

Water Science and Technology Library

Ramakar Jha · V. P. Singh ·  
Vivekanand Singh · L. B. Roy ·  
Roshni Thendiyath *Editors*

# River Hydraulics

Hydraulics, Water Resources and  
Coastal Engineering Vol. 2

 Springer

# Water Science and Technology Library

Volume 110

## **Editor-in-Chief**

V. P. Singh, Department of Biological and Agricultural Engineering & Zachry  
Department of Civil and Environmental Engineering, Texas A&M University,  
College Station, TX, USA

## **Editorial Board**

R. Berndtsson, Lund University, Lund, Sweden

L. N. Rodrigues, Brasília, Brazil

Arup Kumar Sarma, Department of Civil Engineering, Indian Institute of  
Technology Guwahati, Guwahati, Assam, India

M. M. Sherif, Civil and Environmental Engineering Department, UAE University,  
Al-Ain, United Arab Emirates

B. Sivakumar, School of Civil and Environmental Engineering, The University of  
New South Wales, Sydney, NSW, Australia

Q. Zhang, Faculty of Geographical Science, Beijing Normal University, Beijing,  
China

The aim of the *Water Science and Technology Library* is to provide a forum for dissemination of the state-of-the-art of topics of current interest in the area of water science and technology. This is accomplished through publication of reference books and monographs, authored or edited. Occasionally also proceedings volumes are accepted for publication in the series. *Water Science and Technology Library* encompasses a wide range of topics dealing with science as well as socio-economic aspects of water, environment, and ecology. Both the water quantity and quality issues are relevant and are embraced by *Water Science and Technology Library*. The emphasis may be on either the scientific content, or techniques of solution, or both. There is increasing emphasis these days on processes and *Water Science and Technology Library* is committed to promoting this emphasis by publishing books emphasizing scientific discussions of physical, chemical, and/or biological aspects of water resources. Likewise, current or emerging solution techniques receive high priority. Interdisciplinary coverage is encouraged. Case studies contributing to our knowledge of water science and technology are also embraced by the series. Innovative ideas and novel techniques are of particular interest.

Comments or suggestions for future volumes are welcomed.

Vijay P. Singh, Department of Biological and Agricultural Engineering & Zachry Department of Civil and Environment Engineering, Texas A & M University, USA  
Email: [vsingh@tamu.edu](mailto:vsingh@tamu.edu)

All contributions to an edited volume should undergo standard peer review to ensure high scientific quality, while monographs should also be reviewed by at least two experts in the field.

Manuscripts that have undergone successful review should then be prepared according to the Publisher's guidelines manuscripts: <https://www.springer.com/gp/authors-editors/book-authors-editors/book-manuscript-guidelines>

More information about this series at <https://link.springer.com/bookseries/6689>

Ramakar Jha · V. P. Singh · Vivekanand Singh ·  
L. B. Roy · Roshni Thendiyath  
Editors

# River Hydraulics

Hydraulics, Water Resources and Coastal  
Engineering Vol. 2

 Springer

*Editors*

Ramakar Jha  
Department of Civil Engineering  
National Institute of Technology  
Patna, India

V. P. Singh  
Biological and Agricultural Engineering  
Texas A&M University  
College Station, TX, USA

Vivekanand Singh  
Department of Civil Engineering  
National Institute of Technology Patna  
Patna, India

L. B. Roy  
Department of Civil Engineering  
National Institute of Technology Patna  
Patna, India

Roshni Thendiyath  
Department of Civil Engineering  
National Institute of Technology Patna  
Patna, India

ISSN 0921-092X

ISSN 1872-4663 (electronic)

Water Science and Technology Library

ISBN 978-3-030-81767-1

ISBN 978-3-030-81768-8 (eBook)

<https://doi.org/10.1007/978-3-030-81768-8>

© The Editor(s) (if applicable) and The Author(s), under exclusive license to Springer Nature Switzerland AG 2022

This work is subject to copyright. All rights are solely and exclusively licensed by the Publisher, whether the whole or part of the material is concerned, specifically the rights of translation, reprinting, reuse of illustrations, recitation, broadcasting, reproduction on microfilms or in any other physical way, and transmission or information storage and retrieval, electronic adaptation, computer software, or by similar or dissimilar methodology now known or hereafter developed.

The use of general descriptive names, registered names, trademarks, service marks, etc. in this publication does not imply, even in the absence of a specific statement, that such names are exempt from the relevant protective laws and regulations and therefore free for general use.

The publisher, the authors and the editors are safe to assume that the advice and information in this book are believed to be true and accurate at the date of publication. Neither the publisher nor the authors or the editors give a warranty, expressed or implied, with respect to the material contained herein or for any errors or omissions that may have been made. The publisher remains neutral with regard to jurisdictional claims in published maps and institutional affiliations.

This Springer imprint is published by the registered company Springer Nature Switzerland AG  
The registered company address is: Gewerbestrasse 11, 6330 Cham, Switzerland

# Contents

<b>1</b>	<b>Hydraulic Design of Reservoir in Permeable Pavement for Mitigating Urban Stormwater</b> .....	<b>1</b>
	Sanjeev Kumar Suman and Rajnish Kumar	
<b>2</b>	<b>Analytical Expression for Measurement of Discharge Using Conical Obstruction in Small Rectangular Channels</b> .....	<b>13</b>
	Ankur Kapoor, Aniruddha D. Ghare, and Avinash D. Vasudeo	
<b>3</b>	<b>Efficient Numerical Algorithm for Flow Field Around Vertically Submerged Tandem and Aligned Circular Cylinders</b> ....	<b>21</b>
	Abhijit Rout, Soni Parth Kaushikbhai, and Arindam Sarkar	
<b>4</b>	<b>Experimental and Numerical Analyses of Boundary Shear Stress in Non-prismatic Compound Channel</b> .....	<b>37</b>
	Laxmikant Das, Kishanjit Kumar Khatua, and Bhabani Shankar Das	
<b>5</b>	<b>Turbulence Flow Statistics Downstream of Grids with Various Mesh Sizes</b> .....	<b>59</b>
	Pankaj Kumar Raushan, Santosh Kumar Singh, and Koustuv Debnath	
<b>6</b>	<b>Review on Hydraulics of Meandering Rivers</b> .....	<b>71</b>
	Jyotirmoy Barman, Jyotismita Taye, and Bimlesh Kumar	
<b>7</b>	<b>Prediction of Discharge Coefficient for Side Rectangular Weir Using Group Method of Data Handling (GMDH)</b> .....	<b>83</b>
	Ali Shariq, Ajmal Hussain, and Mujib Ahmad Ansari	
<b>8</b>	<b>Enhancement of Energy Dissipation Using Combination of Solid Roller Bucket and Type II Stilling Basin for Ogee Stepped Spillway</b> .....	<b>97</b>
	P. B. Nangare and A. S. Kote	

<b>9</b>	<b>Estimation of Coefficient of Discharge for Side Compound Weir Using the GMDH Technique</b> .....	103
	Mujib Ahmad Ansari, Ajmal Hussain, and Faisal Ahmad	
<b>10</b>	<b>Flow Distributions in a Compound Channel with Diverging Floodplains</b> .....	113
	Bhabani Shankar Das, Kamalini Devi, Jnana Ranjan Khuntia, and Kishanjit Kumar Khatua	
<b>11</b>	<b>Boundary Shear Stress Distributions in Compound Channels Having Narrowing and Enlarging Floodplains</b> .....	127
	Kamalini Devi, Bhabani Shankar Das, Jnana Ranjan Khuntia, and Kishanjit Kumar Khatua	
<b>12</b>	<b>Turbulence Characteristics in a Rough Open Channel Under Unsteady Flow Conditions</b> .....	143
	Jnana Ranjan Khuntia, Kamalini Devi, Bhabani Shankar Das, and Kishanjit Kumar Khatua	
<b>13</b>	<b>Study of Scour Near Pier of Gandhi Setu in Ganga River</b> .....	157
	Binit Kumar and Vivekanand Singh	
<b>14</b>	<b>Optimisation of Hydraulic Design of Uri-II Dam Spillway, Jammu and Kashmir</b> .....	167
	Vankayalapati S. Ramarao and M. R. Bhajantri	
<b>15</b>	<b>Modification of Spillway Ski Jump Bucket Subjected to Higher Tail Water Levels</b> .....	181
	Vankayalapati S. Ramarao and M. R. Bhajantri	
<b>16</b>	<b>Prediction of Submerged Vegetated Flow in a Channel Using GMDH-Type Neural Network Approach</b> .....	191
	Nekita Boraah and Bimlesh Kumar	
<b>17</b>	<b>Turbulent Flow Over a Train of K-Type Roughness</b> .....	207
	Santosh Kumar Singh, Pankaj Kumar Raushan, and Koustuv Debnath	
<b>18</b>	<b>Shifting of Main Course of River Ganga Within the Reach Bhagalpur to Kahalgaon Using Remote Sensing and GIS</b> .....	217
	Chandan Raj and Vivekanand Singh	
<b>19</b>	<b>Depth-Averaged Velocity Distribution in a Meandering Compound Channel Using Calibrating Coefficients</b> .....	229
	Anurag Handique, Arpan Pradhan, C. Sarat Chandra, and Kishanjit Kumar Khatua	
<b>20</b>	<b>Study of Flow Characteristic of Trapezoidal Labyrinth Weir</b> .....	241
	Saurabh Sah, Munendra Kumar, and Deepak Singh	

<b>21</b>	<b>Calibrating Coefficients of Emerged Vegetative Open Channel Flow</b> .....	<b>249</b>
	Priya Shejule, Jnana Ranjan Khuntia, and Kishanjit Kumar Khatua	
<b>22</b>	<b>Trend Analysis of Water Flow and Suspended Sediment Flow of Lower Godavari Basin, India</b> .....	<b>261</b>
	Madhura Aher and S. M. Yadav	
<b>23</b>	<b>Characterization of Flow Turbulence Around Bridge Pier on Rigid Bed Channel</b> .....	<b>277</b>
	Pasupuleti Laxmi Narayana, Praful Vasharambhai Timbadiya, and Prem Lal Patel	
<b>24</b>	<b>Countermeasures Against Local Scouring at Circular Bridge Piers Using Collar and Combination of Slot and Collar</b> .....	<b>289</b>
	Geeta Devi and Munendra Kumar	
<b>25</b>	<b>Influence of Pier Shape and Interference Effect on Local Scour</b> ....	<b>297</b>
	Siva Krishna Reddy, Sruthi Thazhathe Kalathil, Malasani Gopi Chand, and Venu Chandra	
<b>26</b>	<b>Energy and Momentum Correction Coefficients in Compound Open Channel Flow</b> .....	<b>309</b>
	Sarjati Sahoo, Jnana Ranjan Khuntia, Kamalini Devi, and Kishanjit Kumar Khatua	
<b>27</b>	<b>Development of Hydraulic Geometry Equations for Middle Tapi River, India</b> .....	<b>321</b>
	Suhani Choudhary and P. L. Patel	
<b>28</b>	<b>Hydraulic Investigations to Optimize the Design of Spillway and Energy Dissipator for Dri Dam, Arunachal Pradesh—A Case Study</b> .....	<b>333</b>
	P. P. Gadge, R. R. Bhate, M. R. Bhajantri, and V. V. Bhosekar	
<b>29</b>	<b>Scientific Area Calculation of a Landfill in Boragaon Guwahati</b> ....	<b>347</b>
	C. K. Anoop, Abishek Baby, Tina Maria Jacob, and Suresh A. Kartha	
<b>30</b>	<b>Dam Break Analysis for Ukai Dam in Lower Tapi Basin, India</b> ....	<b>357</b>
	Shubham M. Jibhakate and P. V. Timbadiya	
<b>31</b>	<b>3D Modelling of Hybrid River Training Works</b> .....	<b>371</b>
	Riddick Kakati, Vinay Chembolu, and Subashisa Dutta	
<b>32</b>	<b>Effect of Bends on Scour and Deposition Around Causeways</b> .....	<b>379</b>
	Mohammad Athar, Ismeet Singh Saluja, and Humaira Athar	
<b>33</b>	<b>Hydrodynamic Modeling of Urban Flooding and Its Management: A Case Study of Patna, India</b> .....	<b>389</b>
	Biswajit Chakravorty, R. Venkata Ramana, and N. G. Pandey	



<b>34</b>	<b>Loss Coefficient of Expansion in Diverging Channel</b> .....	<b>405</b>
	M. Sahu, S. T. Biswal, and B. Naik	
<b>35</b>	<b>Numerical Modelling of Tidal Hydrodynamics Along River Tapi, Gujarat</b> .....	<b>419</b>
	R. Balaji, J. SatheeshKumar, R. Cornelius, R. Naveen, G. Prasantha, and T. Prince	
<b>36</b>	<b>Study on the Variation of Distribution of Velocity in Accordance with Differential Roughness in a Compound Open Channel</b> .....	<b>429</b>
	Nirjharini Sahoo, Kishanjit Kumar Khatua, and Ramakar Jha	
<b>37</b>	<b>Flow Distribution in Diverging Compound Channel Using LES Models</b> .....	<b>443</b>
	Deepika P. Palai and K. K. Khatua	
<b>38</b>	<b>Using CARTODEM Data for Dam Break Flood Hazard Mapping in a Hilly Terrain</b> .....	<b>455</b>
	Pankaj Mani, Rakesh Kumar, and J. P. Patra	

## About the Editors

**Ramakar Jha** is a Chair Professor at the Department of Civil Engineering and has 30 years of experience in the field of hydrology and water resources engineering. He is presently working as Chair Professor in the Department of Civil Engineering, National Institute of Technology (NIT) Patna-INDIA, which is a Premier Institute in India under the Ministry of Human Resource Development, Government of India. He has served at various levels from Scientist-B to Scientist-E1 at National Institute of Hydrology (NIH), Roorkee, India and as Professor in the Department of Civil Engineering, NIT Rourkela. He has worked and working as Country Co-ordinator of UNESCO-GWADI and Principal Investigator for many International (EU-FP7, DAAD, ADB, AUS-Aid) and National research and consultancy projects (ISRO, DST, MoWR, MHRD). Moreover, he served as Chair for many administrative positions and received a couple of international and national awards for research papers. Presently, he is working as Dr. Rajendra Prasad Chair for Water Resources under the Ministry of Water Resources, Government of India in the Department of Civil Engineering, NIT Patna, Bihar.

**V. P. Singh**, a Texas A&M University Professor of Indian origin, has received a prestigious award for his world-renowned work on water. He is receiving the 2013 Lifetime Achievement Award from the American Society of Civil Engineers-Environmental and Water Resources Institute, otherwise known as the ASCE-EWRI. The award is in recognition of Singh's work in the field of hydrology, which is the study of water in all aspects, such as quality, distribution, preservation, transportation, etc. Some of the work he has done has even created an entire new branch of hydrology—called entropic hydrology—that is connected to the study of entropy, which means essentially the study of order and disorder as it relates to the physical universe. His work is considered fundamental for flood planning and water modelling around the world. Since earning his doctorate degree, Singh has held teaching positions in some of the most well-known universities in the US. He was an Associate Research Professor of Civil Engineering at George Washington University from 1977 to 78, an Associate Professor of Civil Engineering at Mississippi University from 1978 to 81, and an Adjunct Professor as well as the Coordinator of the Environmental and Water

Resources Systems Engineering Program at Louisiana State University from 1999 to 2006 and 2001 to 2006, respectively. He joined Texas A&M University in 2006, where he currently wears a number of different hats. He is a Professor of Biological and Agricultural Engineering, a Professor of Civil and Environment Engineering, and a Caroline and William N. Lehrer Distinguished Chair in Water Engineering (Hydrology). He has authored or edited around 10 published works in the fields of engineering and hydrology.

**Vivekanand Singh** is a Professor at the Department of Civil Engineering and has 28 years of experience in the field of river hydraulics, groundwater, and water resources engineering. He has published research papers in international journals including ASCE Journal. He has done national projects and consultancy during his work at NIT Patna. Prior to this, he was Scientist at National Institute of Hydrology Roorkee. He organized several summer courses, conferences, and workshops. He has been working as Editor in some Indian Journals.

**L. B. Roy** is a Professor at the Department of Civil Engineering and has 33 years of experience in the field of water resources engineering as well as geotechnical engineering. He has been serving the Water Resources Engineering Department for long time and carried out various field-based research activities for different river systems of the region with special emphasis to floods. He has been involved in many research projects and published several research papers in peer-reviewed journals. He has been working for Intellectual Property Rights (IPR) and received awards for various activities.

**Roshni Thendiyath** is an Assistant Professor at the Department of Civil Engineering and has 9 years of experience in the field of water resources engineering. She earned her PhD in Civil Engineering at the University of Pisa, Italy. After obtaining Ph.D., she had joined National Institute of Technology Calicut, India as an ad hoc faculty and later joined National Institute of Technology Patna as an Assistant Professor. She has supervised 2 Ph.D. and more than 30 Master theses. Furthermore, she has been awarded DST-SERB project for the topic, Two Phase flows and Water Quality in Rivers, funded by Department of Science and Technology, MHRD India. Results obtained from her research have been published in nearly 30 papers in international journals and more than 15 papers in international conferences and 3 book chapters. She is active in a variety of professional bodies and she has organized numerous workshops and conferences in her academic career.

# Chapter 1

## Hydraulic Design of Reservoir in Permeable Pavement for Mitigating Urban Stormwater



Sanjeev Kumar Suman and Rajnish Kumar

**Abstract** Green infrastructure stormwater control measures, such as permeable pavement systems, are common practices used for controlling stormwater runoff in a developed country. This paper focus on the permeable pavement as a measure of stormwater mitigation in urban area. A hydraulic design aspect of reservoir stone layer is offered along with solution for the study area. Hydraulic design of the stone reservoir storage area includes depth of reservoir layer, drawdown time and storage volume. The depth of stone reservoir is calculated using the minimum depth approach for a permeable pavement of a given specific region. Rajendra Nagar Patna as study area is considered for design calculation. The depth of reservoir layer is 471 mm corresponding to last three years average annual precipitation of 120 mm. This will store water 7963 m<sup>3</sup> with draw down time of 57 h. Soil beneath reservoir layer having low-infiltration rate, hence required additional measure like drain pipe. In addition, proper maintenance is needed to keep pores of the pavement surface remain open. According to researchers, cost of the permeable pavement is 15–80% less than the other stormwater management measures. Increasing the amount of stormwater infiltrated can result in lower stream flow levels after storm events. Permeable pavement can be used to substantially reduce the volume of stormwater runoff.

**Keywords** Stormwater management · Permeable pavement · Reservoir layer · Hydraulic design

### 1.1 Introduction

Flooding is a significant threat to the world's rising urban population, not only endangering human life but also affecting transportation, causing economic losses, and polluting the environment. Because of the variations in pervious surfaces protected by houses and impervious pavements, built-up areas are vulnerable to floods. Furthermore, due to old or poorly managed drainage networks that cannot cope with the

---

S. K. Suman (✉) · R. Kumar  
Department of Civil Engineering, NIT Patna, Bihar, India 800005  
e-mail: [sksuman@nitp.ac.in](mailto:sksuman@nitp.ac.in)

effects of the rising urban population, the resulting increased surface runoff is often not diverted away from flooded areas. This situation has resulted in the development of alternative methods to improve surface drainage, such as the use of porous asphalt pavements.

The permeable pavement is constructed in such a way that rainwater runoff passes through pavement surface voids and store into underlying stone reservoir. The stone reservoir is used to temporarily accumulate the runoff water and infiltrate. Porous asphalt, pervious concrete, and permeable interlocking concrete pavers are some of the types of permeable pavement that are used in the area. Regardless of the particular specification, all permeable pavements have a standard structure that includes a surface pavement board, an underlying stone aggregate reservoir layer, and a filter layer or fabric placed at the bottom. The reservoir layer's thickness is measured in such a way that it can support both structural and hydrologic purposes. The reservoir layer stores rainwater and maintains the pavement's construction traffic loads. In low-infiltration soils, any or more of the treated water is deposited in an under drain and added to the storm drain grid. If native soil infiltration rates allow, permeable pavement can be engineered without an under drain to allow for maximum runoff infiltration. To infiltrate a part of the filtered runoff, a mixture of these techniques may be used.

Permeable paving is normally intended to handle rainwater that occurs on the pavement surface area, but it may also tolerate run-on from small surrounding impervious areas, such as non-permeable driving lanes or rooftops. However, for some run-on areas, careful sediment management is needed to prevent clogging of the down-gradient permeable pavement. Permeable pavements are found in typically impervious areas such as industrial, institutional, and residential buildings. Permeable paving facilitates a high degree of runoff volume mitigation and nitrogen removal, and it can minimise a construction site's successful impervious cover.

Pervious pavements infiltrate water under the ground surface, thus eliminating standing water problems. This would serve to alleviate worries over mosquito reproduction. Recent research has also discovered that pervious pavement can help mitigate temperatures on and around pavements, thus reducing the urban heat island effect. Porous asphalt pavements are commonly used for parking lots and low-volume roads. Porous asphalt is also used for pedestrian walkways, bridges, driveways, bike paths, and shoulders. Furthermore, porous asphalt pavements are widely used on suburban and urban sidewalks, as well as highways. Porous asphalt pavements may be constructed entirely or partially in conjunction with standard impervious asphalt pavements. Porous asphalt, when constructed in conjunction with impervious pavements or adjacent to building roofs, will adequately contain and treat the additional runoff caused.

Brattebo and Booth (2003) investigated the long-term feasibility of permeable pavement as an alternative to standard impervious asphalt pavement in parking area. Although no surface runoff, almost all rainwater entered into the permeable pavements. According to Sansalone et al. (2012) as a sustainable infrastructure material,

permeable pavement will aid in hydrologic regeneration. The study's findings include measurements and models of filtration and hydraulic conductivity phenomena, as well as the maintenance needs of permeable pavement that is directly loaded by urban drainage. Wei et al. (2015) studied the filtration effects and processes of permeable asphalt pavements (PAP). Pollution rates have been reduced due to the interception and physisorption of porous products used in the PAP. Junqi et al. (2015) investigated the impact of pore water pressure in a saturated asphalt pavement, where fluid velocity and water penetration rate increase, having a negative influence on asphalt mixture ability. The experimental findings indicated that pore water pressure increases with increasing car speed, but pore water pressure lifespan decreases with increasing speed. Meysam et al. (2017) installed a permeable pavement (PP) in urban sidewalks as an alternate low-impact development (LID) to regulate stormwater runoff volume and, as a result, mitigate pollutant discharge into receiving water bodies. This study showed that when PPs are washed on an annual basis, it is anticipated that PPs will be able to work hydraulically and eliminate particulate contaminants over their life cycle by proper maintenance. Miklas and Piotr (2007) reviewed the comprehensive but fragmented literature on primarily permeable pavement systems (PPS), outlining emerging developments in science and industry, and proposing future areas of research and development. The evolution of PPS as a component of sustainable drainage systems is examined in the light of conventional and contemporary urban drainage systems. Justin et al. (2013) investigated impermeable pavements that occupy a large amount of land in cities. Their impact on the hydrological cycle is obvious; acting as a buffer in the soil-atmosphere spectrum, they reduce moisture infiltration and evaporation. Because of perceived hydrologic advantages, porous pavements are starting to replace impermeable alternatives. Pavements have the potential to modify surface moisture and chemical properties, but the results vary depending on pavement porosity and profile shape. According to Fatemeh and Kelly (2013), permeable pavements, a form of structural water responsive urban design structure, will provide additional opportunities for stormwater harvesting and reuse. This research compared three permeable pavements base coarse aggregates to monitor ecosystems and five water collection residence periods to see if they increased stormwater quality. When the findings were compared to current Australian recommendations for water harvesting and reuse, it was discovered that permeable pavements with the chosen base coarse aggregates and residence times would provide water of sufficient quality for reuse for irrigation of green spaces. These findings will aid in the long-term irrigation maintenance of urban green spaces. Murray et al. (2014) investigated the hydraulic conductivity, mechanical properties, and ability of the products to separate particulate and dissolved contaminants (including zinc) from water. According to Martin and Putman (2016), the porosity of porous paving mixtures is crucial to their efficiency and is a widely assessed parameter. However, since there are many methods for measuring a specimen's porosity, this study examined how these various methods related to one another and described where variations in measurements occurred. Hengji et al. (2018) has investigated a special porous asphalt mixture with void ratio 18% or more and discussed their performance. The porosity of porous asphalt paving is critical to its ecological functions, which include

water drainage, noise control, and water purification. Pavement's brittle structure has also resulted in several design flaws. The findings show that porous asphalt with red mud filler at 0.9 FB ratio performed better in terms of ravelling and rutting resistance. Jun et al. (2018) explored porous pavements, which have major benefits in terms of road protection and noise reduction. The internal temperature of the PPM experiment is smaller than that of the asphalt mixture and the OGFC specimens when exposed to the same amount of sunshine. PPM, on the other hand, absorbs more noise than OGFC, especially tyre vibration noise.

The aim of this paper is to propose a hydraulic design of the stone reservoir using minimum depth method and solution for mitigating stormwater in Rajendra Nagar, Patna, Bihar, India.

## 1.2 Types of Permeable Pavement

There are various forms of permeable pavement available. Today, the most common type of paver is pervious concrete, but other alternatives include porous asphalt, interlocking concrete pavers, concrete grid pavers, and plastic reinforced grids filled with gravel or vegetation. Various designs with different structures are also available but these are the most common and adaptable designs. The word pavement usually refers only to the surface layer of a multi-layered structure. Typically, a filter course composed of finer aggregate is installed under the permeable pavement or surface layer (12.5 mm diameter). This filter path is applied over a stone reservoir (37.5–75 mm in diameter), the thickness of which is determined by rainwater management specifications and load bearing requirements. A surface of filter fabric lies on the undisturbed soil under the stone reservoir. Filter fabric can also be used around the sides or perimeter of the permeable surface structure to avoid dirt out of those areas. Figure 1.1 depicts a standard asphalt permeable pavement cross section, while Fig. 1.2 depicts a typical concrete permeable pavement cross section.

## 1.3 Permeable Pavement Design Criteria

### 1.3.1 Reservoir Layer

The reservoir layer is made up of stone under the concrete portion and above the bottom filter layer or underlying soils, as well as the optional infiltration sump. Runoff storage requirements, penetration levels of in situ soils, technical requirements of the pavement sub-base, depth to water table and bedrock, and frost penetration conditions all influence the overall thickness of the reservoir sheet. The reservoir is constructed under the permeable pavement with smooth and double washed stone

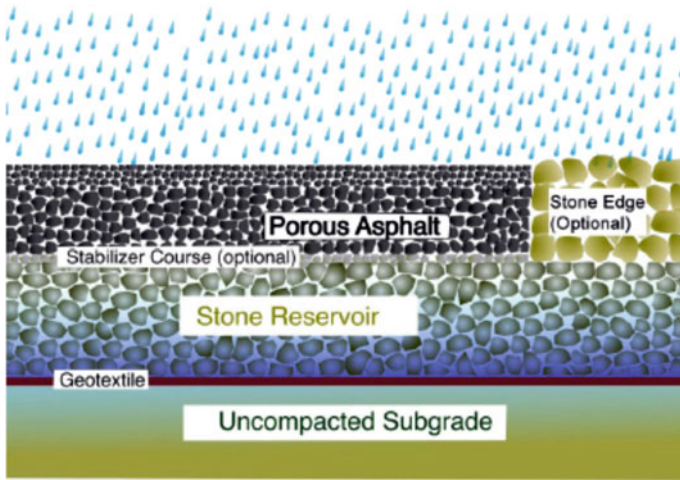


Fig. 1.1 Typical porous asphalt pavement

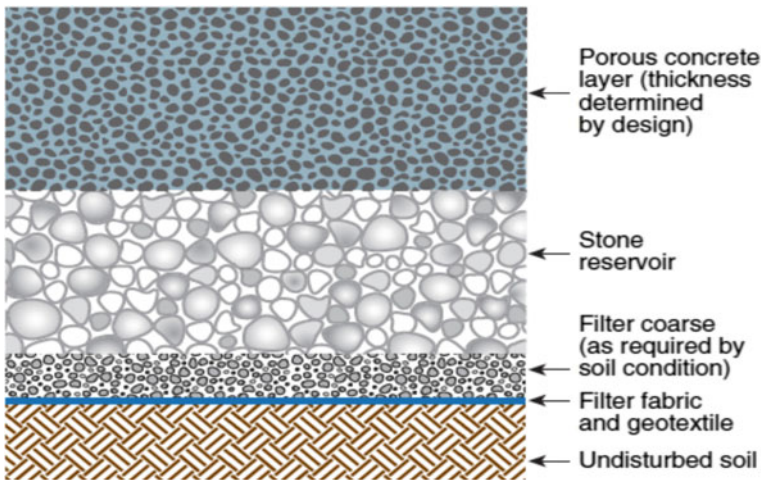


Fig. 1.2 Typical pervious concrete pavement

aggregate which fulfil the requirement of designed traffic as well as storm occurrence. Additional chamber is also constructed in the reservoir layer to store the large volume of water. The reservoir layer's bottom should be perfectly smooth so that runoff will infiltrate uniformly over the whole surface.



### 1.3.2 Hydraulic Design

In the reservoir sheet, permeable concrete is typically sized to hold the construction storm volume or more. The volume of storage in the pavements would account for all underlying infiltration and outflow into any under drains. To reliably calculate the appropriate reservoir depth, the design storm should be routed through the pavement. Eq. 1.1 can be used to calculate the depth of the reservoir layer or infiltration sump used to store the design storm.

$$d_p = \frac{R_c \left( \frac{A_c}{A_p} \right) + P - f.T}{V_r} \quad (1.1)$$

where  $d_p$  = depth of the reservoir layer (or depth of the infiltration sump) in mm,  $R_c$  = runoff from contributing area in mm,  $P$  = design rainfall in mm,  $A_c$  = contributing area in  $m^2$ ,  $A_p$  = permeable pavement surface area  $m^2$ ,  $f$  = infiltration rate in mm/hr,  $T$  = time to fill the reservoir layer in hour,  $V_r$  = void ratio of reservoir layer in decimal (0.30–0.40). The aim is to collect rainwater runoff from building roofs and access roads and transport it to a permeable pavement system in the parking lot.

The design assumptions are made by Eq. 1.1. (i) The contributing drainage area (CDA) is devoid of pervious areas; (ii) For design purposes, the field-tested subgrade soil penetration rate (i) is divided by 2 as a protection consideration to account for possible compaction during construction. If the subgrade is compacted to meet the structural design criteria of the pavement portion, the design infiltration rate of the subgrade soil shall be dependent on calculation of the infiltration rate of the subgrade soil subjected to the compaction requirements and (iii) the porosity ( $\eta_r$ ). Maximum allowable depth of the stone reservoir ( $d_{max}$ ) is computed using Eq. 1.2.

$$d_{max} = \frac{f.T_s}{V_r} \quad (1.2)$$

where  $d_{max}$  = Maximum allowable depth of reservoir layer (mm),  $T_s$  = Maximum allowable storage time (hr).

Check the design feasibility based on the criteria (i) depth of the reservoir layer ( $d_p$ )  $\leq$  maximum allowable depth of reservoir layer ( $d_{max}$ ), (ii) bottom of the reservoir layer at least 60 cm above the seasonal high water table (WT) and (iii) If neither of two, reduce design storm depth or increase permeable pavement surface area.

The reservoir layer's depth cannot be less than the depth needed to satisfy the structural requirements of the pavement. To satisfy structural or broader storage needs, the depth of the reservoir layer may need to be increased. Designers must make certain that the collected water drains from the pavement within 36–48 h. For infiltration designs (no under drains) or designs with infiltration sumps, Eq. 1.4 can be used to measure the drawdown time in the reservoir layer or infiltration sump.

$$t_d = \frac{d_p n_r}{0.5 f} \quad (1.3)$$

where  $t_d$  = drawdown time (day),  $d_p$  = depth of the reservoir layer (mm),  $n_r$  = effective porosity for the reservoir layer (0.40),  $f$  = field-verified infiltration rate for the subgrade.

The drawdown period for designs of under drains should be calculated using the hydrological routing or modelling techniques used for detention structures, with the depth and head calibrated for aggregate porosity. The total storage volume given by the practise,  $S_v$ , should be measured using Eqs. 1.4 and 1.5, or both.  $S_v$  is determined for infiltration designs using Eq. 1.4. Both calculations are found in mixed designs.  $S_v$  is given by Eq. 1.4 for the infiltration sump, and  $S_v$  is provided by Eq. 1.5 for the stone reservoir above the under drain.

$$S_v = A_p \left[ (d_p n_r) + \left( \frac{f \cdot t_f}{2} \right) \right] \quad (1.4)$$

where  $S_v$  = storage volume ( $m^3$ ),  $d_p$  = the reservoir layer depth (mm),  $n_r$  = effective porosity for the reservoir layer (0.35),  $A_p$  = surface area of permeable pavement ( $m^2$ ),  $f$  = infiltration rate of field-verified for the subgrade soils (cm/day). If an impermeable liner is used in the design then  $f = 0$ ,  $t_f$  = time to fill the reservoir layer (day) (assume 2 h or 0.083 day).

$$S_v = d_p n_r A_p \quad (1.5)$$

where  $S_v$  = storage volume ( $m^3$ ),  $d_p$  = reservoir layer depth (mm),  $n_r$  = effective porosity for the reservoir layer (0.40),  $A_p$  = permeable pavement surface area ( $m^2$ ).

## 1.4 Result and Discussion

Rajendra Nagar is a planned colony divided by numbered roads. It has several open spaces like Parks and playing fields. Even though about eighty percent area is impervious and twenty percent area is pervious one. During rainy season most of the area of the Rajendra nagar becomes flooded and mainly the area near to Manul Haque stadium water standing up to a height of 30–60 cm. This situation happens may be due to lack of proper drainage system and increase of impervious area. Study area is shown in Fig. 1.3.

Contributing area ( $A_c$ ) and permeable area, required ( $A_p$ ) are measured from Google map for study area. Gradation of an aggregate used for the reservoir stone layer is indicated in Table 1.1. Assuming void ratio in prosed gradation of aggregates is 40%. Infiltration rate of soil texture that would be beneath the reservoir layer is

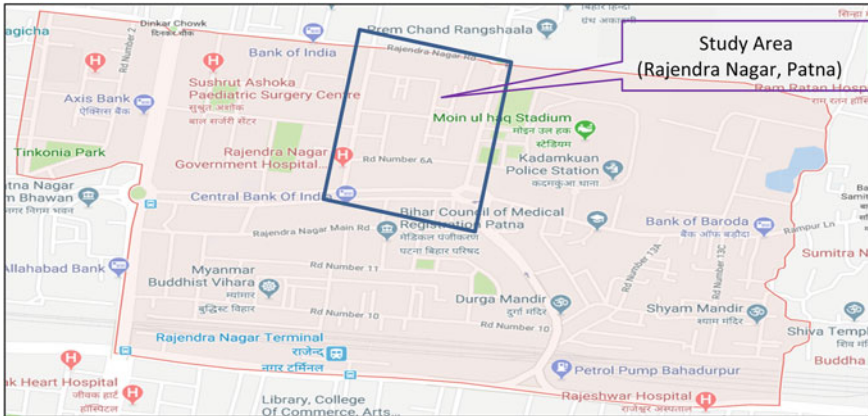


Fig. 1.3 Map of Rajendra Nagar, Patna

Table 1.1 Aggregate gradation for reservoir layer

Sieve size (mm)	Percentage passing	
	AASHTO No.3	AASHTO No.5
63	100	
50	90–100	
37.5	35–70	100
25	0–15	90–100
19	–	2–55
12.5	0–5	0–10
9.5		0–5
Compaction	95%	95%

taken from Table 1.2. Runoff from the impervious surface is considered as ten percent of precipitation because certain loss is assumed. With varying precipitation value, depth of reservoir layer is computed using Eq. 1.1. This computed depth is checked for maximum allowable depth of the reservoir layer. Further draw down time and storage capacity is estimated for the reservoir layer as shown in Table 1.3a, b.

Suppose at 120 mm precipitation and time taken to fill the reservoir layer is 2 h, depth of the reservoir layer comes 471 mm. This is less than maximum allowable depth 594 mm when maximum allowable storage time is 36 h. Where draw down time is 57 h and it can store 7963 m<sup>3</sup> of stormwater. It is found that at high storm water runoff and low-infiltration rate of soil, reservoir layer is not sufficient to mitigate the stormwater. In this contest, additional measure can be applied, like drain pipe.

**Table 1.2** Estimated soil infiltration rates (US, EPA)

Soil texture	Minimum infiltration rate (mm/hr.)
Sand	210.03
Loamy sand	62.23
Sandy loam	25.908
Loam	13.208
Silty loam	6.858
Sand clay loam	4.318
Clay loam	2.286
Silty clay loam	1.524
Sandy clay	1.27
Silty clay	1.016
Clay	0.508

## 1.5 Maintenance and Cost

Openings in the surface of permeable pavements are vulnerable to clogging from moving cars, concrete surface wear, and drainage from surrounding disturbed soils. As a result, it is critical to ensure that surrounding soils are properly protected before, after, and after the construction of permeable pavement. To help avoid clogging, pre-treatment systems may be needed.

The cost of permeable paving is affected by a variety of factors, including supply availability, transportation, site conditions, stormwater management specifications, project duration, contractor expertise, and, in the case of pavers, method of construction (mechanical vs. hand). Long-term operating costs can also be addressed. Using permeable pavement as part of a broader stormwater management effort, on the other hand, will result in considerable long-term savings. A collection of case studies performed throughout the United States showed that the overall capital costs of integrated low-impact construction stormwater management installations (consisting of permeable pavements) is 15–80% less than traditional retention and drainage facilities.

## 1.6 Conclusion

This study explores the permeable pavement and presents a hydraulic design method for mitigating stormwater in urban area. The design result showed that with increase of precipitation, reservoir layer depth increased but it depends upon the infiltration rate. To decrease the fill time, void ratio in the aggregates should be increased. Pervious area in the study area is not sufficient to reduce the stormwater. Therefore, there is a need of increasing the pervious area by implementing permeable pavement

**Table 1.3** Hydraulic design data

P (mm)	R <sub>c</sub> (mm)	A <sub>c</sub>	A <sub>p</sub>	F (FOS = 2)	T	V <sub>r</sub>	d <sub>p</sub>
50	45	31,980	42,223	2.159	2	0.4	199
55	49.5	28,782	39,025	2.159	2	0.4	218
60	54	25,584	48,619	2.159	2	0.4	210
65	58.5	22,386	45,421	2.159	2	0.4	224
70	63	19,188	55,015	2.159	2	0.4	219
75	67.5	15,990	58,213	2.159	2	0.4	223
80	72	12,792	61,411	2.159	2	0.4	227
85	76.5	9594	64,609	2.159	2	0.4	230
90	81	6396	67,807	2.159	2	0.4	233
95	85.5	3198	71,005	2.159	2	0.4	236
100	90	31,980	42,223	3.429	2	0.4	403
105	94.5	31,980	42,223	6.604	2	0.4	408
110	99	31,980	42,223	6.604	2	0.4	429
115	103.5	31,980	42,223	6.604	2	0.4	450
120	108	31,980	42,223	6.604	2	0.4	471
125	112.5	31,980	42,223	6.604	2	0.4	493
130	117	31,980	42,223	6.604	2	0.4	514
d <sub>p</sub>	T <sub>s</sub>	d <sub>max</sub>	Drawdown time (hours)	Storage volume (m <sup>3</sup> )	Remarks		
199	40	215.90	74	3368	d <sub>p</sub> ≤ d <sub>max</sub>		
218	43	232.09	81	3403	d <sub>p</sub> ≤ d <sub>max</sub>		
210	40	215.90	78	4089	d <sub>p</sub> ≤ d <sub>max</sub>		
224	48	259.08	83	4066	d <sub>p</sub> ≤ d <sub>max</sub>		
219	48	259.08	81	4822	d <sub>p</sub> ≤ d <sub>max</sub>		
223	48	259.08	83	5194	d <sub>p</sub> ≤ d <sub>max</sub>		
227	48	259.08	84	5569	d <sub>p</sub> ≤ d <sub>max</sub>		
230	48	259.08	85	5947	d <sub>p</sub> ≤ d <sub>max</sub>		
233	48	259.08	86	6328	d <sub>p</sub> ≤ d <sub>max</sub>		
236	48	259.08	88	6712	d <sub>p</sub> ≤ d <sub>max</sub>		
403	48	411.48	94	6811	d <sub>p</sub> ≤ d <sub>max</sub>		
408	36	594.36	49	6898	d <sub>p</sub> ≤ d <sub>max</sub>		
429	36	594.36	52	7253	d <sub>p</sub> ≤ d <sub>max</sub>		
450	36	594.36	55	7608	d <sub>p</sub> ≤ d <sub>max</sub>		
471	36	594.36	57	7963	d <sub>p</sub> ≤ d <sub>max</sub>		
493	36	594.36	60	8318	d <sub>p</sub> ≤ d <sub>max</sub>		
514	36	594.36	62	8673	d <sub>p</sub> ≤ d <sub>max</sub>		

that can serve for catering the traffic as well as mitigating the stormwater during rainy season. The depth of reservoir layer is 471 mm corresponding to last three years average annual precipitation of 120 mm. This will store water 7963 m<sup>3</sup> with draw down time of 57 h. On the other hand, maintenance of permeable pavement is very important because pores of the pavement are filled after passing vehicles. Installation of permeable pavement can reduce the overall cost by 15–80%, in comparison of other stormwater management measures like a drainage system.

## References

- Brattebo BO, Booth DB (2003) Long-term storm water quantity and quality performance of permeable pavement system. *Water Res* 27:4369–4376
- Fatemeh K, Kelly H (2015) Effect of permeable pavement base course aggregates on storm water quality for irrigation reuse. *Ecol Eng* 77:189–195
- Hengji Z, Hui L, Yi Z, Dawei W, John H, Hanbing W (2018) Performance enhancement of porous asphalt pavement using red mud as alternative filler. *Constr Build Mater* 160:707–713
- Jun C, Xiaojing Y, Hao W, Yangmin D (2018) Evaluation of durability and functional performance of porous polyurethane mixture in porous pavement. *J Clean Prod* 188:12–19
- Junqi G, Chengcheng G, Yutao L (2015) Measurement of pore water pressure in asphalt pavement and its effects on permeability. *Measurement* 62:81–87
- Justin M, Graeme B, Scharenbroch BC (2013) Below ground effects of porous pavements-soil moisture and chemical properties. *Ecol Eng* 51:221–228
- Martin WD, Putman BJ (2016) Comparison of methods for measuring porosity of porous paving mixtures. *Constr Build Mater* 125:299–305
- Meysam K, Madjid D, Massoud T (2017) Evaluation of permeable pavement responses to urban surface runoff. *J Environ Manag* 187:43–53
- Miklas S, Piotr G (2007) Review of permeable pavement systems. *Build Environ* 42:3830–3836
- Murray CA, Snyder KS, Marion BA (2014) Characterization of permeable pavement materials based on recycled rubber and chitosan. *Constr Build Mater* 69:221–231
- Sansalone J, Kuang X, Ying G, Ranieri V (2012) Filtration and clogging of permeable pavement loaded by urban drainage. *Water Res* 46:6763–6774
- Wei J, Sha A, Xiao J, Li Y, Yue H (2015) Experimental study on filtration effect and mechanism of pavement runoff in permeable asphalt pavement. *Const Build Mater* 100:102–110

# Chapter 2

## Analytical Expression for Measurement of Discharge Using Conical Obstruction in Small Rectangular Channels



Ankur Kapoor, Aniruddha D. Ghare, and Avinash D. Vasudeo

**Abstract** Flow measurement in rectangular channels can easily be carried out using measuring flumes. The type of flume used in a particular application depends on the need for precision and cost. Traditional flumes such as cutthroat flumes are usually built with the channel itself by channel side convergence. Their construction or removal involves engineering work on the channel. The authors feel this as the limitation of the traditional flumes; as for similar sections of the network of channels, a new and independent construction of flume is required. The present study negates this drawback and proposes a particular kind of flume for flow measurement in rectangular irrigation channels in which the throat section of the flume is obtained with a cone shaped object, placed at the center of the rectangular channel. The limitation of a fixed structure can be overcome by using a mobile structure that works on the same principle and remains effective in similar situations. The present study involves the use of a cone shaped obstruction to restrict the flow in order to achieve critical condition. An analytical model is developed for discharge measurement in rectangular channels using the conical obstruction. The geometry of the channel at the location of the obstruction becomes complex due to the presence of cone shaped object. The study presents various comprehensive equations defining the flume geometry. The cone shaped obstruction is equipped with a gauge at its upstream side to measure the depth of flow upstream of the critical flow section. The reading of the gauge is directly related to the flow rate. The relation between upstream flow depth and rate of flow is obtained analytically using energy concept. An experiment is performed in the laboratory by observing flow depth after placing a cone in the rectangular channel under free flow condition. The experiment results validated the developed analytical model. The maximum error of the flow discharge obtained

---

A. Kapoor (✉)

Assistant Professor, Department of Civil Engineering, G H Raison Institute of Engineering and Technology, Nagpur 440028, India

A. D. Ghare

Professor, Department of Civil Engineering, Visvesvaraya National Institute of Technology, Nagpur 440010, India

A. D. Vasudeo

Associate Professor, Department of Civil Engineering, Visvesvaraya National Institute of Technology, Nagpur 440010, India

using the analytical approach was found to be 5.19 percent when compared with the actual flow rate. The proposed flume is appropriate for temporary use and can replace the traditional flumes for flow measurement in small conduits. The flume is a simple and affordable device for flow measurement which is easy to construct, carry, and mount. The cone is physically independent of the channel and can be used in different, similar sections of the network of channels. The unit can be quickly fixed and detached for momentary use in open channels. This flume can be used as a mobile device for momentary flow measurement in open channels under free flow condition.

**Keywords** Flow measurement · Measuring flumes · Froude number · Rectangular channel · Conical obstruction

## 2.1 Introduction

Many agricultural processes utilize a huge quantity of water as part of production operations. Agriculture alone uses an estimated 70% of the freshwater withdrawals globally. With severe droughts, shrinking reservoirs, and freshwater shortages in some areas of the world, water conservation has become an important aspect at farm level. Measuring the quantity of water that is used during any process is a decisive component for its efficient management. This quantity is generally gauged through open channels that facilitate flow measurements, more explicitly in volume per unit time. In case of open channels, measurements of continuous flows are usually done by means of hydraulic structures that establish a unique flow—depth relationship. These hydraulic structures can primarily be classified as weirs and control flumes. Weirs are generally accurate and viable in favorable situations, but if the pool or channel section immediately upstream of the weir crest collects sediment, the required vertical flow depth below the crest is correspondingly reduced, thus affecting the accuracy of the device.

The introduction of modified venturi flume by Parshall (1926) obviated many of the objections to the weir, rating flume, or other devices which were then in general use. The accuracy of measurement with this device was completely within practical limits. This device works effectively with comparatively small loss of head, and for free flow, this loss in a standard weir is nearly four times that in the flume. The flume is designed by constricting the flow using channel side convergence to obtain a minimum flow cross section (throat) for the occurrence of critical flow. The flume essentially has a converging section, a throat, and a diverging section. The occurrence of critical flow without the throat section was studied by Robinson and Chamberlain (1960) and Skogerboe and Hyatt (1967) by performing experiments on cutthroat flume. These long-established flumes are permanent devices used for flow measurement in open channels and required to be built while constructing the channel. The flow in a channel can only be measured at locations where these flumes are built. It may also require regular maintenance.



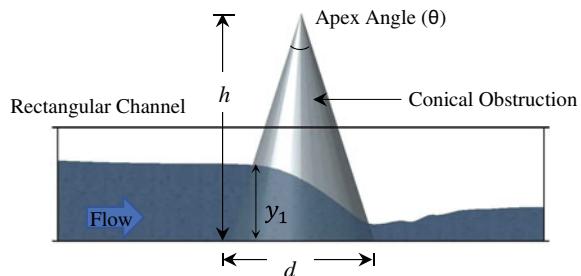
The use of a mobile device which can remove the drawbacks of conventional flumes was practiced by Hager (1985) by inserting a cylinder vertically in a prismatic channel to constrict the flow. The discharge in the channel was characterized as a function of energy of flow at the cylindrical obstruction. The precision obtained with the model proposed by Hager (1985) was  $\pm 5\%$  which was within the acceptable limit. A graphical approach using the upstream energy ( $H$ ) was also proposed when Hager (1988) extended the mobile flume studies for circular channels. Samani et al. (1991) inspired by Hager's work developed a computer model for calibration of circular mobile flume which predicted discharge with an error of 6%. The approach by Samani requires the measurement of flow depth at the cylinder which is the only physical measurement required. A computer model was developed after laboratory experiments were conducted for cylindrical obstruction in trapezoidal channels (Samani and Magallanez 1993) which predicted discharge with an accuracy of nearly 95%. The accuracy of discharge prediction was further increased by Badar and Ghare (2012) with the use of Buckingham's  $\pi$ -theorem of dimensional analysis to deduce a stage—discharge relationship using the dimensionless parameters.

Critical flow condition can also be achieved using two semicircular cylinders by combining the concept of cutthroat and circular flume (Hager 1988) as presented by Samani and Magallanez (2000). The two semicircular cylindrical objects were used to design a simple flume by attaching them to the side walls of the channel. A single equation to measure discharge for any cross section of channel consists of empirical coefficients depending upon flume dimensions as presented by Samani (2017) when a cylindrical obstruction was tested for channels having trapezoidal, rectangular, and circular cross sections.

The use of cylindrical object to obstruct the flow can be replaced with some other object that has similar stability when placed in the flow and can create critical flow in the open channel. Peruginelli and Bonacci (1997) tested a movable pier-shaped object in rectangular channel and found that the prism can be a good alternative to the commonly studied cylindrical object which was also supported by the range of acceptable error obtained from the proposed equation for discharge measurement.

The present study focuses on development of analytical expression to predict discharge in small rectangular channel and encourages the use of cone shaped hollow object to obstruct flow (Fig. 2.1) to create critical flow condition. The authors used cone in this study due to its geometrical construction that makes it more stable against

**Fig. 2.1** Schematic diagram of rectangular flume with conical obstruction



the strong current of flow as compared to the commonly used cylindrical object of similar height. The use of cone as mobile obstruction was first proposed by Hager (1986). The better stability of cone is due to its center of gravity which is positioned more toward its base. The cone is physically independent which can be moved to any similar section of the channel network to measure rate of flow. A gauge is attached on the outer surface of the cone to measure the flow depth at the upstream of the critical section. The depth measured at the face of cone upstream of critical section is related to the rate of flow in the channel. In the present study, the development of discharge equation using energy concept has been described. The study also includes the laboratory testing of the flume.

## 2.2 Development of Analytical Expression for Computation of Flow Rate

Flow measurement in open channels is governed by the concept of critical flow. Critical flow condition in rectangular channel can be created by forming a contracted section using a cone shaped object placed in the middle of the channel. The specific energy and Froude number equations are applicable in this case. Assuming uniform distribution of velocity throughout the channel, the upstream energy of flow can be given by

$$H = y + \frac{Q^2}{2gA^2} \quad (2.1)$$

where  $Q$  = flow rate;  $H$  = upstream energy of flow;  $y$  = upstream flow depth;  $A$  = upstream flow area.

Assuming a horizontal flume and infinitesimally small loss in energy between upstream and critical section, the energy upstream of the critical section equals the energy at the critical section and can be pronounced as

$$H_c = y_c + \frac{Q^2}{2gA_c^2} = H \quad (2.2)$$

in which  $H_c$ ,  $y_c$ , and  $A_c$  are the energy, flow depth, and area at the critical section, respectively.

Critical flow condition is achieved at the least cross-section of the channel, for which the Froude number equals 1. The flow at the critical section can be described by conventional Froude number equation as

$$F^2 = \frac{Q^2}{gA_c^3} \left( \frac{\partial A_c}{\partial y} \right) = 1 \quad (2.3)$$

where  $\partial A_c/\partial y$  is the derivative of cross—sectional area at critical section with respect to the flow depth, which signifies the top width of the flow.

From Eqs. (2.2 and 2.3),

$$H = y_c + \frac{A_c}{2\left(\frac{\partial A_c}{\partial y}\right)} \quad (2.4)$$

If a conical obstruction of height  $h$  and base diameter  $d$  is placed with its axis vertical, inside a rectangular channel with bed width  $B$ , then the critical flow condition is expected to occur at the central location of the cone. The cross—sectional area of flow at the critical point  $A_c$  as the function of flow depth can be expressed as

$$A_c = (B - d)y_c + \frac{d}{2h}y_c^2 \quad (2.5)$$

If the energy upstream of the critical flow section can be measured, then Eqs. (2.3, 2.4, and 2.5) can be simultaneously used to determine  $y_c$  and  $Q$ . The upstream flow depth is measured at the cone face with the help of a gauge attached to the cone. The gauge reading can be a representative of the upstream energy if a uniform velocity distribution and parallel flow lines are assumed. In that case, the cone acts as a piezometer and the reading of the gauge would be equal to the upstream energy ( $H$ ). Equations (2.4 and 2.5) are solved to obtain critical flow depth  $y_c$  which can be used to obtain  $Q$  using Eq. (2.3).

### 2.3 Experimental Analysis

The 0.6-m-wide rectangular channel used in the laboratory was 21 m long having 0.5 m high side walls. A digital flow meter was also attached to the channel to measure actual discharge flowing through it. A hollow cone shaped object of height ( $h$ ) 0.885 m was designed for a contraction ratio of 60% having base diameter ( $d$ ) 0.36 m with apex angle ( $\theta$ ) 23° and tested for free flow condition. The cone was placed vertically at the center of the channel to confine the flow area and create critical flow condition. For proper handling, it was cut from the top and, therefore, looks like a frustum (shown in Fig. 2.2) having top diameter 0.12 m with effective height 0.6 m. The hollow frustum of the cone enables the additional weight to be placed over the obstruction to provide more stability against the strong current of flow. Moreover, the geometry of the cross-section is not affected as the effective height of the obstruction is still more than the side walls of the channel.

The flow depth was recorded using the gauge attached on the curved surface of the obstruction facing the flow. An electromagnetic flow meter was used to measure

**Fig. 2.2** Photograph of conical obstruction from upstream



the rate with which the flow is passing through the rectangular flume. The flume was tested for three different discharge rates viz.  $0.032 \text{ m}^3/\text{s}$ ,  $0.042 \text{ m}^3/\text{s}$ , and  $0.052 \text{ m}^3/\text{s}$ .

The flow depth measured at the face of cone ( $y_1$ ) replicates the upstream energy ( $H$ ) of the flow assuming uniform velocity distribution and neglecting curvature of flow lines. This upstream energy ( $H$ ) is replaced in Eq. (2.4) to obtain depth of flow at critical section ( $y_c$ ). The flow depth and cross-sectional area at the critical section is used to predict discharge using Eq. (2.3). Table 2.1 shows the comparison of measured and predicted discharge for the laboratory flume.

The difference in the values of measured and predicted discharge is due to the assumption of no energy loss between the upstream of obstruction and critical section. The non-uniform velocity distribution and the curvature of flow lines as the flow passes around the object may also incur some error in the prediction of discharge using mobile obstruction in open channels. The last column of Table 2.1 for percentage (%) error between the measured (using flow meter) and predicted discharge (using Eq. 2.3) shows that the proposed flume predicts flow rate with decent accuracy having maximum percentage difference of 5.19% when compared with measured flow rate.

**Table 2.1** Comparison of predicted and measured flow rates

S. No	$y_1$ (m)	$Q_0$ ( $\text{m}^3/\text{s}$ )	$Q_p$ ( $\text{m}^3/\text{s}$ ) [Eq. 2.3]	Error (%)
1	0.172	0.0320	0.0321	-0.31
2	0.203	0.0420	0.0418	0.48
3	0.225	0.0520	0.0493	5.19

## 2.4 Conclusions

A simple device for flow measurement for open channels is presented in this study. The device consists of a conical obstruction placed vertically inside a rectangular channel which is easy to fabricate, inexpensive, and portable. The flume does not require widespread transition at the upstream. The conical obstruction decreases area of flow creating critical condition. The measurement of head is made at the cone surface facing the flow. The measured upstream head at the cone face is utilized in predicting discharge with the help of Eqs. (2.3 and 2.4). The comparison made between the measured and predicted flow rates shows that the error obtained using the proposed approach is within acceptable limit. The experiment is performed for level flumes under free flow condition with a contraction ratio of 60%. However, the effect of submergence and sloping flumes can result in substantial error. The present study and the experiments are carried out for rectangular channels which can be extended for other cross sections as well. Cones with different heights and apex angles may be experimentally tested for use as obstructions in open channels. Comprehensive experiments with different contraction ratios should be performed to further refine the proposed model on the lines of studies presented here.

## References

- Badar AM, Ghare AD (2012) Development of discharge prediction model for trapezoidal canals using simple portable flume. *Int J Hydraul Eng* 1(5):37–42. <https://doi.org/10.5923/j.ijhe.20120105.02>
- Hager WH (1985) Modified venturi channel. *J Irrig Drain Eng* 111(1):19–35. [https://doi.org/10.1061/\(ASCE\)0733-9437\(1985\)111:1\(19\)](https://doi.org/10.1061/(ASCE)0733-9437(1985)111:1(19))
- Hager WH (1986) Modified trapezoidal venturi channel. *J Irrig Drain Eng* 112(3):225–241. [https://doi.org/10.1061/\(ASCE\)0733-9437\(1986\)112:3\(225\)](https://doi.org/10.1061/(ASCE)0733-9437(1986)112:3(225))
- Hager WH (1988) Mobile flume for circular channel. *J Irrig Drain Eng* 114(3):520–534. [https://doi.org/10.1061/\(ASCE\)0733-9437\(1988\)114:3\(520\)](https://doi.org/10.1061/(ASCE)0733-9437(1988)114:3(520))
- Parshall RL (1926) The improved venturi flume. *Trans ASCE* 89:841–880
- Peruginelli A, Bonacci F (1997) Mobile prisms for flow measurement in rectangular channels. *J Irrig Drain Eng* 123(3):170–174. [https://doi.org/10.1061/\(ASCE\)0733-9437\(1997\)123:3\(170\)](https://doi.org/10.1061/(ASCE)0733-9437(1997)123:3(170))
- Robinson AR, Chamberlain AR (1960) Trapezoidal flumes for open channel flow measurement. *Trans Am Soc Agric Eng* 3(2):120–124, 128
- Samani Z (2017) Three simple flumes for flow measurement in open channels. *J Irrig Drain Eng* 2–5. [https://doi.org/10.1061/\(ASCE\)IR.1943-4774.0001168](https://doi.org/10.1061/(ASCE)IR.1943-4774.0001168)
- Samani Z, Magallanez H (1993) Measuring water in trapezoidal canals. *J Irrig Drain Eng* 119(1):181–186. [https://doi.org/10.1061/\(ASCE\)0733-9437\(1993\)119:1\(181\)](https://doi.org/10.1061/(ASCE)0733-9437(1993)119:1(181))
- Samani Z, Magallanez H (2000) Simple flume for flow measurement in open channel. *J Irrig Drain Eng* 126(2):127–129. [https://doi.org/10.1061/\(ASCE\)0733-9437\(2000\)126:2\(127\)](https://doi.org/10.1061/(ASCE)0733-9437(2000)126:2(127))
- Samani Z, Jorat S, Yousaf M (1991) Hydraulic characteristics of a circular flume. *J Irrig Drain Eng* 117(4):558–566. [https://doi.org/10.1061/\(ASCE\)0733-9437\(1991\)117:4\(558\)](https://doi.org/10.1061/(ASCE)0733-9437(1991)117:4(558))
- Skogerboe GV, Hyatt ML (1967) Rectangular cut throat flumes. *J Irrig Drain Eng Div* 98(4):569–583

# Chapter 3

## Efficient Numerical Algorithm for Flow Field Around Vertically Submerged Tandem and Aligned Circular Cylinders



Abhijit Rout, Soni Parth Kaushikbhai, and Arindam Sarkar

**Abstract** A comparative analysis of the experimental and numerical results on flow fields around submerged tandem and aligned cylinders is presented. The flow characteristics were measured using Acoustic Doppler Velocimeter (ADV), and the cylinders were aligned 0 and 20° over horizontal plane rigid beds. The results are validated using steady numerical simulation using COMSOL 5.3. Experiments were conducted with two unsymmetrical cylinders of upstream cylinder diameter 3 cm and downstream cylinder diameter 7.5 cm, separated by 2.5 times the spacing i.e., 18.75 cm, under completely submerged conditions. A submergence ratio (depth of water to height of cylinder) of 1.4 was taken. A fully developed flow condition with an average flow velocity of 0.1165 m/s was ensured for both the arrangement. For numerical simulation, all the parameters and boundary conditions remain the same as experimental. The computational domain was limited around the cylinder to reduce the computational time. The horizontal distributions of time averaged three dimensional velocities at various radial loci on different horizontal planes have been plotted. Streamlines are plotted to study the flow features. The results collectively delineate the changes in the characteristics of the flow field at the wake of the upstream cylinder brought to effect by the presence of a larger downstream cylinder. A weak sheltering effect by the upstream cylinder on the downstream cylinder for 20° angular alignment especially differentiates its flow field characteristics from that of the linear tandem arrangement of the cylinders at 0°.

**Keywords** Tandem · Staggered · Submerged · Turbulent flow · Vortex shedding · Wake

---

A. Rout · S. P. Kaushikbhai · A. Sarkar (✉)  
School of Infrastructure, Indian Institute of Technology Bhubaneswar, Bhubaneswar, India  
e-mail: [asarkar@iitbbs.ac.in](mailto:asarkar@iitbbs.ac.in)

A. Rout  
e-mail: [ar18@iitbbs.ac.in](mailto:ar18@iitbbs.ac.in)

S. P. Kaushikbhai  
e-mail: [pks15@iitbbs.ac.in](mailto:pks15@iitbbs.ac.in)

### 3.1 Introduction

In engineering, because of its common occurrence in many forms, cylinder-like structures can be found either alone or in groups in the designs for bridge piers, supports of offshore structures, etc. These structures become fully submerged during high floods, sudden release or high tides. The flow characteristics around these structures become much more complex due to the complex interaction of flow around and over them. There are several comprehensive studies available in literature on flow pattern and turbulent flow around a single, isolated partially submerged circular cylinder (Morkovin 1964; Gerrard 1978; Coutanceau and Defaye 1991; Williamson 1996; Zdravkovich 1997, 2003). Due to wider applications, arrangements of multiple cylinders have become popular, but direct application of the results derived for a single cylinder may be erroneous for fully submerged groups. A complete understanding of flow fields of multiple cylinders involves complex interactions between the vortices, wakes and shear layers. The basic arrangements of cylinders are tandem and side-by-side configuration, which have received numerous attentions (Sumner 2010). Though the staggered configuration is commonly found in engineering applications, relatively few studies are available for the same (Sumner 2010). The present work focuses on flow behaviour around two fully submerged cylinders arranged in tandem and staggered configuration.

Flow regimes of tandem cylinders have been classified based on the spacing ratios as per the studies carried out by Zdravkovich (1987). The regime in case of tandem cylinders is identified as wake interference, and it occurs when one cylinder is near or submerged into the wake of other. Two closely separated cylinders may give rise to most generic flow features like flow separation, reattachment, vortex formation, recirculation (Eswaran et al. 2013). Thus, flow around tandem cylinders provide a good model to understand the flow physics around multiple cylinders. Most of the researches of the tandem configurations refer to two partially submerged cylinders of equal diameter (Mittal et al. 1997; Lin et al. 2002; Alam et al. 2003; Xu and Zhou 2004; Carmo and Meneghini 2006; Sumner 2010; Ashtiani and Kordkandi 2013). Ljungkrona et al. (1991a,b) studied the spacing at which the shear layers got separated from the upstream cylinder without reattachment onto the downstream cylinder. Zhou and Yiu (2006) reported two different types of flow structures depending on the reattachment of the shear layers from the upstream cylinder on the upstream or downstream side of downstream cylinder. Sumner (2010) has reviewed the experimental and numerical investigations on the flow around two partially submerged cylinders of equal diameter arranged in different configurations.

Above studies show detailed investigations on flow field around partially submerged tandem cylinders with equal diameter. However, considering the case when cylinders are with unequal diameters, such as piggyback pipeline (commonly found in the offshore oil and gas industry), only few studies are reported (Hiwada et al. 1979; Igarashi 1982; Zdravkovich 1987; Alam and Zhou 2008; Yangyang et al. 2014). Igarashi (1982) investigated flow around tandem cylinders with large diameter cylinder located upstream. Alam and Zhou (2008) reported the effect of small

cylinder on a large downstream cylinder using variation of flow structures, Strouhal number and forces on downstream cylinder in the co-shedding regime. A number of studies considered the effect of large cylinder on small downstream cylinder. It was shown that either the vortex shedding from large cylinder or its lift decreased with appropriate placement of the small cylinder (Strykowski and Sreenivasan 1990; Mittal and Raghuvanshi 2001; Dalton et al. 2001; Sarkar 2014). Zhao et al. (2005, 2007) reported the effect on both vortex shedding and hydrodynamic forces due to the relative position of small cylinder.

There may be number of geometrical configurations based on the distance between the cylinders and their relative angle to the approach flow. Laboratory studies on each of these configurations are time consuming and expensive since a large number of variables need to be considered. However, few numerical studies for tandem circular cylinders (Meneghini et al. 2001; Jester and Kallinderis 2003; Kitagawa and Ohta 2008) are carried out. Most of these studies are based on 2D finite element model.

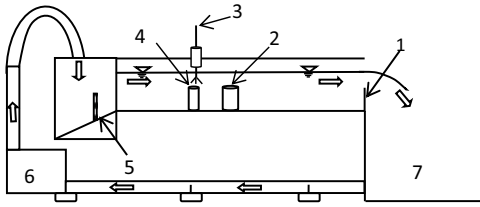
The main objective of the present study is to carry out detailed experimental as well as numerical investigations of flow pattern around tandem and aligned arrangement of fully submerged circular cylinders of unequal diameter on rigid flat bed. All the measurements were taken by an Acoustic Doppler Velocimeter (ADV). The contours of the time averaged velocity components and flow patterns at various sections are presented and discussed for different experimental runs. Furthermore, all the runs are simulated using numerical models and experimental results are validated. The obtained results are used in summarizing the effect of different arrangement of cylinders, velocity and unequal diameter of cylinder. In results and discussions, flow behaviour in horizontal plane, effect of Reynolds number, and spectrum analysis are discussed.

## 3.2 Experimental Setup and Procedure

### 3.2.1 Experimentation

The experiments were conducted at the Water Resources Engineering Laboratory of the School of Infrastructure Department of the Indian Institute of Technology Bhubaneswar, India. The experiments were performed in 10 m long, 0.8 m wide, and 0.8 m deep laboratory flume as shown in Fig. 3.1. Both sides of the flume were made of glass. The water depth in the flume was regulated by tailgates. The flow rate was adjusted using a calibrated butterfly valve. The measuring section was located 5 m away from the flume inlet to ensure a fully developed turbulent flow. Two Perspex cylinders in tandem or aligned were glued to the bed of the flume within the measuring section. The two cylinders were of equal height ( $h = 25$  cm) but of different diameters, i.e.,  $D_1 = 3$  cm (upstream cylinder) and  $D_2 = 7.5$  cm (downstream cylinder). The  $D_2$  cylinder was positioned 18.75 cm ( $L = 2.5D_2$ ) downstream to the upstream cylinder for tandem configuration. Yangyang et al. (2014) reported that maximum flow field





Sr no.	Component
1	Tailgate
2	D/S Cylinder
3	ADV
4	U/S Cylinder
5	Vertical screen
6	Pump
7	Tank

**Fig. 3.1** Schematic of the experimental setup

interactions occur for  $L/D_2 = 2.5$ , for two tandem cylinders of varying diameters  $D_1$  and  $D_2$  ( $D_2 > D_1$ ) separated by distance  $L$ . Whereas, for staggered configuration, downstream cylinder was aligned at  $20^\circ$  and  $P/D_2$  ratio was kept approximately 2.7, where  $P$  is the inclined spacing between the aligned cylinders. For equal diameter cylinders in staggered configuration, shear layer reattachment occurs for range of  $P/D = 1.125-4$  and  $\alpha = 0-20^\circ$  (Sumner 2010). The experiments were run for an average velocity  $U$  of 0.1165 m/s. Vertical perforated screens were installed at the inlet to prevent formation of any large scale disturbances and to achieve a fully developed turbulent flow. To ensure a fully developed flow at the measurement section, velocity measurements were taken 1 m ahead of the test section. All the experiments were done for fully submerged condition. Depth of water was maintained at 0.35 m by adjusting the tailgates. A point gauge with an accuracy of 0.1 mm was used for measuring the free surface of water. Velocity data were obtained at different radial sections as shown in Fig. 3.2. The instantaneous three dimensional velocity components were measured by a SonTek made 5-cm Acoustic Doppler Velocimeter (ADV). The ADV operates on a pulse-to-pulse coherent Doppler shift to provide instantaneous three dimensional velocity components, for which frequency was set at 50 Hz. In the present study, few noisy results (taken very near to bed) because of the disturbance of reflected signals were filtered. The same problem was reported by Snyder and Castro (1999)

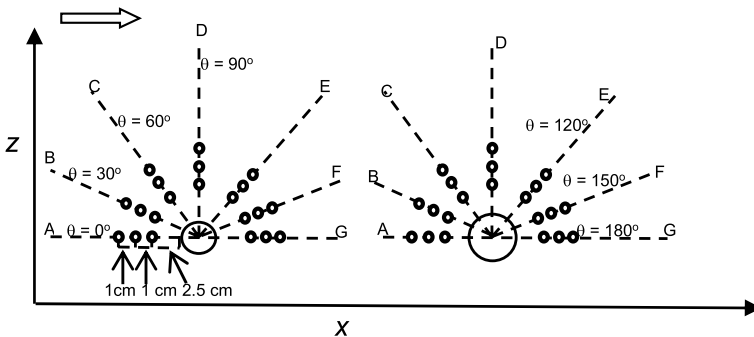


**Fig. 3.2** Measurement section layout at different radial directions

and Beheshti and Ashtiani (2010). The sampling duration was taken as 120 s. The minimum duration of sampling for low standard errors was ranged between 60 and 90 s (Buffin-Belanger and Roy 2005). All the obtained data were processed and filtered using WinADV software as described in Ashtiani and Kordkandi (2012). Modified raw data were used in investigating the flow features.

### 3.2.2 *Coordinate Systems and Sections of Measurements*

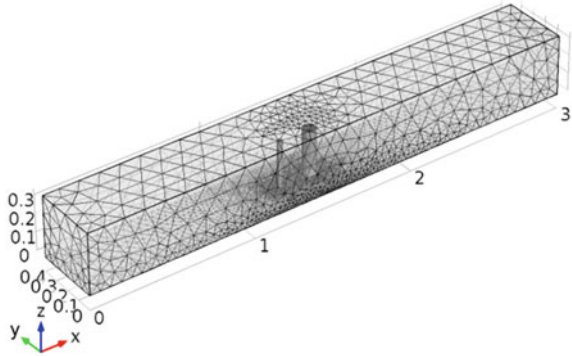
Figure 3.2 is a two dimensional spatial presentation of all the sections at which the instantaneous velocity readings were taken along radial directions at discrete vertical levels from the bed around the vertically submerged circular cylinders. Along the radial directions (lines), sections are numbered in increasing order away from the cylinders starting from 1 for first section. The locus of each observation taken is represented by polar coordinates ( $\theta$ ,  $r$ , and  $z$ ). Along  $\hat{x}\hat{z}$  plane, line A ( $\theta = 0^\circ$ ) and line G ( $\theta = 180^\circ$ ) represent the upstream and downstream lines respectively for both the cylinders. The remaining lines are along the  $\hat{y}\hat{z}$  plane where  $\theta$  changes for line B ( $\theta = 30^\circ$ ), line C ( $\theta = 60^\circ$ ), line D ( $\theta = 90^\circ$ ), line E ( $\theta = 120^\circ$ ) and line F ( $\theta = 150^\circ$ ). On each line, instantaneous velocity is recorded at three consecutive sections from the outer surface of the pier at 2.5, 3.5, and 4.5 cm respectively. The minimum horizontal distance of the first section was 2.5 cm due to the limitation of constant length of ADV receiver. The vertical resolution up to 12 cm above the bed as well as 10 cm below the water surface was 1 mm, and for the remaining 6 cm at mid depth from 10 to 15 cm, the vertical resolution taken was 2 mm. The measurements could not be recorded for the top 5 cm from free surface due to limitation of ADV.

### 3.2.3 *Numerical Model*

#### 3.2.3.1 *Computational Domain, Boundary Conditions, and Grid Generation*

Figure 3.3 represents a 3.0 m long, 0.4 m wide and 0.35 m deep computational domain containing two circular vertical tandem cylinders of diameters  $D_1 = 3.0$  cm and  $D_2 = 7.5$  cm along its central vertical plane. The domain consisted of single phase flow. The two cylinders were completely submerged in water. The turbulent flow around submerged tandem cylinders was simulated using the Reynolds-Averaged Navier–Stokes (RANS) equations with a  $k$ - $\epsilon$  turbulence model on a three dimensional grid. The computational domain was discretized with user-defined meshes. Non-uniform staggered grid was used, and the enclosed area of two cylinders was refined with respect to other areas of the flow field. Four numbers of simulations were computed using 4010, 10,981, 25,550, and 37,850 mesh elements, and finally 25,550 elements were used in the simulations after checking the grid independency. Extremely fine

**Fig. 3.3** Computational domain and mesh



meshes were used at the edge, toe and surface of the tandem cylinders in order to simulate large velocity gradients. Coarser mesh was used for rest of the domain. Boundary layers have also been created around the solid boundary. Generalized Minimal Residual (GMRES) iterative solver was used for simulation. At the inlet boundary (left), the transverse and vertical velocity components were set to be zero. A normal inflow velocity of 0.1165 m/s was provided at the inlet of the domain, and the hydrostatic pressure was applied at the outflow. At the outlet (right) boundary, the gradients of the velocity and turbulent quantities in the flow direction were set to zero and a reference pressure of zero was given. The top of the domain was assigned a symmetric boundary condition which indicates no shear stress along the top surface and no normal flow through top surface. No-slip boundary condition (zero velocity) was applied at the surface of the cylinder wall. Number of 3D simulation runs were carried out for flow investigation around tandem and aligned arrangement of cylinders. Post processing of results was done to extract necessary data. Flow behaviour at near bed level (i.e.,  $z/h = 0.08$ , where  $z$  is the depth of section from bottom, and  $h$  is the height of cylinder), and mid-cylinder level (i.e.,  $z/h = 0.5$ ) were investigated and discussed. For investigation on the effect of Reynolds number, runs were simulated at different velocities. Diameter of the larger cylinder was considered in calculating the Reynolds number, which were varied in the range  $190-4 \times 10^5$ .

### 3.2.3.2 Grid Independence

The results of any numerical simulation vary with grid size especially when a particular parameter has high gradients within the domain. Generally, simulations start with a mesh of higher size and gradual refinement is done till the changes observed in the results at any particular location are smaller than a pre-defined acceptable error. Since the results around the cylinder are of interest, staggered mesh is provided with more refinement near cylinders and at the gap between two cylinders. Adoption of proper mesh is necessary because coarser mesh leads to deviation from true results, and the use of finer mesh takes long time in simulation. Selection of proper mesh was carried

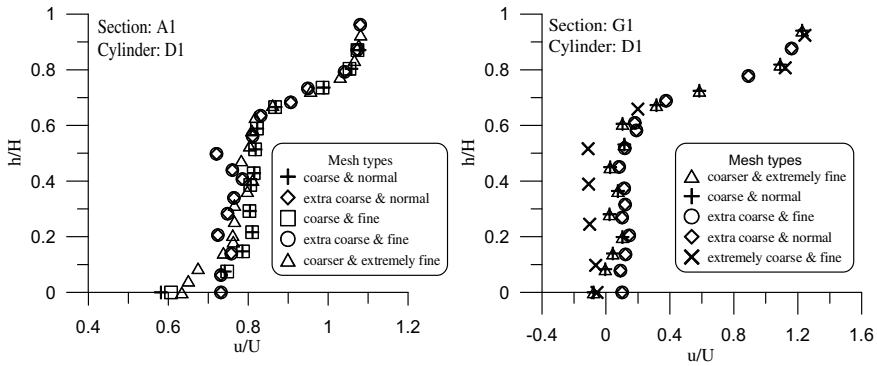


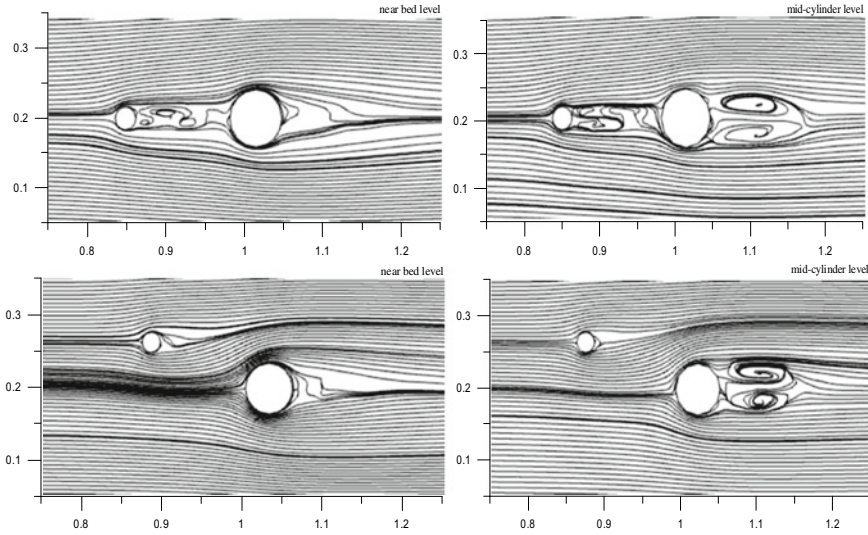
**Fig. 3.4** Results of grid independence test at two different locations

out from the comparison of results of simulations with different meshes. Meshes of large element size like coarse, coarser, extra coarse, extreme coarse, extremely coarse were tried for domain of water, while meshes with small element size like fine, finer, extra fine, extreme fine, extremely fine were tried for around cylinder and in the gap between the cylinders. The results of grid independency are shown in Fig. 3.4. From the observations of the velocity profile at different meshes, a staggered mesh with coarser refinement at water domain and extremely fine refinement for the domain of interest was adopted.

### 3.3 Results and Discussions

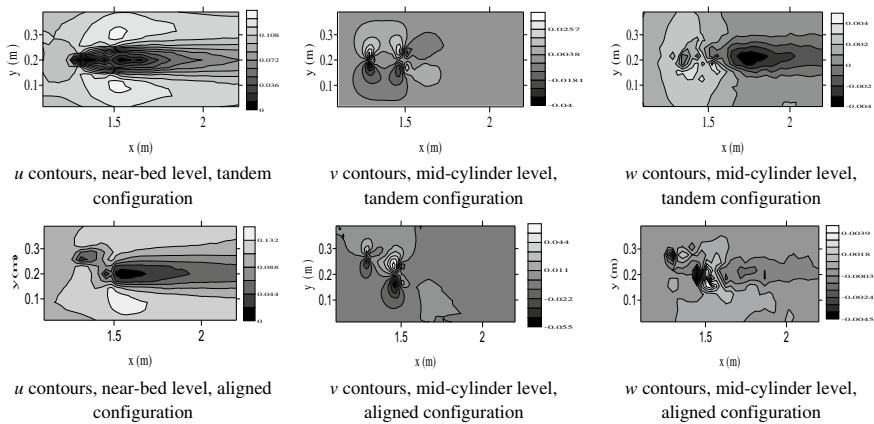
#### 3.3.1 Flow Field in Horizontal Plane

Figure 3.5 shows the patterns of streamlines for two circular cylinders of unequal diameters in tandem and  $20^\circ$  alignment at centre-to-centre spacing equals to  $2.5D_2$  and  $Re = 4500$ . In both the cases, flow behaviour upstream of the smaller cylinder is similar to that of single cylinder, but behind the cylinder this similarity decreases due to presence of larger cylinder at downstream side. For tandem arrangement, vortex street is observed at the gap between two cylinders. For aligned cylinder, fully developed recirculation zone is not visible behind the smaller cylinder. The numerical simulation fails to represent the vortex street of smaller cylinder. However, slight deviation of wake region towards upstream is visible; this is due to the presence of larger downstream cylinder. Vortices are in the form of two incomplete elliptical shapes, and size of these vortices is comparatively larger at mid cylinder depth. The presence of larger cylinder has confined the streamline growth of recirculation region in the downstream of smaller cylinder. From the figure it is evident that the recirculation is not developed near bed level behind the larger cylinder. This is



**Fig. 3.5** Flow patterns at around  $Re = 4500$  for tandem and staggered configurations

due to the effect of bed resistance on the flow. However, at the mid-cylinder depth, complete recirculation is visible in the form of two complete ellipses of streamlines. Contours of the time-averaged streamwise, transverse and vertical velocity components at different horizontal planes are presented in Fig. 3.6. An increase in streamwise velocity around the sides of the cylinders due to contraction of flow area is evident. The flow around the wake region accelerated leading to transport of extra fluid, which was also reported by Ahmed and Rajaratnam (1998) and Ashtiani and Kordkandi (2013). Reverse flow is also observed throughout the gap between the



**Fig. 3.6** Velocity contours at different locations ( $u$ : streamwise,  $v$ : transverse,  $w$ : vertical)

tandem cylinders. Ashtiani and Kordkandi (2013) also reported that the presence of the downstream cylinder makes the reverse flow region extend further than that in the single pier case. The wake region behind the downstream cylinder is smaller and weaker than that of the upstream cylinder as the velocity of approaching flow decreased due to the sheltering effect of the upstream cylinder. The reverse flow near the bed is stronger than that at the upper level near the free surface, which indicates the presence of co-shedding regime in front of the downstream cylinder. It is also evident that the transverse velocity is high at the sides of cylinders. Deflections of transverse velocity are high near the bed as the separated shear layers curve towards each other.

Downflow is visible in front of the upstream cylinder, which is similar to the single cylinder case. However, flow at the gap is in upward direction, and the extent of upflow increases at the upstream of the downstream cylinder. This interaction prevented the formation of the horseshoe vortex at the base of the downstream cylinder. Upflow in the gap reaches its maximum value at the upper level of the submerged cylinder. Behind the downstream cylinder, a small downflow is observed.

### 3.4 Effect of Reynolds Number

#### 3.4.1 Effect of $R_e$ in Tandem Configuration

The flow around tandem and aligned circular cylinders is sensitive to both  $R_e$  and  $L/D$ . Number of investigations were carried out for flow over equal diameter circular cylinders in tandem configuration (Igarashi 1982, 1984; Strykowski and Sreenivasan 1990; Dalton et al. 2001; Xu and Zhou 2004; Alam and Zhou 2008). In case of unequal diameters, wake characteristics are differed because of the interference of the wake generated from upstream cylinder on downstream cylinder. Numerical simulations were carried out for different values of free-stream velocity and corresponding Reynolds number  $R_e = \rho U_0 D / \mu$ , where  $\rho$  is the density of water,  $D$  is the diameter of larger cylinder,  $U_0$  is the free-stream velocity and  $\mu$  is the dynamic viscosity. Streamlines at different Reynolds number are presented in Fig. 3.7. Shear layers formed behind the downstream cylinder are evidently disturbed because of vortices shed from the upstream cylinder, which was also supported from the observations of Bearman and Wadcock (1973), Xu and Zhou (2004) and Gao et al. (2013).

As shown in the figure, fully developed recirculation of shear layers is observed at low Reynolds number ( $R_e = 187.5$ ), which is similar to the case of equal diameter cylinders. Two elliptical shape vortices are formed in the gap which extends up to the front surface of larger cylinder alternatively, which confirms the presence of alternate reattachment regime in the gap, which is similar with the results of Carmo and Meneghini (2006), for numerical simulations around partially submerged cylinders at lower Reynolds number. At high velocity of flow ( $R_e = 37,500$  and  $R_e = 412,500$ ), shear layers roll up in the gap and a pair of quasi-stationary eddies are

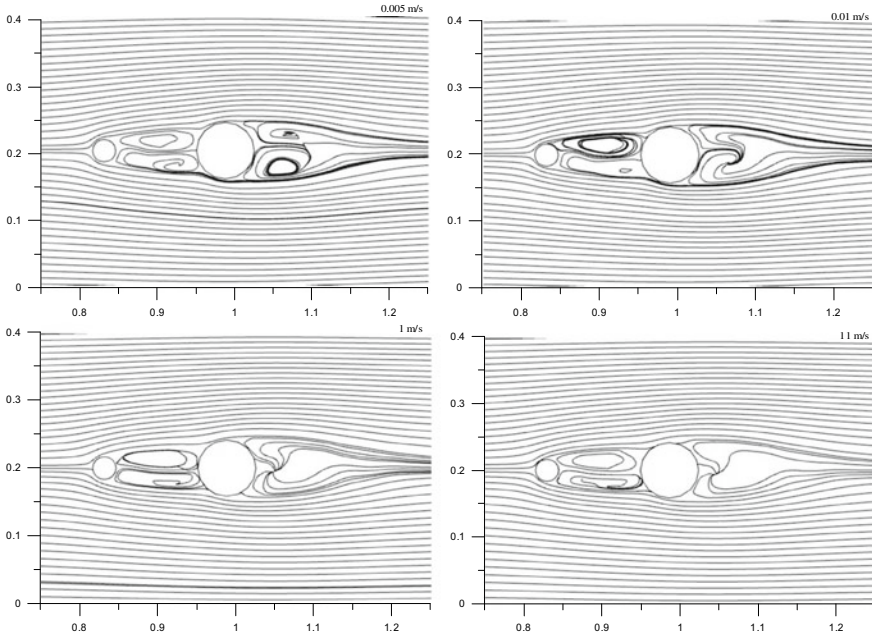


**Fig. 3.7** Flow patterns at different Reynolds number for tandem configuration

formed, which also confirms the results of Alam et al. (2003), for nearly same range of  $L/D$  and  $Re = 65,000$  in case of partially submerged cylinders. In contrast, numerical simulations of Kitagawa and Ohta (2008), for  $L/D = 2$  and  $Re = 22,000$ , showed alternate reattachment of shear layers on the downstream cylinder. With increase in Reynolds number, width of eddies is found to decrease in the gap. Whereas, for very small value of Reynolds number, vortices are found behind the downstream cylinder. Comparatively weaker but larger wake is observed behind the larger cylinder at high velocity because the shear layers in the lee of the larger cylinder begin to swirl and distort themselves. The wake behind the larger cylinder extends up to three times diameter from the centre of the larger cylinder.

### 3.4.2 Effect of $Re$ in Staggered Configuration

Investigation of flow patterns for aligned cylinders was still more complex due to the interaction of separated shear layers with the vortex streets. In the present study, investigations were carried out only on aligned configuration of inclination angle  $20^\circ$  in the present study. There were few numerical studies on flow around partially submerged circular cylinders for aligned configuration (Mittal et al. 1997; Jester and Kallinderis 2003; Akbari and Price 2005; Sumner 2010; Zhao et al. 2010).

However, there are no data available on the effect of  $R_e$  on staggered configuration of circular cylinders of unequal diameter. Flow pattern at the upstream of smaller cylinder is the same as in single cylinder case, but flow pattern at the upstream of larger cylinder is deviated due to the wake effect of the smaller cylinder. As evident from the figure, for very low Reynolds number, vortex street of the smaller cylinder is unsymmetrical and deviated towards the upstream outer side. Vortex street behind the larger cylinder further extended more than three times the diameter from the centre of the larger cylinder. Flow is accelerated in the gap from the sides of larger cylinder. As shown in Fig. 3.8, eddies formed behind the larger cylinder are not symmetrical as the flow is deviated on the side opposite of the smaller cylinder. At around  $R_e = 4500$ , vortex street of smaller cylinder deviated and the extent of wake zone behind the larger cylinder decreased. However, at higher values of Reynolds number, wake zones of both the cylinders remain confined. The smaller size of the upstream cylinder had little influence on the flow pattern of downstream cylinder, which is markedly different from the equal diameter cylinder case.

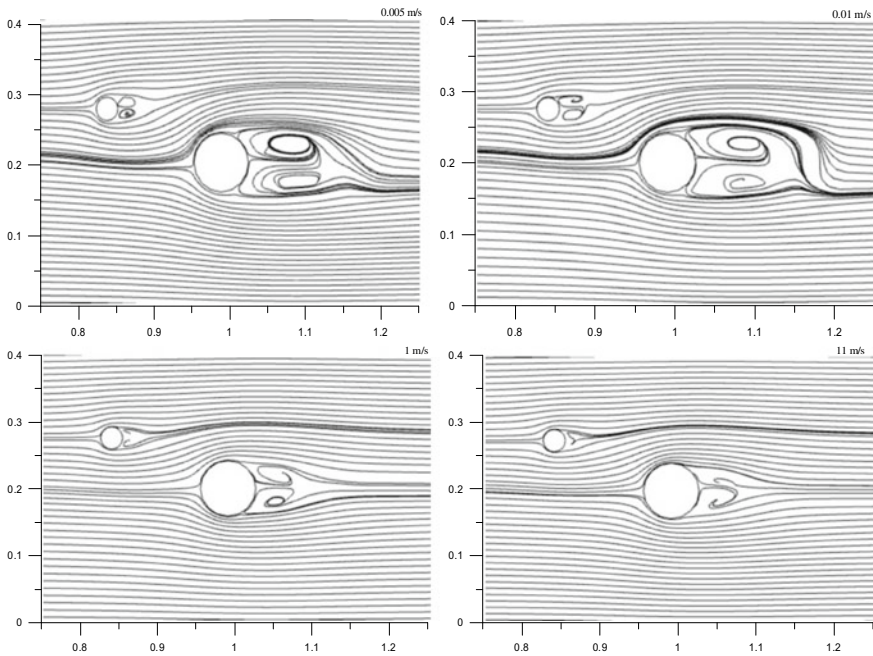


**Fig. 3.8** Flow patterns at different Reynolds number for aligned configuration



### 3.5 Spectral Analysis

Power spectra analysis of the instantaneous velocity measurements at different locations in the wake of both the cylinders were carried out to determine the dominant vortex shedding frequency, the results of which are presented in Fig. 3.9a, b. The first digit of the title given in the plots indicates cylinder number (1 for smaller and 2 for larger cylinder) and remaining title indicates section details, i.e., 1D2 means 3.5 cm away from the side of smaller cylinder, whereas Y-axis indicates power spectra  $S(f)$  in  $m^2/s$ . The dominant vortex shedding frequency was determined using Fast Fourier Transformation (FFT) of auto-covariance function of the velocity time-series data. The power associated with the peak frequency indicates the strength of vortices formed by the cylinder, which were used to explain the entrainment capacity of wake vortices to entrain and move bed sediments from the sides and rear of the cylinders, although not shown here. For tandem configuration, the lowest peak is found at upstream of larger cylinder (Section A2 for downstream cylinder), which indicate that the vortices shed from the smaller cylinder weakened even before reaching the larger cylinder. However, the higher peaks are found at the sides of the larger cylinder.

For aligned configuration, similar to the earlier case, the lowest peak is found at just upstream of the larger cylinder. Strength of vortices is high at the side and downstream of larger cylinder. High strength of wake vortices is found downstream of the gap rather than the outer side of the cylinders. Strength of vortices in the gap increases as they move away further from the gap. This is because of the interaction between the vortices shedding from each cylinder. Strength of vortices is higher in the case of staggered configuration.

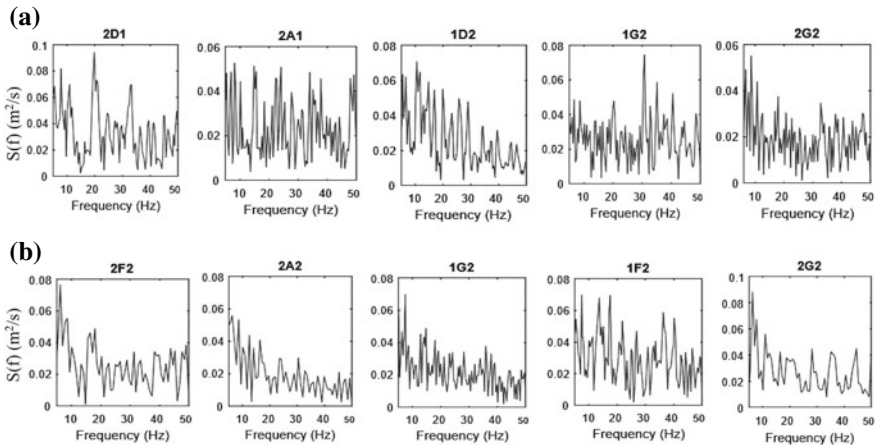


**Fig. 3.9** **a** Spectral analysis for circular cylinders in tandem configuration. **b** Spectral analysis for circular cylinders in 20° aligned configuration

### 3.6 Conclusions

The effects of two cylinders in tandem and aligned configuration on the flow field were investigated experimentally as well as numerically. Measurements of the flow characteristics were carried out using ADV. The computational domain was limited close to the cylinders to reduce the time of simulation. Suitable mesh was selected from the observations of the grid independence test. Results obtained from the computational domain were validated from the experimental results. Flow patterns, velocity contours, and spectral analysis at different locations were presented at different locations. Furthermore, the effect of Reynolds number has been reported.

For tandem cylinders, alternate reattachment is observed between the two cylinders at very low Reynolds number. Flow patterns are demonstrated to be sensitive to Reynolds number. Absence of reattachment in staggered cylinders is due to the relatively small diameter of upstream cylinder. Complete recirculation of flow is not observed near the bed level because of the effect of bed resistance. The streamwise velocity increases between the two piers which changes the behaviour of vertical and transverse deflections. The results collectively delineate the changes in the characteristics of the flow field at the wake of the upstream cylinder brought to effect by the presence of a larger downstream cylinder. The wake behind the larger cylinder extends up to three times diameter from the centre of the larger cylinder for the tandem cylinders. A weak sheltering effect is observed on the downstream cylinder aligned at an angle of  $20^\circ$  with the upstream cylinder, as a result of which the approach flow velocity increases near downstream cylinder. Strength of vortices is high at the immediate downstream sides of both the cylinders and low at just upstream of the larger cylinder. Strength of vortices increases at the downstream in the gap. Further, spectral analysis for tandem configuration shows low frequency of vortex shedding at upstream of larger cylinder, whereas the strength of the shed vortices is high at the sides of the larger cylinder for aligned cylinders.

**Acknowledgements** The authors gratefully acknowledge the Department of Science and Technology (DST), Government of India, for providing the research funds.

### References

- Ahmed F, Rajaratnam N (1998) Flow around bridge piers. *J Hydraul Eng* 124(3):288–300
- Akbari MH, Price SJ (2005) Numerical investigation of flow patterns for staggered cylinder pairs in cross-flow. *J Fluid Struct* 20:533–554
- Alam MM, Zhou Y (2008) Strouhal numbers, forces and flow structures around two tandem cylinders of different diameters. *J Fluid Struct* 24:505–526
- Alam M, Moriya M, Takai K, Sakamoto H (2003) Fluctuating fluid forces acting on two circular cylinders in a tandem arrangement at a subcritical Reynolds number. *J Win Eng Ind Aero* 91:139–154
- Ashtiani BA, Kordkandi AA (2012) Flow field around side-by-side piers with and without a scour hole. *Euro J Mech B/fluids* 36:152–166

- Ashtiani BA, Kordkandi AA (2013) Flow field around single and tandem piers. *Flow Turbul Combust* 90:471–490
- Bearman PW, Wadcock AJ (1973) The interaction between a pair of circular cylinders normal to a stream. *J Fluid Mech* 61:499–511
- Beheshti AA, Ashtiani BA (2010) Experimental study of three dimensional flow field around a complex bridge pier. *J Eng Mech* 136:143–154
- Buffin-Belanger T, Roy AG (2005) 1 min in the life of a river: selecting the optimal record length for the measurement of turbulence in fluvial boundary layers. *Geomorphology* 68:77–94
- Carmo BS, Meneghini JR (2006) Numerical investigation of the flow around two circular cylinders in tandem. *J Fluid Struct* 22:979–988
- Coutanceau M, Defaye J (1991) Circular cylinder wake configurations: a flow visualization survey. *Appl Mech Rev* 44:255–305
- Dalton C, Xu Y, Owen JC (2001) The suppression of lift on a circular cylinder due to vortex shedding at moderate Reynolds numbers. *J Fluid Struct* 15:617–628
- Eswaran M, Goyal P, Dutta A, Reddy GR, Singh RK, Vaze KK (2013) Numerical investigation of Strouhal frequencies of two staggered bluff bodies. In: COMSOL conference. Bangalore
- Gao YY, Wang XK, Tan DS, Tan SK (2013) Particle image velocimetry technique measurements of the near wake behind a cylinder-pair of unequal diameters. *Fluid Dynam Res* 45:045504
- Gerrard JH (1978) The wakes of cylindrical bluff bodies at low Reynolds number. *Philos Trans R Soc Lond A* 288:351–382
- Hiwada M, Taguchi T, Mabuchi I, Kumada M (1979) Fluid flow and heat transfer around two circular cylinders of different diameters in cross-flow. *Bull JSME* 22:715–723
- Igarashi T (1982) Characteristics of a flow around two circular cylinders of different diameters arranged in tandem. (First report). *Bull JSME* 201:349–357
- Igarashi T (1984) Characteristics of the flow around two circular cylinders arranged in tandem. (Second report, unique flow phenomenon at small spacing). *Bull JSME* 27:2380–2387
- Jester W, Kallinderis Y (2003) Numerical study of incompressible flow about fixed cylinder pairs. *J Fluid Struct* 17:561–577
- Kitagawa T, Ohta H (2008) Numerical investigation on flow around circular cylinders in tandem arrangement at a subcritical Reynolds number. *J Fluid Struct* 24:680–699
- Lin JC, Yang Y, Rockwell D (2002) Flow past two cylinders in tandem: Instantaneous and averaged flow structure. *J Fluid Struct* 16:1059–1071
- Ljungkrona L, Norberg C, Sunden B (1991b) Free-stream turbulence and tube spacing effects on surface pressure fluctuations for two tubes in an in-line arrangement. *J Fluid Struct* 5:701–727
- Ljungkrona L, Noberg C, Sunden B (1991a) Free-stream turbulence and tube spacing effects on surface effects on surface pressure fluctuations for two tubes in an in-line arrangement. *J Fluid Struct* 5:701–727
- Meneghini JR, Saltara F, Siqueira CLR, Ferrari JA Jr (2001) Numerical simulation of flow interference between two circular cylinders in tandem and side-by-side arrangements. *J Fluid Struct* 15:327–350
- Mittal S, Raghuvanshi A (2001) Control of vortex shedding behind circular cylinder for flows at low Reynolds numbers. *Int J Numer Methods Fluids* 35:421–447
- Mittal S, Kumar V, Reghuvanshi A (1997) Unsteady incompressible flows past two cylinders in tandem and staggered arrangement. *Int J Numer Methods Fluids* 25:1315–1344
- Morkovin MV (1964) Flow around circular cylinder—a kaleidoscope of challenging fluid phenomena. In: Hansen AG (ed.) *Proceedings of the symposium on ASME fluid engineering division conference fully separated flows*. Philadelphia, USA, p 102118
- Sarkar A (2014) Scour and flow around submerged structures. *Water Manag* 167:65–78
- Snyder WH, Castro IP (1999) Acoustic Doppler velocimeter evaluation in stratified towing tank. *J Hydraul Eng* 125(6):595–603
- Strykowski BJ, Sreenivasan KR (1990) On the formation and suppression of vortex shedding at low Reynolds numbers. *J Fluids Mech* 218:71–107
- Sumner D (2010) Two circular cylinders in cross-flow: a review. *J Fluid Struct* 26:849–899

- Williamson CHK (1996) Vortex dynamics in the cylinder wake. *Annu Rev Fluid Mech* 28:477–539
- Xu G, Zhou Y (2004) Strouhal numbers in the wake of two inline cylinders. *Exp Fluid* 37:248–256
- Yangyang G, Stephane E, Xikun W, Keat ST (2014) Experimental study on the flow around two tandem cylinder with unequal diameters. *J. Ocean Univ China* 13:761–770
- Zdravkovich MM (1987) The effect of interference between circular cylinders in cross flow. *J Fluid Struct* 1:239–261
- Zdravkovich MM (1997) *Flow around circular cylinders: Fundamentals*, vol 1. Oxford University Press, Oxford, UK
- Zdravkovich MM (2003) *Flow around circular cylinders: Applications*, vol 2. Oxford University Press, Oxford, UK
- Zhao M, Cheng L, Teng B, Liang DF (2005) Numerical simulation of viscous flow past two circular cylinders of different diameters. *Appl Ocean Res* 27:39–55
- Zhao M, Cheng L, Teng B, Dong G (2007) Hydrodynamic forces on dual cylinders of different diameters in steady currents. *J Fluid Struct* 23:59–83
- Zhao M, Cheng L, Zang Z (2010) Experimental and numerical investigation of local scour around a submerged vertical circular cylinder in steady currents. *J Coastal Eng* 57:709–721
- Zhou Y, Yiu MW (2006) Flow structure, momentum and heat transport in a two-tandem-cylinder wake. *J Fluid Mech* 548:17–48

# Chapter 4

## Experimental and Numerical Analyses of Boundary Shear Stress in Non-prismatic Compound Channel



Laxmikant Das, Kishanjit Kumar Khatua, and Bhabani Shankar Das

**Abstract** As boundary shear stress is an important parameter in open channel flow so experiments are carried out in non-prismatic compound channel. These experimental channels comprising of rectangular main channel, two symmetrically disposed diverging flood plains. The boundary shear stress distribution cannot be determined easily as they depend upon the velocity field, the shape of the cross section, and the boundary roughness. Variation of shear on flood plain and main channel with respect to the relative flow depth and divergence angle has been demonstrated. The present experimental non-prismatic compound channel is having diverging flood plain. Here, experimentations were done with two water depth ratio ( $D_r$ ) such as 0.4 and 0.5 and two diverging angle such as  $5.93^\circ$  and  $9.83^\circ$ . As a complementary study of the experimental research undertaken in this work, one numerical hydrodynamic tools, viz., three-dimensional CFD model (ANSYS—FLUENT) is applied to simulate the flow in non-prismatic compound channel. This study aims to validate ANSYS—FLUENT simulations of open channel flow by comparing the data observed in the hydraulics laboratory of the National Institute of Technology, Rourkela. In this study, I have used four turbulence models to validate the result up to the at most accuracy. The four models are as follows: LES,  $k-\varepsilon$ ,  $k-\omega$ , and SST. The experimental results were taken as the reference, and all the models simulation result of boundary shear stress is compared with it, among the four models LES was given the approximate result and was taken as the best model for the analysis of boundary shear stress for non-prismatic compound channel.

**Keywords** Depth ratio · Turbulence model · Non-prismatic compound channels · ANSYS

---

L. Das (✉)  
Savitribai Phule Pune University, Pune 411007, India

K. K. Khatua  
National Institute of Technology, Rourkela 769008, India

B. S. Das  
National Institute of Technology Patna, Bihar 800005, India

## 4.1 Introduction

Every living being needs at least water to survive. The main source of water is rainwater, and it is not available throughout the year. Nowadays due to globalization and industrialization the cycle, period, nature, quality, quantity, etc., of the rainfall and rainwater is disturbed. This disturbance affects human as well as natural vegetation. So, to equalize the water cycle and make water available at every situation, hydraulic structures like dams and artificial reservoirs are build. However, these structures are built to store water and to convey this water further, channels or canals are constructed. Channels or canals are an artificial path constructed to convey water to desired place which mostly work on gravitational flow concept. To design these channels or canals various design parameter are to be considered. Depth average velocity and boundary shear stress plays a vital role in fluid flow running throughout the cross section of an open channel. However, study of these parameters is required to overcome hydraulic and engineering problems. The boundary shear stress depends upon the shape of the channel and the depth average velocity depends upon cross-sectional area and discharge (Myers and Elsayy 1975; Bathurst et al. 1979; Ghosh and Jena 1971; Knight 1981; Knight et al. 1992; Khatua and Patra 2010).

The main aim of this research is that analysis of boundary shear stress in non-prismatic compound channel by both experimental and numerical analysis. In this research work, a trial was made to validate the numerical models such as LES model, k- $\epsilon$  Model, k- $\omega$  model, and SST model for non-prismatic compounds channels.

From the experimental analysis, we got point to point data from the wetted perimeter of the various sections of the channel and further plotted in graphs and analyzed the distribution of boundary shear stress. The analysis shows that the boundary shear stress is maximum in the main channel, and it gradually decreases as we move from main channel to flood plain. The boundary shear stress distributions are plotted from the data computed from the ANSYS using four turbulence model for different sections, which was compared with the boundary shear stress graph plotted from the experimental data. It was found that the obtained graphs were not coinciding at all with the three models such as k- $\epsilon$  , k- $\omega$ , and SST but it was not perfectly coinciding but with less error LES model is valid for finding the boundary shear stress in non-prismatic compound channel flow. Hence, we found out that the LES model can be applied for the analysis of boundary shear stress in compound channel flow.

The current work open wide scope for the upcoming future investigations such as LES model for other types of channel having different channel geometry and of various hydraulics sections can be carried out. The data that we have got here can be used to validate with the data of other investigations.

### 4.1.1 Non-Prismatic Compound Channel

A non-prismatic compound section is one either cross section or slope or both cross section and slope changes and channel is termed as non-prismatic compound section. It is very clear that only the artificial channel can be prismatic sections because of its irregular shapes which is caused by nature.

Mainly non-prismatic compound channel is broadly divided into two types:

- i. Non-prismatic compound channel having converging flood plains
- ii. Non-prismatic compound channel having diverging flood plains

So in this research area, my focus was only on compound channel having diverging floodplain (Fig. 4.1).

## 4.2 Methodology

Here, the experiment is conducted in a compound channel having diverging flood plains inside a concrete flume measuring in  $20 \times 2 \times 0.5$  m the hydraulic engineering laboratory of the National Institute of Technology Rourkela, India. Here, we have taken the three diverging angle such as  $5.93^\circ$ ,  $9.83^\circ$ , and  $14.7^\circ$  and of depth ratio 0.2, 0.3, 0.4, and 0.5. Mainly the channel is made up of cement concrete. The details about the channel used in current research work are given in Fig. 4.2 and also can be found in Das and Khatua (2018) (Table 4.1 and Figs. 4.3 and 4.4) (Table 4.2).

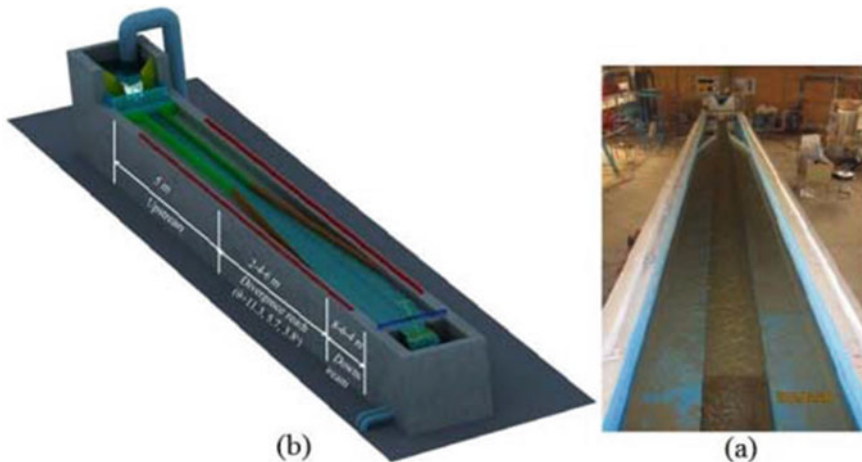


**Fig. 4.1** a The view of the non-prismatic compound channel b Schematic of 3-D view of the non-prismatic compound channel

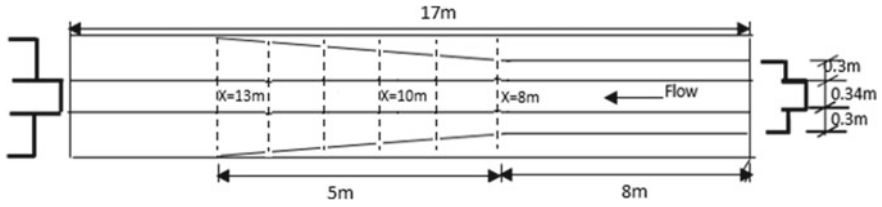


**Fig. 4.2** Experimental channel having diverging angle  $5.93^\circ$

**Table 4.1** Details of experimental parameters for diverging compound channel having diverging length 5 m and of diverging angle  $5.93^\circ$

Serial. No	Item	Diverging compound channel
1	Main channel geometry	Rectangular
2	Flood plain geometry	Diverging
3	Width of the main channel	34 cm
4	Full depth main channel	11.3 cm
5	Top width of channel measured before divergence started	94 cm
6	Divergence length	500 cm
7	Slope of the channel	0.002
8	Experimental position Sect. 4.1	8 m from outlet
9	Experimental position Sect. 4.2	9 m from outlet
10	Experimental position Sect. 4.3	10 m from outlet
11	Experimental position Sect. 4.4	11 m from outlet
12	Experimental position Sect. 5	12 m from outlet
13	Experimental position Sect. 6	13 m from outlet
14	Flume size	$20 \times 2 \times 0.4$ m

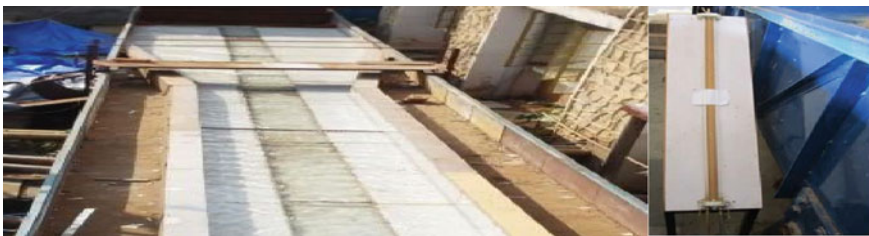


**Fig. 4.3** Experimental flume and inclined manometer



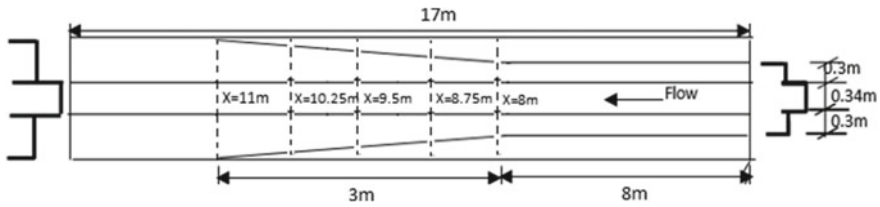


Fig. 4.4 Experimental channel having diverging angle 9.83°

Table 4.2 Details about the channel sections of diverging length 3 mm and of diverging angle 9.83°

SL. No	Item	Diverging compound channel
1	Main channel geometry	Rectangular
2	Flood plain geometry	Diverging
3	Width of the main channel	34 cm
4	Main channel full depth	11.3 cm
5	Top width of main channel measured before divergence	94 cm
6	Divergence length	500 cm
7	Slope of the channel	0.002
8	Experimental position at section 1	8.75 m from outlet
9	Experimental position at section 2	9 m from outlet
10	Experimental position at section 3	9.5 m from outlet
11	Experimental position at section 4	10.25 m from outlet
12	Experimental position at section 5	10 m from outlet
13	Flume size	20 × 2 × 0.4 m

### 4.2.1 Measurement of Boundary Shear Stress

The local boundary shear stress was measured using a Preston tube which is having a diameter of the 4.77 mm. It is considered as an outer diameter. Basically, a Preston tube is consisting of mainly two isolated tubes; one tube is named as static tube and another tube is named as a dynamic tube. The main function of the static tube is that it was fixed at the middle of flow depth and its main function is to measure the pressure due to static head of flow. The dynamics tube was placed in such a manner mostly within the boundary shear layer, which is mainly facing into the flow and it is basically measured the dynamics pressure head. As far as local boundary shear stress was concern it was measured around the wetted perimeter of channel at 10mm vertical intervals on the walls. So, before any reading was taken checks were made that there must be no air bubble in the either tube of inclined manometer. In every week manometer should be cleaned. The main functions of the inclined manometer are that it was used to measure the pressure difference between the static tube and the dynamic tube, delta which was then converted into boundary shear stress using

a most important formula known as Patel's calibration equations for the case of the smooth boundaries. Keeping in mind the end goal to check the exactness of slanted point of the manometers, after each investigation, when pumps were turned off and water surface was steady, both the static and dynamic head weights were recorded and any contrasts between them was utilized as a change consider in the limit shear stress measurement.

As far as methodology is concern for experimental analysis experimentation is done in experimental channel and boundary shear stress is found out using Patel's formula (Preston 1954; Patel 1965).

$$\Delta p = (\Delta h) \sin \theta \quad (4.1)$$

$$x^* = \log_{10} \left( \frac{\Delta p d^2}{4 \rho v^2} \right) \quad (4.2)$$

$$y^* = \log_{10} \left( \frac{\tau d^2}{4 \rho v^2} \right) \quad (4.3)$$

Here,  $d$  is the external diameter of the Pitot tube (0.477 mm) and  $v$  the kinematic viscosity ( $1.004 \times 10^{-6} \text{ m}^2/\text{s}$ ) and  $\Delta p$  the difference in static and dynamic pressure  $x^*$  is found using (3) and given the value and its respective range, we find  $y^*$  using the following:

$$y^* = 0.5x^* + 0.037 \quad (4.4)$$

$$0 \leq y^* < 1.5$$

$$0 \leq x^* < 2.9$$

$$y^* = -.0060x^{*3} + 0.1437x^{*2} - 0.1381x^* + 0.8287 \quad (4.5)$$

$$1.5 \leq y^* < 3.5$$

$$2.9 \leq x^* < 5.6$$

$$x^* = y^* + 2 \log_{10}(1.95y^* + 4.02) \quad (4.6)$$

$$3.5 \leq y^* < 5.3$$

$$5.6 \leq x^* < 7.6$$

And hence  $\tau$  can be calculated using these equation.

## 4.2.2 Numerical Model Analysis

For numerical analysis here ANSYS (FLUENT) software was used and analysis is done with four models such as LES,  $k-\varepsilon$ ,  $k-\omega$ , and SST.

### 4.2.2.1 Turbulence Modeling

The stream which was diverted is turbulent in natural conditions. Turbulent stream is a stream step by step set depicted by riotous and stochastic property changes. It is generally having joins low force dispersion more energy convection, and snappy variety of weight and speed in space and time (Larocque et al. 2012, 2013).

Turbulence mainly carried out when the inertness propels in the liquid get the chance to be gigantic stood out from gooey strengths, and is conducted by actually a high Reynolds Number. Basically, turbulence is unpredictable which is mainly the dimensional time ward eddying development as well as the various significant scale eddies. The trio geometric humor of turbulent streams is rotted into two unique parts, i.e., means sections and variance part, which is doubtlessly comprehended as Reynolds decay. Here, the spatial character of turbulence not covers the swirls with a various ranges of scales. Here in the turbulence, mainly disconnected liquid particles which is mainly responsible for the development of the eddying when they come closure together which is mainly responsible for the fruitful exchange of warmth, weight, and force. The turbulence in winding channel is flighty and the stream structure incorporated into it makes vulnerability in gauge of stream factors. Especially, in NPCC, the qualifications of the average velocity within the main channels and these structures are summed by a large amount of the shear layers. In the both of the longitudinal and vertical heading, this extensive shear layer area is made. The anisotropy furthermore over homogeneity of turbulent structure causing assistant ebb and flow, which makes the speed plunge and impacts the stream factors. Consequently, here in review an effort is done to see the impact of the turbulence in winding cannal. Joining turbulence, CFD acknowledges those actuate velocity area furthermore a fluctuating rate a piece provided for as.

$$u = \bar{u} + u' \quad (4.7)$$

Here, the Navier–Stokes momentum equation is given by as follows:

$$\frac{\partial(\rho u_i u_j)}{\partial x_j} = \frac{\partial \rho}{\partial x_i} + \frac{\partial y}{\partial x_j} \left( \frac{\partial u_j}{\partial x_j} \right) \quad (4.8)$$

Now next thing is that we need to substitute  $\bar{u} + u'$  for  $u$  in Eq. (4.2) and which leads to gives the averaging of the term:

$$\frac{\partial \bar{u}}{\partial x} = \frac{\partial(\bar{u} + u)}{\partial x} = \frac{\partial u}{\partial x} \quad (4.9)$$

Furthermore the above non-linear equations become

$$\frac{\partial(uu)}{\partial x} = \frac{\partial \bar{u}\bar{u}}{\partial x} + \frac{\partial u'u'}{\partial x} \quad (4.10)$$

Now, the Navier–Stokes equations become

$$\frac{\partial \bar{u}}{\partial x_j} = 0 \quad (4.11)$$

$$\frac{\partial \rho_{ij}}{\partial x_i} = -\frac{\partial \rho}{\partial x_j} + \frac{\partial}{\partial x_j} \left( \mu \frac{\partial \bar{u}}{\partial x_j} \right) - \frac{\partial \rho(u'j u'j)}{\partial x_j} \quad (4.12)$$

The term given above in the equations  $\frac{\partial \rho(u'j u'j)}{\partial x_j}$  is called as “Reynolds stress”.

### 4.2.3 Models Descriptions and Governing Equation

So here we have taken four models to validate the results. These are  $K-\epsilon$  model,  $K-\omega$  model, LES, and SST. So below there is a detailed description about the models and also for the Governing Equation. Numerical models are used here.

- LES model
- $K-\epsilon$  model
- $K-\omega$  model
- SST model.

#### 4.2.3.1 LES Model

The governing equations of LES are acquired by sifting the fractional differential conditions administering the stream field. There are contrasts between the incompressible and compressible LES administering conditions, which prompt the meaning of another filtering operation (Salvetti et al. 1997).

Statistically, individual might consider separating the velocity field into a resolved and subgrid part. The determined part of the field denotes the “large” eddies, while the subgrid portion of the velocity denotes the “small scales” whose effect on the resolved field is involved through the subgrid scale model. Formally, one might think of filtering as the convolution of a function with a filtering kernel  $G$ :

$$\overline{u_i}(\vec{x}) = \int G(\vec{x} - \vec{\varepsilon})u(\vec{\varepsilon})d\vec{\varepsilon} \quad (4.13)$$

Resulting in

$$u_i = \overline{u_i} + u'_i \quad (4.14)$$

where  $\overline{u_i}$  the resolvable scale is part and  $u'_i$  is the subgrid-scale part. However, most practical (and commercial) applications of LES practice the grid itself as the filter (the box filter) and do no explicit filtering. More evidence about the theory and application of filters is found in the LES filters article.

This page is mainly focused on LES of incompressible flows. For compressible flows, see Favre averaged Navier–Stokes equations. The filtered equations are developed from the incompressible Navier–Stokes equations of motion

$$\frac{\partial u_i}{\partial t} + u_j \frac{\partial u_i}{\partial x_j} = -\frac{1}{\rho} \frac{\partial p}{\partial x_i} + \frac{\partial}{\partial x_j} \left( \nu \frac{\partial u_i}{\partial x_j} \right) \quad (4.15)$$

#### 4.2.3.2 The k-ε Model

**k-ε model** is a general model used in CFD for the purpose of simulation of the mean flow characteristics for turbulent flow conditions. It is often a two equation model in which a general description of turbulence by means of two transport equations (PDEs) is given. The basic thing for the k-ε model was to the mixing length model, as well as to find to algebraically prescribing turbulent length scales in moderate to high complexity flows.

The first transported variable mainly determines the energy in the turbulence which is called as turbulent kinetic energy (k).

The second transported variable is the turbulent dissipation (ε) which determines the rate of dissipation of the turbulent kinetic energy.

- (1) The *k-ε* model focuses on the mechanisms that affect the turbulent kinetic energy (per unit mass) *k*.
- (2) The instantaneous kinetic energy *k(t)* of a turbulent flow is the sum of mean kinetic energy *K* and turbulent kinetic energy *k*:

$$(a) k = \frac{1}{2}(U^2 + V^2 + W^2) \quad (4.16)$$

$$(b) k = \frac{1}{2}(U'^2 + V'^2 + W'^2) \quad (4.17)$$

$$(c) k(t) = K + k \quad (4.18)$$

- (3)  $\epsilon$  is the dissipation rate of  $k$ .  
 (4) If  $k$  and  $\epsilon$  are known, we can model the turbulent viscosity as

$$V_t \propto \nu \propto k^{\frac{3}{2}} \frac{k^{\frac{3}{2}}}{\epsilon} = \frac{k^2}{\epsilon} \quad (4.19)$$

### K equation:

Model (simplified) equation for  $k$  after using Boussinesq assumption by which the fluctuation terms can be linked to the mean flow is as follows:

$$\frac{\partial k}{\partial t} + U_i' \frac{\partial k}{\partial x_i} = v_i \left[ \frac{\partial U_j}{\partial x_i} + \frac{\partial U_i}{\partial x_j} \right] \frac{\partial U_j}{\partial x} + \frac{\partial}{\partial x_i} \frac{v_t}{\sigma_k} \frac{\partial k}{\partial x_i} - \epsilon + \nu \frac{\partial^2 k}{\partial x_i^2} \quad (4.20)$$

With  $v_t = 0.09 \frac{k^2}{\epsilon}$

### Model Equation for $\epsilon$ :

A model equation for  $\epsilon$  is derived by multiplying the  $k$  equation by  $(\epsilon/k)$  and introducing model constants:

$$v_t = C_v \frac{k^2}{\epsilon} \quad (4.21)$$

$$\frac{\partial \epsilon}{\partial \tau} + \frac{\partial U_j \epsilon}{\partial x_i} = \frac{\partial}{\partial x_i} \left[ \left( \nu + \frac{v_t}{\sigma_k} \right) \frac{\partial \epsilon}{\partial x_i} \right] + C_{z1} P \frac{\epsilon}{K} + C_{z2} P \frac{\epsilon^2}{K} \quad (4.22)$$

$$\text{where } P = v_t \left( \frac{\partial U_j}{\partial x_i} + \frac{\partial U_i}{\partial x_j} \right) \frac{\partial U_j}{\partial x_i}$$

Empirically, the closure coefficients are given below

$$\sigma_k = 1, C_{z1} = 1.44, C_{z2} = 1.92, C_v = 0.09, \sigma_\epsilon = 1.33$$

### 4.2.3.3 The $k$ - $\omega$ Model

#### Overview

The first ever two equations model is the  $k$ - $\omega$  turbulence model in which the turbulent kinetic energy ( $k$ ) and also the turbulence frequency ( $\omega$ ) is involved, it is also called as  $k$ - $f$  model as the solution of this model having turbulent kinetic energy  $k$  and also the turbulence frequency  $\omega$ . In other way  $\omega$  can be defined as the  $\epsilon/k$  and where  $\epsilon$  is defined as the rate of dissipation of  $\epsilon$ .

It seems to be k- $\omega$  model is not as popular as the k- $\epsilon$  model, still it was having lot of advantages as compared to k- $\epsilon$  model is.

- The low Re version model is very economical, predictable, and elegant as compared to the low Re version k- $\epsilon$  models, because in here it does not need for any of the wall distances calculations, its additional source terms and its damping functions mainly based on the friction velocity.
- It is reported that it is used to perform better in flows with adverse pressure gradients and also it's perform better in transitional flows.
- This model is mainly numerically very stable and also it produces the approximately gives better results.

The main disadvantage of the k- $\omega$  model as of k- $\epsilon$  model is it is very sensitive to the freestream boundary condition for  $\omega$  in free shear flows (Cater and Williams, 2008).

#### Details Description About the Model

The summarization of the k- $\omega$  model:

$$\frac{\partial}{\partial t} \left( \frac{\rho}{k} \right) + \nabla(\rho \times U \times k) = \nabla \left( \rho \times \left( v_t + \frac{v_t}{k} \right) \nabla k \right) + \rho \times (P_k -) \quad (4.23)$$

$$\begin{aligned} & \frac{\partial}{\partial t} (\rho \times \omega) + \nabla(\rho \times U \times \omega) \\ & = \nabla \left( \rho \times \left( v_t + \frac{v_t}{\omega} \right) \nabla \omega \right) + \rho \times \omega \left( f_1 \times C_{1\omega} \times \frac{P_k}{k} - f_1 \times C_{1\omega} \times \frac{P_1}{k} - f_2 \times C_{2\omega} \times \omega \right) \end{aligned} \quad (4.24)$$

The equations of the various parameters used above are given below

$$V_t = f_\mu \times C_\mu \times \frac{k}{\omega} \quad (4.25)$$

$$P_k = v_t \times \left( \frac{\partial U_i}{\partial X_j} + \frac{\partial U_j}{\partial X_i} \right) \frac{\partial U_i}{\partial X_j} \quad (4.26)$$

$$\epsilon = C_D \times \omega \times k \quad (4.27)$$

wherein:  $\rho$  is the density of the fluid;  $\nu_l$  and  $\nu_t$  are the viscosities of the laminar and the turbulent flow of the fluids;  $P_k$  is the volumetric production rate of k; and  $f_\mu$ ,  $f_1$  and  $f_2$  are mainly the damping functions of low Re.

The constant which are generally used in the k- $\omega$  models are as follows:

$$\sigma_k = 2.0, \sigma_\omega = 2.0, C_\mu = 1.0, C_D = 0.09, C_{1\omega} = 5/9, C_{2\omega} = 3/40.$$

Mainly the damping functions, in the high Re model which are set to unity, are defined by

$$f_{\mu} = \left( \frac{1}{40} + \frac{R_T}{R_K} \right) / \left( 1 + \frac{R_T}{R_K} \right) \quad (4.28)$$

$$f_1 = \left\{ \frac{1}{f_{\mu}} \right\} \times \left( 0.1 + \frac{R_T}{R_W} \right) / \left( 1 + \frac{R_T}{R_K} \right) \quad (4.29)$$

$$f_2 = \left( \frac{8}{15} + \left( \frac{R_T}{R_B} \right)^4 \right) / \left( 1 + \left( \frac{R_T}{R_B} \right)^4 \right) \quad (4.30)$$

The value of Reynolds number is given below

$$R_T = \frac{k}{(\omega \times \nu l)} \quad (4.31)$$

where  $R_B = 8$ ,  $R_K = 6.0$ ,  $R_W = 2.7$ , and  $R_T$  is the Reynolds number of the turbulent model. In specific area where  $R_T$  is of high value, than there  $f_{\mu}$ ,  $f_1$ , and  $f_2$  tend to very small which is trends to be unity.

#### 4.2.3.4 SST Model

##### Introduction

The SST model was displayed and created by Menter, the primary point of building up this demonstrated model is that of exact plan of  $k-\omega$  model show in the close divider area with freestream autonomy of the display in far field. To accomplish this, the SST model is changed over into a detailing. The SST model is like as of standard demonstrate  $k-\omega$  model, however incorporates the accompanying refinements:

- The standard display and changed model are both duplicated by a mixing capacity and both models are included. The mixing capacity is intended to be one in close divider locale, which actuates the standard model, and zero far from the surface, which enacts the changed display.
- The SST show consolidates a damped cross dispersion subsidiary term in the condition.
- The meaning of turbulent consistency is changed to represent the vehicle of the turbulent shear stretch.
- Other modifications were also done in addition with a cross diffusions term in  $\omega$  equation and there is a blending function which is mainly put for ensuring that the model equations behave appropriately in both near wall and far field zones.

##### Transport Equations for SST Model

The SST model has a similar form to standard  $k-\omega$  model:



$$\frac{\partial}{\partial t}(\rho k) + \frac{\partial}{\partial x_i}(\rho k u_i) = \frac{\partial}{\partial x_i} \left( \Gamma_k \frac{\partial k}{\partial x_j} \right) + G_k - Y_k + S_k \quad (4.32)$$

$$\frac{\partial}{\partial t}(\rho \omega) + \frac{\partial}{\partial x_i}(\rho \omega u_i) = \frac{\partial}{\partial x_i} \left( \Gamma_\omega \frac{\partial \omega}{\partial x_j} \right) + G_\omega - Y_\omega + D_w + S_w \quad (4.33)$$

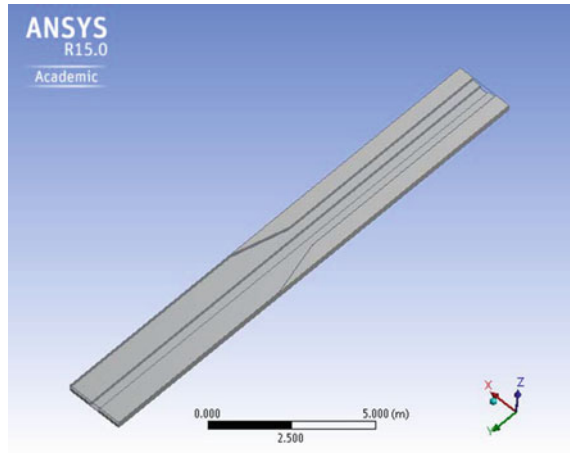
In these equations,  $G_k$  indicates the formations of turbulence kinetic energy because of mean velocity gradients,  $G_\omega$  indicates the formations of  $\omega$ ,  $\Gamma_r$ , and  $\Gamma_w$  indicates the effectiveness diffusivity of  $k$  and  $\omega$ , respectively, which are mainly calculated as described below  $Y_k$  and  $Y_\omega$  indicates the scattering of  $k$  and  $\omega$  due to turbulence. Here,  $D_w$  mainly represents the cross diffusion term. The term used here which are  $S_k$  and  $S_w$  are user defined source terms.

#### 4.2.4 Methodology of ANSYS (Fluent)

The process for obtaining numerical solution in case of fluid flow is based upon the above given equation and usually has four steps in it. The explanation of four steps is given below.

- (a) Identification of problem
  1. To define suitable goals.
  2. Identifying the domain of solution.
- (b) Pre-Processing
  1. In geometry setup designing a solid model to define the domain.
  2. Design or modification of mesh grid.
- (c) Solver
  1. Set up the Physics
    - Adding the flow conditions (i.e., laminar, turbulent, etc.)
    - Boundary condition and temporal conditions are given
  2. Defining numerical models to find solutions of the applicable equations.
  3. Convergence of iterations of equation till the desired satisfaction in result is obtained.
  4. Through solver setting find the solutions to the equation.
    - First step is Initialization
    - Second one is control of solution
    - Third one being monitoring the solution
- (d) Postprocessing
  1. Seeing the results through eyes and scrutinizing the results.

**Fig. 4.5** Geometry of the non-prismatic compound channel having diverging flood plains



2. Plots of X–Y.
3. Drawing of contours, streamlines, etc.

#### 4.2.4.1 Preprocessing

In the first step, problem statement is fitted into the system by user. There are many steps such as geometry, computational grid's properties, different kinds of models to be used, quantity of Eulerian states, time step size, and numerical solutions.

##### Geometry Creation:

First and principal phase in CFD analysis is the creation of geometry of the flowing fluid in Geometry fluid. For creation of geometry, prediction happens from the reference of coordinate axis. Streamwise direction of fluid flow is represented by Y-axis. X-axis denotes the width of the channel and is directed in the lateral direction. Z-axis is used for representing the vertical axis, i.e., the depth of water. It is Y direction in which water flows. The simulation was performed on a non-prismatic compound channel. Below given figure shows the cross-sectional geometry of the prismatic bar (Fig. 4.5).

While constructing model, there is an additional consideration. It is to classify a part of the geometry which is potential location for conducting few analyses and for implementing boundary condition on selected domain. Below given is a list of geometric parts used in a non-prismatic compound channel of the diverging flood plain channel.

In order to know the domain, various types of generated surfaces are given below.

1. Center line

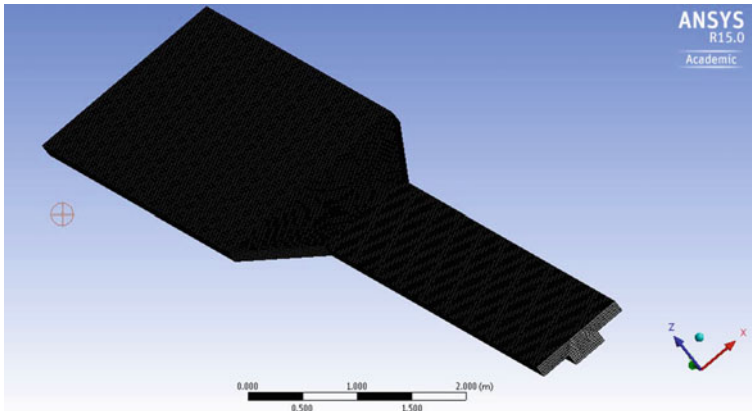


**Fig. 4.6** Meshing of the non-prismatic compound channel

2. Channel Bottom
3. Side wall
4. Free surface
5. Outlet
6. Inlet

### Mesh Generation

This step is the second one but the most important step in the analysis of numerical solutions. In this step, grid needs to be set. This grid is related to the construction of geometry. Non-linear equations used are non-linear partial differential equations. These equations take the whole of fluid domain as continuum. The problem was made easier by simplifying the equations. These equations can be directly solved by very low Reynolds numbers. The simplification process is called as discretization. The work is developed by subdividing the geometry into different parts. The factors at these parts were processed numerically. Taking the help of Cartesian coordinates, the fluid flow describing equations were solved. They were continuity equation, momentum equation, etc. Two schemes are required for CFD analysis. They are spatial discretization scheme and time marching scheme. What meshing does is that it divides the entire spectrum into countable number of nodes. Finite element, finite difference, and finite volume are the three various methods to discretize the domains. The finite element method divides the domain into elements (Fig. 4.6).

As far as transient problems an appropriate time steps are needed to be specified. To catch the required elements of liquid stream with in a space, the time step ought to be adequately little yet not all that much little which may bring about misuse of computational power and time. Spatial and time discretization is connected, as apparent in the Courant number (Table 4.3).

**Table 4.3** Meshing statistics

Statistics	
Nodes	311,283
Elements	262,080
Mesh metric	None

### 4.3 Result

The experimental result is got from the non-prismatic compound channel of NITR flume as given in Fig. 4.7.

The numerical analysis result got from ANSYS software including all four models is given in (Table 4.4 and Fig. 4.8).

**Fig. 4.7** Boundary shear stress distribution for diverging compound channel

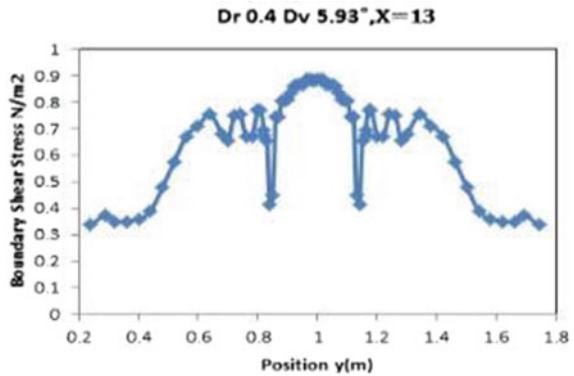


**Table 4.4** Values of the various parameters used in the numerical analysis with the respective relative depth (Dr)

SL NO	Relative Depth (Dr)	Total Flow Depth (m)	Main Channel Depth (m)	Discharge (m <sup>3</sup> /sec)	Area of the cross Sections (m <sup>2</sup> )	Velocity (m/s)
01	0.2	0.113	0.141	0.030	0.11574	0.259
02	0.3	0.113	0.161	0.041	0.12254	0.330
03	0.4	0.113	0.118	0.055	0.13172	0.418
04	0.5	0.113	0.226	0.067	0.14464	0.463

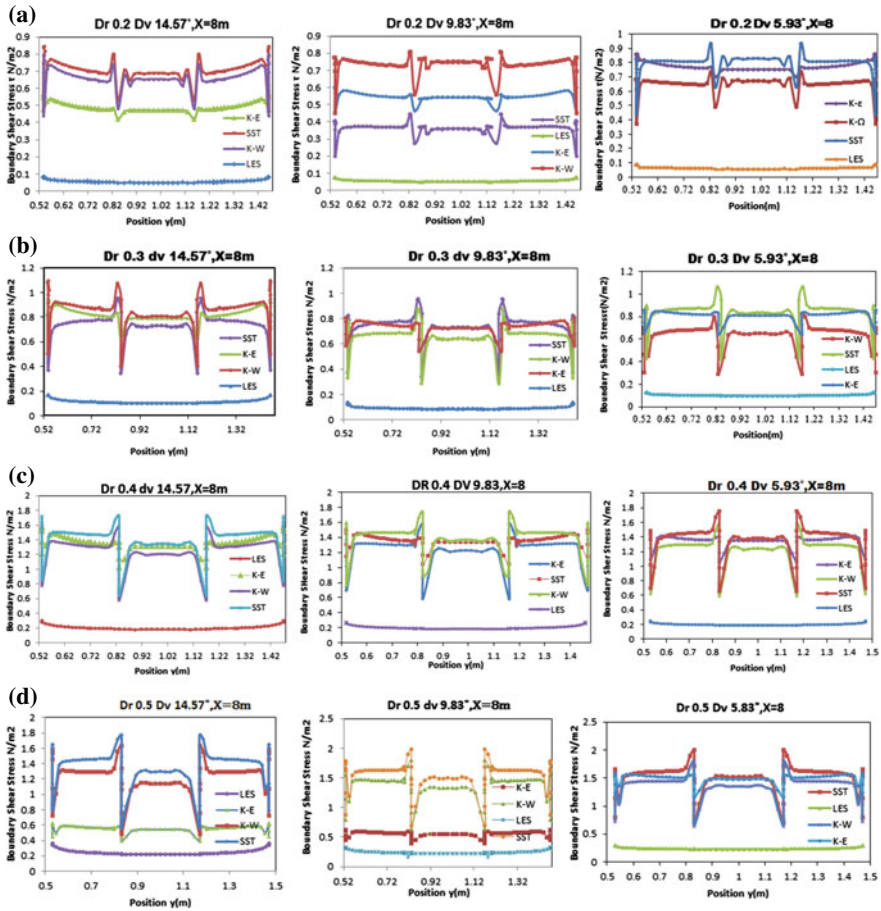


**Fig. 4.8** **a** Showing the variation of the boundary shear stress of fixed  $Dr = 0.2$ . **b** Showing the variation of the boundary shear stress of fixed  $Dr = 0.3$ . **c** Showing the variation of the boundary shear stress of fixed  $Dr = 0.4$ . **d** Showing the variation of the boundary shear stress of fixed  $Dr = 0.5$

### 4.3.1 Validation of Numerical Result with the Experimental Result

The four numerical models namely LES,  $k-\epsilon$ , model,  $k-\omega$  model, and SST model were applied in two diverging angle and of two depths ratio and the results were obtained, then the results were compared with experimental results.

Experiment has conducted for two diverging angles that is  $5.93^\circ$  and  $9.83^\circ$ . So here comparison was made with numerical result and also the experimental result to show which turbulence model is fit to give the good result with less error percentage (Das et al. 2017).

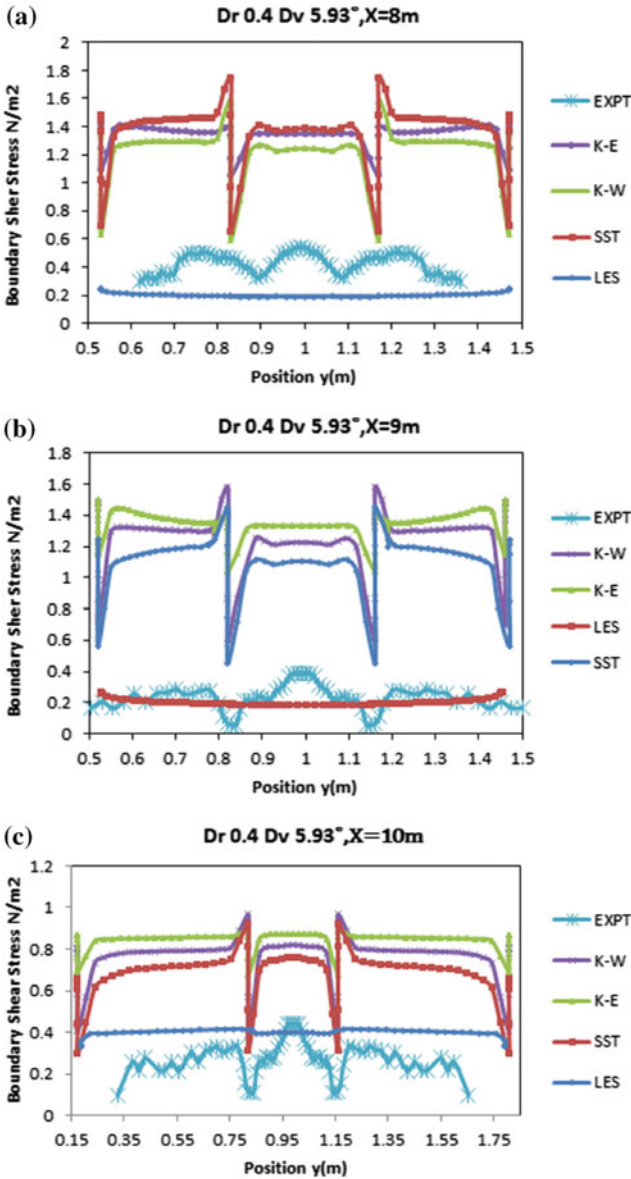


**Fig. 4.9** **a** Comparison of boundary shear stress in section  $x = 8$  m. **b** Comparison of boundary shear stress in section  $x = 9$  m. **c** Comparison of boundary shear stress in section  $x = 10$  m. **d** Comparison of boundary shear stress in section  $x = 12$  m. **e** Comparison of boundary shear stress in section  $x = 8$  m (Diverging angle  $9.83^\circ$ ). **f** Comparison of boundary shear stress in section  $x = 11$  m (Diverging angle  $9.83^\circ$ ). **g** Comparison of boundary shear stress in section  $x = 8$  m (Diverging angle  $9.83^\circ$ ). **h** Comparison of boundary shear stress in section  $x = 8.75$  m (Diverging angle  $9.83^\circ$ ). **i** comparison of boundary shear stress in section  $x = 10.25$  m (Diverging angle  $9.83^\circ$ ). **j** Comparison of boundary shear stress in section  $x = 11$  m

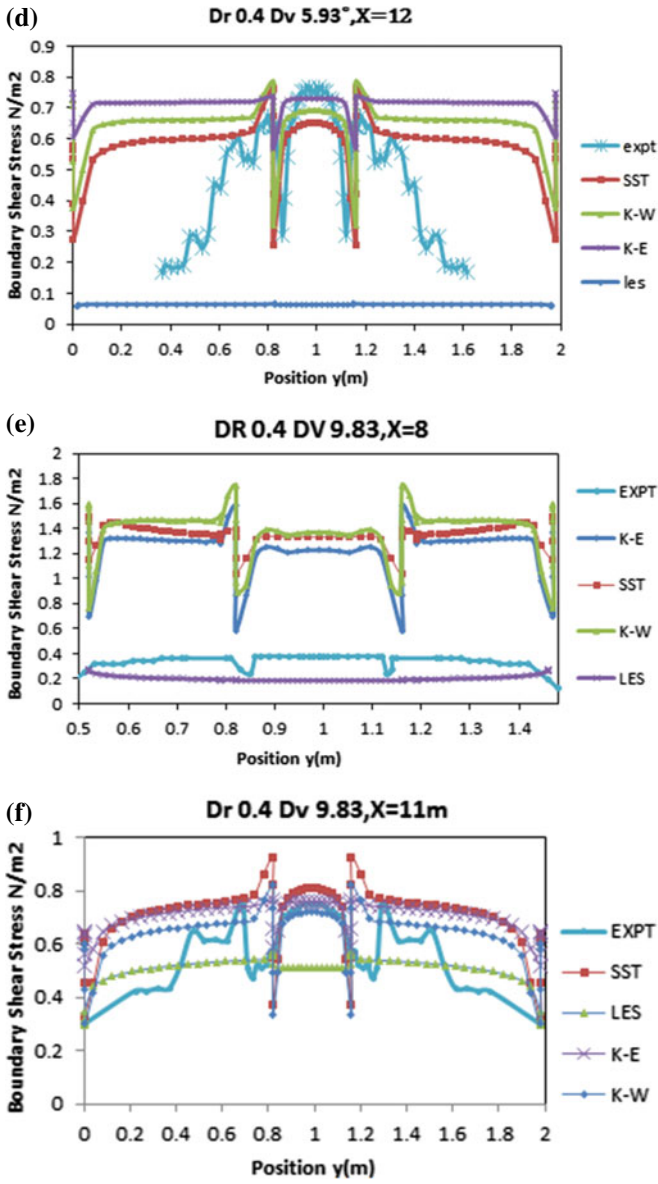
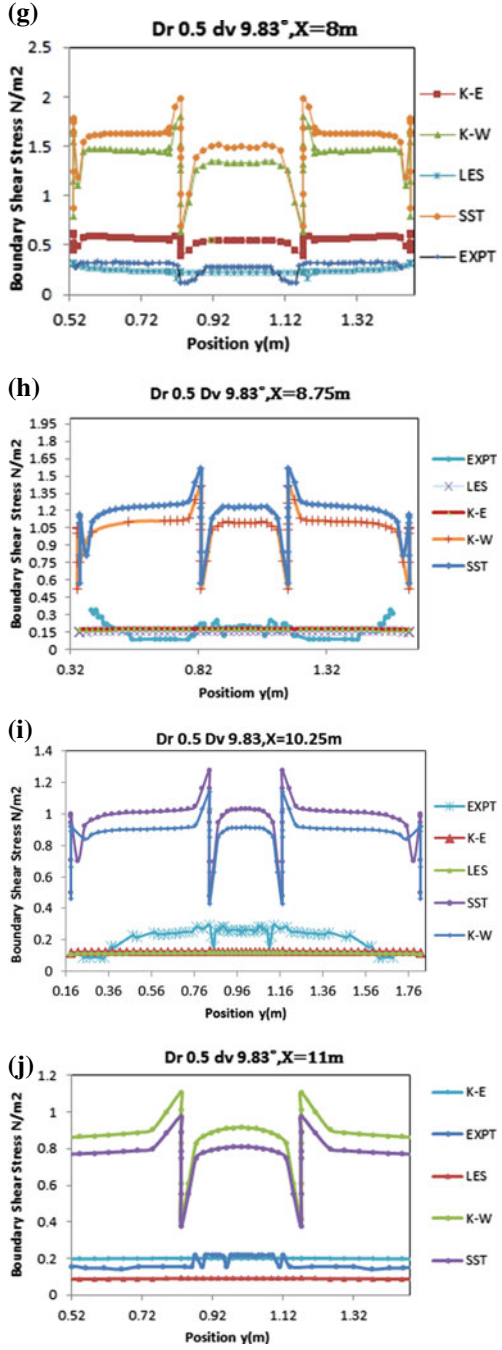


Fig. 4.9 (continued)

Fig. 4.9 (continued)





#### 4.3.1.1 Numerical result validations of 5.93°

Similarly, here also from channel geometry experimental data were taken from the six sections ( $X = 8, 9, 10, 11, 12, 13$  m) with two different depth ratio such as  $Dr = 0.4$  and  $0.5$  and numerical models also applied along these sections. Above here  $X$  represents distance of the section from inlet of the channel. Graphs showing the comparison were given in next page .

In the above graphs, we can analyze and compare very nicely that boundary shear stress distribution of experimental results of the channel having  $Dr = 0.4$  and of  $5$  m diverging length shows a symmetrical pattern with ANSYS results at the different measurement sections of channel. Among all the turbulence models applied here in most of sections such as Fig. 4.9a–c, LES model was giving most approximate result as compared to other models here used. As from the above figure, we have concluded about the distributions of boundary shear stress that (i) numerical analysis proved to be in good agreement with the experimentation, (ii) boundary shear stress increases along the diverging part of the flume.

#### 4.3.1.2 Numerical result validation for 9.83° (3 m diverging length)

Similarly, here also from channel geometry experimental data were taken from the five sections ( $X = 8, 8.75, 9.5, 10.25, \text{ and } 11$  m) with two different depth ratio such as  $Dr = 0.4$  and  $0.5$  and numerical models also applied along these sections.

In the above graphs, we can analyze and compare very nicely that boundary shear stress distribution of the experimental results of channel  $Dr = 0.4$  and  $0.5$  of  $3$  m diverging length shows a symmetrical pattern with ANSYS results at different measurement sections of the channel. Among all the turbulence models applied here in most of the sections such as Fig. 4.9d–f, LES model was giving most approximate result as compared to other models here used. As from above comparison we have concluded that the distributions of boundary shear stress that (i) numerical analysis proved by giving good agreement with the experimentation, (ii) boundary shear stress increases along the diverging part of the flume.

### 4.4 Conclusion

From the experimental analysis, we got point to point data from the wetted perimeter of the various sections of the channel and further plotted in graphs and analyzed the distribution of boundary shear stress. The analysis shows that the boundary shear stress is maximum in the main channel, and it gradually decreases as we move from main channel to flood plain. The boundary shear stress distributions are plotted from the data computed from the ANSYS using four turbulence model named as LES model,  $k-\epsilon$  model,  $k-\omega$ , model, and SST model for different sections, which was compared with the boundary shear stress graph plotted from the experimental

data. It was found that the obtained graphs are not perfectly coinciding but with less error LES model with respect to others model. Hence, we found out that the LES model is can be applied for the analysis of boundary shear stress in compound channel flows, and it gradually decreases as we move from main channel to flood plain. The boundary shear stress distributions are plotted from the data computed from the ANSYS using four turbulence model named as LES model,  $k-\epsilon$  model,  $k-\omega$  model, and SST model for different sections, which was compared with the boundary shear stress graph plotted from the experimental data. It was found that the obtained graphs are not perfectly coinciding but with less error LES model with respect to others model. Hence, we found out that the LES model is can be applied for the analysis of boundary shear stress in compound channel flow.

## References

- Bathurst JC, Hey RD, Thorne CR (1979) Secondary flow and shear stress at river bends. *J Hydraul Div* 105(10):1277–1295
- Cater JE, Williams JJR (2008) Large eddy simulation of a long asymmetric compound open channel. *J Hydraul Res* 46(4):445–453
- Das BS, Khatua KK (2018) Flow resistance in a compound channel with diverging and converging floodplains. *J Hydraul Eng* 144(8):04018051
- Das BS, Khatua KK, Devi K (2017) Numerical solution of depth-averaged velocity and boundary shear stress distribution in converging compound channels. *Arab J Sci Eng* 42(3):1305–1319
- Ghosh S, Jena SB (1971) Boundary shears distribution in open channel compound. *Proc Inst Civ Eng* 49(4):417–430
- Khatua KK, Patra KC (2010) Evaluation of boundary shears distribution in a meandering channel. In: *Proceedings of ninth international conference on hydro-science and engineering*. IIT Madras, Chennai, India, p 74
- Knight DW (1981) Boundary shears in smooth and rough channels. *J Hydraul Div Am Soc Civil Eng* 107(7):839–851
- Knight DW, Yuan YM, Fares YR (1992) Boundary shears in meandering channels. In: *Proceedings of the Institution Symposium on Hydraulic research in nature and laboratory Paper No.11017*, vol. 118. Wuhan, China, pp 151–159
- Larocque LA, Imran J, Chaudhry MH (2013) 3D numerical simulation of partial breach dam-break flow using the LES and  $k-\epsilon$  turbulence models. *J Hydraul Res* 51(2):145–157
- Larocque LA, Imran J, Chaudhry MH (2012) Experimental and numerical investigations of two-dimensional dam-break flows. *J Hydraul Eng* 139(6):569–579
- Myers RC, Elsayw EM (1975) Boundary shears in channel with flood plain. *J Hydraul Div* 101
- Patel VC (1965) Calibration of the Preston tube and limitations on its use in pressure gradients. *J Fluid Mech* 23(01):185–208
- Preston J (1954) The determination of turbulent skin friction by means of Pitot tubes. *J R Aeronaut Soc* 58(518):109–121
- Salvetti MV, Zang Y, Street RL, Banerjee S (1997) Large-eddy simulation of free-surface decaying turbulence with dynamic subgrid-scale models. *Phys Fluids* 9(8):2405–2419

# Chapter 5

## Turbulence Flow Statistics Downstream of Grids with Various Mesh Sizes



Pankaj Kumar Raushan, Santosh Kumar Singh, and Koustuv Debnath

**Abstract** An experimental approach was performed to examine the interaction between the rigid boundary and grid turbulence of different mesh sizes. Three unlike mesh sizes ( $M_1$ ,  $M_2$  and  $M_3$ ) were used having a constant diameter ( $d$ ) and cross-section. Variation of mean velocities in stream-wise and vertical direction, turbulent intensities, Reynolds shear stresses and turbulence kinetic energy at the different locations of the grid  $M_1$ ,  $M_2$  and  $M_3$  are discussed. The time series of velocity was measured by an acoustic Doppler velocimetry (ADV). The measured data of velocity fluctuations were used to understand the variations of turbulent characteristics behind the grids with rigid boundary interaction.

**Keywords** ADV · Grid turbulence · Mesh sizes · Flume experiment · Mean velocity · Turbulence kinetic energy

### 5.1 Introduction

Turbulence created due to the grid is a conventional problem since the theory of isotropic turbulence has been developed to understand the transport phenomenon in turbulent flow. Therefore, to achieve the nearly isotropic turbulence by an experimental method, the grid turbulence is a convenient way. Turbulence generated due to the grid can be mainly divided into close and far-field regions. Closed to the grid region, the formation of wakes is generated, and the turbulence generated mainly depends upon the size of the grid, whereas far away from the grid, homogeneous isotropic turbulence can be observed as suggested by Batchelor (1953). A broad study has been executed in the region away from the grid for the authentication of homogeneous isotropic turbulence [HIT] (Detailed study are provided in Batchelor

---

P. K. Raushan (✉) · K. Debnath

Department of Aerospace Engineering and Applied Mechanics, Indian Institute of Engineering Science & Technology, Shibpur, Howrah 711103, India

S. K. Singh

Department of Mechanical Engineering, SRM Institute of Science and Technology, Kattankulathur 603203, India

1953). Mohamed and LaRue (1990) suggested that the nearly isotropic flow can be observed at far-field region of the grid and the homogeneity of the flow also depend on grid geometry. Further, Krogstad and Davidson (2011) suggested that in the adjacent zone the grids act in an alike way that of fractal grids, whereas in the zone away from the grid it follows the classical decay. Grzelak and Wierciński (2017) performed an experiment in the presence of the grid with different mesh sizes over the rigid flat surface. Recently, the study on the passive grid was performed by Vita et al. (2018). They suggested that for  $x \approx 5Mx$  the isotropic and homogeneous flow can be achieved. More recently, Raushan et al. (2018, 2019) investigated experimentally that far-field region of the grid is also affected by rigid boundary and it produces its own dissipative mechanism as result the homogeneity of the flow in grid turbulence is affected.

The objective of the present work is to comprehend the turbulence flow characteristics produced by the grid of three different mesh sizes and their interaction with rigid boundary. The present paper reported in four parts. The first part is introduction related to grid-generated turbulence; the second parts deal with the experimental set with grid configurations and measurement technique of fluid velocity, the third part contains the results and discussion based on our experiment for the study of grid-generated turbulence for different mesh sizes. Finally, the conclusions have been presented in the four-part.

## 5.2 Experimental Setup and Procedure

Experiments of different grid cases were performed in the water channel facility at the IEST, Shibpur, India. The detail description of the experimental setup is provided in our recent studies (Singh et al. 2016). The schematic of the experimental setup of the water channel with grids having three mesh sizes is provided in Fig. 5.1. The details description of the experimental condition are given in Raushan et al. (2018, 2019). The coordinate system for the considering the origin as shown in (Fig. 5.1) and the instantaneous three-dimensional velocity field were recorded at upstream and downstream of the grids by using the ADV instrument. The experimental geometry for the grid had three different mesh sizes, solidity ratio, mesh Reynolds number and experimental condition are given in Table 5.1. The calculation made for the grid solidity ratio ( $\sigma$ ) is used from the formula,  $\sigma = (d_b/M)(2 - d_b/M)$  which is described in (Raushan et al. 2018, 2020a), and it also is presented in Table 5.1.

To maintain the stability of the flow as well as similar pressure drop for the same flow condition, the value of the grid solidity ratio here used is lower than 0.5 [Cardesa et al. 2012]. The instantaneous velocity data was recorded by ADV for the duration of 300 s with the sampling rate of 40 Hz. The detailed processing method for the time-series data, measuring technique and filtering method was used here is provided in (Singh and Debnath 2016, 2017; Raushan et al. 2020b).

The time-averaged of turbulence characteristics such as variation of mean velocities, turbulent intensities and Reynolds shear stresses are computed by using standard

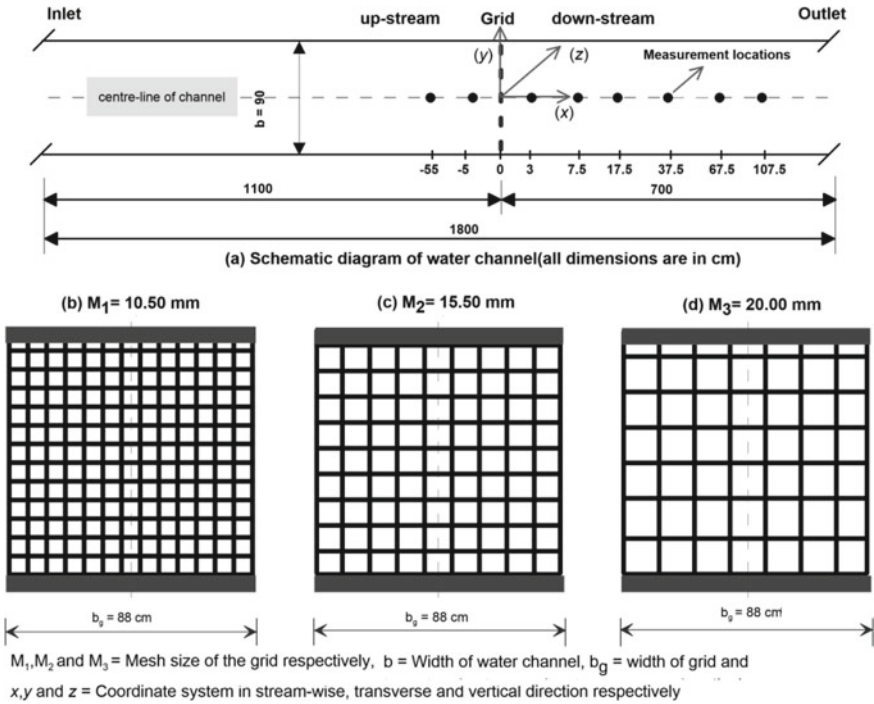


Fig. 5.1 Schematic of experimental setup with grids of different mesh sizes

procedure (Nezu and Nakagawa 1993; Singh et al. 2017, 2018). Further, for ease of compression, the turbulence quantities are normalized by the shear velocity ( $u_* = 0.012$  m/s), which is calculated from log-law (for detail refer Singh and Debnath 2017) and therefore the following normalized nomenclature is used here.

$$\hat{u} = \bar{u}/u_*, \hat{w} = \bar{w}/u_*, u^+ = u_{r.m.s}/u_*, w^+ = w_{r.m.s}/u_* \text{ and } uw^+ = \overline{u'w'}/u_*^2 \quad (5.1)$$

### 5.3 Experimental Results and Discussion

#### 5.3.1 Variation of Time-Averaged Velocity

The profile of  $\hat{u}$  and  $\hat{w}$  is plotted in Figs. 5.2 and 5.3 with  $z/h$  for the grid having three mesh sizes, and it is compared with the without grid condition in fully developed region.

**Table 5.1** Experimental conditions

Representation of Grid (mm)	solidity ratios ( $\sigma$ )	Dia of the bar( $d$ ) (mm)	Stream-wise maximum velocity ( $U_0$ ) (m/s)	Mesh Reynolds Number ( $Re_M$ )	Water depth ( $h$ ) (m)
$M_1 = 10.50$	$\sigma_1 = 0.2653$	$d_b = 1.5$	$U_0 = 0.18$	2700	0.22
$M_2 = 15.50$	$\sigma_2 = 0.1841$	$d_b = 1.5$	$U_0 = 0.18$	2790	0.22
$M_3 = 20.00$	$\sigma_3 = 0.1443$	$d_b = 1.5$	$U_0 = 0.18$	3600	0.22

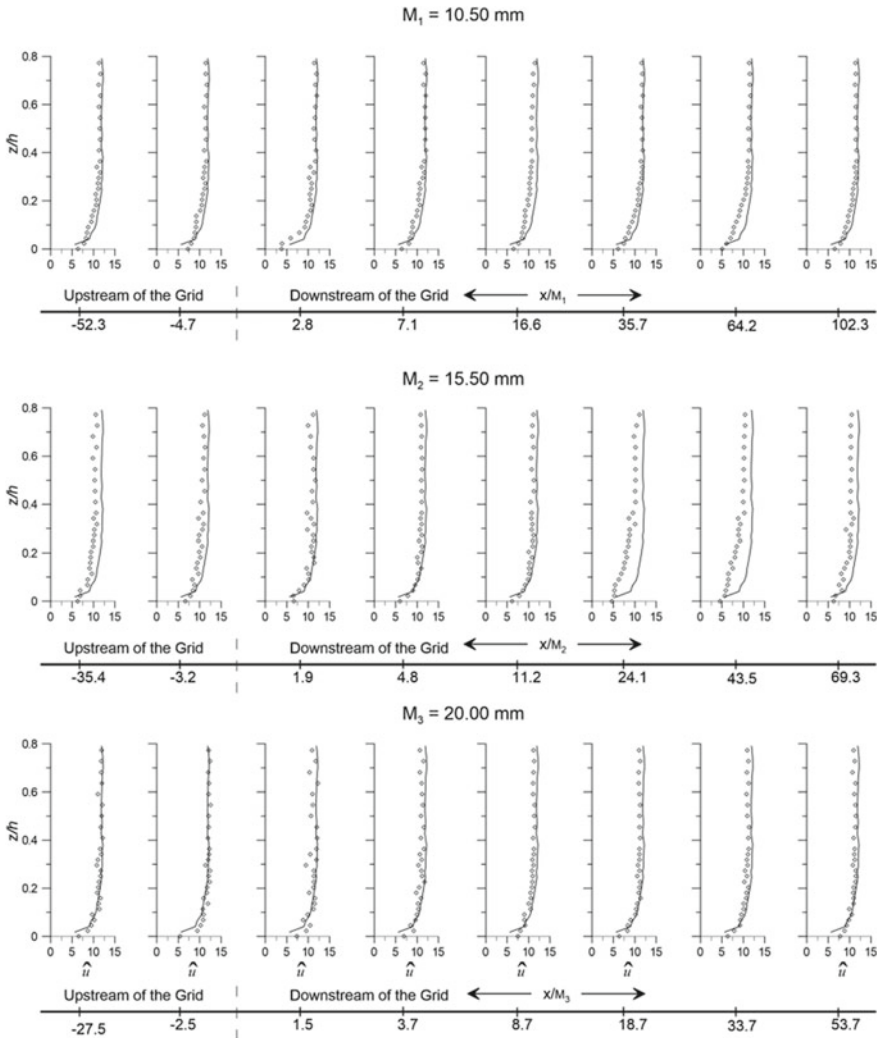


**Fig. 5.2** Evolution of dimensionless mean  $\hat{u}$  at the different locations. Here, solid line represents without grid case

It is observed from the profile that before the grid  $\hat{u}$  and  $\hat{w}$  are almost the same for the entire flow depth comparison to the absence of grid for all three cases. The velocities are enhanced close to the near boundary region for M3 case, which indicates that the velocities are overshooting and the developing of jet pattern that advecting from the grid wires (Torrano et al. 2015; Raushan et al. 2018). As it increases along the downstream distances of the grid, the behaviour of overshooting flow decreases and it is matched to the without grid case data. Observed from Fig. 5.3 reveals that the magnitude of dimensionless vertical mean velocities  $\hat{w}$  is lesser compared to  $\hat{u}$

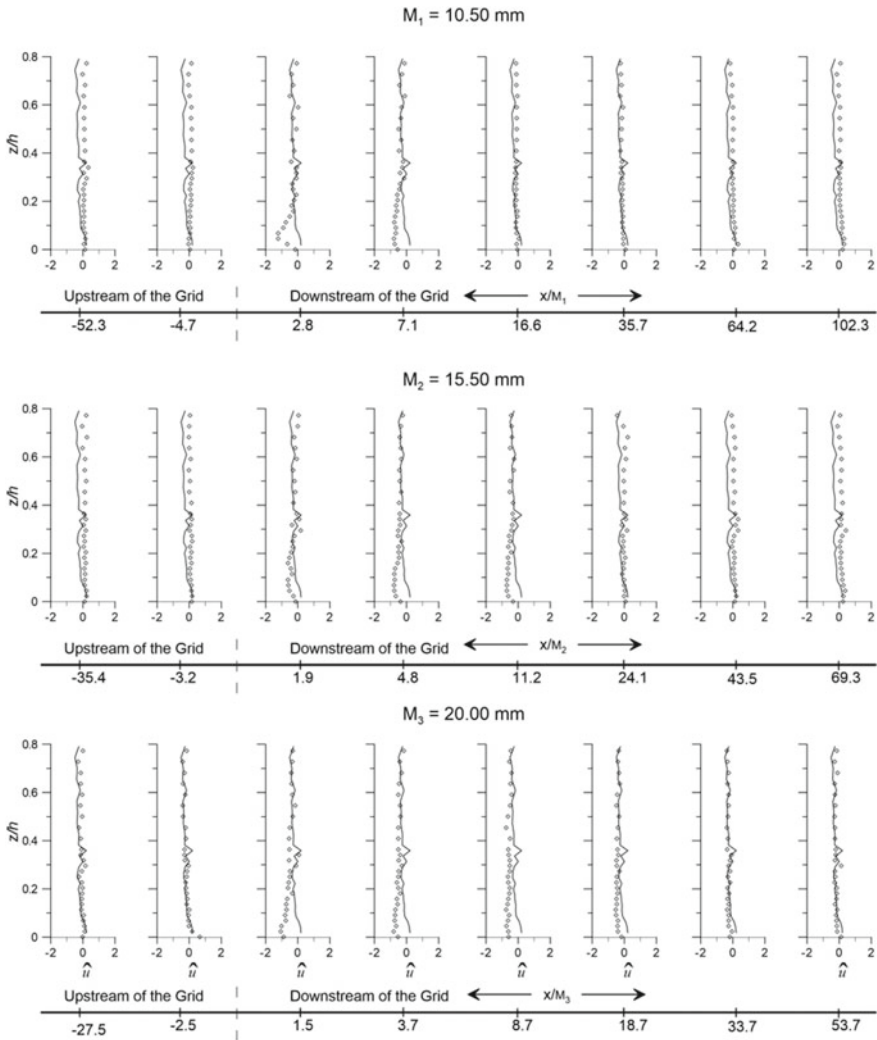


**Fig. 5.3** Evolution of dimensionless mean velocities in the vertical direction at the different locations. Here, solid line represents without grid case

but two important behaviours in the plot are examined due to amend in mesh size of the grid. Behind the grids having three mesh sizes, flow migrates in the downward direction up to  $z/h \leq 0.25$  and afterwards, the vertical velocity profile matched with without grid data.

This is probably because  $M_1$  type grid produces tubby hindrance in the flow as the contrast to  $M_2$  and  $M_3$ . For smaller mesh sizes ( $M_1$ ), the zone of negative values for mean vertical velocity is  $x/M_1 \leq 7.1$ , whereas for  $M_2$  and  $M_3$ , the zone is extended to  $x/M_2 \leq 11.2$  and  $x/M_3 \leq 18.7$ , respectively.



### 5.3.2 Evolution of Turbulent Intensities and Turbulence Kinetic Energy

The profile of dimensionless turbulent intensities, i.e.,  $u^+$  and  $w^+$  are plotted with  $z/h$  in Figs. 5.4 and 5.5 for three different mesh sizes along with flat rigid surface data for the comparison purpose. At the upstream of the grid, the results show that both the intensities almost matched well compared to the without grid case except near boundary region.

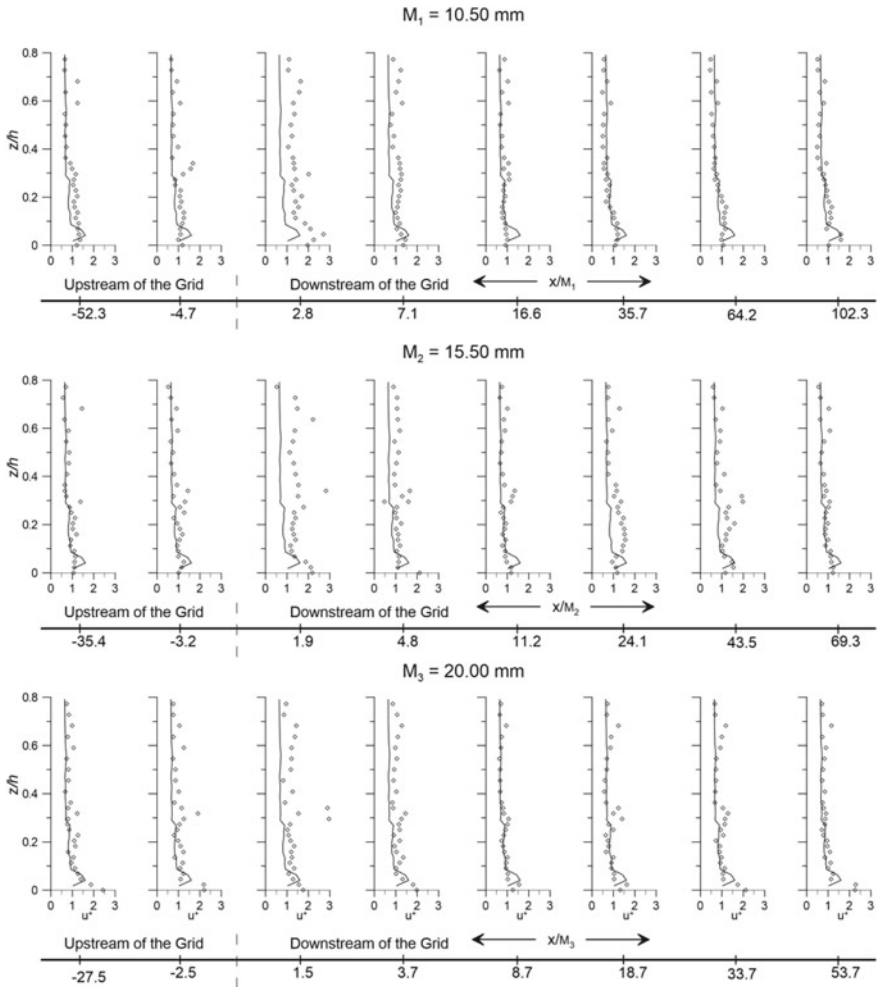


**Fig. 5.4** Evolution of dimensionless mean turbulent intensities along the stream-wise direction at the different locations. Here, the continuous solid line denoting without grid condition

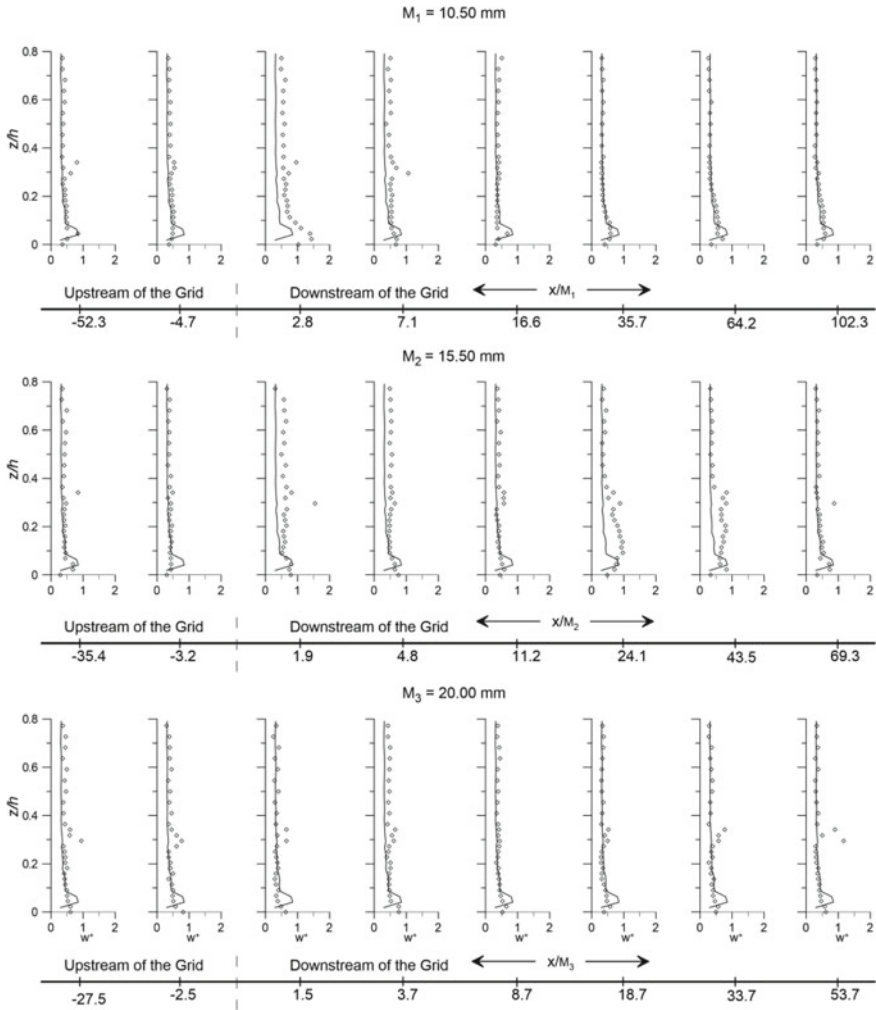


**Fig. 5.5** Evolution of dimensionless turbulent intensities in the vertical direction at the different locations. Here, solid line represents without grid condition

The  $u^+$  and  $w^+$  reduces as the flow reaches closed to the grid because of narrowing upshot and rearrangement of pressure on the upstream side close to the bed. It is also observed that the normalized turbulent intensities increase as the mesh size decreases and the values of these 3, 2 and 1.5 for lower to higher mesh size, respectively, at the downstream of the grid. The magnitude of turbulence intensities is higher compared to the without grid data which is inline with the observation of Raushan et al. (2018). However, the turbulent intensities in vertical direction increase for  $M_1$  compared to the without grid data. It is also to noted that the turbulent value intensities in the stream-wise and vertical direction at the downstream of the grid for the three mesh

sizes are almost matched to the without grid condition for  $x \geq 16.6M_1$ ,  $x \geq 11.2M_2$  and  $x \geq 8.7M_3$ , respectively. Torrano et al. (2015) and Raushan et al. (2018) also that, these results are good agreement with previous work same as that the intensities of turbulence in stream-wise direction decaying behaviour at the downstream along the longitudinal direction.

To understand the decay process, the term turbulent kinetic energy (TKE) per unit density is evaluated from the standard procedure (Raushan et al. 2018) and is normalized by friction velocity ( $k^+ = k/u_*^2$ ). The profile of dimensionless TKE for all the cases are shown in Fig. 5.6, and it is compared with without grid condition. It is observed that just behind the grid in all three cases, the normalized TKE augments against the flow depth compared to the without grid condition. With further increase in  $x/M$  for  $M_1$ ,  $M_2$  and  $M_3$  the profile of  $k^+$  is more or less alike with the profile of without grid case, indicating decaying of turbulence kinetic energy in grid turbulence. The observation from the normalized profile of turbulence kinetic energy is that the production is significantly dominant up to certain mesh sizes in the longitudinal direction. The present results finding from experiment related to the decaying of turbulence kinetic energy are in line with the result of Cardesa et al. (2012) and Raushan et al. (2018).

## 5.4 Conclusions

The finding from the above experimental results is summarized as follows:

- The results show that velocities deficit for the smaller mesh size behind the grid are 10 and 12% more than comparison with the  $M_2$  and  $M_3$  at  $z/h \leq 0.3$  with reference to without grid condition.
- At downstream of  $M_1$ ,  $M_2$  and  $M_3$  the vertical velocity vector in the upward direction up to region  $z \leq 0.25 h$  from the rigid boundary.
- The turbulent intensities in stream-wise direction are increases with the mesh sizes due to the shear layer formation.
- The turbulent kinetic energy is increased by approximately 90% at the downstream of the grids which are similar to turbulent intensities variation. However, it decreases rapidly in the stream-wise direction which signifies that the effect of the interaction of bottom surfaces with the mesh sizes is reduced.

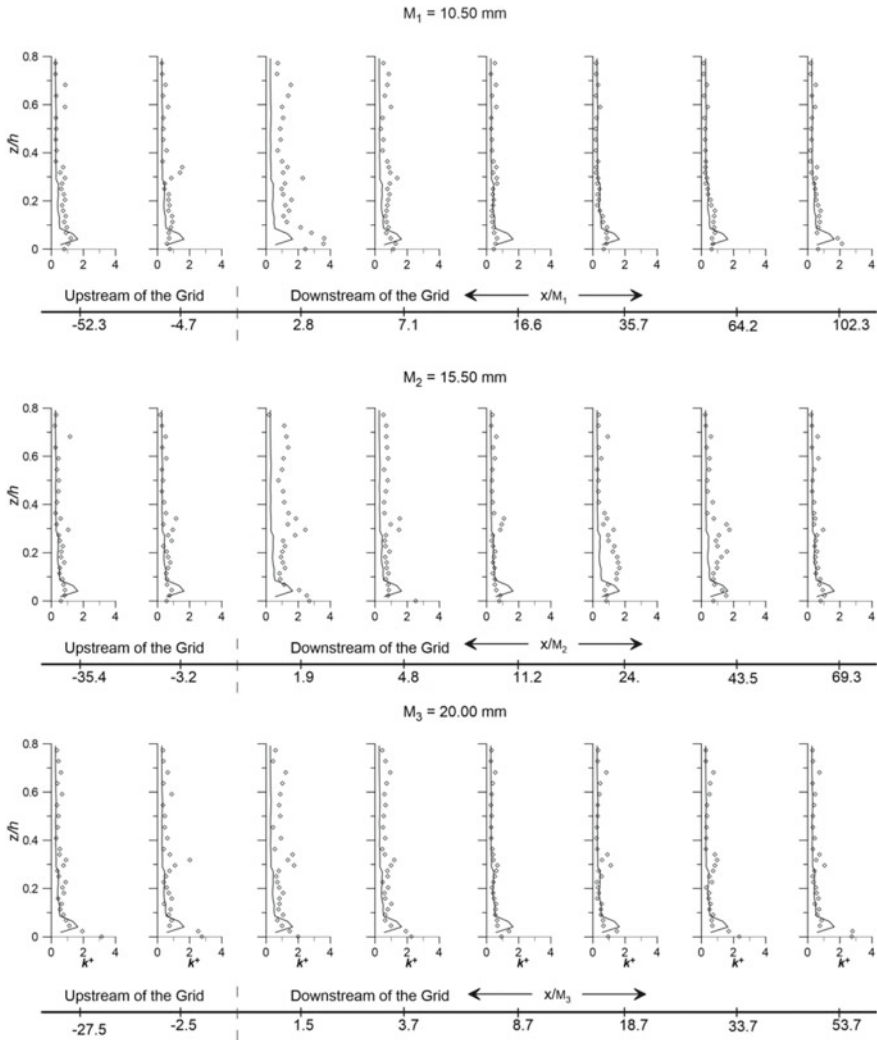


**Fig. 5.6** Evolution of dimensionless turbulent kinetic energy (TKE) at the different locations. Here, solid line represents without grid case

## References

Batchelor GK (1953) The theory of homogeneous turbulence. Cambridge University Press, London

Cardesa JI, Nickels TB, Dawson JR (2012) 2D PIV measurements in the near field of grid turbulence using stitched fields from multiple cameras. *Exp Fluids* 52:1611. <https://doi.org/10.1007/s00348-012-1278-4>

Grzelak J, Wierciński Z (2017) Length scale of free stream turbulence and its impact on bypass transition in a boundary layer. *J Appl Fluid Mech* 10:713–724

- Krogstad P, Davidson PA (2011) Freely decaying, homogeneous turbulence generated by multiscale grids. *J Fluid Mech* 680:417–434
- Mohamed MS, LaRue JC (1990) The decay power law in grid-generated turbulence. *J Fluid Mech* 219:195–214
- Nezu I, Nakagawa H (1993) *Turbulence in open-channel flows*. Balkema CRC Press, Rotterdam A.A
- Raushan PK, Singh SK, Debnath K (2018) Grid generated turbulence under the rigid boundary influence. *J Wind Eng Ind Aerod* 182:252–261
- Raushan PK, Singh SK, Debnath K (2019) Grid-generated turbulence in pulsating flow under the rigid boundary influence. *Eur J Mech B Fluid* 78:291–305
- Raushan PK, Singh SK, Debnath K (2020a) Role of rigid boundary on the decay of turbulence generated by passive-grid for free surface flow. *Proc Inst Mech Eng Part C J Mech Eng Sci* 0954406220942565
- Raushan PK, Singh SK, Debnath K (2020b) Turbulence anisotropy with higher-order moments in flow through passive grid under rigid boundary influence. *Proc Inst Mech Eng Part C J Mech Eng Sci* 0954406220969736
- Singh SK, Debnath K (2016) Combined effects of wave and current in free surface turbulent flow. *Ocean Eng* 127:170–189
- Singh SK, Debnath K (2017) Turbulent characteristics of flow under combined wave-current motion. *ASME J Offshore Mech Arct Eng* 139(2):021102
- Singh SK, Debnath K, Mazumder BS (2016) Spatially-averaged turbulent flow over cubical roughness in wave-current co-existing environment. *Coast Eng* 127:170–189
- Singh SK, Debnath K, Mazumder BS (2017) Turbulence over cube-mounted rough bed using spatiotemporal averaging approach. *Can J Civ Eng* 44(7):504–517
- Singh SK, Raushan PK, Debnath K (2018) Turbulent characteristics of pulsating flow over hydraulically smooth surface. *Eur J Mech B Fluids* 68C:10–19
- Torrano I, Tutar M, Agirre MM, Rouquier A, Mordant N, Bourgoin M (2015) Comparison of experimental and RANS-based numerical studies of the decay of grid-generated turbulence. *J Fluid Eng* 137(6):061203
- Vita G, Hemida H, Andrienne T, Baniotopoulos CC (2018) Generating atmospheric turbulence using passive grids in an expansion test section of a wind tunnel. *J Wind Eng Ind Aerod* 178:91–104

# Chapter 6

## Review on Hydraulics of Meandering Rivers



Jyotirmoy Barman, Jyotismita Taye, and Bimlesh Kumar

**Abstract** A meander is a bend in a sinuous watercourse or river. It consists of a series of turns with curvatures in alternate directions which are connected at the points of inflection or by short straight crossings (Dey). Scientists and researchers are studying the hydrodynamics, morphology, bed topography, etc. of meandering rivers for a very long time. The details of secondary flow become an integral part for some researchers while studying meandering rivers. The role of the centre region cell and the presence of the outer bank cell have also been investigated by many researchers and experts. The centre region cell or helical motion occurs due to unequal forces between centrifugal force and pressure force with flow near the surface directed towards the outer bank and that near the bed directed towards the inner bank. Many of them also tried to find the relation between outer bank circulation cell and bank shear stresses and how it affects bank erosion. Researchers and experts have worked to find out various parameters like mean flow, Reynolds shear stress, turbulent kinetic energy (TKE), etc. and their interactions in meander bends. A lot of field and laboratory experiments have been carried out with different conditions to understand the behaviour of meandering rivers.

**Keywords** Secondary flow · Centre region cell · Outer bank cell · Reynolds shear stress · TKE

---

J. Barman · J. Taye · B. Kumar (✉)  
Department of Civil Engineering, Indian Institute of Technology, Guwahati 781039, India  
e-mail: [bimk@iitg.ac.in](mailto:bimk@iitg.ac.in)  
URL: <http://www.iitg.ac.in/bimk/homepage/index.html#>

J. Barman  
e-mail: [jyoti174104121@iitg.ac.in](mailto:jyoti174104121@iitg.ac.in)

J. Taye  
e-mail: [taye176104022@iitg.ac.in](mailto:taye176104022@iitg.ac.in)

**Fig. 6.1** Meandering River  
(Source laurasriverfeatures.weebly.com)



## 6.1 Introduction

The word meander originated from the Greek word *Maiandros*. A meander is a bend in a sinuous watercourse or river. A meander can be defined as a series of turns, loops, bends or windings in the channel of a river or other watercourse (Fig. 6.1). Sine generated curve closely approximates natural river meanders, and it has become a popular way of considering the path of a meandering stream. A meander contains only one channel that winds its way across the floodplain as opposed to a braided river which consists of a network of small and often temporary islands called braid bars. Meanders are often noticed in a river's mature stages which later in old stages become vigorous. Meandering rivers are formed when the sinuosity (channel length/valley length) of the river is more than 1.5 (Leopold and Wolman 1957). Sinuous river (sinuosity is 1.1–1.5) is the bridge between a straight river (sinuosity <1.1) and a meandering river. The continuous erosion and deposition of the outer and inner banks of the river, respectively, for a very long period of time lead to the formation of a meandering river. The study of meander bends is an integral part of studying meandering rivers. Researchers and experts have worked to find out various parameters like mean flow, turbulence, etc. and their interactions in meander bends. A lot of field and laboratory work have been done to understand the behaviour of the meandering river.

## 6.2 Early Studies

A lot of literature has been produced regarding various aspects of meandering rivers like mechanics of meandering rivers, modelling of meandering rivers, bed topography, etc. and each of these aspects forms a separate and ongoing research topic. Thompson (1876) was one of the first people to explain the formation of cells in secondary currents in curved open channels. Before Thompson (1876) and Boussinesq (1868) obtained the two layer solution flowing in the opposite direction by solving theoretically the problem of viscous fluid flowing in the curved and prismatic open channel of slowly varying curvature. Rozovskii (1957) revised the solution incorporating in mechanics of river bends and later revisited again by Engelund (1974) and Johannesson and Parker (1989).

Rozovskii (1957) was one of the first people to have developed a velocity rotation scheme to separate the secondary flow from the primary flow. Rozovskii have done

field study in the Desna river, Ukraine. The breadth of the study area is 150 m, flow depth is 3.5 m and aspect ratio is 43. The Rozovskii method calculates the cross stream compared to the mean flow direction at each vertical, which forces a zero net discharge in inward and outward directions. As a result, instead of defining the velocity profile in the entire cross section, the strength of the secondary flow is found out at each velocity profile locally. But the Rozovskii method has limitations as it shows the secondary circulation on a local basis and fails to produce the complete details of the cross-stream velocity field. Moreover, in computational fluid mechanics, the velocities are addressed in global coordinates without the need of using correction angles to account for zero net cross-stream discharge.

### 6.3 Field Studies

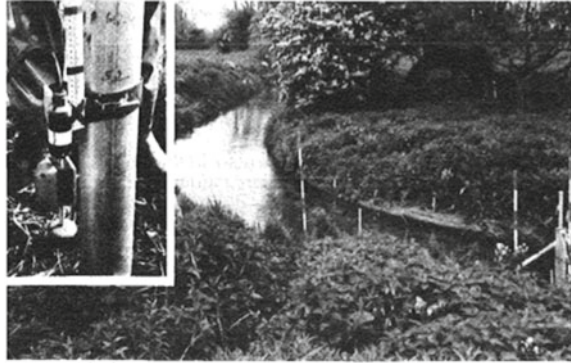
A lot of researchers have worked in natural meandering rivers to see different parameters like mean flow, Reynolds shear stress, TKE, etc. and how does they affect the various aspects like morphology, bed topography, stability of banks, etc. Rozovskii, Vriend, Geldof, Rhoads, Sukhodolov, etc. have given a noteworthy contribution towards this field.

Vriend and Geldof (1983) studied the flow velocity in river bends of shorter reach in two consecutively sharply curved short bends in the river Dommel, the Netherlands, and compared the results with a mathematical model for the depth-averaged main flow velocity. The geometry of the bed and its flow velocity measurements were implemented in a 285 m long section of the river Dommel. Vriend and Geldof did not consider the secondary flow convection because when they applied their mathematical model without any modification to the present flow case, it leads to erroneous results. In the present study of the bends, the mathematical model should describe double-cell pattern formation so that secondary flow convection could be incorporated. From this study, they concluded that the mathematical model they used works in most parts of the two bends if the secondary flow convection is not taken into account. The secondary flow convection is important in the last part of each bend. There is a gradual outward shift of the maximum velocity further downstream of the bend which is due to the retarded adaptation of the flow to the bed configuration and not due to the secondary flow convection. The limitation of this experiment is that it holds good only for sharply curved short bends in steeply banked channels which have a pronounced cross-sectional asymmetry.

Anwar (1986) conducted field measurements around a bend of a small river in Chiselhampton, Oxfordshire (U.K.) (Fig. 6.2). The inner and outer radii of the bend are 19 m and 22 m, respectively. The instantaneous velocities in all three directions, i.e. streamline, lateral and vertical, are analysed. Some contrasting results are found regarding velocity profile, isovels, normal stresses, etc. in the entrance, exit and within the bend. The velocity profile does not follow the logarithmic profile in the bent part as opposed to the straight reach upstream from the bend. The isovels (stream velocity contour line) do not get affected at the bend entrance by the flow curvature, but it



**Fig. 6.2** Bend in flow direction with upstream straight reach

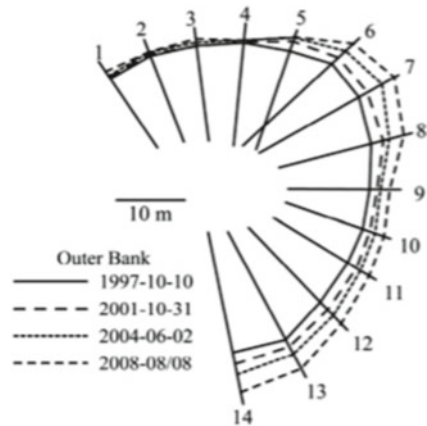


does get affected at the bend exit. The normal stress contours are the same at the bend entrance in three directions. But in the bend, it gets changed greatly where maximum stress occurs near the surface of the outer bank. The shear stresses are maximum at the outer bank near the apex, and it goes on decreasing downstream. The secondary flow played a good part in showing the anomalous behaviour in different parts of the bends.

With the advent of new technology, the study and research of meandering rivers reached new heights. The introduction of Acoustic Doppler Velocimeter (ADV) helped to take measurements of instantaneous velocities in three directions accurately compared to Electromagnetic Current Meter (ECM). Sukhodolov and Kaschtschewaja (2010) performed their experiments in the meander bend of the lowland river Spree in Germany using ADV. The channel considered is 30–40 m wide with a ripple-pool sequence. Other characteristics of the river include arc angle  $\alpha = 150^\circ$ , path length  $S_m = 760$  m, bend wavelength  $\lambda = 485$  m and sinuosity  $\lambda / S_m = 1.57$ . From the study, it can be said that the mean velocity profile is not fully logarithmic and only valid near the riverbed which is in agreement with Booij (2003). They found that the structure of mean and turbulent flow in the meander bend are three-dimensional and highly heterogenous as opposed to Rozovskii (1957) who assumed that shear stress is linearly distributed over the depth, tangential velocity follows the logarithmic law and eddy viscosity is parabolic. The field experiment also concluded that a small counteracting gyre can be seen near the outer bank which is similar to those observed in a laboratory by various researchers.

Engel and Rhoads (2012) studied the co-evolution of flow, bed morphology and channel planform in a compound meander loop in a span of 11 years. They studied the erosion of the outer bank in a meandering river for a span of 10 years. They did their study in the upper portion of the Embarras river watershed in Champaign County, Illinois. The study reveals the migration of the outer bank to a substantial amount in a span of 11 years (Fig. 6.3). They concluded that bank erosion and channel migration are driven by velocity and turbulence in the near-bank. The TKE magnitudes are greatest near the bank toe, downstream of the bend apex. The factors like failed bank blocks and flow deflection by point bars can increase or decrease the

**Fig. 6.3** Location of the outer bank during 11-year study



development of high velocities and TKE near the bank toe. The study also supports the hypothesis that compound loops gravitate towards planform complexity and not towards a stable meander form. The study suggests that rates and patterns of bank erosion and planform evolution can get influenced by local effects on the flow from failed blocks of bank material. Mathematical models don't consider the local effects and their influence on bank erosion and near-bank flow fields.

Engel and Rhoads (2017) studied the compound meander bend along Sugar Creek in McLean County, Illinois, USA. They examined the turbulent structure in the near-bank of the meandering channel as opposed to that of Sukhodolov (2012) who examined the patterns of turbulence only in the central region of the channel. The study of turbulence structure in the outer bank has been done in remarkable detail. The results showed a difference in vertical profiles of streamwise-vertical Reynolds stresses near the outer bank of meander bends to that of wide straight channels which is due to the effects of curvature-induced helical motion and local frictional effects associated with complex bank morphology in meandering channels. Some of the past work has shown the presence of an outer bank circulation cell (SOC) which acts as a counteracting effect on the outer banks of the meander bends (Blanckaert and Graf 2002; Blanckaert et al. 2013). This SOC is not observed clearly in this study either by ADCP or ADV measurements.

## 6.4 Laboratory Studies

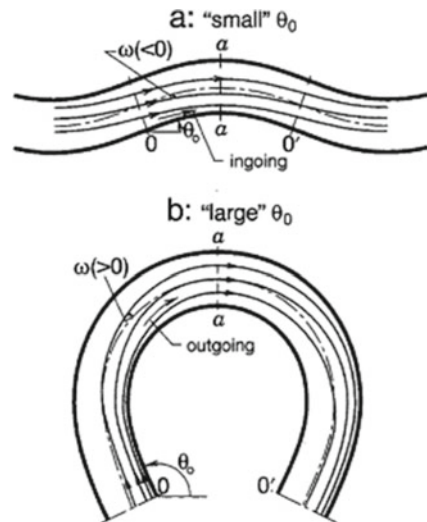
Laboratory studies have got an upper hand over field studies in the sense that conditions like bend angle, type of sand, discharge, etc. are in control of the person performing the experiment. But to replicate the exact nature of the river and its turbulence is very difficult. Another problem which comes in the way is the scaling problem. Most of the meandering rivers are big with a large width-to-depth ratio.

Many researchers have tried to study the behaviour of the meandering river by performing experiments in the laboratory using various conditions.

Silva (1995) developed a method in sine-generated meandering open channels to compute rough turbulent steady-state flows. The cross section of the flow is rectangular with constant width and periodic fluid motion. Silva tried to determine the initial flow both theoretically and experimentally. The theoretical part concerns the rationalisation of the equations of motion. The experimental part has two objectives. The first is whether the initial flow is really ingoing for small angles and outgoing for large angles or whether it is always of an ongoing nature as predicted by computations produced till that time (Fig. 6.4). The experiment is conducted in a laboratory using two meandering channels of 40 cm width. One is a small sinuous channel of  $30^\circ$  angle and another one is a large sinuous channel of  $110^\circ$  angle. The total length of the small sinuous channel is 5.4 m and that of the large sinuous channel is 18.6 m. After performing both theoretically and experimentally, Silva concluded that the flow in sine-generated meandering channels with an initial bed is not of a standard (ingoing) nature. It varies depending on the angle, breadth by height ratio and part of resistance factor due to friction factor, i.e. for small deflection angle between longitudinal channel axis and x-axis, the flow is ingoing whereas for large values it is outgoing. Silva also concluded that cross circulation is not necessary to explain the occurrence of point bar in the neighbourhood of the apex in the inner bank. This is an important conclusion as it explains the occurrence of point bar in large natural meander rivers with a large breadth-to-height ratio where cross circulation is hardly present.

Graf and Blanckaert (2002) have found some interesting results while doing laboratory experiments. They took a  $120^\circ$  meander bend with a flume of constant curvature of sand bed in vertical banks. They observed that the velocity distribution curve

**Fig. 6.4** Convergence and Divergence zones of meandering flows



in the bend deviates from the logarithmic profile (Fig. 5a). Furthermore, in addition to the classical helical motion (Thompson 1876; Rozovskii 1957) in the clockwise direction, they also observed the outer bank cell turning in anticlockwise direction (Fig. 5b). This bank cell acts as an outer-bank-protecting buffer zone, by keeping the core of maximum velocity away from the erosive bank. After analysing the data, they found that there is a reduction of shear stresses in the outer bank relative to the main channel. Though the experiment yielded good results, there are some limitations related to the experiment like the parameters were measured at 1 cross section (60°) only and limitations with measuring velocities and turbulence quantities near the boundaries.

Abad and Garcia (2009) did some extensive experiments in the laboratory and have used a different approach to study various parameters and their interactions. They

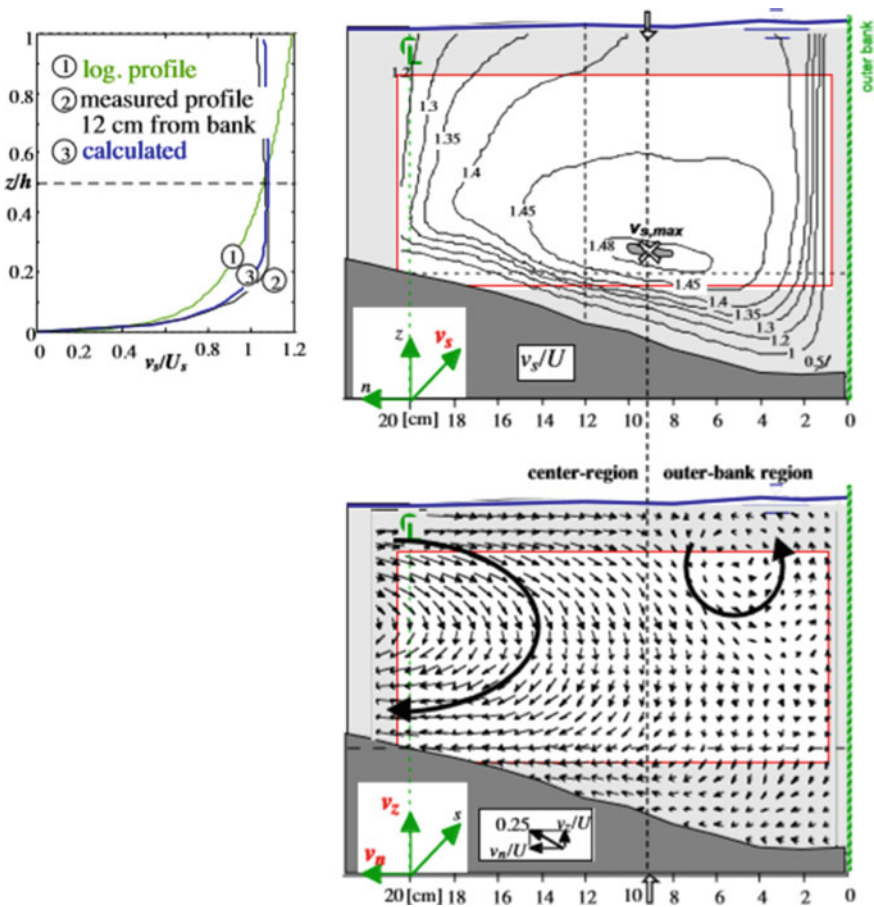


**Fig. 6.5** a Measured and calculated  $v_s$ -profile at 12 cm from outer bank compared to logarithmic profile; b downstream velocity,  $v_s/U$ ; c cross-stream motion  $(v_n, v_z)/U$

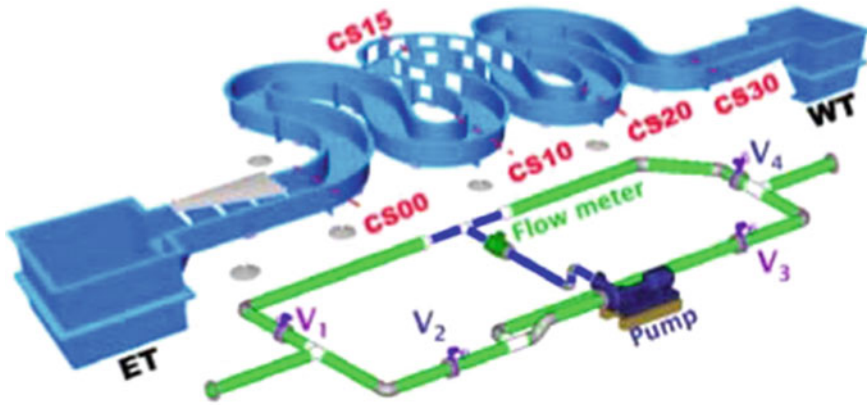


**Fig. 6.6** Meandering channel showing upstream valley orientation (ET to WT) and downstream valley orientation (WT to ET)

took a 200° compound bend (Kinoshita) flume and have considered flow in upstream and downstream skewed and compared the results (Fig. 6.6). They have modified the setup compared to Anwar (1986) who took a simple meander of 35° bend. It is asymmetric in nature and a rectangular smooth channel. They found that the bend which is oriented downstream the valley showed fully developed secondary flows, more developed bedforms along the bed and likely higher shear stresses along the bed and banks. They observed that there is a perfect correlation between turbulent kinetic energy ( $k$ ) with local curvature. The normal stresses  $\tau_{ss}$  have the major contribution to  $k$ , except downstream of the apex, where shear stresses  $\tau_{nm}$  are prevalent. The shear stress  $\tau_{sn}$  are the largest, with local maxima at the inner and outer banks. The limitation of this experiment is that the channel considered is rectangular and the results and patterns of flow will not necessarily match with the self-formed channels with developed pool and point bar topography.

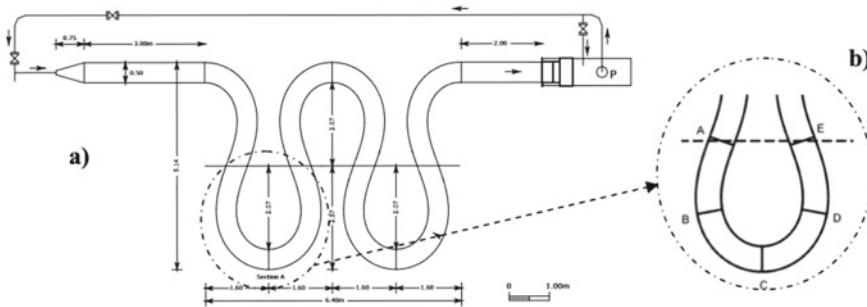


**Fig. 6.7** a) a plane view of the experimental apparatus; b) measurement sections

Jamieson et al. (2010) performed laboratory experiments in two different cases: developing and equilibrium beds. He performed the experiments on a  $135^\circ$  constant curvature flume with a sand bed. After analysing the data found from the experiments, he found that the thalweg migrated towards the outside wall through the bend rather than encroaching the outside wall as found out by previous researchers (Matsuura and Townsend 2004). This result indicates the presence of an outer bank circulation cell which rotates in opposite direction to that of the principal secondary flow cell. Due to this, the increase in outward flow is prevented from affecting the outer bank. The study goes well with Blanckaert and Graf (2002) with a difference that Blanckaert and Graf (2002) took data only from the outer half of a single cross section which makes it impossible to review the presence and growth of the outer bank circulation cell in other regions of the bend. From the study, he also concluded that the magnitude and distribution of normal stresses and turbulent kinetic energy are concentrated over the thalweg and the magnitude increases through the first half of the bend. The streamwise-cross-stream and cross-stream vertical Reynolds stresses increase as flow moves through the bend and the streamwise vertical stresses near-bank become less dominant. It was also found that the magnitudes of streamwise-cross-stream stresses at the outer bank are high relative to other stresses.

Termini (2009) conducted experiments to study the secondary circulation and how it affects the bank shear stress distribution and influences the bank stability. The experiment is conducted in a laboratory that follows a sine-generated curve of deflection angle  $110^\circ$ . The width of the channel is 0.5 m and has a rectangular cross section (Fig. 6.3). The experiment is conducted on two width-to-depth ratios, i.e. one is  $B/h < 10$  and the other  $B/h > 10$ . Termini concluded that for  $B/h < 10$ , a counter-rotating circulation starts to form near the free surface of the outer bank which increases till it reaches the apex section and decays at bend exit. This conclusion is in contrast with  $B/h > 10$  where the outer bank circulation forms only in the apex section. The formation of the outer bank circulation cell, mainly in  $B/h < 10$ , allows the banks to be stabilised as the values of bank shear stress are low.

## 6.5 Research in India

Research from India studied the behaviour of meandering rivers and got fairly good results. Patra et al. (2004) have done experiments in a laboratory to study the behaviour of meandering channels with and without floodplains. Without floodplains, meandering channel behaviour was studied extensively to some extent, but limited study on meandering channels has been done with floodplains. Patra et al. gave a modified power law for the vertical distribution of longitudinal velocity in meandering channel where secondary circulation across the flow is functional because the traditional power law gives different distributions in open channel and natural or lab channels. The distribution of tangential velocity in the longitudinal, radial and vertical directions in the present meandering channels for both in-bank and overbank flow conditions are found to give good results.

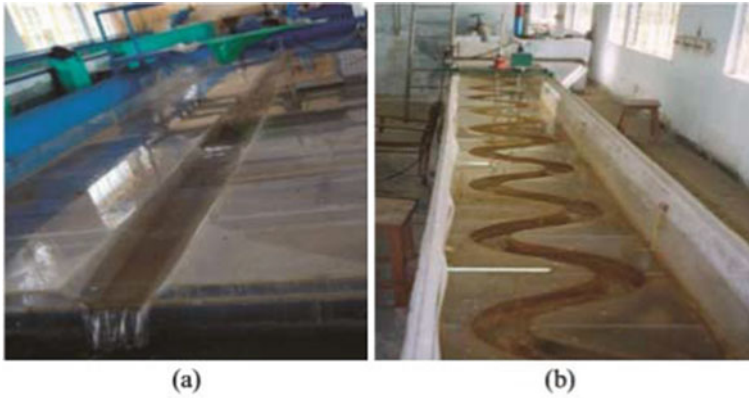


**Fig. 6.8** a Straight channel; b Meandering channel

Khatua et al. (2013) predicted stage-discharge for meandering channels. Stage-discharge relationship is quite easy to find in straight channels but due to variation of river geometry and hydraulic properties, it's quite difficult in meandering rivers. The experiment is conducted in a laboratory using straight and meandering channels (Fig. 6.8). The experiments are carried out to see the effect of channel geometry and sinuosity on the variation of roughness coefficient in a meandering channel. It depends on sinuosity, aspect ratio, longitudinal slope of the channel and Reynolds number of the flow. With flow depth, flow resistance in terms of Chezy's  $C$  also changes. After finding the roughness coefficient by using dimensional analysis, the stage-discharge relationship can be adequately predicted in a meandering channel.

## 6.6 Conclusion

This review paper has followed the works on the behaviour of meandering channels by different researchers. It showed the past works of researchers and scientists using various experimental setups in laboratories and fields with different conditions. They found out various parameters like velocity, Reynolds shear stress, TKE, etc. and examined the effect on the bank stability. From this study, it can be concluded that the distribution of velocity, shear stresses and turbulent kinetic energy in the meander bends varies with respect to straight channels. The presence of outer bank circulation cells has also been suggested by various authors. After so many years of work, the structure of turbulence in the meander bends is still not clear. Future work on the turbulent structure in meander bends should focus on the fluid stresses exerted on the adjacent boundary accurately. Research should also be conducted to analyse the structure of turbulence around failed blocks of bank material and to know how curvature-induced turbulence is enhanced by the development of bank blocks. Further work can be done regarding the seepage condition in meandering rivers and how it

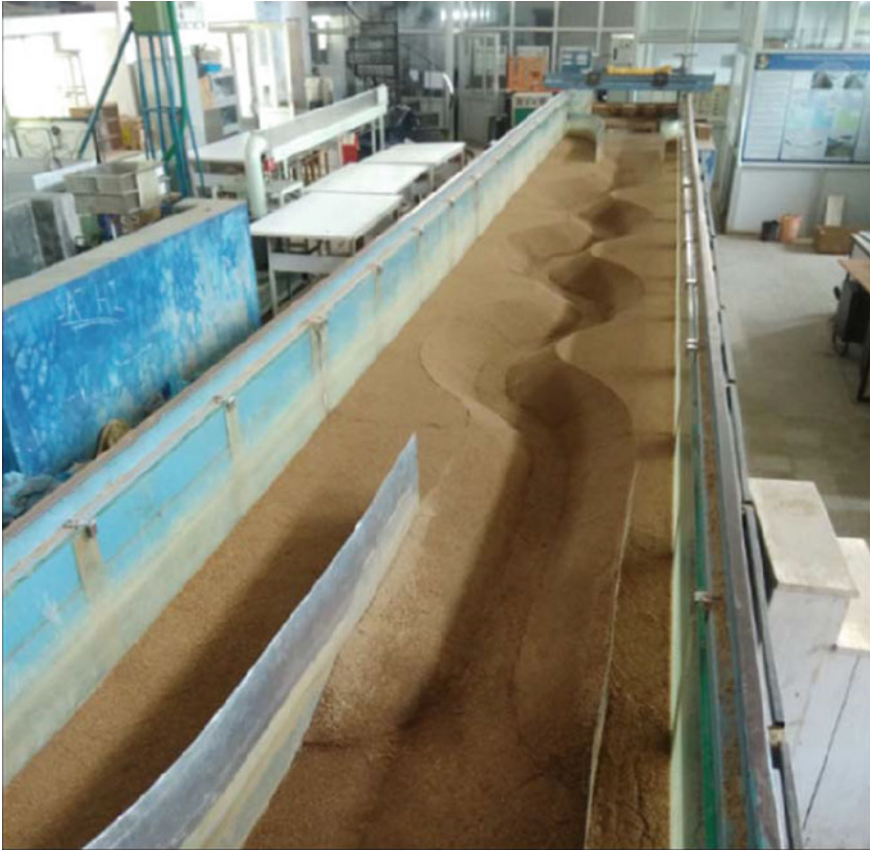


**Fig. 6.9** Meandering channel flume at IIT Guwahati

affects the turbulence structure in the outer bank of the bend. Work on meandering channels and studies of their behaviour have been initiated in the Water Resources Laboratory of Civil Department, Indian Institute of Technology, Guwahati (Fig. 6.9).

## References

- Abad JD, Garcia MH (2009) Experiments in a high-amplitude Kinoshita meandering channel: 1. Implications of bend orientation on mean and turbulent flow structure, *er Resour. Res* 45:1–19
- Anwar HO (1986) Turbulent structure in river bend. *J Hydr Eng* 112:657–669
- Blanckaert K, Kleinhans MG, McLelland SJ, Uijttewaai WSJ, Murphy BJ, van de Kruijs A, Parsons DR, Chen Q (2013) Flow separation at the inner (convex) and outer (concave) banks of constant-width and widening open-channel bends. *Earth Surf Proc Land* 38(7):696–716
- Booij R (2003) Modeling the flow in curved tidal channels and rivers. In: *Proceedings of the International Conference on Estuaries and Coasts*, pp 786–794



- Boussinesq J (1868) Mémoire sur l'influence des frottements dans les mouvements réguliers des fluides; XII - Essai sur le mouvement permanent d'un liquide dans un canal horizontal à axe circulaire. *Journal de mathématiques pures et appliquées 2e série, Tome XIII*, 413
- Da Silva AMF (1995) Turbulent flow in sine-generated meandering channels. Queens University, Kingston, Ontario, Canada
- Engel FL, Rhoads BL (2012) Interaction among mean flow, turbulence, bed morphology, bank failures and channel planform in an evolving compound meander loop. *Geomorphology* 163–164:70–83
- Engel FL, Rhoads BL (2017) Velocity profiles and the structure of turbulence at the outer bank of a compound meander bend. *Geomorphology* 295:191–201
- Engelund F (1974) Flow and bed topography in channel bends. *J Hydraul Div* 100(11):1631–1648
- Graf WH, Blanckaert K (2002) Flow around bends in rivers, 1–9. In: 2nd international conference new trends in water and environmental engineering for safety and life: eco-compatible solutions for aquatic environments
- Jamieson EC, Post G, Rennie CD (2010) Spatial variability of three-dimensional Reynolds stresses in a developing channel bend. *Earth Surf Process Landf* 35(1029)–1043:1029–1043
- Johannesson H, Parker G (1989) Linear theory of river meanders. *River Meandering*, 12:181–213
- Khatua KK, Patra KC, Nayak P (2013) Stage-discharge prediction for meandering channels. *Int J Comput Exp Meth* 1(1):80–92
- Leopold LB, Wolman MG (1957) River channel patterns: braided, meandering, and straight. US Government Printing Office
- Matsuura T, Townsend R (2004) Stream-barb installations for narrow channel bends—a laboratory study. *Can J Civil Eng* 31(3):478–486
- Patra KC, Kar SK, Bhattacharya AK, Asce AM (2004) Flow and velocity distribution in meandering compound channels. *J Hydraul Eng* 130(5):398–411
- Rozovskii IL (1957) Flow of water in bends of open channels. Academy of Sciences of Ukraine, Kiev
- Sukhodolov A, Kaschtschejewa E (2010) Turbulent flow in a meander bend of a lowland river: field measurements and preliminary results. *River Flow 2010—Dittrich, Koll, Aberle & Geisenhainer (eds)*
- Sukhodolov AN (2012) Structure of turbulent flow in a meander bend of a low land river. *Water Resour Res* 48:1–21
- Termini D (2009) Experimental observations of flow and bed processes in large-amplitude meandering flume. *J Hydraul Eng* 135(7):575–587
- Thompson J (1876) On the origin of windings of rivers in alluvial plains, with remarks on the flow of water round bends in pipes. *Proc R Soc London* 25(171-178):5–8
- Vriend BHJ De (1983) Main flow velocity in short river bends. *J Eng* 109(7):991–1011

# Chapter 7

## Prediction of Discharge Coefficient for Side Rectangular Weir Using Group Method of Data Handling (GMDH)



Ali Shariq, Ajmal Hussain, and Mujib Ahmad Ansari

**Abstract** A side rectangular weir is used as a flow diversion structure, having spatially varied flow with decreasing discharge. They have various applications in the field of river, hydraulic, environmental and irrigation engineering. In this study, group method of data handling (GMDH) with two types of transfer function, namely quadratic polynomial one variable and quadratic polynomial two variable, were used to estimate the coefficient of discharge for sharp-crested side rectangular weir. On the basis of the F-test, it is found that the upstream Froude number is the most influencing parameter for the estimation of the coefficient of discharge. On the basis of dimensional analysis, it is observed that the coefficient of discharge depends on the ratio of the crest height to the length ( $P/L$ ), ratio of breadth of the main channel to length ( $B/L$ ), approach flow Froude number ( $F_1$ ) and ratio of the upstream depth to length ( $y_1/L$ ) of sharp-crested side rectangular weir. The coefficient of correlation ( $R = 0.93$ ), average absolute deviation ( $AAD = 2.99$ ) and mean absolute percentage error ( $MAPE = 3.078$ ) show better performance of the present GMDH model. Finally, the results indicated that the GMDH model could provide more accurate predictions than those obtained by traditional regression models.

**Keywords** Side rectangular weir · Coefficient of discharge · Froude number · GMDH

### 7.1 Introduction

The side weirs are broadly utilized in wastewater-treatment plants, river-intake facilities, river-control structures and irrigation canals. They commonly release surplus discharge into an off-stream capacity (for flood control) or to pass excess water into another channel. The study of flow divergence from the main river to another river, primary channel to secondary channel, or canal to sub-canal are essential aspects for hydraulic engineering. There are many hydraulic structures used to divert the excess

---

A. Shariq (✉) · A. Hussain · M. A. Ansari  
Department of Civil Engineering, Zakir Hussain College of Engineering & Technology, Aligarh Muslim University, Aligarh 202002, India  
e-mail: [alishariq@zhcet.ac.in](mailto:alishariq@zhcet.ac.in)

discharge which are weirs, spillway, sluice gate, orifice, etc. Spatially varied flow with decreasing discharge is observed in side weirs and side orifices that are used for diverting water from irrigation or drainage systems, for controlling the water depth in a canal and in flood schemes relief on the river.

An extensive amount of literature is available on different shapes of side weirs due to its broad scope of applications in environmental, hydraulic and water resource engineering. De Marchi (1934) provided the first theoretical approach related to the hydraulics of a rectangular side weir in a rectangular channel. Most of the earlier theoretical analyses were limited to the flow over different shapes of side weirs in circular, triangular and rectangular main channels (Hager 1987; Vatankhah 2012; De Marchi 1934; Emiroglu et al. 2011; Ranga Raju et al. 1979; Shariq 2016).

Many Researchers studied the side weir and proposed different forms of discharge coefficient equations for the different shapes. Flow hydraulics over a side weir in a rectangular channel has been experimentally as well as analytically studied by many researchers (Ranga Raju et al. 1979; Subramanya and Awasthy 1972; Shariq et al. 2018; Hager 1987; Ansari et al. 2019; Emiroglu et al. 2011). Many researches have been conducted for providing the discharge coefficient models in simple rectangular side weirs (Hager 1987; Singh et al. 1994; Ranga Raju et al. 1979; Jalili and Borghei 1996; Emiroglu et al. 2011; Shariq et al. 2018). De Marchi (1934) stated the first theoretical analyses related to the flow over a rectangular side weir in a rectangular flume taking an assumption that total energy is constant along the length of the side weir.

Recently, the GMDH network is being used in various fields to forecasting and modeling the behaviors of complex systems or unknown ones based on a different set of multi-input–single-output data pairs (Amanifard et al. 2008). In addition, the GMDH approach is applied in various researches such as conservation of energy, economic and engineering geology and control engineering system identification (Amanifard et al. 2008; Srinivasan 2008; Najafzadeh et al. 2013; Ansari and Muzzammil. 2014; Ansari 2014 etc.).

The present study aims to re-analyze the databases and to develop a GMDH model for the estimation of discharge coefficient of rectangular side weir.

Discharge coefficient of rectangular side weir can be expressed as a function of approach velocity of flow, crest length of side weir ( $L$ ), crest height ( $P$ ), breadth of main channel ( $B$ ), breadth of secondary channel ( $b$ ), density of water ( $\rho$ ) and dynamic viscosity of water ( $\mu$ ).

$$C_d = f(\rho, \mu, B, g, V, L, y_1, P, b) \quad (7.1)$$

This equation can, alternatively, be written as

$$C_d = f\left(y_1/L, P/L, B/L, F_1\right) \quad (7.2)$$

Such a functional relationship can be used to develop the GMDH model.

**Table 7.1** Range of data collected from the literature for side weir

Parameter	Unit	Range of data	
		Min	Max
Q <sub>1</sub>	m <sup>3</sup> /s	0.00914	0.041
Q <sub>2</sub>	m <sup>3</sup> /s	0.0063	0.02803
B/L	–	0.66	1.97
y <sub>1</sub> /L	–	0.182	1.46
P/L	–	0.0895	0.7915
F <sub>1</sub>	–	0.15	0.77

## 7.2 Data Collection

The data sets presented by Bagheri et al. (2014) and Shariq et al. (2018) were used in this study. Shariq et al.'s (2018) experimental setup consisted of the main channel of length, width and depth as 12.8 m, 0.29 m and 0.39 m, respectively. A side weir (i.e.  $P/L = 0.317$  m, 0.55 m and 0.7915 m) was built at a distance of 8.20 m from the starting end of the primary channel in the right wall of the primary channel. Discharge that passes over the rectangular side weir was moved into the secondary channel of length, width and height as 4.18 m, 0.2 m and 0.35 m, respectively. Bagheri et al.'s (2014) experimental setup consisted of a horizontal rectangular flume of length, width and height as 8 m, 0.4 m and 0.6 m, respectively. All the experiments were conducted under subcritical flow conditions. All the measurements were taken with an accuracy of 0.5 mm. The range of data collected from the literature for the present study is shown in Table 7.1.

## 7.3 Analysis of Data, Results and Discussion

### 7.3.1 *F*-test

An *F*-test is a parametric test in which the researcher draws out an inference about the data that is drawn from the given population. It is generally used for comparing statistical models that have been fitted to a data set, in order to identify the model that best fits the population from which the data were sampled.

When the *F*-value of any parameter as compared to the *F*-value of another parameter is very low, then the lowest *F*-value parameter can be dropped because that parameter is treated as not affecting the whole value of the equation (Shariq et al. 2018; Hussain et al. 2016). The effect of non-dimensional parameters ( $B/L$ ,  $P/L$ ,  $y_1/L$  and  $F_1$ ) on the coefficient of discharge ( $C_d$ ) was investigated by *F*-Test as shown in Fig. 7.1.

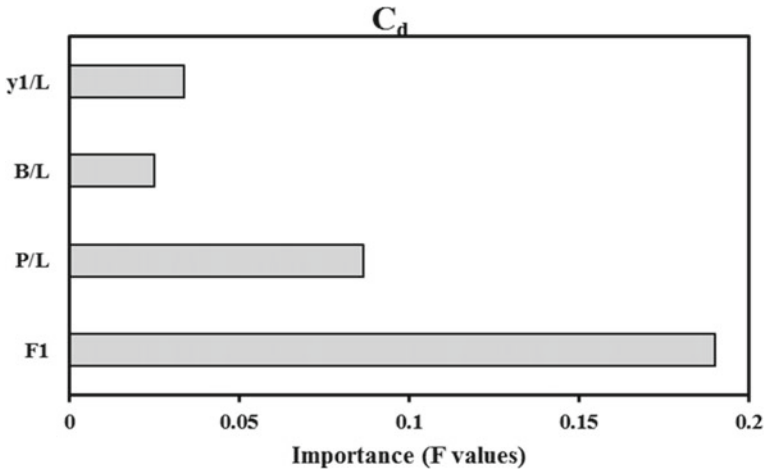


Fig. 7.1 Importance of different independent parameters on  $C_d$

### 7.3.2 Effect of Dimensionless Parameters on $c_d$

The effect of the dimensionless parameters  $F_1$ ,  $y_1/L$ ,  $P/L$  and  $B/L$  achieved by dimensional analysis on the observed  $C_d$  was examined. A thorough data analysis shows that  $F_1$ ,  $P/L$ ,  $B/L$  and  $y_1/L$  are the influencing parameters which could affect the  $C_d$ . The variation of  $C_d$  with upstream Froude number while the other parameter is taken as a constant is shown in Fig. 7.2, which clearly shows that  $C_d$  decrease with an

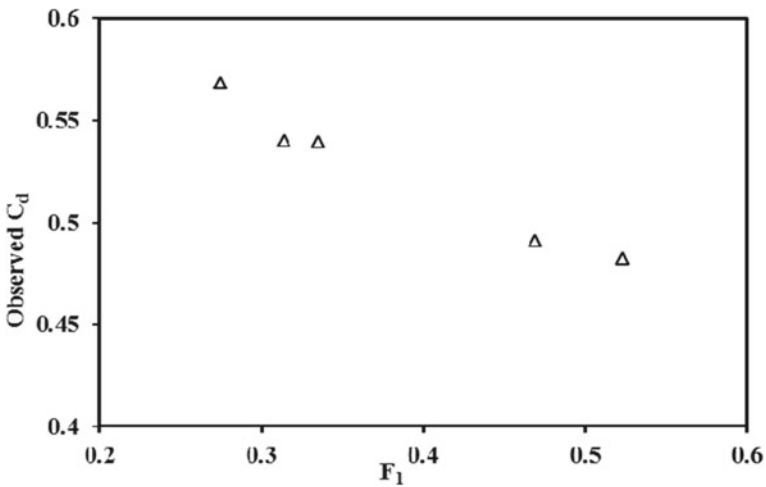


Fig. 7.2 Variation of  $C_d$  with upstream Froude number when  $y_1/L = 0.74$ ,  $B/L = 1.45$  and  $P/L = 0.317$

increase of upstream Froude number when other influencing parameters were taken as constant. The variation of  $C_d$  with a ratio of upstream depth to crest length is shown in Fig. 7.3, which clearly reveals that  $C_d$  increase with an increase of the ratio of upstream depth to crest length ( $y_1/L$ ) when other influencing dimensionless parameters were constant. The variation of  $C_d$  with  $P/L$  is shown in Fig. 7.4, which shows that  $C_d$  decreases with an increase of the ratio of crest height to crest length ( $P/L$ ) when other influencing dimensionless parameters remain constant. Variation of  $C_d$  with the ratio of the breadth of the channel to crest length is shown in Fig. 7.5, which

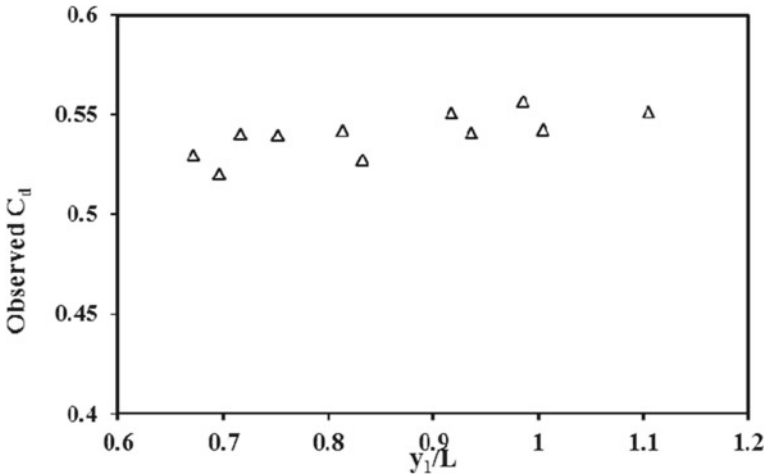


Fig. 7.3 Variation of  $C_d$  with  $y_1/L$  when  $F_1 = 0.33$ ,  $B/L = 1.45$  and  $P/L = 0.317$

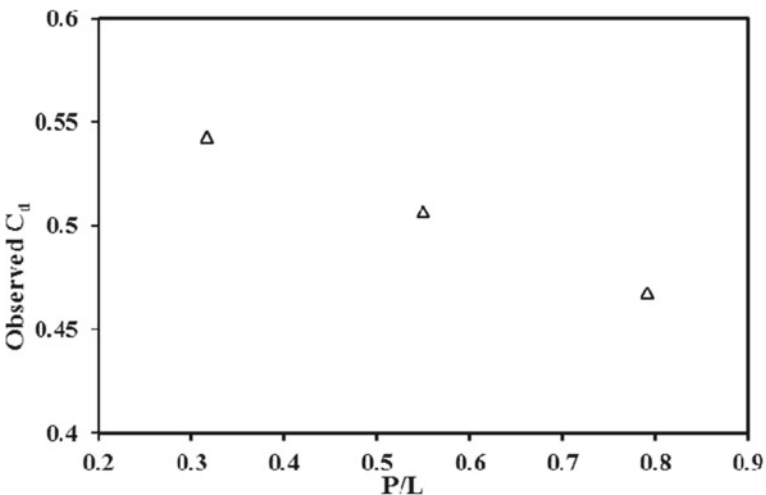


Fig. 7.4 Variation of  $C_d$  with  $P/L$  when  $F_1 = 0.32$ ,  $B/L = 1.45$  and  $y_1/L = 1.00$

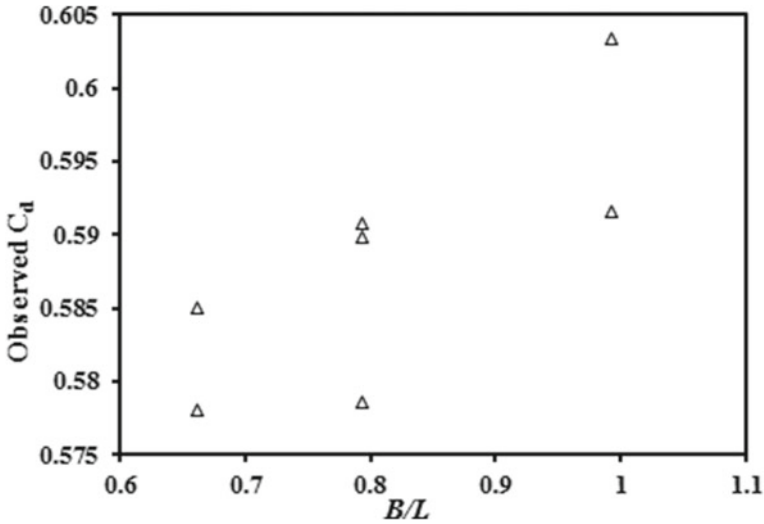


Fig. 7.5 Variation of  $C_d$  with  $B/L$  when  $F_1 = 0.55$ ,  $P/L = 0.133$  and  $y_1/L = 0.287$

clearly indicates that  $C_d$  increases with an increase of  $B/L$  when other influencing dimensionless parameters were constant.

### 7.3.3 Proposed GMDH Model for Coefficient of Discharge of Rectangular Side Weir

The results of Group Method of Data Handling networks are presented in this section. In the present study, the polynomial functions of two different types, i.e. quadratic one variables and quadratic two variables of the GMDH network are used and are written as

Quadratic function: one variable

$$\hat{y} = G(x_i x_j) = a_0 + a_1 x_j + a_3 x_i^2 \tag{7.3}$$

Quadratic function: two variables

$$\hat{y} = G(x_i x_j) = a_0 + a_1 x_i + a_2 x_j + a_3 x_i x_j + a_4 x_i^2 + a_5 x_j^2 \tag{7.4}$$

In addition, the results obtained by the GMDH model are compared with those using the available Regression model, viz., Ghodsian (1997) and Shariq et al. (2018). The proposed GMDH network yielded a correlation coefficient of 0.94.

One of the important properties of the GMDH networks is analytical equations which can be obtained using different types of polynomial functions. Analytical Eqs. (7.5–7.16) obtained by the GMDH network for predicting the coefficient of discharge of rectangular side weir are presented as follows:

$$[C_d]_4^1 = 0.9363 - 0.5918 * B/L + 0.2117(B/L)^2 \quad (7.5)$$

$$[C_d]_2^2 = - 2.765 * 10^{12} + 1.747 * 10^{12} * (B/L) - 6.251 * 10^{11} * (B/L)^2 \\ + 2.953 * 10^{12} * [C_d]_4^1 + 54.934 * ([C_d]_4^1)^2 + 8.637 * B/L * [C_d]_4^1 \quad (7.6)$$

$$[C_d]_6^1 = 0.4267 + 0.041 * (y_1/L) + 0.0678 * (y_1/L)^2 + 1.110 * F_1 \\ - 1.043 * F_1^2 - 0.83(y_1/L) * F_1 \quad (7.7)$$

$$[C_d]_9^1 = 0.9 - 0.406 * B/L + 0.1328 * (B/L)^2 - 0.452 * P/L \\ + 0.1317 * (P/L)^2 + 0.166 * B/L * P/L \quad (7.8)$$

$$[C_d]_5^2 = - 2.006 + 3.634[C_d]_6^1 - 0.644([C_d]_6^1)^2 - 4.372[C_d]_9^1 \\ - 1.462([C_d]_9^1)^2 - 3.965[C_d]_6^1[C_d]_9^1 \quad (7.9)$$

$$[C_d]_1^3 = - 0.883 + 0.665[C_d]_2^2 - 1.496([C_d]_2^2)^2 + 3.518[C_d]_5^2 \\ - 4.249([C_d]_5^2)^2 - 2.921[C_d]_2^2[C_d]_5^2 \quad (7.10)$$

$$[C_d]_{13}^1 = 0.635 - 0.228B/L + 0.127 * (B/L)^2 + 0.713F_1 - 0.288F_1^2 \\ - 0.526(B/L)(F_1^2) \quad (7.11)$$

$$[C_d]_{14}^1 = 0.707 - 0.178y_1/L + 0.093(y_1/L)^2 + 0.38P/L + 0.079(P/L)^2 \\ + 0.140(y_1/L)(P/L) \quad (7.12)$$

$$[C_d]_{12}^2 = - 3157 + 8.822[C_d]_{13}^1 - 0.7027([C_d]_{13}^1)^2 + 3.135[C_d]_{14}^1 \\ - 4.302([C_d]_{14}^1)^2 - 13.053[C_d]_{13}^1[C_d]_{14}^1 \quad (7.13)$$

$$[C_d]_{15}^2 = - 4.119 + 0.172y_1/L + 0.103(y_1/L)^2 + 15.558[C_d]_9^1 \\ - 12.62([C_d]_9^1)^2 - 0.621(y_1/L)([C_d]_9^1) \quad (7.14)$$

$$[C_d]_{11}^3 = - 0.267 + 7.907[C_d]_{12}^2 - 5.628([C_d]_{12}^2)^2 - 5.975[C_d]_{15}^2$$



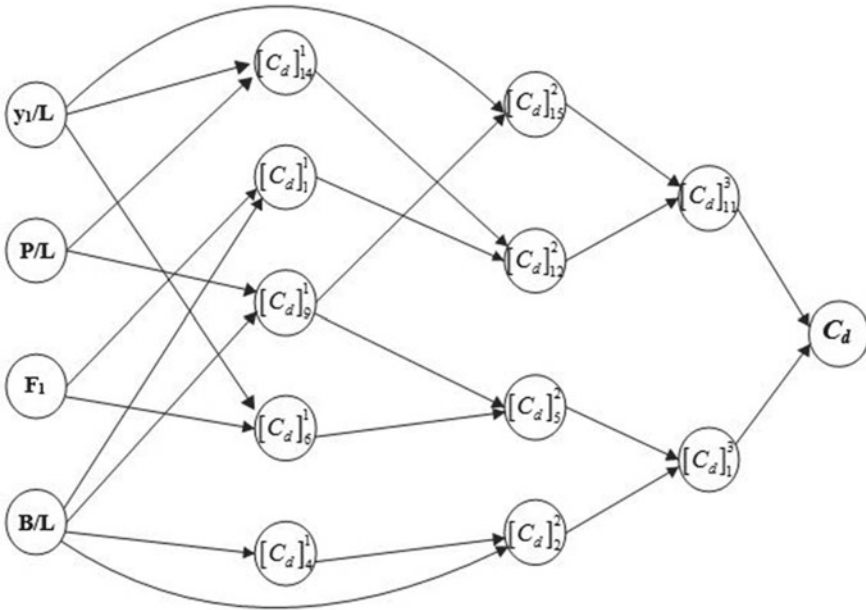


Fig. 7.6 Network Architecture of the GMDH model for predicting coefficient of discharge

$$- 17.703([C_d]_{15}^2)^2 - 24.149[C_d]_{12}^2[C_d]_{15}^2 \tag{7.15}$$

$$C_d = 0.215 - 4.222[C_d]_1^3 + 11.118([C_d]_1^3)^2 + 4.246[C_d]_{11}^3 + 3.451([C_d]_{11}^3)^2 - 13.648C_{d11}^3[C_d]_{11}^3 \tag{7.16}$$

In the above equations, the subscript and superscript of each parameter represent the number of pertaining layers and neurons, respectively. The recommended structure of the GMDH network for predicting the coefficient of discharge contains 5 selective neurons in the first layer, 4 selective neurons in the second layer and 2 selective neurons in the third layer, respectively, and a selective neuron in the output layer (5-4-2) is presented in Fig. 7.6.

The predicted values of coefficient of discharge have been plotted against its observed values for training, and validation sets are shown in Fig. 7.7 for the GMDH model.

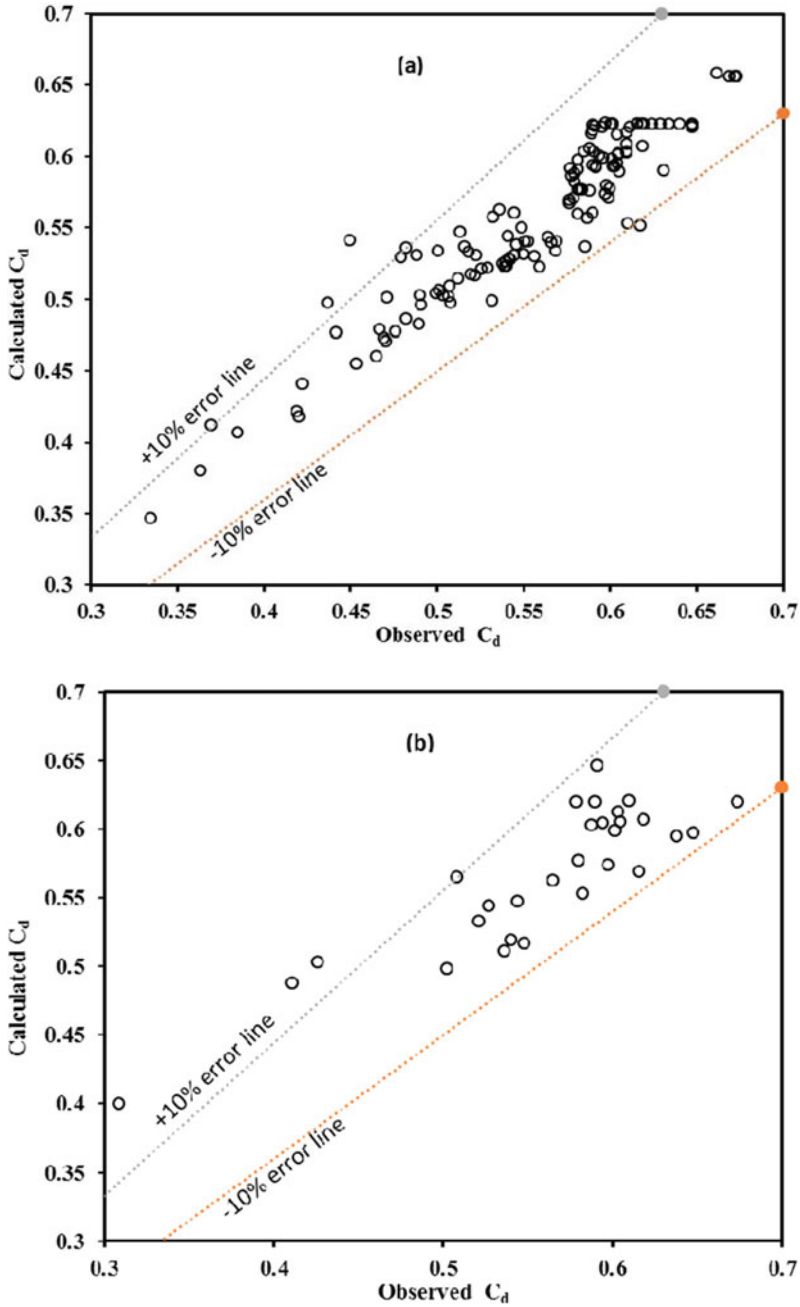


**Fig. 7.7** **a** Comparison between values of  $C_d$ , using the present GMDH model for training data sets. **b** Comparison between values of  $C_d$ , using the present GMDH model for validation data sets

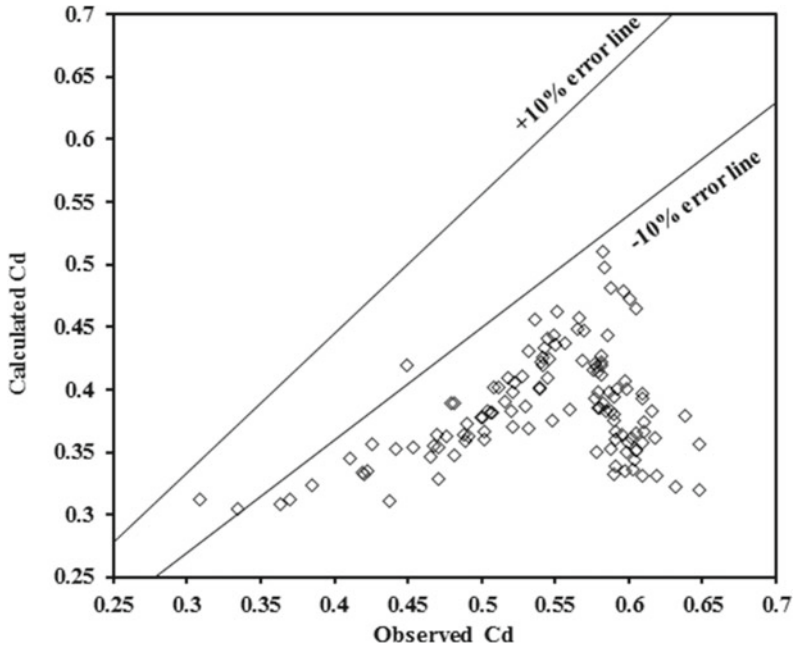


Fig. 7.8 Comparison between values of  $C_d$  for Ghodsian (1997) model

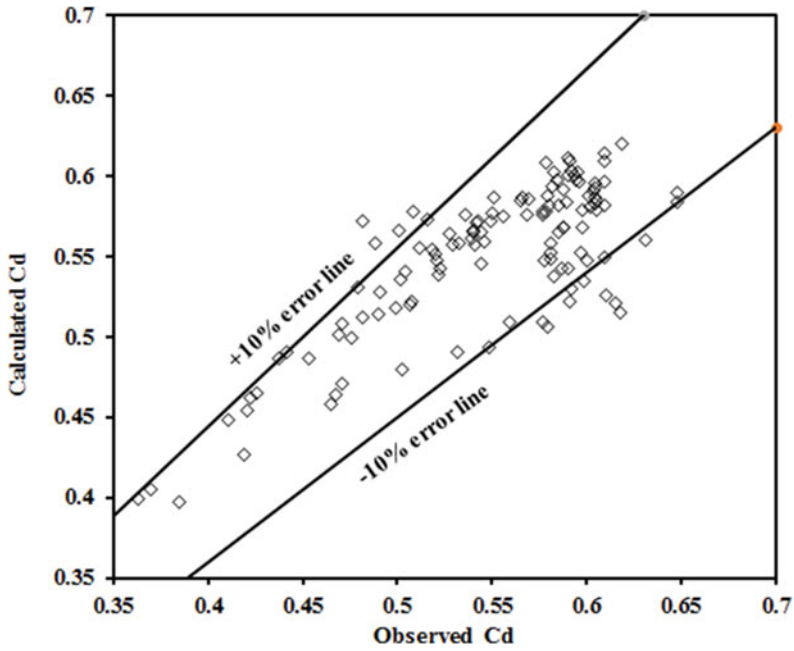


Fig. 7.9 Comparison between values of  $C_d$  for Shariq et al. (2018) model

### 7.3.4 Verification of Previous Available Relationships for $C_d$

Most of the available data collected from the literature have been first used to check the accuracy of the previous available models for estimation of the coefficient of discharge. The range of influencing dimensionless parameters used in this study is shown in Table 7.1. The selected available equations in the literature are those proposed by Ghodsian (1997) and Shariq et al. (2018) and are listed in Table 7.2. The comparison between the observed and estimated values of coefficient of discharge of side rectangular weir,  $C_d$ , using the available equations in the literature are shown in Figs. 7.7, 7.8 and 7.9 qualitative performance of these equations is presented in Table 7.2. Figures 7.7, 7.8 and 7.9 report that none of the previously available equations have been able to estimate the coefficient of discharge values for rectangular side weir. Therefore, the GMDH model along with corresponding quadratic function with one variable and two variable polynomials (Eqs. 7.5–7.16) is recommended for general use to estimate the coefficient of discharge of rectangular side weir.

## 7.4 Conclusion

In this study, the Group Method of Data Handling (GMDH) method is used to estimate the coefficient of discharge for side rectangular weir. The variation of  $C_d$  with upstream Froude number shows that  $C_d$  decreases with an increase of upstream Froude number. It was also observed that the approach flow Froude number is the most influencing parameter for the flow through rectangular side weir. Therefore, its effect on  $C_d$  for side weir is apparent. The variation of  $C_d$  with  $P/L$  indicates that  $C_d$  decreases with an increase of  $P/L$ . The variation of  $C_d$  with  $y_1/L$  indicates that  $C_d$  is directly proportional to  $y_1/L$ . Observed and calculated values of the coefficient of discharge of rectangular side weir using the GMDH model for all data sets are compared graphically, which declares that the estimated coefficient of discharge was within  $\pm 10\%$  of the observed values, which is a satisfactory estimation of the coefficient of discharge for rectangular side weir. The qualitative performance of the proposed GMDH model reveals that it has the lowest *MAPE* (3.078) and *AAD* (2.99) and the highest *R* (0.93) as compared to previously available predictors.

**Table 7.2** Performance parameters of existing and present models

S. no.	Source	Discharge coefficient equations for rectangular side weirs	R	MAPE	AAD
1	Ghodsian (1997)	$C_d = (1 - 0.63F_1^{0.33})[0.611 + 0.075(\gamma_1 - P)/P]$	Training Testing All	28.213 28.413 28.242	29.21 29.25 29.22
2	Shariq et al. (2018)	$C_d = \left\{ \begin{array}{l} 1.1308 - 1.5396\left(\frac{P}{L}\right)^{0.0394} - 0.1492(F_1)^{0.8292} \\ + 0.0105\left(\frac{\gamma_1}{L}\right)^{3.6295} + 0.487\left(\frac{B}{L}\right)^{-0.0357} \end{array} \right\}^{0.2322}$	Training Testing All	4.85 4.55 4.79	4.69 4.54 4.623
3	GMDH model	Equations 7.5–7.16	Training Testing All	3.223 5.945 3.078	3.08 5.30 2.99

## References

- Amanifard N, Nariman-Zadeh N, Farahani MH, Khalkhali A (2008) Modeling of multiple short-length-scale stall cells in an axial compressor using evolved GMDH neural networks. *J Energy Convers Manage* 49(10):2588–2594
- Ansari MA (2014) Sediment removal efficiency computation in vortex settling chamber using artificial neural networks, water and Energy International, Central Board of Irrigation and Power (CBIP). New Delhi 71(1):54–67
- Ansari MA, Muzzammil M (2014) Application of group method of data handling for prediction of peak floods. International conference ICEFT -2014 on Eco-friendly technologies for sustainable growth, 27–28 March, 2014, Anjuman-i-Islams M.H. Saboo Siddik College of Engineering, Mumbai, 115–119
- Ansari MA, Hussain A, Shariq A, Alam F (2019) Experimental and numerical study for the estimation of coefficient of discharge for side compound weir. *Can J Civ Eng* 46(10):887–895
- Bagheri S, Kabiri-Samani AR, Heidarpour M (2014) Discharge coefficient of rectangular sharp-crested side weirs Part I: traditional weir equation. *Flow Meas Instrum* 35:109–115
- De M (1934) G. Essay on the performance of lateral weirs. *L Energia Electrica Milano*, vol. 11, No. 11, Italy, 849–860
- Emiroglu ME, Agaccioglu H, Kaya N (2011) Discharging capacity of rectangular side weirs in straight open channels. *Flow Meas Instrum* 22:319–330
- Ghodsian M (1997) Elementary discharge coefficient for rectangular side weir. In: *Proceeding of 4th international conference on civil engineering*, Tehran, pp 36–42
- Hager WH (1987) Lateral outflow of side weirs. *J Hydraul Eng ASCE* 113(4):491–504
- Hussain A, Ahmad Z, Ojha CSP (2016) Flow through lateral circular orifice under free and submerged flow conditions. *Flow Measur Instrum Elsevier* 36(10):32–35
- Jalili MR, Borghei SM (1996) Discussion of Discharge coefficient of rectangular side weir, by Singh R, Manivannan D, Satyanarayana TJ. *Irr. Drain Eng, ASCE*, 122(2):132
- Najafzadeh M, Barani GA, Hessami Kermani MR (2013) Abutment scour in clear-water and live-bed conditions by GMDH network. *Water Sci Technol* 67(5):1121–1128
- Ranga Raju KG, Prasad B, Gupta SK (1979) Side weirs in rectangular channels. *J Hydraul Div ASCE* 105(5):547–554
- Singh R, Manivannan D, Satyanarayana T (1994) Discharge coefficient of rectangular side weirs. *J Irr Drain Eng ASCE* 120(4):814–819
- Shariq A, Hussain A, Ansari MA (2018) Lateral flow through the sharp crested side rectangular weirs in open channels. *Flow Measur Instrum Elsevier, Elsevier* 59:8–17
- Shariq A (2016) Flow characteristics of side weirs in open channel. Master's Thesis, Aligarh Muslim University, Aligarh, India
- Subramanya K, Awasthy SC (1972) Spatially varied flow over side weirs. *J Hydraul Div ASCE* 98(1):1–10
- Srinivasan D (2008) Energy demand prediction using GMDH networks. *Neuro Comput* 72(1–3):625–629
- Vatankhah A (2012) Analytical solution for water surface profile along a side weir in a triangular channel. *Flow Meas Instrum* 23(1):76–79

# Chapter 8

## Enhancement of Energy Dissipation Using Combination of Solid Roller Bucket and Type II Stilling Basin for Ogee Stepped Spillway



P. B. Nangare and A. S. Kote

**Abstract** One of the most critical factors in the design of a hydraulic system is the energy dissipation arrangement for high-velocity flow in an ogee spillway. The release of excess water from crest to toe of the ogee spillway generates a large amount of kinetic energy. This would result in scour and erosion on the spillway's downstream face. Many different forms of energy dissipators have been used for ogee spillways in the past. However, they have energy dissipation, scouring, and erosion issues. The aim of this study is to create a physical working model of an ogee stepped spillway with a combination of solid roller bucket and type II stilling basin as an energy dissipator for the Khadakwasla dam in Pune (India). Two sets of phase models for a design discharge of 2700 m<sup>3</sup>/s were used in laboratory experiments. The non-dimensional parameter ( $yc/h$  0.8), nappe flow, and Froude number must be held within acceptable limits with 12 and 9 steps, respectively. The model results show that the 9-step model (Set 2) achieved 80.24% energy dissipation for a 4 m head with a controlled value of non-dimensional parameter up to 0.69, which is the highest energy dissipation among all sets of subject models. As a result of the current model analysis, it was discovered that the combination of a solid roller bucket and a type II stilling basin is the best energy dissipator for an ogee stepped spillway.

**Keywords** Energy dissipation · Solid roller bucket · Type II stilling basin · Non-dimensional parameter · Ogee stepped spillway

### 8.1 Introduction

The ogee spillway's terminal structure plays a major role in dissipating surplus water so as to safeguard dam structures. There is a risk of spillway bed erosion due to the very high discharge of excess floods. As a function, the energy dissipator must be

---

P. B. Nangare (✉)  
AISSMS COE, Savitribai Phule Pune University, Pune 411001, India  
e-mail: [pbnangare@aissmscoe.com](mailto:pbnangare@aissmscoe.com)

A. S. Kote  
DIT, Savitribai Phule Pune University, Pimpri, Pune 411018, India

reliable and adequate under all situations in order to effectively dissipate the specific energy and control erosion. For eliminating the effect on a spillway, various types of energy dissipators are used in ogee spillways, such as stilling basins, roller buckets, flip buckets, and stilling basins. Although the hydraulic jump type II stilling basin is commonly used as an energy dissipator for ogee spillways, it is costly in the long run (Tung and Mays 1982). The use of steps on an ogee profile is a good option.

Roughness components are used to minimize flow acceleration and terminal velocity. Cavitation is reduced as a result of the reduced velocity and cushioning effect of the entrained air. Excessive air entrainment creates positive pressure on the spillway bed, which aids in energy dissipation (Sorensen 1985). Bucket type energy dissipators have been used in the United States, Europe, and India. The roller bucket was used for the first time in the design of the Grand Coulee Dam in the United States. Over a sloping apron or horizontal stilling basin, this allows for the use of a comparatively shorter structure with significant cost savings. Each of these methods seems to have its own set of limitations, and none of them has been specifically designed to dissipate more energy (Bhosekar et al. 2012). There is a significant concern, and wide measures could be taken to utilize the combined effects of solid roller buckets and hydraulic jump type II stilling basins for ogee profile spillways. Although the ogee spillway of the Khadakwasla dam in Pune has a stilling basin form of energy dissipator with friction blocks, it has been troubled by scouring and erosion for the past 15 years. As a result, an attempt has been made to develop a working model for the Khadakwasla dam's ogee stepped spillway. As an energy dissipator, a solid roller bucket and a type II stilling basin are combined.

## 8.2 Methodology

The Froude model law and the following assumptions are used to create a working model of an ogee stepped spillway (Chaft et al. 2010).

- i. Over the crest of the ogee spillway, the operating head is greater than 1.4 times the design head (Chatiola and Jurdi 2004).
- ii. A solid roller bucket is submerged in tailwater 1.1–1.4 times the depth of the post jump.
- iii. A solid roller bucket should have a Froude number of at least 4.5.
- iv. In the riverbed, the solid roller bucket is suitable only for hard rock.

With a model scale ratio of 1:33, an ogee stepped spillway model and energy dissipators have been developed. For evaluating the performance of an ogee stepped spillway, this model uses a combination of hydraulic jump-type stilling basin (type II) and solid roller bucket as energy dissipators. For discharge of 0.0052–0.0063 m<sup>3</sup>/s, the experiments are carried out in a 6 m long, 300 mm high, and 300 mm deep hydraulic flume. For two sets of phase models, a combination of solid roller bucket and type II stilling basin is used as an energy dissipator. The first set (Set 1) included 12 steps with a rise of 4.0 cm and a tread of 3.3 cm, while the second set (Set 2)



**Table 8.1** Comparison of specific energy and energy dissipation for ogee stepped spillway

Provisions	Spillway models	Head (m)	Froude number ( $Fr_1$ )	Specific energy (E) (m)	Energy loss ( $\Delta E$ ) (m)	Energy dissipation (ED) (%)	Average ED (%)	Non-dimensional parameter ( $y_c/h < 0.8$ )
V Notch-Up	Set 1	4	5.53	0.798–0.857	0.058	79	78.14	0.78
		5.5	5.01	0.804–0.877	0.073	78.72		0.87
		6.5	4.68	0.806–0.850	0.095	77.21		0.92
V Notch-Down		4	5.53	0.797–0.846	0.049	80		0.78
		5.5	5.02	0.806–0.850	0.044	76.39		0.87
		6.5	4.75	0.808–0.854	0.046	77.53		0.92
V Notch-Up	Set 2	4	5.53	0.798–0.857	0.059	80.24	78.29	0.69
		5.5	5.02	0.803–0.871	0.067	78.79		0.78
		6.5	4.76	0.806–0.901	0.095	76.39		0.82
V Notch-Down		4	5.53	0.797–0.846	0.044	79.63		0.69
		5.5	5.02	0.801–0.849	0.048	77.53		0.78
		6.5	4.76	0.805–0.850	0.045	77.21		0.82

included 9 steps with a rise of 4.5 cm and a tread of 5.0 cm, and so on. For an ogee spillway with a slope of 0.75:1, steps are provided on the spillway chute.

### 8.3 Results and Discussions

Experiments are carried out with this working model at heads of 4 m, 5.5 m, and 6.5 m using V notch. V notch is provided at the end of the stilling basin for controlling tailwater depth. Table 8.1 compares the specific energy and energy dissipation results with the following sets of configurations for varying heads and discharges.

The experimental results show that the energy dissipation increases as the length of steps increases, with the highest energy dissipation achieved with the lowest non-dimensional parameter value (0.69). The percentage of energy dissipation decreases with rising operational head and increases with decreasing rise-tread ratio of steps and step number in both sets of ogee stepped spillway models. Due to the combination of energy dissipators, the solid roller bucket performs well by increasing tailwater depth by 0.23 m over the stilling basin. The tailwater depth is preserved in a range of 1.1–1.4 times post jump in both sets of models by having a movable V notch on the stilling basin. It has been observed that the Froude number also decreases with an increase in head and discharge. The intensity of velocity is reduced as a result of the longer steps, which decreases the load of energy dissipation on the solid roller bucket and reduces the length of the stilling basin (Chanson 1994). The 9-step model of an ogee stepped spillway (Set 2) with the lowest non-dimensional parameter achieved 80.24% energy dissipation for a 4 m head (0.69).

### 8.4 Conclusion

For different heads and discharge, the experiments are conducted using a combination of energy dissipator models with 12 steps (Set 1) and 9 steps (Set 2) models. The stepped spillway with a combination of solid roller bucket and type II stilling basin model (Set 2) was found to dissipate 80.24% of energy. Among other devices, this is the optimal energy dissipation. For a 4 m head, this model maintained a 0.23 m tailwater depth, a non-dimensional parameter of 0.69, and a Froude number of 5.53.

### References

- Bhosekar VV, Patnaik S, Bhajantri MR, Sunderlal BS (2012) Limitations of spillway roller bucket. *Int J Water Energy* 69(7):47–54
- Chaft C, Hazzab A, Seddini A (2010) Study of flow and energy dissipation in stepped spillways. *Jordan J Civil Eng* 4(1):1–11

- Chatiola JG, Jurdi BR (2004) Stepped spillway as an energy dissipater. *Canadian Water Resour J* 29(3):147–158
- Chanson H (1994) Comparison of energy dissipation nappe and skimming flow regime on stepped chutes. *J Hydra Res IAHR* 32(2):213–218
- Sorensen RM (1985) Stepped spillway hydraulic model investigation. *J Hydraul Eng ASCE* 111(12):1461–1472
- Tung YK, Mays LW (1982) Optimum design of stilling basins for overflow spillway. *J Hydra Div ASCE* 108(10):1163–1178

# Chapter 9

## Estimation of Coefficient of Discharge for Side Compound Weir Using the GMDH Technique



Mujib Ahmad Ansari, Ajmal Hussain, and Faisal Ahmad

**Abstract** A sharp-crested side compound weir is a flow diversion structure provided in one or both sidewalls of a channel to spill/divert water from the main channel. It is widely used in irrigation, hydraulic and environmental engineering. The mechanism of flow through the compound side weir is complicated, and it is difficult to establish a model to accurately predict the coefficient of discharge. In this study, the group method of data handling network with quadratic polynomial, ratio and linear two-variable functions was used to predict the coefficient of discharge for side compound sharp-crested weir. The discharge coefficient of compound side weir has a high correlation with three dimensionless parameters including upstream Froude number ( $F_1$ ), ratio of weighted crest height of side weir to crest length of side weir ( $P/L$ ) and the ratio of upstream flow depth to crest length of side weir ( $y_1/L$ ). Therefore, a new model for the determination of coefficient of discharge of side rectangular sharp-crested compound weir was developed. Results of the GMDH model were also compared with the available regression model, and it was found that GMDH results were better than that of the regression model. The performance of the present model is based on the coefficient of correlation ( $R = 0.8489$ ), mean absolute percentage error ( $MAPE = 17.62$ ) and average root means square error ( $RMSE = 16.10$ ). On the basis of sensitivity analysis, it was found that ( $P/L$ ) was the most effective parameter for the prediction of coefficient of discharge.

**Keywords** Side compound weir · Coefficient of discharge · Froude number · GMDH

### 9.1 Introduction

Flow through side weir represents gradually varied flow with non-uniform discharge. The discharge in the channel varies along the length of the channel due to lateral withdrawal of water from the main channel. A side weir is a flow diversion structure,

---

M. A. Ansari (✉) · A. Hussain · F. Ahmad  
Department of Civil Engineering, Zakir Hussain College of Engineering & Technology, AMU,  
Aligarh 202002, India  
e-mail: [maansari@zhcet.ac.in](mailto:maansari@zhcet.ac.in)

which is widely used in irrigation, environmental and hydraulic engineering as a head regulator. Side weirs are also used in channel systems, river-control structures, irrigation canals, water and wastewater-treatment plants and for stormwater overflow from urban drainage systems. The various hydraulic structures used to divert flow are weirs, spillways, sluice gates, orifices, etc. (Ansari et al. 2019; Hussain et al. 2010, 2011, 2014, 2016; Swamee et al. 1994; Ramamurthy et al. 1986). The flow over a side weir is a typical case of spatially varied flow. A side weir is designed to divert a certain amount of discharge, and therefore knowing an accurate discharge is important.

Due to the use of various geometric and hydraulic shapes of the side weir, extensive research work has been conducted from different viewpoints for different types of side weir. Probably, the first theoretical approach to the hydraulics of a side weir in a rectangular channel was reported by De Marchi (1934). Most of the earlier experimental studies and theoretical analysis were limited to the flow over side weirs in a rectangular channel (e.g. De Marchi 1934; Emiroglu et al. 2011; Ranga Raju et al. 1979; Uyumaz and Smith 1991; Shariq et al. 2018) triangular channel (Vatankhah 2012a), trapezoidal channel (Cheong 1991), and circular main channels (Vatankhah 2012b; Hager 1987). Normally, weirs are generally rectangular in shape and have a limitation in cases where there is a need to divert flow discharges varying from low- to high-water levels. Therefore, a new shape of side weirs has been presented known as compound side weirs. Despite analyzing a wide range of reliable experimental data collected in the present investigation having a wide range of hydraulic and geometrical variables, the problem of coefficient of discharge for sharp-crested side compounds has remained inconclusive. It is felt that it is partly due to the complexity of the phenomenon involved and partly because of the limitation of the analytical tool commonly used by most of the earlier investigators, namely statistical regression.

Recently, the GMDH network is used in many fields to forecast and model the behaviors of unknown or complex systems based on different sets of multi-input–single-output data pairs (Amanifard et al. 2008). In addition, the GMDH approach is applied in different researches such as energy conservation, economics and engineering geology, and various areas of hydraulics and water resources engineering (Amanifard et al. 2008; Srinivasan 2008; Najafzadeh et al. 2013; Ansari and Muzzammil. 2014; Ansari 2014 etc.).

Discharge coefficient of side compound weir can be expressed as a function of the average velocity of flow over the cross section of the basin ( $V$ ), upstream depth of flow in channel ( $y_1$ ), acceleration due to gravity ( $g$ ), crest length of side weir ( $L$ ), width of main channel ( $B$ ), weighted crest height of side weir ( $P$ ), width of diverted channel ( $b$ ), dynamic viscosity of water ( $\mu$ ) and density of water ( $\rho$ ). The schematic view of the side compound weir is shown in Fig. 9.1. Due to different crest heights of upper and lower weirs in a compound weir, the crest height should be replaced with the weighted crest height  $P$  as follows:

$$P = \frac{P_1 L_1 + P_2 L_2 + P_3 L_3}{L}$$

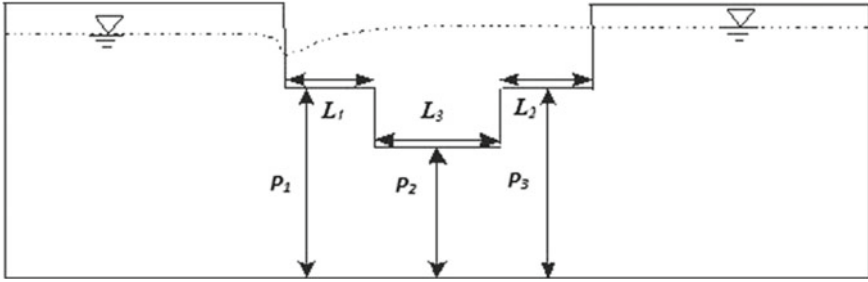


**Fig. 9.1** Schematic view of side compound weir

where  $P_1, P_2, P_3, L_1, L_2$  and  $L_3$  are the parts of side compound weir as shown in Fig. 9.1.

The functional relationship for the compound side weir may be expressed as

$$C_d = f(P, L, B, g, V, y_1, b, \rho, \mu, , L) \tag{9.1}$$

Using the Buckingham- $\pi$  theorem, non-dimensional equations in functional forms can be written as follows:

$$C_d = f\left(\frac{P}{L}, \frac{B}{L}, \frac{y_1}{L}, F_1, \frac{b}{L}, \frac{\mu}{\rho VL}\right) \tag{9.2}$$

So that  $F_1$  represents the approach flow Froude number. The influence of the Reynolds number,  $R_e = PVL/\mu$ , is relatively insignificant,  $b/L$  and  $B/L$  are constant in the present study, hence, may be dropped from Eq. (9.2). The final functional relationship for  $C_d$  may, therefore, be expressed as

$$C_d = f\left(\frac{P}{L}, \frac{y_1}{L}, F_1\right) \tag{9.3}$$

To see the effect of various parameters on the coefficient of discharge,  $C_d$ , and to establish a relationship among the dependent and independent parameters of Eq. (9.3), experimental programmes are carried out in the present study.

## 9.2 Experimental Programe

The data sets for four different weighted crest heights, i.e. 7.5 cm, 8.5 cm, 11.5 cm and 12.5 cm of side compound weir obtained by Ansari et al. (2019) have been used in this study. The experimental setup of Ansari et al. (2019) consisted of a primary flume of length, width and depth of 12.8 m, 0.29 m and 0.39 m, respectively. Discharge through the side weir was passed into a diversion channel of length, width and

**Table 9.1** Range of data collected for side weir in the present study

Parameter	Unit	Range of data	
		Min	Max
$Q_1$	m <sup>3</sup> /s	0.0002	0.0785
$Q_3$	m <sup>3</sup> /s	0.0017	0.0293
$B$	m	0.39	0.39
$y_1$	m	0.124	0.345
$L$	m	0.20	0.20
$P$	m	0.075	0.125
$F_1$	–	0.003	0.495

height of 4.18 m, 0.2 m and 0.35 m, respectively, and then moved to a return channel. Discharge flowing through the side weir was measured by a rectangular sharp-crested weir- $Y_1$  provided at the end of the diversion channel. The total discharge measured by a rectangular sharp-crested weir- $Y_2$  was provided at the end of the channel. The width of each side weir was 20 cm. All side weirs were placed in the groove and leveled with the wall of the channel.

The nappe was fully ventilated during the experimentation. Experiments were performed under free flow through the side compound weir under subcritical flow conditions. The range of data collected in the present work has been listed in Table 9.1.

### 9.3 Analysis of Data, Results and Discussion

The Group Method of Data Handling model has been developed for the prediction of coefficient of discharge of side compound weir. The details are presented here.

#### 9.3.1 Proposed GMDH Model for Coefficient of Discharge of Side Compound Weir

The results of the Group Method of Data Handling networks are presented in this section. In the present study, the polynomials of various types, i.e. quadratic two variables and quadratic one variables of GMDH network, are used as transfer functions and are written as

$$\text{Quadratic (two variable): } \hat{y} = G(x_i x_j) = a_0 + a_1 x_i + a_2 x_j + a_3 x_i x_j + a_4 x_i^2 + a_5 x_j^2 \quad (9.4)$$

$$\text{Quadratic (one variable): } \hat{y} = G(x_i x_j) = a_0 + a_1 x_i + a_2 x_i^2 \quad (9.5)$$

The proposed GMDH network yielded a correlation coefficient of 0.8489 (Training).

One of the important features of GMDH networks is analytical equations which can be obtained using a quadratic polynomial. Analytical Eqs. (9.10–9.20) given by GMDH network for predicting the coefficient of discharge of sharp-crested side compound weir:

$$(C_d)_2^1 = 0.2490 + 0.10045(P/L) + 0.1270(P/L)^2 \quad (9.6)$$

$$(C_d)_4^1 = 0.7586 - 2.3204(F_1) + 2.8375(F_1)^2 \quad (9.7)$$

$$\begin{aligned} (C_d)_1^2 = & -0.6491 - 2.5442(C_d)_2^1 + 9.338707((C_d)_2^1)^2 + 5.8157(C_d)_4^1 \\ & - 1.63915((C_d)_4^1)^2 - 9.1403(C_d)_2^1(C_d)_4^1 \end{aligned} \quad (9.8)$$

$$\begin{aligned} (C_d)_7^2 = & 6.2816e + 0.12 + 2.5338e + 0.12(P/L) + 3.2038e + 0.12(P/L)^2 \\ & - 2.5224e + 0.13(C_d)_2^1 + 3847.706((C_d)_2^1)^2 - 2024.086(P/L)(C_d)_2^1 \end{aligned} \quad (9.9)$$

$$\begin{aligned} (C_d)_9^1 = & 0.1216 + 1.006 + 3.349(P/L) - 0.4081(P/L)^2 \\ & - 2.7011(y_1/L) + 1.2974(y_1/L)^2 - 1.695(P/L)(y_1/L) \end{aligned} \quad (9.10)$$

$$\begin{aligned} (C_d)_8^2 = & -0.7952 + 2.6685(F_1) - 1.6264(F_1)^2 + 3.2315(C_d)_9^1 \\ & - 1.418489(C_d)_9^1{}^2 - 4.26785(F_1)(C_d)_9^1 \end{aligned} \quad (9.11)$$

$$\begin{aligned} (C_d)_6^3 = & -0.7693 + 4.7948(C_d)_7^2 - 6.8864((C_d)_7^2)^2 + 0.2958(C_d)_8^2 \\ & + 0.4054((C_d)_8^2)^2 + 1.1145(C_d)_7^2(C_d)_8^2 \end{aligned} \quad (9.12)$$

$$\begin{aligned} (C_d) = & 0.0502 - 0.7542(C_d)_1^2 + 3.1817(C_d)_1^2{}^2 + 1.4462(C_d)_6^3 + 1.6297((C_d)_6^3)^2 \\ & - 4.4183(C_d)_1^2(C_d)_6^3 \end{aligned} \quad (9.13)$$



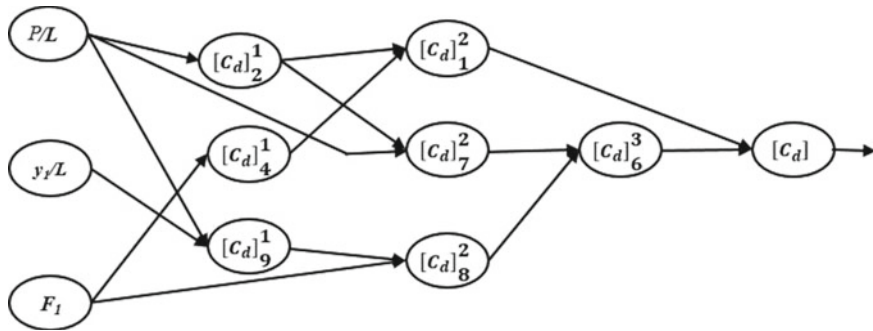


**Fig. 9.2** Structure of present GMDH model  $(C_d)_{\text{Predicted}} = 0.6668(C_d)_{\text{Observed}} + 0.1238$

**Table 9.2** Performance parameter of the present GMDH model

MODEL	<i>R</i>	<i>MAPE</i>	<i>RMSE</i>	Performance
GMDH	0.8159	19.3107	17.4767	All
	0.8489	17.6266	16.1061	Training
	0.7673	25.5045	22.2852	Validation

In the above equations, the subscript and superscript of each parameter represent the number of pertaining layers and neurons, respectively. The proposed structure of the GMDH network containing of 3 selective neurons in the first layer, 3 selective neurons in the second layer, one selective neuron in the third layer, respectively, and a selective neuron in the output layer (3–3–1–1) for predicting the coefficient of discharge ( $C_d$ ) is presented in Fig. 9.2.

The GMDH model has the highest *R* and lowest *MAPE* and *RMSE*, respectively, 0.8489, 17.62 and 16.10 during training and 0.7673, 25.50 and 22.28 during validation. In the end, therefore, the GMDH model with performance parameters given in Table 9.2 is recommended for general use in order to predict the coefficient of discharge of side compound weir.

The predicted values of coefficient of discharge ( $C_d$ ) have been plotted against its observed values for all, training and validation data sets, as shown in Fig. 9.3 for the GMDH model.

### 9.3.2 Sensitivity Analysis

Sensitivity tests were conducted to find out the relative importance of each of the independent parameters (input) on the prediction of coefficient of discharge of sharp-crested side compound weir (output).

Comparison of different GMDH models, with one of the independent parameters removed in each case, is presented in Table 9.3. The results in Table 9.3 show that the ( $P/L$ ) is the most significant parameter for the prediction of coefficient of discharge. The variables in order of decreasing level of sensitivity for the GMDH model are ( $/L, y_1/L$  and  $F_1$ ). However, considering the limitation and uncertainties in the data, a full-fledged network involving all input variables would be desirable.

### 9.4 Conclusion

The following conclusions are drawn from the present study.

A generalized model for predicting the coefficient of discharge of side rectangular sharp-crested side compound weir using the GMDH network has been developed. The predictions based on the GMDH model were generally more satisfactory than those given by traditional regression equations because of low error and high correlation coefficient.

On the basis of sensitivity analysis of the GMDH model, it was observed that ( $P/L$ ) is the most significant parameter. The sensitivity analysis gives the impression that  $F_1$  has only marginal influence on the coefficient of discharge of a sharp-crested side compound weir. But in view of variability in the outcome resulting from the application of different analytical schemes, the GMDH network, which requires all input quantities, may be followed for generality.

**Fig. 9.3 a** Comparison between observed and predicted values of  $C_d$  for the GMDH model. ( $C_d$ ) Predicted =  $0.6850(C_d)$  Observed +  $0.1118$ . **b** Comparison between observed and predicted values of  $C_d$  for the GMDH model ( $C_d$ ) Predicted =  $0.6589(C_d)$  Observed +  $0.1529$ . **c** Comparison between observed and predicted values of  $C_d$  for the GMDH model

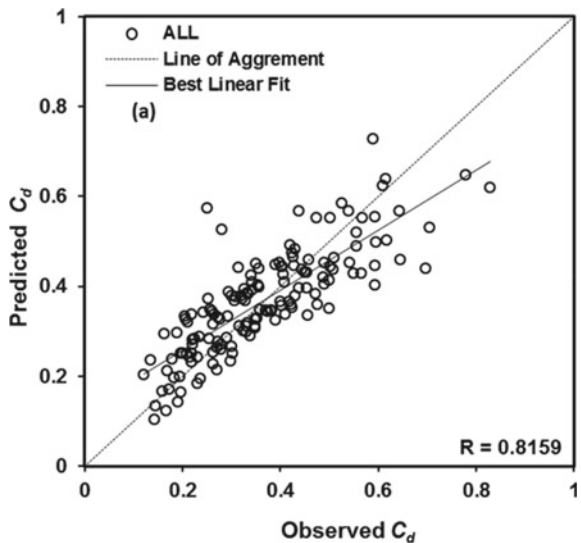
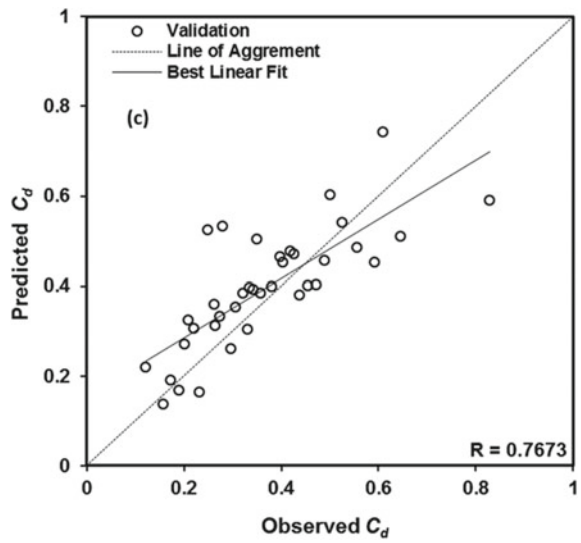
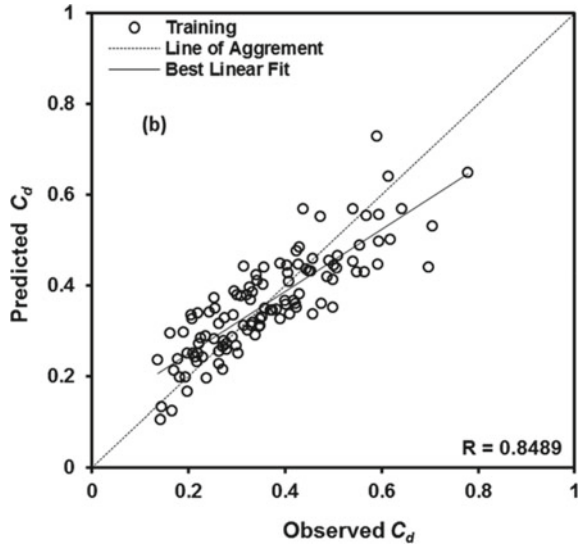


Fig. 9.3 (continued)



**Table 9.3** Sensitivity analysis

Input Variables	<i>R</i>	<i>MAPE</i>	<i>RMSE</i>	Performance
$C_d = f\left(\frac{P}{L}, \frac{y_1}{L}, F_1\right)$	0.8159	19.3107	0.0821	All
	0.8489	17.6266	0.0736	Training
	0.7673	25.5045	0.1037	Validation
$C_d = f\left(\frac{y_1}{L}, F_1\right)$	0.6402	28.5073	0.1091	All
	0.6409	28.1934	0.1068	Training
	0.3432	69.7598	0.9793	Validation
$C_d = f\left(\frac{P}{L}, F_1\right)$	0.7347	22.4617	0.0963	All
	0.7544	21.5161	0.0914	Training
	0.6676	26.6374	0.1191	Validation
$C_d = f\left(\frac{P}{L}, \frac{y_1}{L}\right)$	0.8006	20.3506	0.0850	All
	0.8195	19.4973	0.0797	Training
	0.7673	25.5045	0.1037	Validation

## References

- Amanifard N, Nariman-Zadeh N, Farahani MH, Khalkhali A (2008) Modeling of multiple short-length-scale stall cells in an axial compressor using evolved GMDH neural networks. *J Energy Convers Manage* 49(10):2588–2594
- Ansari MA (2014) Sediment removal efficiency computation in vortex settling chamber using artificial neural networks, Water and Energy International, Central Board of Irrigation and Power (CBIP). New Delhi 71(1):54–67
- Ansari MA, Muzzammil M (2014) Application of group method of data handling for prediction of peak floods. International Conference ICEFT-2014 on Eco-friendly technologies for sustainable growth, 27–28 March, 2014, Anjuman-i-Islams M.H. Saboo Siddik College of Engineering, Mumbai, 115–119
- Ansari MA, Hussain A, Shariq A, Alam F (2019) Experimental and numerical study for the estimation of coefficient of discharge for side compound weir. *Can J Civ Eng* 46(10):887–895
- Cheong H (1991) Discharge coefficient of lateral diversion from trapezoidal channel. *J Irr Drain Eng ASCE* 117(4):461–475
- De M (1934). G.Essay on the performance of lateral weirs. *L Energia Electrica Milano* 11(11):849–860 Italy
- Emiroglu ME, Agaccioglu H, Kaya N (2011) Discharging capacity of rectangular side weirs in straight open channels. *J Flow Measur Instrum* 22:319–330
- Hager WH (1987) Lateral outflow of side weirs. *J Hydraul Eng ASCE* 113(4):491–504
- Hussain A, Ahmad Z, Asawa GL (2010) Discharge characteristics of sharp-crested circular side orifices in open channels. *J Flow Measur Instrumen Elsevier*. 21(3):418–424
- Hussain A, Ahmad Z, Asawa GL (2011) Flow through sharp-crested square side orifices under free flow in open channels. *J Agric Water Manag Elsevier*. 98(10):1536–1544
- Hussain A, Ahmad Z, Ojha CSP (2016) Flow through lateral circular orifice under free and submerged flow conditions. *J Flow Measur Instrumen Elsevier*. 36(10):32–35
- Hussain A, Ahmad Z, Ojha CSP (2014) Analysis of flow through lateral rectangular orifices in open channels. *J Flow Measur Instrumen Elsevier* 36(10):32–35
- Najafzadeh M, Barani GA, Hessami Kermani MR (2013) Abutment scour in clear-water and live-bed conditions by GMDH network. *Water Sci Technol* 67(5):1121–1128
- Ramamurthy AS, Udoyara ST, Serraf S (1986) Square Lateral orifices in open channel. *J Environ Eng* 135(5):292–298
- Shariq A, Hussain A, Ansari MA (2018) Lateral flow through the sharp crested side rectangular weirs in open channels. *Flow Measur Instrumen Elsevier* 59:8–17
- Srinivasan D (2008) Energy demand prediction using GMDH networks. *Neuro Comput* 72(1–3):625–629
- Swamee PK, Pathak SK, Mohan M, Agrawal SK, Ali MS (1994) Subcritical flow over rectangular side weir. *J Irr Drain Eng ASCE* 120(1):212–217
- Uyumaz A, Smith RH (1991) Design procedure for flow over side weirs. *J Irrig Drain Engg, ASCE* 117(1):79–90
- Vatankhah A (2012) Analytical solution for water surface profile along a side weir in a triangular channel. *J Flow Measur Instrumen* 23(1):76–79
- Vatankhah A (2012) New solution method for water surface profile along a side weir in a circular channel. *J Irrig Drain Eng*. [https://doi.org/10.1061/\(ASCE\)IR.19434774.0000483.948-954](https://doi.org/10.1061/(ASCE)IR.19434774.0000483.948-954)

# Chapter 10

## Flow Distributions in a Compound Channel with Diverging Floodplains



**Bhabani Shankar Das, Kamalini Devi, Jnana Ranjan Khuntia, and Kishanjit Kumar Khatua**

**Abstract** During flood, the flow distribution in main channel and floodplain is always an important factor for river engineer to model, accordingly, the measures can be taken in the floodplain area. Experiments on diverging compound channel show that the flow distribution in main channel and floodplains are found to be a function of four non-dimensional geometric and hydraulic parameters such as width ratio, relative flow depth, relative longitudinal distance and flow aspect ratio. This paper presents an empirical-non-linear-multivariable regression model by considering the aforementioned parameters to compute discharge distribution in diverging compound channels. The model is developed using discharge distribution data obtained from present laboratory experiments and with the published data of other researchers on diverging compound channels. The predictive strength of the developed regression model is validated using several major statistics. All deployed statistics have indicated that the developed model is highly significant. The outcome for all diverging compound channels resulted in minimum RMSE and MAPE values as 0.0092 and 4.35%, respectively, when the discharge is predicted using the developed multivariable regression model.

**Keywords** Flow distribution · Diverging compound channel · Multivariable regression analysis · Width ratio · Aspect ratio; relative flow depth

---

B. Shankar Das (✉)

Civil Engineering Department, National Institute of Technology, 800005 Patna, India

K. Devi

Civil Engineering Department, Vidya Jyothi Institute of Technology, Telangana 500075 Hyderabad, India

J. R. Khuntia

Civil Engineering Department, St. Martin's Engineering College, Dhulapally, Secunderabad 500100, Telangana, India

K. K. Khatua

Civil Engineering Department, National Institute of Technology Rourkela, Odisha 769008 Rourkela, India

## 10.1 Introduction

Flow modelling in the compound channel is a challenging task for the river engineer as the shape of floodplain and main channel significantly affect the conveyance capacity. Natural river generally exhibits non-prismatic cross-sectional shape during flooding and known as non-prismatic compound channels. These type of compound channels are broadly classified into three types, viz., diverging, converging and skewed types compound channel depending on the floodplains shape (Chlebek 2009). Over-estimation of floodplain discharge leads to extra cost for protection near floodplain area, whereas underestimation leads to loss of life and property of the country. Thus, knowledge on flow distribution in main channel and floodplain in such channel is very essential. Diverging and converging geometry of floodplains affect significantly to the conveyance estimation process. Flooding rivers usually present flow-width variations that give rise to non-uniform flows in non-prismatic compound geometries. Flow distribution in the diverging compound channel (DCC) is a very important topic in river hydraulics to be investigated from a practical point of view in relation to flood risk assessment, bank protection, navigation and sediment-transport depositional pattern. Very few works were found from the literature on a compound channel with diverging floodplains. Proust (2005) is the first to work on diverging compound channels and presented an independent subsection method to model the flow depth and velocity at the different subsections of prismatic and non-prismatic compound channels. He categorized the compound channel into three subsections such as left floodplain, main channel and right flood plain. Das et al. (2018) divided the compound channel into four sub zone such as left flood plain, right floodplain, upper main channel and lower main channel. Bousmar et al. (2006) discuss the flow behaviour in the compound channel with diverging floodplain for two different diverging angles  $3.81^\circ$  and  $5.7^\circ$ . Later Yonesi et al. (2013) worked on diverging compound channels with differential bed roughness for diverging angles  $3.81^\circ$ ,  $5.7^\circ$  and  $11.3^\circ$ . Das et al. (2020) use the soft computing technique to estimate the discharge in converging and diverging compound channels. Das et al. (2017) and Devi et al. (2021) developed the numerical and analytical model for prediction of depth averaged velocity and boundary shear distribution in prismatic and non-prismatic compound channels without incorporating any flow distribution calculation in the model. Due to non-prismatic effect of the floodplain, the existing traditional methods like single channel method (SCM), divided channel method (DCM) and numerical methods like lateral distribution method (LDM), Shiono and Knight method (SKM) failed to provide accurate stage, discharge and velocity at different sections of the non-prismatic portion (Das et al. 2019).

Wormleaton et al. (1982), Knight and Demetriou (1983), Devi et al. (2017), Devi and Khatua (2019) and Khuntia et al. (2019) show that the vertical apparent shear exists on the interface between the main channel and the floodplain which generally accelerates the flow on the floodplain and resists the flow in the main channel. Knight and Demetriou (1983) developed the flow percentage in main channel (%Q<sub>mc</sub>) model by considering the two non-dimensional parameters, width ratio and relative flow

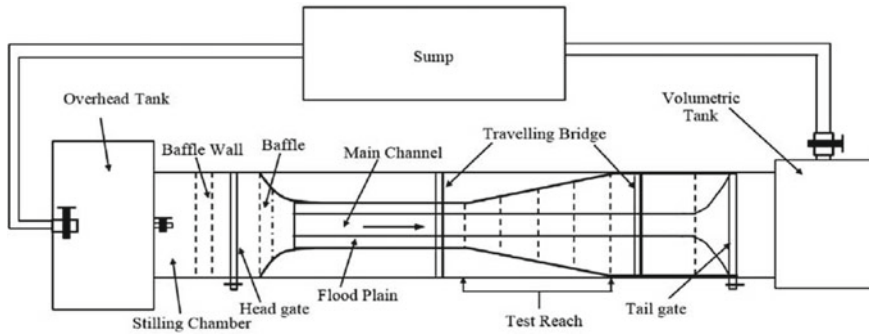


**Fig. 10.1** Plan view of diverging compound channel setup at Hydraulics Engineering Laboratory, NIT Rourkela, India

depth for the prismatic compound channel for width ratio ranges from 1.0 to 3.0. Khatua and Patra (2009) developed the %Q<sub>mc</sub> model for up to 4.0 width ratio. Devi et al. (2016) developed the %Q<sub>mc</sub> model for the straight prismatic compound channel for width ratio ranges from 2.0 to 15.75 by considering four different non-dimensional parameters such as width ratio, relative flow depth, channel side slope and flow aspect ratio. To develop the model for main channel discharge in a diverging compound channel, a large number of data sets is necessary. Therefore, experiments have been conducted in three diverging compound channels at Hydraulics Engineering Laboratory of NIT Rourkela, India, for different flow conditions to study the flow distributions pattern in the floodplain and main channel (Fig. 10.1).

## 10.2 Experimental Setup

Three sets of compound channels with diverging floodplains made up of perspex sheet were fabricated inside a tilting flume of size 22 m long  $\times$  2 m width  $\times$  0.5 m depth. Keeping the geometry of the main channel constant, the diverging length of the fabricated channels were changed to 5 m, 3 m and 2 m. The diverging angles of the floodplains were estimated to be 5.93°, 9.83° and 14.57°, respectively. Figure 10.2 shows the experimental section of three diverging compound channel. Longitudinal bed slope of the channel was maintained at 0.0014, satisfying subcritical flow conditions. The roughness of the floodplain and main channel were alike and the Manning's  $n$  found out as 0.011 from the in-bank experimental runs in the channel. In order to compare the results of experiments in non-prismatic compound channels with different divergence angles ( $\theta$ ) for each selected discharge, the downstream water level was adjusted using the tailgate. It was done in such a way that the backwater profile reached a given depth in the central section of diverging reach at  $x = 14.5$  m,  $x = 15.5$  m and  $x = 16$  m for 5 m, 3 m and 2 m diverging portions of the compound channels, respectively (Fig. 10.3). Water depths were measured



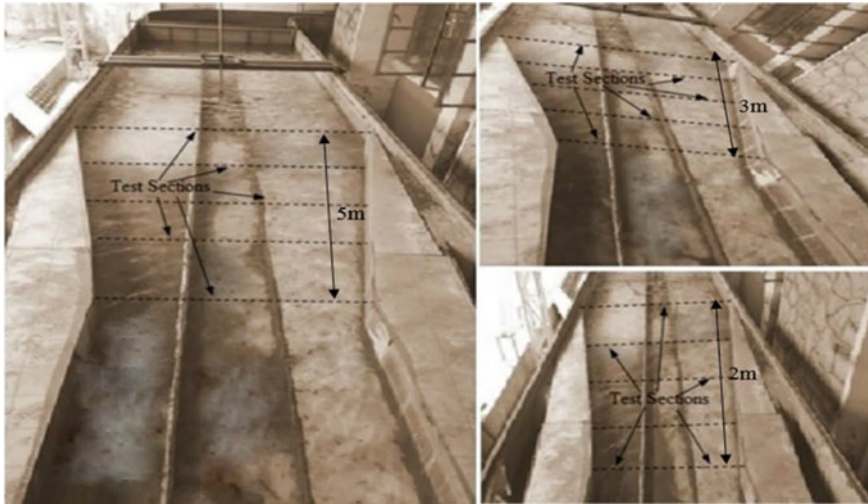


**Fig. 10.2** Experimental sections of three different diverging compound channels ( $5.93^\circ$ ,  $9.83^\circ$ , and  $14.57^\circ$ )

directly with a point gauge located on an instrument carriage. A micro-Pitot tube of 4.77 mm external diameter in combination with suitable inclined manometers as well as 16-MHz Micro-ADV (Acoustic Doppler Velocimeter) were used to measure velocities. Details of experimental setup and procedures are available in Das and Khatua (2018a, b). Summary of experimental characteristics of present test channels is given in Table 10.1.

### 10.3 Discharge Distributions

#### 10.3.1 Flow Percentage in Main Channel and Floodplains

The individual discharges carried by the main channel ( $Q_{mc}$ ) and by the floodplain ( $Q_{fp}$ ) are estimated by summing the product of depth averaged velocity with the respective elementary cross-sectional area ( $\Delta A$ ) over the main channel ( $A_{mc}$ ) and floodplain ( $A_{fp}$ ) zone, respectively. The expressions are given as

$$Q_{mc} = \sum_{mc} U_d \Delta A \quad \text{and} \quad Q_{fp} = \sum_{fp} U_d \Delta A \quad (10.1)$$

The mean velocities of the flow in the main channel ( $U_{mc}$ ) and floodplain ( $U_{fp}$ ) can be evaluated by

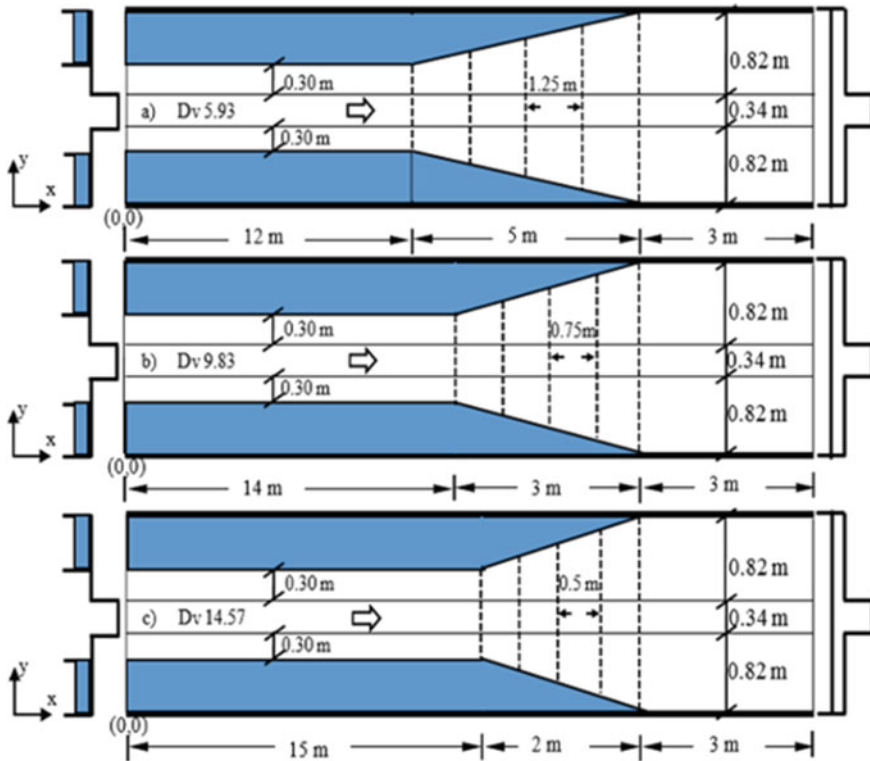


**Fig. 10.3** Schematic view of compound channels with non-prismatic floodplains, diverging from 300 to 820 mm along a length of **a** 5 m (Dv 5.93), **b** 3 m (Dv 9.83) and **c** 2 m (Dv 14.57)

**Table.10.1** Summary of experimental characteristics

Series	Geometry	Relative flow depth, $D_r^{(1)}$	Discharge Q (m <sup>3</sup> /s)	Fr	Re ( $\times 10^5$ )
Dv 5.93	Diverging angle = 5.93° (5 m diverging reach)	0.15,0.20,0.25 0.30,0.40,0.50	0.027, 0.032, 0.037, 0.043, 0.055, 0.067	0.211–0.581	0.471–1.949
Dv 9.83	Diverging angle = 9.83° (3 m diverging reach)	0.15,0.20,0.25 0.30,0.40,0.50	0.025, 0.029, 0.035, 0.041, 0.053, 0.065	0.192–0.544	0.440–1.862
Dv 14.57	Diverging angle = 14.57° (3 m diverging reach)	0.15,0.20,0.25 0.30,0.40,0.50	0.024, 0.028, 0.033, 0.040, 0.051, 0.062	0.189–0.517	0.426–1.801

<sup>(1)</sup>At  $x = 14.5$  m,  $15.5$  m and  $16$  m for Dv5.93, Dv9.83, and Dv14.57, respectively, Fr-Froude number, Re-Reynolds number

$$U_{mc} = \frac{Q_{mc}}{A_{mc}} \text{ and } U_{fp} = \frac{Q_{fp}}{A_{fp}} \quad (10.2)$$

where  $A_{mc}$  and  $A_{fp}$  denote the cross-sectional areas of the main channel and floodplain, respectively. The percentages of flow carried by both subareas are then obtained. Here, the total discharge is utilized as a divisor for calculating percentage discharge using Eq. 10.3.

$$\frac{Q_{mc}}{Q} \times 100 = \%Q_{mc} \text{ and } \frac{Q_{fp}}{Q} \times 100 = \%Q_{fp} \quad (10.3)$$

The percentages of flow carried by the floodplain ( $\%Q_{fp}$ ) are plotted versus longitudinal distance for three diverging compound channels in Fig. 10.4.

$$\% \frac{Q_{mc}}{Q} = 100 - \% \frac{Q_{fp}}{Q} \quad (10.5)$$

### 10.3.2 Results on Flow Distribution

In order to compare the evolution of the discharge distribution along the compound channels with non-prismatic floodplains diverging from 300 to 820 mm along 5 m, 3 m and 2 m lengths, the percentage of discharge in the floodplains were plotted (Fig. 10.4) against the longitudinal distance of diverging portion. Figure 10.4 indicates that for the same relative depth  $\beta$  as the divergence angle increases from  $\theta = 5.93^\circ$  to  $\theta = 14.57^\circ$ , the proportion of flow on floodplains decreases.

## 10.4 Sources of Data

For the development of the model, data has been collected from the present experimental channels and the data from University Catholic de Louvain diverging experimental channel (Bousmar et al. 2006) and from University of Tehran (Yonesi et al. 2013) on smooth diverging compound channel data. The geometric and hydraulic parameters of all the diverging compound channels are presented in Tables 10.2 and 10.3.

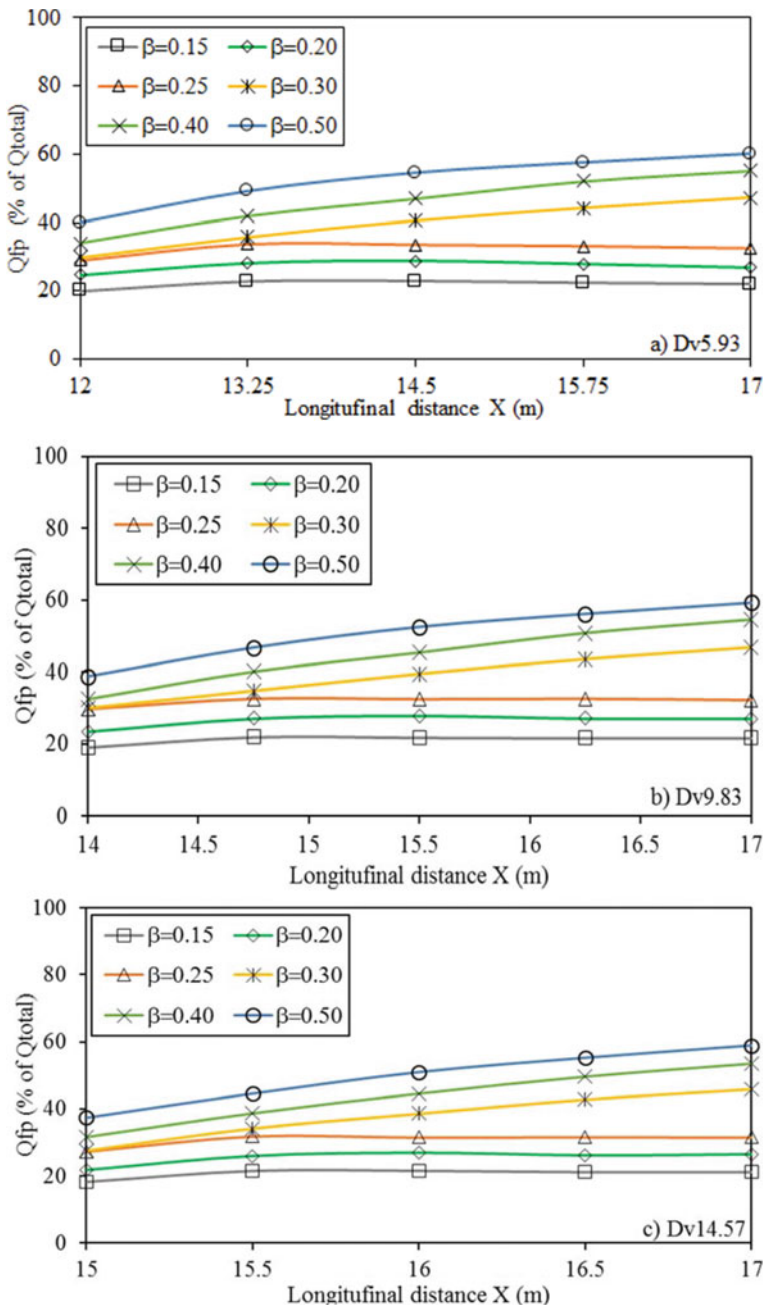


**Fig. 10.4** In steam-wise direction for the diverging portion, percentage of flow at floodplain computed from the total flow **a** Dv5.93 series, **b** Dv9.83 series and **c** Dv14.57 series

**Table.10.2** Details of geometric parameters collected from experimental work and published data for diverging compound channel

Verified test channel	$S_0$	$b$ in (m)	$h$ in (m)	$\theta$ in ( $^\circ$ )	$\alpha$	$\delta$
1	2	3	4	6	5	7
NITR data -Dv5.93	0.0014	0.34	0.113	5.93	5.82–2.76	3.01
NITR data -Dv9.83	0.0014	0.34	0.113	9.83	5.82–2.76	3.01
NITR data -Dv14.57	0.0014	0.34	0.113	14.57	5.82–2.76	3.01
B et al. -Dv3.81	0.00099	0.40	0.05	3.81	3.0–1.0	8.00
B et al. -Dv5.71	0.00099	0.40	0.05	5.71	3.0–1.0	8.00
Y-Dv3.81	0.00088	0.40	0.18	3.81	3.0–1.0	2.22
Y-Dv5.71	0.00088	0.40	0.18	5.71	3.0–1.0	2.22
Y-Dv11.31	0.00088	0.40	0.18	11.31	3.0–1.0	2.22

B et al.- Bousmar et al. (2006, Y-Yonesi et al. (2013), Longitudinal slope- $S_0$ , Main channel width in metre-  $b$ , Main channel depth in metre - $h$ , Diverging angle in degree -  $\theta$ , Width ratio-  $\alpha$ , Aspect ratio-  $\delta = b/h$

**Table.10.3** Details of hydraulic and surface parameters for diverging compound channel collected from experimental work and

Verified Test channel	$Q$ in ( $m^3/s$ )	$n$	$\beta$	$Re$ in ( $\times 10^5$ )	$Fr$
1	2	3	5	6	7
NITR data -Dv5.93	0.026–0.067	0.0095–0.0161	0.146–0.51	0.49–1.58	0.42–0.68
NITR data -Dv9.83	0.025–0.065	0.0093–0.015	0.144–0.52	0.53–1.61	0.44–0.70
NITR data -Dv14.57	0.024–0.062	0.0087–0.0136	0.142–0.51	0.58–1.93	0.51–0.82
B et al. -Dv3.81	0.012–0.020	0.0053–0.025	0.218–0.51	0.34–1.39	0.38–0.86
B et al. -Dv5.71	0.012–0.020	0.0076–0.027	0.253–0.54	0.34–1.30	0.25–0.66
Y-Dv3.81	0.037–0.0615	0.0121–0.0211	0.142–0.36	1.43–1.93	0.24–0.33
Y-Dv5.71	0.037–0.0615	0.0129–0.0207	0.142–0.35	1.35–1.85	0.26–0.362
Y-Dv11.31	0.037–0.0615	0.0122–0.0223	0.143–0.35	1.28–1.74	0.28–0.38

### 10.5 Model Development

In this research, for the development of the mathematical expression for flow distributions in DCC, multivariable regression analysis (MRA) has been adopted. Along with present experimental dataset, other researchers’ dataset on DCC are considered for development of the model. 75% of the total data sets are randomly selected and utilized for the development of the model and the rest 25% of the total data sets are

kept independently for the validation purpose. From the experimental results analyses, the percentage of flow in FP was found to be a function of four non-dimensional parameters as such as width ratio, relative flow depth, relative longitudinal distance and flow aspect ratio, where the non-dimensional parameters are defined as follows:

1. Width ratio ( $\alpha$ ) =  $B/b$ , where  $B$ —total width of the channel,  $b$ —width of the main channel
2. Relative flow depth ( $\beta$ ) =  $(H-h)/H$ , where  $H$ —height of water at a particular section and,  $h$ —bank full depth
3. Flow aspect ratio ( $\delta^*$ ) =  $b/H$  and
4. Relative longitudinal distance ( $Xr$ ) from a reference or origin, i.e., the ratio of the distance ( $l$ ) of the arbitrary reach or section in the longitudinal direction of the channel to the total length ( $L$ ) of the non-prismatic channel and can be expressed as  $Xr = l/L$

Thus, the percentage flow in the main channel can be written as follows:

$$\%Q_{mc} = f(\alpha, \beta, \delta^*, Xr) \quad (10.6)$$

### 10.5.1 Single Regression Analysis

Single regression analysis (SRA) is performed to get the best relationship between the dependent parameter ( $\%Q_{mc}$ ) and each individual independent parameter ( $\alpha$ ,  $\beta$ ,  $\delta^*$ ,  $Xr$ ). In this method, the functional relationship between the variable has been fixed. The plot between the dependent and independent parameters shown in Fig. 10.5a–d. It has been observed from Fig. 10.5a, b, d that the  $\%Q_{mc}$  decreases linearly, logarithmically and exponentially with increase in width ratio, relative flow depth and relative longitudinal distance, respectively, for diverging compound channels. Figure 10.5c depicts that with an increase in flow aspect ratio, the  $\%Q_{mc}$  increases in the diverging compound channel by a power function.

### 10.5.2 Multivariable Regression Analysis

After getting the best relationship between the dependent and independent variables by SRA, multivariable regression analysis has been performed. In this method, the coefficients of each functional parameter have been generated and by multiplying these factors with each individual parameter, the equation for  $\%Q_{mc}$  has been developed as follows:

$$\%Q_{mc} = 78.5 - 7.1\alpha - 23\ln\beta + 8.71\delta^{*0.55} - 31.3e^{-0.39Xr} \quad (10.7)$$

### 10.5.3 Validation of the Model

The developed model is validated by the 25% data which was kept separately before the development of the regression model from the present experimental channel data series and data of Bousmar et al. (2006) and Yonesi et al. (2013) data on the diverging compound channels. Figure 10.6 shows the comparison of actual %Q<sub>mc</sub> and the %Q<sub>mc</sub> computed by the developed multivariable regression model. It is clearly seen in Fig. 10.6 that the predicted values for percentage flow in the main channel lie close to the best fit line which indicates the accuracy of the present model. Further, error analysis has been performed for different diverging compound channels in the next section.

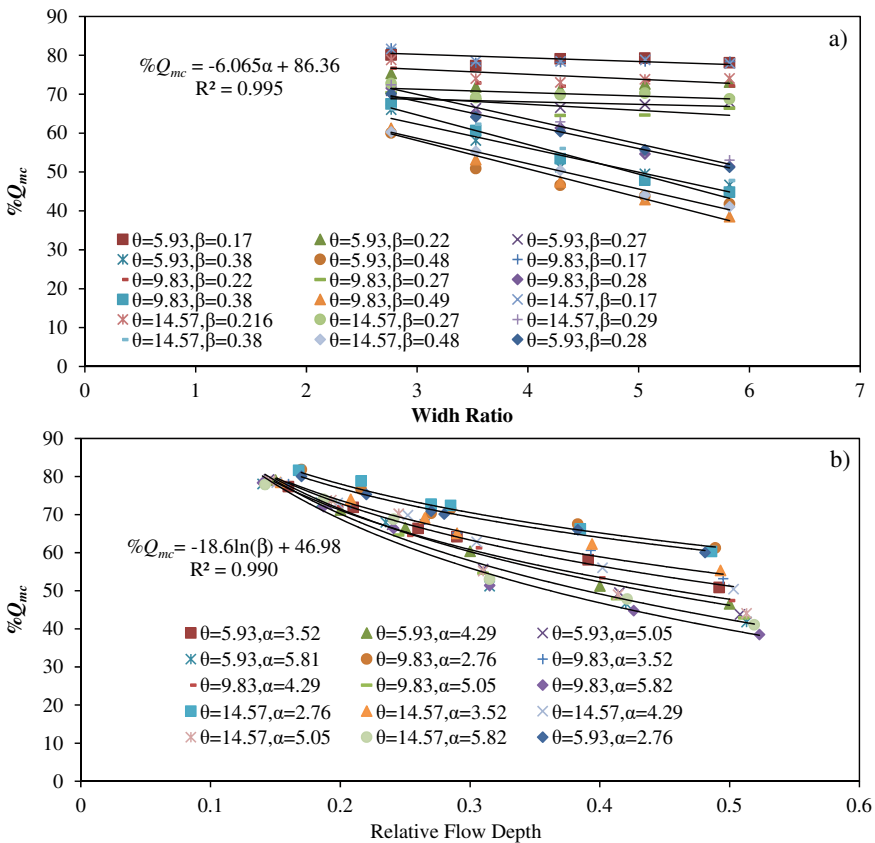


**Fig. 10.5** Variation of %Q<sub>mc</sub> with different independent non-dimensional parameters **a** width ratio, **b** relative flow depth, **c** flow aspect ratio and **d** relative longitudinal distance

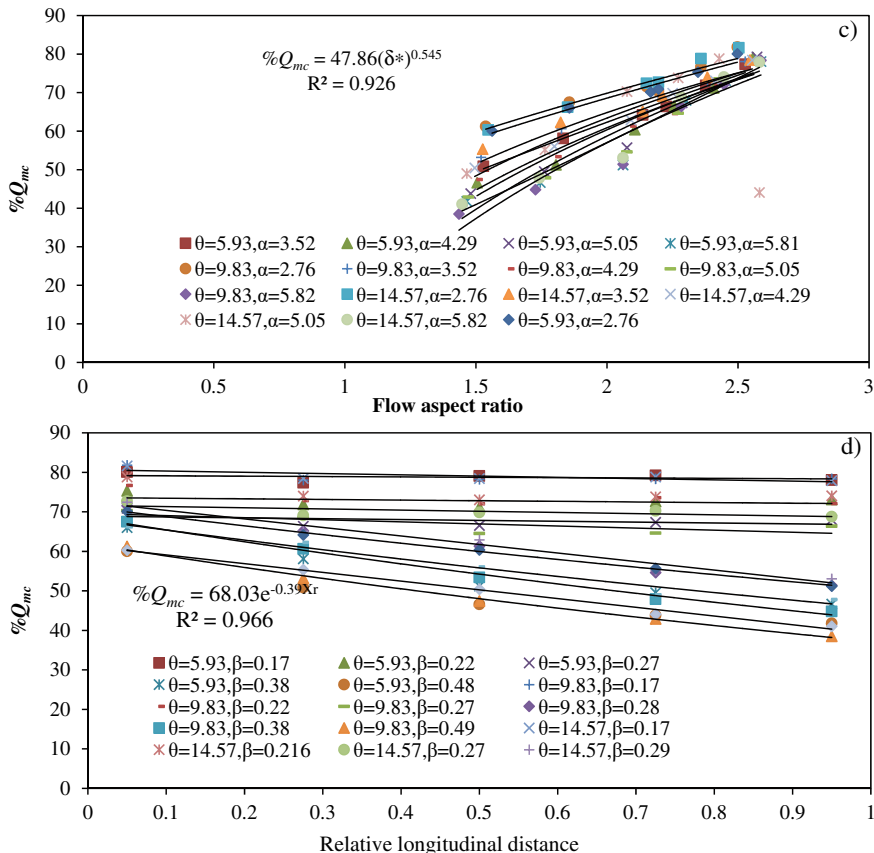
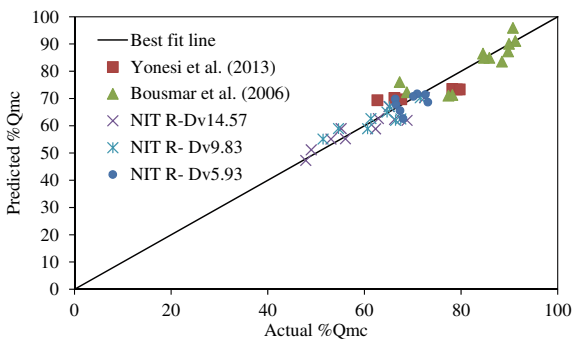


Fig. 10.5 (continued)

Fig. 10.6 Comparison of actual  $\%Q_{mc}$  and predicted  $\%Q_{mc}$  for different diverging compound channels





**Table.10.4** Error in the computation of %Qmc by the present approach in different diverging compound channels

Test channels	MPE	MAPE	RMSE	I <sub>d</sub>	E
NITR Dv5.93	-3.62	2.78	0.0071	0.86	0.90
NITR Dv9.83	-4.81	3.12	0.0085	0.93	0.96
NIT R Dv14.57	3.76	3.22	0.0076	0.88	0.91
Bousmar et al. (2006)	4.63	4.35	0.0092	0.84	0.86
Yonesi et al. (2013)	-2.81	2.58	0.0065	0.89	0.92

## 10.6 Error Analysis

To check the strength of the present model, the error analysis is performed in terms of statistical parameters such as mean percentage error (MPE), mean absolute percentage error (MAPE), root mean square error (RMSE), index of agreement (I<sub>d</sub>) and Nash–Sutcliffe coefficient (E). The detail definition of different error analysis term may be found in Das and Khatua (2018c) and Devi et al. (2016). Table 10.4 shows the error analysis results for the different diverging compound channel. The MPE values lie between -5% to + 5% and MAPE values are less than 5% for all diverging compound channels. From Table 10.4, it also can be seen that the I<sub>d</sub> and E value are greater than 0.85 for all diverging channel cases which depict the accuracy of the developed model.

## 10.7 Conclusions

In the diverging compound channel, the percentage flow in the main channel found to increase linearly, logarithmically and exponentially with increase in width ratio, relative flow depth, and relative longitudinal distance. But with the increase in flow aspect ratio the percentage flow in the main channel found to decrease by a power function. The developed multivariable regression model found to provide good results with the present experimental channel data and other researchers' data on diverging compound channels. In order to check the strength of the present model, error analysis has been performed in terms of mean percentage error (MPE), mean absolute percentage error (MAPE), root mean square error (RMSE), index of agreement and Nash-Sutcliff coefficient (E). The MAPE value found to be less than 5%, and RMSE value less than 0.0095 and I<sub>d</sub> value greater than 0.85, which indicates the good strength of present model for prediction of flow distributions in the diverging compound channels.

## References

- Bousmar D, Proust S, Zech Y (2006). Experiments on the flow in an enlarging compound channel. In: *River flow 2006: Proceedings of international conference on fluvial hydraulics*, pp. 323–332. CRC Press, Taylor & Francis group, Boca Raton, FL
- Chlebek J (2009) Modelling of simple prismatic channels with varying roughness using the SKM and a study of flows in smooth non-prismatic channels with skewed floodplains. PhD dissertation, Univ. of Birmingham
- Das BS, Khatua KK (2018a) Flow resistance in a compound channel with diverging and converging floodplains. *J Hydraul Eng* 144(8):04018051
- Das BS, Khatua KK (2018b) Numerical method to compute water surface profile for converging compound channel. *Arab J Sci Eng* 43(10):5349–5364
- Das BS, Khatua KK (2018c) Water surface profile computation for a compound channel having diverging floodplains. *ISH J Hydraul Eng* 1–14
- Das BS, Devi K, Khatua KK (2019) Prediction of discharge in converging and diverging compound channel by gene expression programming. *ISH J Hydraul Eng* 1–11
- Das BS, Devi K, Khuntia JR, Khatua KK (2020) Discharge estimation in converging and diverging compound open channels by using adaptive neuro-fuzzy inference system. *Can J Civ Eng* 47(12):1327–1344
- Das BS, Devi K, Proust S, Khatua KK (2018) Flow distribution in diverging compound channels using improved independent subsection method. In: *River flow 2018: 9th international conference on fluvial hydraulics* (Vol 40, No. 05068, pp 8 p)
- Das BS, Khatua KK, Devi K (2017) Numerical solution of depth-averaged velocity and boundary shear stress distribution in converging compound channels. *Arab J Sci Eng* 42(3):1305–1319
- Devi K, Das BS, Khuntia JR, Khatua KK (2021) Analytical solution for depth-averaged velocity and boundary shear in a compound channel. In: *Proceedings of the institution of civil engineers-water management*, pp 1–16. Thomas Telford Ltd
- Devi K, Khatua KK, Das BS (2016) Apparent shear in an asymmetric compound channel. *River Flow 2016: Iowa City, USA, July 11–14*
- Devi K, Khatua KK (2019) Discharge prediction in asymmetric compound channels. *J Hydro-Environ Res* 23:25–39
- Devi K, Khatua KK, Khuntia JR (2017) Discharge assessment in an asymmetric compound channel by zero shear interface method. *ISH J Hydraul Eng* 23(2):126–34
- Donald W, Knight John D, Demetriou (1983) Flood Plain and Main Channel Flow Interaction. *J Hydraul Eng* 109(8):1073–1092
- Khuntia JR, Devi K, Khatua KK (2019) Flow distribution in a compound channel using an artificial neural network. *Sustain Water Resour Manag* 5(4):1847–1858
- Khatua KK, Patra KC (2009) Flow distribution in meandering compound channel. *J Hydraul Eng* 15(3):11–26
- Proust S (2005) *Ecoulements non-uniformes en lits composés: effets de variations de largeur du lit majeur* (Doctoral dissertation, Doctorat de Mécanique des fluides, INSA de Lyon)
- Wormleaton PR, Allen J, Hadjipanos P (1982) Discharge assessment in compound channel flow. *J Hydraul Div* 108(9):975–994
- Yonesi HA, Omid MH, Ayyoubzadeh SA (2013) The hydraulics of flow in non-prismatic compound channels. *J Civ Eng Urban* 3(6):342–356

# Chapter 11

## Boundary Shear Stress Distributions in Compound Channels Having Narrowing and Enlarging Floodplains



Kamalini Devi , Bhabani Shankar Das , Jnana Ranjan Khuntia ,  
and Kishanjit Kumar Khatua 

**Abstract** Compound channels are basically described as two stage open channels having main river and its adjoining floodplains. The momentum transfer phenomenon at the junction of main channel and floodplain is very crucial to be understood to estimate the discharge. The difference in water depth and roughness between the two zones generally causes momentum exchange at the interface. It is simple to quantify this momentum exchange for uniform flow conditions in river; however, for non-uniform flow condition the quantification is complex as the flow properties change in both longitudinal and lateral directions. Therefore, a study has been done on overbank flow with non-uniform flow condition, and stage discharge relationships are analyzed for accurate modeling. As natural rivers may have different configurations, so two different types of channels that are converging and diverging channels are considered and flow variables at different longitudinal positions are analyzed. Two discharge predicting models are developed which can be used for flow in natural rivers. These models depend on the non-dimensional forms of geometric and flow parameters and the percentage of the boundary shear forces carried by the adjacent floodplains. So it is required to analyze and estimate the boundary shear force distribution carried by main channel and non-prismatic floodplains before predicting flow. So, two different equations are proposed for percentage shear carried by converging and diverging floodplains. In addition, the developed models give simple ways for the quantification of percentage boundary shear force and provide accurate discharge result through non-prismatic channels. The predictions of the models are then compared with the

---

K. Devi (✉)

Department of Civil Engineering, Vidya Jyothi Institute of Technology, Hyderabad, Telangana 500075, India

B. S. Das

Department of Civil Engineering, National Institute of Technology, Bihar Patna 800005, India

J. R. Khuntia

Department of Civil Engineering, St. Martin's Engineering College, Dhulapally, Secunderabad, Telangana 500100, India

K. K. Khatua

Department of Civil Engineering, National Institute of Technology, Rourkela, Odisha 769008, India

models of other researchers. The prediction efficiency of the present model is found better than the models of previous researchers.

**Keywords** Momentum exchange · Non-uniform flow · Diverging floodplain · Converging floodplains · Stage-discharge relationships

## 11.1 Introduction

Compound channels are the typical patterns of flooded rivers. The study of these channels have become vital for environmental, ecological, and design issues. The behavior of flow in rivers for both in bank and overbank flow conditions have been widely investigated. It is found that many investigators have done their research under uniform flow conditions; however, in natural rivers the flow pattern is generally non-uniform flow. So the applications of models which are developed for uniform flow conditions are found to give spurious results for non-uniform flow conditions. For practical point of view, the uniform flow condition in a flooded river channel is ideal and is considered as a theoretical reference flow as stated by Proust (2005). So understanding and analyzing the non-uniform flow in compound channels become a universal research area nowadays. Bousmar and Zech (1999), Bousmar et al. (2004), Rezaei (2006), Proust et al. (2006), and Rezaei and Knight (2009) have analyzed the non-uniform flow in laboratory flumes. In laboratory environments, diverging and converging channels constructed as non-uniform flow are usually acquired in these types of non-prismatic compound channels. It is proved by many investigators that momentum transfer at junction of main channel and floodplain causes non-uniformity of the boundary shear stress distribution along the subsection perimeters. Moreover, the distribution of boundary shear force in subsections is also indispensable for investigating the sediment transport problems. Knight and Hamed (1984), Khatua et al. (2012), Mohanty et al. (2014), Devi et al. (2017), Khuntia et al. (2018) and Devi and Khatua (2020) developed models for distribution of boundary shear force for compound channels with homogeneous and non-homogeneous roughness by incorporating the momentum exchanges at junctions. For non-prismatic compound channels, Naik et al. (2017) developed a relationship to estimate percentage boundary shear force carried by floodplains of a converging compound channel as a function of geometric and hydraulic parameters. However, for diverging floodplains, there is less work found on lateral boundary shear distribution as well as on percentage shear force carried by floodplains (Das et al. 2020). Here, models are developed for percentage boundary shear force distribution in converging and diverging compound channels as a function of different geometric and hydraulic parameters of non-prismatic compound channels. Further, this distribution of boundary shear force is related to find out the discharge through the channels.

## 11.2 Experimental Setup

In this paper, the non-uniform steady flows are considered to be occurred in non-prismatic compound channels with narrowing and enlarging floodplains. The non-uniform steady flows are also occurred in prismatic geometries (Proust et al. 2013). Due to less availability of data sets, this type of flow condition is not considered here. In present research, two non-uniform flow geometric channels are considered. Firstly narrowing compound channels, where the upstream geometry gets reduced toward downstream as shown in Fig. 11.1a and second one is enlarging one where the upstream geometry gets enlarged along flow direction (Fig. 11.1b).

There are many investigations devoted for the modeling of boundary shear distribution in subsections of a compound channels under uniform flow condition (Khatua et al. 2011; Mohanty and Khatua 2014). As the cross section of a non-prismatic compound channel changes with the longitudinal distance, the flow depth varies in longitudinal direction. In a consequence, the distributions of the flow variables such as boundary shear and discharge vary longitudinally although the discharge remains constant. To study the variation, experiments are performed inside the flume having dimensions as 22 m long  $\times$  2 m wide  $\times$  0.5 m depth, for different geometric and hydraulic conditions. Three sets of experiments are conducted in compound channels having enlarging floodplains (enlarging angle  $5.93^\circ$ ,  $9.83^\circ$ , and  $14.57^\circ$ ) with six different relative flow depths (0.15, 0.20, 0.25, 0.30, 0.40, and 0.50). In this study, the available experimental data sets of previous investigators (both narrowing and enlarging compound channels) along with the data sets of own experimental channels are utilized (Das et al. 2019). The exchange of momentum at the interface between the main channel and the floodplains also strongly affects both boundary shear and velocity distribution.

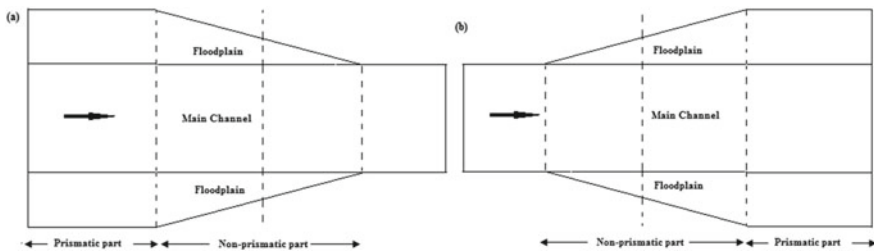


**Fig. 11.1** Top view of the compound channels with **a** narrowing geometries and **b** enlarging geometries

### 11.3 Preliminary Analysis

#### 11.3.1 Development of Boundary Shear Distribution Model

The boundary shear distributions for symmetric and asymmetrical straight compound channels are developed early by previous investigators. Figure 11.2 demonstrates the boundary elements of an overbank flow section. Boundary elements from *a* to *g* comprising the wetted perimeter denotes inclined floodplain wall of length  $\sqrt{2}(H - h)$ , left flood plain of width  $b_{f1}$ , main channel left side slope  $\sqrt{2}h$ , bed width of channel  $b$ , main channel right side slope  $\sqrt{2}h$ , right flood plain width  $b_{f2}$ , flood plain wall of inclined length  $\sqrt{2}(H - h)$  (Devi et al.). To estimate the shear force distribution (per meter length) at each element of the wetted perimeter, shear stresses at each point of the respective element are numerically integrated. To obtain the total shear force (per unit length of the wetted perimeter) of the compound channel, shear forces carried by all the elements are added. This is the total resistance offered by the compound channel, and it is used as a divisor while calculating percentage shear force carried by the flood plain  $\%S_{fp}$  or by other boundary elements.

Previous investigators have developed some equations for calculating  $\%S_{fp}$  as listed below.

1. Knight and Demetriou (1983)

$$\%S_{fp} = 48(\alpha - 0.8)^{0.289}(2\beta)^m \tag{11.1a}$$

2. Knight and Hamed (1984)

$$\%S_{fp} = 48(\alpha - 0.8)^{0.289}(2\beta)^m \left\{ 1 + 1.02\sqrt{\beta}\log\gamma \right\} \tag{11.1b}$$

The exponent *m* can be evaluated from the relation

$$m = 1/[0.75e^{0.38\alpha}] \tag{11.1c}$$

$\gamma$  is the ratio of roughness between flood plain and main channel.

3. Khatua and Patra (2007)

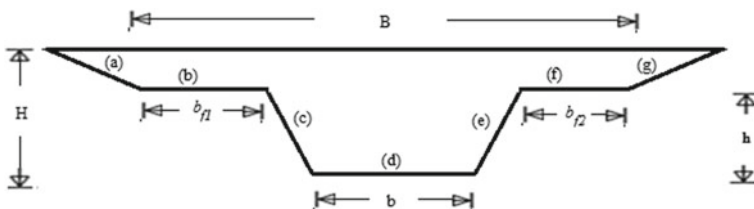


Fig. 11.2 Schematic cross section of symmetrical compound channel

$$\%S_{fp} = 1.23(\beta)^{0.1833}(38Ln\alpha + 3.6262)\left\{1 + 1.02\sqrt{\beta}\log\gamma\right\} \quad (11.1d)$$

4. Khatua et al. (2012)

$$\%S_{fp} = 4.1045\left(\frac{100\beta(\alpha - 1)}{1 + \beta(\alpha - 1)}\right)^{0.6917} \quad (11.1e)$$

5. Mohanty et al. (2013)

$$\%S_{fp} = 3.3254\left(\frac{100\{\beta\alpha\delta - \beta(\delta + 2s)\}}{\beta\alpha\delta + (1 - \beta)(\delta + s)}\right)^{0.7467}\left\{1 + 1.02\sqrt{\beta}\log\gamma\right\} \quad (11.1f)$$

Devi et al. (2016) found that expressions from (11.1a) to (11.1f) are well fitting to symmetric compound channels only. So, they developed a generalized relationship between %S<sub>fp</sub> and %A<sub>fp</sub> for asymmetrical compound channel as

$$\%S_{fp} = 3.576\left\{\frac{100\beta\left(\alpha - 1 - \frac{2.5s}{\delta} + \frac{0.5s}{\delta^*}\right)}{\left(1 + \frac{s}{\delta^*}\right) + \beta\left(\alpha - 1 - \frac{2s}{\delta}\right)}\right\}^{0.717} \quad (11.1g)$$

where width ratio ( $\alpha$ ) = (B/b), relative flow depth ( $\beta$ ) = (H - h)/H, main channel aspect ratio ( $\delta$ ) = (b/h), flow aspect ratio ( $\delta^*$ ) = (b/H), B = Total compound channel width, b = main channel bottom width, H = flow depth over main channel, h = bank full depth and for trapezoidal channel (V:H::l:s) s = side slope of main channel.

All the discussed models are suitable for straight compound channels having different cross-sectional geometries under uniform flow condition. However, for non-uniform flow condition, Naik et al. (2017) gave a boundary shear force model which is well fitted for compound channels having converging floodplains for limited flow and geometric condition only. According to the author’s knowledge, there has been a less work devoted to diverging compound channel and no suitable model has been developed for boundary shear force distribution for this type of channels. Keeping these points in view, this research has been extended to develop a general equation to predict boundary shear distribution for compound channels having non-prismatic floodplains. So, both converging and diverging compound channels are taken into account and separate models are proposed for each of them. For this purpose, experiments have been conducted and additional data sets have been collected from literatures.

For developing a model for any flow variable, the primary task is to make the dependent flow variable as non-dimensional. So, shear force distribution in terms of percentage shear force carried by floodplain (%S<sub>fp</sub>) is made non-dimensional and taken as dependent flow variable. For both converging and diverging compound channels, percentage shear force carried by floodplain (%S<sub>fp</sub>) is analyzed with dimensionless geometric and hydraulic parameters. The geometric and hydraulic parameters are selected investigating their dependencies on the percentage shear

force on floodplain ( $\%S_{fp}$ ). Width ratio, relative flow depth, flow aspect ratio ( $\delta^*$ ), relative longitudinal distance ( $X_r$ ), Reynolds no ( $Re$ ), and Froude's no ( $Fr$ ) are taken as the non-dimensional independent parameters which are influencing the shear force of non-prismatic compound channels. Width ratio ( $\alpha$ ) is defined as the ratio of the total width of compound channel to bottom width of the main channel, relative flow depth ( $\beta$ ) is defined as the ratio between the flow depth over floodplain ( $h$ ) to the total flow depth over main channel ( $H$ ), relative longitudinal distance ( $X_r$ ) is the ratio between the distance ( $l$ ) of a arbitrary reach of the non-prismatic reach in longitudinal direction to the total length ( $L$ ) of the non-prismatic reach. Flow aspect ratio ( $\delta^*$ ) is the ratio between the main channel bed width to the flow depth over it (Devi and Khatua 2019). As the behavior of flow in converging and diverging compound channels is notably different as investigated by previous researchers, so it needs to model the percentage shear force on floodplain ( $\%S_{fp}$ ) individually for these channels.

For developing the models of  $\%S_{fp}$ , converging and diverging experimental data sets from previous investigations are considered here and the details of their geometric, hydraulic, and roughness parameters are tabulated in Tables 11.1 and 11.2 (Das and Khatua 2017). Based on the experimental results of large numbers

**Table 11.1** Details of geometric parameters for all types of channel collected from experimental work and published data for diverging and converging compound channel (Das and Khatua 2018)

Verified test channel	$S_0$	$b$ in (m)	$h$ in (m)	$\theta$ in ( $^\circ$ )	A	$\delta$
1	2	3	4	6	5	7
NITR data-Dv5.93	0.0014	0.34	0.113	5.93	5.82–2.76	3.01
NITR data-Dv9.83	0.0014	0.34	0.113	9.83	5.82–2.76	3.01
NITR data-Dv14.57	0.0014	0.34	0.113	14.57	5.82–2.76	3.01
B et al.-Dv3.81	0.00099	0.40	0.05	3.81	3.0–1.0	8.00
B et al.-Dv5.71	0.00099	0.40	0.05	5.71	3.0–1.0	8.00
Y-Dv3.81	0.00088	0.40	0.18	3.81	3.0–1.0	2.22
Y-Dv5.71	0.00088	0.40	0.18	5.71	3.0–1.0	2.22
Y-Dv11.31	0.00088	0.40	0.18	11.31	3.0–1.0	2.22
NK-Cv5	0.0011	0.50	0.10	5.00	1.0–1.8	5.00
NK-Cv9	0.0011	0.50	0.10	9.00	1.0–1.8	5.00
NK-Cv12.38	0.0011	0.50	0.10	12.38	1.0–1.8	5.00
B-Cv3.81	0.00099	0.40	0.05	3.81	1.0–3.0	8.00
B-Cv11.31	0.00099	0.40	0.05	11.31	1.0–3.0	8.00
R-Cv1.91	0.002003	0.398	0.05	1.91	1.0–3.0	7.96
R-Cv3.81	0.002003	0.398	0.05	3.81	1.0–3.0	7.96
R-Cv11.31	0.002003	0.398	0.05	11.31	1.0–3.0	7.96

B et al.—Bousmar et al. (2004), Y—Yonesi et al (2013), NK—Naik and Khatua (2016), B—Bousmar (2002), R—Rezaei (2006), Longitudinal slope- $S_0$ , Main channel width in meter— $b$ , Main channel depth in meter— $h$ , Diverging angle in degree— $\theta$ , Width ratio— $\delta$ , Aspect ratio— $\delta$



**Table 11.2** Details of hydraulic and surface parameters for all types of channel collected from experimental work and published data for diverging and converging compound channel (Das and Khatua 2018; Das et al. 2019)

Verified test channel	$Q$ in (m <sup>3</sup> /s)	$N$	$\beta$	$Re$ in ( $\times 10^5$ )	$Fr$
1	2	3	5	6	7
NITR data-Dv5.93	0.026–0.067	0.0095–0.0161	0.146–0.51	0.49–1.58	0.42–0.68
NITR data-Dv9.83	0.025–0.065	0.0093–0.015	0.144–0.52	0.53–1.61	0.44–0.70
NITR data-Dv14.57	0.024–0.062	0.0087–0.0136	0.142–0.51	0.58–1.93	0.51–0.82
B et al.-Dv3.81	0.012–0.020	0.0053–0.025	0.218–0.51	0.34–1.39	0.38–0.86
B et al.-Dv5.71	0.012–0.020	0.0076–0.027	0.253–0.54	0.34–1.30	0.25–0.66
Y-Dv3.81	0.037–0.0615	0.0121–0.0211	0.142–0.36	1.43–1.93	0.24–0.33
Y-Dv5.71	0.037–0.0615	0.0129–0.0207	0.142–0.35	1.35–1.85	0.26–0.362
Y-Dv11.31	0.037–0.0615	0.0122–0.0223	0.143–0.35	1.28–1.74	0.28–0.38
NK-Cv5	0.043–0.062	0.010–0.014	0.15–0.30	0.47–1.46	0.64–0.83
NK-Cv9	0.042–0.059	0.012–0.0163	0.15–0.30	0.40–1.61	0.56–0.76
NK-Cv12.38	0.040–0.054	0.011–0.0176	0.15–0.30	0.50–1.73	0.58–0.70
B-Cv3.81	0.010–0.020	0.0087–0.0226	0.213–0.53	0.33–1.32	0.26–0.60
B-Cv11.31	0.010–0.020	0.009–0.0341	0.18–0.53	0.28–1.31	0.29–0.58
R-Cv1.91	0.015–0.040	0.0083–0.0141	0.18–0.52	0.42–1.45	0.56–0.81
R-Cv3.81	0.014–0.025	0.0093–0.0196	0.15–0.50	0.38–1.81	0.35–0.71
R-Cv11.31	0.013–0.023	0.0097–0.0183	0.19–0.50	0.42–1.92	0.38–0.76

B et al.—Bousmar et al. (2004), Y—Yonesi et al (2013), NK—Naik and Khatua (2016), B—Bousmar (2002), R—Rezaei (2006), Observed discharge in m<sup>3</sup>/s— $Q$ , Manning’s roughness coefficient— $n$ , Relative depth— $\beta$ , Reynolds number— $Re$ , Froude number— $Fr$

of published data sets, two individual equations are proposed for converging and diverging compound channel.

The most important task in developing the new boundary shear distribution model is to find out the most significant parameters controlling the boundary shear force distribution in compound channels. Due to the inherent variability of flow caused by interaction mechanism in compound channel, a large numbers of independent parameters may influence the boundary shear distribution. Hence, it makes difficulties in deriving the functional relationships between boundary shear forces with the independent parameters. The  $\%S_{fp}$  is primarily depending on the width ratio ( $\alpha$ ), relative flow depth ( $\beta$ ), and flow aspect ratio. In addition with these three non-dimensional parameters, three other influencing parameters, i.e., Reynolds number ( $Re$ ), Froude number ( $Fr$ ), and relative longitudinal distance ( $X_r$ ) are considered for development of the  $\%S_{fp}$  model for non-prismatic compound channels. So,  $\%S_{fp}$  may be functionally defined as

$$\%S_{fp} = F(\alpha, \beta, \delta^*, Re, Fr, X_r) \tag{11.2}$$

Figures 11.3, 11.4, 11.5, 11.6, 11.7, and 11.8 graphically presents the variation of  $\%S_{fp}$  value with relative flow depth, width ratio, flow aspect ratio, Reynolds number, Froude number, and relative longitudinal distance, respectively, for converging compound channel. The functional relationships that are existing between the  $\%S_{fp}$  with  $\alpha, \beta, \delta^*, Re, Fr, X_r$  are linear, exponential, logarithmic, power, logarithmic, and linear, respectively, for all converging compound channel considered.

Similarly for all the diverging compound channels the variations between the dependent parameter  $\%S_{fp}$  with the non-dimensional independent parameter are analyzed. The best relationships between  $\%S_{fp}$  and  $\alpha, \beta, \delta^*, Re, Fr, X_r$  are shown in Figs. 11.9, 11.10, 11.11, 11.12, 11.13, and 11.14. The functional relationships that are

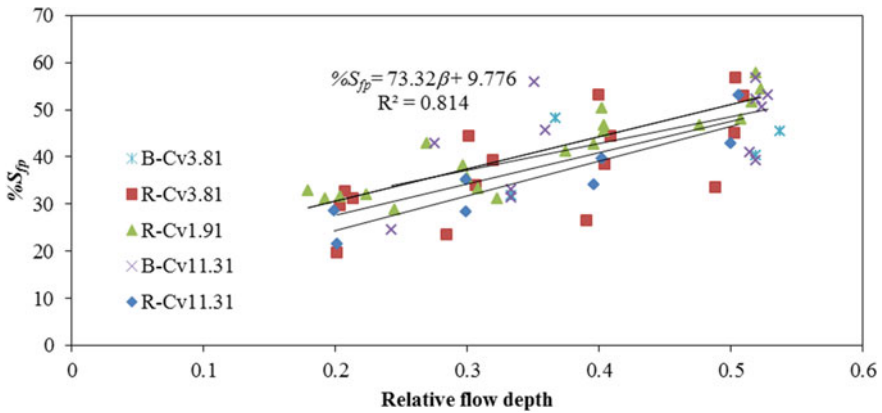


Fig. 11.3 Variation of  $\%S_{fp}$  with relative flow depth for converging compound channel

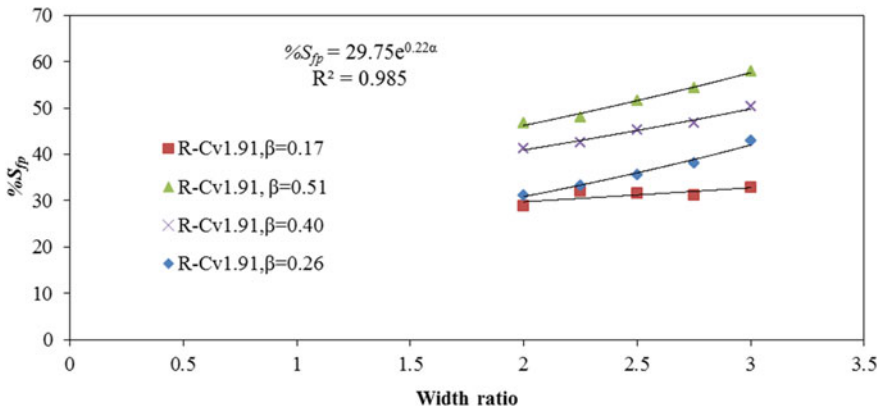


Fig. 11.4 Variation of  $\%S_{fp}$  with width ratio for converging compound channel

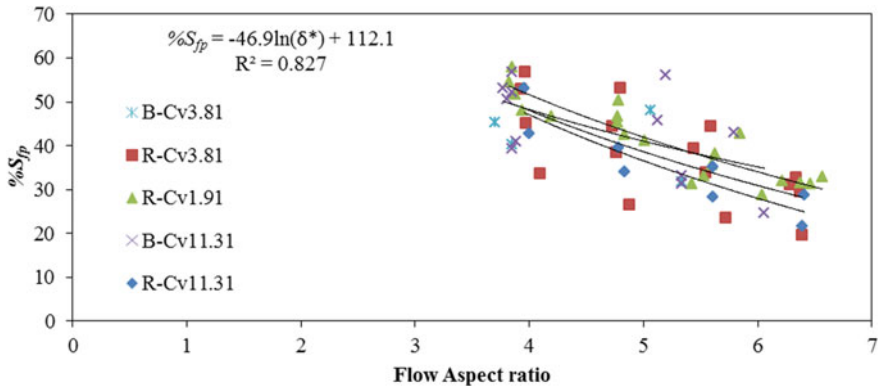


Fig. 11.5 Variation of  $\%S_{fp}$  with flow aspect ratio for converging compound channel

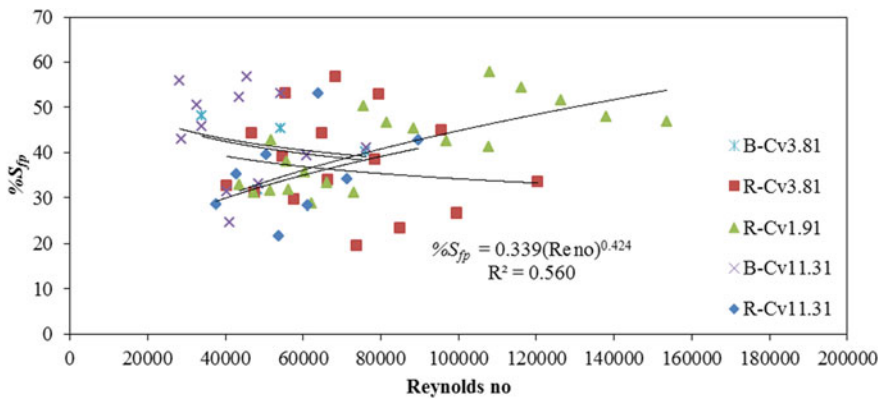


Fig. 11.6 Variation of  $\%S_{fp}$  with Reynolds number for converging compound channel

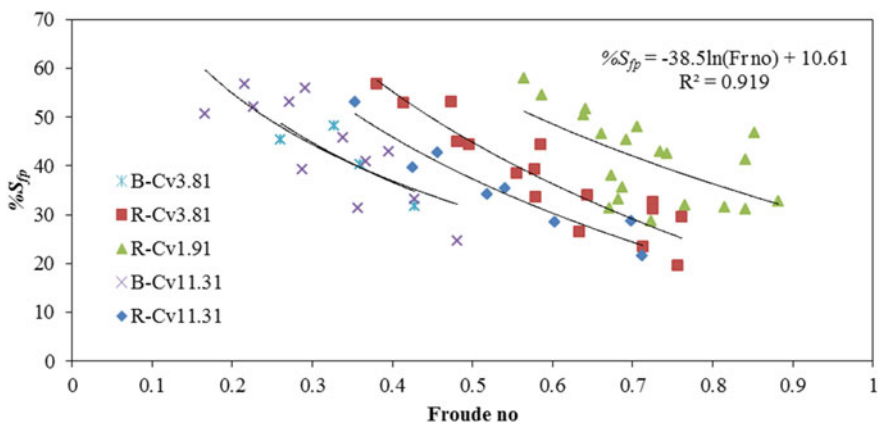


Fig. 11.7 Variation of  $\%S_{fp}$  with Froude number for converging compound channel

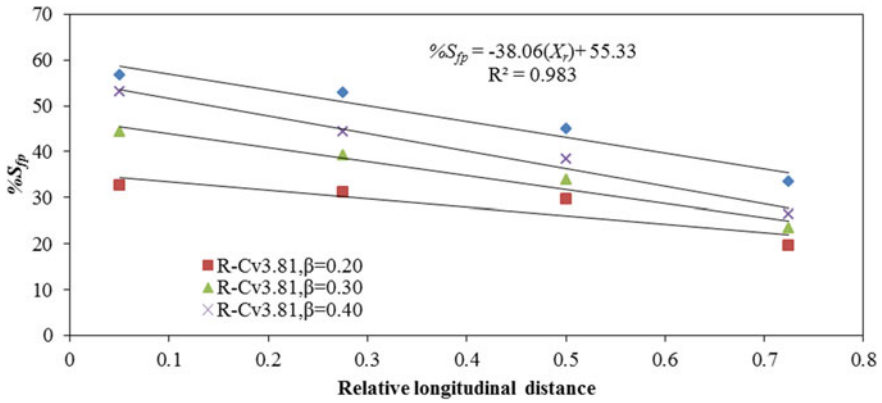


Fig. 11.8 Variation of  $\%S_{fp}$  with relative longitudinal distance for converging compound channel

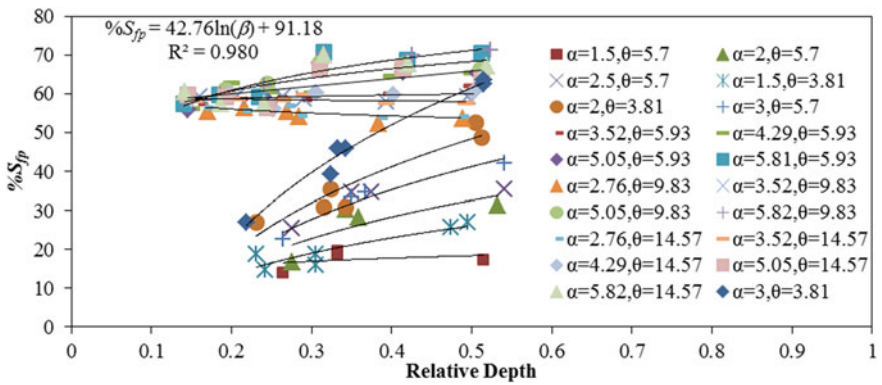


Fig. 11.9 Variation of  $\%S_{fp}$  with relative flow depth for diverging compound channel

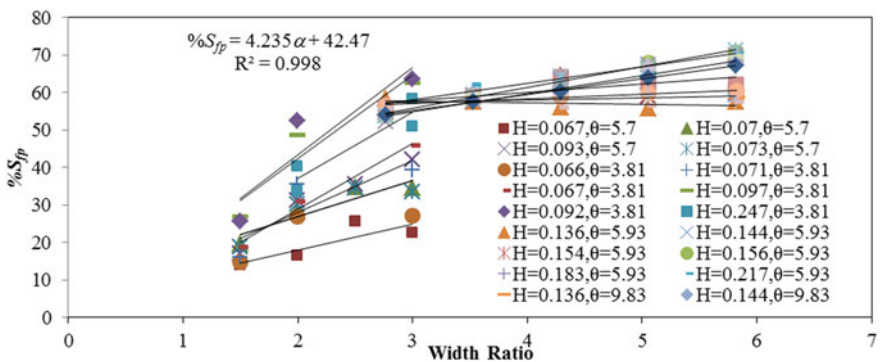


Fig. 11.10 Variation of  $\%S_{fp}$  with width ratio for diverging compound channel

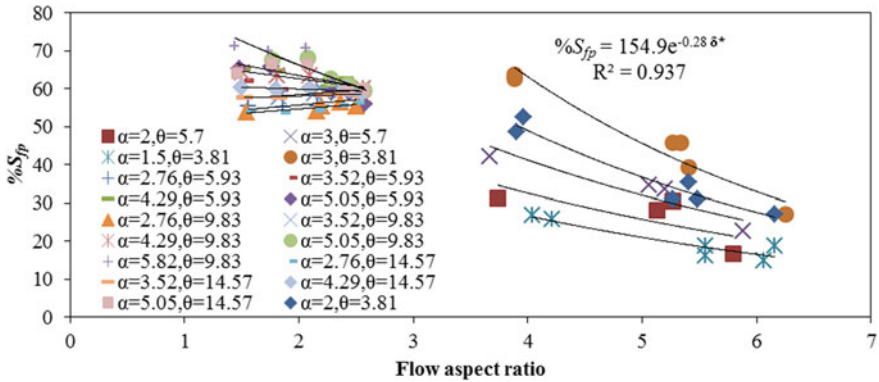


Fig. 11.11 Variation of  $\%S_{fp}$  with flow aspect ratio for diverging compound channel

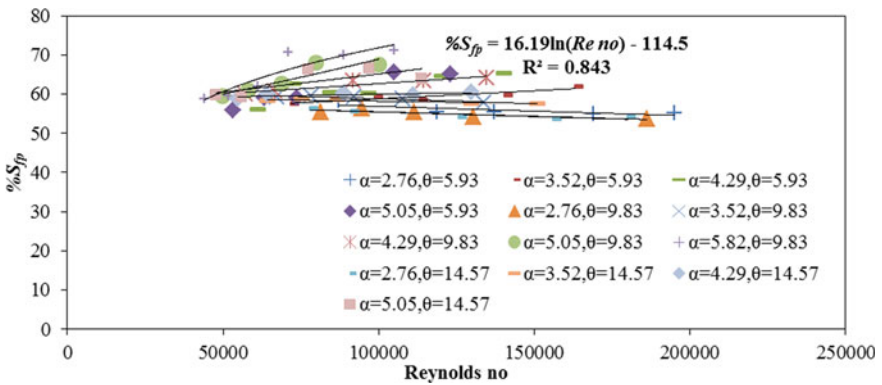


Fig. 11.12 Variation of  $\%S_{fp}$  with Reynolds number for diverging compound channel

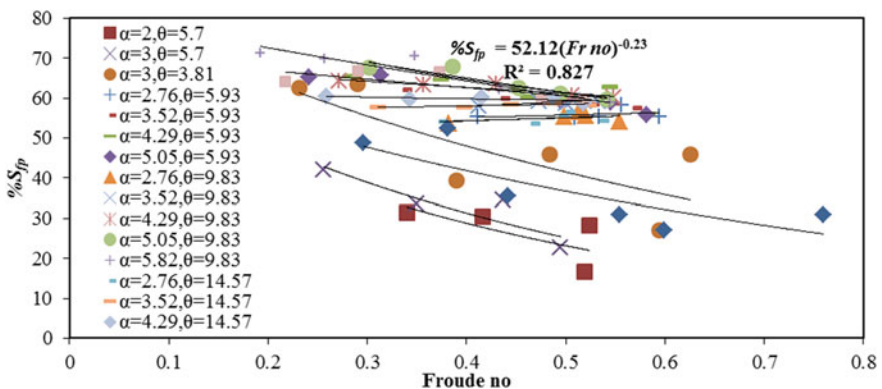
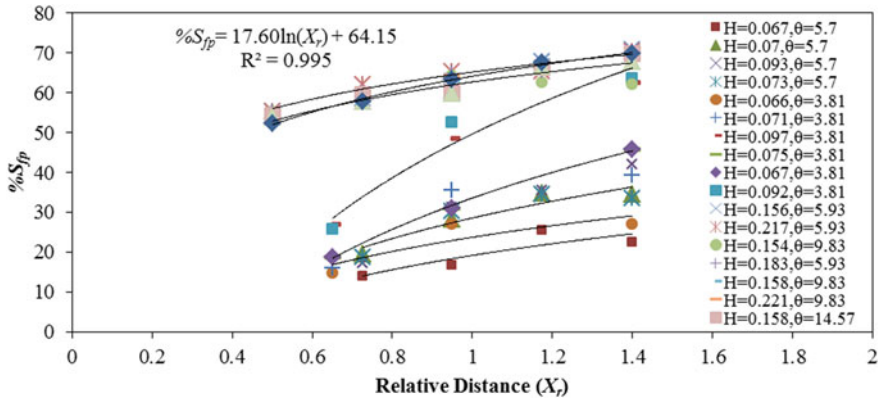


Fig. 11.13 Variation of  $\%S_{fp}$  with Froude number for diverging compound channel



**Fig. 11.14** Variation of  $\%S_{fp}$  with relative distance for diverging compound channel

existing between the  $\%S_{fp}$  with  $\alpha, \beta, \delta^*, Re, Fr, X_r$  are logarithmic, linear, exponential, logarithmic, power, and logarithmic, respectively, for all diverging compound channel considered.

### 11.3.2 Formulation of the Multi-variable Regression Model

Six numbers of possible single regression models between dependent parameter and independent parameters are selected with highest coefficient of determination ( $R^2$ ). Based on the relationships obtained by analyzing the large numbers of published data sets, individual formulations have now been developed using multi-variable regression analysis. Compiling all the individual relationships two generalized formulae are developed for converging and diverging compound channels. Finally, the models of  $\%S_{fp}$  with high coefficient of determination ( $R^2$ ) of 0.90 are obtained.

For converging compound channels

$$\%S_{fp} = -188 + 40e^{0.22\alpha} + 148\beta + 59\ln\delta^* + 0.0634Re\ no^{0.424} - 2.28\ln(Fr\ no) + 6.63X_r \tag{11.3}$$

For diverging compound channels

$$\%S_{fp} = 223 + 3.32\alpha + 11.15\ln\beta + 113e^{-0.28\delta^*} - 11.35\ln Re\ no - 79Fr\ no^{-0.23} + 3.52\ln X_r \tag{11.4}$$

The resulted equation of percentage shear force on floodplains  $\%S_{fp}$  has now been applied to both non-prismatic data sets of previous investigators. Figure 11.15 demonstrates the predicted  $\%S_{fp}$  verses the experimental  $\%S_{fp}$  values for various

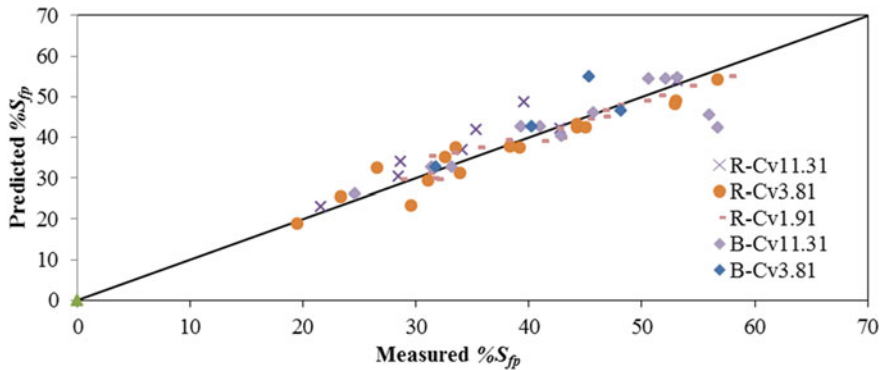


**Fig. 11.15** Comparison of predicted  $%S_{fp}$  with experimental predicted  $%S_{fp}$  for various converging compound channels

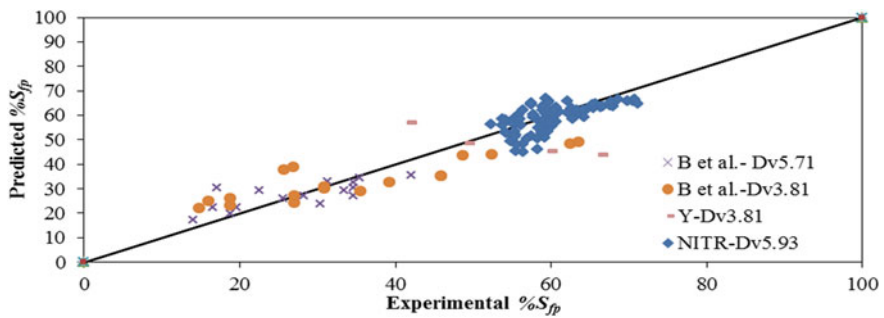


**Fig. 11.16** Comparison of predicted  $%S_{fp}$  with experimental predicted  $%S_{fp}$  for various diverging compound channels

converging compound channels. Similarly Fig. 11.16 demonstrates the predicted  $%S_{fp}$  versus the experimental  $%S_{fp}$  values for different diverging compound channels. These figures indicate the good agreement of models results with their actual values as they are very close to the line of good agreement.

The above expressions, i.e., Eqs. (11.3) and (11.4), are used for successfully estimating the percentage shear force on floodplain any selected location along the length of the channel where the six independent non-dimensional parameters are known. The efficiency of the models shows that they can be applied in natural rivers with minimum errors. For determining the water surface profile in converging compound channels, the equation developed by Rezaei (2006) can be used.

## 11.4 Conclusions

It is observed from the experimental data sets that the variations of flow variables along the stream-wise direction for narrowing and enlarging floodplains are not similar. So, individual models for percentage boundary shear force in floodplains have been proposed for such channels through multi-variable regression model. The models are expressed in terms of non-dimensional parameters such as width ratio, relative flow depth, flow aspect ratio, Reynolds number, Froude number, and relative longitudinal distance. These models will be helpful in accounting the apparent shear stress at the interface. The magnitudes of apparent shear stress at the interface are enumerated for both the converging and diverging compound channels. The applicability of the model is verified against the published data sets of previous investigators.

## References

- Bousmar D, (2002) Flow modelling in compound channels, momentum transfer between main channel and prismatic or non-prismatic floodplains. *Unité de Génie Civil et Environnemental* 326
- Bousmar D, Zech Y (1999) Momentum transfer for practical flow computation in compound channels. *J Hydraul Eng* 125(7):696–706
- Bousmar D, Wilkin N, Jacquemart JH, Zech Y (2004) Overbank flow in symmetrically narrowing floodplains. *J Hydraul Eng* 130(4):305–312
- Das BS, Khatua KK (2018) Flow resistance in a compound channel with diverging and converging floodplains. *J Hydraul Eng* 144(8):04018051
- Das BS, Devi K, Khatua KK (2019) Prediction of discharge in converging and diverging compound channel by gene expression programming. *ISH J Hydraulic Eng* 1–11
- Das BS, Devi K, Khuntia JR, Khatua KK (2020) Discharge estimation in converging and diverging compound open channels by using adaptive neuro-fuzzy inference system. *Can J Civ Eng* 47(12):1327–1344
- Devi K, Khatua KK (2019) Discharge prediction in asymmetric compound channels. *J Hydro-Environ Res* 23:25–39
- Devi K, Khatua KK (2020, December). Boundary shear distribution in a compound channel with differential roughness. In: *Proceedings of the institution of civil engineers-water management*, vol 173, no 6. Thomas Telford Ltd, pp 274–292
- Devi K, Khatua KK, Khuntia JR (2017) Boundary shear stress distribution for a two-stage asymmetric compound channel. *Arab J Sci Eng* 42(3):1077–1091
- Khatua KK, Patra KC (2007) Boundary shear stress distribution in compound open channel flow. *ISH J Hydraulic Eng* 13(3):39–54
- Khatua KK, Patra KC, Mohanty PK (2011) Stage-discharge prediction for straight and smooth compound channels with wide floodplains. *J Hydraul Eng* 138(1):93–99
- Khatua KK, Patra KC, Mohanty PK (2012) Stage-Discharge Prediction for Straight and Smooth Compound Channels with Wide Floodplains. *J Hydraulic Eng* 138(1):93–99. [https://doi.org/10.1061/\(ASCE\)HY.1943-7900.0000491](https://doi.org/10.1061/(ASCE)HY.1943-7900.0000491)
- Khuntia JR, Devi K, Khatua KK (2018) Boundary shear stress distribution in straight compound channel flow using artificial neural network. *J Hydrol Eng* 23(5):04018014
- Knight DW, Demetriou JD (1983) Flood plain and main channel flow interaction. *J Hydraul Eng* 109(8):1073–1092



- Knight DW, Hamed ME (1984) Boundary shear in symmetrical compound channels. *J Hydraul Eng* 110(10):1412–1430
- Mohanty PK (2013) Flow analysis of compound channels with wide flood plains. Doctoral dissertation, NIT Rourkela, India
- Mohanty PK, Khatua KK (2014) Estimation of discharge and its distribution in compound channels. *J Hydrodyn Ser B* 26(1): 144–154
- Naik B, Khatua KK (2016) Boundary shear stress distribution for a converging compound channel. *ISH J Hydraulic Eng* 22(2):212–219
- Naik B, Khatua KK, Wright NG, Sleigh A (2017) Stage-discharge prediction for converging compound channels with narrow floodplains. *J Irrig Drain Eng* 143(8):04017017
- Proust S (2005) Ecoulements non-uniformes en lits composés: effets de variations de largeur du lit majeur. Doctoral dissertation, Ph.D. thesis, INSA Lyon, Lyon, France, 362 p. <http://cemadoc.cemagref.fr/cemoa/PUB00018439>
- Proust S, Riviere N, Bousmar D, Paquier A, Zech Y, Morel R (2006) Flow in compound channel with abrupt floodplain contraction. *J Hydraulic Eng* 132(9):958–70
- Proust S, Fernandes JN, Peltier Y, Leal JB, Riviere N, Cardoso AH (2013) Turbulent non-uniform flows in straight compound open-channels. *J Hydraul Res* 51(6):656–667
- Rezaei B, (2006) Overbank flow in compound channels with prismatic and non-prismatic floodplains. Doctoral dissertation, University of Birmingham, UK
- Rezaei B, Knight DW (2009) Application of the Shiono and Knight Method in compound channels with non-prismatic floodplains. *J Hydraul Res* 47(6):716–726
- Yonesi HA, Omid MH, Ayyoubzadeh SA (2013) The hydraulics of flow in non-prismatic compound channels. *J Civil Eng Urban* 3(6):342–356

# Chapter 12

## Turbulence Characteristics in a Rough Open Channel Under Unsteady Flow Conditions



Jnana Ranjan Khuntia , Kamalini Devi , Bhabani Shankar Das ,  
and Kishanjit Kumar Khatua 

**Abstract** The majority of open channel flows of interest to hydraulic engineers and hydrologists are unsteady. In unsteady flow cases, some aspects of flow (velocity, depth, viscosity, pressure, etc.) will be evolving in time. However, more numbers of issues identified with the unsteady flow have been roughly accepting as steady flow (for example, constant peak discharges in floodplains). Very few experimental investigations have been conveyed in previous literature to examine turbulence qualities in an open channel flow under unsteady flow states over rough beds. The present study investigates the vertical and horizontal fluctuating velocity profiles under unsteady flow states in a rectangular open channel. An experiment is conducted to observe the turbulence characteristics under unsteady flow conditions in a rough bed open channel for two different flow depths. One identical hydrograph is passed repeatedly through the rectangular flume with a fixed rough bed. The dense rough mat is used as a rough bed which replica of a dense grass bed. The flow patterns are investigated at both lateral and longitudinal positions over three different cross-sections by using a micro Pitot tube and Acoustic Doppler Velocimeter (ADV). For two given flow depths, the velocities on both the rising and falling limbs are observed and analyzed. Hysteresis effect loop between stage-discharge ( $h \sim Q$ ) rating curve between the rising and falling limbs is illustrated. Turbulence characteristics, i. e., variations of lateral and vertical Reynolds stresses, are analyzed from measured fluctuation velocities.

---

J. R. Khuntia (✉)

Department of Civil Engineering, St. Martin's Engineering College, Dhulapally, Secunderabad, Telangana 500100, India

J. R. Khuntia · K. K. Khatua

Department of Civil Engineering, National Institute of Technology, Rourkela, Odisha 769008, India

K. Devi

Department of Civil Engineering, Vidya Jyothi Institute of Technology, Hyderabad, Telangana 500075, India

B. S. Das

Department of Civil Engineering, National Institute of Technology, Patna, Bihar 800005, India

**Keywords** Open channel flow · Unsteady flow · Rough bed · Hydrograph · Fluctuating velocity · Hysteresis loop · Reynolds stress

## 12.1 Introduction

Flows in the regular waterways, rivers, and channels are frequently unsteady. At the point when discharge changes gradually, the issue of unsteady flow can be comprehended with the state of steady flow (Mahmood and Yevjevich 1975). However, in some extraordinary cases, for example, reservoir activities, where discharge fluctuates quickly, the learning of steady flow may prompt unique or mistaken outcomes when managing issues of sediment transport, scour, deposition, etc. (Song and Graf 1996). So, the study of unsteady open channel flow has become an important issue for hydraulic engineering. An understanding of the mean velocity, bed shear stress, and turbulence characteristics under unsteady open channel flow conditions is needed, e.g., to predict the flood passage (hysteresis in the stage-discharge relationships between falling and rising limbs) and the river morphology processes dependent on unsteady effects. There are very few literatures found on the experimental investigation in unsteady flow over the rough bed. Tu and Graf (1992) used micro propellers to study the velocity distribution in unsteady open channel flow. They obtained the friction velocity as well as the shear stress distribution, but the turbulence was not measured.

Previous experimental research (Nezu et al. 1994a, b; Anwar and Atkins 1980; De Sutter et al. 2001; Ahanger et al. 2008; Bombar et al. 2011; Martin and Jerolmack 2013) investigated unsteady flow events in a laboratory fixed bank sand-bed channels using hydrographs of different shapes (e.g., trapezoidal, triangular, etc.) and varying characteristics. General conclusions from the literature suggest that few experimental works have been done in response to unsteady flow event hydrograph. Despite this research, to date, no systematic effort has been done for the shape of the unsteady flow event hydrograph over a fixed rough bed and their flow variables. De Sutter et al. (1970, 2001) and Hu et al. (2012) state that a dynamic hydrograph showed hysteresis effects. This means, for the same discharge value, a higher water height was obtained in the falling limb than the rising limb.

Velasco et al. (2003) considered the impact of turbulence on flow in an open channel utilizing plastic plants seeded in a gravel bed. Their outcomes uncovered that minimal value of friction factor is obtained for totally flexible plants under favorable conditions where the relative deflection of plant height was within the range of 0.4–0.5. Huai et al. (2012) investigated the flow characteristics of turbulent open channel flow with submerged vegetation. They experimented by separating the flow into three sections in vertical direction from bed to water surface level. The three layers are basal non-vegetated layer, inner vegetation layer, and upper vegetation layer. Suspended vegetation in open channels impedes flow, for which the longitudinal velocity distribution in vertical direction was deviated from the basic logarithmic law. Further, the Mixing length theory was implemented to find the boundary shear

stress in the internal and non-vegetation layers. Some hydraulic parameters were determined by using the data sets of Plew's laboratory measurements.

Dupuis et al. (2017) investigated the flow characteristics on longitudinal roughness changes of submerged dense rough bed and emerged rigid vegetation by using artificial dense plastic grass and wooden cylinders, respectively. Turbulence production and magnitude of secondary currents were increased by the presence of emergent rigid elements over the floodplains. The mixing layer development in longitudinal direction is also investigated for two stage open channel flow.

The main objective of the present study is to investigate the fluctuating velocities (i.e.,  $u'$ ,  $v'$  and  $w'$ ) and Reynolds stresses (i.e.,  $\overline{u'v'}$  or  $\rho u'v'$ ,  $\overline{v'w'}$  or  $\rho v'w'$  and  $\overline{u'w'}$  or  $\rho u'w'$ ) by laboratory experimentation under unsteady flow conditions over the rough bed. Also, Reynolds stresses have been compared at a lower depth case as well as a higher depth case in both rising and falling limbs of a hydrograph.

## 12.2 Experimental Set-up and Procedures

The experiments were carried out in a 12 m long, 0.6 m wide and 0.6 m deep recirculating, rectangular, tilting flume in the Hydraulics Engineering Laboratory (H. E. Lab.) of Civil Engineering, National Institute of Technology Rourkela (Khuntia et al. 2018a, 2019). The flume has glass walls in the testing section and the rest walls and bottom are of mild steel. The bottom of flume has been modified as a rough bed by fixing rigid grass along the channel bed. A schematic diagram of the experimental set-up is shown in Fig. 12.1. Photographs of the experimental set-up, H. E. Lab., NITR are shown in Fig. 12.2. An electromagnetic flowmeter is fitted with an inlet pipe upstream to measure the flow discharges. Three-point gauges are fixed to measure the flow depth at different positions along the centre line of the flume. A longitudinal slope ( $S_0$ ) of approximately 1.2 cm in 10 m was considered and kept unchanged throughout the experimental program.

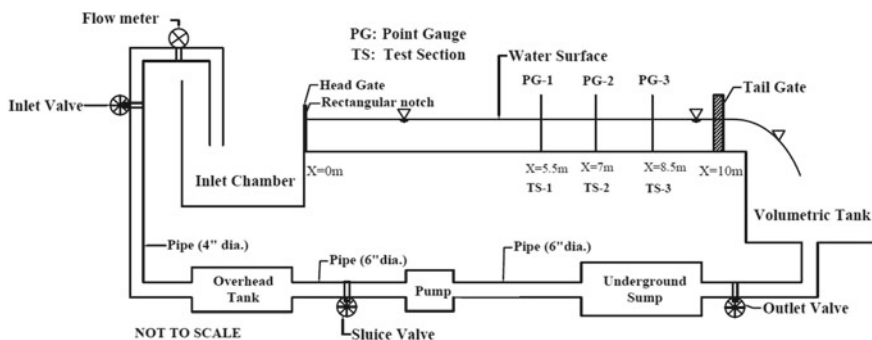
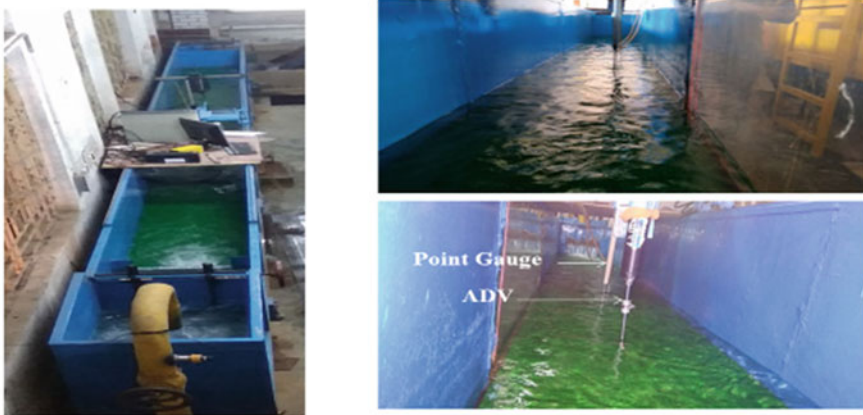


Fig. 12.1 A schematic diagram of the experimental set-up, NITR



**Fig. 12.2** Photographs of experimental set-up, H. E. Lab., NITR

A downstream tail gate is provided to maintain uniformity of flow for this experiment. The tailgate was fixed at a particular height to achieve the given flow depths in steady uniform cases. The same tail gate opening was maintained to achieve the respective flow depths in unsteady flow cases. The measurement of the flow variables has not been done other than the desired flow depth. To get the desired flow depth for the hydrograph, different tail gate settings with several experimental runs have been performed. Rails are provided to support and guide an instrument carriage to run laterally and longitudinally on the top of the flume walls to cover all the test points. The velocity fields were measured by a SonTek Micro 16 MHz Acoustic Doppler velocimeter (ADV). The sampling rate is 50 Hz (the maximum), and the acquisition duration is 60 s. The sampling volume of ADV is located approximately 5 cm below the down-looking probe and was set to be a minimum of  $0.09 \text{ cm}^3$ . The 5 cm distance between the probe and sampling volume is assumed to minimize the flow interference. ADV can record the three directional velocities  $U$ ,  $V$ , and  $W$  in  $X$ -direction: along flume bottom,  $Y$ -direction: lateral to flume bottom and  $Z$ -direction: vertical to flume bottom, respectively. The cross-section distribution of velocities was measured at three different positions or sections (see Fig. 12.1), at  $x = 5.5, 7$ , and  $8.5 \text{ m}$ . Then, a Preston tube of outer diameter  $4.77 \text{ mm}$  was used to measure the velocities at the boundary along the whole perimeter of the flume. The geometry and roughness parameters of the experiment are given in Table 12.1.

The flow behavior at the measuring sections remained similar to that in a long straight natural open channel with a mild bed slope. The ability to reproduce each hydrograph was essential given that only three-point velocities could be observed on each limb during a single run. In the present work, only one hydrograph was studied with successful 198 runs. For maintaining the same flow depth, repetition of the experiments on the same hydrograph has been performed. More runs were taken for the same hydrograph to cover all the measuring points at three different positions for two different flow depths.

**Table 12.1** Geometry and roughness parameters for this experiment

Sl no.	Item description	Parameters
1	Channel type	Straight
2	Geometry of channel section	Rectangular
3	Channel base width ( $b$ )	0.6 m
4	Depth of channel	0.6 m
5	Bed slope ( $S_0$ )	0.0012
6	Length of flume	12 m
7	Length of test channel ( $X$ )	10 m
8	Nature of surface bed	Dense rigid grass
9	Flow condition	Unsteady
10	Manning's $n$ of bed material	0.0304

To obtain meaningful and representative values for the mean flow variables, it was fundamental that flow conditions could be consistently repeated, thus minimizing any underlying variability in the unsteady flows. To establish the bulk flow parameters that characterized a hydrograph, estimations were made amid all independent runs for the given hydrograph. The corresponding data for each variable was then ensemble-averaged (i.e., by moving average method) and smoothed. For the steady flows, including the hydrograph base flow, a time of 10 min (600 s) elapsed when a flow was established until the point when measurements were taken or an unsteady flow hydrograph was started. This was guaranteed that flows were fully developed and in equilibrium condition. In each hydrograph run, two same depths of flow have been selected in each for rising and falling cases. For each depth of flow in rising or falling cases, measurements are performed at three positions. Substantial differences between these profiles for the same flow depth in rising and falling cases are observed. Two turbulence characteristics, i.e., mean kinetic energy and turbulent kinetic energy will be calculated and analyzed for the same flow conditions. The variations of these two turbulent characteristics along the three given sections have been demonstrated (Khuntia et al. 2018a, 2019, 2020).

### 12.3 Results and Discussions

A total of 198 hydrographs was investigated during the experimental repetition. The flow and depth hydrograph in an unsteady flow run has shown in Fig. 12.3. The hysteresis effect of stage-discharge ( $h \sim Q$ ) rating curve between rising and falling limbs is illustrated in Fig. 12.4.

To study the hydrograph, one skewness parameter  $\eta = T_r/T_f$  was proposed by Wang et al. (1997), where  $T_r$  and  $T_f$  are the duration of time for rising and falling limbs. This shape parameter represents hydrograph asymmetry. Based on this definition, one asymmetric hydrograph with the peak skewed toward the rising limb (i.e.,  $\eta$

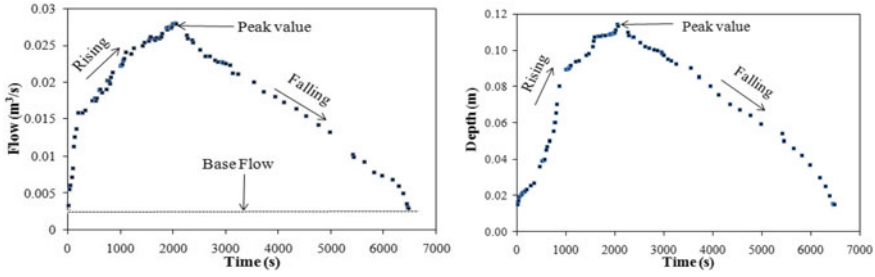
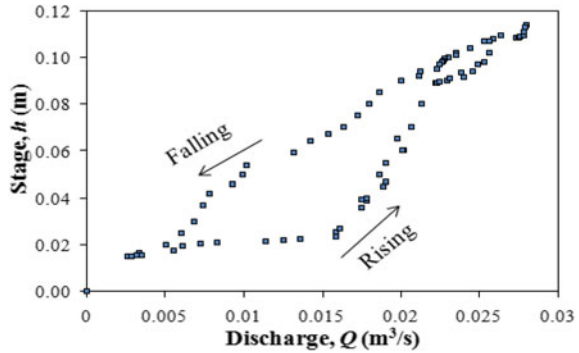


**Fig. 12.3** Flow and depth hydrograph in an unsteady flow run

**Fig. 12.4** Hysteresis effect in stage-discharge curve



= 0.46, referred to as ‘skew-rising’ or ‘left-skewed’ hydrograph) was observed over rigid grass bed (Fig. 12.3). The range of hydraulic parameters used in the experimental run of the hydrograph is given in Table 12.2.

After analyzing the variation of depth-averaged velocity and bed shear stress of a dense rigid rough bed for both steady and unsteady flow conditions, a comparison

**Table 12.2** The range of hydraulic parameters used in the experimental runs

Particulars	Value
Slope	0.0012
No of test runs	198
Base flow (m <sup>3</sup> /s)	0.0025
Water depth in base flow	0.015 m
Water depth at peak	0.114 m
Time duration for rising limb ( $T_r$ )	2040s
Time duration for falling limb ( $T_f$ )	4440 s
Total duration of Hydrograph ( $T$ )	6480 s
Range of Reynolds’s number	400–26,970
Range of Froude number	0.10–0.42

of these flow variables has been made for both the rising and falling limb cases for a given flow depth. Before analyzing the ADV data, possible spectral analysis has been done. The measured data were despiked by an algorithm based on the acceleration thresholding strategy (Goring and Nikora 2002; Khuntia et al. 2018b), which was fit for recognizing and substituting spikes in two stages. The threshold values ( $\pm 1-1.5$ ) for despiking were determined by trial and error basis, for which the velocity power spectra gave an acceptable fit to the Kolmogorov  $-5/3$  scaling-law in the inertial subrange.

### 12.3.1 Reynolds Shear Stress Distributions

In addition to the mean velocity, vegetation also affects the turbulence intensity and the diffusion. These turbulence intensities affect the roughness coefficients and also responsible for generating Reynolds stress within stem areas. The Reynolds stress is defined as the time-averaged instantaneous velocity fluctuation in one direction multiplied by the coincident instantaneous velocity fluctuation in another direction. In vegetative flows, there is the possibility of turbulence occurrence due to the vegetation type and density of vegetation. For open channel flow the respective instantaneous velocity fluctuation components, i.e.,  $u'$ ,  $v'$ , and  $w'$  in longitudinal, transverse, and vertical directions were calculated to determine the Reynolds stress components, i.e.,  $\overline{u'v'}$ ,  $\overline{u'w'}$ , and  $\overline{v'w'}$ . The turbulence characteristics can be evaluated by the instantaneous Reynolds stress value for each Reynolds stress plane over the sampling period. The Reynolds stress for all three planes is seen to be substantially higher for the test with vegetation (Dorcheh 2007). The three Reynolds stresses are calculated as per the following equations:

$$\overline{u'v'} = \frac{\sum u' \times v'}{N_T}, \quad \overline{u'w'} = \frac{\sum u' \times w'}{N_T}, \quad \overline{v'w'} = \frac{\sum v' \times w'}{N_T} \quad (12.1)$$

where  $N_T$  is total number of data taken at a single point. In the present study, all the three Reynolds stresses (i.e.,  $\overline{u'v'}$  or  $\rho u'v'$ ,  $\overline{v'w'}$  or  $\rho v'w'$  and  $\overline{u'w'}$  or  $\rho u'w'$ ) along the vertical direction of the channel have been observed and analyzed which are shown in Figs. 12.5, 12.6, and 12.7.

In the beginning section ( $x1/X = 0.55$ ), Reynolds stress component ( $\rho u'v'$ ) is higher as compared to the other two components of Reynolds stress (i.e.,  $\rho v'w'$  and  $\rho u'w'$ ). In lower flow depth cases, the magnitude of Reynolds stress is less as compared to higher flow depth cases. Also, all three turbulent components reduce their magnitude gradually toward the surface of the water. In falling limbs, the magnitude of  $\rho u'v'$  is also higher than that of two other Reynolds stresses (i.e.,  $\rho v'w'$  and  $\rho u'w'$ ). But, in both rising and falling limb cases, Reynolds stresses are decreasing toward the free surface of the flow depth. The range of Reynolds stresses has varied from  $-15$  to  $5 \text{ N/m}^2$  but in the only case of falling limb and higher flow depth case,



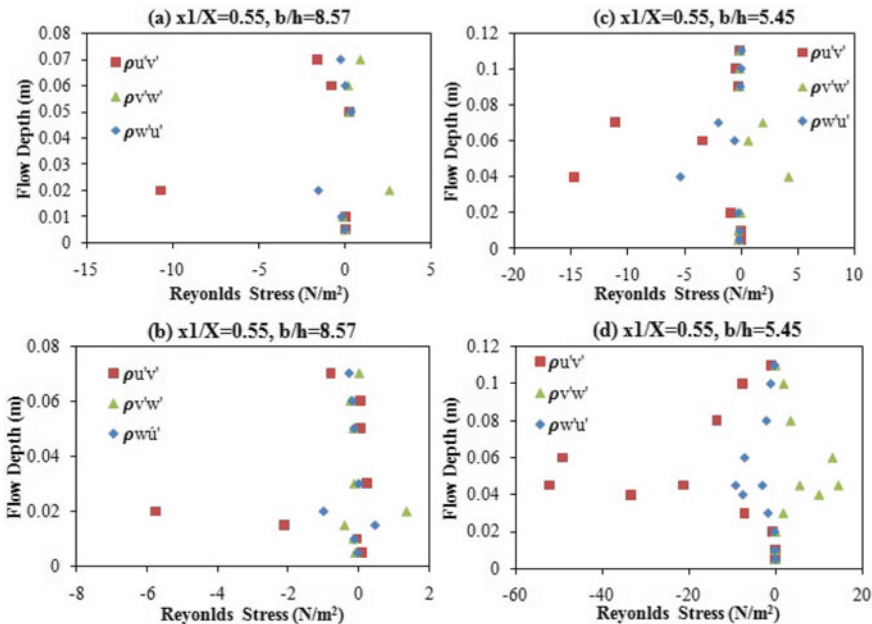


**Fig. 12.5** Vertical variation of Reynolds shear stress at section 1 ( $x1/X = 0.55$ ), **a** and **c** rising limb, **b** and **d** falling limb, respectively

and it varies from  $-55$  to  $20$  N/m<sup>2</sup>. More fluctuations that occur in higher flow depth due to more inertia force cause high turbulence in this section. This is because of unsteadiness that causes all the fluctuating velocities  $u'$ ,  $v'$ , and  $w'$ .

In intermediate section, at section 2 (i.e.,  $x2/X = 0.70$ ) in the rising limb, more fluctuations in three Reynolds stresses have been observed in the lower flow depth case, but the higher magnitude in the case of  $\rho u'v'$  only. But, in the rising limb case of higher flow depth fluctuation in Reynolds stresses are less as compared to the other three conditions (i.e., Fig. 12.8a, b and d). This may be due to that when the depth of flow for unsteady flow increases more fluctuating of velocity is expected to occur near the side walls due to local friction as well as turbulence due to unsteadiness. This is because of unsteadiness that causes all the fluctuating velocities  $u'$ ,  $v'$ , and  $w'$ . The range of Reynolds stresses has varied from  $-7$  to  $1$  N/m<sup>2</sup>. In falling limbs, the variations of  $\rho u'v'$  and  $\rho u'w'$  are more than the magnitude of  $\rho v'w'$ . The range of Reynolds stresses varied from  $-2.4$  to  $0.7$  N/m<sup>2</sup>.

When moving toward the downstream section ( $x3/X = 0.85$ ), in rising limb case the magnitude of  $\rho u'v'$  more as compared to the other two components of Reynolds stress (i.e.,  $\rho v'w'$  and  $\rho u'w'$ ). The same variation was observed in this section as in Section 1 ( $x1/X = 0.55$ ) except in the case of falling limb in lower flow depth case. This may be due to that, when the flow approached toward downstream section less fluctuating of velocity are expected to occur due to less effect of local friction as well as turbulence due to unsteadiness. In falling limb, the more fluctuation observed in

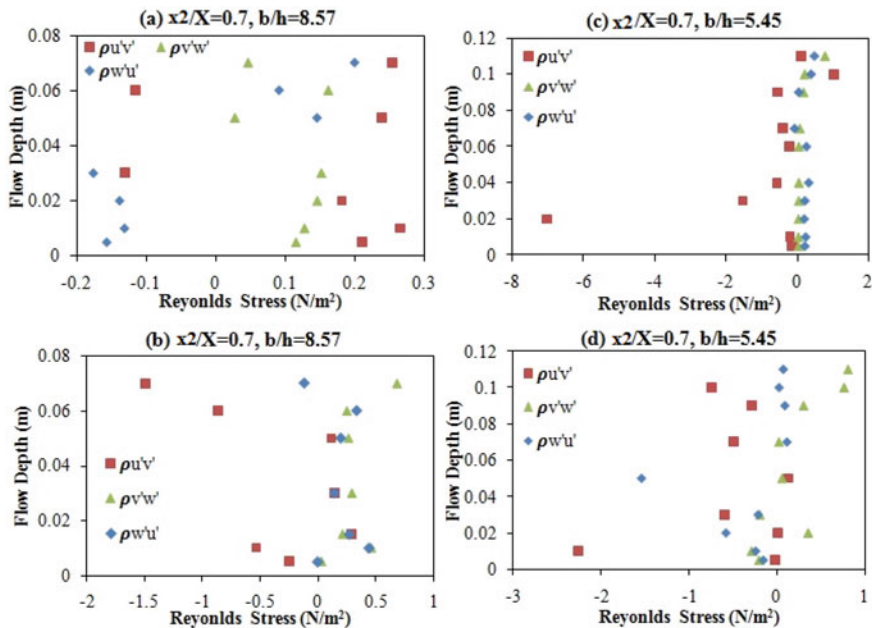


**Fig. 12.6** Vertical variation of Reynolds shear stress at section 2 ( $x_2/X = 0.70$ ), **a** and **c** rising limb, **b** and **d** falling limb, respectively

Reynolds stresses in the case of lower flow depth as compared to the higher flow depth. The range of Reynolds stresses varied from  $-6$  to  $1.8 \text{ N/m}^2$  in the case of rising limb. But, in case of falling limb in low flow depth case, the range varied from  $-0.4$  to  $0.3 \text{ N/m}^2$  and in high flow depth case varied from  $-55$  to  $18 \text{ N/m}^2$ .

Also, in the present research work, all the three Reynolds stresses (i.e.,  $\overline{u'v'}$  or  $\rho u'v'$ ,  $\overline{v'w'}$  or  $\rho v'w'$  and  $\overline{u'w'}$  or  $\rho u'w'$ ) along the lateral direction of the channel have been observed and analyzed which are shown in Figs. 12.8, 12.9, and 12.10.

Interesting results are obtained in all the Reynolds stresses (i.e.,  $\rho u'v'$ ,  $\rho v'w'$ , and  $\rho u'w'$ ) except for some locations. In rising limb, at lower depth of flow, the higher magnitude of  $\rho u'v'$  (acting in the vertical plane along the flow direction) is found near the central region of the channel as compared to Reynolds stress in the other two directions (i.e.,  $\rho v'w'$  and  $\rho u'w'$ ). Toward the wall, the Reynolds stress value is found to be same at the beginning of the sections (Section 1,  $x_1/X = 0.55$ ). This is because of unsteadiness causes all the fluctuating velocities  $u'$ ,  $v'$ , and  $w'$ . This indicates that the fluctuating of velocity in all directions is found to be same except the central region. At the central region higher fluctuating of longitudinal velocity causes higher magnitude of  $\rho u'v'$ . When the flow reaches toward the downstream Section 2, ( $x_2/X = 0.70$ ), the higher magnitude of  $\rho u'v'$  are found to be more uniform. Gradually, the Reynolds stress ( $\rho u'v'$ ) falls in the central region while rising towards both the walls of the last Section 3 ( $x_3/X = 0.85$ ), indicating the fluctuation of turbulence is higher near the walls. For higher depth of flow, the nature of Reynolds stress is found to be

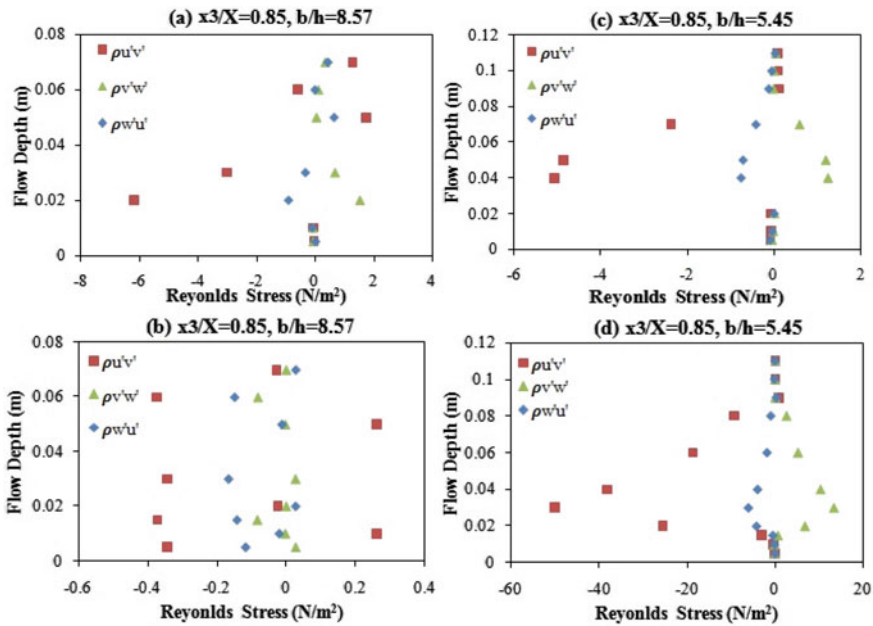


Fig. 12.7 Vertical variation of Reynolds shear stress at section 3 ( $x_3/X = 0.85$ ), a and c rising limb, b and d falling limb, respectively

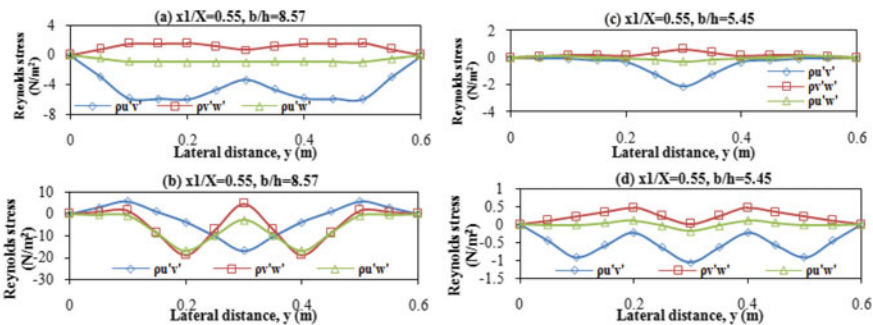
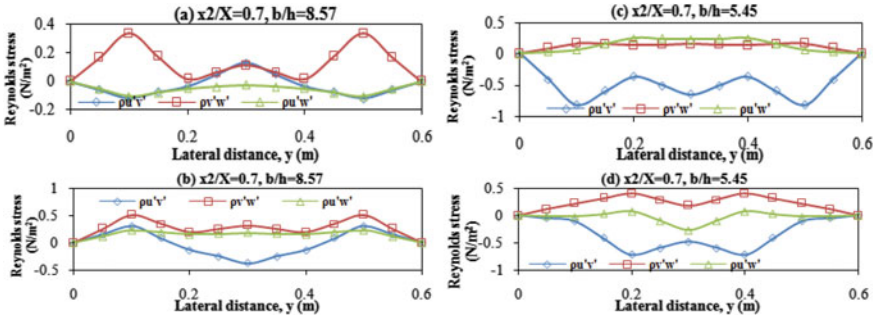
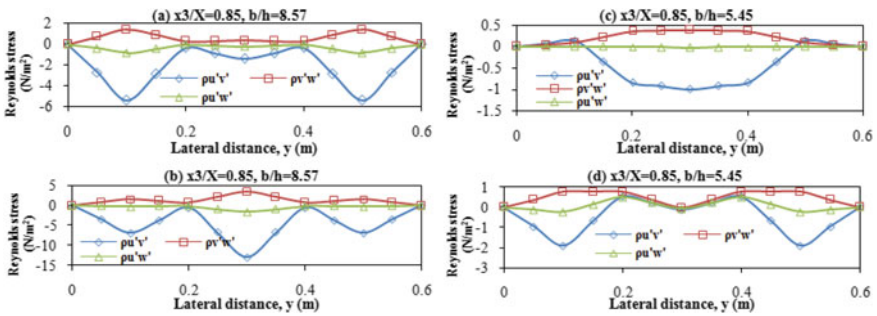


Fig. 12.8 Lateral variation of Reynolds shear stress at section 1 ( $x_1/X = 0.55$ ), a and c rising limb, b and d falling limb, respectively

in opposite nature that had happened in low depth of flow cases. Here, in Section 1, the higher value of  $\rho u'v'$  are found to be near the wall regions, whereas in Section 3 the higher magnitude of  $\rho u'v'$  are found in the central regions. This may be due to that when the depth of flow for unsteady flow increases more fluctuating of velocity are expected to occur near the side walls due to local friction as well as turbulence due to unsteadiness.



**Fig. 12.9** Lateral variation of Reynolds shear stress at section 2 ( $x_2/X = 0.70$ ), **a** and **c** rising limb, **b** and **d** falling limb, respectively



**Fig. 12.10** Lateral variation of Reynolds shear stress at section 3 ( $x_3/X = 0.85$ ), **a** and **c** rising limb, **b** and **d** falling limb, respectively

In the case of falling limb, all the Reynolds stresses are of lesser magnitude in the range  $\pm 0.5 \text{ N/m}^2$ . At Section 1, Reynolds stress ( $\rho u'v'$ ) value is found to be maximum in the central region of the channel. But the other two Reynolds stresses (i.e.,  $\rho v'w'$  and  $\rho u'w'$ ) are having two peak values at the middle third regions and least value of the central region. In Section 2, the peak values of  $\rho u'v'$  is found in the central region. There is a peak drop of  $\rho u'v'$  is noticed in the central region of the channel. Similarly, in Section 3, there is a sudden drop in  $\rho u'v'$  is noticed, but with a high magnitude in range ( $\pm 15 \text{ N/m}^2$ ). For higher depth of flow, the range of Reynolds stress value is less as compared to that of the low depth of flow. At Section 1, there are three peaks of  $\rho u'v'$  is noticed which occurred in the central region and two middle third points. At Sections 2 and 3, the central peak diminishes and only two peaks lie at two middle third points. As compared to lower depth of flow in high flow depth, the range of Reynolds stress is of smaller magnitude ( $\pm 2 \text{ N/m}^2$ ). In lower depth of flow, the range of Reynolds stress is  $\pm 20 \text{ N/m}^2$ , this is due to the dominating effect of both bottom turbulence and bed friction.

## 12.4 Conclusions

The following concluding remarks have been drawn from this study:

1. An experiment has been conducted to investigate the turbulence characteristics in terms of Reynolds stress variation under unsteady flow conditions in a rough open channel for two different flow depths each in rising and falling limbs of hydrograph.
2. In the case of lower flow depth and rising limb, the magnitude of Reynolds stress is less as compared to higher flow depth cases. Also, all the three turbulent components reduce their magnitude gradually toward the surface of the water.
3. In rising limb, more fluctuations in three Reynolds stresses have been observed in the lower flow depth case, but the higher magnitude in case of  $\rho u'v'$  only. But, in the rising limb case of higher flow depth fluctuation in Reynolds stresses are less as compared to the other three conditions (i.e., Fig. 12.8a, b and d).
4. At the downstream sections, in the rising limb case the magnitude of  $\rho u'v'$  more as compared to the other two components of Reynolds stress (i.e.,  $\rho v'w'$  and  $\rho u'w'$ ). In falling limbs, more fluctuation was observed in Reynolds stresses in the case of lower flow depth as compared to the higher flow depth.
5. In the rising limb, for lower depth of flow near the wall region, the magnitude of Reynolds stress value is higher as compare to that of the higher depth of flow. But in the case of falling limb at higher depth of flow, less magnitude of Reynolds stresses have been observed as compared to the lower depth of flow.
6. The present study is a direct measurement of turbulence characteristics. So, this may help to solve any turbulence models (i.e., Spalart–Allmaras (S-A) model,  $k-\varepsilon$  model,  $k-\omega$  model, and Menter's Shear Stress Transport (SST) model etc.), especially in unsteady flow conditions.

## References

- Ahanger MA, Asawa GL, Lone MA (2008) Experimental study of sediment transport hysteresis. *J Hydraul Res* 46(5):628–635
- Anwar HO, Atkins R (1980) Turbulence measurements in simulated tidal flow. *J Hydraul Div* 106(8):1273–1289
- Bombar G, Elçi Ş, Tayfur G, Güney MŞ, Bor A (2011) Experimental and numerical investigation of bed-load transport under unsteady flows. *J Hydraul Eng* 137(10):1276–1282
- De Sutter R, Huygens M, Verhoeven R (1970) Unsteady open channel flow registrations in a test flume with circular cross-section. *WIT Trans Model Simul* 17
- De Sutter R, Verhoeven R, Krein A (2001) Simulation of sediment transport during flood events: laboratory work and field experiments. *Hydrol Sci J* 46(4):599–610
- Dorcheh SAM (2007) Effect of rigid vegetation on the velocity, turbulence, and wave structure in open channel flows. Doctoral dissertation, Cardiff University, UK
- Dupuis V, Proust S, Berni C, Paquier A (2017) Compound channel flow with a longitudinal transition in hydraulic roughness over the floodplains. *Environ Fluid Mech* 1–26

- Goring DG, Nikora VI (2002) Despiking acoustic Doppler velocimeter data. *J Hydraul Eng* 128(1):117–126
- Hu J, Yang S, Fu X (2012) Experimental investigation on propagating characteristics of sinusoidal unsteady flow in open-channel with smooth bed. *Sci China Technol Sci* 1–11
- Huai W, Hu Y, Zeng Y, Han J (2012) Velocity distribution for open channel flows with suspended vegetation. *Adv Water Resour* 49:56–61
- Khuntia JR, Devi K, Proust S, Khatua KK (2018a) Depth-averaged velocity and bed shear stress in unsteady open channel flow over rough bed. In: *River Flow 2018, E3S web of conferences*, vol 40, p 05071
- Khuntia JR, Devi K, Khatua KK (2018b) Prediction of depth-averaged velocity in an open channel flow. *Appl Water Sci. Springer* 8(6):1–14
- Khuntia JR, Devi K, Khatua KK (2019) Turbulence characteristics in a rough open channel under unsteady flow conditions. *ISH J Hydraulic Eng* 1–12
- Khuntia JR, Proust S, Khatua KK (2020) Unsteady open-channel flows over rough bed with and without emergent rigid vegetation: A laboratory experiment. In: *River Flow 2020*. CRC Press, Taylor & Francis, pp 1527–1535
- Mahmood K, Yevjevich V (eds) (1975) *Unsteady flow in open channels*, vol 1. Water Resource Publisher, Fort Collins, Colo
- Martin RL, Jerolmack DJ (2013) Origin of hysteresis in bed form response to unsteady flows. *Water Resour Res* 49(3):1314–1333
- Nezu I, Kadota A, Nakagawa H (1994a) Experimental study on turbulent structures in unsteady open-channel flows. In: *Proceedings of the symposium on fundamentals and advancements In hydraulic measurements and experimentation*, ASCE, Buffalo, New York, pp 185–193
- Nezu I, Nakagawa H, Jirka GH (1994) Turbulence in open-channel flows. *J Hydraulic Eng* 120(10):1235–1237
- Song TC, Graf WH (1996) Velocity and turbulence distribution in unsteady open-channel flows. *J Hydraul Eng* 122(3):141–154
- Tu H, Graf WH (1992) Vertical distribution of shear stress in unsteady open-channel flow [hydrographs were investigated in a gravel-bed flume]. In: *Proceedings of the institution of civil engineers: water maritime and energy*, vol 96, pp 63–69
- Velasco D, Bateman A, Redondo JM, DeMedina V (2003) An open channel flow experimental and theoretical study of resistance and turbulent characterization over flexible vegetated linings. *Flow Turbul Combust* 70(1):69–88
- Wang Z, Lin B, Nestmann F (1997) Prospects and new problems of sediment research. *Int J Sediment Res* 12(1):1–5

# Chapter 13

## Study of Scour Near Pier of Gandhi Setu in Ganga River



Binit Kumar  and Vivekanand Singh

**Abstract** In this paper, an attempt has been made to carry out the study of scour depth at one of the piers of the Gandhi Setu in Ganga River near Gaye Ghat, Patna. Different parameters of the different empirical equations have been calculated by collecting soil samples from the site and analyzed in the laboratory. Based on these parameters, the scour depth is calculated by using different empirical equations given by different researchers such as Shen et al., the Modified Laursen, Jain and Fischer and Lacey's. The actual scour was also measured near one of the piers of Gandhi Setu in Ganga River at Patna, in-situ measurement using the rope attached with heavy weight. It was found that the scour depth measured manually matches satisfactorily with the scour depth computed using Lacey's empirical formula.

**Keywords** Scour near Pier · Gandhi Setu · River Ganga · Flood discharge · Empirical equations for Scour

### 13.1 Introduction

Scour is the removal of sediment such as gravel and sand from the bed of stream around the piers and abutments of a bridge, which causes lowering of bed level. The main cause of the scour is the swiftly moving water, which may scoop out scour holes near the structures. The main concern in stability of bridges founded in the river beds is the lowering of river-bed level, known as local scour. Scouring is one of the main factors for the failure of bridges. In India and all over the world, there are failures of bridges every year. Oliveto and Hager (2002) proposed a relationship for the determination of the time-dependent scour depth at the pier, as a function of time. An accurate estimation of scour depth below stream bed during design is important since this determines the foundation levels of the bridge elements such

---

B. Kumar (✉)

Department of Civil Engineering, IIT Roorkee, Roorkee 247667, India

V. Singh

Department of Civil Engineering, NIT, Ashok Rajpath Patna, Patna, India

e-mail: [vsingh@nitp.ac.in](mailto:vsingh@nitp.ac.in)

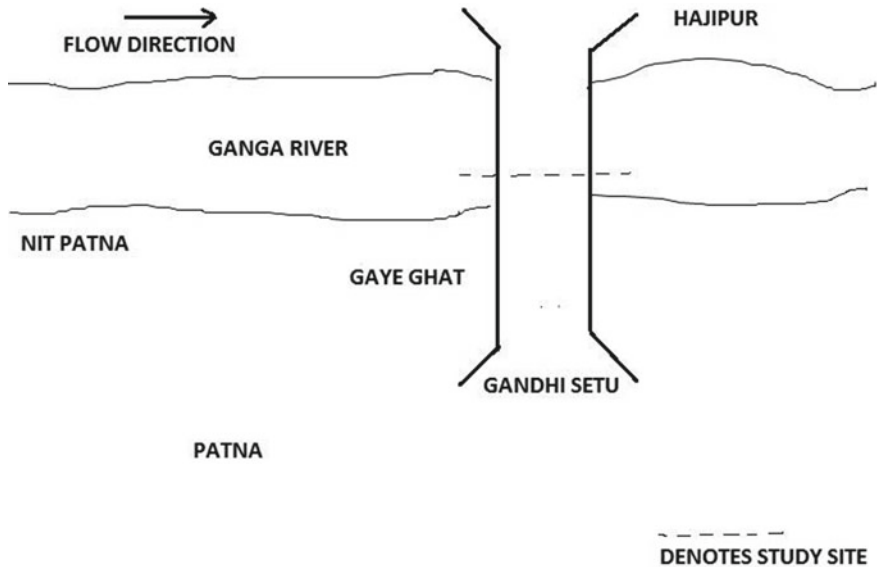


**Fig. 13.1** Schematic diagram of the Gandhi Setu on River Ganga at Gaye Ghat, Patna

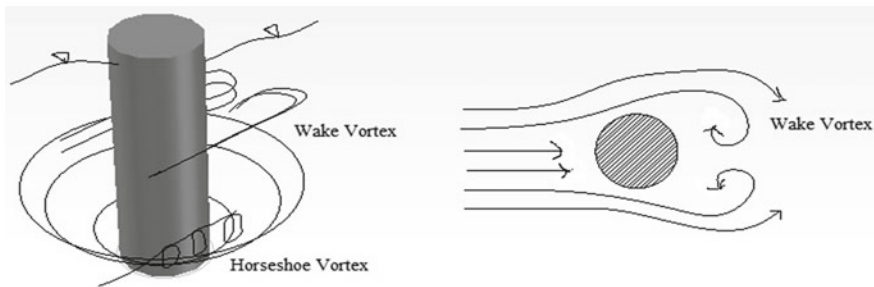
as pier, abutment, guide bank, spur and groynes. (Kothyari 2007). Gandhi Setu is the road bridge constructed on river Ganga at Gaye ghat, Patna. The River Ganga is an alluvial river, which carries high discharge during monsoon, i.e. July–September, and has a great impact of scouring near the pier of the bridge. After serving for more than 30 years, some of the piers of the bridge have been sunken, which caused the bridge damaged. Gandhi Setu is very important for Bihar particularly the people of North Bihar. Due to scouring, there is a lot of failure of bridges all over the world so prediction of scouring must be done in order to save the bridges from damages and failures.

Figure 13.1 shows the schematic diagram of Gandhi Setu on River Ganga at Gaye Ghat, Patna. It connects all the districts headquarter of north Bihar to the capital town Patna. In fact, this bridge is the lifeline of the people of north Bihar. They are dependent directly or indirectly on this bridge for several purposes like commercial, industrial, transportation, etc. This bridge was constructed in the year 1982. The length of the bridge is 5575 m and it is the longest bridge in India. There are 47 spans and having a total number of piers equal to 40. The Setu has 45 intermediate spans having a length of 121.065 m each and also an outer span with a length of 65.530 m each. The River Ganga is an alluvial river, which carries a high discharge during the flood along with huge sediment in monsoon season (i.e. July–September). After serving for more than 30 years, some of the piers of the bridge have been sunken and some have got damaged. This can be seen clearly in Fig. 13.2. Many bridges fail all over the world due to scour near the pier, so prediction of scouring should be carried





**Fig. 13.2** Gandhi Setu with damaged span on River Ganga at Gaye Ghat, Patna



**Fig. 13.3** Flow around a circular pier in a scour hole (Richardson and Davis 2001)

out to prevent from damages and failures. Keeping this in mind, this study has been carried out.

Figure 13.3 (Richardson and Davis 2001) shows the schematic view of the development of the flow in the vicinity of a circular pier which is situated in the scour hole. As it can be seen from Fig. 13.2, wake vortices formation occurs in the downstream of the pier due to the convergence of the flows which was separated in front of the pier. Besides the mean flow strikes the pier at the middle, so that portion of approaching flow is forced to move down at the front area of the pier. Therefore, when this portion arrives at the channel bed, the horseshoe vortex is formed near the base of the pier and hence results in the local scour at the pier.

## 13.2 Methods to Predict Scour Depth

Various empirical equations for the prediction of scour near the pier are as follows:

1. The Modified Laursen by Neil (1964).
2. Shen et al. (1969).

3. The Colorado State University or CSU Formula (1975).
4. The Jain and Fischer (1979).
5. The Modified Froelich Formula (1999).
6. Lacey's Equation.
7. Field measurement at site (2015).

### Modified Laursen by Neil (1964) Equation

In the period 1956, Laursen and Toch gave the design curve in order to find the scour depth. Later, in the year 1964, Neil used this design curve and discovered the explicit equation for the prediction of the scour depth, which is given below:

$$\frac{D_S}{b} = 1.35 \left( \frac{H}{b} \right)^{0.3} \quad (13.1)$$

where  $D_S$  is the scour depth from bed level,  $b$  is the width of the pier (m) and  $H$  is the water depth (m).

### Shen et al. Equation (1969)

Shen et al. (1969) equation included the Froude number in their scour depth prediction equation, which is given below:

$$\frac{D_S}{b} = 3.4(F)^{\frac{2}{3}} \left( \frac{H}{b} \right)^{\frac{1}{3}} \quad (13.2)$$

where  $D_S$  is the scour depth from the bed level (m),  $F$  is the Froude number and all the variables remain the same as discussed earlier.

### Colorado State University or CSU Formula

This equation was developed during the period 1975 and it has used the data of laboratory which was known at that period. The formula is given below:

$$\frac{D_S}{b} = 2.2(F)^{0.43} \left( \frac{b}{H} \right)^{0.65} \quad (13.3)$$

### The Jain and Fischer Equations (1979)

Jain and Fischer found the new equation in the year 1979 related to the prediction of scour of bridge pier and the equation can be known as:

$$\frac{D_S}{b} = 1.84(F)^{0.25} \left( \frac{H}{b} \right)^{0.3} \quad (13.4)$$

### The Modified Froelich Formula (1999)

The two researchers named Fischenich and Landers done a great job in the year 1999 and modified the previous equation and now the equation developed by them included angle of flow attack and safety of factor.

$$D_s = 2 \left( \frac{\theta}{90} \right)^{0.13} \left( \frac{b}{H} \right)^{0.43} (F)^{0.61} + 1 \quad (13.5)$$

where  $\theta$  is the angle of attack.

### Lacey's Equation

Lacey's method of estimating scour depth of flow in loose bed alluvial rivers was developed by Lacey (1929) mainly based on observations made in canals in India and Pakistan. This method is used to predict the scour depth near the pier of the bridge in the alluvial river of India for the design of road and railways bridges. Lacey's equation is given below:

$$D_s = 0.47 \left( \frac{Q}{f} \right)^{\frac{1}{3}} \quad (13.6)$$

where  $Q$  is the discharge in  $\text{m}^3/\text{s}$  and  $f$  is the average silt factor of all the samples.

### Field Measurement of Scour near Pier

Manual measurement of scour depth near bridge pier was done with the help of a string and heavy weight, which was tightened in the string, and a boat was engaged to go near the pier. A heavy stone was tied with the string and then it was released deep inside the water at different places all around the pier, and depths from the water surface were measured.

### Estimation of Different Parameters

Computation of scour depth using various empirical equations requires grain size, silt factor of bed materials, discharge and velocity of flow in the river. The parameters which are required for the determination of scour depth by different empirical equations are given below:

- (a) Silt factor.
- (b) Velocity.
- (c) Froude number.

### Silt Factor

The silt factor of the bed materials has been computed using the Formula (13.7):

$$f = 1.76 \sqrt{d_m} \quad (13.7)$$

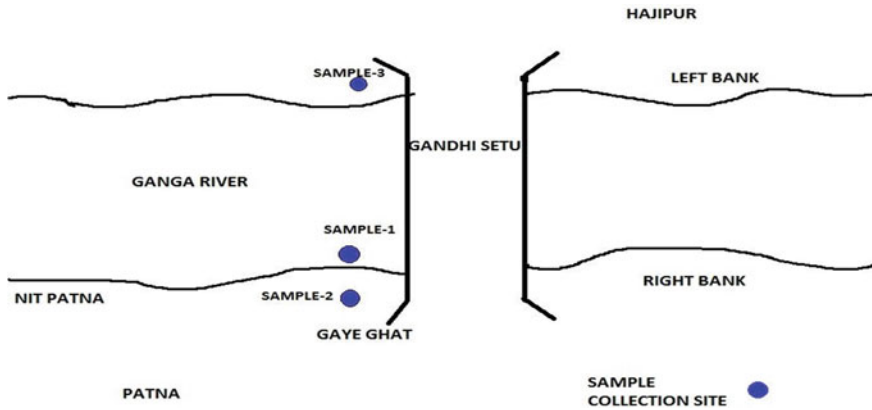


Fig. 13.4 Location of sampling site in River Ganga at Gaye Ghat

where  $d_m$  is the mean size of the bed materials.

Three soil samples were collected for the grain size analysis from the river bed near the said pier of Gandhi Setu as shown in Fig. 13.4. The silt factors have been computed using the mean size of the three samples. Two soil samples were collected from the two sides of the river just after water and one sample was taken inside the river deep into the water. Sample number 1 was inside the river under water and sample numbers 2 and 3 were from the bed of the river just away from water, which can be seen from Fig. 13.4. The grain size analysis of all the samples has been done in the laboratory using Hydrometer for fine grains and a mechanical sieve shaker. The curves were drawn for the percent finer vs grain size of the particles, and the mean size of the bed materials ( $d_{50}$ ) for all the samples has been computed and then silt factors have been computed using Eq. (13.7). The average of all three silt factors has been taken for the average value of the silt factor.

The hydrometer analysis was done for soil sample 1 and mechanical sieve analysis was done for soil samples 2 and 3. The mean size of the bed materials were 0.03, 0.21 and 0.18 mm, for soil samples 1, 2 and 3, respectively. The silt factors for all the three samples were computed using Eq. (13.7) and were 0.31, 0.81 and 0.75, respectively. The average value of the silt factor is 0.63, which is used for the scour analysis.

### Velocity Calculation by Floating Method

The velocity was determined at the Gaye Ghat, Patna, during the monsoon season and it was very difficult to measure the velocity using a current meter or any equipment, so the surface velocity was measured by float method and a coefficient was used to compute the mean velocity of the flow. Three surface velocities were computed and mean values were computed accordingly. The coefficient used is 0.7 and the final mean velocity was computed as 4.2 m/s.

### Determination of Froude Number

Froude number is computed as given below assuming a wide rectangular stream:

$$F = \frac{V}{\sqrt{gy}} \quad (13.8)$$

where  $F$  = Froude number;  $v$  = velocity,  $g$  = acceleration due to gravity and  $y$  = flow depth. The average flow depth measured was 8.8 m. The Froude number computed is 0.45.

## 13.3 Results and Discussion

The main purpose of this study is to compare the scour depth predicted by different empirical equations and the field or In-situ measured scour depth near the pier of Gandhi Setu at Gaye Ghat, Patna. The scour measurement was done with the help of a string, heavy weight and a boat. A heavy weight was tied with the string and it was released deep inside the water at different places all around the pier. This field measurement can be done with the help of an eco-sounder instrument also but here it is done by manual measurement. Generally, the flood recedes in the month of October, so the manual measurement was done during the last week of October. The pier is located few meters inside the river from the bank and a boat was hired to reach this point. Since the measurement is to be done manually, there is a need for a heavy weight. Water depth was measured from the bank to the pier, at different places. So the water depth from the bed level is known from the measurement. The boat was tied just opposite to the flow of water near the pier and the depths of water were measured. Finally, the depth of bed level from the water surface was measured along the three sides of the pier except for the flow side because it was very difficult to make the boat stationary.

Three measurements were taken at each side at an interval of one meter starting from the pier, which is shown in Fig. 13.5. It was also observed that the shape of the pier was rectangular and the width of the pier was 3 m. In Fig. 13.5, the plan view of measurement of the depth of bed levels from the water surface is shown along the flow direction and across the flow direction. Figure 13.6 presents the sectional view of the measured depth near the pier. The maximum scour has occurred near the pier and it decreases away from the pier.

### Comparisons of all the Empirical Equations and the Field Measured Data

The scour depth computed using the empirical equations has been compared with the field measured scour depth. Table 13.1 presents the maximum scour depth computed using all the empirical equations mentioned here with the field measured scour depth. It can be seen that the maximum scour depth computed by Lacey's equation matches

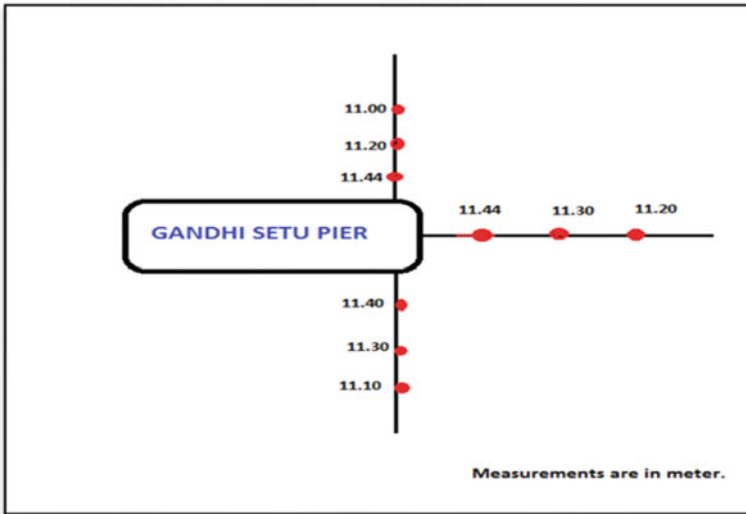


Fig. 13.5 Plan view of the depth measurement points near the pier

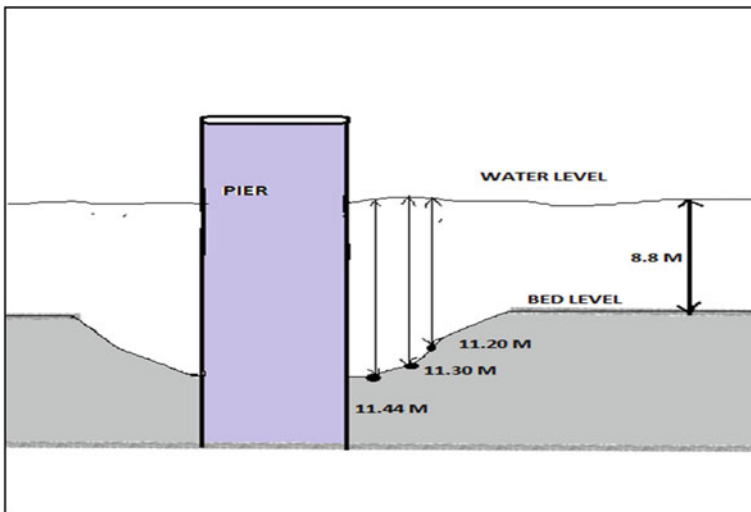


Fig. 13.6 Sectional view of the depth measurement point near the pier

Table 13.1 Maximum scour depth computed using empirical equations and field measured data

Methods	Lacey's equation	Modified Laursen	Shen et al.	CSU formula	Jain and Fischer	Modified Froelich	Field data
Scour depth (m)	2.81	5.59	8.57	6.82	6.24	7.44	2.64

well with the field measured scour depth. The remaining empirical equations do not match even.

It can be seen from Table 13.1 that the scour depth computed from all the empirical equations is a larger value as compared to field measured scour depth except for Lacey's equation. The reasons for the different values of the scour depth by all the empirical equations may be as follows:

- The scour depth calculated by the Modified Laursen equation is approximately double the measured scour depth. This may be due to that this equation doesn't include the velocity of flow, Froude number and angle of attack effects on scour depth.
- The scour depth calculated by Shen et al. is approximately triple the measured value. This may be due to that this equation doesn't include velocity of flow and bed conditions, and later on, some correction factors were added.
- CSU again has not considered the flow angle of attacks and bed conditions at that time, and later on, correction factors were added.
- The above two equations,
- the Jain and Fischer (1979) and the Modified Froelich (1989), considered the angle of flow attack negligible because the flow of angle of attack was equated with the shape of the pier, i.e. circular but the pier is rectangular and we cannot nullify the effect of angle of flow of attack.
- Lacey's theory worked on the conditions prevailing in India so the scour depth value matched with the field measured value. It dealt with the bed condition, i.e. of alluviums and so it is matched well to the measured value. Added to this, the pier shape, velocity of flow and bed conditions are all included in this equation.

Here the shape of the pier of Gandhi Setu is rectangular and according to Chang et al. (2004), the scour depth of circular pier is 90% of the rectangular pier and 80% of the nose-shaped pier bridge. If the shape of the pier is considered to be circular, then according to Chang et al. (2004), the predicted scour depth will change to 90% of the rectangular-shaped pier. Table 13.2 presents the scour depth by all the methods considering the circular-shaped pier. If the shape of the pier is considered to be nose, then according to Chang (1980), the predicted scour depth will change to 80% of the rectangular-shaped pier, which is shown in Table 13.3.

**Table 13.2** Scour depth value for circular pier computed using empirical equations

Methods	Lacey's equation	Modified Laursen	Shen et al.	CSU Formula	Jain and Fischer	Modified Froelich
Scour depth (m)	2.52	5.03	7.70	6.13	5.61	6.69

**Table 13.3** Scour depth value for nose-shaped pier computed using empirical equations

Methods	Lacey's equation	Modified Laursen	Shen et al.	CSU formula	Jain and Fischer	Modified Froelich
Scour depth (m)	2.11	4.47	6.85	5.40	4.99	5.95

## 13.4 Conclusions

In this study, the scour depth near the pier of Gandhi Setu in the alluvium of River Ganga is computed using different empirical equations and compared with the field measured scour depth. It was observed that the measured value of scour depth matches well with the value calculated by Lacey's equation. Lacey's equation value is matching with the measured depth so we can say that this equation is appropriate for the calculation of scour depth. It was also found that the scour equations, which include several parameters affecting scour depth, give better result than those which includes less parameters. Scour depth computed by other empirical equations differs from the measured scour depth. The percentage difference of the scour depth from field measured value and computed using Lacey's equation is 6%, the Modified Laursen 111%, Shen et al. is 224%, CSU Formula is 158%, the Jain and Fischer is 136% and the Modified Froelich 181%.

## References

- Chang WY, Lai JS, Yen CL (2004) Evolution of scour depth at circular bridge piers. *J Hydraulics Eng* 130(9):905–913
- Froelich DC (1989) Local scour at bridge abutments. In: National conference on hydraulic engineering, New York, pp 13–18
- Jain SC, Fischer EE (1979) Scour around bridge piers at high Froude numbers. Federal Highway Administration, Washington, DC
- Kothyari UC (2007) Indian practice on estimation of scour around bridge piers-A comment. *Sadhana* 32(June 2007):187–197
- Lacey G (1964) A general theory of flow in Alluvium. *Proc J.I.C.E. (London)* 27:16
- Landers MN, Mueller DS (1996) Evaluation of selected pier-scour equations using field data. *Transp Res Rec* 1523:186–195
- Laursen EM, Toch A (1956) Scour around bridge piers and abutments. Bulletin no. 4. Iowa Highway Research Board, Ames, Iowa
- Neill CR (1964) River bed scour, a review for bridge engineers. Contract No. 281. Research Council of Alberta, Calgary. Alberta, Canada
- Oliveto G, Hager WH (2002) Temporal evolution of clear-water pier and abutment scour. *J Hydraul Eng (ASCE)* 128(9):811–820
- Oliveto G, Hager WH (2005) Further results to time-dependent local scour at bridge elements. *J Hydraul Eng (ASCE)* 131(2):97–105
- Richardson EV, Davis SR (2001) Evaluating scour at bridges. Federal Highway Administration Hydraulic Engineering Circular No. 18, 4th edn, FHWA NHI 01-001
- Shen HW, Schneider VR, Karaki S (1969) Local scour around bridge piers. *Proc ASCE* 95(6):1919–1940



# Chapter 14

## Optimisation of Hydraulic Design of Uri-II Dam Spillway, Jammu and Kashmir



Vankayalapati S. Ramarao and M. R. Bhajantri

**Abstract** Optimisation of hydraulic design of spillway involves verification of designs of various components of spillway which includes crest profile of spillway and bottom profile of breast wall, adequacy of spillway spans to pass the design flood, the sufficiency of divide walls and training walls, location of trunnion of gates, assessing the performance of energy dissipator, assessing the scour downstream of ski-jump bucket, design of pre-formed plunge pool, location of head regulator/power intake structure and upstream and downstream protection subjected to design floodwaters. Hydraulic model studies play a key role in optimising the designs of various components of the spillway as mentioned above. Hydraulic design of spillway of Uri-II dam was optimised in CWPRS, Pune, by conducting hydraulic model studies. Uri-II H.E. Project was envisaged as a run-of-the-river scheme on the River Jhelum in Uri Tehsil of Baramulla District of Jammu and Kashmir. It has a power generation capacity of 240 MW (4 units of 60 MW each) utilising a gross head of about 130 m. The project consists of a 52 m high and 173 m long concrete gravity dam with a 4.27 km long headrace tunnel (8.4 m diameter), a restricted orifice-type surge shaft (25 m diameter), two 5 m diameter steel-lined penstocks, four 3.5 m diameter bifurcated steel-lined penstocks, an underground powerhouse and a horseshoe shaped tailrace tunnel 3.77 km in length. The spillway is designed to pass design outflow flood of 4850 m<sup>3</sup>/s at FRL El. 1241 m and also to flush the sediment deposited in the reservoir into the river downstream. A breast wall spillway has been proposed with four low-level orifices of size 9 m wide × 11.4 m high (originally 12 m high) with crest level at El. 1217 m. The ski-jump bucket is provided for energy dissipation with invert at El. 1210.19 m and lip at El. 1213 m. The project was completed and all four units were commissioned and the 4th unit in July 2014. Hydraulic model studies enabled optimisation of various components of spillway by optimising the size of spillway spans and design of natural plunge pool and suggesting downstream hill slopes protection. Optimised hydraulic design was made by assessing the discharging capacity of the spillway, validating crest profile with pressures on the spillway surface, the performance of energy dissipation arrangement for the entire range of discharges, flow conditions in the reservoir upstream of the spillway and

---

V. S. Ramarao (✉) · M. R. Bhajantri  
SED Division, Central Water and Power Research Station, Khadakwasla, Pune, Maharashtra  
411024, India

head regulator, flow conditions downstream of the spillway and head regulator and requirement of a natural plunge pool with expected scour levels. This paper provides detailed information on the hydraulic model studies carried out on the spillway and energy dissipator of Uri-II dam spillway, Jammu and Kashmir.

**Keywords** Uri-II hydroelectric project · Spillway · Breast wall · Ski-jump bucket · Scour · Plunge pool

## 14.1 Introduction

Dams are provided with spillways to dispose off excess floods safely to downstream without causing excessive erosion. Sometimes spillways are also used for disposing off sediments from the reservoir. Efficient hydraulic designs are needed to achieve the objects of the spillway as mentioned above. The designs fetch better results if they are tested by hydraulic model studies. Hydraulic model studies permit to modify the designs for improved performance since one or more modifications may be tested before finalising the effective design. Optimisation of hydraulic design of spillway involves verification of designs of various components of the spillway that includes crest profile of spillway and bottom profile of breast wall, adequacy of spillway spans to pass the design flood, the sufficiency of divide walls and training walls, location of trunnion of gates, assessing the performance of energy dissipator, assessing the scour downstream of ski-jump bucket, design of pre-formed plunge pool, location of power intake structure and upstream and downstream protection subjected to design floodwaters, and optimisation of spillway of Uri-II dam was done in CWPRS, Pune.

India is endowed with an enormous hydro-power potential and Arunachal Pradesh and Jammu and Kashmir have a huge amount of share in that. Uri-II H.E. Project was conceived as one of the projects under the 50,000 MW power initiative taken by Govt. of India in 2003. Uri-II H.E. Project is envisaged as a run-of-the-river scheme on the River Jhelum in Uri Tehsil of Baramulla District of Jammu and Kashmir. It has a power generation capacity of 240 MW (4 units of 60 MW each) utilising a gross head of about 130 m. The project was completed and all four units were commissioned and the 4<sup>th</sup> unit in February 2014. The spillway is designed to pass design outflow flood of 4850 m<sup>3</sup>/s at FRL El. 1241 m and also to flush the sediment deposited in the reservoir into the river downstream. A breast wall spillway has been proposed with four low-level orifices of size 9 m wide × 12 m high with crest level at El. 1217 m. The ski-jump bucket is provided for energy dissipation with invert at El. 1210.19 m and lip at El. 1213 m. Figure 14.1 shows the location map of the project and Fig. 14.2 shows the cross section of the spillway. Hydraulic model studies were carried out in CWPRS, Pune, on a 1:50 scale Froudian comprehensive 3D model for making the efficient design of the Uri-II dam spillway.

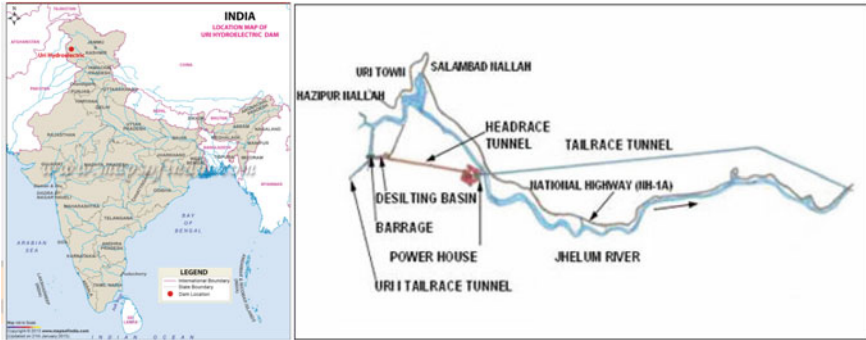


Fig. 14.1 Location of the project (Source <https://www.mapsofindia.com/maps/dams/uri-hydroelectric-dam.html> & <http://www.nhpcindia.com>)

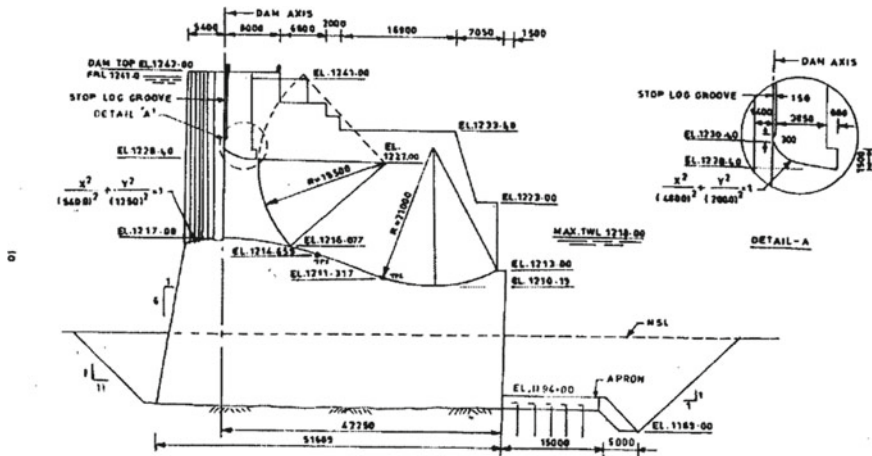


Fig. 14.2 Cross section of the spillway

### 14.2 Model Studies on 1:50 Scale 3D Comprehensive Model (CWPRS Technical Report Nos. 4210, 2005 and 4265, 2005)

Physical hydraulic model studies are very much useful in dealing with complex flow phenomena of spillways and energy dissipators. Since the construction cost of the project is in thousands of crores of rupees, an amicable solution to flow problems if available before construction of dams optimises the various design components of the project in terms of techno-economic feasibility. In that way, hydraulic model studies play a vital role in dealing with dams. Design verification or modifications are made in the spillway and the power intake model is based on studies carried out for assessing discharging capacity of the spillway, flow conditions upstream of the

spillway and upstream and along intake/head regulator, pressures on spillway profile, the performance of energy dissipation arrangement (ski jump in the present case), flow conditions downstream of the spillway and scour downstream of the spillway.

### ***14.2.1 Optimisation of Size of Spillway spans—Discharging Capacity of Spillway***

Discharging capacity of spillway is a very important aspect to be reckoned with as far as dam safety is concerned and is primarily governed by the number and size of spillway spans. The spillway is required to pass the entire design flood within the permissible reservoir water levels without encroaching them. Further, as per IS 11223-1985, the spillway discharging capacity is to be verified for 10% gate inoperative condition (BIS 11223, 1985). Design modifications are subjected to these criteria. The number and area of spillway may be enhanced or reduced depending upon these criteria. For the Uri-II dam spillway, studies indicated that the discharging capacity of the spillway is more than adequate as Probable Maximum Flood (PMF) can be passed at El. 1234.5 m against FRL El. 1241 m. With 10% of inoperative gates (i.e. through three gates), PMF can be passed through the spillway at reservoir water level El. 1239.5 m. Thus, CWPRS suggested to reduce the size of spans and thereby the size of gates by 0.6 m to optimise the design. After adjusting to the modified size of the opening, i.e. 9 m × 11.4 m, the studies were conducted and found the satisfied discharging capacity of the spillway. Positive pressures along the bottom profile of the breast wall also contributing to discharging capacity of the breast wall spillway. The height of piers in ski-jump bucket portion is sufficient to contain the water surface profile of the issuing jets over the spillway glacis. The discharging capacity of the spillway curve for ungated and gated operation is shown in Fig. 14.3 (CWPRS Technical Report Nos. 4210, 2005).

### ***14.2.2 Flow Conditions Upstream of Spillway, Over Spillway and in Front of Head Regulator***

Flow conditions upstream of the spillway for various discharges up to design discharge of 4850 m<sup>3</sup>/s for ungated as well as partial gate operation conditions show that the flow approaching the spillway was straight and forward with a velocity ranging from 1 to 2.5 m/s for ungated operation and 0.5 m/s to 1.5 m/s for gated operation with a reservoir at FRL El. 1241 m for discharges of 1212.5 m<sup>3</sup>/s and 4850 m<sup>3</sup>/s, respectively. Water surface profiles show that the trunnion of the radial gates was well above the water profile for the entire range of all discharges. The water conductor system of the project consists of a head regulator with two bays each 12.5 m wide on the left bank with an open power channel 540 m long. The

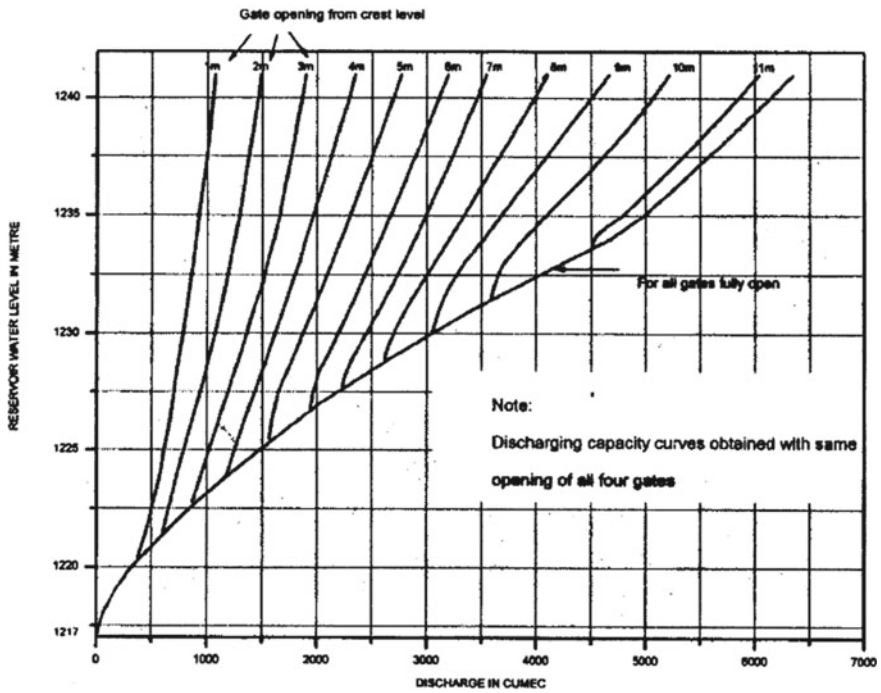
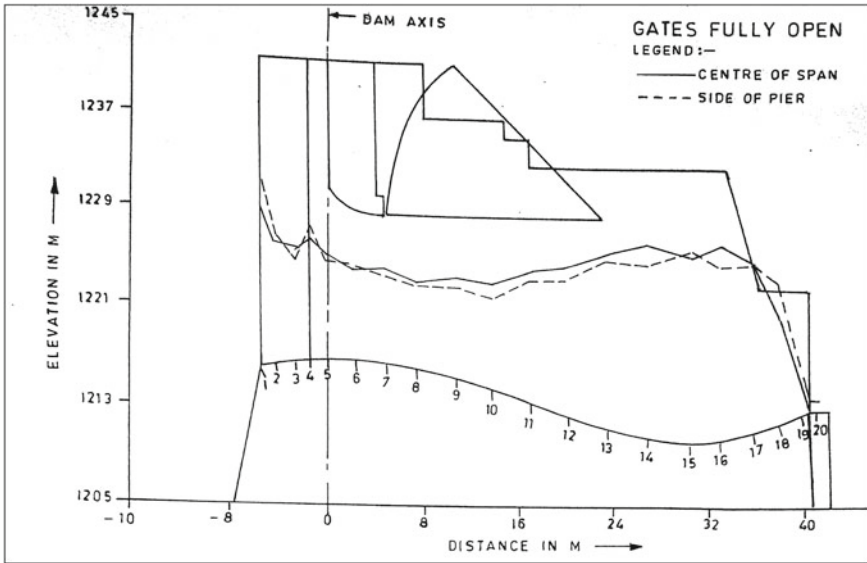


Fig. 14.3 Discharging capacity of the spillway for full and partial gate operation

axis of the head regulator is aligned at 150 degrees from the dam axis. The channel has been designed for a discharge of 253 m<sup>3</sup>/s, considering 20% flushing discharge at a maximum velocity of 2.25 m/s. The maximum portion of the power channel is in cutting, mainly in the overburden. Flow conditions upstream of the head regulator show that the head regulator is able to draw the design discharge of 253 m<sup>3</sup>/s smoothly. Thus, the flow conditions upstream of the spillway and head regulator were satisfactory.

### 14.2.3 Suitability of Profile of Spillway for Passage of Flood

The profile of spillway glacis should be such that the spillway should pass various incoming floods including the design flood without allowing negative pressures affecting the spillway profile thereby causing cavitation damage to the profile. Hence, the hydraulic model should be tested for various floods with the ungated and gated operation of the spillway. Hydraulic model studies indicated that the spillway profile is acceptable and may not be subjected to cavitation damage. Figure 14.4 shows the



**Fig. 14.4** Pressure profile over the glacis of the spillway for  $Q = 4850 \text{ m}^3/\text{s}$ , ungated operation of the spillway

pressure profile over the glacis of the spillway for  $Q = 4850 \text{ m}^3/\text{s}$ , ungated operation of the spillway. Also, studies indicated that the profile of the breast wall of the spillway is acceptable.

#### 14.2.4 Performance of Ski-Jump Bucket

Ski-jump bucket is a popular type of energy dissipator which is suited when the tail water levels are low near to the dam location. The ski-jump bucket is required to push the jet issuing over the spillway glacis, far away from the spillway and thereby reducing the velocities downstream of the spillway to a minimum limit. The performance of the ski-jump bucket was observed for various discharges by maintaining tail water levels at 300 m downstream of the dam axis. For the gated operation of the spillway, clear ski-jump action was observed and the maximum observed throw distance of the ski-jump jet is about 40 m from the bucket lip. The flow in the river downstream beyond the point of impingement of the jet remained supercritical with a high velocity of the order of 15–23 m/s pushing the tail water up to about 300 m downstream of the dam axis. The flow conditions in the river further downstream are violent with the concentration of flow towards the left bank. With gates fully open, the throw of the ski-jump jet is reduced to about 20 m from the bucket lip and it is seen impinging on the excavated slope downstream of the apron. This causes piling up of water downstream of the bucket lip for discharges of 3637.5

$\text{m}^3/\text{s}$  (75% of PMF) and above, thereby submerging the lip of the bucket and lower nappe of the jet. During the initial years of operation of the spillway, the impact of the ski-jump jet on the river bed and high-velocity supercritical flow downstream would result in progressive erosion of the river bed, forming a natural plunge pool. Thereafter, the excess energy of the ski-jump jet will get dissipated in the plunge pool and the flow conditions downstream will improve.

### ***14.2.5 Flow Conditions in the Open Channel of Head Regulator***

Flow conditions in the open channel downstream of head regulator for the design discharge of  $253 \text{ m}^3/\text{s}$  with reservoir water level FRL El. 1241 m and with/without spillway operating were such that the flow in the channel is sub-critical having a velocity of about 2.5 m/s without fluctuations throughout its length. Photo 14.1 shows flow conditions in the open channel downstream of the head regulator for discharge of  $253 \text{ m}^3/\text{s}$  in the channel.



**Photo 14.1** Flow conditions in open channel downstream of head regulator

### 14.2.6 Assessment of Scour Downstream of Spillway

Analysis of scouring downstream of the spillway is complicated by the complex hydraulic and geological conditions. An accurate evaluation of the parameters determining the erosion resistance of the rock is difficult. Many researchers have developed empirical or semi-empirical formulae considering various hydraulic as well as geological parameters. There is a wide variation in the estimated depth of scour by these researchers. Figure 14.5 shows a schematic diagram of factors affecting scour downstream of spillway ski-jump bucket. Table 14.1 shows empirical formulae given by various researchers for the prediction of scour depth. However, these formulae do not indicate the exact scour pattern. In view of these limitations, a qualitative idea of the likely scour pattern and scour depth could be obtained in the model by reproducing the riverbed erodible with non-cohesive material with rigid banks.

where

$q$  = discharge intensity ( $\text{m}^3/\text{s}/\text{m}$ ),

$H$  = Reservoir water level—elevation of bucket lip (m),

$H_{cr}$  = critical depth of flow (m),

$H_1$  = Reservoir water level—Tail water level (m),

$H_2$  = Velocity head at bucket lip (m),

$\phi$  = exit angle or lip angle (radians),

$D$  = size of material lining the bed (mm),

$d_s$  = depth of scour below Tail water level (TWL) and

$d_w$  = Tail water depth above ground level.

In the studies, the river portion downstream of spillway up to chainage 200 m downstream of dam axis was reproduced using sand of mean size ( $d_{50}$ ) of about 2 mm. The scour studies were conducted for the entire range of discharges passed with full as well as partial gate openings and maintaining tail water levels downstream. From studies, it was observed that while passing PMF with the ungated operation, the scour reached up to El. 1187 m at chainage 95 m downstream of dam axis, and for PMF

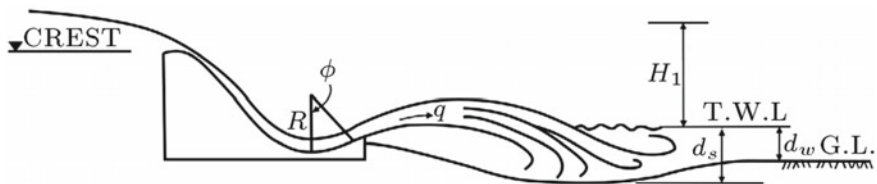


**Figure 14.5** Schematic diagram of factors affecting scour downstream of spillway ski-jump bucket (Nagikhani et al. 2015)



**Table 14.1** Empirical formulae for prediction of scour depth (Khatsuria 1992)

S. no.	Researcher	Formula
1	Damle, ultimate (1966)	$0.65 (qH)^{0.65}$
2	Damle, probable (1966)	$0.54 (qH)^{0.65}$
3	Damle, minimum (1966)	$0.36 (qH)^{0.65}$
4	Shixia (1987)	$1.6 * 2.44 * (H_{cr}^{0.89}) * (H^{0.11})$
5	Martins (1975)	$1.50 * q^{0.6} * H_1^{0.1} 1.50 * q^{0.6} * H_1^{0.1}$
6	Chee and Kung (1973)	$1.66 * q^{0.6} * H_2^{0.2} * \phi^{0.1} / d^{0.1} 1.66 * q^{0.6} * H_2^{0.2} * \phi^{0.1} / d^{0.1}$
7	Veronese (1937)	$1.9 * q^{0.54} * H_1^{0.225} 1.9 * q^{0.54} * H_1^{0.225}$

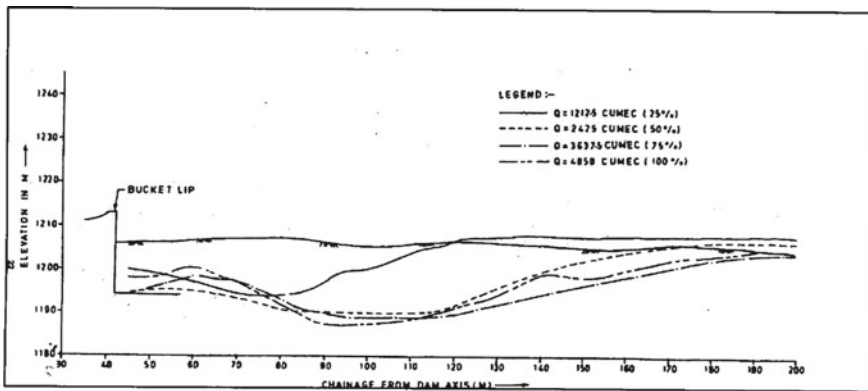


**Fig. 14.6** Scour profiles for various discharges for ungated operation of spillway (CWPRS Technical Report No. 4265, 2005)

with the gated operation, the deepest scour reached up to El. 1186 m at chainage 115 m downstream of dam axis. Figure 14.6 shows the scour profiles for spillway for the ungated condition for various discharges. The observed deepest scour level was compared with those calculated from the various formulae proposed by different researchers (Damle et al. 1966; Shixia 1987; Martins 1975; Chee and Kung 1973; Veronese 1937) and showed in Table 14.2. It was observed that these were in a close match with Damle’s formulae. Damle’s equations are reliable tools for the prediction of scour downstream of ski-jump spillways (Khatsuria 2013).

**Table 14.2** Comparison of values of scour depth obtained from empirical formulae with physical model studies

Discharge intensity, cumec/m	Head, m	qH	Damle, ultimate scour depth	Damle, probable scour depth	Damle, minimum scour depth	CWPRS model studies	Wang scour depth	Martins scour depth	Chee Kung scour depth	Veronese scour depth
134.7	21.5	2896.5	35.0	29.1	19.4	27.8	51.0	38.3	47.6	52.5
101.0	18.5	1864.2	28.1	23.3	15.5	25.2	42.3	32.0	38.9	44.2
67.4	15.2	1021.2	20.8	17.3	11.5	21.3	32.5	24.9	29.3	34.8
33.7	11.1	373.9	12.6	10.4	7.0	16.4	20.8	16.2	18.2	23.2

### 14.2.7 Flow Conditions Downstream of Spillway and Recommendations to Prevent Downstream Erosion

Flow conditions downstream of the spillway are assessed to prevent excessive erosion of topography and to suggest remedial measures to prevent it. The flow conditions in the river downstream of the spillway showed that the flow in the river downstream beyond the point of impingement of the jet remained supercritical with a high velocity of the order of 15–23 m/s pushing the tail water up to about 300 m downstream of dam axis. The flow conditions in the river further downstream were violent with the concentration of flow towards the left bank. However, study with the river bed reproduced erodible indicated that after the formation of plunge pool (because of erosion of river bed due to impact of ski-jump jet), the flow in the river downstream would remain sub-critical with a velocity of the order of 4–5 m/s. In order to protect the banks near the abutments against scour caused by return currents, it was suggested to extend the training walls as shown in Fig. 14.7. It was also recommended to keep the top level of the extended wall suitably above the maximum tail water level and the walls are anchored into the fresh rock on the banks. Moreover, the hill slope above the wall may have to be protected by providing cladding or shotcreting as per conditions at the site.

The construction of the project is completed based on recommendations of CWPRS, Pune, in respect of optimisation of the spillway, and all the four units are in

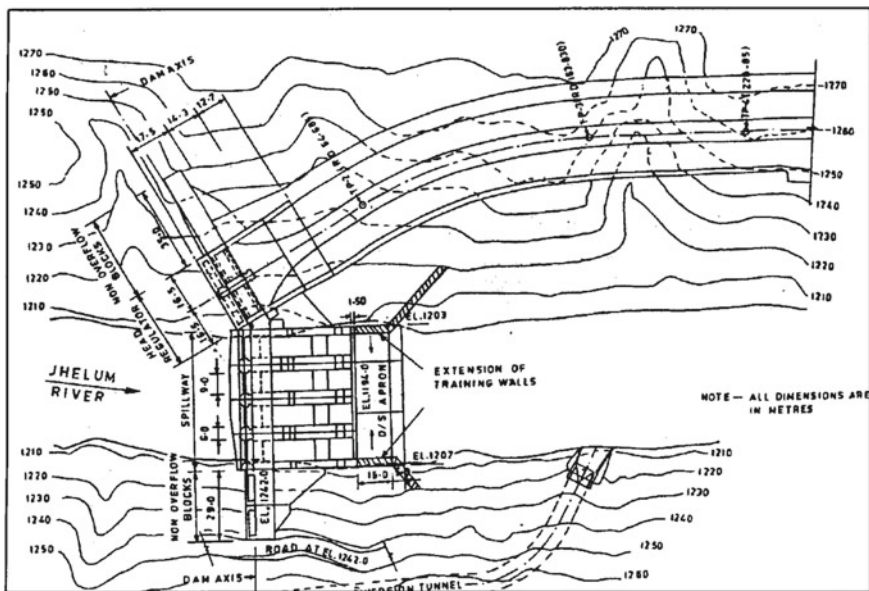


Fig. 14.7 Extension of training wall downstream of spillway to prevent bank erosion



**Photo 14.2** Downstream view of spillway Commissioned Uri-II H. E. Project, Jammu and Kashmir (<https://www.hccindia.com/markets/hydro-power>)

operation since 2014. Photo 14.2 shows Downstream view of spillway Commissioned Uri-II H.E. Project, Jammu and Kashmir.

### 14.3 Conclusions

Optimisation of spillway and its various components can be better carried out of hydraulic model studies and it is the best and only effective way for many decades. The optimisation of the Uri-II dam spillway was done effectively in CWPRS based on the results obtained from model studies:

1. Spillway orifice opening was reduced by about 5% (0.6 m) since model studies revealed that the design discharge of  $4850 \text{ m}^3/\text{s}$  can be passed through three spans at reservoir water level El. 1239.5 m as against FRL El. 1241 m. This reduces the quantity of material in construction and also reduces the size of gates and thereby reduces the maintenance cost of gate operation and thus overall economises the cost of work.
2. As a measure of downstream bank protection, to protect the banks near the abutments against scour caused by return currents, it was suggested to extend the training walls from bucket lip and flared further.
3. Natural plunge pool with scour profile up to El. 1186 m was recommended to eliminate uncontrolled erosion of river beds and banks and to achieve effective

energy dissipation of violent ski-jump jets, as scour studies showed that the deepest scour would reach up to El. 1186 m at chainage 115 m downstream of dam axis for design discharge of 4850 m<sup>3</sup>/s passed with partial gate operation.

**Acknowledgements** The authors are grateful to Director, CWPRS, for his encouragement and support in writing the technical paper. The authors are grateful to the Design/Project Engineers of NHPC for awarding the work of conducting hydraulic model studies to CWPRS and providing valuable inputs/suggestions during the course of the studies. The help of all CWPRS staff in conducting the studies is gratefully acknowledged.

## References

- BIS 11223 (1985) Guidelines for fixing spillway capacity  
 Bureau of Indian Standards (1985) Criteria for Hydraulic design of bucket type energy dissipators. IS: 7365–1985, 2nd revision  
 Chee SP, Kung T (1973) Stream geometry of water jet basins. In: Proceedings of hydraulics conference, Canadian society of civil engineers  
 CWPRS Technical Report No. 4210 (2005) Hydraulic Model Studies for Uri dam spillway, Stage-II, Jammu and Kashmir  
 CWPRS Technical Report No. 4265 (2005) Additional hydraulic model studies for scour downstream of Uri-II H. E. Project, Jammu and Kashmir  
 Damle PM, Venkatraman CP, Desai SC (1966) Evaluation of Scour below Ski-jump Buckets of Spillways. In: Proceedings of CWPRS Golden Jubilee Symposium, Pune, India, vol I, pp 154–163  
<http://www.nhpcindia.com/projects>  
<https://www.hccindia.com/markets/hydro-power>  
<https://www.mapsofindia.com/maps/dams/uri-hydroelectric-dam.html>  
 Khatsuria RM (1992) State of art on computation, prediction and analysis of scour in rocky beds downstream of ski jump spillways. CWPRS Memorandum  
 Khatsuria RM (2013) Predicting scour below ski jump spillways—Damle equation. Hydrotopics  
 Martins RBF (1975) Scouring of rocky river beds by free jet spillways. *Water Power Dam Construct* 27(4):1975  
 Naghikhani A, Noori R, Sheikhian H, Ghiasi B (2015) Estimating scour hole dimensions of ski jump downstream of dams using granular computing model. *J Hydraulics* 9(3):45–60  
 Shixia W (1987) Scouring of river beds below sluices and dams—Design of Hydraulic structures. In: Proceedings of the international symposium on design of hydraulic structures, Colorado State University, USA, August, 1987, pp 295–304  
 Veronese A (1937) Erosion de fond en aval d'une decharge, IAHR meeting for hydraulic works, Berlin

# Chapter 15

## Modification of Spillway Ski Jump Bucket Subjected to Higher Tail Water Levels



Vankayalapati S. Ramarao and M. R. Bhajantri

**Abstract** Spillways are provided to dispose off excess flood safely to downstream without causing excessive erosion. To dissipate the energy of flood, energy dissipators are provided for spillways. Ski jump buckets are one of the popular types of energy dissipators provided for spillways when the available tail water depths are very low, so that the clear ski jump forms and throws the flood away from the toe of the spillway, preventing the undermining of the spillway. However, depending upon the site conditions, ski jump buckets are provided where tail water levels are even at higher levels. In such typical conditions, submerged ski jump action occurs and the efficiency of energy dissipation arrangement may get reduced. As such, the performance of these designs is to be verified by conducting hydraulic model studies, since there are no exact codal provisions existing to have a flawless design. The optimization of ski jump bucket subjected to higher tail water levels can be done by studying its performance for various discharge conditions and making necessary modifications for getting clear ski jump action, without having hydraulic jump formation or submerged ski action in the bucket region which reduces energy dissipation and undermines spillway foundation. The submerged action of ski jump would also have an effect on the scour development downstream of the spillway and in the design of pre-formed plunge pool. A case study is presented in this paper where ski jump bucket of the spillway of Punatsangchhu-II H.E. Project, Bhutan, was optimized for coping up with prevailing higher tail water levels, by hydraulic model studies conducted on 1:70 scale geometrically similar physical hydraulic model in CWPRS, Pune.

**Keywords** Punatsangchhu-II hydroelectric project · Spillway · Breast wall · Ski jump bucket · Scour · Plunge pool

---

V. S. Ramarao (✉) · M. R. Bhajantri  
SED Division, Central Water and Power Research Station, Khadakwasla, Pune, Maharashtra  
411024, India

## 15.1 Introduction

One of the key issues that concern the safety of any dam is the performance of the spillway. The spillway is designed to dispose off excess flood safely to downstream for which a suitable energy dissipator must be provided. Among various types of energy dissipators, the ski jump bucket type of energy dissipator is the popular type, which requires minimum maintenance compared to other types. Ski jump bucket-type dissipators are provided when the available tail water levels are low so that clear ski jump action forms and jump is thrown away from the lip of the spillway preventing its undermining. Sometimes, ski jump buckets are provided for spillways even when the tail water levels are higher and allowing submerged ski jump action. Modifications to the design of spillway or energy dissipator are required if their performance is not satisfactory. Hydraulic model studies are the best tool to finalize the design of spillway and its components as the studies are carried out for various operating conditions whereas the design of the same may be based on guidelines set for limited operating conditions. The optimization of the design of ski jump bucket energy dissipator of Punatsangchhu H.E. Project, Stage-II, Bhutan, was done by conducting hydraulic model studies in CWPRS, Pune.

Punatsangchhu-II H.E. Project is under construction as a run-of-river scheme on the Punatsangchhu River in Western Bhutan. The project is located downstream of Punatsangchhu-I H.E. Project. The project envisages the construction of an 86 m high (from deepest foundation level) concrete gravity diversion dam to generate 1020 MW of power utilizing a design head of 236 m at an underground power house.

The main spillway consists of seven sluices of dimensions 8 m (W)  $\times$  13.2 m (H) to pass a probable maximum flood of 11,723 m<sup>3</sup>/s and Glacial Lake Outburst Flood (GLOF) of 4300 m<sup>3</sup>/s at Full Reservoir Level (FRL) at El. 843 m.

The Maximum Water Level (MWL) is also at El. 843 m and the Minimum Draw-down Level (MDDL) is at El. 825 m. The crest of the spillway is at El. 797 m. An auxiliary spillway in the form of ogee with a crest at El. 839 m is equipped with a vertical lift gate of size 4 m (W)  $\times$  4 m (H) at the centre of the main spillway.

Ski jump bucket has been provided as an energy dissipator for both main and auxiliary spillways. Ski jump bucket for the main spillway has invert of bucket and lip were originally at El. 776.756 m and El. 783.086 m, respectively. A pre-excavated plunge pool is provided downstream of the ski jump bucket for effecting energy dissipation.

## 15.2 Performance of Ski Jump Bucket for Higher Tail Water Levels

The purpose of ski jump bucket is to throw away the jet impinging from the spillway glacis to a faraway distance and thereby preventing the undermining of the spillway structure. Ski jump bucket design depends mainly upon the prevailing tail water

levels which make or spoil the formation of clear ski jump action. Trajectory bucket-type energy dissipator is considered more suitable when (a) Tail water depth is much lower than the sequent depth of hydraulic jump, thus preventing the formation of the jump; (b) By locating at a higher level, it may be used in case of higher tail water depths also, if economy permits; (IS 7365: 2010). Hence, the model studies are essential to study the performance of ski jump buckets. For the Punatsangchhu-II dam spillway, the performance of ski jump bucket was tested on 1:70 geometrically similar scale hydraulic model.

### 15.2.1 The Original Design of Energy Dissipator and Its Performance

The original design of the spillway consisted of a sluice spillway with 7 spans of size 8 m (W) × 13.2 m (H) with the equation of crest profile as  $x^2 = 192y$ , to dispose off the maximum flood of 16,023 m<sup>3</sup>/s, including GLOF. The breast wall bottom profile conforms to the equation  $x = 0.1597 * y^{2.4}$ . The energy dissipator was in the form of ski jump-type bucket with an invert at El. 776.756 m and of radius 35 m. The elevation of the lip of the bucket was at El. 783.086 m and with a lip angle of 35°. Figure 15.1 shows the cross section of the spillway with the original design of ski jump bucket energy dissipator.

Hydraulic model studies were conducted on a 1:70 G.S. 3-D comprehensive model to assess the performance of ski jump bucket was found unsatisfactory for an original design for the entire range of discharges for the gated and ungated operation of the spillway. The bucket lip was getting submerged. It was observed that the extent of submergence of the lip was of the order of 8–20 m for the different ranges of discharges due to existing higher tail water levels. Submerged ski action with aerated surface rollers (hydraulic jump) riding over the bottom jet could see in the bucket. Ski jump bucket was susceptible to tail water levels as the hydraulic jump was seen forming in the bucket for a slight increase in tail water levels. Hence, it was necessary to modify the existing ski jump bucket by raising the elevations of bucket invert and

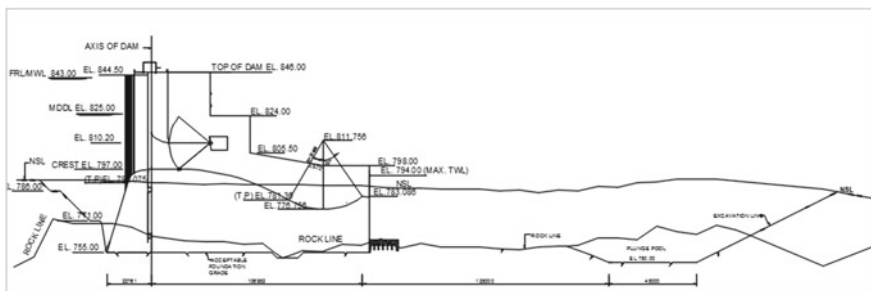
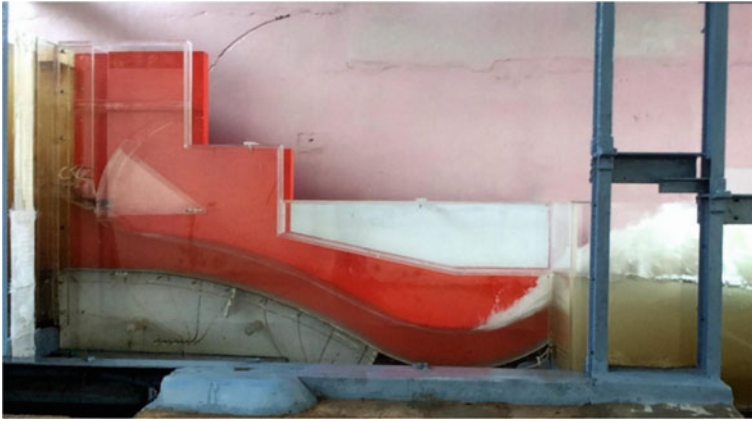


Fig. 15.1 Cross section of the original energy dissipator of the spillway





**Photo 15.1** Performance of original ski jump bucket (Discharge through the spillway,  $Q = 16,023 \text{ m}^3/\text{s}$ , at Full Reservoir Level (FRL))

bucket lip, and the modified design was to be verified for the performance of the modified energy dissipator. Photo 15.1 shows the performance of the original ski jump bucket (Discharge through the spillway,  $Q = 16,023 \text{ m}^3/\text{s}$ , at Full Reservoir Level (FRL)). It shows the formation of roller action in the bucket due to higher tail water levels negating the clear ski jump action.

### 15.2.2 *Modifying Ski Jump Bucket*

Modification of ski jump bucket involves modifying the radius and angle of the lip of the bucket, which in turn modifies elevations of bucket invert and lip. The fixation of bucket invert elevation depends on the site and tail water conditions. The elevation of bucket lip shall in any case be above the maximum tail water level in order to (1) prevent material entering the bucket that causes abrasion and (2) counter cavitation damage due to submergence fluctuations (Vischer and Hager 1998). For a clear flip action, the lip shall have to be kept above the maximum tail water level.

The ski jump bucket of Punatsangchhu-II dam was modified by raising the invert level to El. 780.72 m with a radius of 35 m and the elevation of the lip of the bucket was raised to El. 787.052 m with lip angle  $35^\circ$ . Figure 15.2 shows the cross section of the modified energy dissipator.

The performance of the modified energy dissipator was observed on the 3-D comprehensive model (CWPRS T.R. No. 5410 2016). While passing discharges of 25, 50, 75 and 100% of design discharges, maintaining tail water levels as per tail water rating curve is as shown in Fig. 15.3. From the studies, it was observed that performance of the energy dissipator was improved and functioning satisfactorily for all discharge conditions. The formation of rollers/ hydraulic jump in the bucket lip

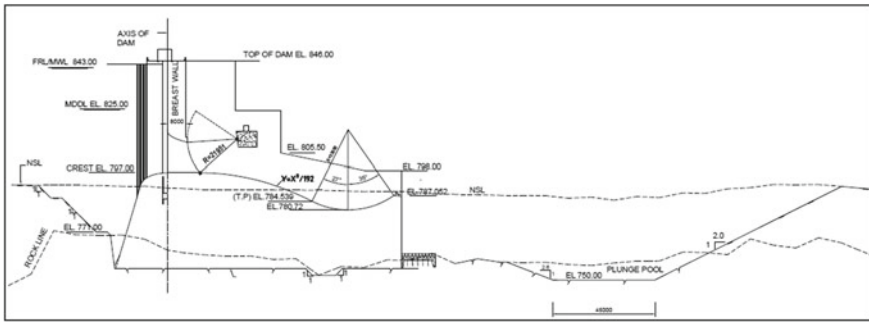


**Fig. 15.2** Cross section of the modified energy dissipator of the spillway

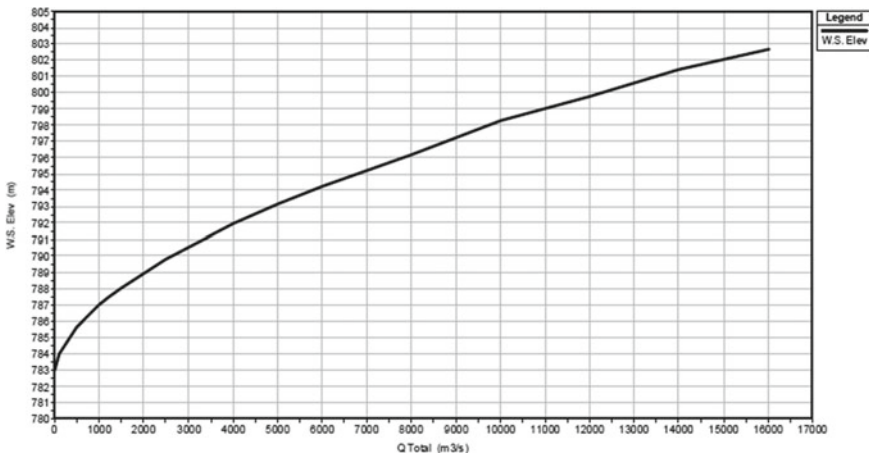


**Fig. 15.3** Tail water rating curve

was completely eliminated with the modification in energy dissipation arrangement. Photos 15.1 and 15.2 show the performance of the energy dissipator for the original and modified ski jump bucket, respectively.

According to the literature, submergence of more than 70 percent of the depth required for the formation of the hydraulic jump may adversely affect the proper performance of the trajectory bucket. The safe maximum submergence may be assumed to be equal to the critical depth ( $d_c$ ) over the lip elevation (IS 7365). Both the criteria were analysed to obtain minimum submergence levels for the formation of clear ski jump for various operating conditions and tabled as Table 15.1.

From Table 15.1, it is known that the clear ski jump action prevails when tail water level is substantially below the elevation of 70% of sequent depth above invert/elevation of critical depth above the lip of the bucket. Even marginal difference in elevations of tail water and both referred criteria was not allowing the clear jump



**Photo 15.2** Performance of modified ski jump bucket (Discharge through the spillway,  $Q = 16,023 \text{ m}^3/\text{s}$ , at Full Reservoir Level (FRL))

to form. Figure 15.4 shows the plot of submergence levels of ski jump buckets above bucket lip for the same criteria.

### 15.2.3 Scour Downstream of Spillway

When the energy of water jet issuing from the spillway glacis exceeds the strength of river bed downstream of the spillway or the energy is not dissipated fully in the downstream, the foundation of the dam and spillway would be subjected to scour and long-term scour process which may endanger the dam/spillway and also downstream river channel, and hence, attention must be given to ensure the safety of the structure. Prediction of plunge pool scour holes is very difficult because scour process varies with many factors including hydraulic, morphologic and hydrologic conditions, as well as characteristics of the structure and flow regulation rule (Annandale 2006). Physical model studies would be the most reliable method for the prediction of scour depth. Hydraulic model studies were conducted in CWPRS, Pune, to assess the maximum scour downstream of the spillway and for the design of the plunge pool (CWPRS Technical Report, 5607 2018). Studies indicated that the deepest scour elevation reached up to El. 768 m at chainage 210 m downstream of dam axis for discharge of  $11,723 \text{ m}^3/\text{s}$  (PMF) passed with the gated operation, and with the ungated operation of the spillway, it reached up to El. 769 m at chainage 195 m. For 75% of PMF with the gated and ungated operation, the deepest scour depth reached up to El. 769 m at chainage 200 m and El. 770 m at 180 m, respectively. For 60% of PMF, scour depth reached up to El. 770 m at 215 m and El. 772 m at 175 m for gated and ungated operation, respectively. For 25% of PMF, scour depth reached up to El.

**Table 15.1** Ski jump submergence levels

S. no.	Profile	Discharge, $Q$ ( $m^3/s$ )	FRL/RWL (m)	Max tail water level (m)	Intensity, $q$ ( $m^3/s/m$ )	Elevation of critical depth ( $d_c$ ) above lip	Sequent depth above invert, $d_2$	Elevation of 70% of $d_2$ , above invert	Remarks
1	Original profile	16,023	839.4	802.64	286.13	803.4	39.5	804.4	Ski jump was not forming
		11,723	823.98	799.6	209.34	799.6	31.1	798.5	
		8792.25	815.56	797.2	157.00	796.7	25.6	794.7	
		7033.8	812	795.45	125.60	794.8	22.6	792.6	
		2930.75	804.7	790.5	52.33	789.6	14.4	786.8	
		16,023	843	802.64	286.13	803.4	40.4	805.0	
		11,723	843	799.6	209.34	799.6	35.4	801.5	
		8792.25	843	797.2	157.00	796.7	31.2	798.6	
		7033.8	843	795.45	125.60	794.8	28.2	796.5	
		2930.75	843	790.5	52.33	789.6	18.8	789.9	
2	Modified profile	16,023	839.4	802.64	286.13	807.3	38.5	807.7	Ski jump was forming
		11,723	823.98	799.6	209.34	803.5	30.0	801.7	
		8792.25	815.56	797.2	157.00	800.6	24.5	797.9	
		7033.8	812	795.45	125.60	798.8	21.5	795.8	
		2930.75	804.7	790.5	52.33	793.6	13.6	790.2	
		16,023	843	802.64	286.13	807.3	39.4	808.3	
		11,723	843	799.6	209.34	803.5	34.6	805.0	
		8792.25	843	797.2	157.00	800.6	30.6	802.1	
		7033.8	843	795.45	125.60	798.8	27.7	800.1	
		2930.75	843	790.5	52.33	793.6	18.5	793.6	

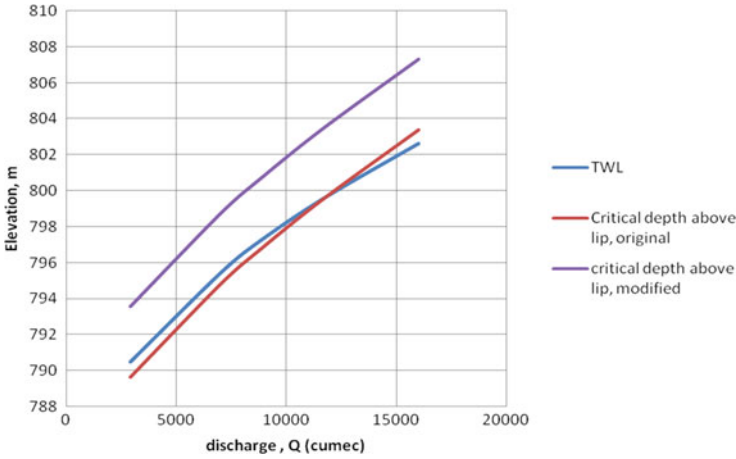


Fig. 15.4 Plot of submergence levels of ski jump bucket above bucket lip

771 m at 195 m and El. 772.5 m at chainage 160 m for gated and ungated operation, respectively.

Based on observed scour profiles, it was recommended by CWPRS that the bottom elevation of the pre-formed plunge pool may be kept the same as the existing rock line against the proposed plunge pool bed at El. 750 m to optimize the design for the greater economy by avoiding the additional excavation of the plunge pool of the order of 7 m. Since the average elevation of the rock line is about El. 757 m, it could be considered as the bed level of the pre-formed plunge pool. Figure 15.5 shows water surface profile from ski jump bucket lip and scour profiles in the scour pit while passing discharge of 11,723 m<sup>3</sup>/s through spillway (PMF), at Full Reservoir

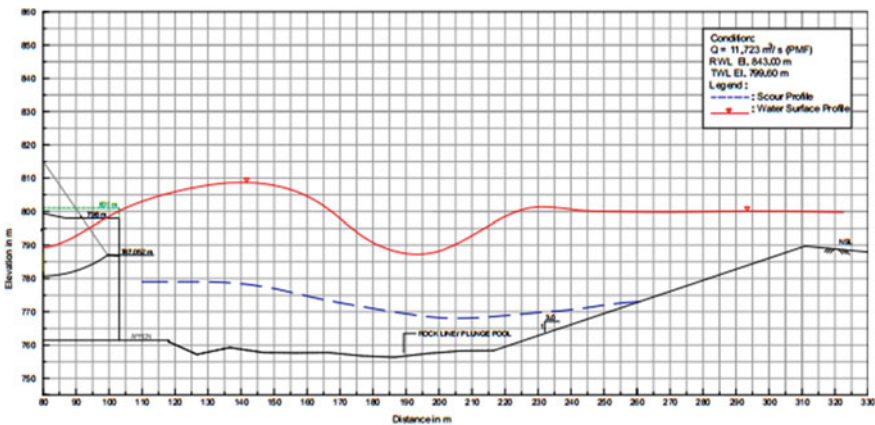


Fig. 15.5 Water surface and scour profiles (Discharge through the spillway, Q = 11,723 m<sup>3</sup>/s, at Full Reservoir Level (FRL))

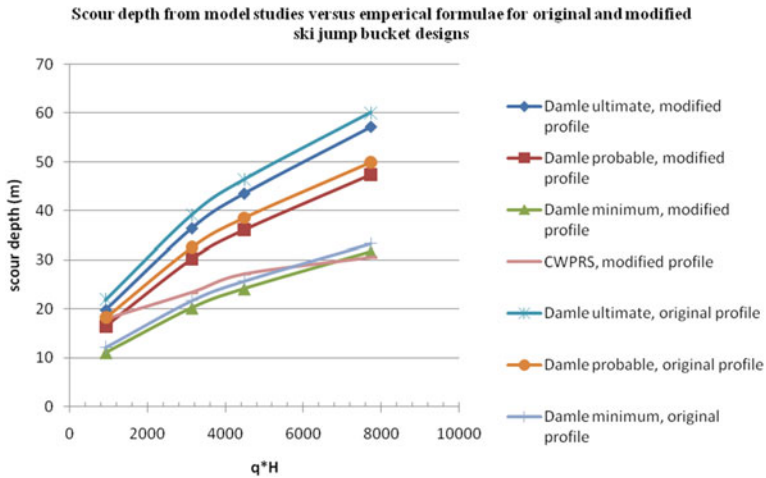


Fig. 15.6 Plot of comparative scour depth obtained from model studies and empirical formulae

Level (FRL) of El. 843 m. The rock line of the river bed downstream of the spillway is also shown in the figure. The obtained scour depth values were compared with the available eminent formulae (Damle et al. 1966), as shown in Fig. 15.6 and found that the values are nearly in agreement with them but not these formulae giving exact values, which indicates the importance of the hydraulic model studies.

### 15.3 Conclusions

Spillways are meant for disposing off the flood safely to downstream, and satisfactory performance of energy dissipators is essential for the same. Modifications to the design of spillways and energy dissipators are essential if their performance is not satisfactory and not suiting to the dam safety criteria. Designs of spillway and energy dissipator are to be verified for varying discharges, and hydraulic model studies are the best possible tool for the same. For the Punatsangchhu-II dam spillway, modifications were required for the energy dissipator of the spillway to improve the performance of ski jump bucket due to prevailing higher tail water levels. The lip and invert levels of the energy dissipator were raised for improving the performance. By modifying the profile, there was an improvement observed in the performance of the energy dissipation arrangement. Scour studies indicated that the observed scour depth is low so that the depth of the plunge pool was optimized by recommending the bottom elevation of plunge pool matching with rock line reducing the cost of excavation. The project is under construction with the adoption of recommendations made by CWPRS, Pune.

**Acknowledgements** The authors are very much grateful to Director for his continued encouragement in writing technical papers. The authors are also grateful to the project authorities of Punatsangchhu-II H.E. Project, Bhutan, for their support in providing required data during model studies. The support of the staff of the SED Division is herewith acknowledged.

## References

- Annandale GW (2006) Scour technology. McGraw-Hill, New York, p 2006
- CWPRS Technical Report No. 5410 (2016) Hydraulic model studies for spillway of Punatsangchhu H.E. Project Stage-II, Bhutan, 1:70 Scale 3-D Comprehensive Model, April 2016
- CWPRS Technical Report No. 5607 (2018) Hydraulic model studies for assessment of scour downstream of spillway of Punatsangchhu H.E. Project, Stage-II, Bhutan, 1:70 Scale 3-D Comprehensive Model, July 2018
- Damle PM, Venkatraman CP, Desai SC (1966) Evaluation of scour below ski-jump buckets of spillways. In: Proc., CWPRS golden jubilee symp., Pune, India, vol I, pp 154–163
- IS: 7365-2010. Criteria for hydraulic design of bucket type energy dissipators. Bureau of Indian Standards, New Delhi, 110002
- Vischer DL, Hager WH (1998) Dam hydraulics. Wiley, England

# Chapter 16

## Prediction of Submerged Vegetated Flow in a Channel Using GMDH-Type Neural Network Approach



Nekita Boraah and Bimlesh Kumar

**Abstract** The study of flow in the vegetative channel is not new to existing concerns. The effect of vegetation in river systems with regards to its preservation is of much importance. The aquatic plants that thrive in water have been found to control the mean flow and turbulence of flow of river systems. Even the morphology of a channel can be affected by the submerged and emergent vegetation. The important parameter of any channel mainly velocity profile is influenced a lot due to the height and flexibility of submerged aquatic plants. This also impacts the transport of sediment in the channel. Apparently, the presence of plant life in a channel decreases the mean discharge and sediment load potential and leads to the accumulation of sediment in the channel due to additional drag produced by the presence of vegetation. Literature status reveals that the scope in this field is vast as not much has been contributed so far. Also, the studies mostly reveal the use of conventional methods to indicate the relationship between the different parameters. To develop models for relating the parameters and to predict future scope, soft computational techniques are used to simplify the otherwise complex equations. Studies indicate the use of neural networks in association with PSO techniques, also GA has been reported. This study has been conducted with the help of another soft-computing technique which analyses polynomial neural networks, Group Method of Data Handling (GMDH). This technique has been reported to be in extensive use in the field of hydraulics. This approach, as an advanced tool, has been modelled to predict the resistance due to flow–vegetation interaction in a submerged vegetated channel. The main aim of this approach is the development of an explicit model which optimises the parameters and predicts the unknown input–output mapping. The results generated by the model have been found to be sufficiently good. The model has been developed in the interest of predicting future outputs by capturing the related relationship of input–output mapping. It is designed so as to analyse the influence of various parameters on the velocity profile.

---

N. Boraah (✉)

School of Hydro-Informatics, Department of Civil Engineering, NIT Agartala, Agartala, India

B. Kumar

Department of Civil Engineering, IIT Guwahati, Guwahati, India

e-mail: [bimk@iitg.ac.in](mailto:bimk@iitg.ac.in)



**Keywords** Flow–vegetation interaction · Flow resistance · Neural networks · GMDH approach · Data modelling

## 16.1 Introduction

Vegetation in a channel is found to affect channel characteristics in many ways as recent studies have indicated too (Jha and Kumar 2013). The main factors found to affect vegetated flow are environmental as well as plant characteristics. Environmental factors mainly include water temperature and surface characteristics, while plant characteristics include vegetation density, the height of submergence, flexibility of vegetation, geometry and spacing of placement of vegetation, also mean flow velocity, and channel morphology. The flow resistance exerted on vegetation is generally classified by the relative depth of flow to the height of vegetation (Ree 1949). Also, a study indicated that bends with riparian vegetation are seen to control five times as much detectable erosion as compared to bends without vegetation during flood events (Beeson and Doyle 1995). Mainly, it is found to affect sediment transport in a channel. The problem of sediment transport is so intricate that for the formulation, it needs exact equations, either empirical or regression. An investigation of sediment transport has indicated extensive use of regression equations for the formulation of equations. Choi and Kang have used the Reynolds stress model for modelling open channel flows with vegetation (Choi and Kang 2004). Experimental studies reported the analysis of vegetation concentration and depth/vegetation height ratio influence on the computed velocity profiles so that a new expression for mixing length could be established based on Prandtl's mixing length (Carollo et al. 2002). But, these equations seemed to lack appropriate functional formulation and a feasible inaccurate clustering effect of influential points and cluster of points. This has resulted in a realisation that there is a need for the development of new and robust modelling procedures which overcomes the limitations of the predictable techniques and also, builds up models for the prediction of sediment transport problems in channels.

As a huge number of computational resources have already been reported, there has been the development of various statistical models that are purely based on the analysis of previous data of an event. Also, different algorithms were evolved based on the methodology of the events. This has encouraged the modellers to develop models that are precise with the ability to explain the inconsistency in data to a suited satisfactory level and predict the state variables corresponding to the combination of circumstances that are entirely new to the model developed. Neural network models have been found to be effective in solving various engineering issues. The main aim of using neural networks is the optimisation of parameters. The popularity of neural networks is that they can capture nonlinear complex interactions between input and output parameters and also, its ability to self-adapt (Muhammad et al. 2018).

Group Method of Data Handling (GMDH) is a set of different algorithms that forms a potentiality to determine the interlinkages in data, choose a model or network that forms an optimal structure, and intensify the accuracy of prevailing algorithms. GMDH algorithm formulates a model as a family of neurons where different pairs of them in each layer are interconnected through a quadratic polynomial to produce new neurons in the next layer which helps in mapping input with output (Amanifard et al. 2008). This approach, as an advanced tool (Muhammad et al. 2018), has been modelled to predict the resistance due to flow–vegetation interaction in a submerged vegetated channel. This approach has been widely used in different fields to model input–output mapping. It has been used to envisage discharge coefficient in a side weir (Ebtehaj et al. 2015). GMDH in coordination with genetic algorithm has been used in modelling and Pareto-based optimisation of heat transfer and flow coefficients in microchannels (Amanifard et al. 2008). In modelling and multi-objective optimisation of a variable value-timing spark ignition engine, GMDH is used to obtain a polynomial neural network model, and using this PNN, a multi-objective evolutionary algorithm is used for optimisation (Atashkari et al. 2007). A review of the problems that can be solved by the algorithms of GMDH indicates that the selection of an algorithm relies on the problem type, noise variance level, sufficient sample points, and also on the presence of only continuous variables in the sample (Ivakhnenko and Ivakhnenko 1995). Further, GMDH-type neural network has also been used for the development of an artificial neural network which was optimised using the multi-objective genetic algorithm to find an explicit polynomial model for friction factor (Besarati et al. 2015).

This paper attempts to formulate a different analysis to model the flow-sediment problem by predicting the flow in a vegetated channel. Other than deriving just an expression, it aims at developing a flow-prediction model using the GMDH approach.

## 16.2 Analytics of Flow–Vegetation Interaction

Numerical modelling, empirical (Kouwen and Fathi-Moghadam 2000), and theoretical relations have been developed in various forms in order to depict the transformation in flow affected by vegetation. A study on channels affected by submerged and unsubmerged vegetation indicated that for unsubmerged vegetation, an increase in flow depth but not topping the vegetation is likely to cause a diminutive change in the mean velocity; as a result of which flow resistance tends to increase with depth. For partially submerged vegetation, studies comprehend that Manning's coefficient  $n$  increases with flow depth. Petryk and Bosmajian (1975) in their flow-resistance model suggested that the energy slope of the flow can be decomposed into the energy gradients caused by the boundary shear stress and the vegetation, respectively. They formulated that Manning's  $n$ , representing the total resistance induced by the boundary friction and vegetation, can also be predicted based on vegetation

density, hydraulic radius, and boundary roughness. For completely submerged vegetated areas, Manning's  $n$  is found to increase in proportion to the  $2/3$  power of the hydraulic radius and the square root of the vegetation density, but it is independent of the roughness of the channel bottom (Wu et al. 1999).

Rouse identified flow resistance and classified it into four components. With the help of the Weishbach resistance coefficient  $f$ , he formulated resistance as a dimensionless symbolic function given as (Yen 2002):

$$f = F(\mathbf{R}, \mathbf{K}, \eta, \mathbf{N}, F, \mathbf{U}) \quad (16.1)$$

where  $\mathbf{R}$  = Reynolds number,  $\mathbf{K}$  = relative roughness, expressed as  $k_s/R$ ,  $k_s$  represents equivalent wall surface roughness and  $R$  represents hydraulic radius pertaining to the flow,  $\eta$  = geometry of cross-section,  $\mathbf{N}$  = non-uniformity of the channel profile wise and plan wise,  $F$  = Froude number,  $\mathbf{U}$  = degree of unsteadiness of flow, and  $F$  pertains to the function. Yen extended this study by explaining resistance phenomena with the inner and outer laws of boundary layer theory. Also, he discussed about the linear and nonlinear-separation approach to alluvial channel resistances. The analysis extended that if vegetation is present in flow, it has a great effect on the velocity distribution and hence, flow resistance. He further deduced the symbolic function in Eq. (16.1) as:

$$f = F(\mathbf{R}, F, \mathbf{N}, \mathbf{L}_v, \mathbf{J}, \mathbf{D}, \mathbf{M}) \quad (16.2)$$

where  $\mathbf{R}$ ,  $F$ ,  $\mathbf{N}$  have been discussed in Eq. (1) and  $\mathbf{K}$  has been expanded to include symbolic non-dimensional vegetation parameters,  $\mathbf{L}_v$  for representative geometry measure,  $\mathbf{J}$  represents flexibility,  $\mathbf{D}$ , the relative submergence, and  $\mathbf{M}$ , its density distribution on channel bed. Also, as the flow advances through the vegetated channel, where the height of the plant to the depth of flow ratio,  $K/H > 1/2$ , the drag of vegetation offers more resistance than that from bed shear. Form drag is mainly affected by plant properties that include the ratio  $K/H$ , the amount of submergence of the plant,  $K > H$ , plant density, and flexibility (Neary 2003). A study conducted by Lopez and Garcia reveals that vegetation-induced flow has been found to lower the suspended sediment transport capacity (Lopez and Garcia 1998). Also, the channel flow modelling through vegetation is a function of many more variables than discussed earlier. The discussion reveals the dependency on fluid properties, properties of flow, channel, and vegetation characteristics. Assuming flow to be steady and uniform, for a homogeneous vegetation of fixed height and diameter, the flow-vegetation interaction can be equated as:

$$f(u, h, k, i, m, C_D, D) = 0 \quad (16.3)$$

where  $u$  = mean flow velocity,  $h$  = flow depth,  $k$  = height of vegetation,  $i$  = channel slope,  $D$  = diameter of cylindrical vegetation,  $m$  = number of cylinders per square metre horizontal area, and  $C_D$  = drag coefficient. The condition of submergence,  $h \gg 5k$ , is valid only when vegetation does not block the way of flow in the channel (Galema 2009). Also, a condition of  $5k > h > k$  is followed when the density of vegetation is relatively more than the depth of flow. As a result, there is a notable change in the velocity profile of the channel. This study focusses on predicting the flow velocity of a submerged vegetated channel, so that the velocity parameter  $u$  is considered as a dependent variable that depends on the various other factors as shown in Eq. (16.1). Keeping this in view, Eq. (16.1) can be written as:

$$u = f(h, k, i, m, C_d, D) \quad (16.4)$$

### 16.3 Modelling Using GMDH-Type Neural Network

The focal attraction of research efforts nowadays includes two key features: system identification and modelling complex processes using input–output mapping. Already, system identification techniques have been used many times in various fields for modelling and predicting the behaviour of complex systems using input–output data. But, the foremost toil is to apprehend the mathematical input–output connection explicitly which is almost difficult, i.e., not readily distinguishable. So, soft-computing techniques that concern computation of a vague environment have received noteworthy consideration. Soft-computing constitutes of components, fuzzy-logic, neural network, and genetic algorithms, and these components have revealed prodigious ability in resolving complex nonlinear system identification (Nariman-Zadeh et al. 2005). Among these methods comes an approach that is self-organising in nature and works with nonlinear network models and uses an amalgamation of quadratic polynomial in a multilayer system, known as the Group Method of Data Handling or GMDH (Najafzadeh and Sattar 2015). For modelling complex systems and identification, this multivariate analysis technique has been quite convenient.

GMDH has been utilised in such a way so as to evade the difficulty of having a prior understanding of the mathematical model of the considered process. The beauty lies in the fact that it can be used to model complex systems without having detailed knowledge of the systems. The main idea of GMDH lies in building an analytical function in a feed-forward network that is based on a quadratic node transfer function whose coefficients are obtained by regression technique. Also, the model coefficients in this method are estimated by means of the least-squares method. In this paper, the GMDH-type neural network has been effectively used to model and predict the velocity, as a function of important input parameters in flow–vegetation interaction (Fig. 16.1).

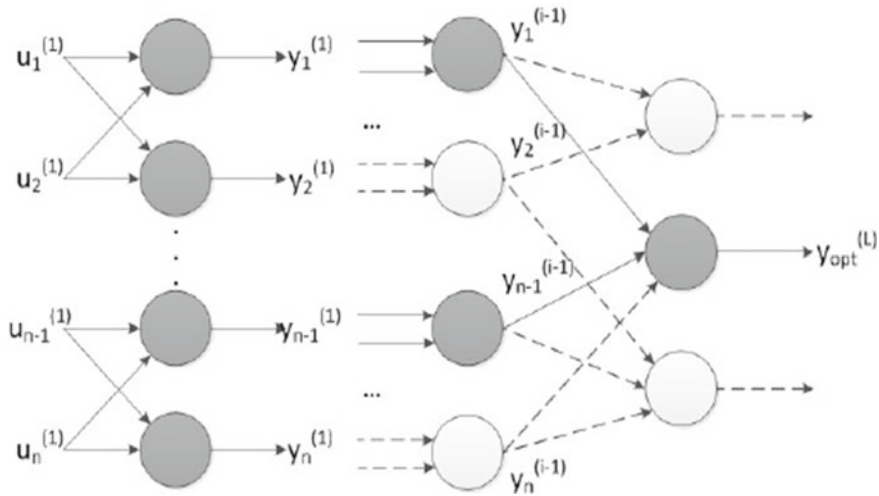


**Fig. 16.1** Schematic structure of a GMDH neural network (Sobolewski 2014)

The GMDH algorithm represents a model as a set of neurons. Different pairs of neurons in each layer are connected through a quadratic polynomial and thus produce new neurons in the next layer. This demonstration is used in modelling to map inputs to outputs. The proper explanation of the detection problem is to hit upon a function,  $\hat{f}$ , that approximates the actual function,  $f$ , to a sufficient accuracy to predict the actual output  $y$  for a given input vector  $X = (x_1, x_2, \dots, x_n)$  as  $\hat{y}$ . Therefore, for a given  $M$  number of observations of multiple input and single output data pairs, the system can be defined as:

$$y_i = f(x_{i1}, x_{i2}, \dots, x_{in}), \text{ for } i = 1, 2, \dots, M \tag{16.5}$$

A GMDH-type neural network can be trained to predict the output values for any set of input vectors, as demonstrated below:

$$\hat{y}_i = \hat{f}(x_{i1}, x_{i2}, \dots, x_{in}), \text{ for } i = 1, 2, \dots, M \tag{16.6}$$

In the determination of a GMDH-type network, the actual struggle that emerges, for which the square of the differences between the actual output and the computed one is optimal, is:

$$\sum_{i=1}^M \left[ \hat{f}((x_{i1}, x_{i2}, x_{i3}, \dots, x_{in}) - y_i) \right]^2 \rightarrow \min \tag{16.7}$$

The relation between the input–output variables can be articulated by a discrete form of the Volterra functional series, as follows:

$$y = a_0 + \sum_{i=1}^n a_i x_i + \sum_{i=1}^n \sum_{j=1}^n [a_{ij} x_i x_j] + \sum_{i=1}^n \sum_{j=1}^n \sum_{k=1}^n [a_{ijk} x_i x_j x_k] + \dots \quad (16.8)$$

This form of the series is known as the Kolmogorov–Gabor polynomial (Farlow 1984). This full form of mathematical description can be denoted by a partial quadratic polynomials system consisting of only two input variables (neurons), represented in the following form.

$$\hat{y} = G(x_i, x_j) = a_0 + a_1 x_i + a_2 x_j + a_3 x_i x_j + a_4 x_i^2 + a_5 x_j^2 \quad (16.9)$$

## 16.4 Results and Discussion

Group Method of Data Handling (GMDH) was used to illustrate the performance of the system in sight. The complete modelling and study have been carried out by means of the neural network toolbox incorporated in MATLAB<sup>®</sup> software (The MathWorks Inc., Natick, MA, USA) (Jha and Kumar 2013). Documentations of the ample records for various vegetation types that review hydraulic properties were collected from numerous sources (Galema 2009). Table 16.2 demonstrates the collection of observations that have been reviewed while carrying out present studies. The total number of observations was taken to be 446 in the modelling. The development of the GMDH model used 74% of the observations as training sets and the rest 26% have been assigned for testing. A hit and trial method was employed to arrive at the optimal parameters for the GMDH modelling. The model devised parameters are the maximum number of neurons in a layer, the maximum number of layers, and the amount of selection pressure in a layer. The program had to be iterated many times in order to discover an optimal value of the model devised parameters. The number of neurons remains unidentified so a GMDH-type neural network has to be selected carefully. With the occurrence of numerous layers along with neurons and a complicated structure, there arises a tendency of an overtrained network that might memorise outputs. Also, if the neurons are too few, it may fabricate a network that is unable to describe the variability in the data presented. As such, neuron number had to be assumed appropriately, which was recognised by assembling numerous trials of the training algorithm, every time changing the number of neurons in a single hidden layer. Each time, only the neuron numbers were altered without varying the algorithmic changes. Again, the ANN transfer functions were also decided using a hit and trial method. The transfer function after undergoing various trials suggested a combination of tan and log sigmoid functions to be used for the hidden layer and also, the input layers. This amalgamation proved to provide the best correlation coefficient values. However, the output layer witnessed a linear transfer function (Table 16.1).

**Table 16.1** Equations suggested for flow-velocity analysis in a vegetative channel

Author(s)	Formulation(s)
Stone and Shen (2002)	$u = \sqrt{\frac{2g}{C_d m D}} \sqrt{i} (1 - D\sqrt{m}) \sqrt{\left(\frac{h}{k} - \frac{1}{4}\pi m D^2\right) \frac{h}{k}}$
Velzen et al. (2003)	$u = \sqrt{\frac{2g}{C_d m D}} \sqrt{i} + 18(h - k)^{3/2} \frac{\sqrt{i}}{k} \log \frac{12(h-k)}{16k^{0.7}}$
Baptist et al. (2007)	$u = \left( \sqrt{\frac{2g}{C_d m D}} \sqrt{i} \sqrt{k} + \frac{\sqrt{g}}{0.4} \ln\left(\frac{h}{k}\right) \sqrt{i} \right) \sqrt{h}$
Huthoff (2007)	$u = \sqrt{\frac{2g}{C_d m D}} \sqrt{i} \left( \sqrt{\frac{k}{h}} + \frac{h-k}{k} \left( \frac{h-k}{1-D\sqrt{m}} \right)^{2/3} \right)$

Sixteen neurons were adopted in a layer for the neural network because of the best correlation coefficient, as compared to different numbers of neurons. Thereafter, a number of runs were tried with various constant parameters so that the assessment of the number of neurons alone can be evaluated. The final network architecture of the GMDH-type neural network analysed is 6-16-1. The model prediction in terms of training, testing, and all sets have been demonstrated in Fig. 16.2. In addition, Table

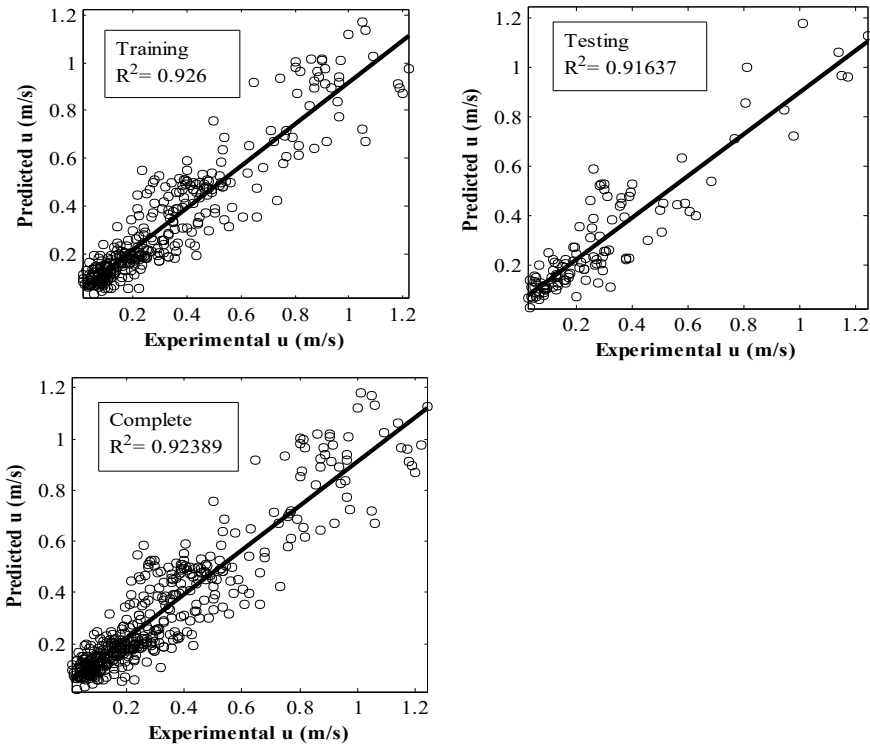


**Fig. 16.2** Modelled results obtained from GMDH-based approach

16.1 lists the formulae that have been worked on to enumerate the ability of prediction. The principal factors chosen to determine the efficiency of the model prediction are Root-Mean-Square Error (RMSE) and coefficient of determination ( $R^2$ ). RMSE is employed to measure the standard difference between the predicted and the computed values. It is found to serve well in portraying the prediction power of a model. Another parameter,  $R^2$ , is used to assess the model performance.  $R^2$  is otherwise expressed as the squared ratio between the covariance and the multiplied standard deviations of the observed and predicted values. So, it estimates the combined dispersion against the single dispersion of the observed and predicted series. Table 16.3 incorporates the performance analysis of the model based on the coefficients. Of the empirical forecasting formulations listed, the equation given by Baptist et al. (2007) envisages effectively in comparison to all other efficiency criteria (RMSE and  $R^2$ ).

## 16.5 Conclusion

Flow–vegetation interactions are vital as it provides a realistic interest to the problems faced by hydraulic engineers, including prediction of flood-peaks, risk and reliability of floods, sediment transport investigation, and enhancement of river restoration schemes by the examination of hydraulic performance. In an actual sense, the forecasting techniques which exist prove to be too complicated, and also their number is inadequate in terms of applicability. Due to the availability of huge databases of both rigid and flexible submerged vegetation conditions, the present work aims at articulating a neural network model depicting mean velocity in a vegetative channel based on all the significant parameters. So, the quality effect of all the parameters can be observed while predicting flow velocity in a vegetated channel. The results generated by the model have been found to be sufficiently good when compared to different parameters affecting flow–vegetation interactions. Also, it is known that the precision in the accuracy of a model is bound to be affected by errors. For an accurate flow-velocity prediction, the determination of flow depth and drag coefficient due to vegetation, also Manning's coefficient could be considered, need to be made more accurately. It is also important to understand that the process is as well dependent on the variability of flow velocity with different parameters. Mostly, field applications need exposure to nonlinearity and non-parametric evaluations that are the characteristics of a neural network model. To compare with the empirical predictors, the performance of the present model is better than the existing forecasting techniques.



**Table 16.2** Data summary of hydraulic as well as vegetation characteristics (Galema 2009)

Source	$D (m)$		$m (m^{-2})$		$k (m)$		$C_d$		$h (m)$		$i$		$u$	
	Max value	Min value	Max value	Min value	Max value	Min value	Max value	Min value	Max value	Min value	Max value	Min value	Max value	Min value
<i>Rigid Submerged Vegetation</i>														
Murphy et al. (2007)	0.0064	0.006	800	250	0.0139		1	0.61	0.467	0.088	0.000596	0.00000055	0.197	0.013
Poggi et al. (2004)	0.004	0.004	1072	67	0.12		1.5	1.5	0.6	0.6	0.00032	0.00004	0.313	0.3
Stone and Shen (2002)	0.0127	0.00318	696	173	0.124	0.124	1.11	0.96	0.314	0.151	0.04402	0.00009	0.502	0.017
Meijer et al. (1998a)	0.008	0.008	256	64	1.5	0.45	1	0.96	2.5	0.99	0.00205	0.00055	1.242	0.175
Dunn et al. (1996)	0.0064	0.0064	384	42	0.12		1.13	1.13	0.335	0.164	0.01607	0.00359	0.854	0.308
Shimizu (1994); Tsujimoto (1994)	0.0015	0.001	10,000	2500	0.046	0.041	1		0.1052	0.0631	0.00886	0.001	0.331	0.096
Tsujimoto and Kitamura (1990)	0.0015	0.0015	2500	2500	0.046		1.46		0.095	0.073	0.00703	0.001	0.331	0.117

(continued)

**Table 16.2** (continued)

Source	$D (m)$		$m (m^{-2})$		$k (m)$		$C_d$		$h (m)$		$i$		$u$	
	Max value	Min value	Max value	Min value	Max value	Min value	Max value	Min value	Max value	Min value	Max value	Min value	Max value	Min value
Einstein and Banks (1950)	0.0064	0.0064	108	3	0.038		1.4		0.108	0.073	0.01024	0.00774	1.2	0.8
<i>Flexible Submerged vegetation</i>														
Carollo et al. (2005)	0.0045	0.0045	44,000	28,000	0.082	0.044	1		0.272	0.061	0.05	0.001	1.047	0.211
Järvelä (2003)	0.003	0.0028	512	12,000	0.295	0.155	1		0.7065	0.306	0.0051	0.0002	0.33	0.072
Rowinski and Kubrak (2002)	0.000825	0.000825	10,000	2500	0.165	0.165	1.35		0.2475	0.1962	0.0174	0.0087	0.2948	0.1587
Meijer et al. (1998b)	0.0057	0.0057	254	254	0.165	0.155	1.81		2.5	1.75	0.00208	0.00109	0.393	0.142
Ikeda and Kanazawa (1996)	0.00024	0.00024	20,000	20,000	0.045	0.04	1		0.19	0.142	0.00641	0.00247	0.385	0.349
Tsujimoto et al. (1993)	0.00062	0.00062	10,000	10,000	0.065	0.061	2		0.16	0.1	0.01076	0.00051	0.606	0.078

(continued)

**Table 16.2** (continued)

Source	$D(m)$		$m(m^{-2})$		$k(m)$		$C_d$		$h(m)$		$i$		$u$	
	Max value	Min value	Max value	Min value	Max value	Min value	Max value	Min value	Max value	Min value	Max value	Min value	Max value	Min value
Tsujimoto et al. (1991)	0.0015	0.0015	2500	2500	0.0419	0.0238	3.14	3.14	0.11	0.07	0.007	0.001	0.4836	0.0945
Murota (1984)	0.00024	0.00024	4000	4000	0.06	0.048	2.75	2.75	0.116	0.092	0.00383	0.0005	0.258	0.085
Ree and Crow (1977)	0.005	0.005	1076	1464	0.305	0.203	1		0.751	0.242	0.0021	0.00042	0.427	0.046
Kouwen et al. (1969)	0.005	0.005	5000	5000	0.1	0.05	3		0.4	0.149	0.01001	0.0005	0.609	0.03
Fenzl (1962)	0.00238	0.00238	1808	11	0.152	0.051	1.17	1.07	0.181	0.058	0.00285	0.00163	0.289	0.052

**Table 16.3** Comparison of performance analysis of different predictors

Methodolgy	R <sup>2</sup>	RMSE
GMDH approach	0.93	0.108
Stone and Shen (2002)	0.6	0.37
Velzen et al. (2003)	0.55	0.35
Baptist et al. (2007)	0.61	0.26
Huthoff (2007)	0.68	3.11

## References

- Amanifard N, Nariman-Zadeh N, Borji M, Khalkhali A, Habibdoust A (2008) Modelling and Pareto optimization of heat transfer and flow coefficients in microchannels using GMDH type neural networks and genetic algorithms. *Energy Convers Manage* 49(2):311–325
- Atashkari K, Nariman-Zadeh N, Golcu M, Khalkhali A, Jamali A (2007) Modelling and multi-objective optimization of a variable valve-timing spark-ignition engine using polynomial neural networks and evolutionary algorithms. *Energy Convers Manage* 48(3):1029–1041
- Baptist MJ, Babovic V, Rodraguez Uthurburu J, Keijzer M, Uittenbogaard RE, Mynett A, Verwey A (2007) On inducing equations for vegetation resistance. *J Hydraul Res* 45(4):435–450
- Beeson CE, Doyle PF (1995) Comparison of bank erosion at vegetated and non-vegetated channel bends. *JAWRA J Am Water Resour Assoc* 31(6):983–990
- Besarati SM, Myers PD, Covey DC, Jamali A (2015) Modeling friction factor in pipeline flow using a GMDH-type neural network. *Cogent Eng* 2(1):1056929
- Carollo FG, Ferro V, Termini D (2002) Flow velocity measurements in vegetated channels. *J Hydraul Eng* 128(7):664–673
- Carollo FG, Ferro V, Termini D (2005) Analyzing turbulence intensity in gravel bed channels. *J Hydraul Eng* 131(12):1050–1061
- Choi S, Kang H (2004) Reynolds stress modeling of vegetated open-channel flows. *J Hydraul Res* 42(1):3–11
- Dunn C, Lopez F, Garcia MH (1996) Mean flow and turbulence in a laboratory channel with simulated vegetation (hes 51)
- Ebtehaj I, Bonakdari H, Zaji AH, Azimi H, Khoshbin F (2015) GMDH-type neural network approach for modeling the discharge coefficient of rectangular sharp-crested side weirs. *Eng Sci Technol Int J* 18(4):746–757
- Einstein HA, Banks RB (1950) Fluid resistance of composite roughness. *EOS Trans Am Geophys Union* 31(4):603–610
- Farlow SJ (1984) Self-organizing methods in modeling: GMDH type algorithms, CRC press
- Fenzi RN (1962) Hydraulic resistance of broad shallow vegetated channels. University of California, Davis
- Galema A (2009) Evaluation of vegetation resistance descriptors for flood management. Master thesis, University of Twente, Enschede, The Netherlands
- Huthoff F (2007) Modeling hydraulic resistance of floodplain vegetation
- Ikeda S, Kanazawa M (1996) Three-dimensional organized vortices above flexible water plants. *J Hydraul Eng* 122(11):634–640
- Ivakhnenko AG, Ivakhnenko GA (1995) The review of problems solvable by algorithms of the group method of data handling (GMDH). *Pattern Recognit Image Anal C/c of Raspoznavaniye Obrazov I Analiz Izobrazhenii* 5:527–535
- Järvelä J (2003) Influence of vegetation on flow structure in floodplains and wetlands. In: *Proceedings of the 3rd symposium on river, coastal and estuarine morphodynamics (RCEM)*. Madrid, pp 845–856
- Jha A, Kumar B (2013) Particle swarm optimization neural network for flow prediction in vegetative channel. *J Intell Syst* 22(4):487–501

- Kouwen N, Unny TE, Hill HM (1969) Flow retardance in vegetated channels. *J Irrig Drain Div* 95(2):329–342
- Kouwen N, Fathi-Moghadam M (2000) Friction factors for coniferous trees along rivers. *J Hydraul Eng* 126(10):732–740
- Lopez F, Garcia M (1998) Open-channel flow through simulated vegetation: suspended sediment transport modeling. *Water Resour Res* 34(9):2341–2352
- Meijer DG (1998a) Modelproeven overstroemde vegetatie. Technical report PR121, HKV consultants, Lelystad, The Netherlands
- Meijer DG (1998b) Modelproeven overstroemde vegetatie. Technical report PR121, HKV consultants, Lelystad, The Netherlands
- Muhammad MM, Yusof KW, Mustafa MRU, Zakaria NA, Ab Ghani A (2018) Prediction models for flow resistance in flexible vegetated channels *International Journal of River Basin Management* 1–11
- Murota A (1984) Turbulence structure in vegetated open channel flows. *J Hydrosoci Hydr Eng. Jpn* 2(1):47–61
- Murphy E, Ghisalberti M, Nepf H (2007) Model and laboratory study of dispersion in flows with submerged vegetation. *Water Resour Res* 43(5)
- Najafzadeh M, Sattar AMA (2015) Neuro-fuzzy GMDH approach to predict longitudinal dispersion in water networks. *Water Resour Manage* 29(7):2205–2219
- Nariman-Zadeh N, Darvizeh A, Jamali A, Moeini A (2005) Evolutionary design of generalized polynomial neural networks for modelling and prediction of explosive forming process. *J Mater Process Technol* 164:1561–1571
- Neary VS (2003) Numerical solution of fully developed flow with vegetative resistance. *J Eng Mech* 129(5):558–563
- Petryk S, Bosmajian III G (1975) Analysis of flow through vegetation. *J Hydraul Div* 101(7):871–884
- Poggi D, Porporato A, Ridolfi L, Albertson JD, Katul GG (2004) The effect of vegetation density on canopy sub-layer turbulence. *Bound-Layer Meteorol* 111(3):565–587
- Ree WO (1949) Hydraulic characteristics of vegetation for vegetated waterways. *Agric Eng* 30(4):184–189
- Ree WO, Crow FR (1977) Friction factors for vegetated waterways of small slope. Publication ARS-S-151
- Rowinski PM, Kubrak J (2002) A mixing-length model for predicting vertical velocity distribution in flows through emergent vegetation. *Hydrol Sci J* 47(6):893–904
- Shimizu Y (1994) Numerical analysis of turbulent open-channel flow over a vegetation layer using a  $\kappa$ - $\epsilon$  turbulence model. *J Hydrosoci Hydraul Eng JSCE* 11(2):57–67
- Sobolewski L (2014) Predicting the corrections for the polish timescale UTC (PL) using GMDH and GRNN neural networks. In: European frequency and time forum (EFTF). IEEE, pp 475–478
- Stone BM, Shen HT (2002) Hydraulic resistance of flow in channels with cylindrical roughness. *J Hydraul Eng* 128(5):500–506
- Tsujimoto T, Kitamura T (1990) Velocity profile of flow in vegetated-bed channels. *KHL ProgIve Rep* 1:43e55
- Tsujimoto G, Hayakawa N, Ichiyama M, Fukushima Y, Nakamura Y (1991) A study on suspended sediment concentration and sediment transport mechanism over rippled sand bed using a turbulence model. *Coast Eng Jpn* 34(2):177–189
- Tsujimoto T (1993) Turbulent structure of open-channel flow over flexible vegetation. *KHL-Communication* 4:37–46
- Tsujimoto T (1994) Flow and suspended sediment in a compound channel with vegetation. *Proc 1st Int Sym Habitat Hydraulics, Trondheim, Norway*, 357–370
- Velzen EV, Jesse P, Cornelissen P, Coops H (2003) Stromingsweerstand vegetatie in uiterwaarden. RIZA, Arnhem

Wu F-C, Shen HW, Chou Y-J (1999) Variation of roughness coefficients for unsubmerged and submerged vegetation. *J Hydraul Eng* 125(9):934-942  
Yen BC (2002) Open channel flow resistance. *J Hydraul Eng* 128(1):20-39

# Chapter 17

## Turbulent Flow Over a Train of *K*-Type Roughness



Santosh Kumar Singh, Pankaj Kumar Raushan, and Koustuv Debnath

**Abstract** Detailed experimental investigations are reported in this paper to study the turbulent flow characteristics in wave-current flow over the bed-mounted ribs at equal spacing. Regular wave is generated by wave-maker at frequency  $f = 1$  and 2 Hz which is installed at the entrance of the wave flume. The measurements were performed at the developed zone between the two consecutive ribs. The results show that mean stream-wise velocity changes significantly with the induced wave over turbulent current. Further, it is observed that the recirculation length changes slightly with a superposition of wave over current.

**Keywords** ADV · Rib roughness · *k*-type · Flume experiment · Mean velocity · Reynolds shear stress

### 17.1 Introduction

The perception of a boundary layer (BL) is mainly owing to Prandtl in Connelly et al. (2006), as suggested by White (Prandtl 1904), who directed that the results of friction inside the fluid are substantial only in a very thin layer near to the bottom wall. The use of BL theory has numerous significant solicitations, e.g., the estimation of flow parting and skin friction drag. Many experimental and numerical studies have been performed to highlight two-dimensional (2D) TBL flow above the flat surface and in the framework of a zero pressure gradient due to its simplicity in terms of physics and geometry (Raushan et al. 2018; Singh et al. 2018a, b). The furthest condition for the fully developed three-dimensional free surface flows is the acquaintance of the required length for the development of the flow (Singh et al. 2018c, 2017a). Indeed, in free surface flow (e.g., open channel), the velocity gradients in the entrance and close

---

S. K. Singh (✉)

Department of Mechanical Engineering, SRM Institute of Science and Technology, Kattankulathur, Chennai 603203, India

P. K. Raushan · K. Debnath

Department of Aerospace Engineering and Applied Mechanics, Indian Institute of Engineering Science and Technology, Shibpur, Howrah 711103, India

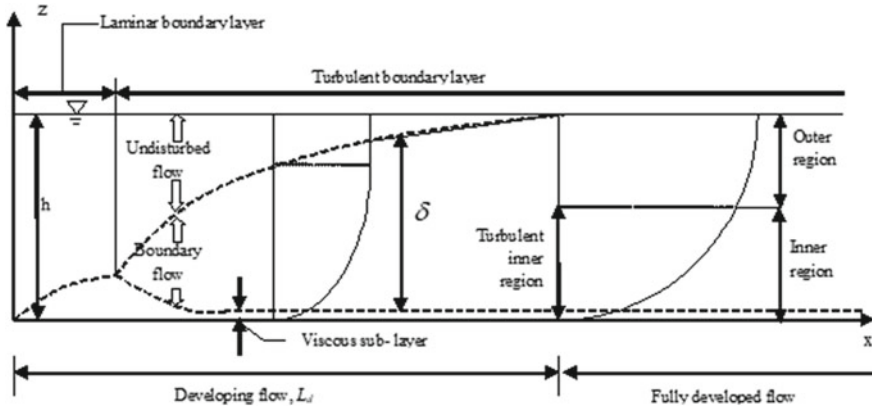


Fig. 17.1 Schematic representation of the growth of a 2D boundary layer over a smooth surface

to the bottom wall are larger due to the growing BL (see Fig. 17.1). Figure 17.1 shows the schematic view of the evolution of a 2D TBL over a flat surface. The presence of the no-slip boundary situation at the bottom of the surface impedes the flow, affecting a stream-wise average velocity profile  $\bar{u}(z)$  (where  $z$  is the bottom-normal coordinate direction), which horizontally combines to the outer free-stream velocity,  $u_0$ . The bl thickness  $\delta(x)$  (where  $x$  is the stream-wise direction) is ruminated to be the position at the surface at which the local average velocity is 99% of the free-stream velocity. As shown in Fig. 17.1, the BL thickness cultivates with rising distance,  $x$ , from the leading edge and reaches the surface where the flow characteristics are constant. The turbulent characteristics of flow reach a self-similar state beyond the fully develop length in the channel. Further, the flow over the rough bed is encountered frequently in nature and finds applications in numerous fields of engineering and basic science. Hence, numerous works have been performed by hydraulic engineers to comprehend the flow statistics over the rough bed. The extensive review of the current state of the art on the subject was presented in Singh et al. 2017b; Singh et al. 2016a, b), whereas the effect related to the surface wave on a rough bed is emphasized in Singh et al. (Singh and Debnath 2017a). Despite the significant work on flow over the rib roughness in a steady flow environment, comparatively less attention has been given to the turbulent characteristics in wave-induced flow over a rough bed. In this work, mean velocity, turbulent intensity, and Reynolds shear stress have been assessed in developed and fully developed flow for steady and wave-induced flow cases.

## 17.2 Experiments

Experiments were conducted in the IEST, Shibpur water-wave facility that has 18 m long, 0.9 m wide, and 0.9 m high test section (Fig. 17.2). The facility is capable of generating turbulent current over a rough bed using a pump and a wave-maker





**Fig. 17.2** Photograph of the experimental setup mounted with rib roughness at  $p/k = 11$

generates surface wave over unidirectional current; for details see (Singh and Debnath 2016). The facility is the same as described in detail by Singh et al. (Singh et al. 2018d). The water depth during the experiment was kept constant, i.e.,  $h = 20$  cm throughout the channel. The fluctuations of the velocity in all three directions were measured by ADV which is fixed at the instrument carriage (Fig. 17.2). The roughness elements were made of wood and coated with waterproof paint. The length of the roughness element (square rib) is 89 cm long and the side length of the square ribs is measured 2.5 cm and is placed in the entire flume as shown in Fig. 17.2. The pitch length  $l$  was selected in such a way to attain isolated roughness flow based on Perry et al. 1969. Picky attention was given to the change in flow characteristics due to the addition of surface waves of  $f = 1$  and 2 Hz on a steady flow. Three different tests were conceded out in this study: (1) steady flow over the flatbed, (2) steady flow tests over bed mounted with ribs at constant  $p/k$ , and (3) test over the bed-mounted rib in presence of regular wave over study current.

The measurement of velocity fluctuations in all three directions was performed at 12 stream-wise locations ( $x = 1, 2, 3, \dots, 12$  m) in the direction of flow, and the eight verticals at the developed zone between the consecutive rib were also measured using a 40 MHz sontek micro-ADV (micro-acoustic Doppler velocimeter). The data analysis technique and flow parameters for various cases are detailed in Singh et al. (2018a), Singh et al. (2015), Singh and Debnath (2017b). For all experimental runs, the water depth  $h$  was kept at 20 cm, flow discharge  $q = 0.063$  m<sup>3</sup>/sec, Reynolds



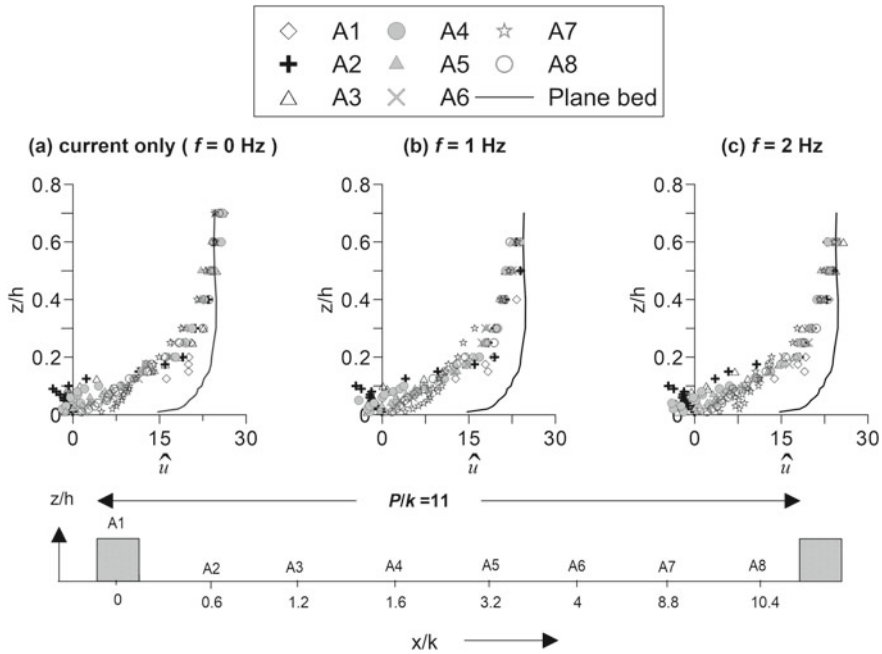


**Fig. 17.4** Plot of mean velocity profile at location A1–A8 over the rib (solid line represents data for plane bed case)

at location A6. Further increase in distance from the rib, i.e., at A7,  $\hat{u}$  is positive close to the bed indicating the vertical A7 is outside the recirculation region. Beyond location A7, the  $\hat{u}$  shows zero value close to the bed for induced wave and steady flow cases, suggesting a point of separation due to the downstream rib. Further, it is observed that near the free surface, the  $\hat{u}$  decreases compared to without rib case for all the wave-induced conditions.

### 17.3.2 Variation of Turbulence Intensities Within the Cavity of the Rib

Figure 17.5a–c represents the variation of normalized  $x$ -component of turbulence intensity ( $u^+ = \sigma_u/u_*$ ) for steady current and wave with steady current together with the smooth bed data for comparison

At location A1, a maximum value of turbulent intensity is observed in comparison to without rib for all the flow cases. Further, with a shift in the location (A3), the normalized turbulent intensity first increases in the zone  $0.14 \leq z/h \leq 0.38$  and afterward reduces for all the cases whereas, for higher surface wave frequency, the turbulent intensity increases in the same location in comparison to current-only and

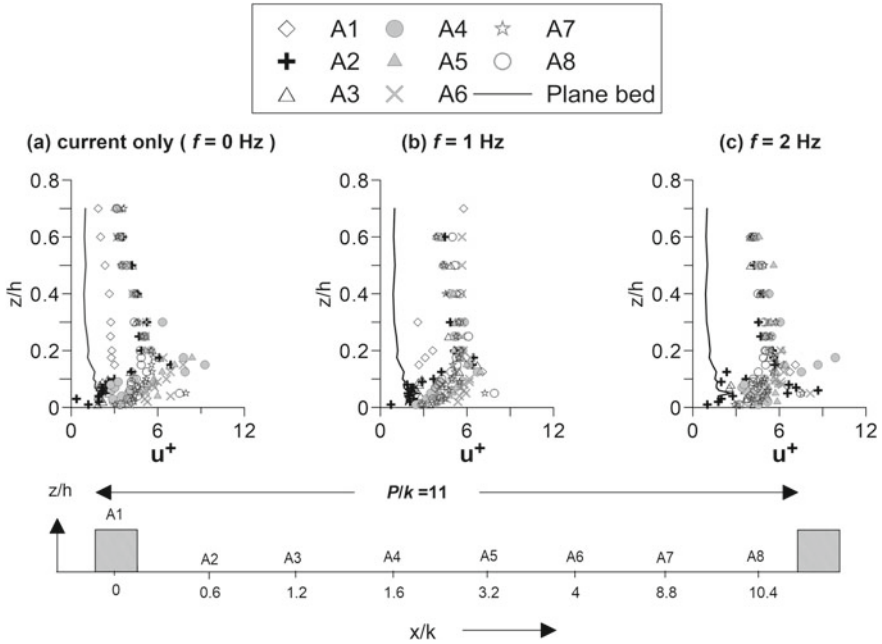


**Fig. 17.5** Plot of stream-wise turbulence intensity at locations A1–A8 for steady flow and wave-induced cases (solid line represents data for plane bed case)

lower surface wave frequency case. At locations A7 and A8, the  $u^+$  profile shows different behaviours and it overlapped with the plane bed profile. At vertical A5, the  $u^+$  value is utmost at  $z/h = 0.19, 0.17,$  and  $0.15$  for steady flow and wave-induced cases, respectively. The data demonstrate the changes in the  $u^+$  profiles close to the surface (Fig. 17.5b, c) due to a higher frequency of waves at all locations.

Figure 17.6a–c characterizes the variation of  $w$ -component of turbulent intensity for steady flow and wave-induced cases, together with that of without rib case for comparison. The profile of vertical turbulent intensity shows a similar trend as observed in stream-wise turbulent intensity for all the cases. At location A1, the maximum value of  $w^+$  is observed at vertical A1 at the level  $z/h = 0.19, 0.17,$  and  $0.16,$  and thereafter, it reduces for all three cases.

At the downstream locations (A2, A3), the variation in vertical turbulent intensity profile is alike for all the cases studied here. At further downstream (A4), at level  $z/h = 0.1,$  the maximum value in vertical turbulent intensity is observed and at vertical A5 to A8, the maximum value in vertical turbulent intensity shifted to the level  $z/h = 0.05$  for all the cases.

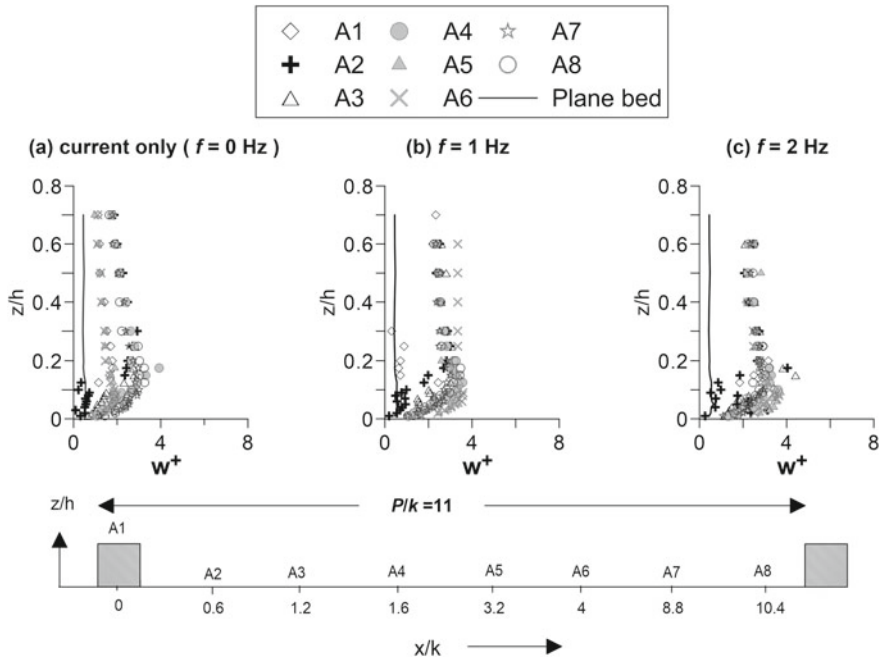


**Fig. 17.6** Plot of vertical turbulence intensity at locations A1–A8 for steady flow and wave-induced cases (solid line represents data plane bed case)

### 17.3.3 Reynolds Shear Stress

Figure 17.7a–c shows the variation of the normalized shear stress profile for steady flow and wave-induced cases along with the without rib profile for comparison. At location A1, the shear stress increases and reaches a maximum at  $z/h = 0.3$ , and beyond this, it merges with the without rib profile in all three cases.

For the current flow case, at location A4, close to the bed, the shear stress profile is zero and then it increases and reaches a peak value at about  $z/h = 0.3$  and afterward, it gradually diminishes and merges with the value of without rib data. The shear stress profiles for steady flow show similar nature as observed in wave-induced cases. Figure 17.7a–c reveals that at locations A5 and A6, the Reynolds stress amplifies to the highest value at about  $z/h = 0.1$  and afterward diminishes and coincides with that of without rib profile. It is also observed that at locations A5 and A6, shear stress profiles show identical behaviour for three cases. At location A8, the shear stress profile closely follows the pattern of without rib profile for three different cases. For steady flow at the location A8, the shear stress profile increases compared to the without rib in between  $z/h = 0.16–0.4$ , and beyond this, the profile remains unchanged compared to that of the without rib. For  $f = 1$  and 2 Hz, shear stresses become negative at  $z/h = 0.05$ , and thereafter, it increases and matches with without rib profile.

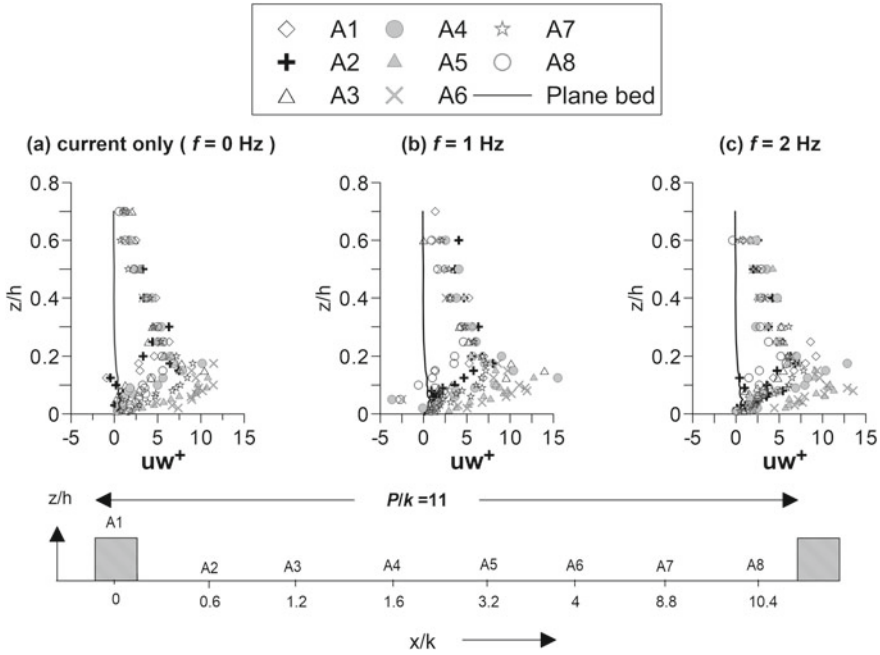


**Fig. 17.7** Plot of shear stress profile at locations A1–A8 for both steady flow and wave-induced cases (solid line represents data plane bed case)

### 17.4 Conclusion

An effort has been made in this work to comprehend the nature of flow over a bed with  $k$ -type roughness at fixed spacing epically in wave-induced conditions. Experiments were executed for three dissimilar flow states: (a) steady flow without rib roughness, (b) steady flow with rib roughness having  $p/k = 11$ , and (c) wave-induced flow over the rib roughness. An ADV was employed to gather the turbulent fluctuations inside the cavity. Analysis from the experimental data suggests that TBL development is observed at 11 m from the entrance of the channel (Singh and Debnath 2017b; White 1991). The thickness of TBL enlarges after the addition of waves on a steady flow. Further, the measurement between the cavity indicates that recirculation and the point of reattachment modified significantly due to the addition of surface waves on turbulent current. Profiles of  $u$  and  $w$ -component of turbulence intensities are nearly alike in nature. However, towards the surface, further raise in turbulence intensities are observed at a high frequency of wave compared other two cases. At the location A6, the highest value in shear stress is observed at  $z/h = 0.1$  in all conditions. The results of this work may be useful for the improvement and validation of numerical models.

## References

- Connelly S, Schultz MP, Flack KA (2006) Velocity-defect scaling for turbulent boundary layers with a range of relative roughness. *Exp Fluid* 40:188–195
- Prandtl L (1904) Über flüssigkeits bewegung bei sehr kleiner reibung [motion of fluids with very little viscosity]. *Verhaldlg iii int Math Kong* 484–491
- Raushan PK, Singh SK, Debnath K, Mukherjee M, Mazumder BS (2018) Distribution of turbulent energy in combined wave current flow. *Ocean Eng* 167:310–316
- Singh SK, Raushan PK, Debnath K, Mazumder BS (2018a) Effect of surface wave on development of turbulent boundary layer over train of rib roughness. *J Offshore Mech Arct Eng* 141(6):061101
- Singh SK, Raushan PK, Debnath K, Mazumder BS (2018b) Turbulent oscillatory flow along unidirectional current over square ribs. *Can J Civ Eng* 45(4):248–262
- Singh SK, Raushan PK, Debnath K, Mazumder BS (2018c) Combined effect of wave and current in rough bed free surface flow. *Ocean Eng* 160:20–32
- Singh SK, Debnath K, Mazumder BS (2017a) Turbulence over cube-mounted rough bed using spatiotemporal averaging approach. *Can J Civ Eng* 44(7):504–517
- Singh SK, Debnath K, Mazumder BS (2017b) Reply to the discussion by Li and Li on “Turbulence over cube-mounted rough bed using spatiotemporal averaging approach”. *Can J Civ Eng* 46(1):69–71
- Singh SK, Debnath K, Mazumder BS (2016a) Spatially-averaged turbulent flow over cubical roughness in wave-current coexisting environment. *Coast Eng* 114:77–85
- Singh SK, Debnath K, Mazumder BS (2016b) Changes in turbulent flow structure over rough-bed under combined wave-current motions. *ISH J. Hydraul. Eng.* 22(3):305–313
- Singh SK, Debnath K (2017a) Turbulent flow characteristics in a rectangular channel under the influence of cube-mounted rough bed. *ISH J Hydraul Eng* 23:167–176
- Singh SK, Debnath K (2016) Combined effect of wave and current in free surface turbulent flow. *Ocean Eng* 127:170–189
- Singh SK, Raushan PK, Debnath K (2018) Turbulent characteristics of pulsating flow over hydraulically smooth surface. *Eur J Mech B/Fluids* 68C:10–19
- Singh SK, Debnath K, Mazumder BS (2015) Turbulence statistics of wave-current flow over a submerged cube. *J Waterw Port Coast Ocean Eng* 142(3):04015027
- Singh SK, Debnath K (2017) Turbulence characteristics of flow under combined wave-current motion. *J Offshore Mech Arct Eng* 139(2):021102
- White FM (1991) *Viscous fluid flow*. Macgraw, New York, pp 335–393

# Chapter 18

## Shifting of Main Course of River Ganga Within the Reach Bhagalpur to Kahalgaon Using Remote Sensing and GIS



Chandan Raj and Vivekanand Singh

**Abstract** The lateral movement of the river channel within its Khadir over time is a universal phenomenon. Various processes of the fluvial-geomorphological environment, such as frequent occurrence of floods, deposition of sediment, the capture of lower courses of tributaries by the main channel, failure of the bank and avulsion, are predominant factors behind the channel dynamics. In this study, shifting of main course, bank-lines and the variation of the sinuosity index were computed from the year 1973–2018 within the reach Bhagalpur to Kahalgaon, in the state of Bihar, India. The area near both the banks is densely populated and has many important structures. Shifting of river banks put these structures under risk of failure and dwelling area under risk of submergence in flood seasons. It has abandoned its original course and huge sandbars have been formed in the middle of the stream. These sandbars are hindering vessel navigation too. The dynamics of channel adjustment in terms of lateral shifting can be beautifully illustrated by the application of modern geoinformatics tools, i.e., remote sensing and Geographic Information System (GIS). From the study of USGS satellite images using ARC-GIS, it has been found that the main course and bank-line has been shifted significantly during this period. The study of the width of the active channel and the position of main course indicates that both the left and right banks have changed significantly due to the erosion and deposition of sediment during monsoon period of each year. During the period 1973–2018, the river has moved toward its left bank and has become more sinuous in nature. This study highlights a significant message of immense vulnerability of the Ganga river and also points towards its geomorphological instabilities in this reach of the river.

**Keywords** Bankline shifting · Fluvial-geomorphology · Sinuosity Index · Bank-line · Remote sensing and GIS

---

C. Raj (✉) · V. Singh  
Department of Civil Engineering, National Institute of Technology Patna, Patna,  
Bihar 800005, India  
e-mail: [chandan.ce16@nitp.ac.in](mailto:chandan.ce16@nitp.ac.in)

V. Singh  
e-mail: [vsingh@nitp.ac.in](mailto:vsingh@nitp.ac.in)



## 18.1 Introduction

River channel shifting is very critical among geomorphological and river management problems. Lateral shifting of river is defined as positional change of a river channel due to variations in water and sediment discharge. It is always associated with bank erosion or streambed erosion due to turbulent flow conditions (Yang et al. 1999). Lateral migration of river is a catastrophic local and regional change process (Hickin and Nanson 1984). Dynamic equilibrium of a river can be disturbed by any one of the factors, whether it is natural, anthropogenic or manmade. In order to maintain its equilibrium, river undergo self-adjustment through fluvial processes.

Lateral shifting of river is geomorphological phenomena, and is very burning issue for most of the rivers throughout the world. Detailed study of channel migration is very important for documenting the erosion hazard and changes in planform and land use characteristics, as well as for understanding reasons behind those changes. In recent years, various researchers have studied this phenomenon (Debnath et al. 2017; Dewan et al. 2017; Hossain et al. 2013; Kummur et al. 2008; Nanson and Hickin 1986; Nigam et al. 2016; Thakur 2014). In the present study, the change in the planform of river Ganga has been studied between Bhagalpur and Kahalgaon from the year 1973–2018 using remote sensing and GIS. This stretch of river Ganga is highly affected by problems of flood, erosion and migration of main course (Hazarika et al. 2015; Jayanth et al. 2016; Rawat and Kumar 2015). Remotely sensed data have been used for study, which gives imprint of river channel over area for different time period. This method made possible study of river migration in less time with better accuracy and low-cost effective manner.

The River Ganga is one of the most important religious rivers in India. It is also known for disastrous reasons, especially in monsoon season, when discharge is very high. When it flows through Bihar, India, it is in mature stage. Low bed-slope gradient and decreases in velocity of streamflow cause aggradation in river bed. Aggradation reduces discharge carrying capacity of the river. During the season of high flood, water either overtop banks or its bank fail in action. Soft soil cover, high discharge, low velocity, and water laden with silt, all these factors induce meandering of the river, and causes severe erosion in concave bends (Deb et al. 2012). Huge amount of fertile land lost every year due to shifting of river (Debnath et al. 2017). In the present study area, massive erosion take place every year affecting people living there. Huge amount of agricultural land gets eroded. In this region, areas on the bank of river are highly populated also having many important infrastructures. National Highway No. 80 also get damaged due to flood water. There is need to study the shifting trend over time–space domain and its severity on areas, so that concerned authorities can take preventive steps to minimize disastrous impact. Taking into consideration of earlier studies and severity of channel migration, this study has been aimed to quantify amount of river on spatial and temporal basis.

### 18.2 Study Area

The Ganga River reach between Bhagalpur to Kahalgaon has been considered, which is lying in Bihar, India. The study area has been shown in Fig. 18.1. Bhagalpur is the district town of Bihar State, is located in the middle of eastern part of the state. The area of the district is 2569 km<sup>2</sup>, having population of 3,037,766 (Census 2011). River Ganga flow through middle of the district. This district is home to the Vikramshila Gangatic Dolphin Wildlife Sanctuary, which is 50 km in length. This study is based on channel shifting due to bank erosion of Ganga River. So, the study area comprises only river part and area near its bank affected by erosion hazards. The geographical extent of study area is from 25°12' N to 25°19' N and 87°01' E to 87°14' E, with an area of about 314 km<sup>2</sup>.

Ganga river enters the study area in Bhagalpur and ends at Kahalgaon, after flowing about 38 km in length. In this stretch, river is continuously changing its planform because it is in mature stage and plain is formed by loose alluvium. This

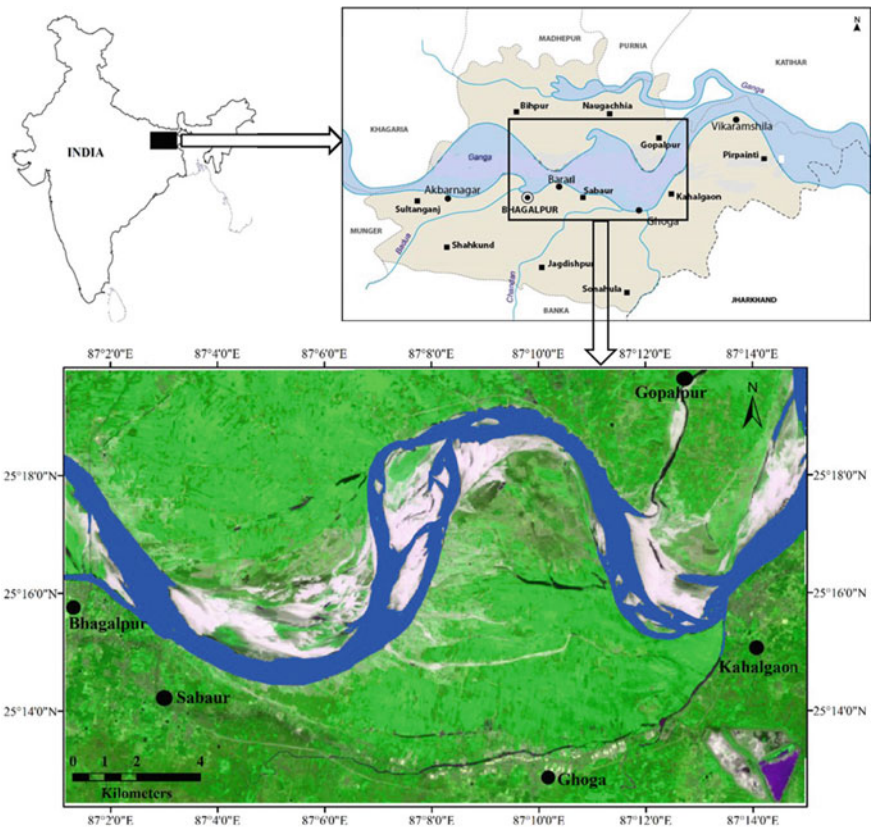


Fig. 18.1 Study area (Ganga river)

loose and unconsolidated soil stratum is highly vulnerable to erosion. The direction of flow is from west to east. Many islands and sandbars are also formed in this stretch, some of them are old and some are newly formed. Old and vegetated islands are called 'Diara' in local language where agricultural activities are performed in lean period.

### **18.3 Erosion in Study Area**

The river Ganga shows dynamic nature of its river course almost every year. This dynamic nature is due to natural factors like discharge, soil characteristics, topography, geological characteristics etc., and also due to man-made factors like construction of barrages, deforestation etc. This stretch of river face river bank failure almost every year. In Gopalpur, dozen of houses had disappeared in 72 h only in year 2018. In this stretch of river, bank erosion occurs firstly due to high pressure of water on bank wall, and secondly due to submerged and stagnated water seepage as groundwater. It weakens porous soil profile and dissects the bank deep root. And as result after recession of flood bank collapses (Keshkar et al. 1996).

### **18.4 Social and Economic Aspect of River Bank-Line Shifting**

River bank shifting has also led to administrative problems. Villages situated on the bank of river lost its boundary due to erosion. This has also become a matter of local dispute. People from affected area shift to nearby village, increasing administrative problems. They lost their agricultural land and became landless and without livelihood. They demand for their re-allocation/ rehabilitation from government. Government has to go through long procedure for their rehabilitation. People search their shelter themselves, and often take shelter on road side making huts. It results in high rate of road accidents. The neo- refugees like situation prevail with many social problems. Poverty and local conflicts increase crime. A social grouping and conflicts between victims and non-victims get started. Geomorphological process of river comes with many unseen problems directly associated with our life.

### **18.5 Methodology**

Satellite imagery gives an imprint of a river. Thus, remote sensing and GIS technique is very suitable for this study. ArcGIS and its extensions have been used for the

study, which is highly sophisticated software for analysis of mapped information, and provides infrastructure for managing geographical information.

In this study, shifting of bank-line and sinuosity have been computed and analyzed. Landsat scenes have been taken from 1973 to 2018 at the interval of every fifth year. All these data were collected from USGS site (<http://earthexplorer.usgs.gov/>). Selection of images is based on cloud cover and its availability. Here only dry season images (i.e. January to March) have been used as water level remain normal and sky are mostly cloud free in this period. These selected images are processed for distortion and rectified as per requirement. Finally, each image has been clipped for the getting study reach. Clear boundary between land and water is required for study of river planform. For extraction of river boundary several methods are described in previous studies. Some are manually done, and in some work, it has been extracted automatically using GIS software. Previous record showed that automated result is unreliable because it is based on reflectance of riverine features (Dewan et al. 2017). Different features having similar reflectance give errors in result. Thus, manual digitization of river boundary is more accurate process (Gupta et al. 2013; Yang et al. 1999). In this study, manual digitization of river boundary has been used. Multispectral data comprising of band combination 4-5-3 clearly distinguishes land and water boundary. During digitization of the river bank, similar zooming level of 1:100,000 has been kept for consistency in method because scale is an important factor in analysis of channel boundary (Tiegs and Pohl 2005). A georeferenced spatial dataset representing river boundary was finally obtained for each year of study.

In order to calculate amount of bank-line and centerline shifting, fixed cross sections have been drawn which is shown in Fig. 18.2. Bank-lines for two successive

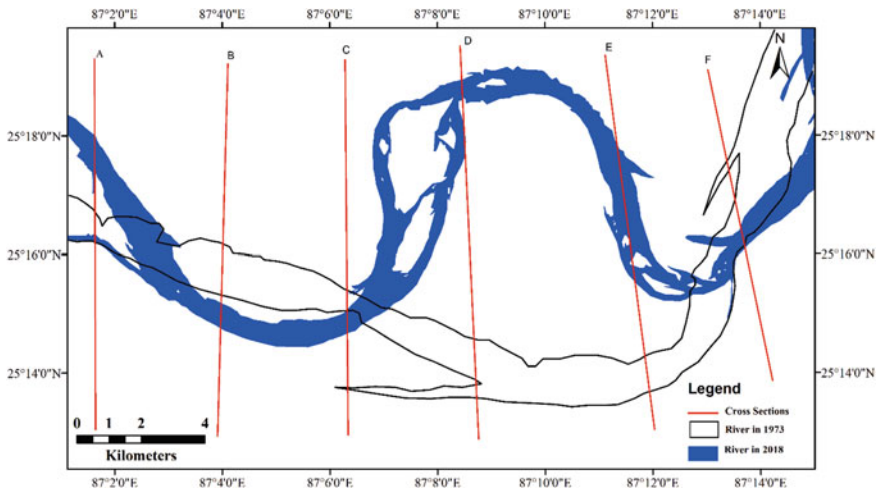
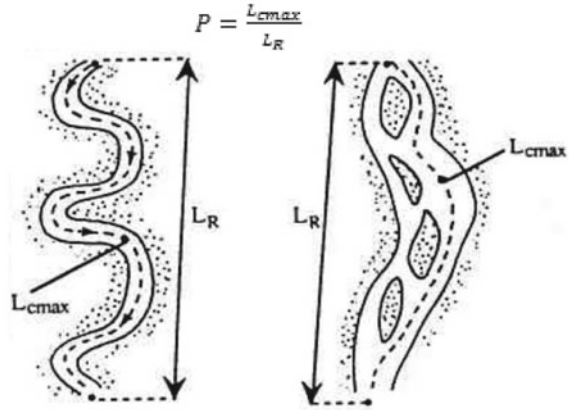


**Fig. 18.2** Cross sections across Ganga for measuring temporal (1973–2018) shift along each cross section

**Fig. 18.3** Sinuosity (Source Friend and Sinha (1993))



years i.e. 1973–1975, 1975–1980 and so on have been overlaid and compared to calculate amount of shift.

A sign convention has been adopted to study bank-line shifting. Left bank shifting towards left direction (i.e. erosion) is marked with positive sign, whereas left bank shifting towards right direction (i.e. accretion) is marked with negative sign. Similarly, right bank shifting towards right (i.e. erosion) is marked with positive and right bank shifting toward left (i.e. accretion) is marked with negative sign.

Sinuosity is the measure of deviation of flow path from a straight path. Many researchers have defined it in different ways. This study adopted sinuosity defined by Friend and Sinha (1993). It is defined as “Ratio of mid-channel length of widest channel ( $L_{cmax}$ ) to overall length of channel belt reach measured along a straight line ( $L_R$ )”. Figure 18.3 shows the  $L_{cmax}$  and  $L_R$  in meander and braided rivers (Friend and Sinha 1993). Sinuous,  $P$  is given as:

$$P = \frac{L_{cmax}}{L_R}$$

## 18.6 Results and Discussions

Regular shifting of the river Ganga has been analyzed at different sections along the river between Bhagalpur and Kahalgaon. The river has meandered in this reach and hence sinuosity has also been measured and analyzed.

Shifting of the left bank along selected cross sections (A, B, C, D, E, and F) have been shown in Fig. 18.4 a and b for each interval of time. In the year 1973, the river was flowing almost straight from CS (Cross Section) A to E. Left bank start eroding and continuously goes on shifting northward from year 1973 to 1995, which can

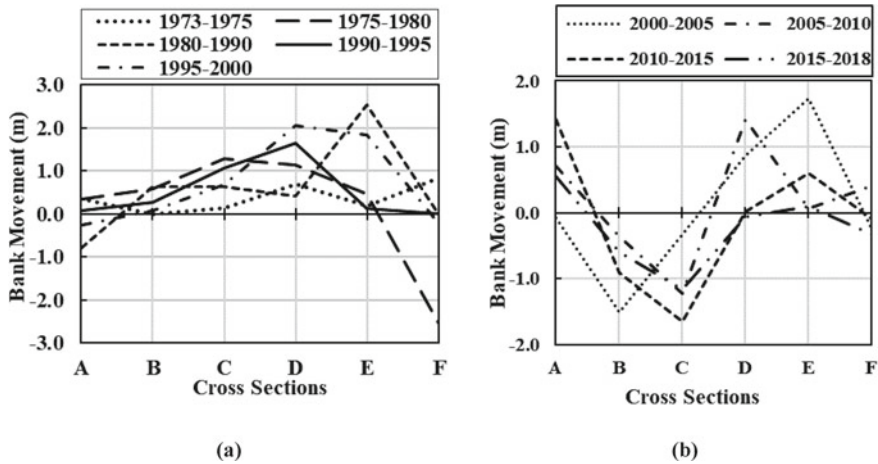


Fig. 18.4 Left bankline shifting along cross sections, 1973–1995 (a); 2000–2018 (b)

be clearly seen in Fig. 18.4 a. During the years 2000 to 2018, southward shifting (i.e. accretion) of the left bank-line was observed at cross sections CS-A to CS-D. However, the stretch beyond CS-D to CS-F continues shifting northward. Further erosion of left bank between the CS-D and CS-E has been restricted from the year 2005 onwards due to construction of left bank protection.

Figure 18.5 a and b shows the shifting of right bank along predefined cross sections. Right bank has shifted northward due to accretion in the stretch CS-A to CS-E in duration 1973–1995. Further, it has shifted southward due to erosion between CS-B to CS-C after 2000. However, stretch CS-C to CS-E continues shifting northward due to accretion. In a whole, it is observed that right bank has shifted northward

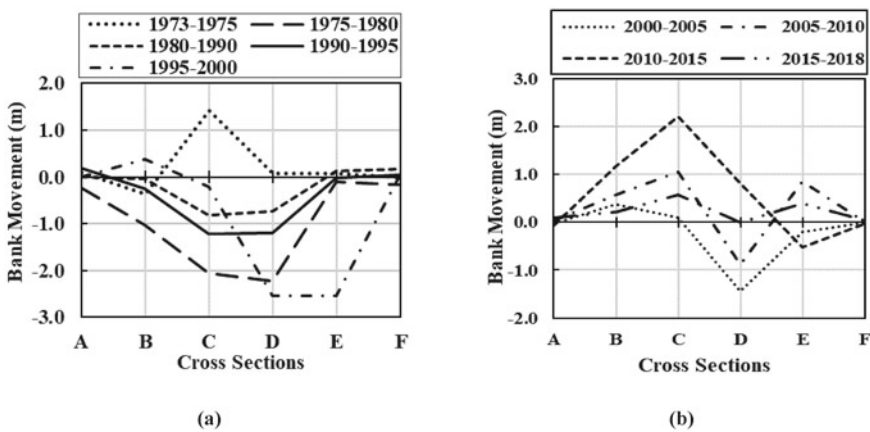


Fig. 18.5 Right bankline shifting along cross sections, 1973–1995 (a); 2000–2018 (b)

as a result of accretion. This accretion formed the vast attached bar and some narrow stream. These bars get vegetated along time and people started agricultural activities in the lean period. Analysis of shifting of the both bank-lines revealed that river has undergone drastic change in its planform. People living in the areas close to both banks are affected every year due to these shifting. Their agricultural land and dwelling areas disappeared because of erosion.

Table 18.1 presents temporal variation of left and right bank-lines in terms of erosion and accretion from 1973 to 2018 with an interval of every 5 years. Amount of per year shifting has been shown. It can be seen that the Left bank undergone more shifting compared to right bank and it is continuous. However, the left bank shows less accretion compared to right bank. Right bank faces more accretion than left bank of the river.

Sinuosity is an important parameter after bank-line shifting to describe planform change of a river. Temporal change of morphological parameters width of the river and sinuosity is presented in Table 18.2. It has been calculated from historical maps between year 1973–2018.

Result shows mean width of the river undergoes moderate change in the study reach from year 1973 to 2018. It varies from maximum 2.05 km in 1975 to 1.19 km in 1980. There is abrupt increase in river width from 1973 (1.47 km) to 1975 (2.05 km). This abrupt change may be due to blockage of flow after commissioning of Farakka Barrage in year 1975. River Ganga flowing in alluvium plain, is in mature stage in this stretch. Erosion is easy because of loose alluvial soil. Hence river goes on continuous expansion and contraction. The river is facing erosion at one bank and accretion at the other so its gross width is increased without showing major variation in waterway width. Overall width of the river is in increasing trend with minor variation.

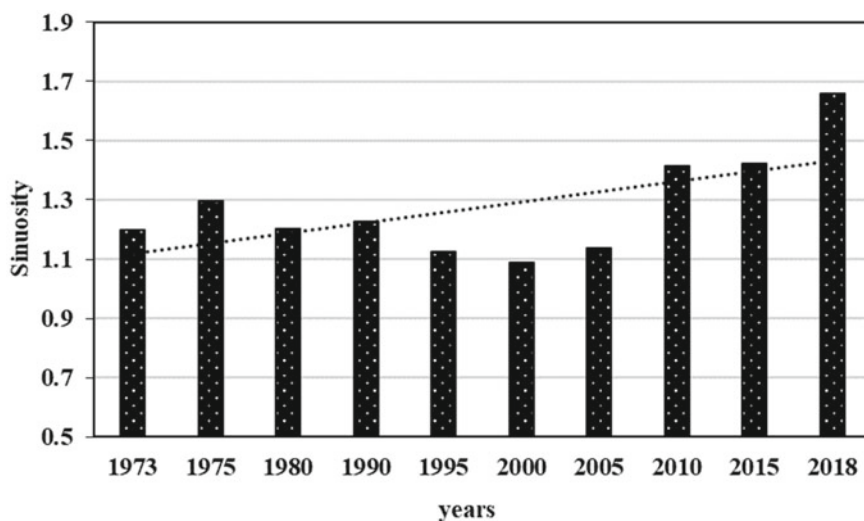
Study showed that sinuosity had changed considerably over time between Bhagalpur and Kahalgaon. Figure 18.6 shows the time interval wise sinuosity and it is in increasing trend from 1.20 (1973) to 1.66 (2018) in the study reach. This increase

**Table 18.1** Temporal variation of left and right bankline shifting

Time period	Left bank-line shifting		Right bank-line shifting	
	Erosion (m y <sup>-1</sup> )	Accretion (m y <sup>-1</sup> )	Erosion (m y <sup>-1</sup> )	Accretion (m y <sup>-1</sup> )
1973–1975	220.28	0	209.86	181.02
1975–1980	152.59	505.30	0	193.87
1980–1990	104.89	79.26	14.72	53.05
1990–1995	127.80	0	23.52	134.30
1995–2000	233.06	47.66	29.49	352.35
2000–2005	259.20	107.63	46.61	83.47
2005–2010	130.10	157.76	124.96	88.50
2010–2015	136.05	177.05	278.65	41.47
2015–2018	108.47	178.56	87.01	0

**Table 18.2** Temporal change of width and sinuosity

Year	Mean channel width (Km)	% Change in mean channel width	Sinuosity	% Change in sinuosity
1973	1.47		1.20	
1975	2.05	39.8	1.30	8.06
1980	1.19	-41.9	1.20	-7.22
1990	1.49	25.1	1.23	2.19
1995	1.60	7.5	1.13	-8.39
2000	1.20	-24.9	1.09	-3.24
2005	1.07	-11.1	1.14	4.52
2010	1.52	41.8	1.41	24.16
2015	2.02	33.0	1.42	0.55
2018	1.76	-12.7	1.66	16.76

**Fig. 18.6** Change in sinuosity

may be due to blocking of sediment by Farakka barrage. The result showed decrease in the sinuosity from 1990 to 2000. This decrease may be contributed to process of meandering when river length shortens before changing course from one side to the other side. However, it showed increasing trend (Fig. 18.6). In general increase in sinuosity is associated with increase in bank erosion, because it causes decrease in streamflow velocity. This decrease in streamflow velocity is combined action of low river bed gradient, siltation and backwater effect after construction of barrage. This particular reach of the Ganga had sinuosity ranged between 1.13 (1995) to 1.66



(2018). Between years 1973–2018, overall sinuosity of the River Ganga study reach had increased, which resulted in an increase on overall length of 9.70 km study reach.

## 18.7 Conclusions

Under the combined action of erosion, accretion and human interventions, the River Ganga had experienced significant morphological change. Accurate quantification of this change is a challenging task. To detect long-term morphological change through remote sensing is a practical approach. In this study, shifting of river has been calculated and analyzed using multiple Landsat images of the Ganga from Bhagalpur to Kahalgaon for the of period 1973–2018. Figure 18.2 also shows complete shifting of the river in this period within study area. During this study period, the river has migrated towards the north by maximum of 9.5 km. Massive erosion has completely changed planform of the river. About 8174 hectares of land has been lost in this study area only in the period of study. Almost Straight River has completely become sinuous. Its sinuosity has increased from 1.20 (1973) to 1.66 (2018). Formation of bars is also seen in the study reach.

## References

- Census (2011) “District Census Handbook Bhagalpur” Directorate of Census Operations Bihar. [https://www.censusindia.gov.in/2011census/dchb/1022\\_PART\\_B\\_DCHB\\_BHAGALPUR.pdf](https://www.censusindia.gov.in/2011census/dchb/1022_PART_B_DCHB_BHAGALPUR.pdf) (Retrieved 20 November 2018)
- Deb M, Das D, Uddin M (2012) Evaluation of meandering characteristics using RS & GIS of Manu River. *J Water Resour Prot* 4(March):163–171
- Debnath J, Das (Pan) N, Ahmed I, Bhowmik M (2017) Channel migration and its impact on land use/land cover using RS and GIS: A study on Khowai River of Tripura, North-East India. *Egypt J Remote Sens Space Sci Auth Remote Sens Space Sci* 20(2):197–210
- Dewan A, Corner R, Saleem A, Rahman MM, Haider MR, Rahman MM, Sarker MH (2017) Assessing channel changes of the Ganges-Padma River system in Bangladesh using Landsat and hydrological data. *Geomorphology* 276:257–279
- Friend PF, Sinha R (1993) Braiding and meandering parameters. *Geol Soc Lond Spec Publ* 75(1):105–111
- Gupta N, Atkinson PM, Carling PA (2013) Decadal length changes in the fluvial planform of the River Ganga: Bringing a mega-river to life with Landsat archives. *Remote Sens Lett* 4(1):1–9
- Hazarika N, Das AK, Borah SB (2015) Assessing land-use changes driven by river dynamics in chronically flood affected Upper Brahmaputra plains, India, using RS-GIS techniques. *Egypt J Remote Sens Space Sci Auth Remote Sens Space Sci* 18(1):107–118
- Hickin EJ, Nanson GC (1984) Lateral Migration Rates of River Bends. *J Hydraul Eng* 110(11):1557–1567
- Hossain MA, Gan TY, Baki ABM (2013) Assessing morphological changes of the Ganges River using satellite images. *Quat Int Elsevier Ltd INQUA* 304:142–155
- Jayanth J, Ashok Kumar T, Koliwad S, Krishnashastry S (2016) Identification of land cover changes in the coastal area of Dakshina Kannada district, South India during the year 2004–2008. *Egypt J Remote Sens Space Sci Auth Remote Sens Space Sci* 19(1):73–93

- Keshkar et al (1996) Report of experts' committee for bank erosion problem of River Ganga-Padma in the districts of Maida and Murshidabad. Planning Commission Govt. of India, pp 1–71
- Kummu M, Lu XX, Rasphone A, Sarkkula J, Koponen J (2008) Riverbank changes along the Mekong River: remote sensing detection in the Vientiane-Nong Khai area. *Quatern Int* 186(1):100–112
- Nanson GC, Hickin EJ (1986) A statistical analysis of bank erosion and channel migration in western Canada. *Geol Soc Am Bull* 97:497–504
- Nigam MK, Katiyar SK, Mittal SK (2016) Change Detection in course of River Ganga near Kanpur using remote sensing & GIS techniques. *Int J Sci Eng Res* 7(7):762–765
- Rawat JS, Kumar M (2015) Monitoring land use/cover change using remote sensing and GIS techniques: a case study of Hawalbagh block, district Almora, Uttarakhand, India. *Egypt J Remote Sens Space Sci Auth Remote Sens Space Sci* 18(1):77–84
- Thakur PK (2014) River bank erosion hazard study of river Ganga, upstream of farakka barrage using remote sensing and GIS. *Our Natl River Ganga Lifeline Millions* 9783319005:261–283
- Tiegs SD, Pohl M (2005) Planform channel dynamics of the lower Colorado River: 1976–2000. *Geomorphology* 69(1–4):14–27
- Yang X, Damen MC, van Zuidam R, a. (1999) Satellite remote sensing and GIS for the analysis of channel migration changes in the active Yellow River Delta, China. *Int J Appl Earth Obs Geoinf* 1(2):146–157

# Chapter 19

## Depth-Averaged Velocity Distribution in a Meandering Compound Channel Using Calibrating Coefficients



Anurag Handique, Arpan Pradhan, C. Sarat Chandra,  
and Kishanjit Kumar Khatua

**Abstract** The precise prediction of the depth-averaged velocities, lateral shear stresses, and boundary shear stresses are necessary to access the flow capacity and flow variations related to flood events in meandering channels. The accurate assessment of the distribution of velocities, conveyance, and bed shear stress distribution is significant for flood management schemes, bank protection studies, and sediment dynamics on meandering channels. This work proposes a new approach for assessing the depth-averaged velocities laterally across a meandering compound channel. The experimental evaluation was done in Hydraulic Laboratory in the National Institute of Technology Rourkela (NITR), Odisha, India. The apex section was considered for estimating the boundary shear stress through experimentation. The meander cross-section is split into five distinctive panels for studying the flow phenomenon for overbank flow. The results indicated that the boundary shear stress causes a notable change in the secondary flow coefficient ( $K$ ). The new model provides the variation of depth-averaged velocity ( $U_d$ ) across the cross-section of the meandering compound channel, which includes the bed-generated friction, secondary flows, and lateral shear turbulence.

**Keywords** Meandering compound channel · Lateral depth-averaged velocity · Velocity distribution · Secondary flow coefficient · Boundary shear stress

### 19.1 Introduction

Rivers are considered to be a blessing to society and one of the essential parts of nature. The river plays a vital role in every living being in its way. Some of our basic needs related to water, such as drinking, cleaning, washing clothes, etc., are also being fulfilled by a river. Furthermore, human-made channels are of great importance from the early days as these are of great worth in producing power for different industries. Rivers have always been an attraction of researchers around the globe from many disciplines. The river curves, commonly known as meanders, are so ubiquitous; as the

---

A. Handique (✉) · A. Pradhan · C. S. Chandra · K. K. Khatua  
Civil Engineering Department, National Institute of Technology, Rourkela 769008, India

river tries to flow in the way having the least flow resistance, eventually, meandering occurs. In meandering rivers, erosion of sediment takes place from each meander's outer arc, and deposition occurs on the inner arc further downstream. Subsequently, the individual meanders grow larger in due course of time. Meandering rivers often exhibit asymmetrical nature, with the outer bend of the meandering section having the deepest section. The velocities in the deeper sections are relatively higher, which triggers erosion in the outer bend (Sankalp et al. 2015). However, the inner bend velocities are on the slower side, which can't carry the sediment load. Consequently, it deposits the load on a string of point bars. Natural alluvial rivers commonly consist of a curved main channel along with floodplains on either one side or both. The settlement of human civilization on the floodplains can induce a significant flood hazard causing serious damage to human life and property. During a flood event, the depth of flow in the river increases, resulting in the submergence of the main channel. To convey this excess water, floodplain flow takes place.

The flow process in a meandering compound channel is much more complicated than in the case of a straight or skewed channel. The mechanism of generation of main channel secondary flow is different in instances of a meandering geometry as compared to a straight one. In this regard, the flow characteristics in a meandering channel vary significantly as compared to a straight geometry. Accordingly, it is obligatory to account for the variations in velocity, bed shear stress, secondary flow, and discharge in a meandering compound channel. The river engineers traditionally use the subdivision techniques to predict flood water levels in case of overbank flows in compound channels. The methods are one-dimensional and do not provide an accurate estimation. The inefficiency can be attributed to the exclusion of the effects like a turbulent exchange, momentum transfer, and secondary current. Therefore, the simple 1-D methods cannot meet the requirements of some river engineering problems. Thus, the essence of some advanced techniques is highly felt to predict the river flow parameters.

Shiono and Knight (1991) proposed a more polished method, obtained by depth-averaging the streamwise Reynolds averaged Navier–Stokes (RANS) equations. This method was an efficient method for the prediction of rivers' conveyance capacity having overbank flow more accurately. Furthermore, this method also provided the distributions of depth-averaged velocity and bed shear stress across the cross-sectional domain of the channel. The Shiono and Knight Method (SKM) is based on three hydraulic parameters, namely the bed friction factor ( $f$ ), depth-averaged secondary flow ( $K$ ) and lateral eddy viscosity ( $\lambda$ ). Bed friction factor ( $f$ ) represents the boundary friction, lateral eddy viscosity ( $\lambda$ ) represents the lateral mixing and turbulence, and depth-averaged secondary flow ( $K$ ) represents the secondary flows. The application of SKM involves dividing the channel into the required numbers of panels or sections, and then the equations of SKM are incorporated into each section or panel. Subsequently, the requisite boundary conditions are applied to each panel boundaries. Later, the SKM equations are solved for obtaining the depth-averaged

velocities, and local boundary shear stresses at the defined panels across the cross-section. While modelling the hydraulic parameters in SKM, there might be some difficulties, including whether these parameters accurately depict the energy loss mechanisms for which they are prescribed.

The process involved in the secondary flow coefficient  $K$  calibration for integrating the secondary flow effects is still tricky. Abril and Knight (2004) proposed an approach, which considered fixed values of  $K$  for both main channel and floodplain domains. Devi and Khatua (2017) developed some equations which combine the variations involved in secondary flow coefficients with geometrical factors of the channel, the relative depth ( $\beta$ ) and width ratio ( $\alpha$ ). Alawadi et al. (2018) suggested that the approach presented by Devi and Khatua (2017) is more reliable compared to the approach given by Abril and Knight (2004).

An improved method for finding lateral depth-averaged velocity is modelled by Liu et al. (2014), which accounted for the distribution of depth-averaged velocities laterally through a half meander in a compound channel. Liu et al. (2014) also modelled the parameter  $K$  by considering the equation of momentum and continuity. But Liu has done the experiments in the compound meandering channel at Sichuan University in China. The experimentation involved a channel having a particular sinuosity, width ratio ( $\alpha$ ), and relative depth ( $\beta$ ), giving a certain set of results. But for a different set of relative depth ( $\beta$ ), sinuosity, and width ratio ( $\alpha$ ), the results may not follow the same trend, so proper modelling of the hydraulic parameters should be done for a broader range of data.

## 19.2 Theoretical Background

The Shiono Knight Method is an essential tool for obtaining the lateral variations in depth-averaged velocities. The Shiono Knight Method (SKM) is based on depth-averaged quasi 2D Reynold's averaged Navier–Stokes equation (RANS) in the x-direction.

$$v \frac{\partial^2 \bar{u}}{\partial y^2} + v \frac{\partial^2 \bar{u}}{\partial z^2} - \frac{\partial \overline{u'v'}}{\partial y} - \frac{\partial \overline{u'v'}}{\partial z} + \left[ \frac{\partial h}{\partial x} - S_o \right] = \frac{\partial \bar{u}\bar{v}}{\partial y} + \frac{\partial \bar{u}\bar{v}}{\partial z} \quad (19.1)$$

For steady and uniform flow, the simplified form of the streamwise RANS equation is as follows

$$\rho \left[ \frac{\partial \bar{u}\bar{v}}{\partial y} + \frac{\partial \bar{u}\bar{w}}{\partial z} \right] = \rho g S_o + \frac{\partial}{\partial y} (-\rho \overline{u'v'}) + \frac{\partial}{\partial z} (-\rho \overline{u'v'}) \quad (19.2)$$

where  $\rho$  is the density of water,  $S_o$  is the bed slope,  $g$  is the acceleration due to gravity, the temporal mean velocities are being represented by  $\bar{u}$ ,  $\bar{v}$ ,  $\bar{w}$  in the x, y and z directions, respectively.  $u'$ ,  $v'$  and  $w'$  represents the components of fluctuations from the mean velocities in x, y and z directions, respectively.

The mean velocity in the z-direction ( $\bar{w}$ ) is assumed to be zero. Adopting the eddy viscosity approach Shiono and Knight simplified the above equation. Reynold’s shear stress  $(-\rho\overline{u'v'})$  (onthelateralplane),  $(-\rho\overline{u'w'})$  (onthetheverticalplane) are being denoted by  $\tau_{yx}$  and  $\tau_{zx}$  respectively. Now integrating the above equation over the flow depth H, the following equation is obtained,

$$\int_0^H \rho \left[ \frac{\partial \overline{uv}}{\partial y} + \frac{\partial \overline{uw}}{\partial z} \right] dz = \rho \frac{\partial H(\overline{uv})_d}{\partial y} \text{ and } \int_0^H \rho g S_o dz = \rho g H S_o \tag{19.3}$$

According to eddy viscosity theory transverse shear stress,  $\tau_{yx} = \rho \epsilon_{yx} \frac{\partial U}{\partial y}$  where  $\epsilon_{yx}$  is the eddy viscosity which is equal to  $\lambda H U_*$  where  $\lambda$  is the dimensional eddy viscosity and  $U_*$  is the shear velocity represented by  $U_* = \sqrt{\frac{\tau_b}{\rho}}$  where  $\tau_b$  is the boundary shear stress.

Now, according to the relationship, frictional factor,  $f = \frac{8\tau_b}{\rho U^2}$

Moreover,

$$\epsilon = \lambda H U_* = \lambda H \left( \frac{f}{8} \right)^{\frac{1}{2}} U \tag{19.4}$$

$$\tau_{yx} = \rho \lambda H \left( \frac{f}{8} \right)^{\frac{1}{2}} U \frac{\partial U}{\partial y} \tag{19.5}$$

Now we can write,

$$\int_0^H \frac{\partial}{\partial y} (-\rho\overline{u'v'}) dz = \int_0^H \frac{\partial \tau_{yx}}{\partial y} dz = \frac{\partial}{\partial y} \left( \rho \lambda H^2 \left( \frac{f}{8} \right)^{\frac{1}{2}} U \frac{\partial U}{\partial y} \right) \tag{19.6}$$

and

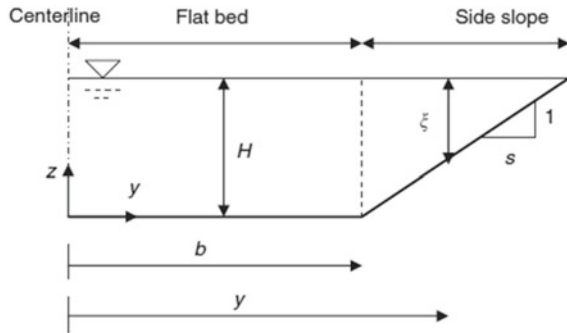
$$\int_0^H \frac{\partial}{\partial z} (-\rho\overline{u'w'}) dz = \int_0^H \frac{\partial \tau_{zx}}{\partial z} dz = \tau_b \frac{(1+s^2)^{\frac{1}{2}}}{s} = \frac{f}{8} \rho U^2 \frac{(1+s^2)^{\frac{1}{2}}}{s} \tag{19.7}$$

Finally, the simplified form of Shiono Knight method can be expressed as followed

$$\rho \frac{\partial H(\overline{uv})_d}{\partial y} = \rho g H S_o + \frac{\partial}{\partial y} \left( \rho \lambda H^2 \left( \frac{f}{8} \right)^{\frac{1}{2}} U_d \frac{\partial U_d}{\partial y} \right) - \frac{f}{8} \rho U^2 \frac{(1+s^2)^{\frac{1}{2}}}{s} \tag{19.8}$$

The term  $\rho \frac{\partial H(\overline{uv})_d}{\partial y}$  represents secondary flow whose variations are studied by Shiono and Knight from the experimental dataset. They stated that the shear stress

**Fig. 19.1** Trapezoidal section



induced due to secondary flow declines linearly on either side of a maximum value at the junction of the main channel and floodplains. On the Eq. (19.8) right-hand side, the first term is the gravitational force term; the second and third term results from Reynold’s shear stress in  $xy$  plane and the  $x-z$  plane, respectively. The secondary flow term has been replaced by a parameter  $K$  which is called the secondary flow coefficient. So,  $\rho \frac{\partial H(\bar{w})_d}{\partial y} = K$ . Furthermore, to get the depth-averaged velocity distribution, we have to know the parameters  $f$ ,  $\lambda$ , which represents bed friction factor and dimensional eddy viscosity in the lateral direction, respectively. These all three parameters  $f$ ,  $\lambda$  and  $K$  are collectively called calibrating coefficients (Fig. 19.1).

According to Shiono and Knight, the analytical solution for finding depth-averaged velocity differs between the constant bed region and side slope region. For constant depth region, the analytical solution for  $U_d$  is

$$U_d = [A_1 e^{\gamma_1 y} + A_2 e^{\gamma_2 y} + k]^{\frac{1}{2}} \tag{19.9}$$

where

$$k = \frac{8gHS_o}{f} \left[ 1 - \frac{K}{\rho gHS_o} \right], \gamma_1 = \frac{1}{H} \left( \frac{2}{\lambda} \right)^{\left( \frac{1}{2} \right)} \left( \frac{f}{8} \right)^{\left( \frac{1}{4} \right)}, \gamma_2 = \gamma_1$$

For side slope region, the analytical solution for  $U_d$  is,

$$U_d = (A_3 \xi^\alpha + A_4 \xi^{-(\alpha+1)} + \omega \xi + \eta)^{\frac{1}{2}} \tag{19.10}$$

where

$$\alpha = -\frac{1}{2} + \frac{1}{2} \sqrt{1 + \frac{(1+s^2)^{\frac{1}{2}}}{\lambda} (8f)^{\frac{1}{2}}}$$

$$\omega = \frac{gS_o}{\left(\frac{f}{8}\right)\frac{(1+s^2)^{\frac{1}{2}}}{s} - \frac{\lambda}{s^2}\left(\frac{f}{8}\right)^{\frac{1}{2}}}$$

$$\eta = -\frac{K}{\rho\left(\frac{f}{8}\right)\frac{(1+s^2)^{\frac{1}{2}}}{s}}$$

$$\xi = H + \frac{y+b}{s} \text{ (for positive } y)$$

$$\xi = H - \frac{y-b}{s} \text{ (for negative } y)$$

$A_1, A_2, A_3, A_4$  are the unknown coefficients which can be determined by applying proper boundary conditions.

To apply the Shiono Knight method, the channel cross-section is split into a requisite number of distinctive panels, and the equations of SKM are incorporated in each panel. The relevant boundary conditions are integrated into each panel boundaries. The equations of SKM are solved to obtain the depth-averaged velocities, and boundary shear stresses across the cross-section.

### 19.3 Calibrating Coefficients

To apply this model the calibrating coefficients, which are bed friction factor ( $f$ ), dimensional eddy viscosity ( $\lambda$ ) and secondary flow coefficient ( $K$ ) has to be found out accurately. The process by which we can determine these coefficients are as follows.

**Bed Friction Factor ( $f$ ):** The bed friction factor or Darcy Weisbach friction factor ( $f$ ) can be found out by back-calculating from the equation  $f = \frac{8\tau_b}{U_d^2}$  knowing the mean depth-averaged velocity and boundary shear stress in each panel. But as there is no experimental data available so we cannot get the depth-averaged velocity term to use this particular equation. So, the equation  $f = \frac{8gn^2}{R^3}$  as proposed by Huai et al. (2008) is used to find out the bed friction factor.

**Dimensional Eddy Viscosity ( $\lambda$ ):** Shiono and Knight (1991) proposed that in a straight compound channel dimensional eddy viscosity ( $\lambda$ ) changes slightly in the main channel and the change is significant in the floodplain. Later, Abril and Knight (2004) proposed an equation  $\lambda = \lambda_{mc}(1.2D_r^{-1.44} - 0.2)$  to determine the dimensional eddy viscosity, but this equation does not give satisfactory results in meandering compound channels. So it is best to calibrate from the measured velocity data. Without the experimental data, some fixed values of  $\lambda$  are assumed. Abril and Knight (2004)



proposed a fixed value of  $\lambda_1 = 0.07$  for the main channel. For side, slope domain  $\lambda_2$  is considered as 0.03 while for floodplain  $\lambda$  is taken as  $\lambda_2/D_r^{1.5}$  ( $D_r$  is relative depth) which is equal to 0.7.

**Secondary Flow Coefficient ( $K$ ):** Secondary flow coefficient ( $K$ ) is a difficult parameter to determine. Omran (2008) has mentioned two empirical formulas for determining  $K$  in both the main channel and floodplain. Those formulas are based on relative depth  $D_r = \frac{H-h}{H}$  and  $(B/b)$  ratio. Although the formulae given by Omran (2008) becomes ineffective when it comes to meandering compound channels. Devi and Khatua (2017) proposed a much reliable method to find out the secondary flow coefficient ( $K$ ) which can be found out using the boundary shear stress data by the following equations.

For the main channel,

$$k_{mc} = \frac{(\tau_{bmc})_{avg}}{\rho g H S_0} \quad (19.11)$$

For floodplain,

$$k_{fp} = \frac{(\tau_{bfp})_{avg}}{\rho g (H - h) S_0} \quad (19.12)$$

where,  $(\tau_{bmc})_{avg}$  and  $(\tau_{bfp})_{avg}$  are the averaged boundary shear stress in the main channel and floodplains respectively (Figs. 19.2 and 19.3).

Now, the expressions for finding out secondary coefficients are

$$K_{mc} = \rho g H S_0 (1 - k_{mc}) \quad (19.13)$$

$$K_{fp} = \rho g (H - h) S_0 (1 - k_{fp}) \quad (19.14)$$



**Fig. 19.2** The experimental flume in Hydraulic Laboratory, NIT, Rourkela

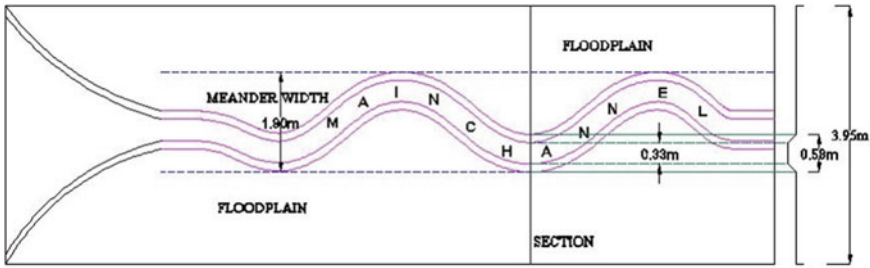


Fig. 19.3 Plan view of the flume in Hydraulic Engineering Laboratory, NIT, Rourkela

### 19.4 Experimental Setup

The experimentation was performed in a trapezoidal meandering channel with a sinuosity 1.22 in Hydraulic Laboratory in NITR, India. The channel section has a side slope of 1:1, bottom width of 0.33, while the full-bank depth being 0.125 m having a valley slope of 0.00165. Perspex sheets with a roughness coefficient ( $n = 0.01$ ) are used to fabricate the bed of the channel domain. The plan view and the photographs of the channel are represented as follows.

### 19.5 Measurement of Boundary Shear Stress

An effective technique was proposed by Preston (1954) for assessing the bed shear stress. The approach is applicable to the smooth boundaries, which involves experimentation with a Preston tube. A non-dimensional relationship was presented by Preston, which associates between the boundary shear stress ( $\tau$ ), and pressure difference  $\Delta P$  obtained from the Preston tube.

$$\frac{\tau d^2}{4\rho v^2} = F\left(\frac{\Delta P d^2}{4\rho v^2}\right) \tag{19.15}$$

Here,  $d$  represents Preston tube’s outer diameter,  $\rho$  is the flow medium’s density of the,  $v$  represents the fluid’s kinematic viscosity, and  $F$  signifies an empirical function.

Patel (1965) expanded the research further, and he gave two non-dimensional parameters which can relate the pressure difference directly with the boundary shear stress

$$x^* = \log_{10}\left(\frac{\Delta P d^2}{4\rho v^2}\right) \quad y^* = \log_{10}\left(\frac{\tau d^2}{4\rho v^2}\right) \tag{19.16}$$

After finding out the values of  $x^*$ , the  $y^*$  values can be found out with the help of these following expressions

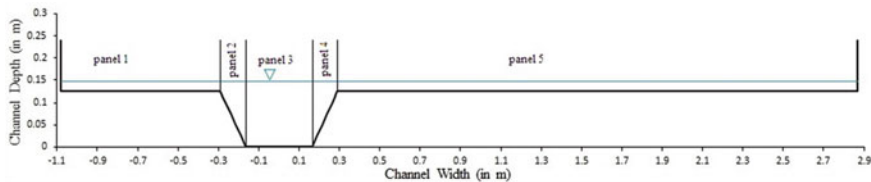


**Fig. 19.4** Cross-section of the flume at bend apex with the divided panels

$$y^* < 1.5 \quad y^* = 0.5x^* + 0.037 \quad (19.17)$$

$$1.5 < y^* < 3.5 \quad y^* = 0.8287 - 0.1381x^* + 0.1437x^{*2} - 0.006x^{*3} \quad (19.18)$$

$$3.5 < y^* < 5.3 \quad x^* = y^* + 2 \log_{10}(1.95y^* + 4.10) \quad (19.19)$$

The differential pressure readings are obtained using a pitot tube on the points, which are already predefined, across all the channel sections. The manometer affixed to the pitot tube furnishes the difference in static and dynamic pressures. After that, the differential pressure can be obtained from the vertical manometer readings by  $\Delta P = \rho g \Delta h$ . Where  $\Delta h$  is the head difference between the static and dynamic pressure,  $g$  is the gravitational acceleration, and  $\rho$  is water density.

## 19.6 Boundary Conditions

In the present study, only the bend apex section is considered. Therefore, to determine the unknown constants, and for the application of the model, the channel cross-section is divided into five representative panels (Fig. 19.4). The following boundary conditions are applied on the edge of each panel shown in Fig. 19.4.

1.  $U_i^2 = U_{i+1}^2$
2.  $\frac{\partial U_i^2}{\partial y} = \frac{\partial U_{i+1}^2}{\partial y}$

where,  $U_i$  and  $U_{i+1}$  represents the depth-averaged velocities in the  $i$ th panel and  $(i + 1)$ th panel respectively.

## 19.7 Results and Discussions

The experiments were conducted in Hydraulic Laboratory in the National Institute of Technology, Rourkela, India, utilizing the Preston tube technique at the bend apex. The experimented boundary shear stress data are compared with the datasets

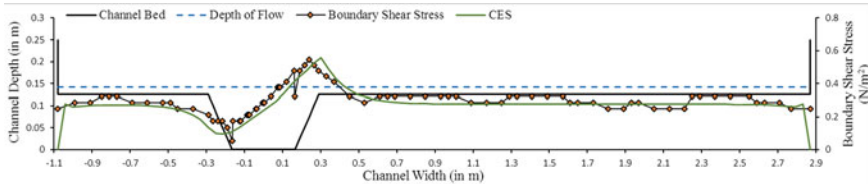


**Fig. 19.5** Comparison of boundary shear stress

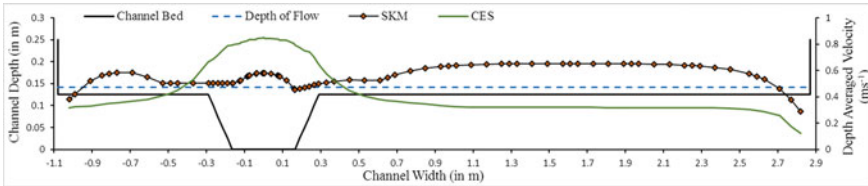


**Fig. 19.6** Comparison of lateral depth-averaged velocity

obtained from Conveyance Estimation System (CES). CES mainly incorporates the quasi-one-dimensional RANS (Reynold’s Averaged Navier–Stokes) equations to obtain the results. The results obtained gave good arguments with the observed datasets (Fig. 19.5).

The averaged boundary shear stress values  $(\tau_b)_{avg}$  are obtained for each panel, as shown in Fig. 19.4. After finding out the values of  $(\tau_b)_{avg}$  we can compute the secondary flow coefficient ( $K$ ) from Eqs. (19.11)–(19.14).

The SKM equations are applied to each of the five panels individually and at the panel boundaries, the boundary conditions are applied to get the value of the unknown coefficients of each panel.

The depth-averaged velocity distribution obtained from SKM is compared with the same obtained from CES software shown in Fig. 19.6.

From Fig. 19.6 it is seen that the profile that is obtained by SKM resembles to the practical case whereas the distribution plot given obtained by CES does not give better results which does not have a resemblance with the practical scenario.

## 19.8 Conclusions

The results obtained are analyzed, and the following conclusions can be made from the study.

1. The model gives the lateral variation of the depth-averaged velocity,  $U_d$  for meandering compound channel and includes the bed’s friction, lateral shear turbulence, and secondary flows.

2. The variation of the model parameters was observed in the study. It is observed that the bed friction factor ( $f$ ) values in the main channel bed were relatively less, whereas it increases in the side slopes and floodplains. The secondary flow coefficient ( $K$ ) was observed to be more in the main channel and relatively less in the floodplains.
3. It is seen from the distribution plot of depth-averaged velocity that it gradually increases towards the edges and decreases finally just before the edge of the compound channel.
4. The approach which is used for determining secondary flow coefficient ( $K$ ) by boundary shear stress approach is much more reliable in case of a meandering compound channel than the empirical equations given by Omran (2008).

## References

- Abril JB, Knight DW (2004) Stage-discharge prediction for rivers in flood applying a depth-averaged model. *J Hydraul Res* 42:616–629. <https://doi.org/10.1080/00221686.2004.9628315>
- Alawadi W, Al WS, Ali R, Al AH (2018) Application of the Shiono and Knight Method in asymmetric compound channels with different side slopes of the internal wall. *Appl Water Sci* 8:1–10. <https://doi.org/10.1007/s13201-018-0663-4>
- Devi K, Khatua KK (2017) Depth-averaged velocity and boundary shear stress prediction in asymmetric compound channels. *Arab J Sci Eng* 42:3849–3862. <https://doi.org/10.1007/s13369-017-2486-2>
- Huai WX, Xu ZG, Yang ZH, Zeng YH (2008) Two dimensional analytical solution for a partially vegetated compound channel flow. *Appl Math Mech (English Ed)* 29:1077–1084. <https://doi.org/10.1007/s10483-008-0811-y>
- Liu C, Wright N, Liu X, Yang K (2014) An analytical model for lateral depth-averaged velocity distributions along a meander in curved compound channels. *Adv Water Resour* 74:26–43. <https://doi.org/10.1016/j.advwatres.2014.08.003>
- Omran M (2008) New developments in predicting stage-discharge curves, velocity and boundary shear stress distributions in open channel flow. *Water Environ J* 22:131–136. <https://doi.org/10.1111/j.1747-6593.2007.00091.x>
- Patel VC (1965) Calibration of the Preston tube and limitations on its use in pressure gradients. *J Fluid Mech* 23:185–208
- Preston J (1954) The determination of turbulent skin friction by means of Pitot tubes. *J R Aeronaut Soc* 58:109–121. <https://doi.org/10.1017/S0368393100097704>
- Sankalp S, Khatua KK, Pradhan A (2015) Boundary shear stress analysis in meandering channels at the bend apex. *Aquat Procedia* 4:812–818
- Shiono K, Knight DW (1991) Turbulent open-channel flows with variable depth across the channel. *J Fluid Mech* 222:617–646

# Chapter 20

## Study of Flow Characteristic of Trapezoidal Labyrinth Weir



Saurabh Sah, Munendra Kumar, and Deepak Singh

**Abstract** A trapezoidal labyrinth weir is characterized by a broken axis in the plan to increase the crest's effective length. Labyrinth weirs provide an increase in crest length for a given channel width, thereby increasing flow capacity for a given upstream head. A physical or experimental study based on the design and analysis of trapezoidal labyrinth weirs is presented in this study. Hydraulic model tests of the weir showed that the behavior of the labyrinth weir was convenient and that the discharge capacity presented a good agreement with theoretical calculations. It is the purpose of this paper to present a satisfactory developed physical model of labyrinth weir flow and provide engineers with a model capable of dealing with a variety of labyrinth weir configurations and flow conditions. The preliminary hydraulic calculations results indicated that hydraulic jump with estimated low Froude numbers ( $Fr_1$ ), of about 2.7–3.0, is supercritical at its downstream, and it enhances with the slope of the weir. This study of labyrinth weir is performed between head to crest ratio, apex width, vertical aspect ratio, approach, and conveyance channel conditions that increased the discharge capacity of labyrinth weir and design of trapezoidal labyrinth weir.

**Keywords** Trapezoidal labyrinth weir · Hydraulic model · Physical model · Froude numbers · Discharge coefficient

### Nomenclature

- A = Inside apex width;
- B = Flume width;
- a,b = Coefficients;
- Cd = Coefficients of discharge for labyrinth weir;
- Fr = Froude Number;
- g = Acceleration due to gravity;

---

S. Sah (✉) · M. Kumar · D. Singh  
Department of Civil Engineering, Delhi Technological University, New Delhi 110042, India

Ht	= Total upstream head on weir;
Ht/P	= Headwater ratio;
l	= Length of one cycle (2L1+A+D);
L	= Effective length of labyrinth =N (2L2+2A);
N	= Number of cycle;
P	= Weir height;
Qo	= Observed discharge;
Qc	= Computed discharge;
R2	= Determination coefficient;
t	= Weir wall thickness;
Va	= Velocity of approach;
W	= Total width of labyrinth weir;
w	= Width of one cycle of labyrinth;
$\theta$	= Vertex angle;
$\alpha$	= Angle of side edge or labyrinth angle;

## 20.1 Introduction

A trapezoidal labyrinth weir is constructed across a stream to increase the water level on the upstream side while allowing excess water to flow down the river's entire length. Labyrinth weirs improve a dam's spillway discharge capacity and are often used for dam renovation projects due to an increase in projected flood inflow to the dam's reservoir. Contributions to the labyrinth weir knowledge base have been made by "Anderson and Tullis (2012, 2013), Bilhan et al. (2011), Crookston and Tullis (2012a, b, 2013), Emiroglu et al. (2010), Garde et al. (2000), Mohamed (2010), Hay and Taylor (1970), Martinez (2005), Kandaswamy and Rouse (1957), Khode et al. (2010, 2012), Lux (1989), Magalhaes and Lorena (1989), Bos (1989), Sobeih et al. (2012), Righetti and Lanzoni (2008), Tullis and Waldron (2005), Tullis et al. (1995, 2007), Venkataraman (1977), Yildiz and Uzupek (1996)". Conclusions made through this study will help extend this knowledge base of labyrinth weir design methods and applications. A trapezoidal labyrinth weir is an efficient way to improve spillway power. To increase the effective crest length, the labyrinth weir is used to change the crest plan shape. The following mathematical expression describes the labyrinth weir (Q) in a channel under free-flow conditions (20.1).

$$Q = \frac{2}{3} C_d \sqrt{2g} L h^{\frac{3}{2}} \quad (20.1)$$

where  $C_d$  represents the discharge coefficient,  $L$  represents the total crest length of the weir,  $g$  represents the acceleration due to gravity, and  $h$  represents the head over the crest.  $C_d$  depends on flow characteristics and geometry of the channel and the weir. This paper presents the experimental study results to investigate the discharging

capacity of a trapezoidal labyrinth weir plan form under the free-flow condition in a rectangular channel. The following equation for  $C_d$  was proposed by conducting experiments of the broad crested curved weir (20.2).

$$C_d = \left( 0.5 + 0.33 \frac{h}{w} + \frac{h}{L} \right)^{0.06} \quad (20.2)$$

Taylor's work was followed up on by Hay and Taylor, who created design standards for labyrinth weirs. For the discharge coefficient of labyrinth weirs, they proposed equation (20.3).

$$C_d = 3.22 + 0.40 \frac{h}{P} \quad (20.3)$$

$C_d$  is the discharge coefficient;  $h$  is the depth of flow over the weir crest, and  $P$  is the weir height. Lux looked into various model studies for the labyrinth weir, and his suggested equation for measuring the discharge of a trapezoidal labyrinth weir is Eq. (20.4).

$$Q = C_d \left( \frac{\frac{W_c}{P}}{\frac{W_c}{P+K}} \right) W_c H_t \sqrt{g H_t} \quad (20.4)$$

where  $Q$  represents the discharge over the labyrinth weir,  $C_d$ , represents the coefficient of discharge,  $H_t$ , represents the total upstream head measured relative to the weir crest,  $W_c$  represents the channel width, and  $P$  represents the weir height. Magalhaes and Lorena measured the discharge coefficient of the labyrinth weir as a function of  $L/W$  and  $H_t/P$  parameters (20.5).

$$Q = C_d W_T 2g H_t^{1.5} \quad (20.5)$$

## 20.2 Experimental Set-Up and Experiments

In order to find out the flow characteristics, discharge carrying capacity of the trapezoidal labyrinth weir, and its accuracy, an experimental setup is built up in "Fluid Mechanics and Hydraulics Research Laboratory" at Delhi Technological University, Delhi, India. The experimental set-up consists of sump, pumping system, collecting tank, rectangular flume, electromagnetic flow-meter, and the different trapezoidal labyrinth weir models. The tests have been performed in a straight rectangular channel of 10 m long, 0.516 m wide, and a height of 0.6 m. The channel is fed by a pump of 20 H.P connected with a series of pipes of 4-inch supply, delivering the discharges up to 50 L/s. The flume supply line calibrates by orifice meter (0.25% uncertainty),



and discharge can adjust with a supply valve's help. A baffle wall and a wood surface dampener are provided to dampen the water surface waves and minimize turbulence. The upstream elevation was constructed higher than the downstream elevation in the tests, resulting in free flow conditions downstream of the weir. For the labyrinth weirs, sheet metal materials with a thickness of 6 mm ( $t$ ) were used. The nappe breakers' upstream apex angle was set at 105 degrees, and the downstream apex shape was rounded. Each model of trapezoidal labyrinth weirs has four cycles. The trapezoidal labyrinth and linear weirs are depicted schematically in (Fig. 20.1). In the experiments, each labyrinth weir model with a sharp-crested shape was tested (Fig. 20.2).

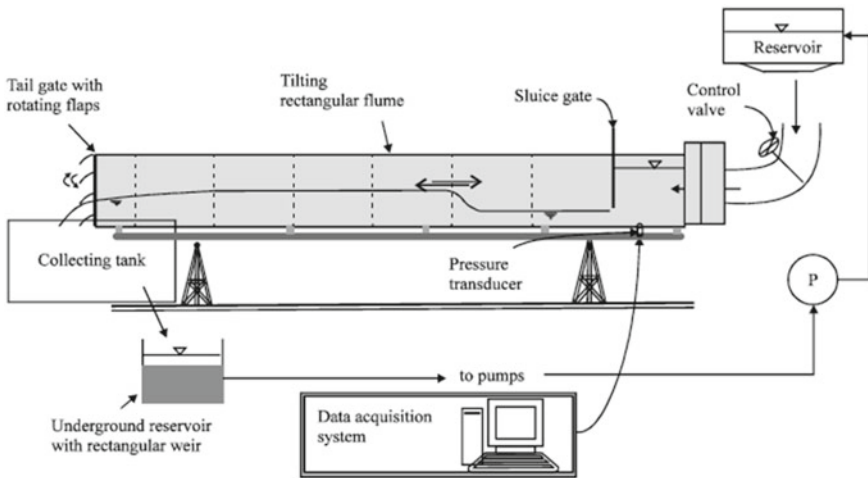


Fig. 20.1 Definition sketch for tilting flume (10 m) length

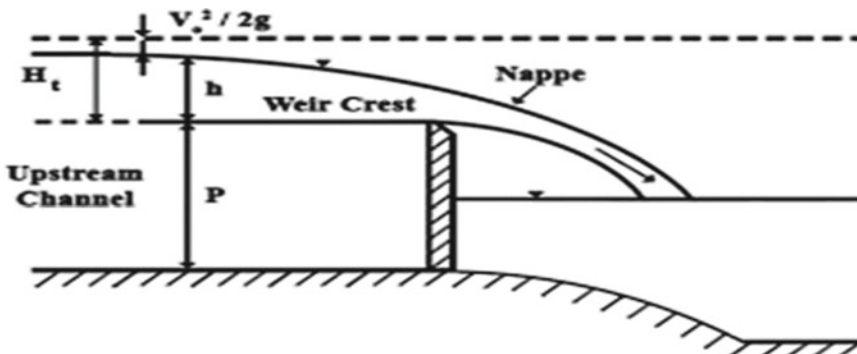


Fig. 20.2 Definition sketch for flow over a sharp-crested weir

### 20.3 Experimental Results and Analysis

Experiments were performed on nine trapezoidal labyrinth weir models with sidewall angles of 12, 15, 18, 21, 24, 30, 36, 42, 48° and linear weir models with a sharp-crested shape similar to labyrinth weir models. The head discharge measurement is taken for weir height of  $P = 15, 20,$  and  $25$  cm. Total of 30 different configurations were examined in these experiments as shown in Table 20.1. The discharge coefficient was computed by labyrinth weir equation no (20.4). In this study, the crest was spaced at a regular interval. The variance of  $C_d$  for trapezoidal labyrinth weirs with  $H_t/P$  is plotted in (Fig. 20.3).

The data is represented in equation form, and correlation analysis is performed on the observed data from each physical model. The fifth-degree polynomial equation given a rational match between  $C_d$  and  $H_t/P$ . As a result, the discharge coefficient ( $C_d$ ) of a trapezoidal labyrinth weir is (20.6)

$$C_d = A_0 + A_1 \left( \frac{H_t}{P} \right) + A_2 \left( \frac{H_t}{P} \right)^2 + A_3 \left( \frac{H_t}{P} \right)^3 + A_4 \left( \frac{H_t}{P} \right)^4 + A_5 \left( \frac{H_t}{P} \right)^5 \quad (20.6)$$

The values of  $C_d$ ,  $A_0$  to  $A_5$ , and  $R^2$  are shown in Table 20.2.

### 20.4 Conclusions

Trapezoidal labyrinth weir can pass large water flow at the minimum head. The labyrinth weir can also be used efficiently to measures discharge metering device in open channel flow. The equation of  $C_d$  for weir has been obtained, which can be employed to find  $C_d$ 's value and  $\theta$  in the corresponding range of the discharge of trapezoidal labyrinth weir. This study has found that trapezoidal labyrinth weir has more efficient than the linear weir and form the ease of construction and the increased discharge capacity. A problem for trapezoidal labyrinth weir is matching the outflow to downstream flow limitation. It is recommended that a study of the trapezoidal labyrinth weir design of physical model be undertaken to study the performances of different shapes and operations. The study recommended a trapezoidal labyrinth weir analysis and design to verify by a physical model study to the same parameter with numerical modeling study for future work.

**Table 20.1** Geometry of the physical model for the weirs that were evaluated in the analysis

S. no	Wc (cm)	P (cm)	L (cm)	N	A (cm)	Lc/Wc	Type of weir
1	206	15	206	4	8	1.0	Linear weir, $\alpha = 90$
2	206	15	304	4	8	1.48	Trapezoidal $\alpha = 48$
3	206	15	355	4	8	1.72	Trapezoidal $\alpha = 42$
4	206	15	437	4	8	2.12	Trapezoidal $\alpha = 36$
5	206	15	544	4	8	2.64	Trapezoidal $\alpha = 30$
6	206	15	605	4	8	2.93	Trapezoidal $\alpha = 24$
7	206	15	757	4	8	3.68	Trapezoidal $\alpha = 21$
8	206	15	837	4	8	4.06	Trapezoidal $\alpha = 18$
9	206	15	904	4	8	4.39	Trapezoidal $\alpha = 15$
10	206	15	987	4	8	4.80	Trapezoidal $\alpha = 12$
11	206	20	206	4	8	1.0	Linear weir $\alpha = 90$
12	206	20	304	4	8	1.47	Trapezoidal $\alpha = 48$
13	206	20	355	4	8	1.72	Trapezoidal $\alpha = 42$
14	206	20	437	4	8	2.12	Trapezoidal $\alpha = 36$
15	206	20	544	4	8	2.64	Trapezoidal $\alpha = 30$
16	206	20	605	4	8	2.93	Trapezoidal $\alpha = 24$
17	206	20	757	4	8	3.67	Trapezoidal $\alpha = 21$
18	206	20	837	4	8	4.06	Trapezoidal $\alpha = 18$
19	206	20	904	4	8	4.38	Trapezoidal $\alpha = 15$
20	206	20	987	4	8	4.79	Trapezoidal $\alpha = 12$
21	206	25	206	4	8	1.0	Linear weir $\alpha = 90$
22	206	25	304	4	8	1.47	Trapezoidal $\alpha = 48$
23	206	25	355	4	8	1.72	Trapezoidal $\alpha = 42$
24	206	25	437	4	8	2.12	Trapezoidal $\alpha = 36$
25	206	25	544	4	8	2.64	Trapezoidal $\alpha = 30$
26	206	25	605	4	8	2.94	Trapezoidal $\alpha = 24$
27	206	25	757	4	8	3.67	Trapezoidal $\alpha = 21$
28	206	25	837	4	8	4.06	Trapezoidal $\alpha=18$
29	206	25	904	4	8	4.39	Trapezoidal $\alpha = 15$
30	206	25	987	4	8	4.81	Trapezoidal $\alpha = 12$

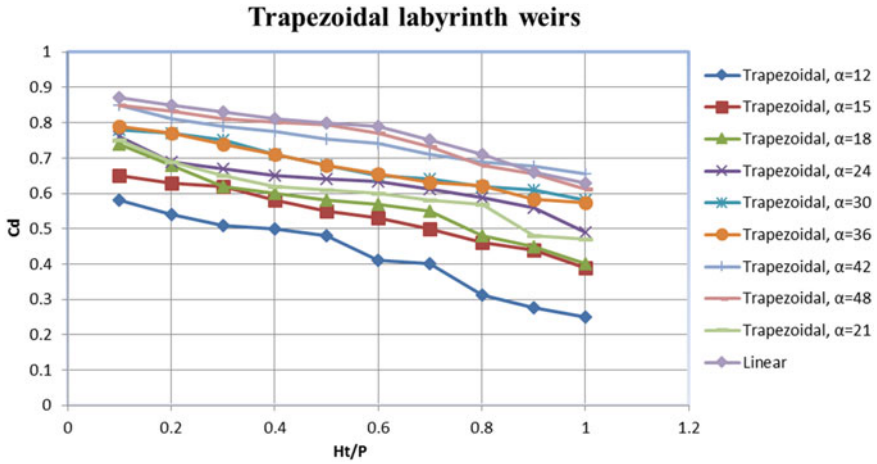


Fig. 20.3 Variation of  $C_d$  versus  $H_t/P$  for different angle of trapezoidal weir

Table 20.2 Discharge coefficient per length of the trapezoidal labyrinth weir

Type of weir model	A0	A1	A2	A3	A4	A5	R <sup>2</sup>
Trapezoidal, $\alpha = 12$	0.4651	2.8456	-16.3511	39.1255	-42.451	16.278	0.9751
Trapezoidal, $\alpha = 15$	0.4701	3.5741	-18.6525	41.2523	-43.056	15.568	0.9874
Trapezoidal, $\alpha = 18$	0.5832	2.2933	-13.8442	30.5824	-31.458	11.259	0.9754
Trapezoidal, $\alpha = 21$	0.6121	1.1546	-9.5436	21.5864	-24.546	8.546	0.9731
Trapezoidal, $\alpha = 24$	0.6517	0.9572	-4.5421	6.1245	-4.895	0.7854	0.9608
Trapezoidal, $\alpha = 30$	0.6614	1.5684	-8.5231	18.5289	-17.145	7.1451	0.9621
Trapezoidal, $\alpha = 36$	0.6781	1.6315	-8.8212	19.0153	-16.458	6.5483	0.9758
Trapezoidal, $\alpha = 42$	0.6798	1.6214	-9.1912	21.4562	-15.564	5.5345	0.9645
Trapezoidal, $\alpha = 48$	0.6896	1.5234	-9.6514	24.5862	-13.548	5.4215	0.9842
Linear, $\alpha = 90$	0.7015	0.9412	-3.5814	2.4586	1.948	-1.8954	0.9513

**Acknowledgements** The author gratefully acknowledges the supports provided by the department of civil engineering, Delhi Technological University, Delhi.

## References

Anderson RM, Tullis BP (2012) Comparison of piano key and rectangular labyrinth weir hydraulics. J Hydraul Eng 138:358–361  
 Anderson RM, Tullis BP (2013) Piano key hydraulics and labyrinth weir comparisons. J Irrig Drain Eng (ASCE) 139:246–253

- Bilhan O, Emiroglu ME, Kisi O (2011) Use of artificial neural networks for prediction of discharge coefficient of triangular labyrinth side weir in curved channels. *J Adv Eng Softw* 42:208–214
- Bos MG (Ed) (1989) Discharge measurement structures. In: International institute for land reclamation and improvement (ILRI) publication, vol 20. Wageningen, The Netherlands
- Crookston BM, Tullis BP (2012a) Arced labyrinth weirs. *J Hydraul Eng (ASCE)* 138:555–562
- Crookston BM, Tullis BP (2012b) Discharge efficiency of reservoir-application specific labyrinth weirs. *J Irrig Drain Eng (ASCE)* 138:564–568
- Crookston BM, Tullis BP (2013) Hydraulic design and analysis of labyrinth weirs. II: nappe aeration, instability, and vibration. *J Irrig Drain Eng (ASCE)* 139:371–377
- Emiroglu ME, Kaya N, Agaccioglu H (2010) Discharge capacity of labyrinth side weir located on a straight channel. *J Irrig Drain Eng (ASCE)* 136:37–46
- Garde RJ, Ranga Raju KG (2000) Mechanics of sediment transportation and alluvial stream problems. Wiley Eastern Limited, New Delhi
- Hay N, Taylor G (1970) Performance and design of labyrinth weir. *J Hydraul Eng (ASCE)* 96:2337–2357
- Kandaswamy P, Rouse H (1957) Characteristics of flow over terminal weirs and sills. *J Hydraul Div* 83:1–13
- Khode BV, Tembhurkar AR, Porey PD, Ingle RN (2010) Determination of crest coefficient for flow over Trapezoidal labyrinth weir. *World Appl Sci J* 12(3):324–329. (ISSN 1818-4952), (© IDOSI Publications, 2011)
- Khode BV, Tembhurkar AR, Porey PD, Ingle RN (2012) Experimental studies on flow over labyrinth weir. *J Irrig Drain Eng ASCE* 138:548-552
- Lux F (1989) Design and application of labyrinth weirs. In: Design of hydraulic structures, vol 89. Balkema, Rotterdam
- Magalhaes A, Lorena M (1989) Hydraulic design of labyrinth weirs. Report no. 736, National Laboratory of Civil Engineering, Lisbon, Portugal
- Martínez J, Reca J, Morillas MT, Ló Pez JG (2005) Design and calibration of a compound sharp-crested weir. *J Hydraul Eng ASCE* 131(2):112–116
- Mohamed HI (2010) Flow over gabion weirs. *J Irrig Drain Eng* 136(8):573–577. (© ASCE 2010)
- Righetti M, Lanzoni S (2008) Experimental study of the flow field over bottom intake racks. *ASCE J Hydraul Eng* 134(1):15–22
- Sobeih MF, Helal EY, Nassralla TH, Abdelaziz AA (2012) Scour depth downstream weir with openings. *Int J Civil Struct Eng* 1(3):259–270
- Tullis BP, Amanian N, Waldron D (1995) Design of labyrinth spillways. *ASCE J Hyd Eng* 121(3):247–255
- Tullis BP, Young JC, Chandler MA (2007) Head-discharge relationships for submerged Labyrinth weirs. *ASCE J Hyd Eng* 133(3):248–253
- Tullis BP, Waldron D (2005) Design of labyrinth spillways. *J Hydraul Eng* 121(3)
- Venkataraman P (1977) Discharge characteristics of an idealized bottom intake. *J Inst Eng* 58(2–3):99
- Yıldız D, Uzuçek E (1996) Modeling the performance of labyrinth spillways. *Int J Hydropower Dams* 3:71–76

# Chapter 21

## Calibrating Coefficients of Emerged Vegetative Open Channel Flow



Priya Shejule, Jnana Ranjan Khuntia, and Kishanjit Kumar Khatua

**Abstract** Vegetation is a crucial element of the river system. In open channel hydraulics, vegetation has a significant effect on flow structure; it offers resistance to the flow and responsible for flood level increase by reducing the carrying capacity of the flood. Researchers throughout the globe have analyzed the resistance provided by vegetation with a theoretical and experimental study. Many flow and channel parameters affect the flow resistance. Out of all these parameters, vegetation is an influential one in vegetative channels. It alters the velocity profiles in an open channel, which affects the roughness coefficients. The roughness coefficients in vegetative channels vary with the flow depths and sections. Therefore, due to the complex structure, it is tedious to come up with a flow model based on previous research. Though it is challenging to determine directly from a field exercise, a laboratory study has been carried out in emergent vegetation at Hydraulics Engineering Laboratory, NITR, to explore the vegetation influence. The Shiono Knight Method (SKM) has been applied to calculate the boundary shear stress and depth-averaged velocity distribution in an open channel flow. For this purpose, three calibrating coefficients, namely bed friction ( $f$ ), dimensionless eddy viscosity ( $\lambda$ ), and transverse gradient for secondary flow ( $\Gamma$ ), have been incorporated to modify the existing SKM. A mathematical model was formulated to find the calibrating coefficients in the channel and compared with the SKM.

**Keywords** Open channel flow · Emergent vegetation · Drag coefficient · Bed friction · Eddy viscosity · Secondary flow coefficient · Depth-averaged velocity · SKM

---

P. Shejule (✉)

Department of Civil Engineering, Indian Institute of Technology Guwahati, Guwahati, Assam 781039, India

J. R. Khuntia

Department of Civil Engineering, St. Martin's Engineering College, Dhulapally, Secunderabad, Telangana 500100, India

P. Shejule · J. R. Khuntia · K. K. Khatua

Department of Civil Engineering, National Institute of Technology, Rourkela, Odisha 769008, India

## 21.1 Introduction

Vegetation offers additional drag forces and hinders the flow capacity of an open channel. Vegetation leads to complex flow structure. It affects the velocity, enlarges the local water level, reduces the flood discharge, and controls the fate of sediments. Vegetation is an essential factor in determining roughness because it affects the flow in a channel. Energy dissipation occurs in a channel due to three factors: (1) bed friction (2) turbulent exchange at the interface responsible for the momentum transfer (3) momentum transfer as a result of mass exchange through subsections (Proust et al. 2009). The most observed influence of vegetation is that it increases the resistance offered to flow and reduces the channel conveyance (Kouwen 1992; Wu et al. 1999). Other vegetation characteristics like vegetation species, density, distribution, flexibility, and the submergence degree of vegetation, affect the channel capacity (Abood et al. 2006). The present study is carried out on a straight simple vegetated rectangular channel. Vegetation in wetlands and open channel strongly influences the flow hindrance, (mean) velocity; mass and turbulence exchange (Ghisalberti and Nepf 2005). Flow resistance coefficient mainly depends on flow depth and discharge proven by Jarvela (2002), who carried out a laboratory study.

For a water resources Engineer, wild growth of vegetation is an inconvenience as it reduces the conveyance of a channel. However, vegetation removal is an expensive process, and it affects the ecological integrity of the river system (Karr 1991).

Vegetation in waterways is classified as follows:

- I. Vegetation naturally occurring on beds and banks of the river.
- II. Artificially planted vegetation.

Velocity in the cross-section varies from section to section due to water surface effects. The velocity distribution in an open channel is three-dimensional and complicated, and it makes the flow modeling difficult (Maghrebi and Givchchi 2009). The hydraulic behavior of flexible submerged vegetation is different from emergent vegetation. Polyethylene plastic strips are used to simulate vegetation (Kouwen et al. 1969). Velocity distribution is considerably impacted by vegetation. When vegetation is introduced in a flowing channel, the vegetation roughness affects the shape of velocity profiles in a stream-wise and vertical direction (Sarma et al. 1983). Khuntia et al. (2016) and Shi et al. (2013) studied the rough bed and vegetation density effect on Manning's coefficient respectively.

Dimensionless geometric and hydraulic factors affects the vegetal drag coefficient (Panigrahi and Khatua 2015). The vertical velocity profile was studied for different discharges and different vegetation densities. Understanding the flow resistance and conveyance capacity is required to determine the stage-discharge characteristics of a reservoir. The Shiono and Knight Method (SKM) (1990) is applied in a two-dimensional approach. This method is obtained after the depth-averaging of the Navier–Stokes equation. Here, the momentum equation is simplified. It is used to derive the depth-averaged velocity and distribution of boundary shear stress. For applying SKM, one has to calibrate factors like ( $f$ ) representing bed shear, ( $I'$ ) representing secondary flow, and ( $\lambda$ ) denoting the lateral shear. Liu et al. (2013) proved that

the prediction of flow velocity and Bed Shear Stress (BSS) are significantly affected by secondary flow, and their ignorance gives inaccurate results. BSS distribution in a channel alters sediment transportation (Yu and Smart 2003).

In the present study, an experiment is performed in a rectangular flume with a rough bed situation at National Institute of Technology, Rourkela, Laboratory.

## 21.2 Theoretical Background

The SKM helps in finding depth-averaged velocity. This method uses the RANS model, i.e., two-dimensional Reynold's Averaged Navier–Stokes equation. The momentum equation is simplified and blended with the continuity equation to get the lateral variation in mean velocity and boundary shear stress. A secondary flow term is introduced in this method, which helps get accurate velocity and BSS results.

For uniform flow, the stream-wise momentum equation is

$$\frac{\partial \tau_{yx}}{\partial y} + \frac{\partial \tau_{zx}}{\partial z} + \rho g S = \rho \left( U \frac{\partial U}{\partial x} + V \frac{\partial U}{\partial y} + W \frac{\partial U}{\partial z} \right) \quad (21.1)$$

where  $x$ ,  $y$ ,  $z$  are the stream-wise, lateral, and vertical directions, respectively.  $\tau_{yx}$  and  $\tau_{zx}$  are the Reynolds stress on the planes perpendicular to  $y$  and  $z$ , respectively;  $\rho$  is the flow density;  $g$  is the acceleration due to gravity;  $S$  is the valley slope;  $U$ ,  $V$ ,  $W$  are the velocity components along the stream-wise, lateral, and vertical directions. Equation (21.1) referred from Liu et al. (2014).

Shiono and Knight (1988) derived the depth-mean-averaged equation by taking the integration of Eq. (21.1) over depth  $H$  as follows:

$$\frac{\partial}{\partial y} \{ H(\rho U V)_d \} = \rho g H S_0 + \frac{\partial H \tau_{yx}}{\partial y} - \tau_b \sqrt{\left( 1 + \frac{1}{s^2} \right)} \quad (21.2)$$

The depth-averaged transverse shear stress ( $\tau_{yx}$ ) is formulated in the form of a lateral gradient of depth mean velocity as follows:

$$\tau_{yx} = \rho \varepsilon_{yx} \frac{\partial U_d}{\partial y} \quad (21.3)$$

where  $\varepsilon_{yx}$  is the depth-averaged eddy viscosity. The eddy viscosity has a dimension of  $\text{m}^2 \text{s}^{-1}$ . It corresponds to local shear velocity  $U^*$  and depth  $H$ , by the dimensionless eddy viscosity coefficient,  $\lambda$ , and expressed as

$$\varepsilon_{yx} = \lambda H U^* \quad (21.4)$$



But, the local shear velocity  $U^* = \sqrt{\frac{\tau_b}{\rho}}$  is influenced by the free shear-layer-turbulence and the secondary flows. The Darcy–Weisbach friction factor  $f = \frac{8\tau_b}{\rho U_d^2}$  is linked to  $U^*$  and  $U_d$ , giving

$$U^* = \sqrt{\frac{1}{8}} f U_d \tag{21.5}$$

The depth-averaged eddy viscosity in (21.1) then given as

$$\varepsilon_{yx} = \lambda H \sqrt{\frac{1}{8}} f U_d \tag{21.6}$$

Substituting (21.5) and (21.3) into (21.2), we get the depth-averaged expression for stream-wise Reynold’s Averaged Navier–Stokes equation as follows:

$$\rho g H S_0 - \frac{1}{8} \rho f U_d^2 \sqrt{\left(1 + \frac{1}{s^2}\right)} + \frac{\partial}{\partial y} \left\{ \rho \lambda H^2 \sqrt{\frac{1}{8}} f U_d \frac{\partial U_d}{\partial y} \right\} = \frac{\partial}{\partial y} \{ H(\rho U V)_d \} \tag{21.7}$$

$H$  = water depth;  $S_0$  is the bed slope;  $U_d$  = depth-averaged stream velocity,  $f$  is Darcy–Weisbach friction factor;  $U, V$  are the velocity components;  $S$  represents the side slope of the channel, and  $\lambda$  = dimensionless eddy viscosity, respectively.

The above form is the clear and reduced version of the SKM. The right side term  $\frac{\partial}{\partial y} \{ H(\rho U V)_d \}$  indicates secondary current ( $\Gamma$ ). On the left side, the first term denotes the gravity term in uniform flow, the second term represents Reynold’s shear stress, and the last term arises due to the bed shear.

Secondary current ( $\Gamma$ ) relies on two factors:

1. The average boundary shear stress represented as ( $\tau_{avg}$ ) and
- 2, Average boundary shear stress per unit length of the (compound) channel denoted as ( $\rho g H S_0$ ).

The reason is that the secondary current flows significantly affect boundary shear stress distribution and the depth average velocity.  $k$  is a factor expressed as the ratio of average boundary shear stress per unit length and average boundary shear stress per unit length of the compound channel. In the case of variable depth, flow depth is taken as average depth all through the domain. So here,  $k$  is given by

$$k = \frac{\tau_{avg}}{\rho g H S_0} \tag{21.8}$$

$\Gamma$  changes along with the flow depth; therefore,  $k$  is represented as a function of dimensionless hydraulic and geometric parameters. In above equation  $\rho g H S_0$  is called as secondary flow factor. Devi and Khatua (2016) gave a simplified formula for  $\tau$  as follows:

$$\Gamma = \rho g H S_0 (1 - k) \quad (21.9)$$

It is observed that the above equation depends on ( $f$ ) representing bed shear, ( $\Gamma$ ) representing secondary flow, and ( $\lambda$ ) representing the lateral shear.

### 21.3 Model Parameters

For applying the SKM approach, it is necessary to calculate three critical factors such as bed friction ( $f$ ), non-dimensional eddy viscosity ( $\lambda$ ), and transverse gradient for secondary flow ( $\Gamma$ ).

Depth-averaged velocity and boundary shear stress are obtained by experimenting in a laboratory using ADV. The Darcy–Weisbach friction factor is then back computed from the obtained experiment (Tang and Knight 2009).

$$f = \frac{8gn^2}{R^{0.33}} \quad (21.10)$$

where  $f$  is the Darcy–Weisbach friction factor,  $n$  is the manning's roughness coefficient,  $g$  represents acceleration due to gravity, and  $R$  represents hydraulic radius.

Dimensionless eddy viscosity is a constant and given by expression as follows:

$$\varepsilon_{yx} = \lambda H U^* \quad (21.11)$$

where  $\varepsilon_{yx}$  is the depth-averaged eddy viscosity;  $H$  represents flow depth;  $U^*$  denotes shear velocity; and  $\lambda$  represents dimensionless eddy viscosity.

Secondary flow term ( $\Gamma$ )

Secondary flow arises because of velocity fluctuations in a turbulent flow. Shiono and Knight (1988) experimented and commented that depth-averaged velocity fluctuates linearly in the lateral direction. Factor  $k$  depends on the geometric and hydraulic parameter given by Eq. (21.8). Thus, secondary flow  $\Gamma$  can be expressed by Eq. (21.9) as

$$\tau = \rho g H S_0 (1 - k)$$

## 21.4 Experimental Setup

The experiment is conducted in a rectangular flume available at the NIT Rourkela laboratory. Rectangular flume has a length of 12 m; flume width 0.6 m and depth 0.6 m. The rectangular flume has a testing section made up of glass. The walls and bottom of the flume are made of mild steel. The rigid grass is fixed along the channel bed to impart roughness. The longitudinal slope denoted by  $S_0$  was set to 0.0012, i.e., 1.2 cm in 10 m and remained constant all through the experiment. The top view of the experimental channel is given in Fig. 21.1. The cross-section of experimental rectangular channel is shown in Fig. 21.2. Point gauges are fixed to measure the flow depth. The test section is 10 m from upstream, where flow stabilizes and uniform flow is observed. A tailgate is installed downstream to achieve uniform flow conditions (Khuntia et al. 2018, 2019).

For supplying water into the channel, an overhead tank is built upstream of a flume. The volumetric tank is constructed at the flume downstream to measure discharge at different depths (Shejule 2019) (Fig. 21.2).

A SonTek Micro-Acoustic Doppler Velocimeter (ADV) of 16 MHz is used to measure flow fields. 50 Hz is the maximum sampling rate, and data acquisition time

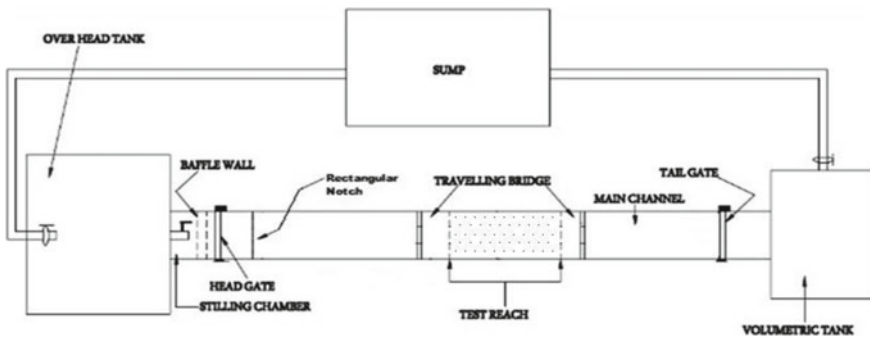


Fig. 21.1 Top view of the experimental flume (channel), hydraulic engineering lab, NIT Rourkela

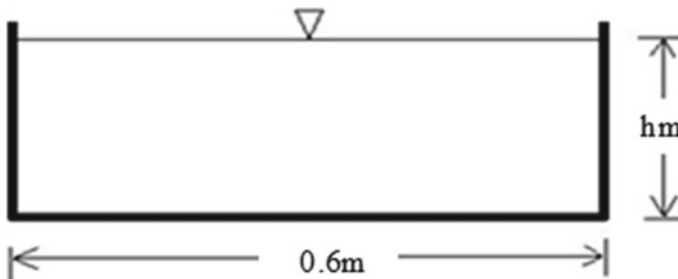


Fig. 21.2 Cross-section of the experimental rectangular channel

**Table 21.1** The roughness and geometrical parameters of a channel

Serial no	Description	Parameter
1.1	Channel description	Straight
1.2	Channel section geometry	Rectangular
1.3	base width ‘b’ of channel	0.6 m
1.4	Depth of channel	0.6 m
1.5	Bed slope ‘ $S_0$ ’	0.0012
1.6	Flume length	12 m
1.7	Test channel length ‘X’	10 m
1.8	Bed surface feature	Rough (Fixed rigid grass)
1.9	Flow condition	Steady flow

is 60 s. ADV sampling volume is placed at a distance of 5 cm below the down probe. 5 cm distance among the probe and sampling volume is considered to minimize flow hindrance. ADV measures the directional velocities  $U, V, W$  in  $x-, y-, z$ -directions, i.e., along, lateral and vertical to the flume bottom, respectively. Steady flow condition is maintained throughout the experiment. To compute velocities at the boundary along channel periphery, ‘Preston tube’ with outer diameter of 4.77 mm is used. Some important channel attributes are presented in the table below (Table 21.1 and Fig. 21.3).



**Fig. 21.3** Photograph of the straight rectangular flume

### 21.5 Results

The variation of depth-averaged velocity along a lateral-distance of a rectangular straight channel is obtained using Conveyance Estimation System (CES) software. It is based on one-dimensional RANS (Reynold’s Averaged Navier–Stokes) approach (Figs. 21.4, 21.5, 21.6, and 21.7).

Graphs are plotted to get the variation in calibrating coefficients  $f$ ,  $\lambda$ , and  $k$  against lateral distance (see Figs. 21.8, 21.9, and 21.10).

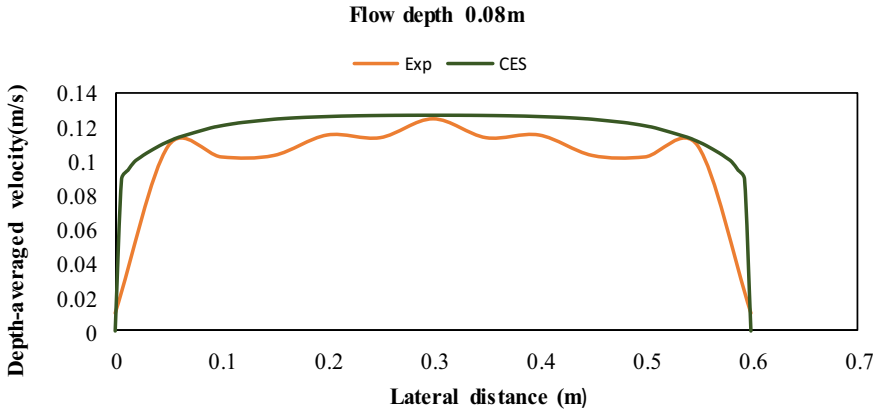


Fig. 21.4 Depth-averaged velocity variation in a rectangular channel for flow depth 0.08 m

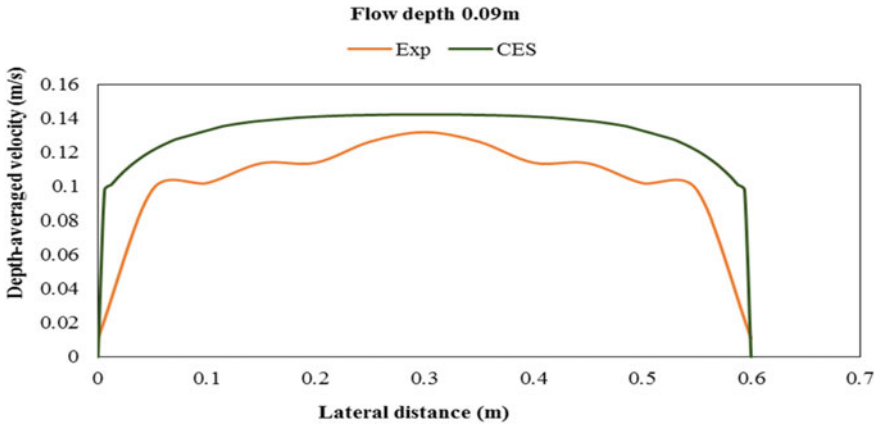


Fig. 21.5 Depth-averaged velocity variation in a rectangular channel for flow depth 0.09 m

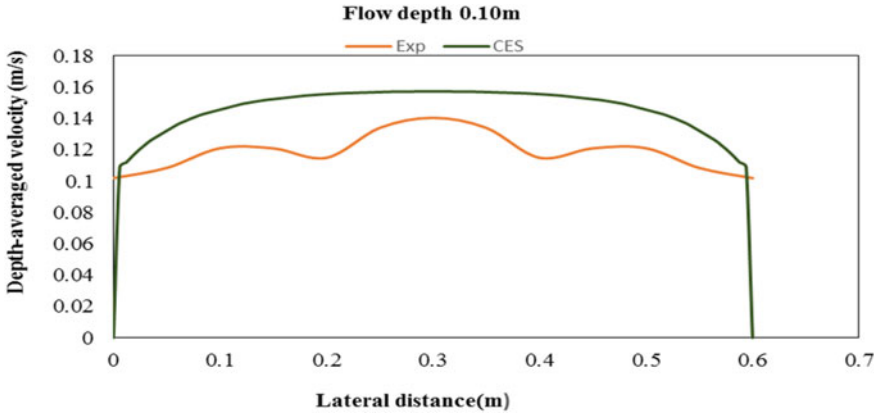


Fig. 21.6 Depth-averaged velocity variation in a rectangular channel for flow depth 0.10 m

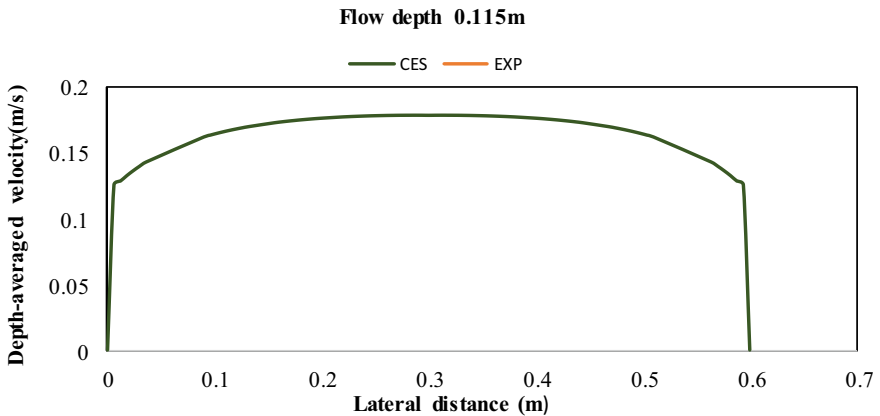


Fig. 21.7 Depth-averaged velocity variation in a rectangular channel for flow depth 0.115 m

## 21.6 Conclusions

1. Experiment on emergent vegetative open channel flow has been performed to find calibrating coefficients used in the RANS equation. These coefficients are helpful to measure the depth average velocity distribution.
2. The friction factor is found to be of uniform value in a lateral direction of the channel. The friction factor value is higher for low depth of flow and lower for high depth of flow.
3. Secondary flow coefficients show an abrupt change for low flow depth in the lateral direction due to vegetation. For high flow depth, it is observed to be of uniform value.

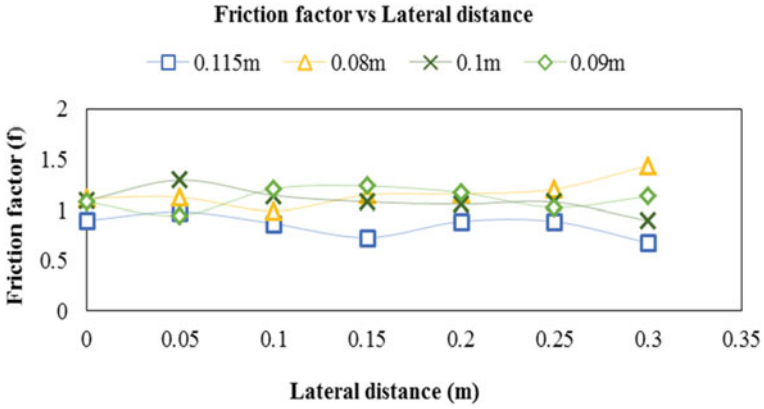


Fig. 21.8 Variation of friction factor against lateral distance

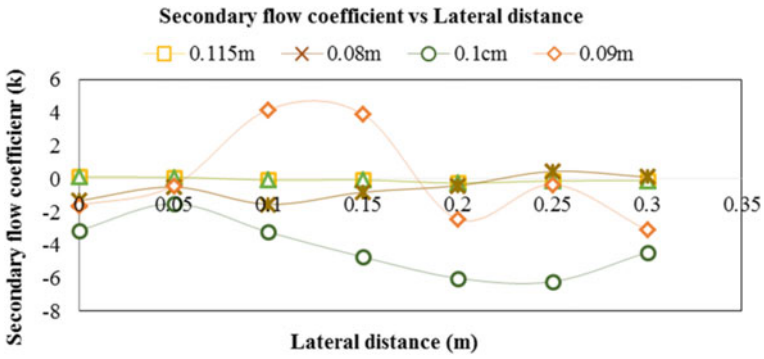


Fig. 21.9 Variation of Secondary flow against lateral distance

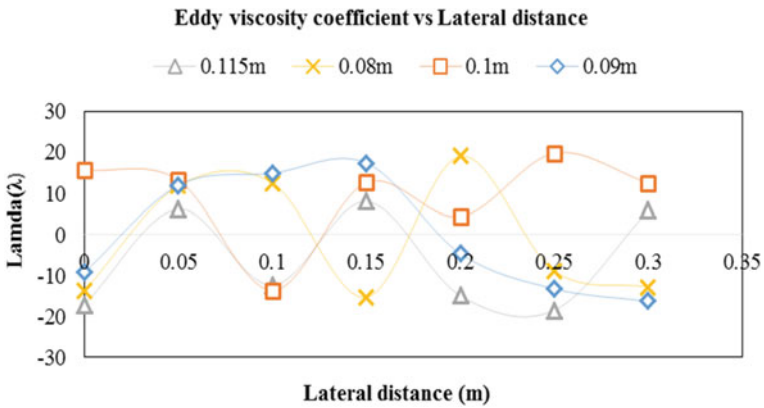


Fig. 21.10 Variation of eddy viscosity against lateral distance

4. Similar to the secondary coefficient, an abrupt change in eddy viscosity is observed for low flow depth.
5. The depth-averaged velocity results obtained using the RANS equation and from the CES software are compared. CES is found to overpredict depth-averaged velocity because of improper accounting of calibrating coefficients. The modeling of calibrating coefficients needs to be done.

## References

- Abood MM, Yusuf B, Mohammed TA, Ghazali AH (2006) Manning roughness coefficient for grass-lined channel. *J Sci Technol* 13(4):317–330
- Devi K, Khatua KK (2016) Prediction of depth averaged velocity and boundary shear distribution of a compound channel based on the mixing layer theory. *Flow Meas Instrum* 50:147–157
- Ghisalberti M, Nepf H (2005) Mass transport in vegetated shear flows. *Environ Fluid Mech* 5(6):527–551
- Jarvela J (2002) Flow resistance of flexible and stiff vegetation: a flume study with natural plants. *J Hydrol* 269(1–2):44–54
- Karr JR (1991) Biological integrity: a long-neglected aspect of water resource management. *Ecol Appl* 1(1):66–84
- Khuntia JR, Devi K, Khatua KK (2016) Variation of local friction factor in an open channel flow. *Indian J Sci Technol* 9(46):1–6
- Khuntia JR, Devi K, Khatua KK (2018) Prediction of depth-averaged velocity in an open channel flow. *Appl Water Sci* 8(6):172
- Khuntia JR, Devi K, Khatua KK (2019) Turbulence characteristics in a rough open channel under unsteady flow conditions. *ISH J Hydraul Eng*, 1–12. <https://doi.org/10.1080/09715010.2019.1658549>
- Kouwen N (1992) Modern approach to design of grassed channels. *J Irrig Drain Eng* 118(5):733–743
- Kouwen N, Unny TE, Hill HM (1969) Flow retardance in vegetated channels. *J Irrig Drain Div* 95(2):329–344
- Liu C, Luo X, Liu X, Yang K (2013) Modelling depth-averaged velocity and bed shear stress in compound channels with emergent and submerged vegetation. *Adv Water Resour* 60:148–159
- Liu C, Wright N, Liu X, Yang K (2014) An analytical model for lateral depth-averaged velocity distributions along a meander in curved compound channels. *Adv Water Resour* 74:26–43
- Maghrebi MF, Givehchi M (2009) Estimation of depth-averaged velocity and boundary shear stress in a triangular open channel. *J. Water Wastewater* 2:71–80
- Panigrahi K, Khatua KK (2015) Prediction of velocity distribution in straight channel with rigid vegetation. *Aquatic Procedia* 4:819–825
- Proust S, Bousmar D, Riviere N, Paquier A, Zech Y (2009) Non-uniform flow in compound channel: A 1-D method for assessing water level and discharge distribution. *Water Resour Res* 45(12)
- Sarma KV, Lakshminarayana P, Rao NL (1983) Velocity distribution in smooth rectangular open channels. *J Hydraul Eng* 109(2):270–289
- Shejule PA (2019) Calibrating coefficients of emerged vegetative open channel flow. MTech thesis, National Institute of Technology, Rourkela
- Shi JZ, Li YH, Hughes JM, Zhao M (2013) Hydrological characteristics of vegetated river flows: a laboratory flume study. *Hydrol Sci J* 58(5):1047–1058
- Shiono K, Knight DW (1988) Two-dimensional analytical solution for a compound channel. In: Proceedings of 3rd international symposium on refined flow modelling and turbulence measurements, pp 503–510. (July 1988)



- Tang X, Knight DW (2009) Analytical models for velocity distributions in open channel flows. *J Hydraul Res* 47(4):418–428
- Wu FC, Shen HW, Chou YJ (1999) Variation of roughness coefficients for unsubmerged and submerged vegetation. *J Hydraul Eng* 125(9):934–942
- Yu G, Smart G (2003) Aspect ratio to maximize sediment transport in rigid bank channels. *J Hydraul Eng* 129(12):927–935

## Chapter 22

# Trend Analysis of Water Flow and Suspended Sediment Flow of Lower Godavari Basin, India



Madhura Aher and S. M. Yadav

**Abstract** In this research, long term daily variation in daily water flow and sediment flow of Lower Godavari Basin is focused. The records of water discharge as well as suspended sediment concentration are collected from six hydrological stations located on Lower Godavari Basin for different time periods of 1969–2015. For analysis, the daily mean values of water discharge  $Q$  ( $\text{m}^3/\text{sec}$ ) and suspended sediment transport rate  $Q_s$  ( $\text{t}/\text{day}$ ) are used. The daily mean water discharge and sediment discharge series were analysed for auto correlations prior to apply trend test. The nature of trend is analysed by using Mann–Kendall test, Sen’s slope estimator test at the significance level of 5%. The test results revealed that out six stations five stations reported decreasing trend in water discharge and two stations (Jagdarpur and Nowrangpur) show significant decreasing trend and remaining one station (Konta) shows increasing trend. Similarly, for sediment discharge, results indicate that all the six stations that reported decreasing trend with three stations (Nowrangpur, Perur and Polavaram) show significant decreasing trend. The abrupt change analysis is carried out at 5% significance level for water discharge and sediment discharge time series. The significant abrupt change occurs from year 1995 for Jagdarpur and Nowrangpur station. Significant decline in sediment discharge is observed for station Jagdarpur, Nowrangpur and Polavaram in year 1994, 1994, 1995, respectively. The significant increasing or decreasing trend is indication of increased human activities and Climatological variations in the catchment area of Lower Godavari Basin.

**Keywords** Lower Godavari basin · Water discharge · Sediment discharge · Mann–Kendall test · Changes point

---

M. Aher (✉) · S. M. Yadav (✉)  
Civil Engineering Department, Sardar Vallabhai National Institute of Technology, 395007, Surat,  
Gujarat, India

## 22.1 Introduction

River discharge along with sediment flow delivers important information to understand the erosion process occurred in the catchment area of basin (Siakeu et al. 2004). The combined effects of modification in climatological parameters such as precipitation, temperature with increased human actions in river basins are responsible for global and regional sediment fluctuation. Walling and Fang (2003) analysed the nature of trends of sediment loads of many important rivers in the world, and found that 50% of the rivers exhibits significantly decreasing or increasing trends. And the maximum rivers are showing intensely decreasing trends. Such alterations can be results of changes in basin precipitation, due to climate change, intensive anthropogenic impacts such as land use changes, deforestation; mining activities and construction of numerous dams. Growing quantity of the river sediment is due to soil erosion process and on the other hand reducing the same quantity due to retention of sediments into the reservoirs (Syvitski et al. 2003, Wang et al. 2012). The primary cause of reduction in sediment load is owing to the construction of dams (Vorosmarty et al. 2003, Walling 2006, 2009). The development of deltas and estuaries, and the coastal erosion can also be studied through the nature of sediment supply (Yang et al. 2002, Mayo et al. 2012, Peng et al. 2010). Drops in sediment supply from rivers to the ocean directly an outcome of the retreat of deltas globally (Day et al. 2009). The Nile River in Egypt (Wiegel 1996); the Ebro River in Spain (Sánchez-Arcilla et al. 1998); the Yangtze, Yellow and Pearl Rivers in China (Yang et al. 2002, Wang et al. 2007); the Colorado River in the United States of America (Carriquiry et al. 2013) are also showing the decreasing trend in terms of sediment transport.

The rivers flowing through the tropical regions of India are very significant because of due to the ecology of coastal area and the thickly populated economic regions which are very much depended on these rivers (Panda et al. 2011). In the broad sense, the rivers in Indian are divided into two systems on the basis of morphotectonic difference and due to this it demonstrated huge difference in terms of sediment supply. It can be evident through, as the Ganga River systems transport annual average sediment load of 2390 t/km<sup>2</sup> and those that of peninsular river systems carry sediment load 216 t/km<sup>2</sup> (Milliman and Meade 1983). The tropical rivers of India receive the maximum rainfall during monsoon season that is near about 80% of the yearly rainfall, and it is having impact on streamflow of the river as well as amount of sediment load carrying capacity (Kale 2002). In opposite to the tropical rivers, the Gangetic rivers carry the continuous flow irrespective of a particular season because of melting of glaciers of from the mountains of Himalayan regions.

The aim of this research is to recognize the nature of trend in the stream flow and suspended sediment flow of the Lower Godavari Basin. The data period from the year 1969–2015 is used for the analysis purpose. Six stream gauging stations located on the Lower Godavari Basin and its tributaries are taken for the consideration. The daily data of water discharge and suspended sediment concentration is collected from the Central water Commission of India (CWC). The frequency of discharge observation of the river is daily and the concentration of suspended sediment is once in a week in

for other than monsoon period, i.e. from October to May and on the daily basis in the monsoon period, i.e. from June to September. Most part of the Lower Godavari Basin is dry from the month of December to June, as the basin receives the rainfall from south west monsoon from the month of June to September. River carries considerable amount of discharge in these months. The amount of the sediment load carried by the tropical river basin of India are mainly influenced due to the different types of rock formations in the catchment area of basin and then it secondarily affected due to the channel slope. The Godavari Basin experiences hot and humid climate for maximum time in the year. The half west part of the basin is covered with the Deccan trap which contributes 50% of the yearly sediment load. The hard rocks of portion in the basin are around 39% that contribute 13% of sediment load and sedimentary rock formation of the Godavari Basin 33% of the yearly sediment load (Panda et al. 2011).

## 22.2 Study Area and Data Set

The Godavari River is third main river in India in relations with its drainage area. Along with some other east flowing major rivers such as Cauvery, Krishna, Brahmani, Mahanadi, Godavari River flows into Bay of Bengal. The Godavari River starts from at Trimbakeshwar village situated in the Nashik district of Maharashtra. From the Arabian Sea, the elevation of river from is 1,067 m. The total length of Godavari River is about 1,465 km. The Godavari River flows through various districts of Maharashtra, Telangana, Andhra Pradesh, Chhattisgarh and Odisha, Karnataka, and minor regions in Madhya Pradesh, and Union territory of Pondicherry. The catchment area of Godavari Basin is 3, 12,812 Sq.km out of that of Lower Godavari Basin is covering area of 24,869 Sq.km. The Godavari Basin extends in between 73°24' and 83°4' east longitudes and 16°19' to 22°34' north latitudes. The Godavari Basin takes maximum of its precipitation during the months from June to September. The mean monsoon and annual rainfall over the basin is 83.5 cm 107.5 cm, respectively. The annual variations in precipitation in between the monsoon period are quite huge varying from 643 mm in the year 1974–1221 mm in the year 1959 (Fig. 22.1).

Due to this there is wide huge variation in annual rainfall in many parts that lies in the basin experiences either frequent floods or severe droughts. Mean annual temperature of the basin varies from 25 to 27 °C. According to IPCC report 2014, Godavari Basin is one of the basins that lay in the category of rivers which will undergo climate changes in the twenty-first century. The major soils formations in the basin are red soil, black soil, alluvium, mixed soils, alkaline soil and laterite soil. Godavari River basin is also covered with variety of land use. The data set from 06 hydrological stations located in Lower Godavari Basin was collected and analysed in the study.

Six streamflow gauging stations namely Polavaram, Perur and Konta are the stations located on the Lower Godavari Basin and Pathagudem, Nowargpur and Jagdalpur stations are located on Sabri and Indravati Rivers (Table 22.1). Polavaram is the last gauging station after which Godavari River confluences into Bay of Bengal.



Fig. 22.1 Location of Godavari River Basin and gauging stations

Table 22.1 List of gauging stations on Lower Godavari Basin

Sr.no	Name of station	Basin	Latitude	Longitude	Series(years)
1	Polavaram	Godavari	17 <sup>0</sup> 50'54"	81 <sup>0</sup> 38'55"	43
2	Perur	Godavari	18 <sup>0</sup> 32'52"	80 <sup>0</sup> 23'04"	46
3	Pathagudaem	Godavari	18 <sup>0</sup> 50'54"	80 <sup>0</sup> 20'52"	46
4	Nowargpur	Godavari	19 <sup>0</sup> 11'56"	82 <sup>0</sup> 31'36"	37
5	Konta	Godavari	17 <sup>0</sup> 49'14"	81 <sup>0</sup> 23'20"	45
6	Jagdalpur	Godavari	19 <sup>0</sup> 66'27"	82 <sup>0</sup> 01'23"	46

## 22.3 Analysis Methods

### 22.3.1 Trend Analysis

The non-parametric trend test, i.e. Mann–Kendall test was initially suggested by Mann in 1945 and then the test is reviewed by Kendall in 1948. The test does not assume any type of distribution, and it is one of the advantages (Serrano and Garcla 1999). The MK test is not sensitive to the outliers as well as any missing values in the data. And the performance of test is good as compared with the other parametric tests in which the data distribution is not normal. Thus, it is extremely suggested by the World Meteorological Organization for the use (Mitchell 1966).

The equations of Mann–Kendall test statistics are as given as below. The standardized Z statistics is calculated as

$$Z = \begin{cases} \{S - 1/\sqrt{S}\} & \text{if } S > 0 \\ \{0\} & \text{if } S = 0 \\ \{(S + 1)/\sqrt{S}\} & \text{if } S < 0 \end{cases} \tag{22.1}$$

where

$$S = \sum_{j=1}^{n-1} \sum_{i=j+1}^n \text{sgn}(x_j - x_i) \tag{22.2}$$

$$\text{sin}(x_j - x_i) = \begin{cases} +1 & \text{if } x_j > x_i \\ 0 & \text{if } x_j = x_i \\ -1 & \text{if } x_j < x_i \end{cases} \tag{22.3}$$

$$\text{Var}(S) = \left\{ n(n - 1)(2n + 5) - \sum_{(i=1)}^n t_i(i - 1)(2i + 5) \right\} / 18 \tag{22.4}$$

where  $t_i$  denotes the number of ties of extent  $i$ .

$x_j$  and  $x_i$  are the sequential data points at times  $j$  and  $i$ , respectively,  $j > i$ ;  $n$  is the length of the time series;  $t_i$  is the  $i$  th group; and represents the summation of all ties (Gilbert 1987; Xu et al. 2004).

The positive value of  $Z$  designates an upward trend and Negative value  $Z$  designates downward trend. The null hypothesis  $H_0$  indicates absence of any trend in the time series, where magnitude of slope is zero. The  $H_a$  is alternate hypothesis is when accepted; it is either increasing or decreasing trend in the time series. 5% significance level was used for analysis.

### 22.3.2 Change Point Analysis

The non-parametric test suggested by Pettit in 1979 is used to evaluate the point of significant variation in the data set (Kiely et al. 1998, 1999). This technique identifies one unknown change point by considering a sequence of random variables  $X_1, X_2, \dots, X_T$  which may have a change point at  $N$  if  $X_t$  for  $t = 1, 2, \dots, N$  has a common distribution function  $F_1(x)$  and  $X_t$  for  $t = N + 1, \dots, T$  has a common distribution function  $F_2(x)$ , and  $F_1(x) \neq F_2(x)$  (Pettitt 1979; Dou et al. 2009).

The non-parametric statistic are calculated as follows:

$$Kt = \max_{1 \leq t \leq T} |U_{t,T}| \tag{22.5}$$

$$U_{t,T} = U_{t-1,T} + \sum_{(j-1)}^T \text{sgn}(X_t - X_j) \quad (22.6)$$

For  $t = 2, \dots, T$   
where

$$\sin\theta = \begin{cases} +1\theta > 0 \\ 0 \text{ if } \theta = 0 \\ -1\theta < 0 \end{cases} \quad (22.7)$$

And

$$p = 2 \exp\{-6 k_T^2 / -6 k_T^2 (T^3 - T^2)\} \quad (22.8)$$

When  $p$  is smaller than the 5% significance level, the obtained trend can be said to significant. The time,  $t$ , when  $K_t$  occurs is the change point time. The MK test and Pettit tests consider that model data of streamflow and suspended sediment discharge time series is not serially correlated and not robust against autocorrelation.

### 22.3.3 Sen's Slope Estimator

The degree of the trend is assessed using nonparametric technique suggested by Sen (1968).

Sen's slope estimator ( $\beta$ ) specified by formula

$$\beta = \text{Median}\left(\frac{x_j - x_i}{j - i}\right) \text{ for } j > i \quad (22.9)$$

## 22.4 Results

### 22.4.1 Mann-Kendall Test

#### 22.4.1.1 Water Discharge

The outcomes of the MK test and Sen's slope estimator's for gradual change in water flow show declining trends at the Lower Godavari Basin from 1969 to 2016 (Table 22.2). For all the station except Konta, the nature of trend in streamflow is found out as a decreasing as value  $Z$  is obtained as negative for all the stations. For station

**Table 22.2** Mann–Kendall test results for water discharge

Sr.No	Station	T	$\rho$ -Value	Sen's slope( $\beta$ ) value	S	Var	Z <sub>m</sub> k	Trend	Significance level
1	<b>Jagdarpur</b>	-0.4	<b>0.00</b>	-1.87	-378	9775	-3.81	<b>Decreasing</b>	<b>Significant</b>
2	Konta	0.099	0.34	1.56	98	10,450	0.94	Increasing	Not significant
3	<b>Nowrangpur</b>	-0.299	<b>0.01</b>	-1.58	-199	5845	-2.58	<b>Decreasing</b>	<b>Significant</b>
4	Pathagudem	-0.055	0.59	-1.80	-57	11,155	-0.53	Decreasing	Not significant
5	Perur	-0.115	0.26	-15.09	-119	11,155	-1.11	Decreasing	Not significant
6	Polavaram	-0.111	0.28	-16.38	-115	11,155	-1.07	Decreasing	Not significant

Values with significant trend are shown in bold



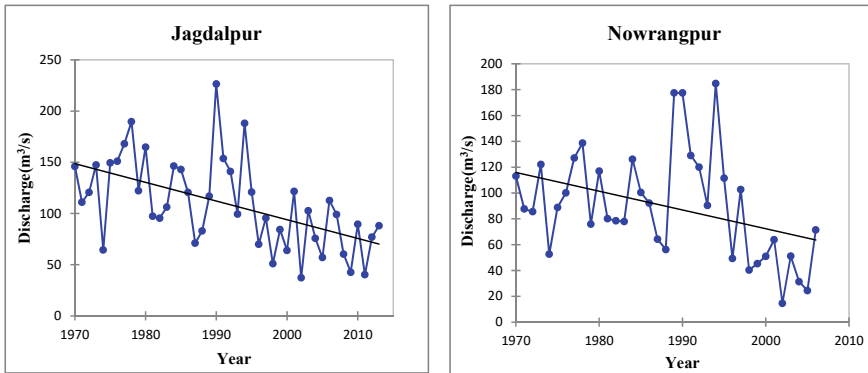


**Fig. 22.2** Result of MK test at Jagdalpur and Nowrangpur stations

Jagdalpur and Nowrangpur, the estimated  $P$  value is 0.00 and 0.015, respectively, these two values are measured as statistically significant, because the estimated  $P$  value is less than significance level 5%. The  $\beta$  value also shows negative slope at the Jagdalpur, Nowrangpur, Pathagedum, Perur and Polavaram stations that indicates that the trend is decreasing. And for station Konta, the ( $\beta$ ) values obtained as 1.56 indicate the increasing trend in water discharge.

The nature of trend with significant decreasing from the year 1969–2015 is represented in Fig. 22.2. Out of six stations five stations are representing decreasing trend and one station shows increasing trend. The  $Z$  values obtained at Jagdalpur and Nowrangpur stations are  $-3.81$  and  $-2.58$ , respectively. And the magnitude of this decreasing trend is  $-1.87$  and  $-1.58$ , respectively, for Jagdalpur and Nowrangpur stations.

#### 22.4.1.2 Sediment Discharge

The MK test and Sen's slope estimator's results for sediment discharge are summarized in Table 22.3. And indicates decreasing trends for all the gauging stations in the Lower Godavari River Basin. For all gauging station  $Z$  value is negative, i.e. trend is decreasing. Statistically decreasing trend is found in sediment discharge for stations Nowrangpur, Perur and Polavaram as the estimated  $p$  values are 0.000, 0.028,  $<0.0001$ , respectively, which are less than the significance level 5%.

The gauging stations Jagdalpur, Konta and Pathagudem also show the declining trend in sediment discharge but it is not considered as statistically significant because the obtained  $p$  values are more than the considered significance level (0.005).

The statistically significant reducing trend plots are drawn in Fig. 22.3. The estimated  $Z$  values at three stations are  $-3.28$ ,  $-2.19$  and  $-4.14$  for Nowrangpur, Perur and Polavaram stations, respectively. All the six stations are representing decreasing trend.

**Table 22.3** Mann-Kendall trend test results for sediment discharge

Sr.No	Station	T	p-value	Sen's slope( $\beta$ ) value	S	Var	Z <sub>mk</sub>	Trend	Significance level
1	Jagdulpur	-0.095	0.36	-175.08	-322	9775	-3.24	Decreasing	Not significant
2	Konta	-0.095	0.36	-128.39	-94	10,450	-1.24	Decreasing	Not significant
3	<b>Nowrangpur</b>	-0.441	<b>0.00</b>	-288.09	-294	5846	-3.28	<b>Decreasing</b>	<b>Significant</b>
4	Pathagudem	-0.114	0.268	-287.77	-118	11,154	-1.1	Decreasing	Not significant
5	<b>Perur</b>	-0.225	<b>0.028</b>	-342.00	-233	11,155	-2.19	<b>Decreasing</b>	<b>Significant</b>
6	<b>Polavaram</b>	-0.424	<b>&lt;0.01</b>	-7810	-439	11,155	-4.14	<b>Decreasing</b>	<b>Significant</b>

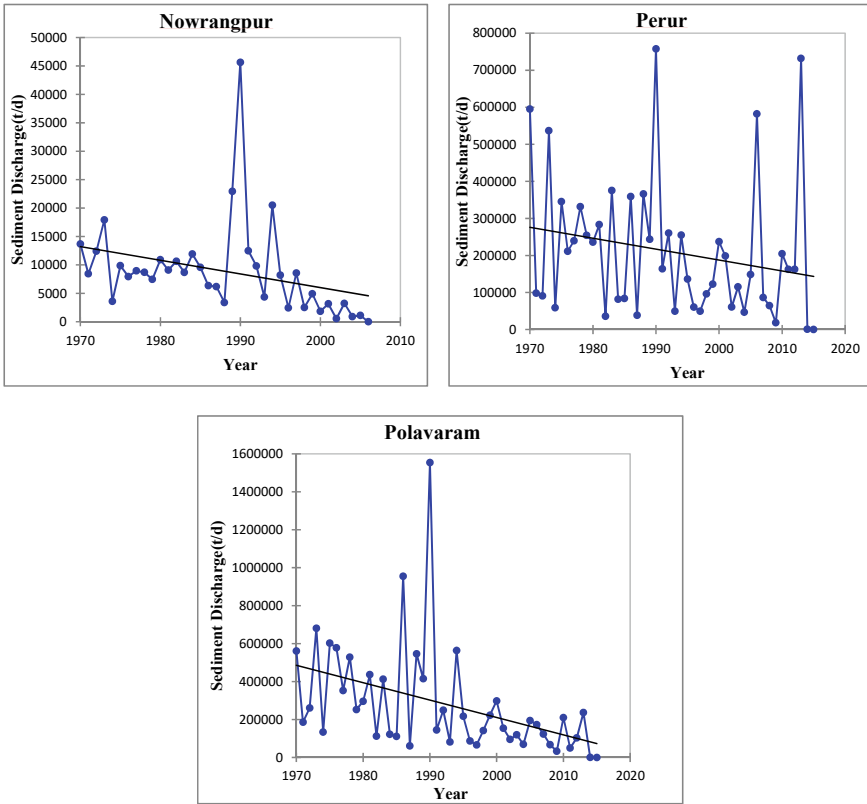


Fig. 22.3 Result of MK test at Nowrangpur, Perur and Polavaram stations

Table 22.4 Change point analysis for water discharge

Sr.no	Station	Series length	$K_T$ Value	$\rho$ -Value	Shift	T
1	Jagdapur	1969–2013	370	<0.0001	Downward	1995
2	Konta	1969–2014	126	0.896	Downward	1974
3	Nowrangpur	1969–2006	248	0.001	Downward	1995
4	Pathagudem	1969–2015	88	0.166	Downward	2013
5	Perur	1969–2015	119	0.664	Downward	1990
6	Polavaram	1969–2005	130	0.886	Downward	1995

## 22.4.2 Change Point Analysis

### 22.4.2.1 Water Discharge

The results of Pettit test of water discharge are given in Table 22.4. The test is carried out at the 0.05 significance level. There is no major sudden change found out at stations Konta, Pathagudem, Perur and Polavaram. It is observed that at stations Jagdalpur and Nowrangpur the statistically abrupt change occurred. And the transition year for both the stations Jagdalpur and Nowrangpur is 1995. The overall transition period for water discharge is 1974–2013.

### 22.4.2.2 Sediment Discharge

The results of Pettit test in sediment discharge are given in Table 22.5. The test is carried out at the 0.05 significance level. The significant change in sediment discharge is observed at the stations Jagdalpur, Nowrangpur and Polavaram. And the transition years for these three stations are 1994, 1994 and 1995, respectively.

## 22.5 Discussion

Mann–Kendall trend test results express that no significant increasing or decreasing trend in water discharge except at Jagdalpur and Nowrangpur stations. Sediment discharge shows significant declining trend at Nowrangpur, Perur and Polavaram stations. It is observed that at station Jagdalpur, water discharge is significantly reduced and sediment discharge also decreased from year 1969–2015 but not significantly. Now for station Polavaram which is the last measuring station on Lower Godavari River though water discharge is not significantly reduced but sediment discharge is reduced significantly. Same is the case with station Perur. For station Nowrangpur, the water discharge and sediment discharge both reduced significantly from year 1969–2006.

**Table 22.5** Change point analysis for sediment discharge

Sr.no	Station	Series length	$K_T$ Value	$\rho$ -Value	Shift	T
1	<b>Jagdalpur</b>	1969–2013	375	<b>&lt;0.0001</b>	Downward	1994
2	Konta	1969–2014	192	0.253	Downward	1992
3	<b>Nowrangpur</b>	1969–2006	264	<b>0.000</b>	Downward	1994
4	Pathagudem	1969–2015	192	0.299	Downward	1995
5	Perur	1969–2015	229	0.102	Downward	1992
6	<b>Polavaram</b>	1969–2005	350	<b>0.001</b>	Downward	1995

After conducting gradual change analysis with MK test, change point analysis is carried out for water discharge as well as sediment discharge. The results indicate that significant change is observed for the water discharge excluding at stations Jagdalpur and Nowrangpur and for sediment discharge, at all the stations except Jagdalpur and Nowrangpur and Polavaram.

### ***22.5.1 Controlling Factors for Water Discharge and Sediment Discharge***

#### **22.5.1.1 Basin Geology**

The rock formations are the key governing factor for the sediment transport. The rock formation of Godavari Basin is classified into three distinct types, i.e. Granites and hard rocks 39%, Deccan traps (48%) and Sedimentary rocks (13%). The sedimentary rocks are located in central as well as lower portion of the basin is Precambrian and Godawana age (Biksham et al. 1988). Sabri and Indravati which are main tributaries of Lower Godavari Basin flowing through granite and vary solid rocks contribute around 16% of yearly sediment load (Biksham et al. 1988). Sabri and Indravati basins consist of scattered existences of sedimentary rock formation.

#### **22.5.1.2 Discharge**

The relative importance of discharge with amount of sediment transport of the river basins has been explored by many researchers. According to Biksham, increase in water discharge in the river may not also be always increasing the sediment transport of the river and on the opposing there are numerous cases that elaborate that with the increase in river discharge had really caused less sediment transport.

#### **22.5.1.3 Impact of Rainfall (Climate) Variability**

Goswami et al. stated that the frequency as well as magnitude of extreme rainfall events is increased in the central part of India that is connected with the global warming. According to DK Panda, rainfall is the primary controller of the sediment transport in the Godavari, Cauvery, Brahmani, Tapi and Mahi basins. Reduction in the precipitation with increasing temperature will have impact on the streamflow in the Godavari Basin. A reduction of 10, 20 and 30% in precipitation and 4% rise in temperature will reduce streamflow (Mishra and Lilhare 2016). The reduction in sediment flux near to zero is owing to the constant decrease in rainfall in Krishna basin (Panda et al. 2011).

### 22.5.1.4 Impacts of Dams and Reservoirs

The constant decrease in the rainfall which with responsible considerable reduction in sediment transport suggests that almost maximum rainfall of the basin have been contributing to the reservoirs during the drought period. Since from 1970s human interference increased in the catchment is the main factor that attributes to decrease in streamflow and sediment load in the Yellow River basin contributing rate is 55–83% and 49.7–87.8%, respectively (Wei et al. 2016). The Narmada basin that provides largest volume of sediment to Arabian sea has now evident to significant reduction in sediment flux (Panda et al. 2011). This trend is attributed due to Sardar Sarovar Dam that captures around 60–80% of sediment loads (Gupta and Chakrapani 2005).

## 22.6 Conclusion

In this research, the Mann–Kendall and Pettit tests are used examine the nature of trends in water flow and sediment flow at six hydrological stations located in the Lower Godavari Basin in India for the duration of 1969–2016.

The following conclusions are made.

1. The Mann–Kendall test exhibited decreasing trend in water discharge at the stations Jagdalpur, Nowrangpur, Patahgudem, Perur and Polavaram, out of which Jagdalpur and Nowrangpur show significant decreasing trend. Increasing trend is observed for the station Konta though the observed trend is not statistically significant with 5% of significance level.
2. The Mann–Kendall test for sediment discharge exhibited declining trend for all the six stations. Out of which stations namely Nowrangpur, Perur and Polavaram indicate significant decreasing trend.
3. Sen's slope test results are in contracted with the Mann–Kendall test results for both streamflow as well as sediment discharge.
4. The change point examination is done to check the transition year of water discharge. Significant downward change is detected at Jagdalpur and Nowrangpur stations from year 1995.
5. Similarly significant reducing trend is observed in sediment discharge for Jagdalpur, Nowrangpur and Polavaram stations from year 1994, 1994 and 1995, respectively.
6. Based on the investigations, which identified the various stations exhibiting significant reduction in water flow and sediment flow, strategic planning needs to be commenced in order to protect the ecology as well as geomorphology of the basin. Further investigation is essential to enumerate the contributing factors such as climate change, climate variability, human influence that affects the streamflow and sediment transport of the Lower Godavari Basin.

## References

- Biksham G, Subramaniya V (1988) Elemental composition of Godavari sediments (Central and Southern India Sub-Continents). *Chem Geol* 70:275–286
- Carrquirry JD, Barranco-Servin LM, Villaescusa JA., Camacho-Ibar VF, Reyes-Bonilla H, Cupul-Magaña AL (2013) Conservation and sustainability of Mexican Caribbean coral reefs and the threats of a human-induced phase-shift. *Environ Change Sustainabil* 2:29–51. <https://doi.org/10.5772/54339>
- Chakrapani GJ (2005) Factors controlling variations in river sediment loads. *Curr Sci* 88(4):569–575
- Day R, Vorosmarty J, Satio C, Giosan Y, Nicholls L, RJ (2009) Sinking deltas due to human activities. *Nat Geosci.* 10:1038
- Dou L, Huang M, Hong Y (2009) Statistical Assessment of the Impact of Conservation Measures on Streamflow Responses in a Watershed of the Loess Plateau, China. *Water Resour Manag* 1935–1949
- Gilbert R (1987) Statistical methods for environmental pollution monitoring
- Gosain AK, Rao S, Basuray D (2006) Climate change impact assessment on hydrology of Indian River basins, special section: climate change and India, vol 90, no 3, pp 346–353
- Kale VS (2002) Fluvial geomorphology of Indian rivers, an overview. *Prog Phys Geogr* 26:400–433
- Kendall MG (1975) Rank correlation methods. Oxford Univ Press, New York
- Kiely G (1999) Climate change in Ireland from precipitation and streamflow observations. *Adv Water Resour* 23:141–151
- Mann HB (1945) Nonparametric tests against trend. *Econometric* 13:245–259
- Miao CY, Shi W, Chen XH, Yang L (2012) Spatio-temporal variability of streamflow in the Yellow River: possible causes and implications. *Hydrol Sci J* 57:1355–1367
- Mishra V, Lilhare R (2016) Hydrologic sensitivity of Indian sub-continental river basins to climate change. *Global Planet Change* 139:78–96
- Mitchell JM (1966) Climate change. (Report of a working group of the Commission for Climatology), Geneva, Switzerland:World Meteorological Organization, WMO Technical note no 79
- Milliman JD, Meade RH (1983) World-Wide delivery of river sediment to the Oceans. *J Geol* 91:1–21
- Panda DK, Kumar A, Mohanty S (2011) Recent trends in sediment load of the tropical river basins of India. *Global Planet Change* 75:108–118
- Peng J, Chen SL, Dong P (2010) Temporal variation of sediment load in the Yellow River Basin, China, and its impact on the Lower reaches and river delta. *CATENA* 83(2–3):135–147
- Pettitt (1979) A Non-parametric test for the change point problem. *Appl Stat* 28:126–135
- SA´Nchez-Arcilla A, Jimé´nez JA, Valdemoro HI (1998) The Ebro delta: morphodynamics and vulnerability. *J Coastal Res*, 14:754–772
- Serrano VL, Garcıa JA (1999) Trend analysis of monthly precipitation over the Iberian Peninsula for the period 1921–1995. *Phys Chem Earth (B)* 24(2):85–90
- Sen PK (1968) Estimates of the regression coefficient based on Kendall’s tau. *J Am Stat Assoc* 63:1379–1389
- Siake J, Oguchi T, Aoki T, Esaki Y, Jarvie HP (2004) Change in riverine suspended sediment concentration in central Japan in response to late 20th century human activities. *CATENA* 55(2):231–254
- Syvıtski JPM (2003) Supply and flux of sediment along hydrological pathways: research for the 21st century. *Global Planet Change* 39:1–11
- Vorosmarty CJ, Green P, Salisbury J, Lammers RB (2000) Global water resources: vulnerability from climate change and population growth. *Sci* 289(5477):284–288
- Walling DE (2006) Human impact on land-ocean sediment transfer by the world’s rivers. *Geomorphology* 79:192–216


- Walling DE (2009) The impact of global change on erosion and sediment transport by rivers: current progress and future challenges. The United Nations World Water Assessment Programme, Scientific Paper 1–23
- Wang Y et al (2012) Contribution of climate and human activities to changes in runoff of the Yellow and Yangtze rivers from 1950 to 2008. *Sci China Earth Sci* 56(8):1398–1412
- Wang HJ, Yang ZS, Satio Y, Liu JP, Sun XX, Wang Y (2007) Stepwise decrease of Huanghe(Yellow river)sediment load (1950–2005): impacts of climate change and human activities. *Global Plant Change* 57:331–354
- Walling DE, Fang X (2003) Recent trends in the suspended sediment loads of the world's rivers. *Global & Planetary Change* 39:111–126
- Wiegel RL (1996) Nile delta erosion. *Sci* 272:338–340
- Xu X-z, Zhang, H-w, Zhang O (2004) Development of check-dam systems ingullies on the Loess Plateau, China. *Environ Sci Policy* 7(2), 79e86. <https://doi.org/10.1016/j.envsci.2003.12.002>
- Yang SL, Zhao QY, Belkin IM (2002) Temporal variation in the sediment load of the Yangtze River and the influences of human activities. *J Hydrol* 263:56–71



# Chapter 23

## Characterization of Flow Turbulence Around Bridge Pier on Rigid Bed Channel



Pasupuleti Laxmi Narayana, Praful Vasharambhai Timbadiya ,  
and Prem Lal Patel 

**Abstract** In current study, flow turbulence statistics generated around a circular bridge pier placed in a rigid bed channel for different flow discharges under constant flow depth are presented. Experimental work in the laboratory flume included measurement of velocity distribution around bridge pier using three-dimensional Micro-Acoustic Doppler Velocimeter to estimate the bottom Reynolds shear stresses, Velocity spectra, and Turbulence Kinetic Energy near the bed and mid flow depth. Power spectra analysis depicted that dominant of Reynolds shear stress, in the present study, is  $uv$  plane than other two planes at flume centerline. The strength of wake vortex is doubled for 27L/s vis-a-vis 22L/s.

**Keywords** Power spectra · Turbulence kinetic energy · Reynolds shear stress · Rigid channel · Wake vortex

### 23.1 Introduction

Local scour around bridge piers is a natural phenomenon and responsible for failure of many river bridges across the globe (Ataie-Ashtiani and Aslani-Kordkandi 2012). As and when an alluvial stream is partially obstructed by immovable bridge piers, the changes in flow pattern around the pier structures are accompanied by formation vortices including horseshoe, wake, and trailing vortices (Kothyari et al. 1992, Sarkar et al. 2016). The drastic changes in shear stress distribution pattern around the pier is responsible for formation of scour hole around the structure (Kothyari et al. 1992). Theoretical treatment in prediction of scour around bridge piers is extremely difficult due to complex turbulence created in the vicinity of hydraulic structure (Raudkivi and

---

P. Laxmi Narayana · P. V. Timbadiya (✉) · P. L. Patel  
Department of Civil Engineering, SVNIT, Surat, Gujarat 395007, India  
e-mail: [pvtimbadiya@ced.svnit.ac.in](mailto:pvtimbadiya@ced.svnit.ac.in)

P. Laxmi Narayana  
e-mail: [d15ce010@ced.svnit.ac.in](mailto:d15ce010@ced.svnit.ac.in)

P. L. Patel  
e-mail: [plpatel@ced.svnit.ac.in](mailto:plpatel@ced.svnit.ac.in)

Ettema 1983). Assessment of turbulence structures around the bridge piers is of prime importance for better understanding the mechanism of scour around the structure and finalizing their orientations, shape, size, and numbers on the river bed. Extensive experimentations were undertaken in previous studies, and many researchers focused on scour around bridge piers to estimate its temporal variations under clear water conditions (Muzzammil and Gangadharaiyah 2003; Dey et al. 1995; Kandaswamy and Melville 1998; Raudkivi and Ettema 1983; Dargahi 2003). Few studies also focused on computations of maximum scour-depth around bridge piers numerically on alluvial sand beds (Kothyari et al. 1992; Melville and Sutherland 1988; Shepard et al. 2014; Melville 1997; Dey 1999; Melville and Chiew 1999). Sarkar et al. (2016) quantified the turbulence by studying the spatial and temporal changes of bed forms around a submerged cylindrical pier of different diameters embedded vertically on the sand bed. The study described associated near-bed turbulence bursting phenomena for constant flow discharge in the channel. Ataie-Ashtiani and Aslani-Kordkandi (2012) performed laboratory experiments to investigate the flow field around side-by-side piers with and without scour hole at constant spacing and first time quantified turbulence around pier in both horizontal and vertical planes. Maity and Mazumder (2014) described the turbulence properties in the region of crescentic scour-hole generated at the upstream of a horizontal short cylinder placed over the sandy beds. However, aforesaid study was not concerned on evolution of hydrodynamics around bridge pier with different discharges under uniform flow condition and hardly, few studies are concerned with submerged pier condition with different pier geometry under constant flow discharge. Characterization of turbulence around bridge piers having significant importance in high flood situations, when piers are in submerged condition, hence, the present study was focused on submerged pier condition under different flow discharges. The objective of present study is to study the temporal variations of bed topography under different flow discharges (uniform flow) to characterize the flow turbulence around bridge pier on rigid bed condition and associated near bed turbulence to understand the movements of horseshoe vortices.

## 23.2 Experimental Set-Up and Data Collection

Experiments were conducted in a recirculating tilting sediment transport flume located in the Advanced Hydraulics Laboratory (AHL) of Sardar Vallabhbhai National Institute of Technology (SVNIT), Surat, Gujarat, India. The experimental channel had the dimensions of 15 m length, 0.89 m width, and 0.6 m height. The flume walls were made of Perspex windows over a distance of 8 m for providing clear view of the flow. The plan and longitudinal section of the flume is shown in Fig. 23.1. The upstream section of the channel was divided into three sub-channels of equal dimensions, and a honeycomb cage was placed at each end of most upstream sub-channel to ensure smooth flow conditions over the working section. The experimental work was carried out using circular pier with diameter, ( $d$ ) of 8.8 cm for varied discharges with constant flow depth under different bed slope conditions. The

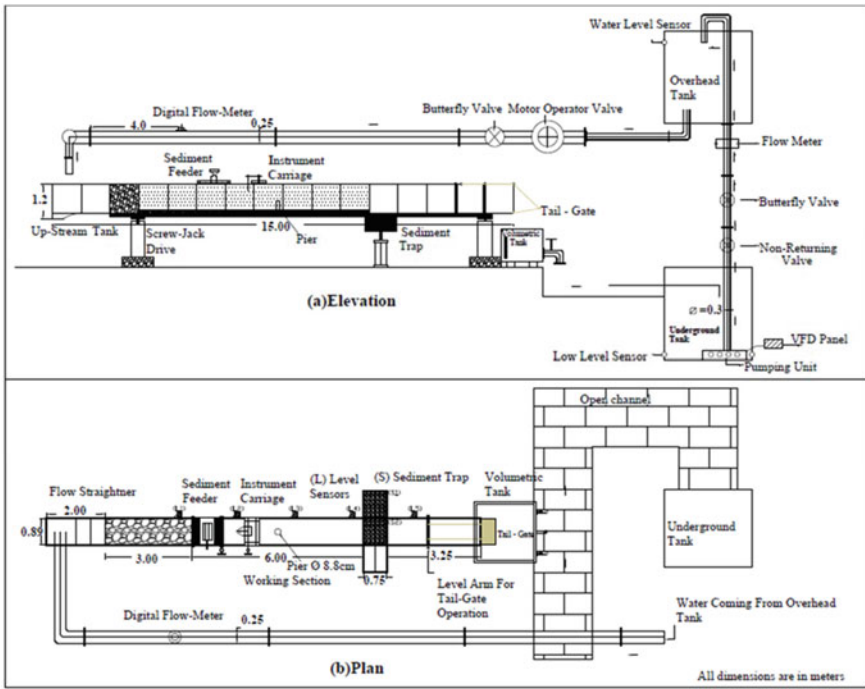
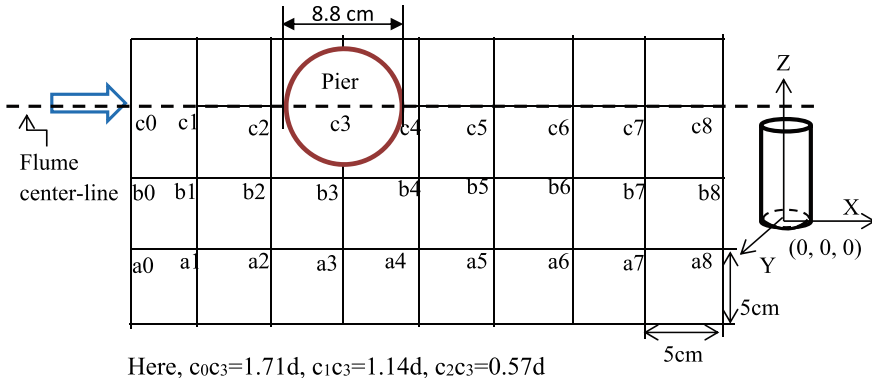


Fig. 23.1 Schematic diagram of experimental set-up

pier size was chosen such that ratio of channel width to pier width was 10.11 to avoid the contraction effects in the flume. The minimum value of ratio of channel width to pier width should be 6.25 to avoid the effect of side wall of channel (Raudkivi and Ettema 1983). The pier was embedded vertically at the flume centerline, and instantaneous three dimensional velocities were measured for 180 s at a sampling rate of 40 Hz using 3D ADV along rows a, b, and c in Fig. 23.2. Here, x-axis is along the flow, y-axis is transverse to the flow, and z-axis is normal to the flow; origin (0, 0, 0) is taken at the center of isolated pier. Experiments were performed under two water discharges (22 L/s and 27 L/s) with constant flow depth (9.5 cm) under uniform flow condition. The slope of the flume was adjusted to maintain the uniform flow (Wang et al. 2016) in the channel.

The velocity measurements were taken at grid points marked in Fig. 23.2 included first velocity profile at 1.0 m upstream to the pier. The Reynolds number,  $R (U_0 d/\nu)$ , ranges from  $2.2 \times 10^4$  to  $3 \times 10^4$ , where  $\nu$  is the kinematic viscosity of the fluid and  $U_0$  is the mean velocity of the approaching flow. The collected ADV data were post processed to remove the noise by eliminating the data points having correlation less than 70% and SNR (Signal to Noise Ratio) less than 15 by an algorithm developed in MATLAB-R2014b<sup>®</sup>, which is similar to that available in public domain WinADV software. Further, the data obtained after filtering against the noise, in-filled using cubic interpolation technique. The time series obtained after removal of noise



**Fig. 23.2** Schematic of the location of data collected by ADV over the isolated pier case

contamination were filtered against possible contamination due to spikes, using a phase space threshold de-spiking technique proposed by Goring and Nikora (2002).

### 23.3 Results and Discussions

Instantaneous velocity components ( $u, v, w$ ) in the Cartesian coordinate system ( $x, y, z$ ) is given as

$$u = \bar{u} + u', v = \bar{v} + v', w = \bar{w} + w' \tag{23.1}$$

where  $\bar{u}, \bar{v}, \bar{w}$ , are the time-averaged velocities in ( $x, y, z$ ) directions and  $u', v', w'$  are the fluctuating components in respective directions. The instantaneous 3-D velocity data were used to compute turbulence parameters like Reynolds shear stresses along all the three planes and vertical velocity distributions around the pier including upstream, sides and downstream of the pier and Turbulence Kinetic Energy,  $K$  (Dey 2014) at both horizontal planes of near bed and mid flow depth. The measured mean velocity distributions are presented at upstream of the pier on vertical planes of both  $u$  and  $w$  components (see Fig. 23.3). In Fig. 23.3,  $x$  is distance from center of the pier upstream along flume center line and  $d$  is the diameter of the pier (8.8 cm);  $U_0$  is the mean velocity;  $z$  is the vertical distance from channel bed at which velocity measurement were taken, and  $z_0$  is the flow depth. The observed vertical velocity components shown in Fig. 23.3a indicates the existence of horse shoe vortices in front of the pier wherein the positive upward velocity in bottom layers indicates the movement of fluid upward and negative downward velocity indicates movement of fluid downward. Figure 23.3b indicates that front flow is not fully developed or effect

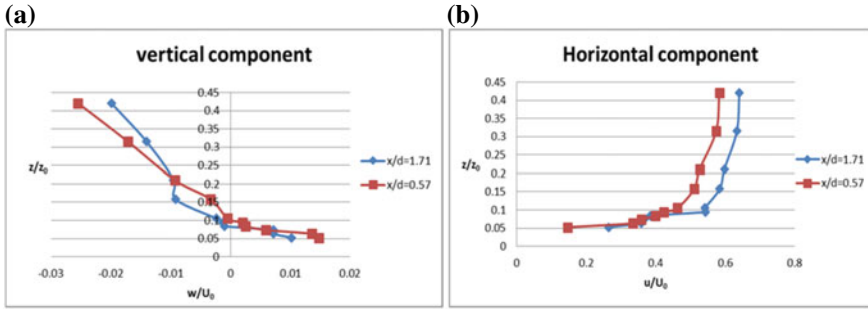


Fig. 23.3 Vertical distribution of  $w$  and  $u$  component upstream of pier on flume centerline

of pier is seen. Velocity contours of horizontal and vertical components are shown in Figs. 23.4 and 23.5 for discharges 22 L/s and 27 L/s, respectively. Both components confirms the formation of horseshoe vortex in the vicinity of pier.

The variations of  $K$  are plotted in Fig. 23.6a, c and b, d for discharges 22L/s and 27L/s, respectively. Further, Fig. 23.6a, b and c, d indicate the variations of  $K$  near the bottom ( $z = 0.5$  cm) and mid flow depth ( $z = 4$  cm) planes, respectively, for aforesaid discharges. Figures 23.6a, c and 23.8b, d indicate clearly that  $K$  is higher for higher discharge in downstream of pier for both bottom and mid flow depth. The

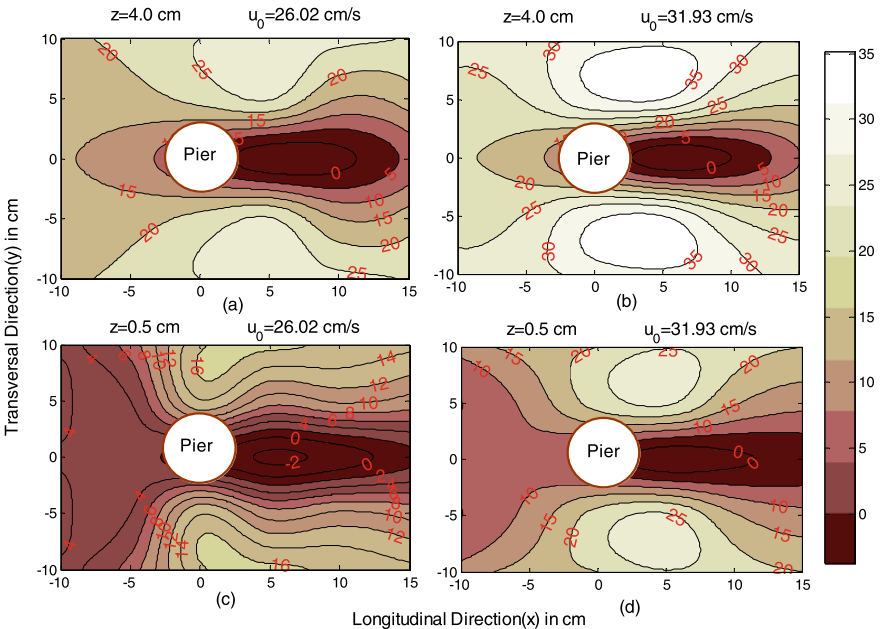
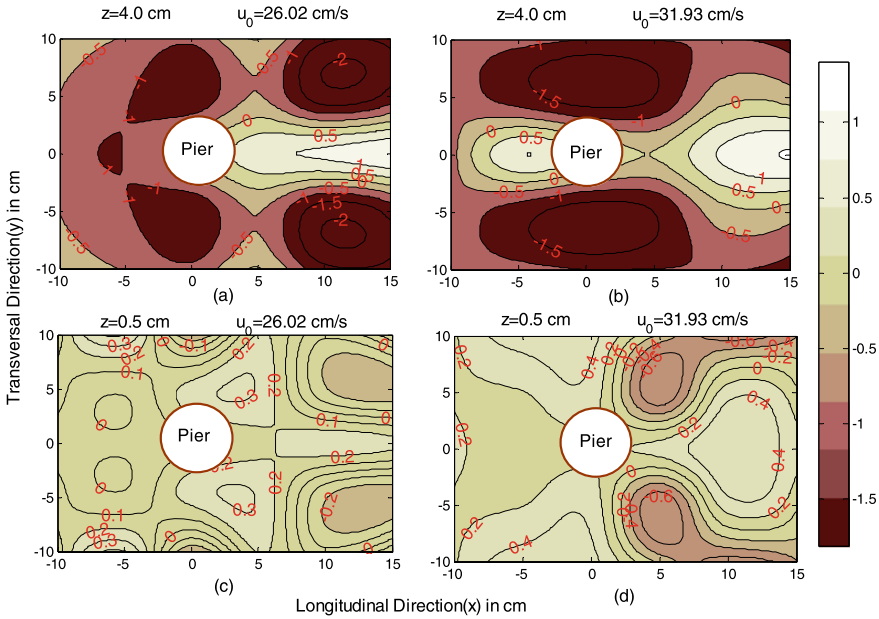
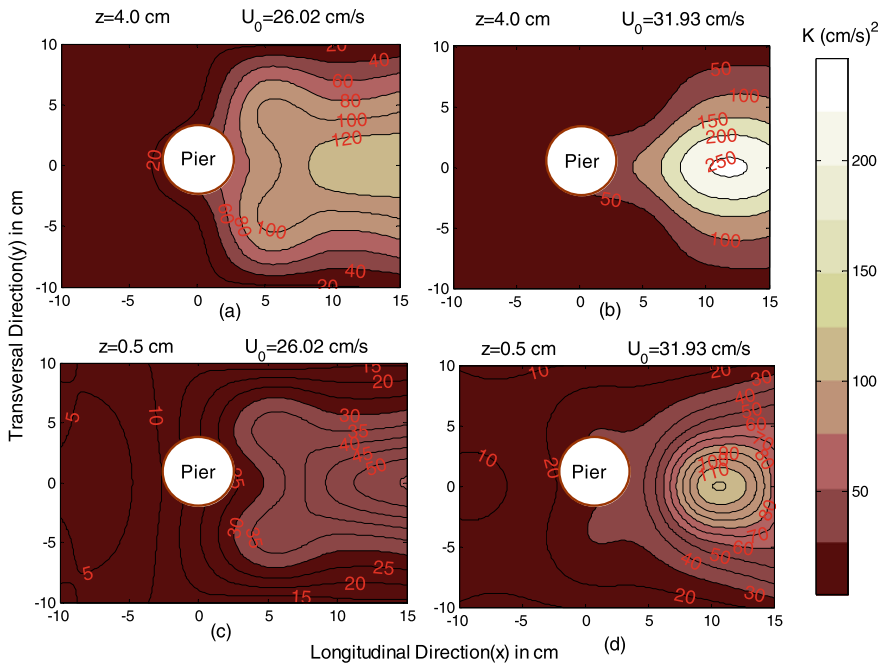


Fig. 23.4 Velocity contours of  $u$ -component for 22 L/s **a**  $z = 4.0$  cm **c**  $z = 0.5$  cm and 27 L/s **b**  $z = 4.0$  cm **d**  $z = 0.5$  cm



**Fig. 23.5** Velocity contours of w-component for 22 L/s **a**  $z = 4.0$  cm **c**  $z = 0.5$  cm and 27 L/s **b**  $z = 4.0$  cm **d**  $z = 0.5$  cm

turbulence kinetic energy, particularly, at mid flow depth plane, is increased from  $120(\text{cm/s})^2$  to  $240(\text{cm/s})^2$  by increasing the discharge just from 22L/s to 27L/s at 10 cm downstream of pier. While comparing K for same discharge at bottom ( $z = 0.5$  cm) and mid flow depth plane ( $z = 4$  cm), it is apparent that the parameter is having exceedingly high value on later plane vis-à-vis bottom plane. The bed shear stresses were also estimated around the bridge pier while normalizing the actual shear stresses ( $\tau_0$ ) with bed shear stress ( $\tau_b$ ) for normal flow condition. The value of shear stresses at  $x/d = -0.56$  is close to zero which, according to Dargahi (1989) and Ahmed and Rajaratnam (1998), is in correspondence with primary flow separation point upstream of the pier. The direction of shear stress for  $x/d \geq -0.56$  is changed, indicating the reverse flows associated with horseshoe vortices. The shear stresses are increased from upstream of the pier to the downstream and reaches a maximum at  $x/d = 2.5$  for discharges 22 L/s and 27 L/s (see Fig. 23.7). Observed maximum in the present study is close to the study of Dey and Barbhuiya (2005), i.e.,  $x/d = 2.6$ . Ataie-Ashtiani and Aslani-Kordkandi (2012) found the maximum value at  $x/d = 2.63$ . Similarly, Ahmed and Rajaratnam (1998) found at  $x/d = 3.63$  for an abutment placed on the plain bed. The power spectrum analysis was performed at different locations around the bridge pier, i.e., upstream, downstream, and near the wake regions, to find the dominant vortex shedding frequency of large scale coherent structures. Velocity spectra were calculated using Fast Fourier Transform (FFT) of auto covariance function of velocity time-series data (Sarkar et al. 2016).



**Fig. 23.6** Contour plots of  $K \text{ (cm/s)}^2$  for 22 L/s **a**  $z = 4.0 \text{ cm}$  **c**  $z = 0.5 \text{ cm}$  and 27 L/s **b**  $z = 4.0 \text{ cm}$  **d**  $z = 0.5 \text{ cm}$

The resultant spectra at different points from center of pier downstream at  $x/d = 0.57, 1.14,$  and  $1.71$  are shown in Figs. 23.8, 23.9, and 23.10, respectively. Figures 23.8, 23.9 and 23.10a, b, c, d indicate velocity power spectra at bottom plane and mid flow planes for aforesaid discharges, respectively. The analyzed results revealed that, for both discharges, cross-stream velocity component ( $v$ -component) dominates other two components at flume centerline downstream of pier at the same frequency of  $0.5 \text{ Hz}$ . The distinct peaks of velocity spectra plots indicates that the frequencies of coherent eddies are shed from the pier boundary layer. The power associated with peaks of this frequency indicates the strengths of vorticity of different kind of vortices formed by the pier (Sarkar et al. 2016; Ataie and Aslani 2012). In turn, the strength of wake vorticity expresses the capacity of the wake vortices to entrain and move sediment bed from the flanks and rear of pier. In the present study, the strengths of wake vortices are maximum for  $v$ -components at near the bed and doubled by increasing the discharge from  $22 \text{ L/s}$  to  $27 \text{ L/s}$  which is in line with variation of  $K$  with discharge as reported in preceding paragraph. In other words, Reynolds shear stress,  $\tau_{uv}$ , contributes maximum shear stress vis-a-vis shear stress in other two planes. Contrary to this, the strengths are increased with increasing in longitudinal distances at mid flow depth (see Figs. 23.8, 23.9 and 23.10).

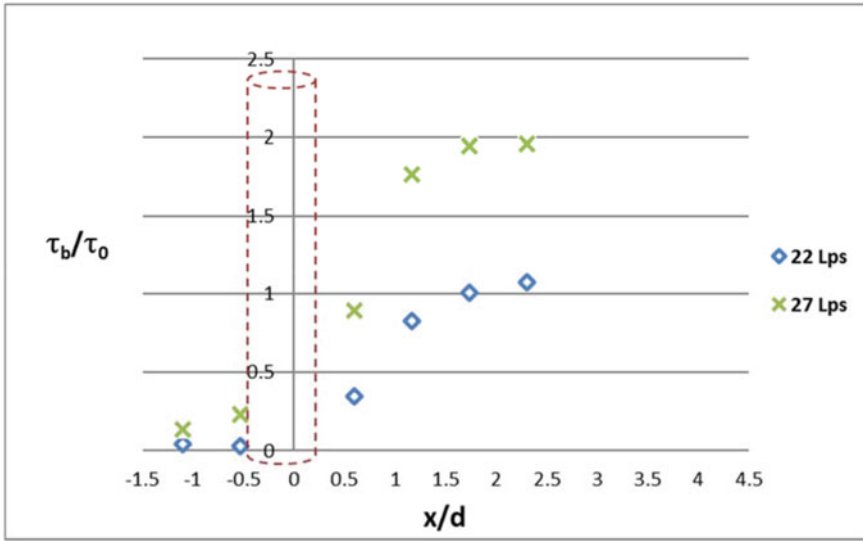


Fig. 23.7 Variations of normalized bed shear stress along flume centerline

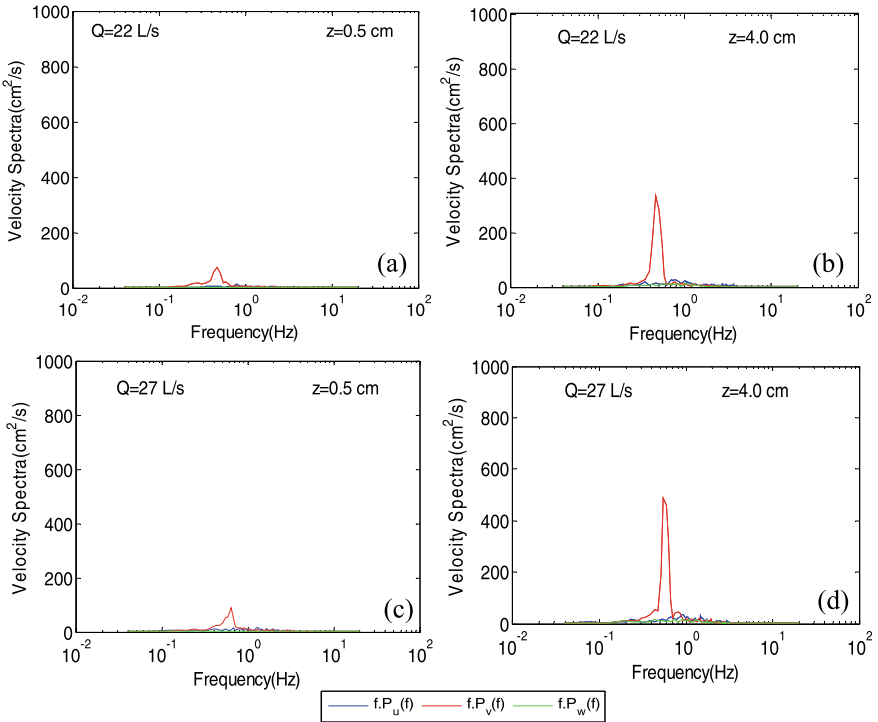


Fig. 23.8 Resultant velocity spectra of u, v, and w velocity at x/d = 0.57 downstream to pier



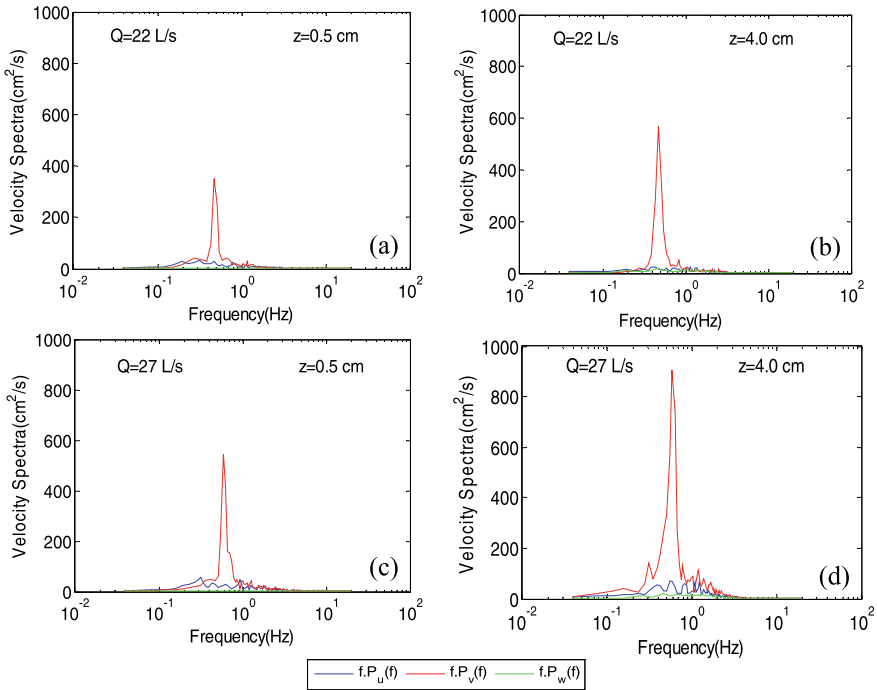
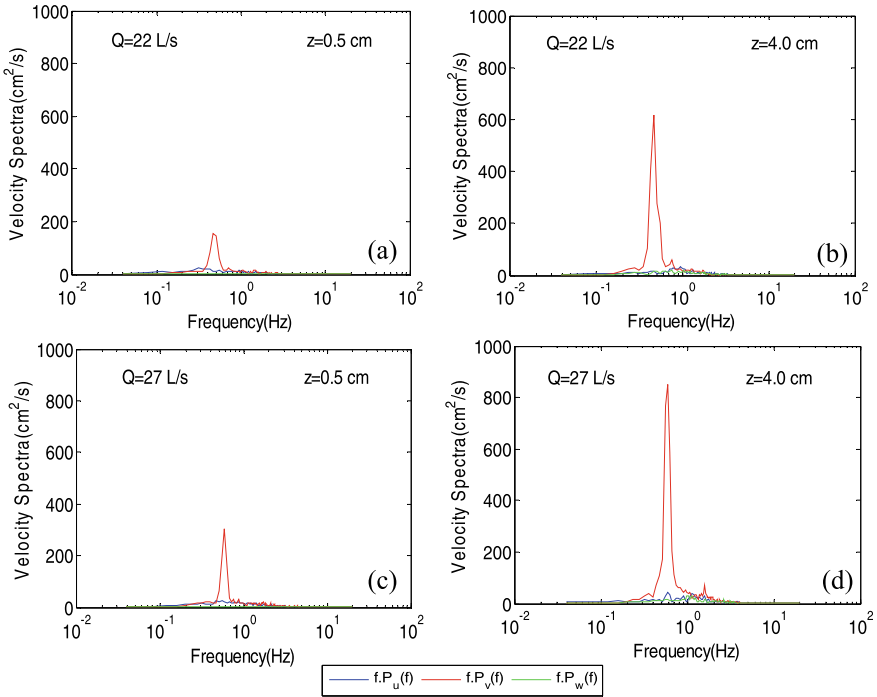


Fig. 23.9 Resultant velocity spectra of u, v, and w velocity at  $x/d = 1.14$  downstream to pier

### 23.4 Conclusions

The flow turbulence has been characterized around single bridge pier on rigid bed channel with two discharges (22L/s and 27L/s) at constant flow depth. The observed vertical velocity components and contours of u and w components had shown clearly the existence of horseshoe vortices adjacent to the pier. The turbulence flow fields on two horizontal planes were studied. The Turbulence Kinetic Energy (K) at mid flow depth plane is increased from  $120(\text{cm/s})^2$  to  $240(\text{cm/s})^2$  by increasing the discharge just from 22L/s to 27L/s at 10 cm downstream of the pier. While comparing K for same discharge at bottom ( $z = 0.5 \text{ cm}$ ) and mid flow depth plane ( $z = 4 \text{ cm}$ ), it is apparent that parameter is having exceedingly high value on later plane vis-à-vis bottom plane. The normalized bed shear stresses are increased from upstream of the pier to the downstream and reaches a threshold point, maximum at  $x/d = 2.5$  for discharges 22 L/s and 27 L/s. Power spectrum analysis depicted the dominance of Reynolds shear stress, on  $uv$  plane via-a-vis other two planes in the centerline of the flume. The strength of wake vortex has been found to be doubled at flow discharge 27L/s compared to 22L/s.



**Fig. 23.10** Resultant velocity spectra of  $u$ ,  $v$ , and  $w$  velocity at  $x/d = 1.71$  downstream to pier

**Acknowledgements** The authors thankfully acknowledge the necessary infrastructural support provided by Centre of Excellence (CoE) on “**Water Resources and Flood Management**”, TEQIP-II, Ministry of Education (MoE), Government of India, for conducting the study reported in the paper.

## References

- Ahmed F, Rajaratnam N (1998) Flow around bridge piers. *J Hydraul Eng* 124(3):288–300
- Ataie-Ashtiani B, Aslani-Kordkandi A (2012) Flow field around side-by-side piers with and without a scour hole. *Eur J Mech B Fluids* 36:152–166
- Dargahi B (1989) The turbulent flow field around a circular cylinder. *Exp Fluids* 8(1–2):1–12
- Dargahi B (2003) Scour mechanism downstream of a spillway. *J Hydraul Res* 41(4):417–426
- Dey S (1999) Time-variation of scour in the vicinity of circular piers. *Proc Inst Civil Eng Water Marit Energy* 136(2):67–75
- Dey S (2014) *Fluvial hydrodynamics*. Springer, Berlin
- Dey S, Barbhuiya AK (2005) Flow field at a vertical-wall abutment. *J Hydraul Eng* 131(12):1126–1135
- Dey S, Bose SK, Sastry GL (1995) Clear water scour at circular piers: a model. *J Hydraul Eng* 121(12):869–876

- Goring DG, Nikora VI (2002) Despiking acoustic Doppler velocimeter data. *J Hydraul Eng* 128(1):117–126
- Kandasamy JK, Melville BW (1998) Maximum local scour depth at bridge piers and abutments. *J Hydraul Res* 36(2):183–198
- Kothiyari UC, Garde RCJ, Ranga Raju KG (1992) Temporal variation of scour around circular bridge piers. *J Hydraul Eng* 118(8):1091–1106
- Maity H, Mazumder BS (2014) Experimental investigation of the impacts of coherent flow structures upon turbulence properties in regions of crescentic scour. *Earth Surf Proc Land* 39(8):995–1013
- Melville BW (1997) Pier and abutment scour: integrated approach. *J Hydraul Eng* 123(2):125–136
- Melville B, Chiew Y (1999) Time scale for local scour at bridge piers. *J Hydraul Eng* 125(1):59–65
- Melville BW, Sutherland AJ (1988) Design method for local scour at bridge piers. *J Hydraul Eng* 114(10):1210–1226
- Muzzammil M, Gangadharaiah T (2003) The mean characteristics of horseshoe vortex at a cylindrical pier. *J Hydraul Res* 41(3):285–297
- Raudkivi AJ, Ettema R (1983) Clear-water scour at cylindrical piers. *J Hydraul Eng* 109(3):338–350
- Sarkar K, Chakraborty C, Mazumder BS (2016) Variations of bed elevations due to turbulence around submerged cylinder in sand beds. *Environ Fluid Mech* 16(3):659–693
- Sheppard DM, Melville B, Demir H (2014) Evaluation of existing equations for local scour at bridge piers. *J Hydraul Eng* 140(1):14–23
- Wang H, Tang H, Liu Q, Wang Y (2016) Local scouring around twin bridge piers in open-channel flows. *J Hydraul Eng* 142(9):06016008-1–06016008-1

# Chapter 24

## Countermeasures Against Local Scouring at Circular Bridge Piers Using Collar and Combination of Slot and Collar



Geeta Devi and Munendra Kumar

**Abstract** Excessive scouring around the bridge pier is a threat to the stability of the bridge. It is vital for human life and bridge safety that some countermeasures against scouring need to be developed. This paper encompasses an experimental investigation on the collar and combination of the slot with a circular and square collar for reducing scour depth around the circular bridge piers. An experimental study was carried out for six different collar and slot arrangements by varying Froude number values under laminar flow conditions. The present study concluded that with the increase in the Froude number depth of scouring increases, increasing the size of the collar plate depth of scouring decreases. The combination of the circular collar and slot gives the minimum scour depth among all the arrangements.

**Keywords** River hydraulics · Scouring · Circular Bridge Pier · Scour protection device · Slot · Collar

### 24.1 Introduction

Local Scour is the leading cause of failure of many bridges inside the river, and it is an unavoidable situation. Therefore, safe designing of the bridges is necessary; it is only possible by the accurate recognition, estimation, and change of bed level around the bridge pier. The interaction between bridge piers and flowing water gives a three-dimensional flow field. On the upstream side of the flow field, a strong pressure gradient generates, and on the downstream side, negative stagnation pressure occurs. The approaching flow field from upstream results in horseshoe vortex formation, and downstream results in the Wake vortex formation. The combination of horseshoe and wake vortex causes the development of local scour (Grimaldi et al. 2009). From past literature, it is clear that the leading cause of the failure of bridge pier is scouring around the piers (Melville and Coleman 2000; Posey 1974; Odgaard 1987; Chiew 1992; Parola 1993; Melville 1999) and other researchers have introduced different countermeasure devices, which are classified into two categories, namely,

---

G. Devi (✉) · M. Kumar  
Department of Civil Engineering, DTU, Delhi 110042, India

Armoring devices and flow-altering devices. Armoring devices include Cable-tied blocks, tetrapods, dolos, placed riprap rocks, flexible mattresses, grout mats, bag anchors, and high-density particles around the pier foundation. Flow altering devices include sacrificial piles placed upstream of the pier, Iowa Vanes, and flow deflectors attached to the pier, such as collars and slots (Zarrat et al. 2006; Melville and Coleman 2000).

The researchers used various countermeasures, and out of them, more researchers considered collars. Collars prevent the reduced scour by preventing the direct impact of flow on the pier and also reduces the horseshoe vortex below the collar (Mashahir et al. 2010). The effect of Local scour is reduced by the collar with the time aspect of the scour development. Collars are adopted mostly because of their existence and scour reduction efficiency (Elsebaie 2013). The total scours around the bridge pier include general scour, contraction scour, and local scour. All over the world number of investigators are researching in scouring, and only limited success has been reported by using different model analyses physically and computationally (M et al. 2007).

## 24.2 Mechanism of Local Scour at Bridge Piers

### 24.2.1 *Traditional Types of Scour Protection and Principles of Working*

In the alluvial channel bed, the Scour hole formation is a matter of discussion in various researches. Engineers must take precautions in designing so that this type of failure cannot occur because they lead to heavy construction and human life loss. There are two approaches to the protection of the foundation of the bridge pier.

1. Placement of protection layer of coarser granular materials or placing of riprap.
2. Protection using Collar or Caissons around the bridge pier (Chiew 1992).

## 24.3 Experimental Program

The present experimental work was conducted in the hydraulics laboratory of Delhi Technological University, Delhi, India, in a 6 m long, 0.3 m wide, 0.45 m deep Flume using a cylindrical pier of 5 cm diameter and 60 cm length. The working section in which the sample was situated was 50 cm upstream from the flume entrance. Experiments were conducted using the bed of cohesionless sand with three different uniform sizes of 0.78 mm, 1.18 mm, and 1.54 mm were laid laterally and 15 cm above the flume bed level. The value of the specific gravity of all the sands was 2.65. For performing the scouring process, the flume was cleaned by allowing free

**Table 24.1** Experimental summary

Sr. No	Experiments
1	For cylindrical pier of diameter 5 cm
2	For cylindrical pier with a collar of diameter (1.5D to 3D)
3	For cylindrical pier with a Square collar of dimension (1.5D × 1.5D to 3D × 3D)
4	For cylindrical pier with Slot of Dim (5 cm × 1 cm)
5	For cylindrical pier with slot and circular collars
6	For cylindrical pier wit square collars

discharge through it. The uniform flow was attained by adjusting the bed slope. The sediment bed was leveled before the commencement of the experiments. For taking the scour depth, a scale on the upstream side of the flow field was enabled.

The present experimental study includes tests to study the effect of the collar, a slot, and a combination of both. The circular and square wooden collar of thickness 4 mm and a slot of dimension 1 cm width and 5 cm height was considered experimental. Collars of varying diameter 1.5D, 2.0D, 2.5D, 3.0D and square collar of varying dimension 1.5D × 1.5D, 2D × 2D, 2.5D × 2.5D, 3D × 3D were used in experiments. An experimental program was conducted in six different sample arrangements by increasing the value of the Froude number. Three sets of the same experiment series were conducted to observe the effects of collar and slot on Scour depth. The experimental summary is tabulated below in Table 24.1.

## 24.4 Analysis of Data

### 24.4.1 Scour Reduction Due to Collar

From various researches, it is concluded that collar users can effectively reduce the scour depth because the collar has a shielding effect against sediment particles erosion (Thomas 1967).

if  $ds_c$  = Depth of Scour at a pier with a collar.

$ds_p$  = Depth of scour at a pier without a collar.

Under the uniform flow condition, we can write:

$$\frac{d_{sc}}{d_{sp}} = f_1 \left( \frac{B}{b}, \frac{H}{Y_o} \right) \tag{24.1}$$

or

$$\frac{d_{sp} - d_{sc}}{dsp} = f_2 \left( \frac{B}{b}, \frac{H}{y_o} \right) \tag{24.2}$$

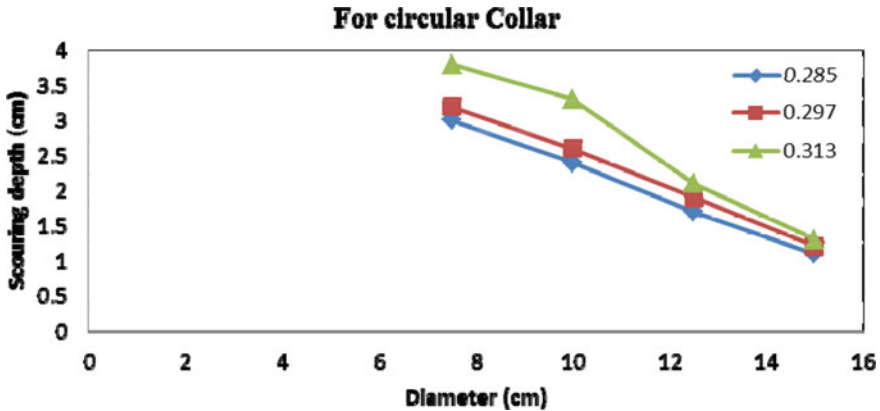


Fig. 24.1 Variation of Scour depth by increasing diameter with different Froude No

Equation (24.2) forms the basis for studying the effect of collar size and elevation on scour depth. An additional parameter of collar thickness should also appear in Eq. (24.2). However, it is not considered because in the present study thickness of the collar is negligible (Kumar et al. 1999).

The deepest scour occurs at the upstream face for the small-sized collar (1.5D), and the minimum scour is observed for the most extensive (3D). As the diameter of the collar increases, the scour depth decreases. It establishes an inverse relationship between collar diameter and scour depth. The pattern of scour depth by increasing diameter and Froude No. is shown in Fig. 24.1 for the circular collar.

Square collars have also been used for evaluating the effect of the collar shape and size on scour depth. Figure 24.2. represents the pattern of scour depth by varying Froude no for square collars.

### 24.4.2 Scour Reduction Due to Slot

The principle of using slots is as follows:

1. To divert the Downflow away from the bed.
2. To reduce the influence of Downflow on the bed.

The Pier slot was located near the bed, and the oncoming flow on the lowermost layer will get accelerated through a slot. This flow forms a horizontal jet, which results in a reduction in scouring potential under uniform flow condition, we can write as: if:

$$ds_s = \text{Depth of scour at a pier with slot}$$

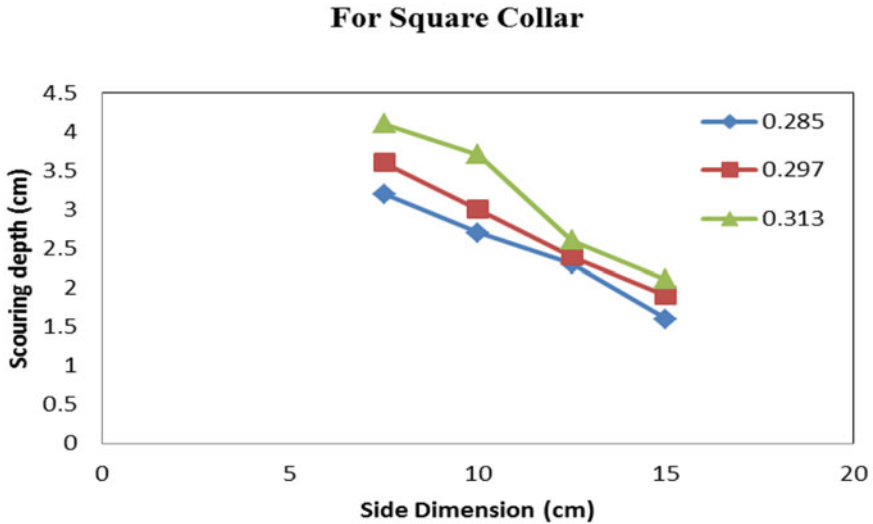


Fig. 24.2 Variation of scour depth by increasing size with different Froude No

$$\frac{ds_s}{ds_p} = f_1\left(\frac{w}{b}, \frac{Y_L}{Y_o}, \theta\right) \tag{24.3}$$

where  $\theta$  = Angle of approach flow with slot axis and  $w$  = Width of slot.

Equation (24.3) represents dimensionless geometric parameters that are related to slot only. The equation’s assumption is the effect of the flow and sediment parameters have been accounted for using  $ds_p$  (Kumar et al. 1999). Figure 24.3 represents the difference in the scour depth by using the slot in comparison to using the only pier. It shows a significant decrease in the scour depth.

### 24.4.3 Scour Reduction Due to a Combination of Slot and Collar

For more reduction, the scour depth combinations of the slot and collars are adapted for the circular and square collar. When the slot is used together with a collar, the results show an improved scour depth reduction. The use of a slot combined with the circular collar reduces the scour depth by nearly 80%. Reduction in scours depth is represented in Fig. 24.4. The combination of the slot and square collar reduces the scour depth by nearly 75%, and its representation is shown in Fig. 24.5.



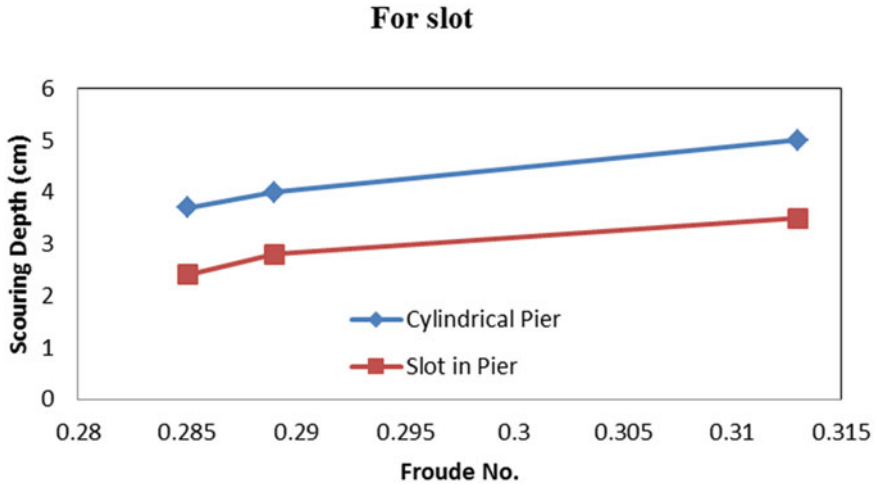


Fig. 24.3 Representation of scour depth reduction by using slot

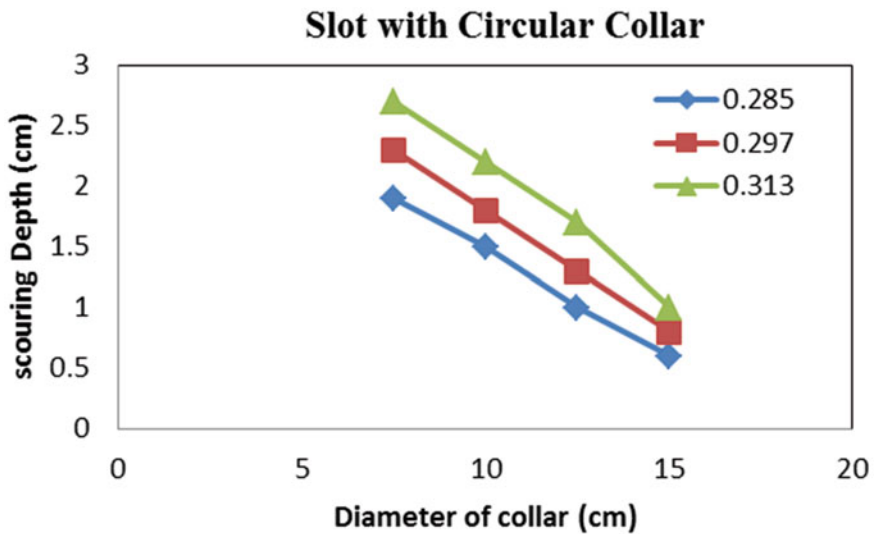
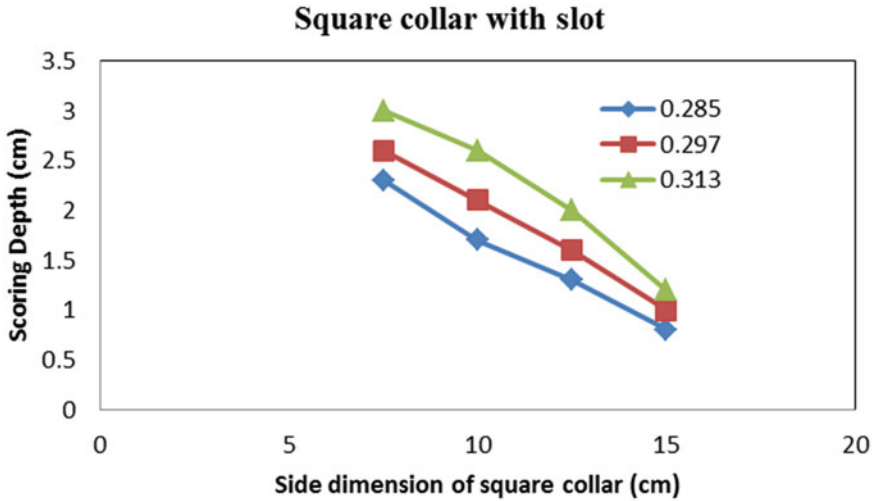


Fig. 24.4 Variation of scour depth by using a combination of slot and circular collar for different Froude No

### 24.5 Conclusion

The present study investigated the effect of the collar, slot, and combination of the two on the bridge pier scour. Experimental results of these protection devices show their efficiency in reducing scouring depth. Following observations were made by experimental work:



**Fig. 24.5** Variation of scours depth by using a combination of slot and square collar for different Froude No

- The extent of Scour depth keep on increasing with the increase in the Froude No. by nearly 3%.
- Scour depth decreases with the increase in the size of the collar. For the circular collar, the scour depth reduction was observed nearly 63% compared to the pier only. The reduction in scours depth was observed for the square collar less than the circular collar; it was 50%.
- By using the slot in the pier value of scouring reduction was observed at 75%. For further reduction in the scour depth combination of slot and collar was adopted. The combination of the slot with the circular collar reduces the scour depth by 83% compared to the single pier scour, and the combination of the slot with the square collar gives the scour reduction value 78%.
- Maximum scour reduction was observed in the case of a combination of the slot, and the circular collar was nearly 83% for the Froude no 0.285 results are shown in Fig. 24.4.

**Acknowledgements** Experimental work was conducted in the hydraulics laboratory at Delhi Technological University, Delhi, and the author is highly grateful to the staff members of the laboratory.




## References

- Chiew Y-M (1992) Scour protection at bridge piers. *J Hydraul Eng ASCE* 118(9)
- Elsebaie IH (2013) An experimental study of local scour around circular bridge pier in sand soil. *Int J Civil Environ Eng* 13(03)
- Grimaldi C, Gaudio R, Calomino F, Cardoso AH (2009) Countermeasures against local scouring at bridge piers: slot and combined system of slot and bed sill. *J Hydraul Eng ASCE* 135(5)
- Kumar V, Ranga Raju KG, Vitta N (1999) Reduction of local scour around bridge piers using slot and collars. *J Hydraul Eng ASCE* 125(12)
- Mashahir MB, Zarrati AR, Mokallaf E (2010) Application of riprap and collar to prevent scouring around rectangular bridge piers. *J Hydraul Eng ASCE* 136(3)
- Melville BW, Hadfield AC (1999) Use of sacrificial piles as pier scour countermeasures. *J Hydraul Eng ASCE*
- Melville BW, Coleman SE (2000) *Bridge scour*. Colorado, USA, 550: Water Resources Publications
- Odgaard AJ, Wang Y (1987) Scour prevention at bridge piers. *Hydr Eng* 87, National Conference, Virginia: R.M. Ragan, ed. 523–527
- Parola AC (1993) Stability of Riprap at Bridge Piers. *J Hydr Eng ASCE* 119:1080–1093
- Posey CJ (1974) Tests of scour protection for bridge piers. *J Hydraul Eng ASCE* 100(12):1773–1783
- Thamer AM, Megat JM, Mohd N, Abdul Halim G, Badronnisa Y, Badronnisa Y, Katayon S (2007) Physical modeling of local scouring around bridge piers in erodible bed. *J King Saud Univ Eng Sci* 19(2)
- Thomas Z (1967) An interesting hydraulic effect occurring at local scour. In: *Proceeding on 12th IAHR Congress*, Netherlands
- Zarrat AR, Mashahir MB, Nazariha M (2006) Reduction of local scour in the vicinity of bridge pier groups using collars and riprap. *J Hydraul Eng ASCE* 154–162

# Chapter 25

## Influence of Pier Shape and Interference Effect on Local Scour



Siva Krishna Reddy , Sruthi Thazhathe Kalathil , Malasani Gopi Chand, and Venu Chandra 

**Abstract** Scour around bridge piers is one of the main reasons for bridge failures. Previous researchers reported that pier shape is an important parameter since it affects the flow field and then scour formation. This study aims (i) to find the effect of pier shape on local scour in comparison with the circular pier shape and (ii) interference effect of different shaped piers placed in tandem arrangement on local scour. Experiments are conducted in a rectangular glass-walled flume with sand of  $d_{50} = 0.56$  mm, under clear-water, and steady flow conditions. Two modified piers are prepared (P2 and P3) with the area equivalent to the area of the circular pier (P1). P1 is a circular pier with diameter  $D (=5$  cm), P2 is a combination of semi-circle and triangle in which pier is oriented to flow direction in either ways (P2a and P2b), and P3 has a groove with projection on semi-circular face of P2. The results showed that compared to P1 the scour depth reduced by 23.5%, 50%, and 55% for P2a, P2b, and P3, respectively, thereby reducing the need for scour countermeasures. From the results of tandem arrangements, it is observed that P1 as front pier and P2a as a rear pier with a clear spacing of  $1.0D$  and P3 as front pier and P1 as a rear pier with the clear spacing of  $1.75D$  given less scour. These observations can be helpful to construct a new bridge adjacent to an existing bridge.

**Keywords** Modified pier shape · Local scour · Interference effect · Tandem arrangement

---

S. K. Reddy · S. T. Kalathil · M. G. Chand · V. Chandra (✉)  
Department of Civil Engineering, Indian Institute of Technology Madras, Tamil Nadu, Chennai  
600036, India  
e-mail: [vc@iitm.ac.in](mailto:vc@iitm.ac.in)

S. K. Reddy  
e-mail: [kvskreddy.09@gmail.com](mailto:kvskreddy.09@gmail.com)

S. T. Kalathil  
e-mail: [tk.sruthi@gmail.com](mailto:tk.sruthi@gmail.com)

M. G. Chand  
e-mail: [gcreddy.m@gmail.com](mailto:gcreddy.m@gmail.com)

## List of Symbols

$D$	Pier diameter (cm)
$d_{50}$	Mean size of bed material (mm)
$d_s$	Maximum scour depth measured below the bed level (cm)
$d_s/D$	Scour depth ratio
$d_{sf}/D$	Scour depth ratio for front pier
$d_{sr}/D$	Scour depth ratio for rear pier
$F_r$	Froude number
$Q$	Flow rate (L/s)
$t$	Time of scour measurement (minutes)
$T$	Total duration of experiment (minutes)
$t/T$	Time scale ratio
$V$	Maximum flow velocity (m/s)
$V/V_c$	Critical velocity ratio
$V_c$	Critical velocity (m/s)
$X$	Clear spacing between two piers in tandem arrangement (cm)
$X/D$	Non-dimensionalised clear spacing
$Y$	Flow depth (cm)
$\sigma_g$	Geometric standard deviation of bed material

## 25.1 Introduction

Bridges play a prominent role in the transportation system of a country. Failure of bridges has adverse effects on its economic run in addition to the loss of lives. Available information on bridge failures across the world includes only a general description with rough statistical data because of limitations in monitoring technologies and inadequate understanding of the failure scenario (Lee et al. 2013). It is found that 45% of bridge failures that occurred in the US were caused by hydraulic scenarios like extreme floods and scour (Choudhury and Hasnat 2015). Accurate estimation of scour depth is required at the design stage itself to avoid such mishaps.

Scour is the lowering of the river bed due to the action of flowing water. Local scour occurs due to the stresses induced around the local area of the pier (Subramanya 1982). Obstruction to flow in the form of bridge piers causes the formation of horseshoe vortex on the upstream side and wake vortex on the downstream side of the pier. This results in an increase in shear stresses and three-dimensional boundary layer separation around the pier, causing sediment erosion (Kothyari 2007). Once the scour depth increases, the horseshoe vortex weakens, and the erosion reduces. Along the downstream of the pier, the strength of the wake vortex decreases with distance from the pier (do Carmo 2005).

Bridge piers are usually designed as circular-type cross-sections (Melville 1975; Melville and Raudkivi 1977). The shape, size, and alignment of the pier influence

the extent of scour (Melville and Sutherland 1988). Scour depth is also dependent on the depth of approach flow and increases with the flow depth when the flow shallowness ratio (ratio of flow depth to pier diameter) is less than 2.6 and beyond which the scour becomes independent of flow depth (Breusers et al. 1977; Chiew 1984; Melville and Sutherland 1988). The scour depth also increases with a decrease of sediment size and sediment gradation (Ettema 1980; Dey et al. 1995; Sumer et al. 1997; Chandra 2003; Kothiyari and Garde 2007). Scour around bridge piers have been widely investigated by several researchers to estimate accurate models of scour depth for design purposes (Shen et al. 1969; Melville 1975; Raudkivi and Sutherland 1981; Raudkivi and Ettema 1983; Sumer et al. 1992; Melville 1997; Melville and Coleman 2000; Richardson and Davis 2001; Barbhuriya and Dey 2004; Dey and Raikar 2007; Kothiyari 2007; Kothiyari 2008; Kumar et al. 2012). Also, temporal variation of scour in steady and unsteady flow conditions have been evaluated to understand the scour phenomenon occurring during events of rainfall and flood for ensuring traffic safety over bridges (Yanmaz and Altinbilek 1991; Kothiyari et al. 1992; Sumer et al. 1992; Melville and Chiew 1999; Oliveto and Hager 2002; Mia and Nago 2003; Yanmaz 2006; Hager and Unger 2010).

Apart from the circular-shaped pier, researchers have also attempted studies with different shaped piers such as rectangular and aerofoil. A considerable reduction in the strength of the horseshoe vortex is observed for streamlined piers, which results in the decrease of the scour depth (Sumer et al. 1997; Ismael et al. 2014). Studies on the flow field and scour depth for different shaped piers such as the rectangular, oblong, trapezoidal, triangular, and lenticular pier found that variation of scour depth in different shaped piers is due to the variation in mean velocities and turbulence associated with the change in the shape of piers (Vijayasree et al. 2017). The scour at the upstream side of piers is proportional to the area exposed to the flow (Al-Shukur and Obeid 2016). Hence research on varied shapes of piers and implementation of the same in the field is of high significance.

Moreover, in actual field scenarios, some of the bridge piers are constructed in a tandem arrangement. This happens when a railway bridge is built adjacent to a road bridge, or a new bridge is built abandoning the old one. In such situations, it is important to estimate the interference effect on both the piers. The equations developed for isolated piers cannot be followed for piers constructed in tandem because of varied scour pattern. Few studies on bridge scour have incorporated tandem arrangement of circular piers at different spacings (Elliot and Baker 1985; Ataie-Ashtiani and Behesti 2006; Keshavarzi et al. 2018). All these studies are confined to circular shaped piers. However, no study has been incorporated in the literature to estimate the scour depth for different shaped piers placed in a tandem arrangement. In the present study, experiments are conducted for circular and modified shaped piers in isolated and tandem arrangements to study the shape effect on pier scour.

## 25.2 Experimental Setup

Experiments were conducted in a rectangular glass-walled flume of length 7.6 m, width 0.5 m, and depth 0.56 m, located in the hydraulics laboratory, IIT Madras, India. The bed slope of the flume is maintained as 0.0002. The test section comprises 5.6 m in length, filled with non-cohesive sediment of  $d_{50} = 0.56$  mm and geometric standard deviation  $\sigma_g = 1.39$ , filled up to a height of 0.25 m. The upstream and downstream portions of the test section were filled with coarse gravel for a length of each 1 m to get fully developed flow and protecting the sediment from washed away with flowing water, respectively. The testing flume is equipped with a regulating valve and tailgate at the upstream and downstream sides, respectively, to regulate the flow depth and flow rate. The corresponding bed and water levels were measured using a digital pointer gauge with an accuracy of 0.05 mm. The bed is leveled before each experiment, and bed levels were taken at 0.25 and 0.5 m distance upstream of the pier test section and 0.25 m at downstream from the pier. Water was allowed gradually into the flume, and the flow rate is measured using a calibrated rectangular notch located at the upstream side of the flume. After attaining the required depth and flow rate, velocity is measured at 1 m distance, upstream of pier location using Acoustic Doppler Velocimetry (ADV). The flow depth ( $Y$ ) is 12 cm, discharge ( $Q$ ) is 15.5 L/s, and maximum flow velocity ( $V$ ) of 0.26 m/s is maintained throughout the study. Experiments were conducted under subcritical flow ( $F_r = 0.24$ ), as well as clear water conditions, with the ratio between maximum flow velocity ( $V$ ) to critical velocity ( $V_c = 0.29$  m/s) is maintained as 0.9, which is less than 1 (Raudkivi and Ettema 1983). Flow through the flume is collected in a sump and re-circulated to the overhead tank using a 40 HP centrifugal pump.

The schematic diagram of various pier models used in this study is shown in Fig. 25.1. The first model (P1) is a circular pier with a diameter ( $D$ ) of 0.05 m. The second model (P2) is a modified shaped pier having an area equal to the first model, with a combination of semi-circular and triangular shapes. The third model (P3) is similar to the second model, but it has a groove at the pier nose in which a metal plate of 3 mm thickness with 5 mm projection fixed. The pier width is set such that the ratio of flume width to pier width is equal to 10 to prevent the effect of flume boundary on scouring (Chiew 1984). Piers were installed at the center of

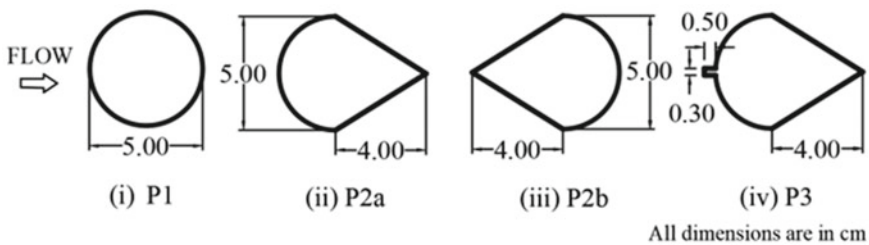


Fig. 25.1 Schematic diagram of pier models

the flume cross-section and 4 m distance from the flume inlet. Initially, experiments were conducted with P1, P2 (blunt nose and a pointed nose), and P3 (groove with projection). The experimental results of P1 are used to compare the results of the other two models. Later, the interference effect on local scour is studied by placing two piers in a tandem arrangement at different clear spacing with a combination (Fig. 25.3) of all three models.

## 25.3 Results and Discussion

Four different models (P1, P2a, P2b, and P3) were tested to evaluate the scour depth and effect of the shape of a pier on scouring formation. The results were presented in the form of non-dimensionalized scour depth, which is the ratio between the scour depth at any instant to the pier diameter ( $d_s/D$ ), plotted against the time scale of ( $t/T$ ) in which  $t$  is the time of scour measurement and  $T$  is the total duration of the experiment ( $T \sim 720$  min). Similarly, the equilibrium scour depth ( $d_s/D$ ) of piers in the tandem arrangement was plotted against a non-dimensional clear spacing ( $X/D$ ) to obtain the interference effect of two piers when aligned to the flow.

### 25.3.1 Isolated Piers

The scour depth around the pier was maximum at the upstream nose due to the downflow and horseshoe vortex formation. Hence, scour measurements were taken only at the pier nose for all the experiments. Figure 25.2 shows the variation of  $d_s/D$  with time for the pier types P1, P2a, P2b, and P3. The plot shows that for P1, equilibrium scour depth was attained at about  $0.6 T$ , whereas for P2a, P2b, and P3, it happened as early as  $0.4 T$ . This shows that modified piers produce less obstruction to the flow and attain a stable state faster. It could also be noted that with the use of P1 pier,  $d_s/D$  is equal to 1.02, which is in close agreement with the findings of Coleman (1971) and Shen et al. (1969), having scoured depth ratios equal to 1.03 and 1.14, respectively. For Mia and Nago (2003),  $d_s/D$  was found to be 1.18. Scour depth values have reduced for modified piers in comparison to the traditional circular piers. Reduction in  $d_s/D$  for P2a, P2b, and P3 is 23.5%, 50%, and 55%, respectively. The lowest value of  $d_s/D = 0.46$  was found for P3 due to the inclusion of a metal plate at the pier nose, which facilitates streamlined flow around the pier.

The proposed pier shapes have asymmetric geometry along the flume width. Even then, the piers were found to be stable during all experiments. In field scenarios, where the vertical load coming on to the pier caps would be greater than the lateral load due to flow, failure chances are not a concern while providing modified shaped piers. Nevertheless, the stresses coming on the pier will be asymmetric due to the shape. This aspect of the modified pier could be analyzed as a future scope.



**Fig. 25.2** Temporal variation of scour depth ratio for isolated piers

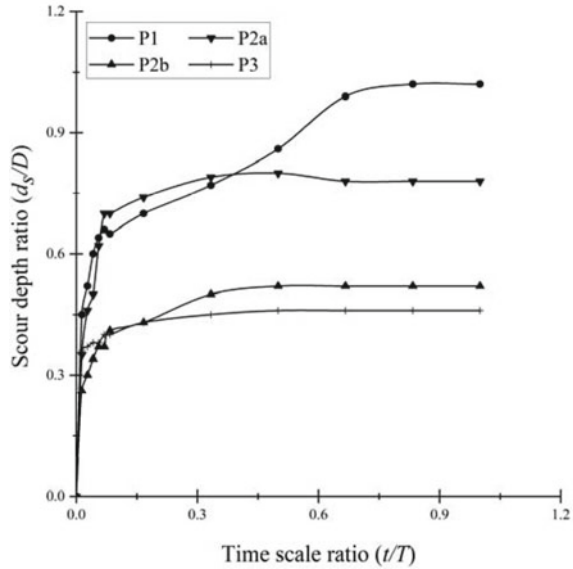
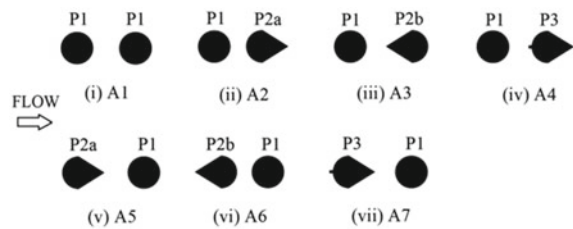


**Fig. 25.3** Different tandem arrangements of pier models



### 25.3.2 Tandem Arrangement

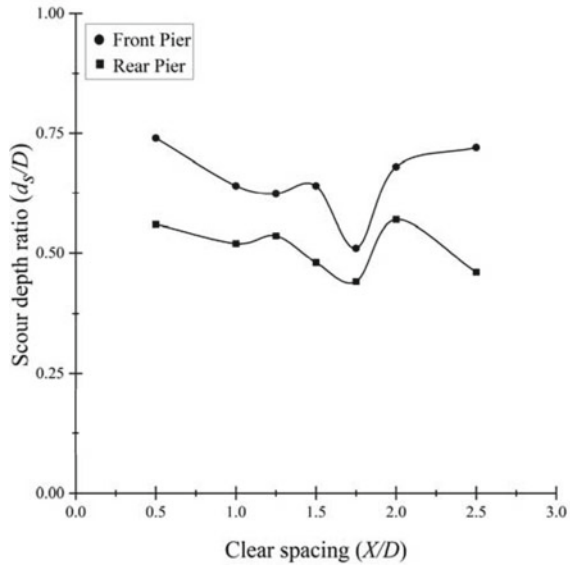
The two modified piers along with the combination of the circular pier model are placed in a tandem arrangement at a different clear spacing of  $0.5D$ ,  $1.0D$ ,  $1.25D$ ,  $1.5D$ ,  $1.75D$ ,  $2D$ , and  $2.5D$ . The piers are aligned to the flow direction to study the interference effect on local scour around both the piers. The various combination of tandem arrangements considered to analyze the interference effect has been shown in Fig. 25.3. The scour depth at the front and rear piers were measured at the face of the piers, and the results are presented in the form of maximum scour depth ratio ( $d_{sf}/D$  and  $d_{sr}/D$ ), where  $d_{sf}$  is scour depth of upstream pier and  $d_{sr}$  is scour depth of downstream pier (Table 25.1). It is found that scour at front pier exceeds rear pier, with all spacings due to sheltering effect from front pier and sedimentation of eroded bed material from the front pier.

Initially, the effect of interference with different clear spacings for two circular piers is tested. Figure 25.4 shows the local scour depth ratio ( $d_s/D$ ) versus clear

**Table 25.1** Variation of scour depth ratio for different tandem arrangements with clear spacings

Tandem piers Arrangement	$X/D = 0.5$		$X/D = 1$		$X/D = 1.25$		$X/D = 1.5$		$X/D = 1.75$		$X/D = 2$		$X/D = 2.5$	
	$d_{sf}/D$	$d_{spr}/D$	$d_{sf}/D$	$d_{spr}/D$	$d_{sf}/D$	$d_{spr}/D$	$d_{sf}/D$	$d_{spr}/D$	$d_{sf}/D$	$d_{spr}/D$	$d_{sf}/D$	$d_{spr}/D$	$d_{sf}/D$	$d_{spr}/D$
A1	0.74	0.56	0.64	0.52	0.62	0.54	0.64	0.48	0.51	0.44	0.68	0.57	0.72	0.46
A2	0.58	0.36	0.35	0.29	0.5	0.43	0.47	0.44	0.42	0.37	0.49	0.36	0.37	0.33
A3	0.42	0.25	0.42	0.34	0.46	0.35	0.36	0.17	0.46	0.3	0.41	0.19	0.5	0.26
A4	0.53	0.33	0.52	0.44	0.42	0.37	0.55	0.55	0.47	0.51	0.47	0.39	0.47	0.34
A5	0.48	0.44	0.48	0.40	0.35	0.37	0.39	0.33	0.45	0.34	0.39	0.37	0.38	0.34
A6	0.4	0.35	0.6	0.4	0.57	0.5	0.46	0.48	0.36	0.5	0.34	0.43	0.45	0.46
A7	0.34	0.35	0.32	0.4	0.30	0.38	0.32	0.40	0.29	0.34	0.34	0.35	0.31	0.38

**Fig. 25.4** Variation in scour depth ratio for different clear spacing between circular piers in tandem arrangement



spacing between the circular piers ( $X/D$ ). The least scour for both the front and the rear pier is observed at a clear spacing of  $1.75D$ , and the corresponding values for  $d_s/D$  for the front and rear pier are  $0.51$  and  $0.44$ , respectively. Whereas the maximum scour depth observed is  $0.74D$  and  $0.57D$  for the front and rear pier, respectively, at  $X = 0.5D$ .

The variation in  $d_s/D$  for different tandem arrangements with clear spacing ( $X/D$ ) is given in Table 25.1. For almost all arrangements, maximum scour depth was observed to be less for the rear pier than the front pier. For arrangements with modified piers as rear piers (A2, A3, and A4), minimum  $d_s/D$  for the front circular pier reduced by 31.4%, 29.4%, and 17.65% for the clear spacing of  $1.0D$ ,  $1.5D$ , and  $1.25D$ , respectively. It could be concluded that, whenever a new bridge is proposed to construct downstream of an existing bridge with circular piers, P2a at a clear spacing of  $1.0D$  is preferable. For arrangements A5, A6, and A7 with circular pier at the rear side,  $d_s/D$  for the rear circular pier is reduced by 22.73%, 20.45%, and 22.73% for the clear spacing of  $1.75D$ ,  $0.5D$ , and  $1.75D$ , respectively. In the case of a new bridge, the upstream of a bridge with circular piers, modified pier P3 at a clear spacing of  $1.75D$ , is recommended. The reduction percentages mentioned here corresponds to the scour at the circular pier. However, if overall scour reduction is analyzed, combinations of piers P1 and P3, i.e., arrangements A4 and A7, showed the least scour at all clear spacings. From the experimental results, it is observed that the pier shape and interference effect of two closely spaced piers affected the flow field and then scour depth.

## 25.4 Conclusions

Scour around piers has been identified as a severe cause for bridge failures for more than six decades. The research conducted in this area has focused more on circular and double-D type of pier cross-sections. A need for a well-designed pier that results in less local scour under different field scenarios exists still. In the present study, three different pier models have been tested in isolated and tandem arrangements. The tested pier shapes include a circular pier (P1), modified pier with an upstream blunt and downstream pointed nose (P2a), modified pier with the upstream sharp and downstream blunt nose (P2b), and a modified P2a shape with a 5 mm projection on the blunt side (P3). Following are the conclusions drawn from the results.

1. The scour depth reduction for the modified piers P2a, P2b, and P3 with respect to P1 is 23.5%, 50%, and 55%. The modified pier P3 showed better performance due to the upstream projection and downstream streamlined shape.
2. The tandem pier experiments were conducted to determine the best-suited pier shape used to construct bridges adjacent to an existing circular pier bridge. It was found that P2a been built downstream of a circular pier at a clear spacing of  $1.0D$  will provide the least sediment erosion at the pier face. In the case of a new bridge at the upstream, P3 could be constructed at a clear spacing of  $1.75D$  in the upstream of a circular rear pier.

**Acknowledgements** We express our sincere thanks to the Science and Engineering Research Board (SERB) for funding this project work.

## References

- Al-Shukur AHK, Obeid ZH (2016) Experimental study of bridge pier shape to minimize local scour. *Int J Civil Eng Tech* 7(1):162–171
- Ataie-Ashtiani B, Beheshti AA (2006) Experimental investigation of clear-water local scour at pile groups. *J Hydraul Eng* 132(10):1100–1104
- Barbhuiya AK, Dey S (2004) Local scour at abutments: a review. *Sadhana* 29(5):449–476
- Breusers HNC, Nicollet G, Shen HW (1977) Local scour around cylindrical piers. *J Hydraul Res* 15(3):211–252
- Chandra V (2003) Effect of waterway constriction and interference of two closely spaced piers on local scour. M.Tech. thesis, Indian Institute of Technology Kanpur, Kanpur, India
- Chiew YM (1984) Local scour at bridge piers. Doctoral dissertation, University of Auckland, Auckland, New Zealand
- Choudhury JR, Hasnat A (2015) Bridge collapses around the world: causes and mechanisms. In: IABSE-JSCE joint conference on advances in bridge engineering-III, IABSE, Dhaka, Bangladesh
- Coleman NL (1971) Analyzing laboratory measurements of scour at cylindrical piers in sand beds. In: *Hydraulic research and its impact on the environment*
- Dey S, Raikar RV (2007) Characteristics of horseshoe vortex in developing scour holes at piers. *J Hydraul Eng* 133(4):399–413

- Dey S, Bose SK, Sastry GL (1995) Clear water scour at circular piers: a model. *J Hydraul Eng* 121(12):869–876
- do Carmo JA (2005) Experimental study on local scour around bridge piers in rivers. *WIT Trans Ecol Environ* 83
- Elliott KR, Baker CJ (1985) Effect of pier spacing on scour around bridge piers. *J Hydraul Eng* 111(7):1105–1109
- Ettema R (1980) Scour at bridge piers. Doctoral dissertation, School of Engineering, University of Auckland, Auckland, New Zealand
- Hager WH, Unger J (2010) Bridge pier scour under flood waves. *J Hydraul Eng* 136(10):842–847
- Ismael A, Gunal M, Hussein H (2014) Use of downstream-facing aerofoil-shaped bridge piers to reduce local scour. *Int J Civil Eng Tech* 5(11):44–56
- Keshavarzi A, Shrestha CK, Melville B, Khabbaz H, Ranjbar-Zahedani M, Ball J (2018) Estimation of maximum scour depths at upstream of front and rear piers for two in-line circular columns. *Environ Fluid Mech* 18(2):537–550
- Kothyari UC (2007) Indian practice on estimation of scour around bridge piers—a comment. *Sadhana* 32(3):187–197
- Kothyari UC (2008) Bridge scour: status and research challenges. *ISH J Hydraul Eng* 14(1):1–27
- Kothyari UC, Garde RJ (2007) Bridge pier scour in gravel bed rivers. *ISH J Hydraul Eng* 13(3):1–14
- Kothyari UC, Garde RCJ, Ranga Raju KG (1992) Temporal variation of scour around circular bridge piers. *J Hydraul Eng* 118(8):1091–1106
- Kumar A, Kothyari UC, Raju KGR (2012) Flow structure and scour around circular compound bridge piers—a review. *J Hydro-Environ Res* 6(4):251–265
- Lee GC, Mohan SB, Huang C, Fard BN (2013) A study of US bridge failures (1980–2012). Technical report MCEER-13-0008, University at Buffalo, State University of New York
- Melville BW (1975) Local scour at bridge sites. Doctoral dissertation, University of Auckland, Auckland, New Zealand
- Melville BW (1997) Pier and abutment scour: integrated approach. *J Hydraul Eng* 123(2):125–136
- Melville BW, Chiew YM (1999) Time scale for local scour at bridge piers. *J Hydraul Eng* 125(1):59–65
- Melville BW, Coleman SE (2000) Bridge scour. Water Resources Publication
- Melville BW, Raudkivi AJ (1977) Flow characteristics in local scour at bridge piers. *J Hydraul Res* 15(4):373–380
- Melville BW, Sutherland AJ (1988) Design method for local scour at bridge piers. *J Hydraul Eng* 114(10):1210–1226
- Mia MF, Nago H (2003) Design method of time-dependent local scour at circular bridge pier. *J Hydraul Eng* 129(6):420–427
- Oliveto G, Hager WH (2002) Temporal evolution of clear-water pier and abutment scour. *J Hydraul Eng* 128(9):811–820
- Raudkivi AJ, Ettema R (1983) Clear-water scour at cylindrical piers. *J Hydraul Eng* 109(3):338–350
- Raudkivi AJ, Sutherland AJ (1981) Scour at bridge crossings. No. RRU Bull. 54, National Roads Board, Road Research Unit, New Zealand
- Richardson EV, Davis SR (2001) HEC-18. Evaluating scour at bridges. *Hydraul Eng Circular* 18
- Shen HW, Schneider VR, Karaki S (1969) Local scour around bridge piers. *J Hydraul Div* 95(6):1919–1940
- Subramanya K (1982) Flow in open channels, 3e. Tata McGraw-Hill Education (India) Private Limited, New Delhi
- Sumer BM, Christiansen N, Fredsoe J (1992) Time scale of scour around a vertical pile. In: The second international offshore and polar engineering conference, International Society of Offshore and Polar Engineers
- Sumer BM, Christiansen N, Fredsøe J (1997) The horseshoe vortex and vortex shedding around a vertical wall-mounted cylinder exposed to waves. *J Fluid Mech* 332:41–70
- Vijayasree BA, Eldho TI, Mazumder BS, Ahmad N (2017) Influence of bridge pier shape on flow field and scour geometry. *Int J River Basin Manage*, 1–21

- Yanmaz AM (2006) Temporal variation of clear water scour at cylindrical bridge piers. *Can J Civil Eng* 33(8):1098–1102
- Yanmaz AM, Altinbilek HD (1991) Study of time-dependent local scour around bridge piers. *J Hydraul Eng* 117(10):1247–1268

# Chapter 26

## Energy and Momentum Correction Coefficients in Compound Open Channel Flow



Sarjati Sahoo, Jnana Ranjan Khuntia , Kamalini Devi ,  
and Kishanjit Kumar Khatua 

**Abstract** Open channels have a wide range of applications directly or indirectly in our day-to-day life. Irrigation canals, waste water channels, sewers etc. are some of the practical examples of free-surface flow channels. Study of the hydraulic properties of open channel is a prime part of river engineering. This article presented a novel approach to model the two energy correction coefficients (kinetic energy and momentum coefficients) by collecting experimental data sets on rough asymmetric channels. In the present work, two sets of experiments were conducted on a compound asymmetric channel having two types of roughness material on the flood plain (plastic mat and gravel). To develop the models a wide range of data sets has been considered which includes asymmetrical compound channels with smooth or differential roughness cases. For the current work, multivariate regression analysis was used to develop ameliorated models to anticipate error-free values of the energy correction factors. Multivariate regression analysis is used to predict dependent variables from a number of independent variables. In this present study, for implementing multivariate regression analysis, the two correction factors (Energy correction factor  $\alpha$  and momentum correction factor  $\beta$ ) were chosen as dependent variable and aspect ratio ( $\delta = b/h$ ), roughness ratio ( $\gamma = n_{fp}/n_{mc}$ ), Reynolds No. ( $R_e$ ) and Froude's No. ( $F_r$ ), width ratio ( $\alpha_1 = B/b$ ), relative depth ( $Dr = (H - h)/H$ ) are taken as independent variable. Error analysis was performed to determine the accuracy of the present models.

---

S. Sahoo (✉) · J. R. Khuntia · K. K. Khatua  
Department of Civil Engineering, National Institute of Technology, Rourkela,  
Odisha 769008, India

K. K. Khatua  
e-mail: [kkkhatua@nitrkl.ac.in](mailto:kkkhatua@nitrkl.ac.in)

J. R. Khuntia  
Department of Civil Engineering, St. Martin's Engineering College, Dhulapally, Secunderabad,  
Telangana 500100, India

K. Devi  
Civil Engineering Department, Vidya Jyothi Institute of Technology, Hyderabad, Telangana  
500075, India

**Keywords** Open channel flow · Energy and momentum correction factors · Multivariate regression analysis · Error analysis

## 26.1 Introduction

Open channels are characterized by existence of a free surface. Open channels include both natural rivers and streams as well as man-made structures like irrigation canals, sewers and laboratory flumes. During flood, as the main-channel cannot accommodate all the water inside it, the excess water inundates the flood plain. When this condition arises, it is called as a compound channel. Open channels are used for irrigation, hydropower, drainage systems etc. Therefore, it is necessary to continuously investigate the open channel flow to achieve a more effective design (Khuntia et al. 2018; Devi et al. 2021). So, to design an open channel, three basic laws of conservation such as conservation of mass, energy and momentum are applied. But for free surface flow applications, the three conservation laws are expressed in terms of continuity equation, energy equation, and momentum equation respectively. Mean velocity is used in these equations, by assuming the flow is to be steady and uniform as well as constant vertically across the cross-section of flow. However, for open channels, the velocity distribution is not uniform (Al-Khatib and Dmadi 1999; Seckin et al. 2009). Due to this assumption, the final values of the energy, momentum and other related calculations resulted with some error (Wali 2013; Fenton 2005). To nullify this error, two correction factors are introduced which are called as energy and momentum correction factor or co-efficient. When the flow is steady or nearly uniform, the error resulted by the above assumption may be neglected. That means there is no need to introduce any corrections to the values of energy and momentum correction factors ( $\alpha = 1$  and  $\beta = 1$ ). But in practical cases, steady and uniform is nearly impossible. That means the values of correction factors are greater than unity and cannot be neglected. So, to have an error free design of open channels, proper assessment of these two factors is very much essential. It's very common in rivers that the flood plain roughness is more than that of main channel roughness, which affects the flow velocities of main channel and flood plain. Due to which the velocity of flow in main channel is more than the velocity of water in flood plain. This difference in flow velocities cause a lot of momentum transfer within the main channel and flood plain. The whole flow becomes very complex as the due to this non uniformity in velocity distribution in lateral direction. In many literatures it has been clearly documented about exchange of momentum by Sellin (1964), Knight and Demetriou (1983). Shape of the velocity distribution curve affects the energy and momentum correction factors. Many researchers like Al-Khatib and Göğüş (1999), Seckin et al. (2009), Mohanty et al. (2012), developed equations to calculate  $\alpha$  and  $\beta$  under certain assumptions and conditions. In the present study, improved models have been developed for correction coefficients specifically for asymmetrical compound channels. For more accuracy, both geometric and hydraulic parameters are considered to develop the model.



## 26.2 Theoretical Analysis

To design an open channel, three basic laws of conservation such as conservation of mass, energy and momentum are applied. But for free surface flow applications, the three conservation laws are expressed in terms of continuity equation, energy equation, and momentum equation respectively. The equations are given below in Eqs. 26.1–26.3 respectively.

*Continuity equation*

$$Q = A_1U_1 = A_2U_2 = \dots = A_nU_n \quad (26.1)$$

*Energy equation*

$$\frac{P_1}{\rho g} + \frac{U_1^2}{2g} + z_1 = \frac{P_2}{\rho g} + \frac{U_2^2}{2g} + z_2 + \sum h \quad (26.2)$$

*Momentum equation*

$$F_r = \rho Q[U_{2x} - U_{1x}] \quad (26.3)$$

where  $Q$  is conveyance,  $A_1$ ,  $A_2$ , and  $U_1$ ,  $U_2$  are area of cross-section and average velocity at Sects. 1 and 2 respectively. Average velocity is used in all the above three equations by assuming the flow as steady and uniform and also constant vertically across the cross-section of flow. But in case of open channel flows, the velocity distribution is non-uniform due to the boundary resistance. These assumptions may result in erroneous data of energy and momentum, which should be corrected while designing hydraulic structures over open channels. To nullify this error, two correction factors are introduced which are called as energy and momentum correction factor or co-efficient.

To estimate these correction coefficients, Eqs. 26.4 and 26.5 are used and the equations are given below.

$$\alpha = \frac{\int_0^A U^3 dA}{U_m^3 A} \quad (26.4)$$

$$\beta = \frac{\int_0^A U^2 dA}{U_m^2 A} \quad (26.5)$$

where

$\alpha$ : energy correction factor,

$\beta$ : coefficient of momentum correction,

$A$ : total area of cross-section,  
 $U$ : flow velocity passing through the small area  $dA$  and  
 $U_m$ : mean or average velocity of flow.

### 26.3 Experimental Setup and Procedures

To perform experiments, a channel was constructed by using mild steel plates and cement concrete in side the Hydraulics Lab of NIT Rourkela. For continuous supply and recirculation of water into the experimental flume, a large reinforced cement concrete (R.C.C) overhead tank and a volumetric tank were constructed at the upstream and downstream side of the flume respectively by using two 10 HP pumps. To reduce the energy of water, a stilling chamber fitted with flow straighteners and also honeycomb structures was provided at the inlet of the flume. In this process, flow uniformity was achieved throughout the length of the flume. Trapezoidal shape was chosen for the main channel cross section with bottom width ( $b$ ) 0.33 m, height ( $h$ ) 0.11 m and side slope 1:1 ( $H:V$ ) over a length of 12 m. Total width of the compound channel is 1.19 m for acquiring width ratio ( $\alpha_1$ ) 3.6 and the bed slope of the channel was maintained at 0.001 by adjusting wheel and gear arrangement provided at inlet of the channel. Experiments were performed on the asymmetric channel with differential roughness having smooth main channel and rough flood plain, by using plastic mat of thickness 15 mm having manning's  $n$  value 0.024 on the flood plain bed. Another set of experiments were performed on the same channel by changing the flood plain roughness from plastic mat to small gravel of Manning's  $n$  value 0.02. Main channel roughness was maintained uniform with side slope and different roughness for flood plain to investigate the momentum transfer and secondary current effect in compound channel. Figure 26.1 shows the layout of NITR channels and Photographs of NITR channels used in the present work are shown in Fig. 26.2.

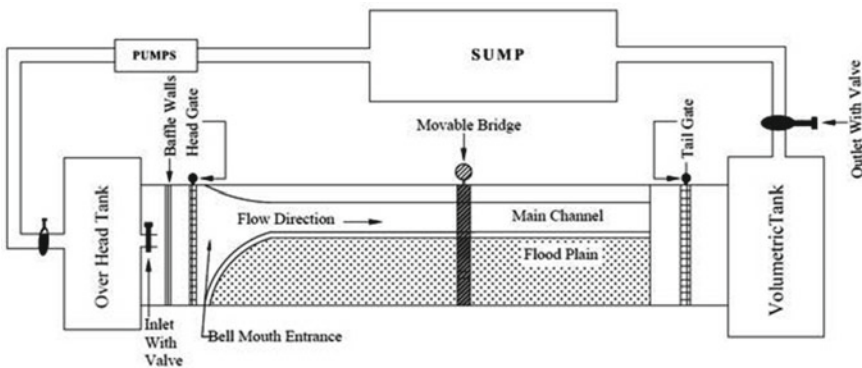


Fig. 26.1 Layout of experimental setup of NITR channels



Fig. 26.2 Photographs of NITR experimental channels used in the present study

## 26.4 Model Development

### 26.4.1 Multiple Regression Analysis

In statistics, regression analysis is done to evaluate necessary relation between variables, which includes various techniques for modelling and analysing several variables. Regression analysis helps us to estimate a proper correlation between a response (criterion) variable and one or more regressor variables (or predictors). More precisely, it enables us to perceive the effect of one varying independent parameter on the dependent parameter while the other independent variables are kept constant. Regression analysis is widely used for predicting and forecasting.

Multiple regression analysis is a capable strategy used to anticipate the obscure estimation of a variable from two or more known variables. More specifically, multiple regression analysis helps us to anticipate the estimation of “y” for given estimation of  $x_1, x_2 \dots x_n$ . We can likewise concentrate the individual impact of the known factors on the obscure parameter. The standard basis of multiple regression is to know more about the association between a few autonomous or predictor factors and a dependent or paradigm variable. Multiple regression analysis is used to predict dependent variables from a number of independent variables.

In this present study, for implementing multiple regression analysis energy correction factor ( $\alpha$ ) and momentum correction factor ( $\beta$ ) were taken as dependent variable and aspect ratio ( $\delta = b/h$ ), roughness ratio ( $\gamma = n_{fp}/n_{mc}$ ), Reynolds number ( $R_e$ ), Froude's number ( $F_r$ ), width ratio ( $\alpha_1 = B/b$ ), relative depth ( $D_r = (H - h)/H$ ) are taken as independent variable. A number of single regression models were developed as one to one relationship between the dependent variable (*DISADF*) and the independent variables (width ratio, aspect ratio, relative depth, friction factor ratio and bed slope). Based on the highest coefficient of regression ( $R^2$ ) values, best single regression models were selected. The properties of the various channels, which were taken for this study given in Table 26.1.

**Table 26.1** Resume of the asymmetrical compound channel data sets

Series	$b(m)$	$B(m)$	$h(m)$	$S_c$	$H(m)$	$S_0$	$n_{fp}$	$n_{mc}$	$Q(m^3/s)$
NIT R1	0.33	1.19	0.11	1	0.134–0.165	0.001	0.024	0.01	0.034–0.0596
NIT R2	0.33	1.19	0.11	1	0.14–0.181	0.001	0.02	0.01	0.0402–0.0820
FCF S06	1.5	4.05	0.15	1	0.15826–0.30185	0.001027	0.01	0.01	0.2235–0.9292
Al-Khatib et al. (2013)	0.1	0.3	0.02	0	0.049–0.110	0.0025	0.015	0.015	0.0033–0.0144
Bousmar (2002)	0.4	0.8	0.05	0	0.0543–0.0912	0.00099	0.0107	0.0107	0.00782–0.02204
Atabay (2001)	0.398	0.8053	0.05	0	0.0593–0.1095	0.002024	0.0091	0.0091	0.015–0.0554
Devi and Khatua 1 (2017)	0.33	1.19	0.11	1	0.12–0.14	0.001	0.01	0.01	0.02873–0.04055
Devi and Khatua 2 (2017)	0.33	1.45	0.11	1	0.12–0.13	0.001	0.01	0.01	0.031461–0.03939
Devi and Khatua 3 (2017)	0.33	1.683	0.11	1	0.125–0.15	0.001	0.01	0.01	0.03024–0.06169
James and Brown T5 (1977)	0.1778	0.4696	0.0508	1	0.05578–0.08016	0.001–0.003	0.012	0.011	0.00708–0.01467
James and Brown T7 (1977)	0.1778	0.8509	0.0508	1	0.05456–0.08168	0.001–0.003	0.011	0.01	0.00558–0.01433
Sun SRC (2007)	0.12	0.27	0.036	0	0.0466–0.0713	0.001	0.0103	0.0103	0.00215–0.00589
Sun STC (2007)	0.12	0.306	0.036	1	0.0475–0.0723	0.001	0.011	0.011	0.00194–0.00558

### 26.5 Results and Discussions

By using the Eqs. 26.4 and 26.5, energy and momentum correction factors were calculated for the present experimental asymmetric compound channel having two types of roughness on flood plain (Plastic mat- roughness-1, small gravel- roughness-2) and presented in the Table 26.2.

The graphs between energy and momentum correction factors and relative depth for both roughness cases were also plotted and given in Figs. 26.3 and 26.4.

From Figs. 26.3 and 26.4 and Table 26.2, it has been observed that the magnitudes of both the correction factors ( $\alpha$  and  $\beta$ ) decrease when the depth of flow increases. The transfer of momentum between the main channel and flood plain becomes very intense in case of low flow depth conditions due more difference in flow velocities of main channel and flood plain. But while considering high flow depth cases, this difference becomes less. That's why the resulted energy and momentum coefficients were higher for low flow depth cases and nearer to one when the flow depth increased for the present experimental channel.

**Table 26.2** Energy and momentum correction factors for the experimental channel

Roughness-1 (NITR 1)			Roughness-2 (NITR 2)		
$H(m)$	$\alpha_1$	$\beta_1$	$H(m)$	$\alpha_1$	$\beta_1$
0.134	1.235	1.080	0.14	1.189	1.066
0.14	1.180	1.054	0.145	1.173	1.065
0.147	1.169	1.045	0.156	1.141	1.040
0.1545	1.123	1.028	0.16	1.124	1.039
0.16	1.122	1.032	0.17	1.089	1.017
0.165	1.108	1.028	0.176	1.069	1.014
–	–	–	0.181	1.057	1.002

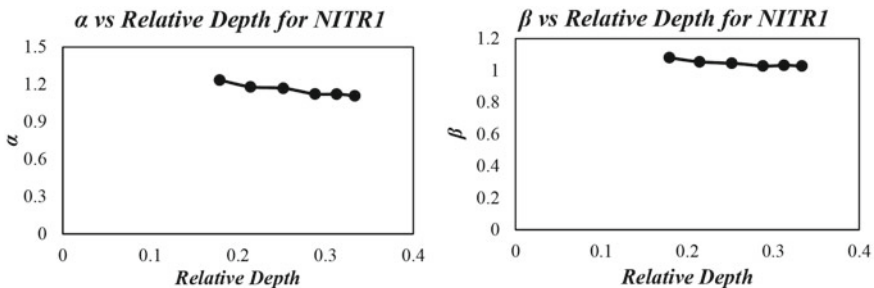


**Fig. 26.3** Variation of  $\alpha$  and  $\beta$  with relative depth for roughness-1

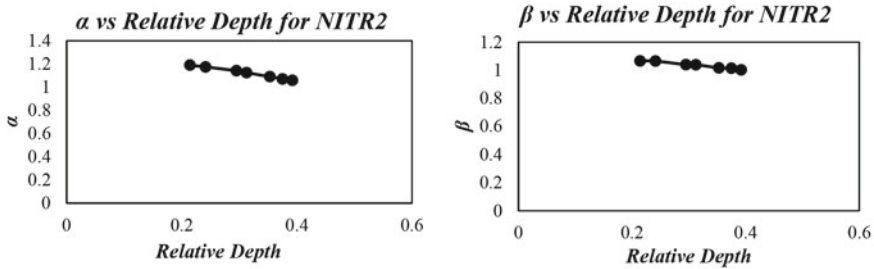


Fig. 26.4 Variation of  $\alpha$  and  $\beta$  with relative depth for roughness-2

### 26.5.1 Regression Models for Asymmetrical Compound Channels

The single regression plots between the dependent parameters ( $\alpha$  and  $\beta$ ) and independent parameters ( $\delta, \gamma, R_e, F_r, \alpha_1, D_r$ ) are given in Figs. 26.5 and 26.6.

The relationships between dependent ( $\alpha$ ) and independent parameters ( $\delta, \gamma, R_e, F_r, \alpha_1, D_r$ ) for energy correction factor are given in Table 26.3.

The relationships between dependent ( $\beta$ ) and independent parameters ( $\delta, \gamma, R_e, F_r, \alpha_1, D_r$ ) for energy correction factor are given in Table 26.4.

Then multiple regression analysis was applied using single regression relationships between the dependent variables ( $\alpha$  and  $\beta$ ) and independent parameters ( $\delta, \gamma, R_e, F_r, \alpha_1, D_r$ ). The proposed models for energy correction factor and momentum correction factor are given by Eqs. 26.6 and 26.7.

$$\alpha = (-0.01\delta) - (0.23\gamma^2) + (0.54\gamma) - (0.054\ln(R_e)) + (0.47F_r^{-0.37}) + (0.006\alpha_1) - (0.33D_r) + 1.06 \tag{26.6}$$

$$\beta = (-0.011\delta) - (0.155\gamma^2) + (0.369\gamma) - (0.00000025R_e) - (0.102F_r) - (0.032\alpha_1) - (0.12D_r) + 1.17 \tag{26.7}$$

### 26.6 Error Analysis

Error analysis is the study of quantification of error, or uncertainty that may be present in a model. Generally, error analysis is done to determine the strength or accuracy of a model. The different types of errors used to determine the accuracy of a model are Mean Percentage Errors (*MPE*), Mean Absolute Percentage Errors (*MAPE*) and Root Mean Square Errors (*RMSE*). For determining the strength of the model presented in this study, MAPE, MPE and RMSE were used. The errors for various channels taken for this model were calculated using the formula given by Eqs. 26.8–26.10.

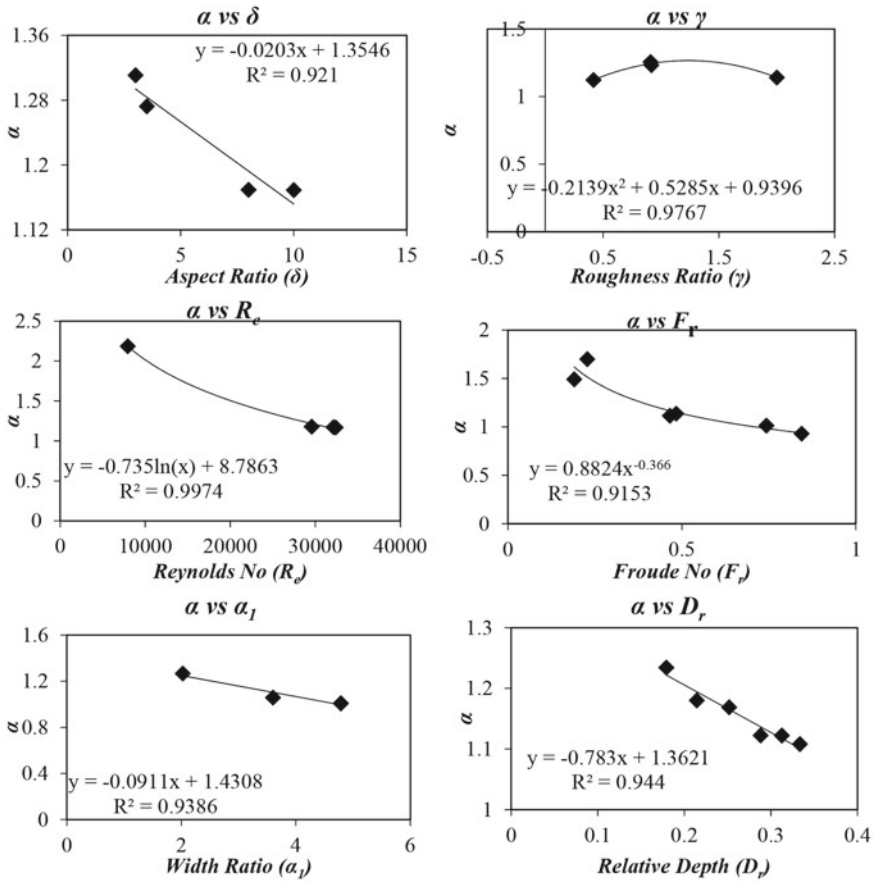


**Fig. 26.5** Energy correction factor versus aspect ratio, roughness ratio, Reynolds number, Froude’s number, width ratio, and relative depth plots with highest  $R^2$  value

$$MAPE = \frac{100}{N} \sum_{i=1}^N \left| \frac{\alpha_{\text{observed}} - \alpha_{\text{predicted}}}{\alpha_{\text{observed}}} \right| \tag{26.8}$$

$$MPE = \frac{100}{N} \sum_{i=1}^N \left( \frac{\alpha_{\text{observed}} - \alpha_{\text{predicted}}}{\alpha_{\text{observed}}} \right) \tag{26.9}$$

$$RMSE = \sqrt{\frac{1}{N} \sum_{i=1}^N (\alpha_{\text{observed}} - \alpha_{\text{predicted}})^2} \tag{26.10}$$

where  $\alpha_{\text{observed}}$  the observed value of energy correction is factor and  $\alpha_{\text{predicted}}$  is the predicted value of energy correction factor using the improved model.

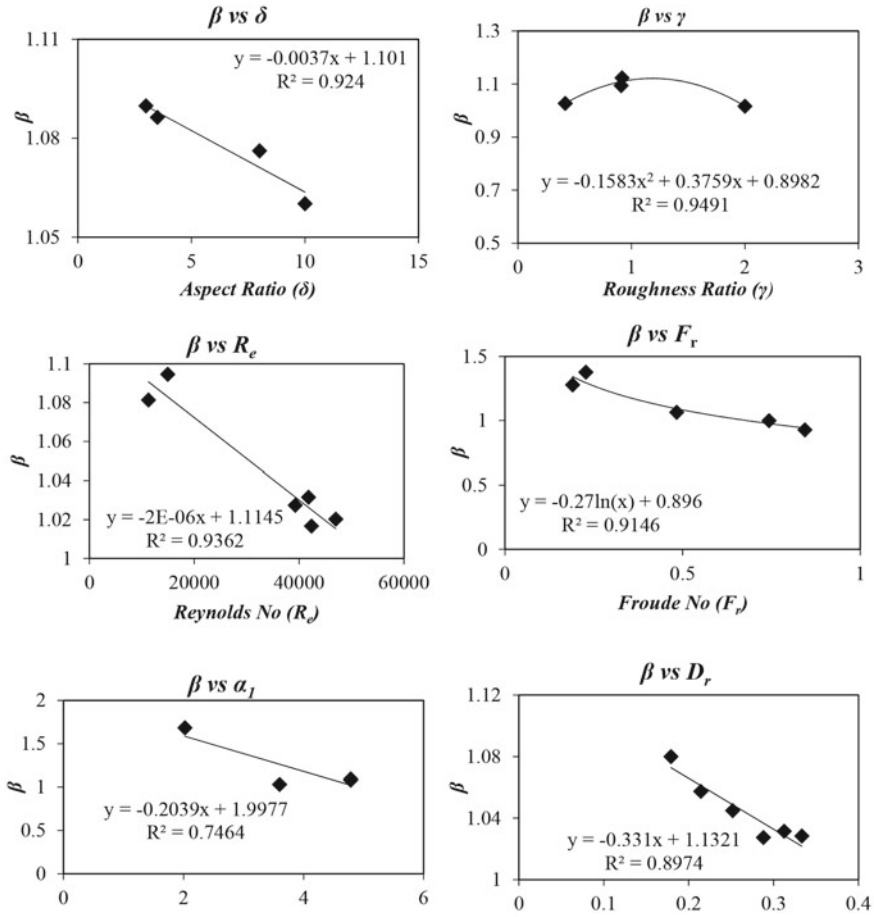


**Fig. 26.6** Momentum correction factor versus aspect ratio, roughness ratio, Reynolds number, Froude’s number, width ratio, and relative depth plots with highest  $R^2$  value

**Table 26.3** Relationships between dependent ( $\alpha$ ) and independent parameters ( $\delta, \gamma, R_e, F_r, \alpha_1, D_r$ ) for energy correction factor

Parameter	Relation	Function	$R^2$
Aspect ratio ( $\delta$ )	$\alpha = -0.0203\delta + 1.3546$	Linear	0.921
Roughness ratio( $\gamma$ )	$\alpha = -0.2139\gamma^2 + 0.5285\gamma + 0.9396$	Polynomial	0.9767
Reynolds no ( $R_e$ )	$\alpha = -0.735\ln(R_e) + 8.7863$	Logarithmic	0.9974
Froude no ( $F_r$ )	$\alpha = 0.8824F_r^{-0.366}$	Power	0.9153
Width ratio ( $\alpha_1$ )	$\alpha = -0.0911\alpha_1 + 1.4308$	Linear	0.9386
Relative depth ( $D_r$ )	$\alpha = -0.783D_r + 1.3621$	Power	0.944



**Table 26.4** Relationships between dependent ( $\beta$ ) and independent parameters ( $\delta, \gamma, R_e, F_r, \alpha_1, D_r$ ) for energy correction factor

Parameter	Relation	Function	R <sup>2</sup>
Aspect ratio ( $\delta$ )	$\beta = -0.0037\delta + 1.101$	Linear	0.924
Roughness ratio( $\gamma$ )	$\beta = -0.1538\gamma^2 + 0.3759\gamma + 0.8982$	Polynomial	0.9491
Reynolds no ( $R_e$ )	$\beta = -2E-06R_e + 1.1145$	Linear	0.9362
Froude no ( $F_r$ )	$\beta = -0.27\ln(F_r) + 0.896$	Logarithmic	0.9146
Width ratio ( $\alpha_1$ )	$\beta = -0.2039\alpha_1 + 1.9977$	Linear	0.7464
Relative depth ( $D_r$ )	$\beta = -0.331D_r + 1.1321$	Linear	0.8974

**Table 26.5** Resulted error from the present models

Correction factor	MPE (%)	MAPE (%)	RMSE
Energy correction coefficient ( $\alpha$ )	-0.715	4.562	0.079
Momentum correction coefficient ( $\beta$ )	-0.358	2.897	0.023

The above equations (Eqs. 26.8–26.10) were used to predict the errors for momentum correction coefficient ( $\beta$ ) by replacing  $\alpha$  with  $\beta$ . The various types of errors are presented in Table 26.5.

From Table 26.5, it has been observed that the MPE is -0.715%, MAPE is 4.562% and RMSE is 0.079 for the model of energy correction coefficient ( $\alpha$ ) and for the model of momentum correction coefficient ( $\beta$ ), the errors are -0.358%, 2.897% and 0.023 as MPE, MAPE and RMSE respectively. As all the error parameters are closer to zero, it has been concluded that both the models are being well predicted for asymmetrical compound channels.

## 26.7 Conclusions

1. Experimental analysis has been performed on the asymmetrical channel to analyse the correction factors ( $\alpha$  and  $\beta$ ).
2. It has been observed that the magnitudes of both the correction factors ( $\alpha$  and  $\beta$ ) decrease when the depth of flow increases.
3. The transfer of momentum between the main channel and flood plain becomes very intense in case of low flow depth conditions due more difference in flow velocities of main channel and flood plain. But while considering high flow depth cases, this difference becomes less.
4. The resulted energy and momentum coefficients were higher for low flow depth cases and nearer to one when the flow depth increased for the present experimental channel.

5. Improved models have been developed for both energy and momentum correction factors using multiple regression analysis. Error analysis was also performed for both the models.

## References

- Al-Khatib IA, Dmadi NM (1999) Boundary shear stress in rectangular compound channels. *Turk J Eng Environ Sci* 23(1):9–18
- Al-Khatib IA, Göğüş M (1999) Momentum and kinetic energy coefficients in symmetrical rectangular compound cross section flumes. *Turk J Eng Environ Sci* 23(3):187–198
- Al-Khatib IA, Abu-Hassan HM, Abaza KA (2013) Development of empirical regression-based models for predicting mean velocities in asymmetric compound channels. *Flow Meas Instrum* 33:77–87
- Atabay S (2001) Stage-discharge, resistance and sediment transport relationships for flow in straight compound channels (Doctoral dissertation, University of Birmingham)
- Bousmar D (2002) Flow modelling in compound channels, momentum transfer between main channel and prismatic or non-prismatic floodplains. *Unité de Génie Civil et Environnemental*, 326
- Devi K, Khatua KK (2017) Depth-averaged velocity and boundary shear stress prediction in asymmetric compound channels. *Arab J Sci Eng* 42(9):3849–3862
- Devi K, Das BS, Khuntia JR, Khatua KK. Analytical solution for depth-averaged velocity and boundary shear in a compound channel. In *Proceedings of the Institution of Civil Engineers-Water Management* 2021 Jun 174(3):143–158. Thomas Telford Ltd
- Fenton JD (2005, September) On the energy and momentum principles in hydraulics. In: *Proceedings of the 31st congress IAHR, Seoul*, pp 625–636
- James M, Brown BJ (1977) Geometric parameters that influence floodplain flow, no WES-RR-H-77-1. Army Engineer Waterways Experiment Station Vicksburg Miss
- Khuntia JR, Devi K, Khatua KK. Boundary shear stress distribution in straight compound channel flow using artificial neural network. *Journal of Hydrologic Engineering*. 2018 May 1–23(5):04018014
- Knight DW, Demetriou JD (1983) Flood plain and main channel flow interaction. *J Hydraul Eng* 109(8):1073–1092
- Mohanty PK, Dash SS, Khatua KK, Patra KC (2012) Energy and momentum coefficients for Wide compound channels. *River Basin Manag* VII 172:87
- Seckin G, Ardıçlıoğlu M, Cagatay H, Cobaner M, Yurtal R (2009) Experimental investigation of kinetic energy and momentum correction coefficients in open channels. *Sci Res Essays* 4(5):473–478
- Sellin RHJ (1964) A laboratory investigation into the interaction between the flow in the channel of a river and that over its flood plain. *La Houille Blanche* (7):793–802
- Sun X (2007) Flow characteristics in compound channels with and without vegetation (Doctoral dissertation, © Xin Sun)
- Wali UG (2013) Kinetic energy and momentum correction coefficients for a small irrigation channel. *Int J Emerg Technol Adv Eng* 3(9). <http://ethesis.nitrkl.ac.in/view/people/Sahoo=3ASarjati=3A=3A.html>, <http://dspace.nitrkl.ac.in/dspace/handle/2080/3166>

# Chapter 27

## Development of Hydraulic Geometry Equations for Middle Tapi River, India



Suhani Choudhary and P. L. Patel

**Abstract** In present study, hydraulic geometry equations are developed for middle Tapi river, India to assess the variation in hydraulic parameters at Bhusawal, Padalse, Sukhwad, Gidhade, and Sarangkhedra stream gauging stations on decadal basis while considering the mean annual discharges of respective periods for the analyses. The insignificant variations in water surface width with the discharge has indicated box shaped cross-section at Sarangkhedra stream gauging station. On other hand, large variations in water surface width with the discharge at Padalse station indicated dish shaped cross section at the same stream gauging station. The nature of hydraulic geometric equations has indicated higher stream powers (higher  $m/f$  values) at upstream gauging stations, i.e., Bhusawal and Padalse, vis-à-vis downstream gauging stations, i.e., Sukhwad, Gidhade and Sarangkhedra stream gauging stations. Present study would be useful in planning appropriate river training structure and design of efficient hydraulic structures in the respective river.

**Keywords** Hydraulic geometry equations · Stream gauging stations · Mean annual discharges · Box shaped cross section · Middle Tapi river

### 27.1 Introduction

Understanding the hydraulic behaviour of alluvial rivers is required in planning efficient hydraulic structures and flood protection measures along respective reaches. Several studies were reported in literature to classify the flows as geomorphologically effective flows. The mean annual discharge was used as the effective discharge in studying the hydraulic geometry of the rivers in the great plains of USA and discovered that mean discharge had a frequency of twenty-five percent (Leopold and

---

S. Choudhary

M.Tech Graduate, Department of Civil Engineering, Sardar Vallabhbhai National Institute of Technology, 395007 Surat, India

P. L. Patel (✉)

Professor, Department of Civil Engineering, Sardar Vallabhbhai National Institute of Technology, 395007 Surat, India

Maddock 1953). The dominant discharge is a hypothetical mean discharge which causes the same morphological changes in the alluvial rivers as is caused by actual varying discharges throughout the year. The bankful discharge was used to study the characteristic of rivers in England (Nixon et al. 1959). The bankful discharge is defined as the discharge which completely fills the stream channel up to the top of the bank. The term bed-generative discharge was defined as the discharge that transports largest volume of coarser material (Menard 1950). The form and shape of the river channel is of major importance in transmission of flow, sediment and their interaction with physical environment. The hydraulic geometry equations provide the information on shape of channel parameters and power of the streams, particularly, during the extreme events. The high magnitude floods of monsoon were considered as geomorphic agents and suggested that Tapi and Narmada rivers, in central India, are characterized by one of the most intense flood regimes in the seasonal tropics (Kale et al. 1994). The effect of floods depends on many controlling factors like magnitude, frequency, rate of sediment movement, flood power, duration of effective flows, and channel geometry (Kale and Hire 2004). The hydraulic geometry equations are having significant importance in planning, designing of hydraulic structures, and management of river engineering and training works (Singh 2003). Present study, involves the development of hydraulic geometry equations along the middle Tapi river, India. Subsequently, the parameters of developed hydraulic equations are linked with available measured cross-sections at the respective stations.

## 27.2 Study Area

The Tapi is the second largest west flowing river in India. It flows from east to west in central and western India between the Godavari and Narmada basins. The Tapi river comes in the category of major rivers of peninsular India with the total length of around 724 km. Out of total length, initial 282 km falls in Madhya Pradesh, 228 km in Maharashtra and remaining 214 km is in Gujarat state. It originates a place called Multai in the Betul district of Madhya Pradesh at an elevation of around 752 m and meets the Arabian Sea in gulf of Cambay after passing through the Surat city. The Tapi river basin covers an area of around 65,145 km<sup>2</sup>, which is almost two percent of the total geographical area of the country.

The middle Tapi begins from Hathnur reservoir in Maharashtra and continues up to Ukai reservoir in Gujarat state. It falls between longitudes 73°35' E to 76°21' E and latitudes of 21° N to 21°45' N and covers a total area of 25,320 km<sup>2</sup> including Girna basin. The average annual rainfall in the middle Tapi basin is 631.5 mm. There are total nine Central Water Commission (CWC) discharge gauging sites located in the middle Tapi basin including Girna basin, i.e., Hathnur, Bhusawal, Dahi-gaon, Savkheda, Malkheda, Gidhade, Morane, Girna dam, and Sarangkhedha. There are also four stream gauging stations of Hydrological Data Users Group (HDUG) of Maharashtra along the middle Tapi river, i.e., Bhusawal, Padlse, Sukhwad and Sarangkhedha. The index map of study area is shown in Fig. 27.1. Table 27.1 shows the data used in present study and their relevant sources.

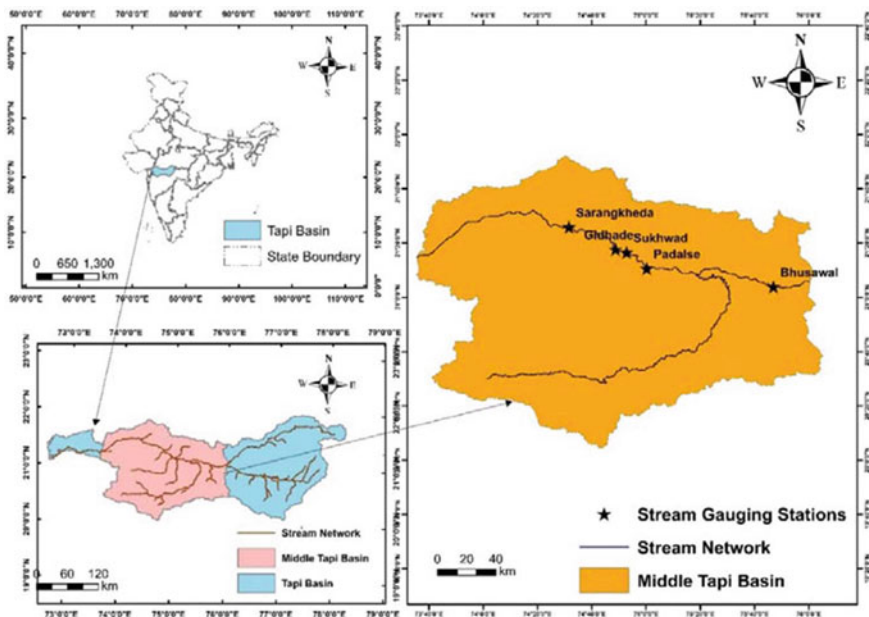


Fig. 27.1 Index map of study area

Table 27.1 Hydrological data used in present study

Station name	Duration		Type of data	Source
	From	To		
Bhusawal	1987	2006	Hourly hzs (absolute gauge)	HDUG, Nashik
	1984	2010	Hourly discharge	HDUG, Nashik
	1967	2004	Hourly hhs (with mean sea level)	CWC, Surat
Padalse	1987	2006	Hourly hzs (water level/stage)	HDUG, Nashik
	1987	2002	Hourly discharge	
Sukhwad	1984	2006	Hourly hzs (water level/stage)	HDUG, Nashik
	1984	2010	Hourly discharge	
Gidhade	1990	2007	Hourly hzs (water level/stage)	CWC, Surat
	1970	2012	Daily discharge and hzs	
Sarangkheda	1984	2006	Hourly (water level/stage)	HDUG, Nashik
	1984	2010	Hourly discharge	HDUG, Nashik
	1984	2010	Daily sediment discharge	CWC, Surat

## 27.3 Results

### 27.3.1 *Development of Hydraulic Geometry Equations for Stream Gauging Stations Along Middle Tapi River*

The quantitative assessment of hydraulic parameters like depth, width, velocity and suspended sediment load and their relation with varying discharges, are required for morphological study of natural streams. The relation between aforesaid variables is termed as hydraulic geometry equations. For developing hydraulic geometry equations at Bhusawal, Padalse, Sukhwad, Gidhade, and Sarangkheda stream gauging stations, measured daily discharges and stage were used. Also, the representative cross sections were developed using the geometry of a particular stream gauging station of ten years. Using decadal best fit cross-section and daily stage data, corresponding cross-sectional area, and top width were estimated. Using cross-sectional area and top width, mean depth of flow of the channel was calculated. As the annual mean discharge is considered the effective discharge for influencing the morphology of channel, the same has been used to develop hydraulic geometry equations on decadal basis at aforesaid stations. Tables 27.2, 27.3, 27.4, 27.5 and 27.6 show the hydraulic geometry equations for the gauging stations at Bhusawal, Padalse, Sukhwad, Gidhade, and Sarangkheda stream gauging stations respectively.

In the hydraulic geometry equations, included in Tables 27.2, 27.3, 27.4, 27.5 and 27.6, the ratio of hydraulic exponent of width ( $b$ ) and hydraulic exponent of depth ( $f$ ), i.e.,  $b/f$ , is a measure of relative variation of channel width with respect to depth. Also, the ratio of hydraulic exponent of velocity ( $m$ ) and hydraulic exponent of depth ( $f$ ), i.e.,  $m/f$  is measure of stream power and sediment transport capacity of the channel. Table 27.7 shows the variation of hydraulic exponents,  $b/f$  and  $m/f$  values on decadal basis at the stream gauging stations along the river.

## 27.4 Discussions

As it can be seen from Table 27.7, that ' $b$ ' values for Bhusawal stream gauging station are 0.126, 0.127, and 0.095 for periods 1984–1990, 1991–2000, and 2001–2010 respectively. The values of  $m/f$  values at the same station are 1.614, 1.486 and 0.925 for periods 1984–1990, 1991–2000, and 2001–2010 respectively. The higher values of  $m/f$  clearly indicate the higher stream power at the same station. The lower values of  $b$  at the Bhusawal stream gauging station indicate vertical sides of the channel at the same station due to insignificant variation in width with the discharge, see Fig. 27.2. The lowest values of  $b$  at Sarangkheda stream gauging station, among all stream gauging stations, indicates that cross section of the same stream gauging station is box shaped, and variation of width with the discharge is negligible, see Fig. 27.3. From Table 27.7, it is clearly indicated that stream power of Gidhade stream gauging station is minimum vis-s-vis other stream gauging stations along

**Table 27.2** At-a-station hydraulic geometry equations using annual mean discharge at Bhusawal

Period	Q versus W	R <sup>2</sup>	Q versus Y	R <sup>2</sup>	Q versus U	R <sup>2</sup>	m + f + b	ack
1984–1990	$W = 191.65 Q^{0.1267}$	0.95	$Y = 0.1441 Q^{0.334}$	0.94	$U = 0.0362 Q^{0.5393}$	0.99	1	0.99
1991–2000	$W = 191.21 Q^{0.1271}$	0.93	$Y = 0.1284 Q^{0.351}$	0.95	$U = 0.0407 Q^{0.5219}$	0.99	1	0.99
2001–2006	$W = 236.74 Q^{0.0956}$	0.95	$Y = 0.0574 Q^{0.4697}$	0.99	$U = 0.0736 Q^{0.4347}$	0.99	1	0.99

**Table 27.3** At-a-station hydraulic geometry equations using annual mean discharge at Padalse station

Period	Q versus W	R <sup>2</sup>	Q versus Y	R <sup>2</sup>	Q versus U	R <sup>2</sup>	m + f + b	ack
1987–1990	$W = 39.407 Q^{0.1508}$	0.99	$Y = 0.2689 Q^{0.3638}$	0.99	$U = 0.0944 Q^{0.4854}$	0.99	1	0.99
1991–2000	$W = 16.344 Q^{0.1645}$	0.99	$Y = 0.1892 Q^{0.3467}$	0.95	$U = 0.3233 Q^{0.4888}$	0.97	1	0.99



**Table 27.4** At-a-station hydraulic geometry equations using annual mean discharge at Sukhwad station

Period	Q versus W	R <sup>2</sup>	Q versus Y	R <sup>2</sup>	Q versus U	R <sup>2</sup>	m + f + b	ack
1984–1990	$W = 292.39 Q^{0.1801}$	0.99	$Y = 0.2801 Q^{0.3598}$	0.99	$U = 0.0122 Q^{0.4601}$	0.99	1	0.99
1991–2000	$W = 296.46 Q^{0.1935}$	0.93	$Y = 0.3413 Q^{0.33}$	0.95	$U = 0.0099 Q^{0.4765}$	0.99	1	0.99
2001–2006	$W = 290.81 Q^{0.134}$	0.95	$Y = 0.245 Q^{0.3807}$	0.99	$U = 0.014 Q^{0.4853}$	0.99	1	0.99

**Table 27.5** At-a-station hydraulic geometry equations using annual mean discharge at Gidhade station

Period	Q versus W	R <sup>2</sup>	Q versus Y	R <sup>2</sup>	Q versus U	R <sup>2</sup>	m + f + b	ack
1981–1990	W = 200.71 Q <sup>0.0891</sup>	0.87	Y = 0.0266 Q <sup>0.6436</sup>	0.99	U = 0.1874 Q <sup>0.2672</sup>	0.99	1	0.99
1991–2000	W = 164.04 Q <sup>0.1235</sup>	0.64	Y = 0.8859 Q <sup>0.6246</sup>	0.95	U = 0.2067 Q <sup>0.2519</sup>	0.99	1	0.99
2001–2006	W = 149.64 Q <sup>0.1339</sup>	0.80	Y = 0.0334 Q <sup>0.6092</sup>	0.99	U = 0.2003 Q <sup>0.2569</sup>	0.99	1	0.99

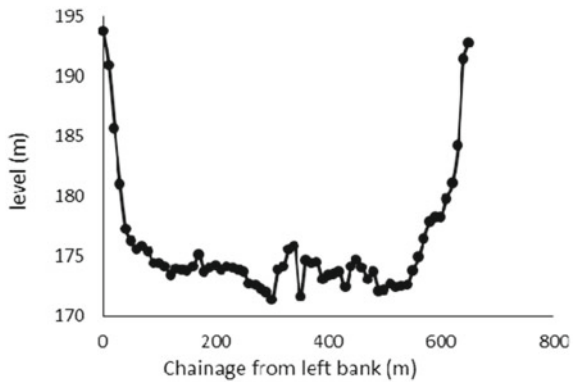
**Table 27.6** At-a-station hydraulic geometry equations using annual mean discharge at Sarangkhedha station

Period	Q versus W	R <sup>2</sup>	Q versus Y	R <sup>2</sup>	Q versus U	R <sup>2</sup>	m + f + b	ack
1981–1990	$W = 392.8 Q^{0.0378}$	0.99	$Y = 0.1286 Q^{0.4603}$	0.99	$U = 0.0198 Q^{0.5019}$	0.99	1	0.99
1991–2000	$W = 386.58 Q^{0.0379}$	0.99	$Y = 0.1215 Q^{0.4579}$	0.99	$U = 0.0213 Q^{0.5042}$	0.99	1	0.99
2001–2010	$W = 386.87 Q^{0.0355}$	0.99	$Y = 0.1196 Q^{0.4495}$	0.99	$U = 0.0216 Q^{0.515}$	0.99	1	0.99

**Table 27.7** Hydraulic exponents of hydraulic geometry equations

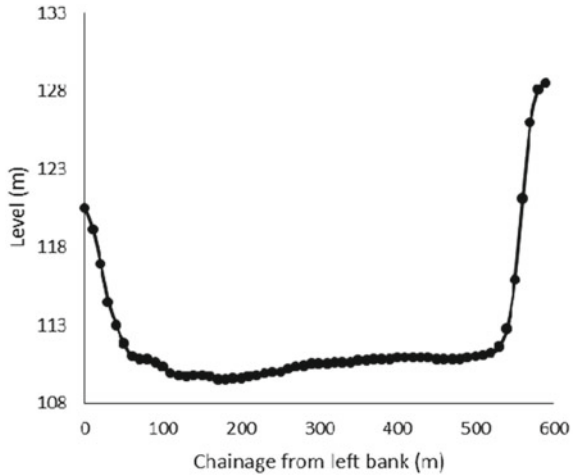
Station	Time period	b	f	m	b/f	m/f
Bhusawal	1984–1990	0.1267	0.334	0.5393	0.379	1.614
	1991–2000	0.1271	0.351	0.5219	0.362	1.486
	2001–2006	0.0956	0.4697	0.4347	0.203	0.925
Padalse	1987–1990	0.1508	0.3638	0.4854	0.414	1.334
	1991–2000	0.1645	0.3467	0.4888	0.474	1.409
Sukhwad	1984–1990	0.1801	0.3598	0.4601	0.500	1.278
	1991–2000	0.1935	0.33	0.4765	0.586	1.443
	2001–2003	0.134	0.3807	0.4853	0.351	1.274
Gidhade	1981–1990	0.0891	0.6436	0.2672	0.138	0.415
	1991–2000	0.1235	0.6246	0.2519	0.197	0.403
	2001–2010	0.1339	0.6092	0.2569	0.219	0.421
Sarangkheda	1981–1990	0.0378	0.4603	0.5019	0.082	1.090
	1991–2000	0.0379	0.4579	0.5042	0.082	1.101
	2001–2010	0.0355	0.4495	0.515	0.078	1.145

**Fig. 27.2** The river cross section at Bhusawal stream gauging station



the river. Invariably, higher power of the stream is clearly seen in upper reaches of the river vis-à-vis lower reaches of the river. The higher stream power in the upper reaches is expected due to larger slope of the streams at the same locations. Further, the power of stream was maximum during the decade 1980–89, followed by period 1990–1999 and 2000–2010.

**Fig. 27.3** The river cross section at Sarangkhedha stream gauging station



## 27.5 Conclusions

The hydraulic geometry equations have been developed at Bhusawal, Padalse, Sukhwad, Gidhade, and stream gauging stations along the middle Tapi river using the mean annual flows for the period 1980–89, 1990–1999 and 2000–2010. The following are the key findings of present study:

- (a) The Bhusawal stream gauging station, located in the upper most part of the reach, indicated maximum stream power along the middle Tapi river.
- (b) Invariably, the stream power of the river has been found to be maximum of at upper reaches of the river vis-à-vis lower reaches.
- (c) The Gidhade stream gauging station reported the minimal stream power, being the least longitudinal slope of the stream at the same location.
- (d) The Sarangkhedha stream gauging station indicated the least variation in water surface width with the discharges due to its box shaped cross section.
- (e) The stream power has been found to be in decreasing order for period 1980–89, 1990–1999 and 2000–2010.

**Acknowledgements** Authors are thankful to central water commission (CWC), Ministry of Jal Shakti, Government of India, and Hydrological Data User's Group (HDUG), Nashik for proving the hydrological and cross-sectional data for the present investigation. Authors owe the thanks to 'Centre of Excellence on Water Resources and Flood Management', Civil Engineering Department, SVNIT Surat, for provisioning the computational support for the reported work.

## References

- Kale VS, Ely LL, Enzel Y, Baker VR (1994) Geomorphic and hydrologic aspects of monsoon floods on the Narmada and Tapi rivers in central India. *Geomorphol Nat Hazards* 157–168
- Kale VS, Hire PS (2004) Effectiveness of monsoon floods on the Tapi river, India: role of channel geometry and hydrologic regime. *Geomorphol* 57(3–4):275–291
- Leopold LB, Maddock T (1953) The hydraulic geometry of stream channels and some physiographic implications. U.S. Geol Surv Prof Pap 252, Washington DC, 1–57
- Menard HW (1950) Sediment movement in relation to current velocity. *J Sediment Res* 20(3):148–160
- Nixon M, Lacey, Inglis (1959) A study of the bank-full discharges of rivers in England and Wales. *Proc Inst Civ Eng* 12(2):157–174
- Singh VP (2003) On the theories of hydraulic geometry. *Int J Sedim Res* 18(3):196–218

# Chapter 28

## Hydraulic Investigations to Optimize the Design of Spillway and Energy Dissipator for Dri Dam, Arunachal Pradesh—A Case Study



P. P. Gadge, R. R. Bhate, M. R. Bhajantri, and V. V. Bhosekar

**Abstract** Etalin Hydroelectric Project (3097 MW) is a run-of-the-river scheme upstream of 3000 MW Dibang Multipurpose Project, utilizing the waters of Dri and Tangon rivers in Dibang Valley of Arunachal Pradesh. Dri limb diversion structure consists of a 101.5 m high and 213.7 m long concrete gravity diversion dam. An orifice spillway has been provided to pass a design flood (PMF) of 11,811 m<sup>3</sup>/s along with Glacial Lake Outburst Flood (GLOF) of 1,170 m<sup>3</sup>/s. A ski-jump bucket is provided for energy dissipation. Hydraulic model studies were conducted at CWPRS, Pune, to determine the efficacy of orifice spillway and energy dissipator for various ranges of discharges and reservoir water levels. The original design of the orifice spillway was found to be suitable in terms of discharging capacity of the spillway and performance of the energy dissipator. However, pressures on the spillway were not found acceptable while passing the low discharges for the gated operation of the spillway. The fluctuating upper nappe was intermittently hitting the trunnion of the radial gate for the design flood. Flow conditions in the bucket were violent due to strong swaying rooster tails generated at the end of piers for higher discharges. Based on the findings from the model studies, the design was modified by raising the crest by 5 m and extending the pier length up to the lip of the bucket to improve the overall performance of the orifice spillway. Modified design helped in finalizing the trunnion elevation of the gate, improving the pressures on the spillway surface and flow conditions in a ski-jump bucket. A need for providing a pre-formed plunge pool was also identified by analyzing the scour profiles. The location and size of the plunge pool were suggested based on the extent of scour observed downstream of the ski-jump bucket. Hydraulic model studies played a very important role in assessing and optimizing the hydraulic performance of spillway and energy dissipator of Dri dam spillway.

**Keywords** Cavitation · Discharging capacity · Energy dissipator · Orifice spillway · Physical model · Plunge pool · Scouring

---

P. P. Gadge (✉) · R. R. Bhate · M. R. Bhajantri · V. V. Bhosekar  
Central Water and Power Research Station, Pune 411024, India

## 28.1 Introduction

Etalin Hydroelectric Project is proposed to be developed by constructing concrete gravity dams on Tangon and Dri rivers and diverting the water through two separate water conductor systems to utilize the available head in a common underground powerhouse located just upstream of the confluence of the two rivers. Dri limb diversion structure consists of a 101.5 m high and 213.7 m long concrete gravity diversion dam with top El. 1047 m. An orifice spillway is designed to pass a design flood (PMF) of 11,811 m<sup>3</sup>/s along with Glacial Lake Outburst Flood (GLOF) of 1,170 m<sup>3</sup>/s through seven orifice openings of size 6.1 m wide × 12.6 m high with crest level at El. 990 m. The FRL/MWL has been fixed at El. 1045 m and MDDL at El. 1039 m. Radial gates have been provided at the downstream face of the breast wall for controlling the outflow discharge. Energy dissipator in the form of a ski-jump bucket of 49 m radius and 30° lip angle with a pre-formed plunge pool is provided at the toe of the spillway. Besides the orifice spillway, one auxiliary spillway bay of size 6 m (W) × 6 m (H) has been provided with a crest at El. 1041 m for passing floating debris. Two power intakes with sill level at El. 1021 m and 41.1 m long inlet tunnel (including transition) are located on the left bank of Dri diversion dam to carry a design discharge of 480 m<sup>3</sup>/s and 528 m<sup>3</sup>/s at MDDL and FRL, respectively. Figures 28.1 and 28.2 show the general layout plan of the project and cross-section of the orifice spillway.

The design of the orifice spillway should be such that the spillway should have the safe discharging potential, acceptable pressure distribution and efficient energy dissipator to minimize the damage downstream of the spillway. CWPRS has carried out the physical model studies on a 3-D comprehensive model to assess the hydraulic

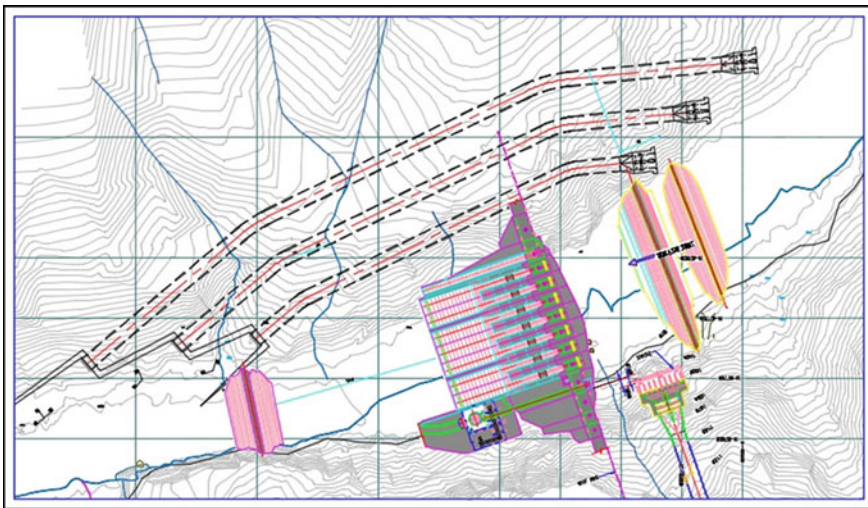


Fig. 28.1 General layout plan of the project



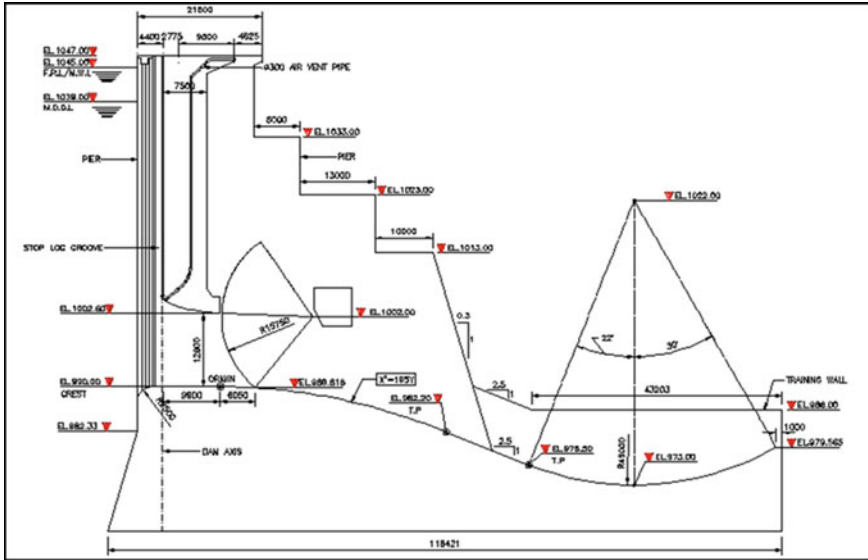
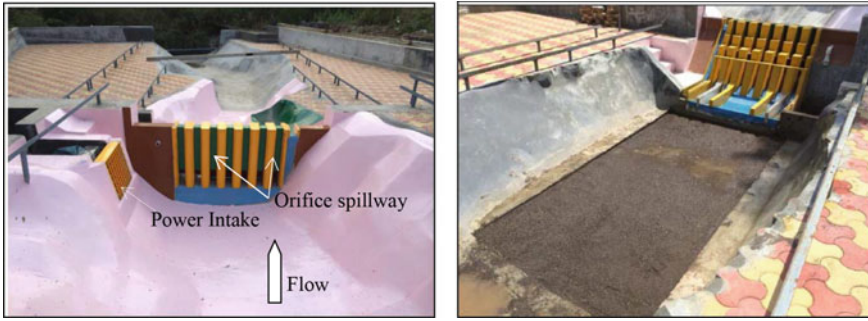


Fig. 28.2 Cross-section of orifice spillway

functioning of the spillway with respect to discharging capacity, cavitation susceptibility over spillway surface, water surface profile to finalize the location of truncheon and height and alignment of training walls, performance of ski-jump bucket type energy dissipator and flow conditions downstream of energy dissipator for a full range of discharges and reservoir water levels.

### 28.2 Physical Model Setup

A 3-D comprehensive model was constructed to a geometrically similar scale of 1:60 based on Froude number similitude. The model incorporates river extent 690 m upstream and 690 m downstream of dam axis, the overflow auxiliary spillway, orifice spillway and the power intake. The riverbed and banks were reproduced in smooth cement plaster. The spillway, piers, breast wall and radial gates were reproduced in Polycarbonate sheet and PVC foam sheets and were painted with P.U. paint to have a very smooth surface. The power intake was fabricated in Perspex. The river portion downstream of the ski-jump bucket lip was reproduced with cohesionless erodible material (sand) of mean size ( $d_{50}$ ) of about 2 mm for assessing the maximum depth of scour and scour pattern for various discharges and gate openings. It was considered appropriate to reproduce the scour pit in the river with rigid sides vertically to avoid collapsing the excess material from the side flanks and filling the scour hole to obtain a near realistic pattern of scour. Figure 28.3a, b shows the upstream and downstream views of the physical model.



a) Upstream view of the model      b) Downstream view of the model

**Fig. 28.3** Upstream and downstream views of the physical model

The model was equipped with suitable inlet and outlet arrangements including discharge measurements. The discharges were measured on Rehbock weir using a hook gauge of 0.1 mm least count in a stilling well. Piezometers were fixed on the spillway surfaces along the centreline for hydrostatic pressure measurement. Water surface measurements were taken using a pointer gauge along the spillway profile and in the downstream channel. Hydraulic model studies were initially carried out for the original design of the structure. Based on the findings obtained from the model, the design was further modified to make the structure economical and hydraulically efficient.

## 28.3 Results for Original Design of Orifice Spillway

Studies were conducted for an original design with crest El. 990 m and width of span 6.1 m for evaluating the performance under various operating conditions. The results obtained from the studies are discussed in the following subsections.

### 28.3.1 Discharging Capacity

Discharging capacity is one of the important hydraulic aspects to be studied in finalizing the design of spillways as most of the dams have failed due to inadequate flood-carrying capacity. The studies indicated that the design discharge of 11,811 m<sup>3</sup>/s (PMF) could be passed at RWL El. 1034 m, and the discharge of 13,957 m<sup>3</sup>/s (18% more than design discharge) could be passed at FRL El. 1045 m with all the gates fully open. With one span inoperative, a discharge of 11,963 m<sup>3</sup>/s could be passed as against the design discharge of 11,811 m<sup>3</sup>/s at FRL El. 1045 m. Check

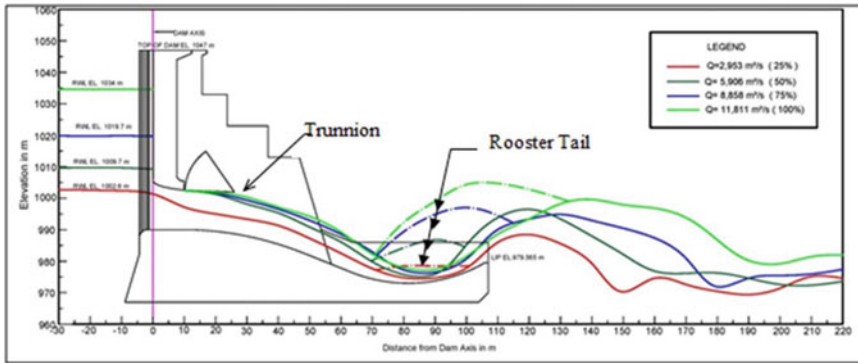


Fig. 28.4 Water surface profiles for original design of orifice spillway

flood of 12,981 m<sup>3</sup>/s (PMF + GLOF) could be passed at RWL El.1040 m with all gates operating under ungated conditions. The discharging capacity of the spillway is found to be adequate.

### 28.3.2 Water Surface Profiles

Water surface profiles were measured along the centerline of the spillway span under various operating conditions. It was observed that the fluctuating upper nappe of the jet issuing from the breast wall opening was touching the trunnion of the radial gate intermittently while passing the design discharge of 11,811 m<sup>3</sup>/s (PMF) at RWL El. 1034 m. The jet was touching the trunnion more frequently when the reservoir water level was at El. 1040 m and above. Therefore, it was suggested to modify the elevation of the trunnion. Minor to very strong pulsating rooster tails for increasing discharges were seen forming due to the interaction of flow emerging from adjoining spans. The top elevation of the training wall was overtopped while passing discharges of 5906 m<sup>3</sup>/s (50% of PMF) and above (see Fig. 28.4). Based on the studies, it was suggested that the heights of training walls should be decided based on the water surface/rooster profiles, bulking of flow due to air entrainment in prototype and free board requirement.

### 28.3.3 Pressures on Spillway Surface

Cavitation is the most complex hydrodynamic phenomenon and can cause serious damage to the spillway surface and is influenced by pressures, velocities and duration of spillway operation (Falvey 1990). The cavitation damage can be assessed by calculating the cavitation index considering the pressure and corresponding velocity

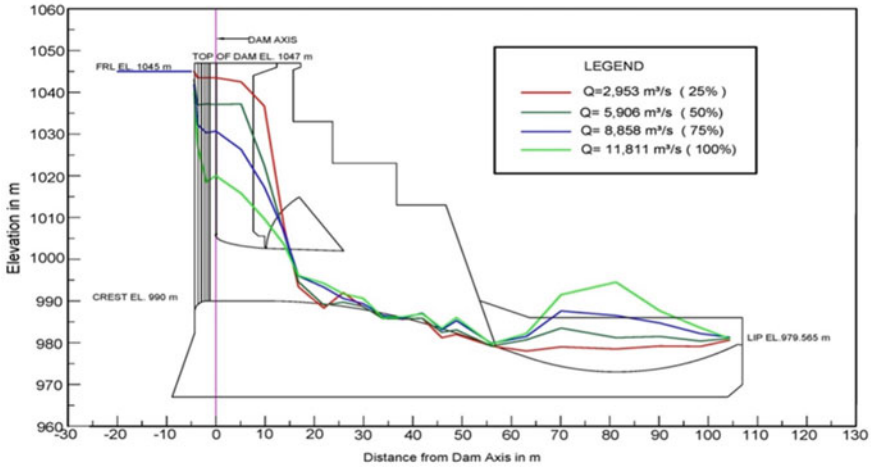


**Fig. 28.5** Pressures along spillway surface for original design of orifice spillway

at a point. Piezometric pressures were measured from the crest up to the bucket lip. The pressures were found to be positive throughout the length of the spillway. The pressures go on decreasing from the crest of the spillway to the start of a ski-jump bucket due to highly accelerated flow and then start rising due to the centrifugal action of flow in the bucket. However, due to the reattachment of rooster tail, redistribution of flow across the width of the bucket and ski-jump jet leaving the bucket lip, the pressures again drop toward the bucket lip. The spillway profile did not show susceptibility for cavitation damage for the entire range of discharges for the ungated operation of the spillway.

Figure 28.5 shows the pressure profiles for the gated operation of the orifice spillway. Minimum pressures of the order of  $-0.15$  to  $-2.12$  m were observed from chainage 22–56 m for the discharge of  $2,953 \text{ m}^3/\text{s}$ . This zone shrinks to chainage 34–46 for discharges higher than  $2,953 \text{ m}^3/\text{s}$ . The corresponding cavitation index was worked out to be less than the critical cavitation index of 0.2. The susceptibility of cavitation damage on the spillway surface was found to be more while passing low discharges at FRL with the gated operation. With an increase in discharge and gate opening, the pressures increased thereby increasing the cavitation index, and the zone of susceptibility shrank. This low-pressure zone necessitates the provision of some cavitation prevention methods for the protection of spillway surfaces. Aeration using different aerator devices is one of the most reliable and economic measures to minimize the possibility of cavitation damage. However, this option was ruled out as the spillway will frequently be operated for silt flushing. During the flushing operation or flood, the boulders varying from size 0.3 to 2.0 m present in the river will flow over the spillway surface which may damage the edges of aerators and there may be the possibility of filling the aerator groove by the flushed silt. The use of surface-resistant material can be proved to be a very costly option so it was considered as the

last possible option. However, it was decided to minimize the cavitating velocities by reducing the head over spillway by raising the crest by 5 m.

Piezometric pressures were also measured on the bottom profile of the breast wall. The maximum negative pressure of 1.23 m was observed for the discharge of 5906 m<sup>3</sup>/s when passed with gates fully open with RWL El. 1009.7 m. The corresponding cavitation index was calculated as 1.84 which was much higher than the critical cavitation index of 0.2. The design of the bottom profile of the breast wall was found to be acceptable in respect of pressures.

### 28.3.4 Performance of Ski-Jump Bucket

The ski action in the bucket was observed for various operations of spillway by maintaining tailwater levels at chainage 300 m downstream of the dam axis. Formation of rooster tails in the bucket from the end of the piers was observed for the ungated and gated operations of the spillway. The intensity of the rooster tails was increased with an increase in discharge and reservoir water level. The rooster tails were hitting the bucket lip up to discharges of 5906 m<sup>3</sup>/s with the ungated operation of the spillway. With the gated operation, the length of the rooster tail increased and height became flatter and the rooster tail was riding over the buried ski-jump profile downstream of the bucket lip. For higher discharges, flow conditions in the bucket were violent because of rooster tails. Hence, it was suggested to extend the intermediate piers up to the lip to improve the flow conditions. Figure 28.6a, b shows the performance of the ski-jump bucket for design discharge 11,811 m<sup>3</sup>/s for the ungated and gated operations of the spillway.

Based on the results obtained from the model studies, it was decided to raise the spillway crest by 5 m to reduce cavitation susceptibility over the spillway surface. It was also suggested to taper the intermediate piers to reduce the violent rooster tails (CWPRS 2016a).



a) Ungated operation of spillway

b) Gated operation of spillway

**Fig. 28.6** Performance of ski-jump bucket with ungated and gated operations of spillway

## 28.4 Results for Modified Design of Orifice Spillway

The spillway design was modified in respect of spillway crest, width of span and trunnion elevation. Spillway crest and trunnion elevation were raised by 5 m and 1.1 m, respectively. Reduction in the hydraulic head was compensated by an increase in the width of the spillway from 6.1 to 6.5 m. The performance of the modified design of the spillway was evaluated in respect of discharging capacity, water and pressure profiles, performance of ski-jump bucket and scour studies downstream of the ski-jump bucket (CWPRS 2016b).

### 28.4.1 Discharging Capacity

The studies indicated that the modified spillway is capable of passing the design discharge of 11,811 m<sup>3</sup>/s (PMF) at RWL El. 1035.4 m and the discharge of 13,765 m<sup>3</sup>/s at FRL El. 1045 m with all the gates fully open. With one span inoperative, a discharge of 11,799 m<sup>3</sup>/s could be passed as against the design discharge of 11,811 m<sup>3</sup>/s at FRL El. 1045 m. Check flood of 12,981 m<sup>3</sup>/s (PMF + GLOF) could be passed at RWL El. 1041 m with all gates operating under ungated conditions. The discharging capacity of the spillway is found to be adequate. The water surface follows the breast wall bottom profile for the entire width for the orifice flow regime, thus making the entire height of the orifice fully effective.

The studies were also conducted for the gated operation of the spillway. The gate openings ranged from 1 to 12 m for various reservoir water levels up to El. 1045 m. The discharging capacity curves for the spillway with all the seven spans operating for various gate openings are shown in Fig. 28.7. The data in terms of the discharges passed through the spillway for various reservoir levels and gate openings would be useful in planning the operation of spillway.

### 28.4.2 Water Surface Profiles

Studies indicated that the modified raised trunnion at El. 1008.10 m was free from the fluctuating upper nappe of the jet issuing from the breast wall opening while passing all ranges of discharges with the ungated operation as shown in Fig. 28.8.

### 28.4.3 Pressures

Piezometric pressures were measured to assess the cavitation susceptibility of the spillway profiles for the gated and ungated operations. The pressures were found to

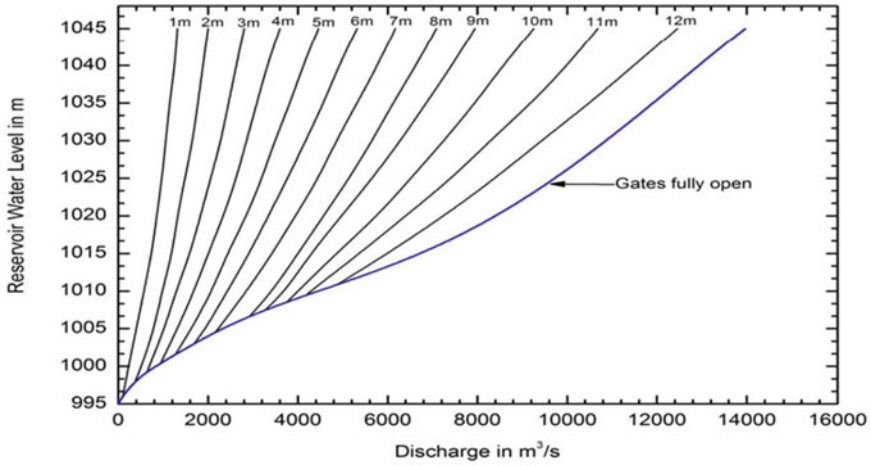


Fig. 28.7 Discharging capacity curve for full and partial operations of gates

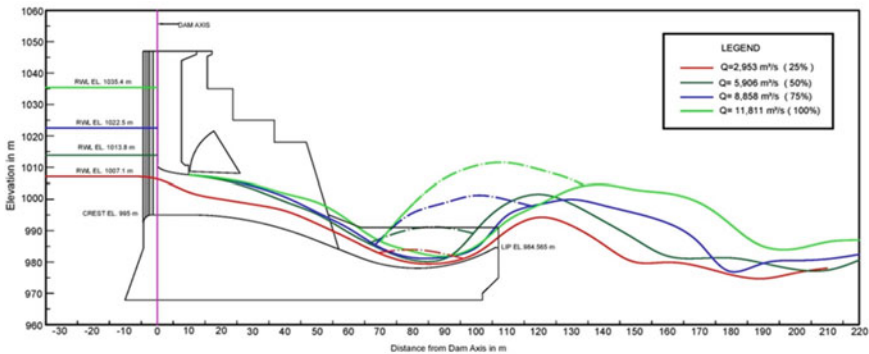


Fig. 28.8 Water surface profiles for modified design of orifice spillway

be positive throughout the length of the spillway for ungated operation. For gated operation, the pressures of magnitude  $-0.20$  to  $-1.03$  m were observed on the spillway bottom profile from chainage 22–52 m for the discharge of  $2,953 \text{ m}^3/\text{s}$ . This zone shrinks to chainage 30–40 for discharges higher than  $2,953 \text{ m}^3/\text{s}$ . However, the corresponding cavitation indices were found to be greater than the critical cavitation index of 0.2. Hence, with a raised crest at El. 995 m, the spillway profile did not show susceptibility for cavitation damage for the gated operation of the spillway. Figure 28.9 shows pressure profiles for various operating conditions of the modified design of the orifice spillway.

Piezometric pressures were also measured on the bottom profile of breast wall along the centerline of the spillway. The maximum negative pressure of 1.16 m was observed while passing the discharge of  $5906 \text{ m}^3/\text{s}$  (50% of PMF) with gates fully

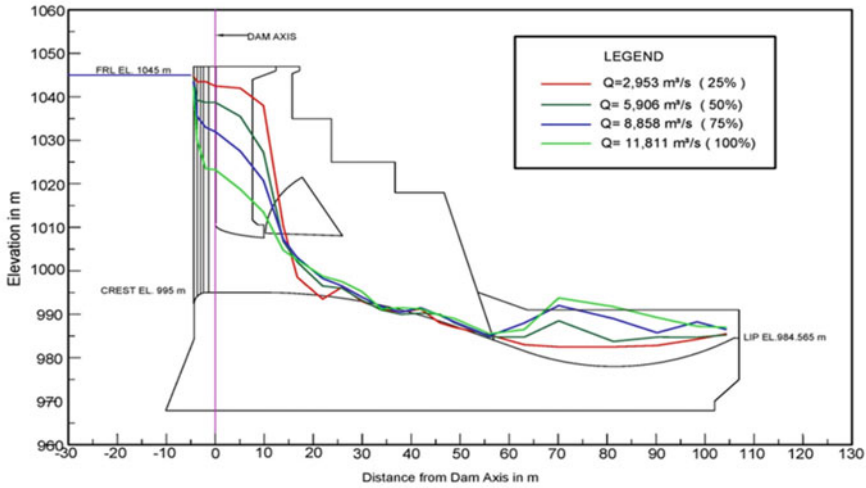


Fig. 28.9 Pressures along spillway surface for modified design of orifice spillway

open. However, the corresponding cavitation index was found to be 2.18 which is much higher than the critical cavitation index of 0.2. As such, the bottom profile of the breast wall is acceptable in respect of pressures.

### 28.4.4 Performance of Ski-Jump Bucket

The performance of a ski-jump bucket of the spillway with extended divide walls was observed for the entire range of discharges up to the PMF of 11,811m<sup>3</sup>/s. A clear ski jump was forming for gated as well as ungated operations of the spillway as shown in Fig. 28.10. Pulsating rooster tails were eliminated in side bays due to



a) Ungated operation of spillway



b) Gated operation of spillway

Fig. 28.10 Performance of ski-jump bucket for extended divide walls



extended divide walls. Formation of hydraulic jump in the bucket and cascading flow over the bucket lip was observed for the low flows. Therefore, a concrete apron properly anchored to the fresh rock and keyed at the downstream end was suggested to be provided for protection of the spillway toe from undermining as the flow will cascade over the lip of the bucket for low discharges and during reservoir flushing.

#### ***28.4.5 Scour Downstream of Spillway***

Scouring is a time-dependent complex dynamic process that is governed by the interaction of three phases, i.e. air, water and rock. It is a three-dimensional phenomenon, strongly influenced by turbulence and the characteristics of rock mass. Maximum scour depth is usually formed downstream of the point of impingement of the ski-jump jet. Retrogression of this scour hole may cause danger to the stability of the dam. Analysis of scouring downstream of the spillway is complicated due to complex hydraulic and geological conditions. An accurate evaluation of the parameters determining the erosion resistance of the rock is difficult. Many researchers have developed empirical or semi-empirical formulae considering various hydraulic as well as geological parameters that are still used for reference. There is a wide variation in the estimated depth of scour by these researchers. Also, these formulae provide values of scour depth but do not indicate the scour pattern. Because of these limitations, a qualitative idea of the likely scour pattern and scour depth could be obtained in the model by reproducing the riverbed erodible with non-cohesive material with rigid banks (Khatsuria 2004).

In view of the above, the experiments were conducted by reproducing cohesionless erodible bed material to assess the extent and pattern of scour so that location, shape and size of the plunge pool can be decided (CWPRS 2016c). The approach of cohesionless erodible bed simulates fully disintegrated rock which results in what is usually considered as established and ultimate scour depth. Following these guidelines and as per standard practice adopted in CWPRS, a cohesionless bed was reproduced for assessment of depth of scour downstream of spillway and location of the plunge pool. The scour studies were conducted for various discharges with full as well as partial gate openings. It was observed that the deepest scour reached up to El. 931.65 m at chainage 265 m downstream of dam axis for a discharge of 11,811 m<sup>3</sup>/s (PMF) passed with the ungated condition. For 75% of PMF, the deepest scour depth reaches up to El. 940 m at chainage 250 m and El. 932.2 m at chainage 270 m for ungated and gated conditions, respectively. For 50% of PMF, scour depth reaches up to El. 947.6 m at 215 m and El. 939.4 m at 260 m for ungated and gated conditions, respectively. For 25% of PMF, scour depth reaches up to El. 952.45 m at 170 m and El. 951 m at chainage 220 m for ungated and gated conditions, respectively. These values are in agreement with the values obtained from established formulae of Damle's probable scour depth values. Studies indicated that the extent of scour hole reached about 270 m downstream for 75% of PMF and even for 25% of PMF it reached up to 220 m. Generally, energy dissipators are designed for 60% of design

discharge. Taking this into account and from the scour profiles obtained from the model studies, possible geometry of the plunge pool was proposed with bottom El. 935 m from chainage 220 to 280 m with longitudinal upstream and downstream slopes. Figure 28.11 shows the scour profiles observed on the model for the ungated operation of the spillway and the proposed design of the plunge pool. Figure 28.12

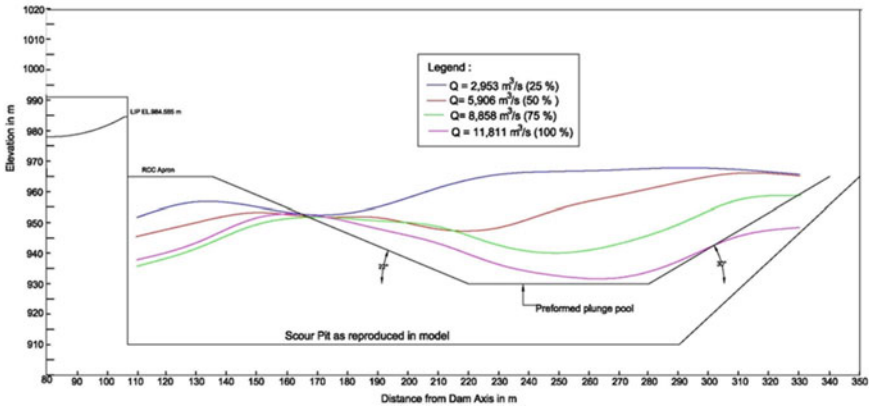


Fig. 28.11 Scour profiles for ungated operation of spillway



Fig. 28.12 Typical scour profile observed in the physical model

shows a typical scour profile observed in the physical model.

Velocities were observed on the spillway profile with extended divide walls and downstream of the scour pit for various operating conditions of the spillway. Velocities of the order of 16–30, 14–26 and 4–9 m/s were observed on bucket invert, bucket lip and downstream of the scour pit at chainage 350 m. The model studies with rigid bed model show the velocities measured at chainage 300 m downstream to be in the range of 8.6–21.12 m/s. However, the present study with erodible riverbed indicated that after the formation of scour hole due to impact of ski-jump jet, the excess energy of flow gets dissipated and the flow in the river downstream would remain sub-critical with the velocity of the order of 4–9 m/s implying the necessity of pre-formed plunge pool.

## 28.5 Conclusion

Hydraulic model studies were carried out on a 1:60 scale 3-D comprehensive model of Dri dam spillway, Arunachal Pradesh. The performance of the spillway was assessed in respect of discharging capacity of the spillway, pressures over spillway surface, water surface profiles, performance of energy dissipator and scour studies at the downstream of the spillway for various ranges of discharges and reservoir water levels. Model studies played a vital role in optimizing the various components of orifice spillway. Hydraulic model studies conducted for the original design of the orifice spillway identified a need for lowering the head by increasing the crest by 5 m to minimize cavitation damage on the spillway surface. It was also suggested to raise trunnion elevation and extend divide walls up to the lip of the bucket to improve the flow conditions in the bucket. Accordingly, the design was modified to improve the performance of the spillway. The conclusions drawn from the studies of modified design are as follows:

- It was observed that a discharge of 13,765 m<sup>3</sup>/s could be passed at FRL El. 1045 m with all gates fully open as against the design discharge of 11,811 m<sup>3</sup>/s. The discharging capacity of the spillway is found to be adequate.
- The water surface follows the breast wall bottom profile for the entire width for the entire range of discharges in the orifice flow regime, thus making the entire height of the orifice fully effective. The raised trunnion of the radial gate was found to be free from the fluctuating upper nappe of the jet issuing from the breast wall opening for all the ranges of discharges. Hence, the raised elevation of trunnion is considered to be adequate.
- The spillway bottom profile with increased crest did not show susceptibility for cavitation damage for gated as well as ungated operations of the spillway. Also, the pressures along the centerline of the bottom of the breast wall were also found to be non-cavitating.

- The performance of a ski-jump bucket with extended divide walls was found to be satisfactory as there was clear ski action for all the discharge conditions, both with the gated and ungated operations of the spillway.
- The present study with erodible riverbed indicated that after the formation of scour hole due to impact of ski-jump jet, the excess energy of flow gets dissipated and the flow in the river downstream would remain sub-critical with the velocity of the order of 4–9 m/s implying the necessity of pre-formed plunge pool.

**Acknowledgements** The authors are thankful to the project and design engineers of Dri dam Etalin Project, Arunachal Pradesh, and WAPCOS Ltd. for constant interaction during the course of studies.

## References

- CWPRS (2016a) Hydraulic model studies for Dri dam spillway, Etalin project, Arunachal Pradesh, 1:60 scale 3-D comprehensive model. Technical Report
- CWPRS (2016b) Hydraulic model studies for assessment of scour downstream of Dri dam spillway, Etalin project, Arunachal Pradesh, 1:60 scale 3-D comprehensive model. Technical Report
- CWPRS (2016c) Hydraulic model studies for discharging capacity for full and partial operation of Dri dam spillway, Arunachal Pradesh, 1:40 scale 2-D sectional model. Technical Report
- Falvey HT (1990) Cavitation in chutes and spillways. Engineering Monograph no 42, USBR Publication, Denver, CO
- Khatsuria RM (2004) Hydraulics of spillways and energy dissipators. Marcel Dekker Publication, New York

# Chapter 29

## Scientific Area Calculation of a Landfill in Boragaon Guwahati



C. K. Anoop, Abishek Baby, Tina Maria Jacob, and Suresh A. Kartha

**Abstract** From the past, management of municipal solid waste has been a serious environmental issue of concern. Unhealthy waste disposal practises pave a way for air, water, soil and land pollution. Scientific landfills are a great solution for this. Scientific landfills are engineered means of confining waste to a small area and covering it with daily layers of earth and compacting it to reduce its volume. Our paper focuses on an unscientific dumpsite located in the outskirts of Guwahati, Boragaon, that proposes the calculation of area for different heights for the same site in a scientific manner. The calculation is done for a period of 20 years (2019–2038) by finding out the future expected population, per capita waste generated and the total municipal solid waste (MSW) generated for the entire city. The term municipal solid waste for the study area refers to the waste which is obtained from domestic, commercial establishments, hotels, restaurants, parks etc. As per our calculation, the total area available for the landfill site is 88,315.26 m<sup>2</sup> and as per the guidelines, in India only 30% of the MSW is recycled and the remaining 70% is deposited in the landfill site, which is being followed in our design. In the design adopted, with the values of density, the loose mass and daily compacted volume is calculated. This is then followed by the calculation of the annually compacted volume. The work includes after the deposition of the daily waste, a layer of soil is provided as a cover so as to prevent the odour problems that occur in the landfill. In the method adopted, volume of cover material is taken to be equivalent to 20% of the volume of recently compacted waste. By adding on the values of annually compacted volume and cover material, volume of

---

C. K. Anoop · A. Baby (✉) · T. M. Jacob

Civil Engineering Department, Viswajyothi College of Engineering and Technology, Vazhakulam, India

A. Baby

APJ Abdul Kalam Technological University, Thuruthiyil House, Puthencruz P.O., Puttumanoor, Ernakulam, Kerala, India

T. M. Jacob

APJ Abdul Kalam Technological University, Vadakkemandapathil House, Aimcombu 6 Th mile Kadanadu P.O, Kottayam, Kerala, India

S. A. Kartha

Civil Engineering Department, Indian Institute of Technology Guwahati, Guwahati, Assam, India  
e-mail: [kartha@iitg.ernet.in](mailto:kartha@iitg.ernet.in)

sanitary landfill is obtained. The total area required is calculated by assuming factor of increase in the additional area required for the access roads, border setback areas, control buildings, sanitary facilities and manoeuvring yards. The factor of increase in the additional area is taken as 25% of the total area to be filled in this case study. The scientific landfill in Boragaon for the 20 years is divided into 4 plots in which each plot is filled within a span of 5 years. The study shows that the proposed area will be filled within the span of first five years and this area is very less as compared to the area for the waste to be accommodated by the year 2038.

**Keywords** Landfill · Solid waste · Area · Population · Environment

## 29.1 Introduction

Waste is an inevitable consequence of satisfying man's need for food, water, air, space, shelter and mobility. Waste are produced from different activities such as household, agricultural activities and hospitals. Waste can be classified into solid waste, liquid waste and gaseous waste. On this basis, source waste can be classified into urban or municipal solid waste, industrial waste, commercial waste and agricultural waste. The term municipal solid waste (MSW) refers to the waste which is obtained from domestic, commercial establishments, hotels, restaurants, parks etc. Solid waste disposal is a major problem because it leads to land pollution if it is openly dumped. Inadequate solid waste management leads to water, land, soil and air pollution.

The most common methods of disposing solid waste is a landfill as shown in Fig. 29.1. Scientific landfills are engineered means of confining waste to a small area and covering it with daily layers of earth and compacting it to reduce its volume. The main components of a landfill are liners, leachate collection system, final cover and gas collection system.

After the installation of the final cover, there are chances for precipitation which percolates through the dumped waste which would contain the minerals and other materials in a landfill, known as leachate which reaches the ground water and pollute the ultimate source of fresh water. Liners are provided to prevent the flow of leachate percolating to the groundwater which is being collected through pipes and stored in a tank.

## 29.2 Boragaon: The Dump Yard of Guwahati

Boragaon is the only dumpsite of the entire Guwahati city at present. The site is located at a distance of 12 km from the city. The coordinates of the site are 26°6'46"N latitude and 91°40'38"E longitude. Our paper focuses on an unscientific dumpsite located in the outskirts of Guwahati, Boragaon, that proposes the calculation of area



**Fig. 29.1** Waste dumped in a landfill site

for different heights for the same site in a scientific manner. The total area available for the dumping of the waste is  $88,316 \text{ m}^2$ , and the site is  $46.9 \text{ m}$  above mean sea level. The existing landfill in Boragaon is chosen by violating all the rules and regulations of Central Public Health and Environmental Engineering Organisation (CPEEHO). At present the waste is just dumped in the site without proper treatment and open burning is also done which causes harmful diseases and other odour problems. Figure 29.2 shows the satellite view of area for dumping the waste in Boragaon.

The major problems faced with dumping waste in Boragaon were flash floods, water logging worsening the situation. The site shares a common boundary with a national wetland which has a linkage with world heritage site of Deeporbeel which is a freshwater lake. The site has also become a home to a bird, The Greater Adjutant Stork which is listed as an endangered species.

### 29.3 Area Calculation Procedure

The area for dumping of waste is divided into 4 square plots such that each plot is assumed to be filled within a span of 5 years and the total area available at the present is  $88,315 \text{ m}^2$ .

Step 1: Calculation of total waste generated.

Total waste generated = population  $\times$  waste generated per person per day

Step 2: Estimation of no of trucks arriving the site.



**Fig. 29.2** The area chosen for the dumping of the waste at Boragaon

Assuming, dimensions of the waste collecting truck to be 1.05 m × 3.6 m × 1.5 m.

So, volume of the truck = 5.67 m<sup>3</sup>.

No of trucks arriving the site per day = (Waste Generated)/(Volume of the truck).

Step 3: Calculation of waste dumped in the landfill.

In case of a scientific landfill, the 30% of the waste arriving the site could be recycled so that only the 70% of the total waste is deposited as the landfill.

So, the waste dumped in the landfill = 0.7 × Total waste generated.

Step 4: Estimation of volume compacted.

Loose density = (Loose mass)/(Volume of waste).

where

Loose density of the waste of the area = 1450 kg/m<sup>3</sup>.

Daily compacted volume = (Loose mass)/(Compacted density).

where

Compacted density of the waste of area = 1150.79 kg/m<sup>3</sup>.

Volume of waste compacted annually = Daily compacted volume × 365 days.



Step 5: Calculation of volume of cover material.

$$\text{Volume of cover material} = 0.2 \times \text{volume of compacted MSW.}$$

where

0.2 is the cover material equivalent to 20% or 25% of the volume of the recently compacted waste.

Step 6: Estimation of volume of sanitary landfill.

$$\text{Volume of sanitary landfill} = \text{Volume compacted annually} + \text{Cover material.}$$

Cover material is the soil provided on each day after compaction so as to reduce the foul smell and spreading of diseases by insects.

Step 7: Calculation of area of sanitary landfill.

$$\text{Area of sanitary landfill} = (\text{Volume of sanitary landfill}) / (\text{Height of heap})$$

where

The height of heap of waste is assumed to 7.5 m, 10 m, 12.5 m, 15 m and 20 m so as to find out the reduced area for the landfill, such that it could be used for more years when compared to that of smaller heights.

Step 8: Calculation of total area required.

$$\text{Total area required} = F \times A.$$

where

F = Factor of increase in the additional area required for penetration roads, border setback areas, control building and sanitary facilities, manoeuvring yard, etc.

A = Area of sanitary landfill.

For the calculation of area of the landfill, the population for proposed period (2019–2038) was forecasted; waste generation and total waste generation was then calculated from the expected population for Guwahati city as shown in Table 29.1.

## 29.4 Sample Calculation

### Area calculation for 2019–2023

$$\begin{aligned} \text{Total waste generated} &= \text{Population} \times \text{waste generated per person per day} \\ &= (832,208.22 + 876,093.94 + 920,874.74 + 974,424.184 + 1,029,124.51) \\ &= 4632725.6 \text{ Kg/day} \\ &= 4632.725 \text{ tonnes/day} \end{aligned}$$

**Table 29.1** Anticipated population and waste generation for Guwahati city for the period from 2019–2038

Year	Population	Waste generation (Kg/capita/day)	Total waste generation (Kg/day)
2019	17,28,725	0.4814	832,208.22
2020	17,94,539	0.4882	876,093.94
2021	18,60,353	0.4950	920,874.74
2022	19,40,311	0.5022	974,424.18
2023	20,20,268	0.5094	1,029,124.51
2024	21,00,226	0.5166	1,084,976.75
2025	21,80,183	0.5238	1,141,979.85
2026	22,60,141	0.5310	1,200,134.87
2027	23,57,282	0.5388	1,270,103.52
2028	24,54,422	0.5466	1,341,587.06
2029	25,51,563	0.5544	1,414,586.52
2030	26,48,703	0.5622	1,489,100.82
2031	27,45,844	0.5700	1,565,131.08
2032	28,63,860	0.5782	1,655,883.85
2033	29,81,876	0.5864	1,748,572.08
2034	30,99,891	0.5946	1,843,195.18
2035	32,17,907	0.6028	1,939,754.34
2036	33,89,027	0.6110	2,070,695.49
2037	34,53,939	0.6200	2,141,442.18
2038	36,22,678	0.629	2,278,664.46

- Since  $1 \text{ m}^3 = 2.41 \text{ tonnes}$ ,  
Waste generated in 2019–2023 will be  $4632.725/2.41 = 1922.29 \text{ m}^3/\text{day}$
- Assuming dimensions of the waste collecting truck to be  $1.05 \text{ m} \times 3.6 \text{ m} \times 1.5 \text{ m}$   
Volume of the truck =  $5.67 \text{ m}^3$ .  
So, no of trucks arriving at the site per day =  $1922.29/5.67 = 339.02 \approx 339$  Trucks
- Assuming 30% of the waste would be recycled and the remaining 70% would only be disposed in the landfill  
Volume of the waste dumped in the landfill =  $0.7 \times 1922.29 = 1345.6 \text{ m}^3$   
Loose density = (Loose Mass)/(Volume of waste)  
=  $1951120 \text{ kg/day}$   
Loose mass =  $1450 \times 1345.6$   
Compacted volume = (Loose mass)/(Compacted density)  
=  $1695.46 \text{ m}^3$   
=  $1951120/1150.79$

- Volume of waste compacted daily =  $1695.46 \text{ m}^3$   
Volume of waste compacted annually =  $1695.46 \times 365$   
=  $618843.4 \text{ m}^3$
- Volume of cover material =  $0.2 \times$  Volume of compacted soil  
=  $0.2 \times 618843.4$   
=  $123768.68 \text{ m}^3$
- Volume of sanitary landfill = volume compacted annually + cover material  
=  $618843.4 + 123768.68$   
=  $742612.08 \text{ m}^3$
- Assuming height of landfill to be 7.5 m  
Area of sanitary landfill = (Volume of sanitary landfill)/(Height of heap)  
=  $742,612.08/7.5$   
=  $99014.94 \text{ m}^2$
- Total area required = Factor of increase in additional area required for penetration  
 $\times$  area of sanitary landfill  
=  $0.25 \times 99014.94$   
=  $24753.74 \text{ m}^2$

Assuming the area as a square plot. The length will be 314.67 m and a height of 7.5 m.

Similarly the values for the landfill area requirement for the various set of years are given in Table 29.2.

## 29.5 Results and Conclusions

The total area calculated (A) for **7.5 m** of height =  $(99,014.94 + 129,067.03 + 168,275.14 + 219,581.24)$ .

$$= \mathbf{6, 15,938.35 \text{ m}^2}.$$

The total area calculated (B) for **10 m** of height =  $(74,261.21 + 96,800.28 + 126,206.36 + 164,685.93)$

$$= \mathbf{4, 61,953.78 \text{ m}^2}$$

The total area calculated (C) for **12.5 m** of height =  $(59,408.97 + 77,440.22 + 100,965.082 + 131,748.74)$

$$= \mathbf{3, 69,563.012 \text{ m}^2}$$

The total area calculated (D) for **15 m** of height =  $(49,507.47 + 64,533.52 + 84,137.57 + 109,790.62)$

$$= \mathbf{3, 07,969.18 \text{ m}^2}.$$

The total area calculated (E) for **20 m** of height =  $(37,130.06 + 48,400.14 + 63,103.18 + 82,342.97)$

$$= \mathbf{2, 30,976.89 \text{ m}^2}$$

The proper disposal of waste is necessary for the preservation of environment and maintenance of a level of public hygiene. In this paper, the landfill area requirement

**Table 29.2** Landfill area requirement in various years

Year	Height of landfill (m)	Area (m <sup>2</sup> )	Dimensions (m × m)
2019–2023	7.5 (A)	99,014.94	314.67 × 314.67
	10 (B)	74,261.21	272.51 × 272.51
	12.5 (C)	59,408.97	243.74 × 243.74
	15 (D)	49,507.47	222.5 × 222.5
	20 (E)	37,130.6	192.69 × 192.69
	7.5 (A)	1,29,067.03	359.25 × 359.25
	10 (B)	96,800.28	311.1 × 311.1
2024–2028	12.5 (C)	77,440.22	278.28 × 278.28
	15 (D)	64,533.52	254.03 × 254.03
	20 (E)	48,400.14	220 × 220
	7.5 (A)	1,68,275.14	410.21 × 410.21
	10 (B)	1,26,206.36	355.25 × 355.25
2029–2033	12.5 (C)	1,00,965.082	317.75 × 317.75
	15 (D)	84,137.57	290.06 × 290.06
	20 (E)	63,103.19	251.2 × 251.2
	7.5 (A)	2,19,581.24	468.59 × 468.59
	10 (B)	1,64,685.93	405.82 × 405.82
2034–2038	12.5 (C)	91,31,748A.074	362.97 × 362.97
	15 (D)	109,790.62	331.35 × 331.35
	20 (E)	82,342.97	286.95 × 286.95

for a period of 20 years that is from 2019–2038 was calculated by assuming different heights of waste of heap. It was found that the area available at present at Boragaon is very less as compared to the area of landfill required by 2038. It is expected that the available area of landfill will be filled in the first span of 5 years if the above-mentioned heights of landfill are used.

## References

- An audit report (Civil -31 March 2011) on Performance audit of Public Private Partnership (PPP) in Solid Waste Management (SWM)
- August H et al (1997) Advanced Landfill liner systems Heron Quay. Thomas Telford, London
- Bagchi A (1994) Design construction monitoring of Landfills, New York, United States of America, Wiley Interscience Publication
- Chhabral T, Paul A, Gulati M (2014) Assessment of municipal solid waste in Northeastern States of India. *Int J Environ Res Devel* 4(4): 275–280 (2014). ISSN 2249–3131
- Christensen TH et al (1997) Landfilling of waste: leachate boundary row. E and FN SPON, London
- Christensen TH et al (1994) Landfilling of waste : barriers boundary row. FN SPON , London
- Delwyn G, Rahardjo H (1993) Soil mechanics for unsaturated soils. Wiley, New York

- Gogoi L, Municipal solid waste disposal: a case study in Guwahati to mitigate manmade disaster. *J Human Soc Sci* 9:3
- Jaramillo J (2003) Guidelines for design, construction and operation of manual sanitary landfill. Lima, Peru
- Kalamdhad A, Characteristics of solid waste generated from Guwahati city and feasibility solution for its management
- Robert M Koerner and David E Daniel (1997) Final covers for solid waste Landfills and abandoned Dumps United states of America
- Sivakumar Babu GL, Reddy KR, Chouskey SK, Kulkarni HS, Prediction of long-term municipal solid waste Landfill settlement using constitutive model
- Worrel WA, Arne Vesilind P (2012) Solid waste engineering. United states of America, Cengage Learning, Boston

# Chapter 30

## Dam Break Analysis for Ukai Dam in Lower Tapi Basin, India



Shubham M. Jibhakate and P. V. Timbadiya

**Abstract** Dam break analysis provides important input on infrastructure development in any area. Surat city having a population of about 50 lakhs is situated in the lower Tapi basin. Further, important industries such as ONGC, Reliance and Kakrapar Atomic Power Station are situated in the said basin. The effect of the Ukai dam break flow in the lower Tapi basin along with Surat city has been carried out in the present study. The inflow hydrograph coming into the said reservoir has been considered as the upstream boundary, while tidal level at the Arabian Sea has taken downstream boundary conditions to carry out the dam break analysis. Total 190 cross sections are used to model 128 km long Lower Tapi River in the 1D hydrodynamic model (MIKE 11). The developed model has been calibrated for the flood of the year 1998 and validated for 2003 and 2006. The dam break flood hydrograph having peak discharge 2,57,885.9 m<sup>3</sup>/s is obtained and stage-discharge relationship at different locations is derived. The stage-discharge curve shows the water level 36.3 m above mean sea level at Surat for aforesaid peak flow. The derived stage-discharge curve, flow velocity, arrival time of flood and its duration were obtained from dam break analysis which can be utilized to prepare flood hazard and risk map of Surat city and the surrounding area.

**Keywords** Lower Tapi basin · Flood · Hydrodynamic (HD) model · Dam break · Stage-Discharge relation · MIKE 11

### 30.1 Introduction

Floods are one of the common natural disasters observed in many parts of the world; they account for more than 40% of natural disaster occurring from the year 1985 which leads to a large amount of economic losses and massive destruction in terms of infrastructure and life of people. Total 539,811 people died and 2,821,895,005 people were affected by flood events that occurred throughout the world during 1980–2009

---

S. M. Jibhakate · P. V. Timbadiya (✉)  
Sardar Vallabhbhai National Institute of Technology Surat, Surat 395007, India  
e-mail: [pvtimbadiya@ced.svnit.ac.in](mailto:pvtimbadiya@ced.svnit.ac.in)

(Doocy et al. 2013). A multipurpose dam resolves various water resources-related issues in the area, and at the same time, sudden failure leads to catastrophic events. Unsteady floods of extreme magnitude in rivers due to sudden failure of dams are found in numerous parts of the world. More than 40% of floods that occurred from 1985 to 2009 are due to sudden changes in climatic conditions. Many dams considered safe in the past are facing maximum flow higher than design high flood level due to change in climate, and land cover leads to increase in the runoff (Rodrigues et al. 2002); such high flows are one of the major cause of dam break occurred in the past. Failure of Malpasset Dam (France) in 1959, Vajont Dan (Italy) in 1963 and failure of Machhu-II dam (Gujarat, India) in 1979 are some of the major dam failure incidents in the world.

The understanding of dam break flood based on past studies such as MacDonald and Langridge-Monopolis (1984) developed the graphical relationship to estimate the breach width, shape and formation time. High-resolution mathematical model to predict the flood caused by the instantaneous 1D dam break flow was developed (Liu et al. 2006). Yochum et al. (2008) developed a 1D HD model in HEC-RAS by using breach geometry for Big Bay Dam failure in March 2004. To calculate the expected value of breach parameter, mathematical expressions were developed using past data (Froehlich, 2008). Goosby et al. (2008) performed the dam break flood inundation study to develop the flood risk maps for the state of Hawaii's Department of Land and Natural (DLNR) using 1D, 2D hydrodynamic modeling. The case study of dam break in southern California is performed by Gallegoes et al. (2009) by modeling in BreZo. Mohapatra (2009) developed rating curves for dam break by performing the hypothetical simulation of dam break flood. Lodhi and Agrawal (2012) analyze the dam break flood using the DAMBRK model for different scenarios along with a combination of different breach parameters. A case study on Gleno dam break in 1923 was performed with the help of available past data and 1D hydrodynamic modeling (Pilotti et al. 2010).

The first law on dam break in European countries was establish in 1968 after the incident of failure of the Malpasset dam. In India, recently, Guidelines for Mapping Flood Risks Associated with Dams was published by Central Water Commission, Govt. of India (CWC 2018). The dam break modeling is an important tool in the hand of a planner to locate critical infrastructure in the basin and is useful in flood Risk mapping. The aforesaid guidelines have mentioned different numerical models which are available to analyze and simulate the dam break flood such as DAMBRK by National Weather Station (NWS), Finite volume model—BreZo, MIKE by DHI, HEC-RAS, NWS SMPDBK, GeoDam-BREACH by FEMA and many other; every model has its own advantages and limitations. Tapi River flows for a 128 km long stretch from the Ukai dam (Capacity = 7414 MCM at FRL), and passes through Surat city before discharging into the Arabian Sea. The Kakrapar Atomic Power Station (KAPS), National Thermal Power Corporation (NTPC), Reliance Industries, etc. are also situated on the bank of Tapi River. Surat city is a thickly populated and highly industrialized city. After the completion of the Ukai dam in 1972, Surat city faced a major flood in the years 1994,1998 and 2006 due to heavy discharge from the Ukai dam. The flood of the year 2006 inundated almost 80% of the city with

a discharge of 25,780 m<sup>3</sup>/s from the Ukai dam which cost the loss of 21,000 crore and 150 lives. The 1D HD model (Timbadiya 2014a), 2D HD model (Ramirez et al. 2016) and integrated 1D-2D HD model (Timbadiya et al. 2014b and Patel et al. 2017) were developed for analysing the flooding situation in Surat city. However, the past studies were missing with the scenario of sudden failure of upstream situated Ukai dam and its consequences on Surat city. Keeping in view that it is important to carry out dam break analysis for the Ukai dam to compute peak flood discharge, peak velocity, arrival time of flood and its duration, the study presented will be useful in the development of flood hazard and flood risk mapping for Surat city and its outskirt area in future.

## 30.2 Study Area

Tapi River is the second largest west-flowing river in India after the Narmada river. It originates from Multai in the Betul district of Madhya Pradesh and covers total 724 km to meet the Arabian Sea. The Tapi is having total 65,145 km<sup>2</sup> area distributed over three states: Madhya Pradesh, Maharashtra and Gujarat. The whole Tapi basin is divided into three sub-basins: (i) Upper Tapi basin from origin to Hathnur, confluence of Purna with main Tapi (29,430 km<sup>2</sup>); (ii) Middle Tapi basin from Hathnur to the Ukai dam and to sea (32,097 km<sup>2</sup>); (iii) Lower Tapi basin from the Ukai dam to sea (3618 km<sup>2</sup>). The average annual rainfall for the Tapi basin for the last 10 years is 870 mm, and for upper, middle and lower Tapi basins for an average year it is 935.5 mm, 631.5 mm and 1,042.3 mm, respectively (Jain et al. 2007). The index map of the Tapi basin is shown in Fig. 30.1. The study reach is 128 km long the lower Tapi River having two existing structures, viz., Kakrapar weir which has Ogee-shaped spillway with a crest elevation of + 48.78 m above mean sea level (MSL) and weir co-efficient of 1.881 (Subramanya 1998) and Singanpur weir of broad crested type with a crest elevation of + 6 m and weir co-efficient of 1.666 (Timbadiya et al. 2011), located at 22.2 km and 103.03 km downstream of the Ukai dam, respectively. The Ukai dam is a multipurpose dam in Lower Tapi basin completed in the year 1972. The top bund level for earthen and masonry dam is located at 80.77 m and 68.68 m, respectively, from the lowest foundation level. The total length is 4927 m out of which 4058 is an earth dam with 425 m long spillway. The Full Reservoir Level (FRL) and top of the dam are 105.156 m and 111.25 m above MSL, respectively, with live storage of 7414 MCM. The reservoir provides irrigation facilities through its left bank main canal and right bank canal through pick up weir, and they also provide partial flood control to the downstream area. The whole Surat city having an area of 326.5 km<sup>2</sup> is divided into seven different zones where the ground elevations vary from -5 m to the 16 m above MSL.

The Surat Municipal Corporation (SMC) carried out the hydrographic survey of Tapi River in the year 2007. The cross-sections of the Tapi river were extracted from AutoCAD drawing based on the hydrographic survey, provided by SMC. The configuration of hydraulic structures along the Tapi river i.e., Kakrapar weir and



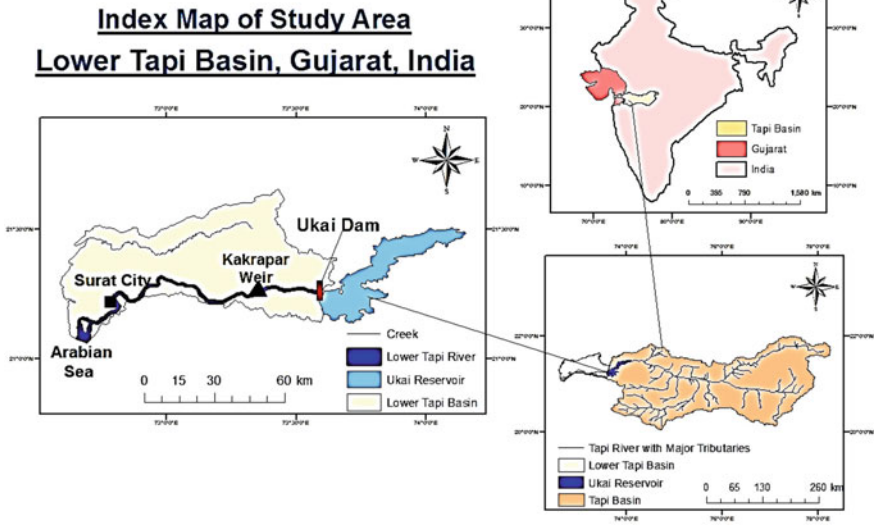
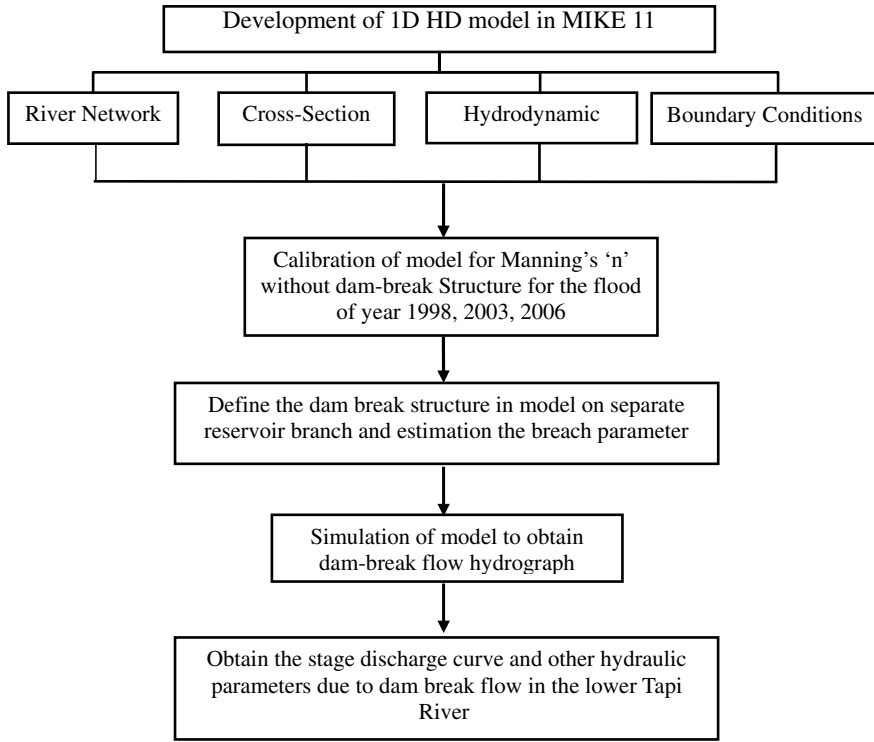


Fig. 30.1 Index Map of Lower Tapi basin showing the location of Ukai dam and Surat city

Singanpur weir were collected from Surat Irrigation Circle (SIC) and SMC respectively. There are four gauging stations available downstream of the Ukai dam on the lower Tapi River, viz., Kakrapar weir (Ch. 22.2 km), Mandavi bridge (Ch. 32.7 km), Ghala Station (Ch. 64.0 km) and Nehru bridge in Surat city (Ch. 106.5 km). The hourly outflow and stage at the Ukai dam and Kakrapar weir for the year 1998, 2009 and 2006 have been collected from SIC. The water levels at Mandavi bridge were collected from State Water Data Center (SWDC), Gandhinagar, Government of Gujarat. The data of Ghala gauging station and Nehru bridge (Surat city) were provided by Central Water Commission (CWC). The hourly tidal levels observed by SIC from December 6, 2009, to January 5, 2010, for both spring and neap Tide have also been collected.

### 30.3 Methodology

The 1D hydrodynamic model was developed for a total stretch of 128 km from the Ukai dam to the Arabian Sea, including two existing structures Kakrapar weir and Singanpur weir. The flow direction is considered to be positive and the maximum distance between two cross sections is 1200 m. Total 190 cross sections have been used to develop the 1D hydrodynamic model; the lowest point of each cross section has been identified and identical lowest point of each cross section is joined to form the thalweg line of the river. For calibration of the model, the outflow from the Ukai



**Fig. 30.2** Methodology for development of 1D HD model for dam break in MIKE 11

dam and tidal level at the Arabian sea is used as upstream and downstream boundary conditions, respectively, for flood simulation of incidents of 1998, 2003 and 2006. The inflow in the Ukai reservoir for the year 2006 is used in the simulation of dam break flow as an upstream boundary condition. The detailed methodology adopted in the present study is shown in Fig. 30.2.

### 30.3.1 Dam Break Simulation of Model

The network editor in MIKE 11 enables to define the dam break structure along with the location of the dam, dam geometry, failure moment mode and selection of breach calculation method in the given river network. The dam is located on the Q-point in the separate reservoir branch (see Fig. 30.3) where momentum equations are replaced by the equation describing the flow through the structure as a broad crested weir (DHI 2013). The point where the dam break structure is located acts as an upstream boundary condition where inflow hydrograph (see Fig. 30.4) is specified. For defining

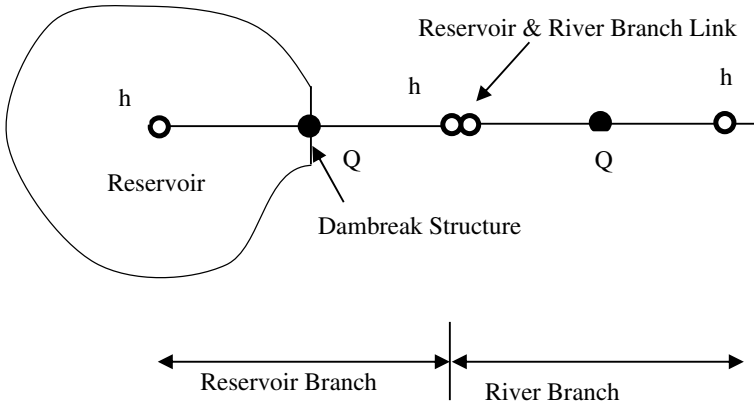


**Fig. 30.3** Typical setup for dam break simulation in MIKE 11 (DHI 2013)

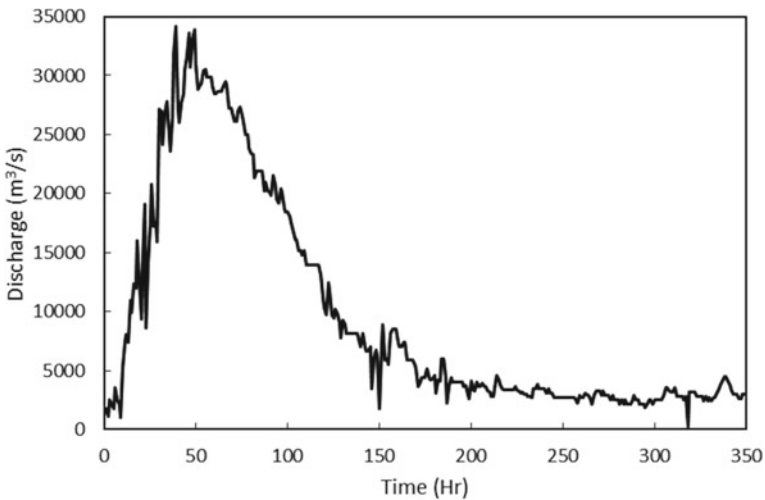


**Fig. 30.4** Hourly inflow hydrograph in Ukai dam during 2006 flood from 6-08-2006 00:00:00 to 20-08-2006 00:00:00

the reservoir storage, the additional flooded area is specified for respective reservoir water level derived from the Capacity-Elevation curve shown in Fig. 30.5.

As per the International Commission on Large Dams (1974), one-third of the embankment dam fails due to insufficient spillway capacity, which results in overtopping of the embankment. For the Ukai dam, the failure moment is specified as water level in the reservoir reaches up-to the top of the dam (+111.25 m) due to heavy inflow, subsequently the dam fails due to overtopping (mode of failure) due to inadequate capacity to hold the inflow. The earthen embankment of the dam gets eroded and develops the breach due overtopping flow of water. The estimation of

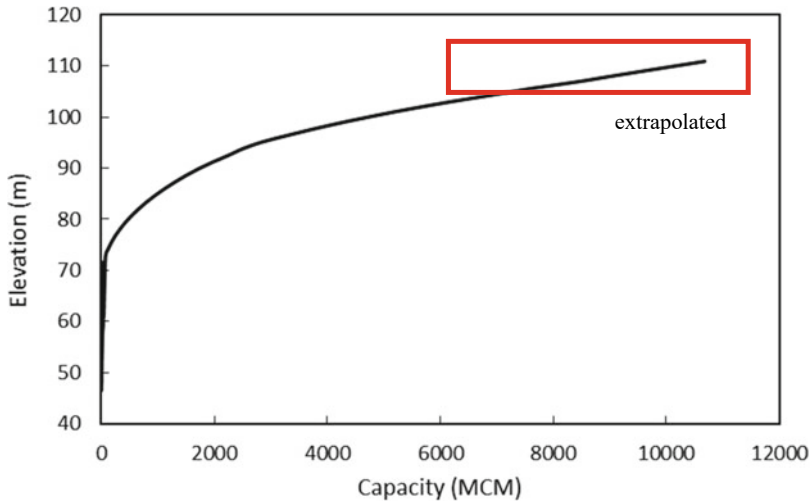


**Fig. 30.5** Capacity Elevation curve for Ukai dam (extrapolated up to 111.25 m)

**Table 30.1** Dam breach parameters and its values for Ukai dam based on Froehlich (2008)

Breach parameter	Formulae	Calculated value for Ukai dam
Average width	$B_{avg} = 0.27K_0V_w^{0.32}H_b^{0.04}$	672 m
Top width	$B_t = B + H_bz$	740 m
Bottom width	$B_b = B - H_bz$	603 m
Side slope	1.0 = Overtopping, 0.7 for other	1.0
Formation time	$t_f = 63.2\sqrt{V_w/gH_b^2}$	8 h

Note  $V_w$  = Volume of water in the reservoir at the time of failure (volume of reservoir)  $m^3$ ,  $H_b$  = breach height (m),  $K_0$  = failure mode co-efficient 1.3 for overtopping failure and 1.0 for other failure

breach parameters is important as it determines the outflow hydrograph after the failure of the dam. Breach parameters such as average width ( $B$ ), average side slope ( $z$ ) and formation time ( $t_f$ ) have been estimated using Froehlich (2008) and tabulated in Table 30.1.

### 30.4 Results and Discussions

#### 30.4.1 Calibration and Validation

To obtain the optimum channel roughness, the comparison between the observed and simulated hourly water levels is performed by calculating root mean square

error (RMSE). The range of channel roughness co-efficient used in calibration for a given type of channel is given in (Chow et al. 1959). The flood event of the year 1998 has been used for calibration, and simulation period is used for 1998 with the highest flow of 19,815 m<sup>3</sup>/sec for the duration from September 15, 1998, 12.00 noon to September 18, 1998, 12.00 noon for a total period of 73 h. The RMSE at different gauging stations were calculated and found that Manning's 'n' = 0.03 shows a close agreement for the observed simulated water level (Table 30.2). The model is validated for the flood of the year 2003 from August 29, 2003, 00:00 to September 1, 2003, 00:00 (73 h) and the flood of the year 2006 from August 6, 2006, 06:00 to August 11, 2006, 06:00 (115 h). Hence, Manning's 'n' = 0.03 is adopted as a roughness value in the present study. Qualitative comparison for simulated and observed discharge at Kakrapar weir and water level at Mandavi bridge, Ghala village and Nehru bridge is shown in Fig. 30.6.

For considering the critical situation in dam break, the reservoir is already at FRL when the inflow is coming into the reservoir. For this study, it is assumed improper timing of gate opening at the time of inflow and the dam fails due to overtopping as water level attains 111.25 m. The reservoir takes 155 h to fill from FRL to top of the dam as a large area undergoes submergence with an increase in the water level of the reservoir. The dam breach statistics for the first 24 h of the flow through breach are given in Table 30.3. Dam break flood hydrograph for discharge just downstream of the dam is shown in Fig. 30.7. The maximum discharge of 2,57,885.9 m<sup>3</sup>/s which is 7.6 times the inflow with a velocity of 18.93 m/s was observed just downstream of the dam. The water level at the various stations for the dam break flow along the channel, downstream of the dam, is shown in Fig. 30.8. The rating curves were developed at Kakrapar weir, Mandavi bridge, Ghala village and Nehru bridge in Surat city as presented in Fig. 30.9 along the channel. The developed rating curves are useful for calculating the water level at different locations on the lower Tapi River for dam break flow. At the same time, it is useful for the development of the flood risk map as well as the design of the levee along the side of the river as flood protection work.

**Table 30.2** Calibration of Manning's n for the channel

Year	Manning's 'n'	RMSE (m)				
		Kakrapar	Mandavi	Ghala	Nehru bridge	Weighted RMSE
1998	<b>0.02</b>	1.0951	1.446	2.4066	1.9413	1.7222
	<b>0.025</b>	1.1095	0.9327	1.7511	1.1685	1.2404
	<b>0.03</b>	1.1278	1.0695	1.5587	0.8471	1.1507
	<b>0.035</b>	1.15	1.5938	1.8662	1.1243	1.4335
2003	<b>0.03</b>	0.2162	2.0203	0.2203	1.4961	0.9882
2006	<b>0.03</b>	1.2404	0.8296	1.9397	0.7914	1.2002

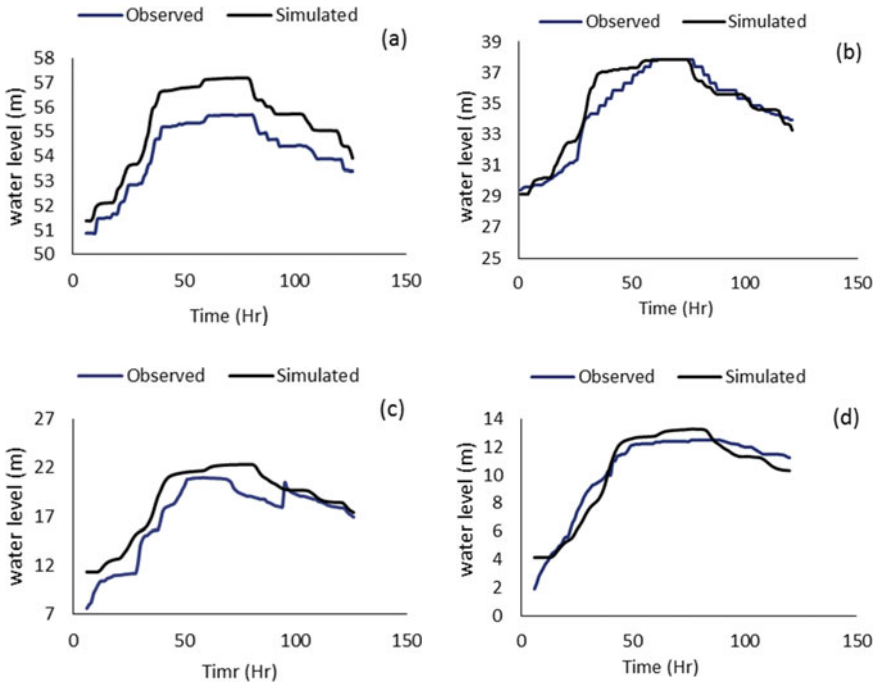


**Fig. 30.6** Qualitative comparison of hourly water level: **a** Kakrapar weir, **b** Mandavi bridge, **c** Ghala village, **d** Nehru bridge, using 1D hydrodynamic model

### 30.5 Conclusions

The dam break analysis for the Ukai dam in the lower Tapi basin has been performed using the inflow of the flood year 2006 into the reservoir in MIKE 11 (HD). Based on aforesaid analyses of the river, the following conclusions can be made:

- (a) The 1D Hydrodynamic model of lower Tapi River in MIKE 11 has been calibrated for 1998, 2003 and 2006 floods, and Manning’s ‘n’ = 0.03 is found to be the most suitable value and is utilized for future simulation.
- (b) The dam break flood hydrograph obtained by the simulating model for the Ukai dam failure results in a peak discharge of 2,57,885.9 m<sup>3</sup>/s, which is 7.6 times more than that of inflow with a maximum velocity of 18.92 m/s when the reservoir fails at 111.25 m.
- (c) The hydraulic parameters computed through simulation (Table 30.3) and rating curves computed along the river (Figs. 30.8 and 30.9) will be helpful in designing flood protection measures and development of flood risk map for downstream area of a dam.

**Table 30.3** Breach statistics for the flow through the breach

Time (Hr)	Discharge through breach (m <sup>3</sup> /s)	Velocity in breach (m/s)	Reservoir water level (m)	Level of breach (m)	Depth of water at breach (m)	Breach bottom width (m)	Breach width at the crest (m)
154.99	0	0.33	111.26	111.24	0.011	0.042	0.052
55.99	0	0.49	111.27	111.23	0.027	0.06	0.1
156.99	0	0.69	111.29	111.19	0.061	0.14	0.25
157.99	0.1	1.04	111.30	111.08	0.141	0.36	0.7
158.99	1.7	1.91	111.31	110.56	0.472	1.39	2.76
159.99	315.6	5.43	111.33	105.34	3.73	11.84	23.65
160.99	56,691.6	15.33	111.28	63.75	29.65	95.01	190.00
161.99	260,228.9	18.93	110.40	42.67	40.97	294.44	431.60
162.99	238,522	9.47	109.01	42.67	59.80	360.6	497.79
163.99	227,304.9	8.74	107.75	42.67	59.54	376.83	513.99
164.99	222,140	8.42	106.47	42.67	58.68	390.83	527.99
165.99	216,031.2	8.12	105.11	42.67	57.68	403.27	540.36
166.99	209,732.1	7.87	103.70	42.67	56.59	414.24	551.40
167.99	203,031.1	7.63	102.27	42.67	55.43	424.20	561.36
168.99	195,660.1	7.41	100.77	42.67	54.17	433.21	570.37
169.99	187,721.6	7.19	99.18	42.67	52.82	441.36	578.52
170.99	179,060.7	6.97	97.48	42.67	51.35	448.73	585.89
171.99	169,725	6.75	95.68	42.67	49.77	455.38	592.54
172.99	154,908.1	6.39	93.20	42.67	47.64	461.17	598.33

(continued)

**Table 30.3** (continued)

Time (Hr)	Discharge through breach ( $m^3/s$ )	Velocity in breach (m/s)	Reservoir water level (m)	Level of breach (m)	Depth of water at breach (m)	Breach bottom width (m)	Breach width at the crest (m)
173.99	141,044.3	6.10	90.48	42.67	45.18	466.02	603.18
174.99	125,321.2	5.74	87.53	42.67	42.54	470.12	607.28
175.99	108,561.3	5.33	84.31	42.67	39.65	473.41	610.57
176.99	90,547.4	4.84	80.78	42.67	36.48	475.89	613.05



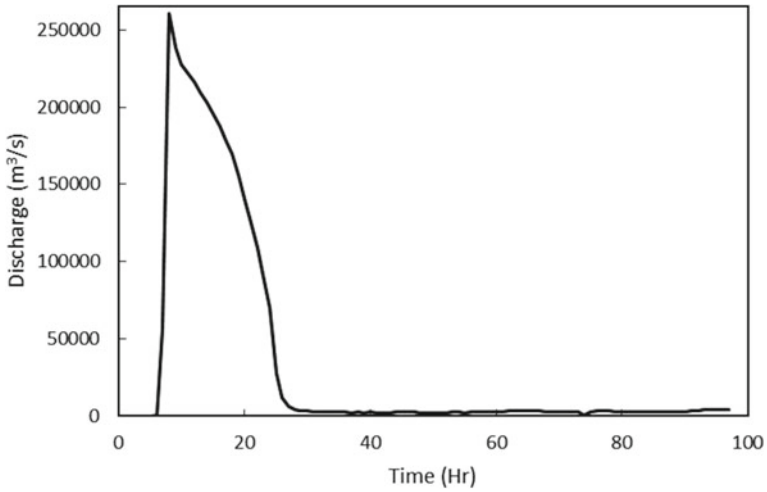


Fig. 30.7 Dam break flood hydrograph downstream of dam

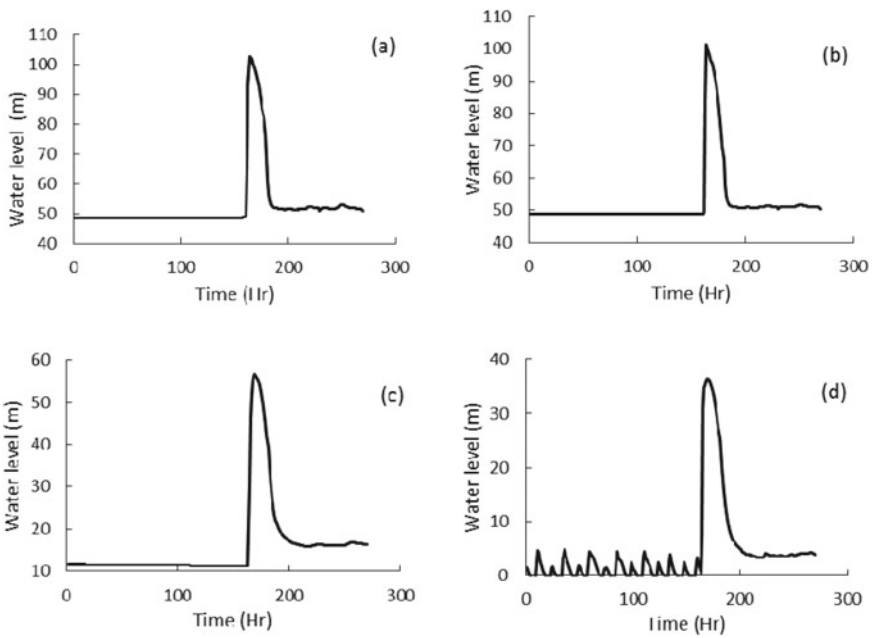
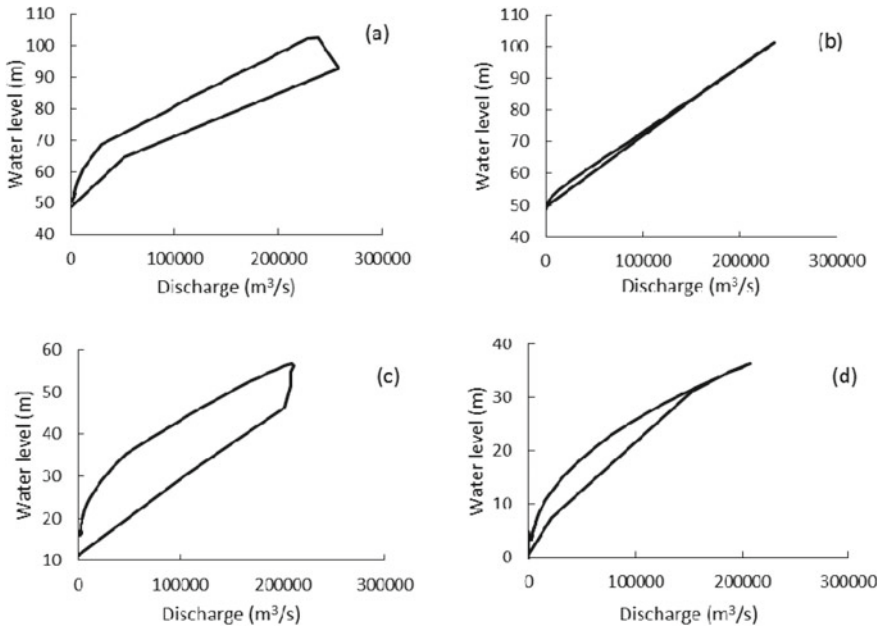


Fig. 30.8 Water level along the channel after the dam break **a** downstream of dam, **b** at Kakrapar weir, **c** Ghala stations and **d** in Surat city



**Fig. 30.9** Rating curves along the channel after the dam break: **a** downstream of dam, **b** Kakrapar weir, **c** Ghala stations and **d** Surat city

**Acknowledgements** The authors are thankful to Centre of Excellence (CoE) on “Water Resources and Flood Management”, SVNIT Surat under TEQIP-II funded by World Bank for providing necessary infrastructural and computational facility for the study. The authors are also grateful to Central Water Commission (CWC), Tapi Division Surat, Surat Municipal Corporation (SMC), State Water Data Centre (SWDC), Gandhinagar, Surat Irrigation Circle (SIC), for providing the relevant data in the present study.

**References**

Central Water Commission (2018) Guidelines for mapping flood risks associated with dams, River Development and Ganga Rejuvenation, Ministry of Water Resources, Govt. of India.  
 Chow VT (1959) Open-channel hydraulics. McGraw-Hill, New York  
 DHI (Danish Hydraulic Institute) (2013) User guide and reference manual to MIKE 11: modeling System for the rivers and channels. Software manual, DHI, Denmark  
 Doocy S, Daniels A, Murray S, Kirsch TD (2013) The human impact of Floods: a historical review of events 1980–2009 and systematic literature review. PLoS currents 1  
 Froehlich DC (2008) Embankment dam breach parameters and their uncertainties. J Hydraul Eng 134(12):1708–1721  
 Gallegos HA, Schubert JE, Sanders BF (2009) Two-dimensional, high resolution modeling of urban dam-break flooding: A case study of Baldwin Hills, California. Adv Water Resour 32:1323–1335  
 Goosby S, Chatman A, Michaud J, Kerper D (2008) Dam break inundation study for the State of Hawaii. Solutions to coastal disasters (2008)

- Jain SK, Agarwal PK, Singh VP (2007) Tapi, Sabarmati and Mahi basins. In: Hydrology and water resources of India. Springer, Dordrecht, pp. 561–595
- Liu Y, Guo Y, Fan WB (2006) Computation of one-dimensional dam-break flow using ENO scheme. In: Computational methods in engineering and science. Springer, Berlin, pp 175–175
- Lodhi MS, Agrawal DK (2012) Dam-break flood simulation under various likely scenarios and mapping using GIS: Case of a proposed dam on River Yamuna, India. *J Mt Sci* 9(2):214–220
- MacDonald TC, Langridge-Monopolis J (1984) Breaching characteristics of dam failures. *J Hydraul Eng* 110(5):567–586
- Mohapatra PK (2009) Rating curves for dam-break flows. *J Hydrol Eng* 15(1):57–60
- Patel DP, Ramirez JA, Srivastava PK, Bray M, Han D (2017) Assessment of flood inundation mapping of Surat city by coupled 1D/2D hydrodynamic modeling: a case application of the new HEC-RAS 5. *Nat Hazards* 89(1):93–130
- Pilotti M, Maranzoni A, Tomirotti M, Valerio G (2010) 1923 Gleno Dam break: Case study and numerical modeling. *J Hydraul Eng* 137(4):480–492
- Ramirez JA, Rajasekar U, Patel DP, Coulthard TJ, Keiler M (2016) Flood modeling can make a difference: disaster risk-reduction and resilience-building in urban areas. In: Hydrology and earth system sciences discussions, pp 1–25.
- Rodrigues AS, Santos MA, Santos AD, Rocha F (2002) Dam-break flood emergency management system. *Water Resour Manage* 16(6):489–503
- Subramanya K (1982) Flow in open channels. Tata McGraw-Hill Publishing Company Limited, New Delhi, pp 150–210
- Timbadiya PV, Patel PL, Porey PD (2011) Calibration of HEC-RAS model on prediction of flood for lower Tapi River, India. *J Water Resour Prot* 3(11):805
- Timbadiya PV, Patel PL, Porey PD (2014a) One-dimensional hydrodynamic modelling of flooding and stage hydrographs in the lower Tapi River in India. *Curr Sci* 106(5):708–716
- Timbadiya PV, Patel PL, Porey PD (2014b) A 1D–2D coupled hydrodynamic model for river flood prediction in a coastal urban floodplain. *J Hydrol Eng* 20(2):05014017
- Yochum SE, Goertz LA, Jones PH (2008) Case study of the big bay dam failure: accuracy and comparison of breach predictions. *J Hydraul Eng* 134(9):1285–1293

# Chapter 31

## 3D Modelling of Hybrid River Training Works



Riddick Kakati, Vinay Chembolu, and Subashisa Dutta

**Abstract** River bank erosion due to unstable banks and high flow variability is usually controlled using permeable and impermeable structures, which are not studied much yet and also cannot solely provide desired velocity reduction. These structures, along with a combination of porcupine screens followed by geobag (i.e., Hybrid layout), are investigated using CCHE3D model for emerged, transition, and submerged flow conditions with respect to porcupine height. An optimum hybrid layout showed velocity reductions of 35% in submerged and 70% in emerged conditions, which further increased with multiple porcupine screens.

**Keywords** Hybrid layout · Porcupine · Geobag · CCHE3D · Velocity reduction

### 31.1 Introduction

Rivers in India are a great source of income and also a boost to the economy. History states that rivers in India were responsible for inland transportation of agricultural goods, machinery, and people. Today, India is an agricultural economy and depends more on our rivers for irrigation purposes.

Rivers are generally meandering in nature, which causes erosion in the outer bank and deposition in the inner bank, hence causes a shift in the thalweg. To reduce the effect of this shift, rivers often tend to change their course or attain a completely new path, which causes a lot of damage to life and property. Various river training methods are practiced now a days to maintain the course of a river along a well-defined path such as guide vanes, groynes, and bank pitching. Stone pitching, gabions, rock riprap, and retaining walls in addition to flow deflectors like spurs and bend weir are the most widely used river bank protection methods in large alluvial rivers (Julien 2002). These river training works can be categorized into permeable and impermeable river

---

R. Kakati (✉) · S. Dutta  
Department of Civil Engineering, IIT Guwahati, Guwahati 781039, India  
e-mail: [riddick.kakati@iitg.ac.in](mailto:riddick.kakati@iitg.ac.in)

V. Chembolu  
Department of Civil Engineering, IIT Jammu, Jammu and Kashmir 181121, India

training works. Permeable works allow flow to pass through them partially, whereas impermeable works do not allow the same. The provision of a particular type of river training work depends on the importance of the area to be protected, as well as the river response to the intervention (Sarker et al. 2011).

Bank erosion is a serious problem, and hence there is a need for effective bank protection measures, which does not alter river response as well as ecology. Due to high cost of these river training works, countries like India have been adopting economic measures of river training. Board fencing, bandalling, jack-jetty systems, and tetrahedral frames are some of the cost effective solutions. Porcupine systems have also been deployed in large rivers like Brahmaputra and Ganga with fairly good results. They cause considerable reduction in the flow velocity resulting in the deposition of sediment with porcupines offering resistance to flow (Aamir and Sharma 2015). From previous research in the area of river bank erosion and protection, it can be seen that flow deflectors like dikes (spurs) and bendway weirs were considered as the most versatile river bank protection techniques in large rivers, where a lot of morphological and hydrodynamic changes are observed (Yoo 2003). Various bank protection measures were installed to confine the flow along main path. But not much studies have been done yet. Hence this study focuses on performance evaluation of some commonly used bank protection measures.

## 31.2 Methodology

The objective of this study is to understand the flow behaviour using 3D modelling and validation with experimental data.

### 31.2.1 CCHE3D Modelling

In this study, three dimensional finite element method based hydrodynamic CCHE3D model is used which is an integrated package developed at the National Centre for Computational Hydroscience and Engineering, the University of Mississippi. It is a numerical model for three-dimensional simulation and analysis of free surface flows like water flows in rivers, lakes, reservoirs, and estuaries, water flow dominated processes of sediment transport, morphological change, water quality, etc. (Zhang and Jia 2009).

These processes are solved with full three-dimensional Reynolds equations and mass conservation equation. In addition, turbulence closure scheme, parabolic eddy viscosity models, mixing length eddy viscosity models, wind driven flow eddy viscosity, and linear and nonlinear  $k-\epsilon$  models are available in this model. This model is developed on the same platform as the CCHE2D model, which is a two dimensional hydrodynamic model, and the results from the 2D model is often used as the initial condition for the 3D simulations. Mesh generation tool is common for both 2D and

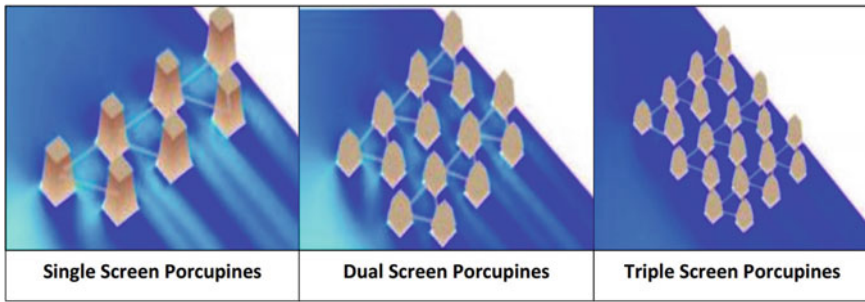


Fig. 31.1 CCHE3D porcupine model setup

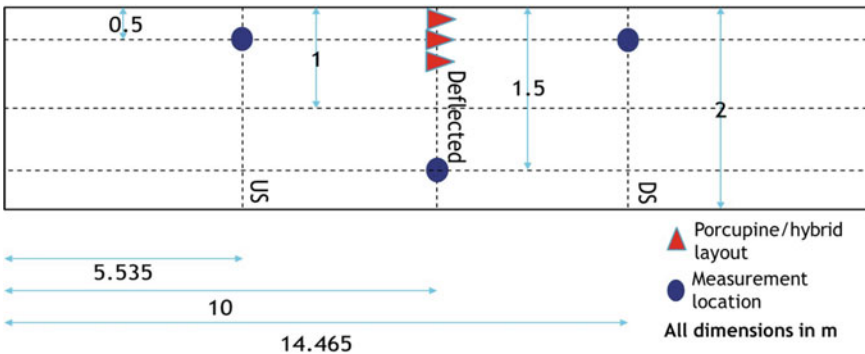


Fig. 31.2 Various locations of velocity measurement

3D, and the 3D mesh is developed based on the 2D mesh by stacking multiple levels. The Graphic User Interface (GUI) helps to drive and manage simulation cases, visualize, analyse and animate the results from simulation. Starting with the mesh, GUI helps to setup parameters, boundary conditions to run the simulation, and visualize the results.

### 31.2.2 Methodology

Considering the computational and modelling difficulties associated with the inclined members in CCHE3D, vertical members were used in this study (Fig. 31.1). The height of the porcupines was 12 cm when placed in the channel. The model was setup for a 20 m long and 2 m wide laboratory channel with different number of porcupines placed in a row, and slope of the bed was kept as mild (Fig. 31.2). Two heights of geobags were used in this study viz. 6 and 12 cm, and they were placed downstream of the porcupine screens in the hybrid layout study. The computational

**Table 31.1** Various parameters used for mathematical modelling

Flow condition	Porcupine height (m)	Geobag height (m)	Distance between porcupine and geobag in hybrid layout (m)
<i>Emergent</i> Q = 0.1128 m <sup>3</sup> /s y = 0.08 m	0.12	0.06	0.06
			0.12
			0.24
	0.12	0.12	0.06
			0.12
			0.24
<i>Submerged</i> Q = 0.3416 m <sup>3</sup> /s y = 0.16 m	0.12	0.06	0.06
			0.12
			0.24
	0.12	0.12	0.06
			0.12
			0.24

mesh for area having length of 20 m and width 2 m is generated using mesh generator. At the porcupine zones, finer grid is generated than other parts of the mesh. The channel is interpolated to get the bed elevation at all mesh nodes, and the geometry file is created. Once the geometry file is created, GUI is used for further analysis, like setting of flow initial and boundary condition and to run the simulations. A uniform roughness height ( $k_s$ ) of 0.0032 is used throughout the domain. Discharge is given as an upstream boundary condition, and the corresponding water level is given as a downstream boundary condition. Initially 2D simulation is carried out, and the results of 2D simulation were further used as the initial condition for the 3D simulation. The flow simulations were carried out for different layouts of porcupine placed halfway along the length of channel. Table 31.1 shows the different layouts of porcupine, water depths, and discharges used for different simulations.

### 31.3 Results and Discussions

It was observed from simulation results that porcupine screens can provide considerable reduction in flow velocity which increases with number of porcupine screens. In emergent case, dual screen porcupines reduced the velocity by 90%, followed by 50% by single screen porcupines. In deflected zone, the velocity increased by 85% in dual screen followed by 42.9% in single screen porcupines. In the transition case, velocity reduction was 9.6% in case of dual screen porcupines followed by 4.4% in case of single screen porcupines. Thus, in case of high submergence, the effect of porcupines in flow deflection and velocity reduction was found to be negligible;

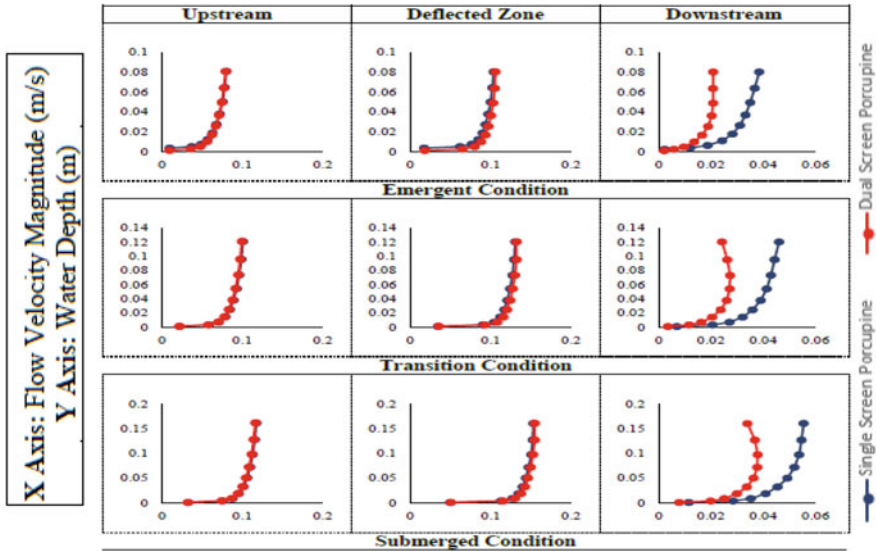


**Fig. 31.3** Comparison of velocity profiles obtained after placing single screen porcupines and dual screen porcupines

hence, porcupines are not suitable for high flow conditions (Fig. 31.3). Hence, a hybrid layout was tested.

Hybrid layout was also found to be most effective in emergent condition. The velocity reduction of a hybrid layout when compared with a geobag layout was found to be almost the same (94.36%). However in deflected region, the velocity of flow increased by 97.85% in dual screen hybrid, followed by 88.60% in single screen hybrid and 76.17% in only geobag layout, respectively. In the transition case, velocity reduction was 91.59% in case of dual screen hybrid, followed by 91.13% in single screen hybrid and 86.78% in only geobag layout. In the deflected region, the velocity of flow increased by 79.85% in case of dual screen hybrid layout, followed by 77.25% in case of single screen hybrid layout and then by 73.10% in case of only geobag layout. In submerged case, velocity reduction was 82.20% in dual screen hybrid and 77.29% in single screen hybrid and only geobag layout. In the deflected region, the velocity of flow increased by 59.49%, 54.21% and 50.25% in dual screen hybrid, single screen hybrid and only geobag layout, respectively.

Finally performance of hybrid layout was compared with that of porcupine and geobag screens placed alone. The results of the study are shown below (Figs. 31.4 and 31.5).



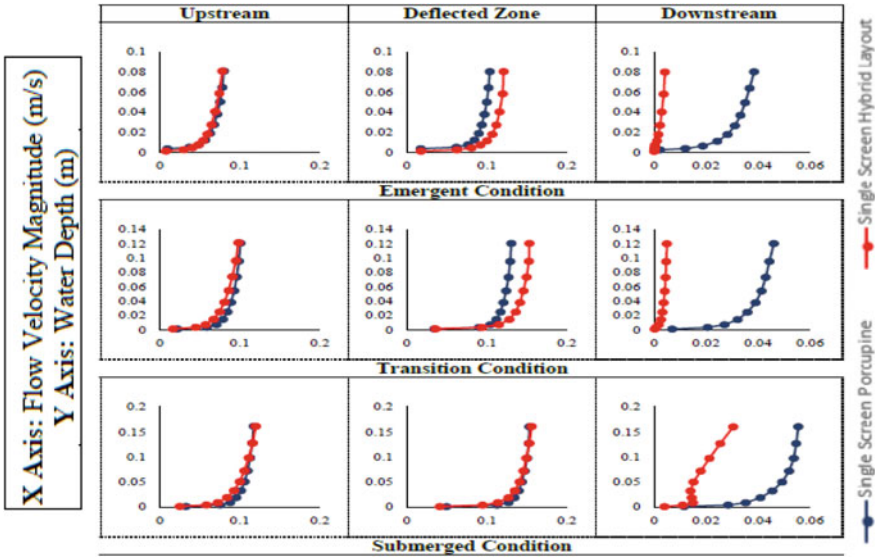


Fig. 31.4 Comparison of velocity profiles obtained after placing single screen porcupines and single screen hybrid layout

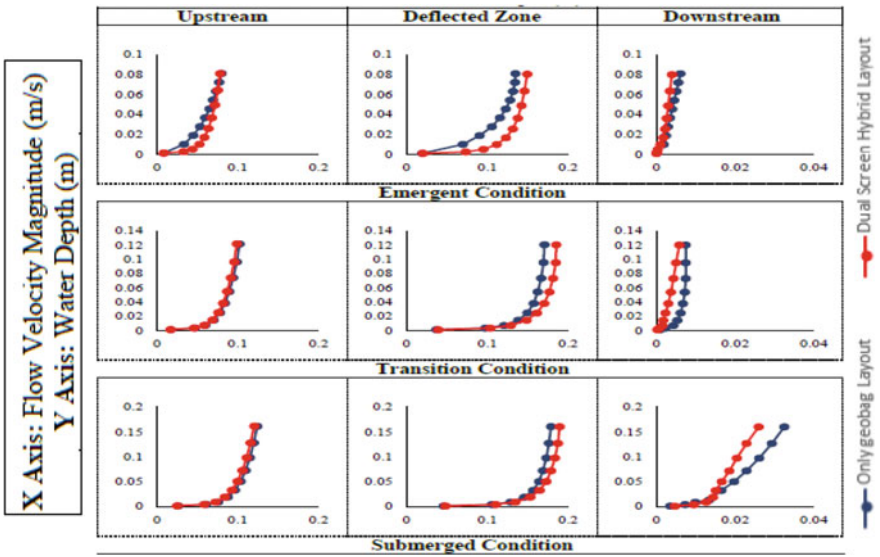


Fig. 31.5 Comparison of velocity profiles obtained after placing only geobag and dual screen hybrid layout

## 31.4 Conclusion

Permeable structures are the cost effective alternative method for training a braided river. The basic principle of permeable elements is to reduce the velocity by offering resistance to flow and promote sediment deposition. In the present study, CCHE3D was setup and permeable structures and hybrid structures were incorporated in the models by increasing the local roughness of the channel at different locations.

1. It was observed that series of porcupines caused considerable reduction in flow velocity and were found to be more effective than single screen porcupines. Thus, there was more energy dissipation by multiple screen porcupines than single screen porcupines.
2. A larger low velocity zone was also observed in multiple screen porcupines when compared to that of single screen porcupines.
3. In case of high submergence, keeping the height of porcupines constant, the effectiveness of porcupines were found to have decreased with increase in water depths.
4. With increase in depth of flow, Manning's coefficient value was found to have a decreasing trend.
5. With the addition of geobag in porcupine layout (hybrid layout), further decrease in velocity as well as increase in low velocity zone was observed, which resulted in increase of sediment deposition.

## References

- Aamir M, Sharma N (2015) Riverbank protection with Porcupine systems: development of rational design methodology. *ISH J Hydraulic Eng* 317–332
- Julien PY (2002) *River mechanics*. Cambridge University Press, Cambridge, U.K.
- Sarker MH, Akter J, Ferdous MR (2011) River bank protection measures in the Brahmaputra-Jamuna River: Bangladesh Experience. *International Seminar on 'River, Society and Sustainable Development*, Dibrugarh
- Yoo KH (2003) Nature friendly River Training Structure using Groynes. *Water Resources Research Department, Korean Institute of Construction Technology, Korea.*
- Zhang Y, Jia Y (2009) *CCHE-MESH: 2D structured mesh generator user's manual-version 3.x*. School of Engineering, The University of Mississippi, Mississippi

# Chapter 32

## Effect of Bends on Scour and Deposition Around Causeways



Mohammad Athar, Ismeet Singh Saluja, and Humaira Athar

**Abstract** This paper presents the experimental investigations of effect of bend on scour and deposition patterns around causeways. Data have been collected in a re-circulatory open channel flow system on three causeway model slabs for two discharge values, i.e., 2.5 and 7.0 l/s. The causeway model slabs were made of cement concrete with 0.75 m length, 0.2 m width, and 0.20 m overall depth. To critically observe the effects of presence of bend on scour and deposition, three locations of causeway slabs were used. The first one is provided in a straight reach in the test channel, the second one is just after the first bend normal to flow, and the third one was an oblique slab provided between the inner and outer curvature of the second bend downstream of the first bend. Data of scour and deposition were recorded after the end of the run. Also photographs were taken. It is concluded that for each discharge, scour and deposition occur in all cases, but at low flow the scour in straight reach is less pronounced. However, scour occurs in second and third causeways due to the presence of bends. At still high values of discharges, scour and deposition both are significant in all the causeways. Since first causeway is straight and normal to flow, there is uniform scour and deposition along the edges of the causeways. The scour and successive deposition occur in other two causeways with high magnitudes, but the location of maximum scour depth shifted. Photographs also support the findings in this investigation.

**Keywords** Causeway · Channel bend · Secondary flow · Scour · Deposition

### Symbol Used

Bc Width of the channel

---

M. Athar (✉) · I. S. Saluja  
Civil Engineering Department, Zakir Husain College of Engineering & Technology, A.M.U,  
Aligarh 202002, U.P, India

H. Athar  
Polymers, Plastics and Composite Division, CSIR-CBRI, Roorkee, India

d50	Sediment size
Dc	Overall depth of the causewa
Lc	Length of the Causeway
Q	Discharge
Sc	Scour depth
x	The lateral distance along the causeway measured from left to right

## 32.1 Introduction

Causeways are mainly preferred in mountainous regions where hilly roads/highways cross many torrential rivers to save the cost of the highway projects (Athar et al. 2017). Causeways serve two purposes, i.e., passing of river water and also to cater the traffic demand simultaneously. The proper design and location (IRC 2008; IS 2000) of the causeways are the important issue as these structures may save the cost of the highway projects. Generally, two types of causeways flushing and vented are in common practice in India and abroad. In flushing type, the crest of the causeway slab is kept in the same level of the river bed on which water and traffic both move at low flow condition. In vented causeway, water move through the vents and the traffic moves on the road surface well above the river bed level. Scour and deposition (Saluja and Athar 2017) are natural phenomena which occur when ever stream or river flow is obstructed due to any obstruction (Athar and Saluja 2017; Saluja and Athar 2017). It is observed in field that many vents of the vented causeways get fully or partially choked with silt due to heavy silt scour and deposition. This situation generally occurs when ever causeways were located where the streams meander (Saluja et al. 2017). In this paper, an attempt has been made to investigate the effect of bends on the scour around flushing type causeways.

### 32.1.1 Location

The proper location of the causeway is an important issue. In no case the causeway should be located at those places where river has meandering patterns. During flood it may happen that due to secondary currents the water may scour the bed materials of rivers from convex side (outer bend of river) and may deposit on concave side (inner bend) resulting choking of many ducts (vents of causeway) as shown in Fig. 32.1.

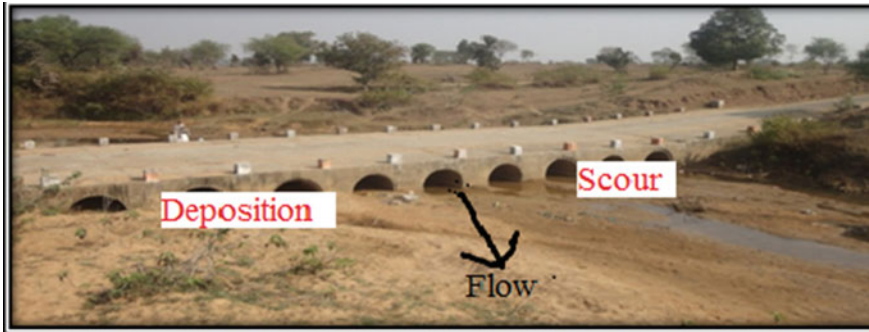


Fig. 32.1 Causeway on Ghosai River, District Shahdol (M.P.)

### 32.1.2 Phenomena of Scour and Deposition

Structures built in rivers and channels are subjected to scour around their foundations. If the depth of scour becomes significant, the stability of the foundations endangered, with a consequent risk to the structure of damage or failure. The factors influencing the development of scour are complex and vary according to the type of structure.

Scour process is caused by sediment transportation resulted from the flow of the fluid. When the sediment rate transported into a certain area is less than that transported out of this area, a scour hole will be existed. Scoured materials when move downstream with flow of water get deposited. The scour and deposition of sediment upstream and downstream of a weir is shown in Fig. 32.2.

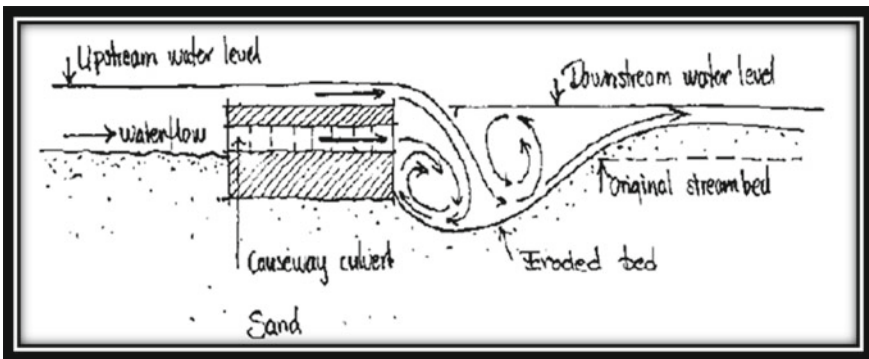


Fig. 32.2 Scour and deposition D/S of a vented causeway

## 32.2 Experimental Set-Up and Procedure

The experimental set-up used in the present study consisted of a 60 m long, 0.75 m wide and 0.60 m deep rectangular open channel having two successive bends. It was a re-circulatory flow system. The experimental set-up is shown in Fig. 32.3. Experiments have been carried out on three model causeway slabs. These slabs have been constructed with cement concrete. The lengths of the two slabs are kept equal to the width of the channel, while length of third slab is kept equals to the perpendicular distance between inner and outer curvatures of the bend. The width and over all depths of each slabs are kept as 0.20 m and 0.20 m, respectively.

### 32.2.1 Installation or Location of Causeway Slabs

The first slab is located in the straight reach of the channel, normal to flow and flushing with the channel bed. The second one is kept just downstream of the first bend normal to flow, and the third one is placed in second bend oblique to flow between inner and outer curvatures as shown in Fig. 32.3. Uniform size of the sand  $d = 0.22$  mm was used to form the channel bed. Flow in the channel has been diverted from an overhead tank through a re-circulatory flow system. To measure flow rate, a pre-calibrated sharp crested rectangular weir has been used at the downstream end of the channel.

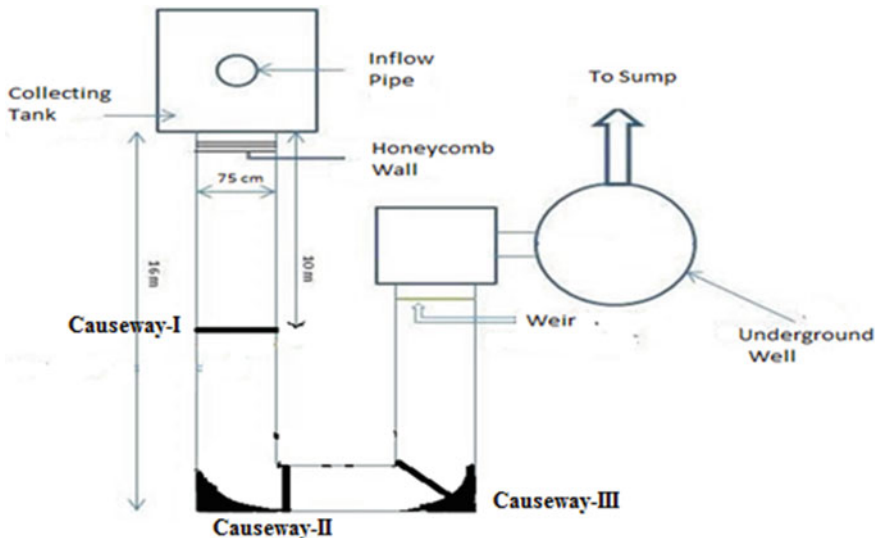


Fig. 32.3 Schematic Diagram of Experimental Setup

### 32.2.2 Procedure

Initially very small quantity of water approximately 1 l/s from the overhead tank was diverted into the test channel at the constant head to maintain the steady uniform flow. Gradually the gate opening is increased till the required flow is maintained in the channel. This was done with the help of pre-calibrated sharp crested weir provided at the end of the test sections. After steady state condition is maintained, the visual observation regarding flow pattern and scour and deposition have been started. Visual observations were taken time to time at each test section and photographs were also been taken at the end of the run.

The data for scour and deposition were collected for two discharge values for all three causeways. Visual observations were first made using coloured balls to see the flow patterns across each causeway slabs. Also, the depths of scour around the upstream faces of each causeway have been measured accurately and carefully.

### 32.3 Data Analysis and Result Presentation

The data for scour depth  $S_c$  collected in the lab for all three causeways are first normalised by dividing them with the sediment size  $d_{50}$ . Similarly, the transverse distance 'x' along the causeways measured from left side to right side has also been normalized by dividing it with channel width  $B_c$ . These data have been plotted as shown in Figs. 32.4, 32.6 and 32.8.

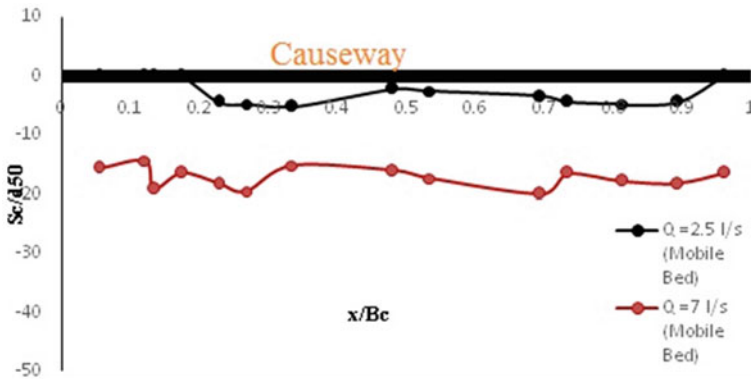


Fig. 32.4 Variation of scour along a causeway-I



**Fig. 32.5** Photogrammetric view of scour around causeway-I

### ***32.3.1 Scour and Deposition Around First Causeway***

It is clear from Fig. 32.4 that at both discharge values, the scour around the edge of the first causeway placed in straight channel and normal to flow is almost uniform and with low magnitudes. This may be attributed to uniform velocity and pressure distribution near and upstream of the causeway. Very small ripples were seen at low value of discharge and moderate dunes at high value of flow. The flow being subcritical and shear velocity is also less than critical shear velocity. Figure 32.5 shows the photogrammetric view of the scour at causeway-I.

### ***32.3.2 Scour and Deposition Around Second Causeway***

Second causeway was located just downstream of the first bend to see the effect of the presence of bend on scour pattern. Since flow is not uniform at upstream of the causeways due to the presence of the bends, the scour and successive deposition which occur along the edges of the causeways is also not uniform. Figure 32.6 show the variation of scour and deposition along the upstream edges of the causeway. The scour starts to occur after one fourth length of the causeway and extends gradually towards the centre from left to right. At centre depth of scour is maximum. The scour hole and its extent can easily be seen in Fig. 32.7.



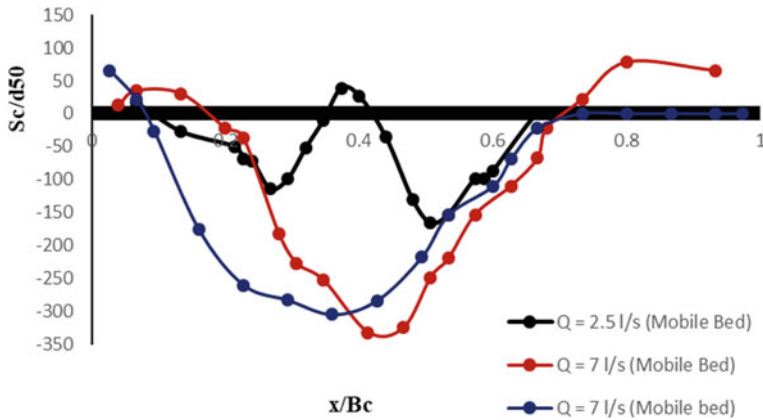


Fig. 32.6 Variation of scour along causeway-II

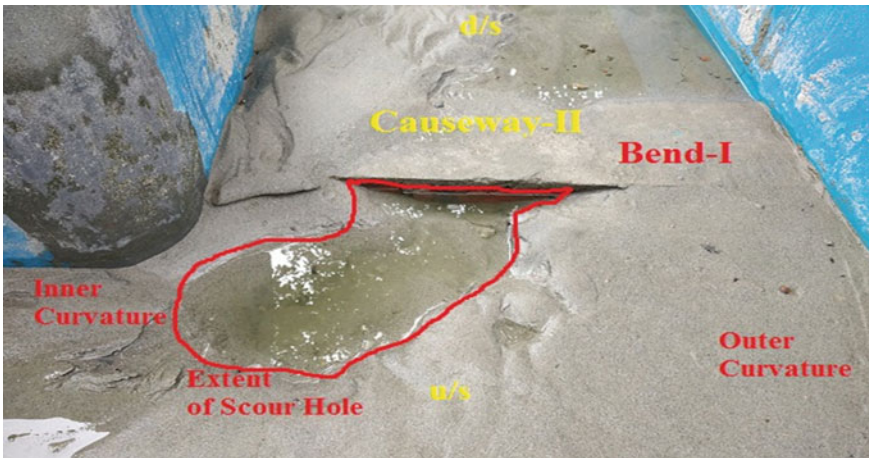


Fig. 32.7 Photogrammetric view of scour around causeway-II

### 32.3.3 Scour and Deposition Around Third Causeway (Upstream Channel Bed Mobile)

In third causeway which is provided in second bend of the channel (Figs. 32.3 and 32.9), the scour and deposition is also not uniform due to non-uniformity of the flow condition upstream of the causeway. At the beginning when the flow passes the causeway, small scour holes started to develop. Also, since the dunes were developed at the upstream of the causeway, the velocity was not uniform. After the elapse of the time, the scour holes were filled up and other holes were developed. This phenomenon

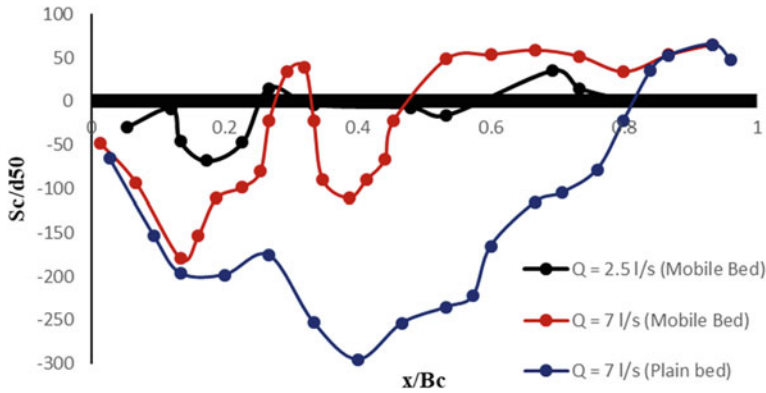


Fig. 32.8 Variation of scour along causeway-III



Fig. 32.9 Photogrammetric view of scour around causeway-III (Mobile Bed)

was continued till the end of the run. Figure 32.9 shows the final photograph of the scour and deposition.

### 32.3.4 Scour and Deposition Around Third Causeway (Upstream Bed Fixed)

An attempt has also been made to keep the channel bed upstream of the third causeway as fixed bed to avoid formation of ripples and dunes. When flow was allowed to pass over this causeway, the scour holes were started to develop along the upstream edge (Figs. 32.8 and 32.9).



**Fig. 32.10** Photogrammetric view of Scour around Causeway-III (Fixed Bed)

The holes were not of uniform depth as approach flow was also not uniform due to obliquity of the causeway. Since no ripples and dunes were formed in the straight portion, no sediment moves towards the causeway holes and no sediment fills the holes. The scour holes were increasing with respect to time. After about one hour it was found that the pattern of the scour in this case was not similar with first case when bed was mobile. The variation of scour along the causeway length is shown in Fig. 32.8. Also this can be clearly seen in Fig. 32.10. The non-uniformity in formation of scour holes fully depends upon velocity distribution. In the bends, velocity is not uniform, hence the scour and successive deposition.

## 32.4 Conclusions

1. The scour around the edge of the first causeway for both the discharges is almost uniform and comparatively small.
2. The scour is more pronounced in second causeway mostly at the centre. The deposition of sediment occurs only at the down streamside of the causeway at inner bend at about 20% of the causeway length. Similar condition was found for the high value of discharge also.
3. In third causeway the scour holes were developed at many places of the causeway. No uniform scour was seen as the bed was mobile, and there was continuous movement of sand towards the causeway.

4. For fixed bed condition, there was no formation of dunes upstream of the causeway. And the scour as well as deposition occur along the edge of about 80% of the length.
5. It is recommended that in no case, causeways should be located at the meandering of streams or where there are bends.

**Acknowledgements** The authors are thankful to the Chairperson, Civil Engineering Department, and A.M.U. Aligarh for providing the experimental facilities. The assistance received by teaching and non-teaching staffs of the hydraulic section is highly acknowledged. The author is also thankful to UGC for providing Maulana Azad National Fellowship.

## References

- Athar M, Adil M, Humaira A (2017) Study of submersible hydraulic structures, a critical review. U.G.C. Approved. *Int J Eng Technol Sci Res (IJETSR)* 4(11). ISSN 2394 2386
- Athar M, Saluja IS (2017) Scour due to rock sills in curved horizontal channels. In: International conference on hydraulics, water resources and coastal engineering (XXII -Hydro-2017), L. D. College of Engineering under the aegis of the Indian Society of Hydraulics at L. D. College of Engineering, Ahmedabad, Gujarat, India.
- IRC (2008) SP: 82–2008 ‘Guidelines for design of causeways and submersible bridges’, Indian Road Congress
- IS (2000) 456–2000 ‘Code of Practice for Design of Reinforced Concrete Structures’, Bureau of Indian Standards, pp 84
- Saluja IS, Athar M (2017) Computation of scour due to rock sills in alluvial channels. U.G.C. Approved. *Int J Eng Technol Sci Res (IJETSR)* 4(12). ISSN 2394 3386
- Saluja IS, Athar M (2017) Scour in curved open channels, a review, U.G.C. Approved. *Int J Eng Technol Sci Res (IJETSR)* 4(12). ISSN 2394 3386
- Saluja IS, Athar M, Ansari SA (2017) Flow characteristics in curved channels, a review paper, U.G.C. Approved. *Int J Comput Math Sci (IJCMS)* 6. ISSN-2347 8527

# Chapter 33

## Hydrodynamic Modeling of Urban Flooding and Its Management: A Case Study of Patna, India



Biswajit Chakravorty, R. Venkata Ramana, and N. G. Pandey

**Abstract** Patna has been facing acute drainage problems due to its topography. In the recent past, Patna was heavily flooded and there was severe waterlogging in the years 1990 and 1997 in the town. Small boats could be seen on the roads. Urbanization, inadequate and choked drainage system adds to the severity of the problem. Efficient drainage and pumping are the only means to dispose of the rainwater of the town. The study presented in the paper simulates stormwater runoff through the drainage networks of Patna town using the hydrodynamic storm water management model (SWMM). The input to the model was extracted from different maps prepared in GIS environment. The digital elevation model (DEM) prepared for the study area was divided into 50 sub-catchments depending on the topography, existing drainage network and the land use pattern of Patna. Satellite data was used for land use classification of Patna. Annual daily maximum rainfall data from 1975 to 2007 were used for the analysis of design storm of Patna town. Extreme value (EVI) distribution was used to find the design storm for 2 to 100 years return periods. The simulation results were calibrated with the observed hydrograph at different outlets of the drains. After calibration, the model was simulated with the existing geometry of the drainage network without any blockage which yielded inadequacy of drainage system to dispose of the runoff even for 2-year return period storm and caused flooding and waterlogging. The dimension of the drains was modified mainly with respect to depth without disturbing the existing network and the model was simulated for return periods from 2 to 25 years as well as for the severe storm observed from 1975 to 2007 till no spilling of the drains were observed.

**Keywords** Runoff · SWMM · Catchments · Flooding and urbanization

---

B. Chakravorty (✉) · N. G. Pandey  
CFMS, NIH, WALMI Complex, Patna 801 505, Bihar, India

R. V. Ramana  
DRC, NIH, Siddrtha Nagar, Kakinada 533 003, AP, India

### 33.1 Introduction

In most urban cities the land surface is covered with impervious material. The natural rainfall-runoff process is altered in an urbanized area. In recent years the higher intensity of rainfall in a short duration is observed more likely due to climate change even reducing the number of rainy days in a year. On top of this, the land use changes, topographical modification and unplanned garbage disposal obstructing natural and man-made drainage system in an urban area add to the menace. If the water stagnates, there is a likelihood of spreading water-borne diseases, which may affect the health of the people. A typical urban land cover consists of impervious rooftops, streets, parking lots etc., allowing far less surface infiltration and retention.

Patna has been facing acute drainage problems due to its flat topography. According to historians and archeologists, once ancient Patna was washed away because of floods of rivers Ganga, Sone and Punpun accompanied by continuous rains for 17 days in the catchments. In the recent past also, Patna was heavily flooded in the year 1975–76 and there was severe waterlogging in the years 1990 and 1997 in the town. Small boats could be seen on the roads. Due to the topographical condition of Patna, storm water does not flow under gravity to river Ganga or Punpun during the period of floods. Pumping is the only means to dispose of the rainwater of the town. The rapid development of new unplanned colonies and their commercial activities without a proper drainage system has aggravated the problem of waterlogging. In order to overcome waterlogging, the storm water drainage system has to be properly designed. Hydrodynamic modeling is a way to understand the problems of urban flooding and to evaluate the performance of the drainage networks. Several mathematical models are in use to model the rainfall-runoff process and generation of floods. The study presented in the paper simulates storm water runoff through the drainage networks of Patna town using the hydrodynamic storm water management model (SWMM).

Modeling of urban flooding and drainage has been attempted by many researchers. Hellweger and Maidment (1999) developed an integrated application for delineating drainage basins and determining surface runoff in a natural watershed using the HEC-HMS (Hydrology Engineering Center–Hydrologic Modeling System). Finberg and Uhrick (1997) discussed integrating GIS database for water distribution and wastewater models in Broward County, Florida. Zellweger and Ferdi (1996) developed an ArcView (GIS) application using the Avenue scripting language to perform the calculation of an SCS-based model, TR-55. Bellal et al. (1996) studied the effect of various urban planning options on rainfall-runoff relationship in urbanized basins using a linked GIS and hydrological model. Barco et al. (2008) developed auto-calibration for the US EPA SWMM model by applying it to a large urban catchment in Southern California. An optimization procedure was incorporated to estimate runoff parameters using 10 storms for calibration and validation. The model after calibration and validation predicted the observed value with reasonable accuracy. Sensitivity analysis showed the impact of the model parameters. The results were most sensitive to imperviousness and impervious depression storage and least sensitive to Manning

roughness for surface flow. Yamaguchi et al. (2012) developed Tokyo storm runoff (TSR) model and tested it for urban runoff analysis using two historical events in small and large urban watersheds. The recent advances in GIS technology and new data availability have opened new possibilities in urban storm runoff modeling. Fletcher et al. (2013) brought out a state-of-the-art on understanding, management and modeling of urban hydrology. Karla and Malik (2014) have used storm-CAD software for evaluating existing storm water drainage networks in Chandigarh, India and found that the computed average runoff coefficient from the model is in good agreement with the rational method runoff coefficient, which was adopted for the study region.

### 33.2 Study Area

The study area is Patna town, capital of Bihar. It is situated on the right bank of river Ganga at latitude  $25^{\circ}37'$  and longitude  $85^{\circ}10'$  having a mean elevation of 50.0 m above the MSL. Patna is a linear city and extending about 30 km long from east to west and 5–7 km from north to south. The city is situated between the river Ganga in the north, river Punpun in the south and river Sone in the west (Fig. 33.1).

Patna has a relatively flat topography with elevation ranging from 47.23 to 51.92 m with a mean elevation of 49.68 m. Field visit was made to evaluate the present condition of the existing draining system. It was found that most of the storm drains were clogged with sand, grass and debris. This has restricted the conveyance system to drain off the runoff volume causing a flood. This study has been made to identify the potential flooding problems and quantify the runoff volumes.

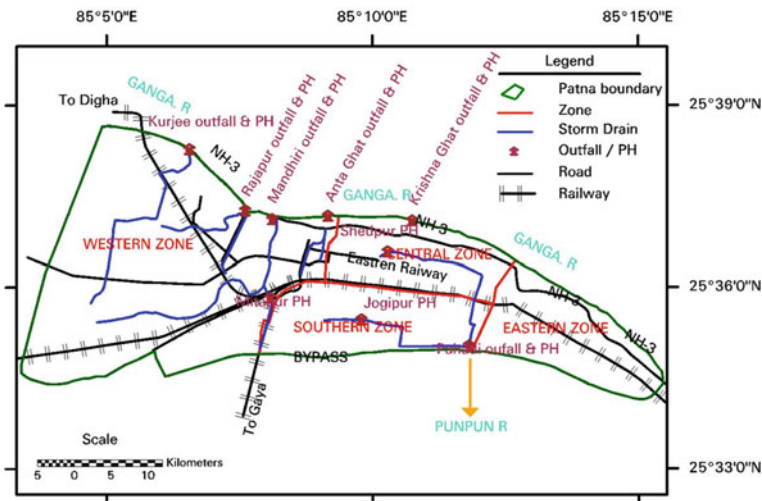


Fig. 33.1 Study area of Patna town

### 33.3 Methodology

Geographic information system (GIS) is a powerful tool to support the spatial database preparation of urban storm water management model. The physically based model SWMM offers input data formats that facilitate sharing and exchange of data with GIS packages. The procedure for GIS to SWMM modeling for urban storm water management involves (i) acquisition and development of base map data layers and coverage required for SWMM, (ii) preprocessing of model input data and parameters in GIS for the input of spatial information into the SWMM model, (iii) interfacing the GIS to the SWMM model, (iv) the SWMM model computation of water surface profile and hydrographs, (v) postprocessing of model output and (vi) analysis of hydrographs, including derivation of depths and extent of flooding in GIS environment.

The data on rainfall, topography, drainage network and remote sensing imagery are needed for the above analysis and to run the SWMM model.

To begin with, the study area was divided into 50 sub-catchments. The delineations were based on the topography of the study area converted to a digital elevation model (DEM), following the existing drainage system and present land use pattern (Figs. 33.2, 33.3 and 33.4). Secondly, infiltration losses were calculated by the inbuilt module in SWMM using the SCS curve number method. Soil conservation service (SCS) suggested an empirical model for rainfall abstractions based on the potential for the soil to absorb a certain amount of moisture. On the basis of field observations, this potential storage  $S$  (millimeters) was related to a ‘curve number’  $CN$  which characterizes the soil type, land use and the initial degree of saturation known as the antecedent moisture condition. The value of  $S$  is defined by the following empirical expression:

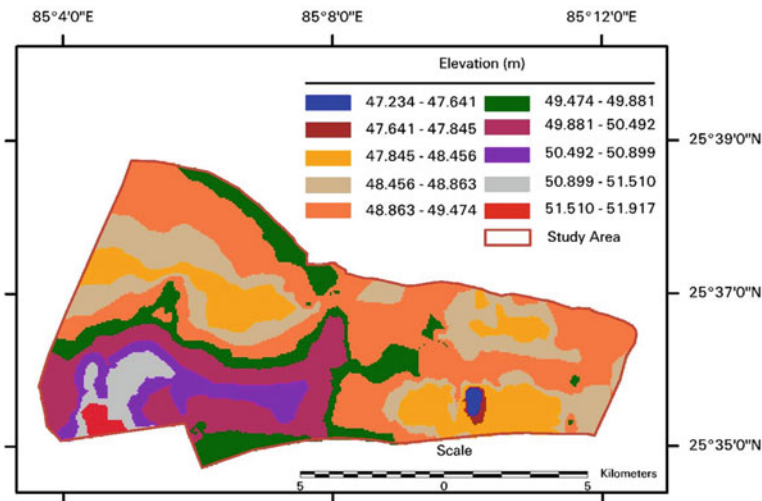


Fig. 33.2 DEM of the study area



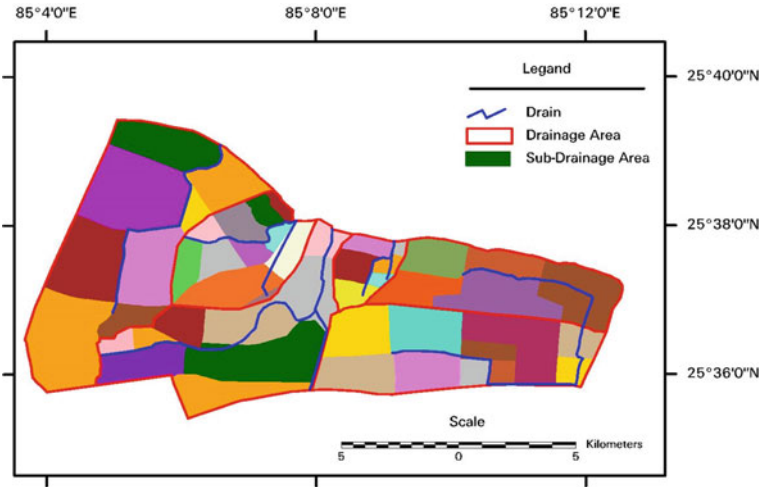


Fig. 33.3 Sub-catchments with drainage networks

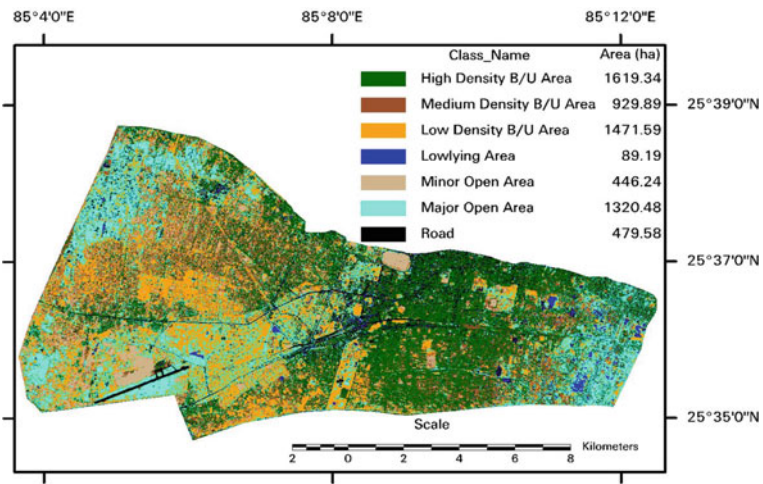


Fig. 33.4 Land use classification using IRS P6-L4MX data

$$S = \frac{25400}{CN} - 254 \tag{33.1}$$

The effective rainfall is computed by the equation:

$$Q(t) = \frac{(P(t) - I_a)^2}{(P(t) + S - I_a)} \tag{33.2}$$

where  $Q(t)$  = accumulated depth of effective rainfall in time  $t$ ,  $P(t)$  = accumulated depth of rainfall in time  $t$ ,  $I_a$  = initial abstraction,  $S$  = potential storage in the soil.

The original SCS method assumed the value of the initial abstraction  $I_a$  to be equal to 20% of the storage potential  $S$ .

$$I_a = 0.2S \quad (33.3)$$

$$Q(t) = \frac{(P(t) - 0.2S)^2}{P(t) + 0.8S} \quad (33.4)$$

Infiltration losses in SWMM have the option to compute it using three methods, viz., Horton's, Green-Ampt and SCS. In the present study, SCS (U.S. Department of Agriculture, Soil Conservation Services, 1994) method was chosen to compute infiltration losses. In the SCS model, the runoff curve number is assigned based on land use classes, soil type and treatment measures. Land use classification of IRS-P6 L4MX-PAN satellite scene of Patna was performed and was classified into seven classes (Fig. 33.4). Patna town has a flat topography. The soil type is mainly silty loam to clay. The average saturated hydraulic conductivity of the clay soils was taken as 0.254 mm/h.

### 33.4 Model Calibration

Calibration is the process of model simulation using a set of input data and comparing the model output with the field observation. The calibration procedure considers the peak flow rate of the event as well as the shape of the hydrograph. After the model is calibrated for a specific storm, it is validated by simulating additional storms and comparing computed output with observed data. The model was calibrated using rainfall data obtained from IMD Patna. Initial calibration showed that the model over-predicted the discharge. This was due to conservative estimates of imperviousness or contributing areas of the drainage basins. A detailed GIS analysis and field investigation was therefore undertaken to determine the effective impervious area. The field investigation produced a relatively accurate delineation of drainage boundaries.

The objective of the application of a catchment model is to determine the peak flow rate and the shape of the hydrograph. The performance of the model with the observed data was evaluated using relative error (RE) and root mean square error (RMSE) criteria.

Relative error (RE) for an arbitrary variable  $x$  is given by:

$$RE = \frac{x_o - x_s}{x_o} \quad (33.5)$$

where  $x_o$  is the observed value of a hydrograph characteristic and  $x_s$  is the simulated value of the same characteristic.

Root mean square error (RMSE) for discharge is given by:

$$RMSE = \sqrt{\frac{\sum_{i=1}^n [Q_o(i) - Q_s(i)]^2}{n}} \tag{33.6}$$

where  $Q_s(i)$  and  $Q_o(i)$  are the simulated and observed discharges, respectively, and,  $n$  is the number of observations in the time series.

After calibration, the model was run to simulate the peak flow. The measured and simulated values of peak flow have been compared in Table 33.1. It is found that relative errors at the four sites varies from -0.90 to -6.20. The negative value indicates that the simulated flow overestimates the observed peak flow. RMSE values indicate that the prediction errors are well balanced. Comparison has been made between the simulated and observed hydrographs (Figs. 33.5, 33.6, 33.7 and 33.8).

**Table 33.1** Calibration of the model results with volume and peak flow

S. No	Name of the outfall	Observed peak flow (m <sup>3</sup> /s)	Simulated peak flow (m <sup>3</sup> /s)	RE (%)	RMSE
1	Kurjee	4.99	5.3	-6.20	0.96
2	Rajpur	17.36	18.04	-3.90	0.94
3	Mandiri	1.11	1.12	-0.90	0.97
4	Phadi	18.65	19.13	-2.40	0.96

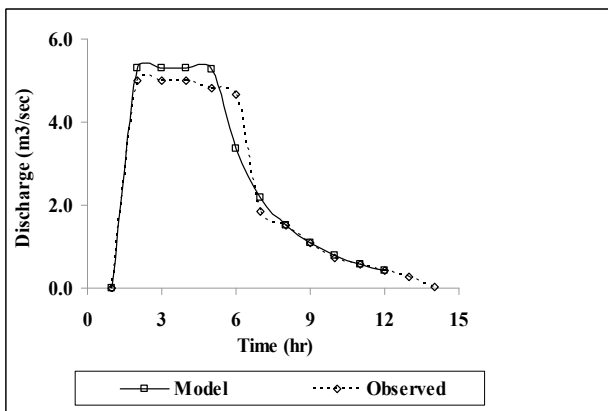


**Fig. 33.5** Calibration for Kurjee outfall hydrograph

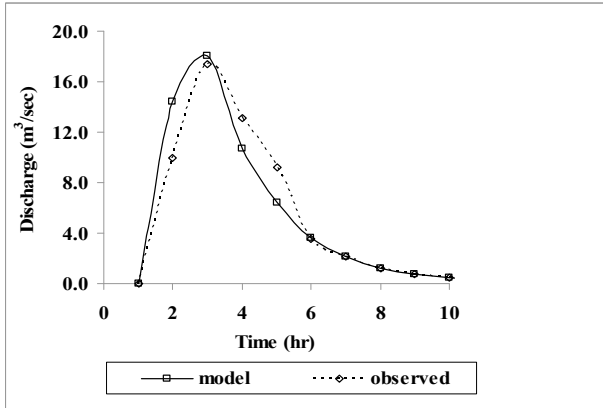


Fig. 33.6 Calibration for Rajapur outfall hydrograph

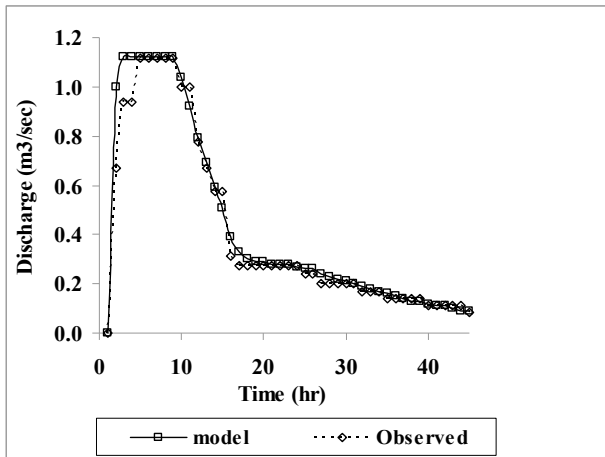


Fig. 33.7 Calibration for Mandiri outfall hydrograph

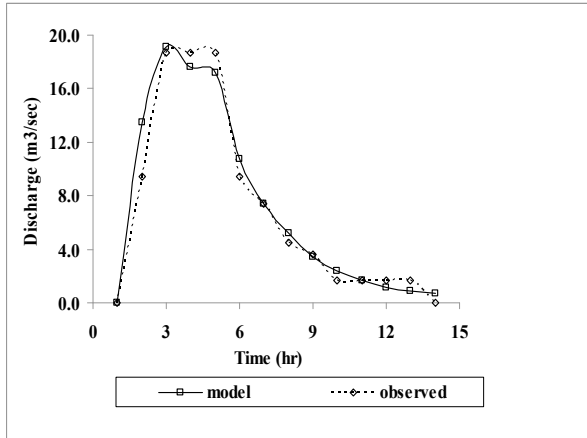


Fig. 33.8 Calibration for Pahadi outfall hydrograph

### 33.5 Design Storm Analysis

The annual daily maximum rainfall data for the past 32 years (1975–2007) was obtained from IMD, Patna. SRRG charts of the most severe storms were also collected and analyzed. Gumble extreme value (EV1) distribution was used to find out the maximum rainfall depth at different return periods (Table 33.2).

Table 33.2 Maximum daily rainfall depth with return periods

Return period	Maximum daily rainfall (mm)	Return period	Maximum daily rainfall (mm)
2	116.78	25	141.46
5	126.66	50	147.59
10	133.20	100	153.68
15	136.89		

**Distribution of Rainfall:** The intensity of rainfall usually varies over the duration. Accurate representation of this temporal variation is important since runoff rates calculated from rainfall-runoff models are usually sensitive to it. The U.S. Department of Agriculture, Soil Conservation Service (SCS, 1986) developed synthetic storm hyetographs. The cumulative hyetographs for 24 h rainfall distributions are shown in Fig. 33.9. Type II curve is selected for distribution to developing the hyetographs for various design storms and observed maximum peak more than the 50 years return period SCS distribution hyetograph. Maximum and minimum peaks observed rainfall intensity of 64.05 mm/h and 20.00 mm/h, as shown in Fig. 33.10.

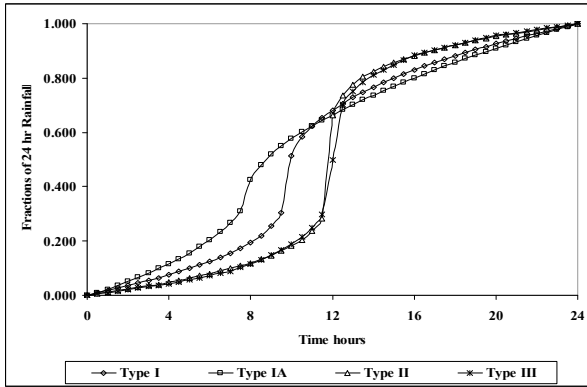


Fig. 33.9 SCS 24 h distributions hyetographs for various curves

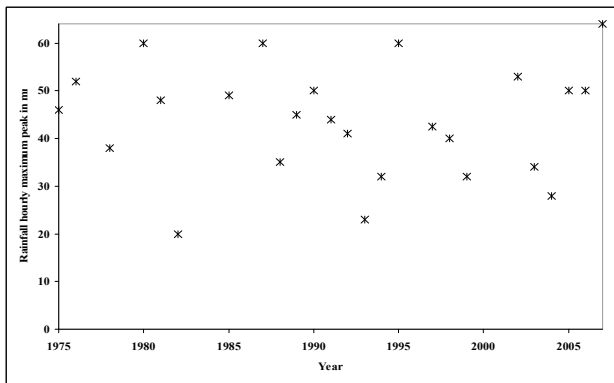


Fig. 33.10 Observed maximum peak hourly rainfall intensity (some missing data)

### 33.6 Routing Design Storm Through Existing Network

A dynamic wave routing procedure was adopted for flow routing. The existing drainage system mostly consists of the brick lining. The roughness coefficient of the drainage system has been considered as 0.012 (SWMM user manual). Runoff generated from each sub-drainage area is passed through a single outlet which is connected to drainage node or junction, again it connects to the main drain and finally conveys the whole discharge to the outfall. Model simulation results of hydrographs of 2-year return period at various outfalls are shown in Fig. 33.11.

In SWMM, flooding will occur whenever the water surface at a node exceeds the maximum defined depth of the drains. Normally such water will be lost from the system. Water elevation profile of drains (Figs. 33.12a–e) reveals that the drains are inadequate to carry flow to the outfalls. This flow spills out along the drains and accumulates in the low-lying areas, causing flood inundation (Table 33.3). From the

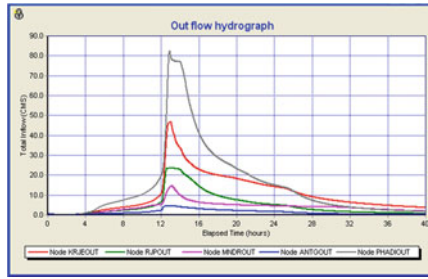
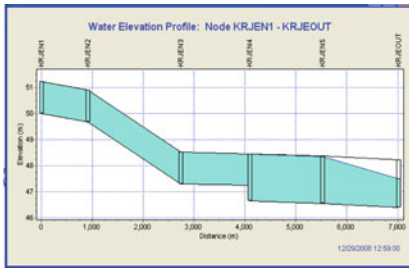
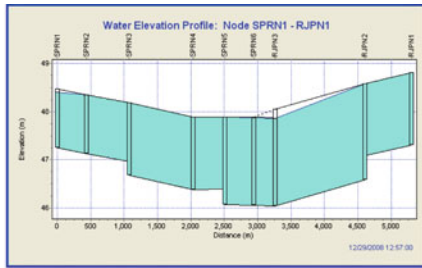


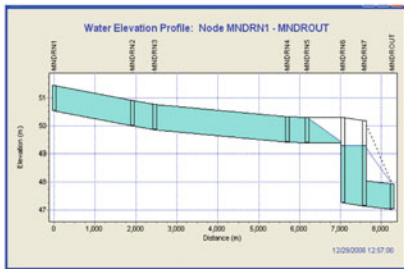
Fig. 33.11 Outfall hydrographs of 2-year return period hyetograph at various outlets



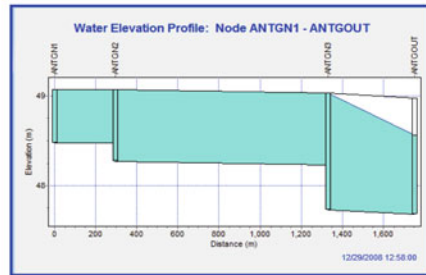
(a)



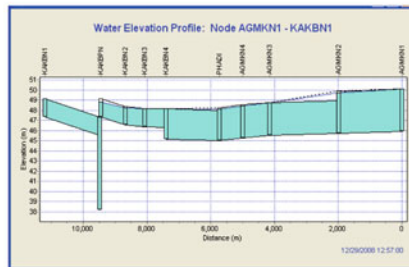
(b)



(c)



(d)



(e)

Fig. 33.12 a Water elevation profile of the Kurjee drain. b Water elevation profile of the SK puri and Boring canal drain. c Water elevation profile of the Mandiri drain. d Water elevation profile of the Antaghat drain. e Water elevation profile of the Kankarbagh and Agumkhan drain

**Table 33.3** Surface flooding of the study area for various return periods

Return period	Rainfall (mm)	Surface flooding (ha-m)	Return period	Rainfall (mm)	Surface flooding (ha-m)
2 years	116.78	126.818	25 years	141.46	194.980
5 years	126.66	152.616	50 years	147.88	213.750
10 years	133.20	170.836	100 years	153.68	233.067
15 years	136.89	181.408			

analysis it is found that the existing drainage system is inadequate even to drain off runoff generated from 2-year return period rainfall. The inundation area with a return period was identified.

Surface flooding maps demarcating the area under inundation have been prepared. The volume of floodwater has also been computed to estimate the depth of ponding using the following formula:

$$V_{j+1} = V_i + \left( \frac{A_j + A_{j+1}}{2} \right) (h_{j+1} - h_j) \tag{33.7}$$

where  $V$  is the volume,  $A$  is the surface area and  $h$  is the associated water elevation in the catchment. DEM of the study area was used with the volume of floodwater to generate surface flooding maps with different return periods for various design storms (Fig. 33.13).

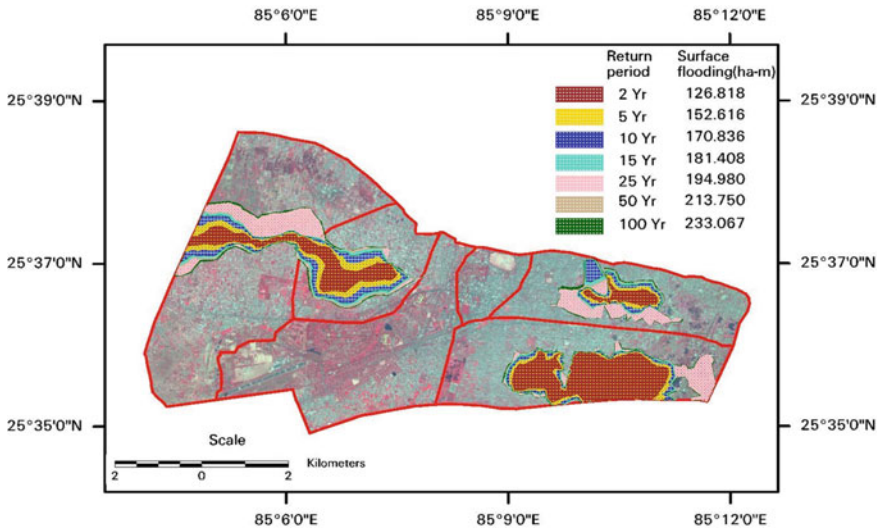


**Fig. 33.13** Surface flooding for various design storm of the design drainage network of the Patna town



### 33.7 Routing Design Storm Through Modified Network

The flow in drains is assumed free-surface flow-through channel having constant cross-sections at different reaches. Manning’s formula was used for the design of the channel assuming uniform flow (friction slope parallel to the bed slope) to accommodate peak flow. The resistance is assumed to be represented by the Manning equation to express the relationship between flow rate ( $Q$ ), cross-sectional area ( $A$ ), hydraulics radius ( $R$ ) and slope ( $S$ ) in open channel:

$$Q = \frac{1}{n} AR^{2/3} \sqrt{S} \tag{33.8}$$

where  $n$  is the Manning roughness coefficient. For steady flow and kinematic wave routing,  $S$  is the conduit slope. For dynamic wave flow routing, it is friction slope  $S_f$ . The existing drainage system was made several decades back. After subsequent developments in the study area, there is no scope at present for widening the channel in most of the locations. The only way out to accommodate peak flow is by changing the geometry of the drainage system without changing the bed slope and roughness coefficient of the channel. For the design of the drainage system for 25 years return period hyetograph, the geometry of the channel was modified and the model was simulated. It may be seen that the modified design as proposed is adequate to convey the storm runoff to the outfalls without any spilling and flooding which is apparent from the system inflow and outflow hydrographs (Fig. 33.14). The outfall hydrograph and water surface elevation profile along the drains show no flooding without spilling

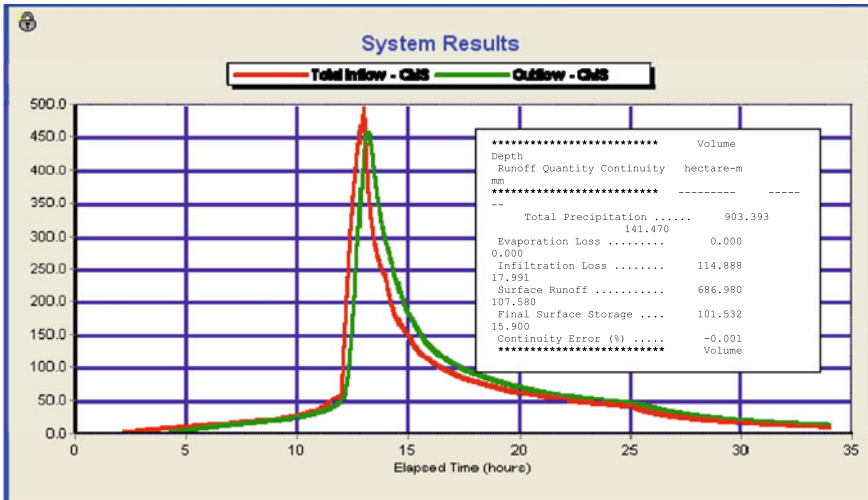
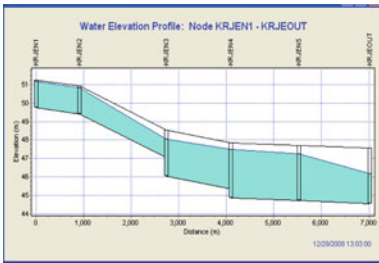
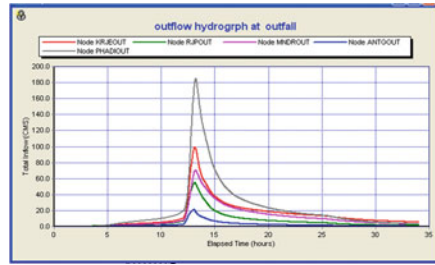
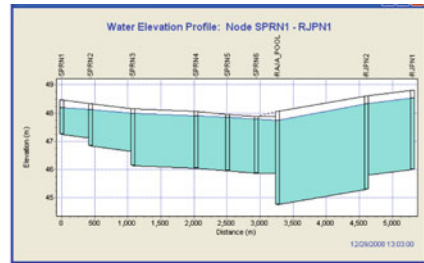


Fig. 33.14 System inflow and outflow hydrograph of the design storm 25-year return period hyetograph and Agamkhan drain

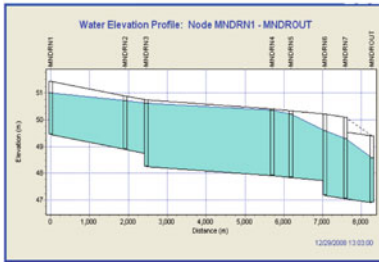
**Fig. 33.15** Outfall hydrograph at the various outfall of the drainage system



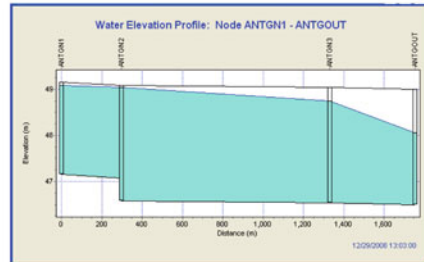
(a)



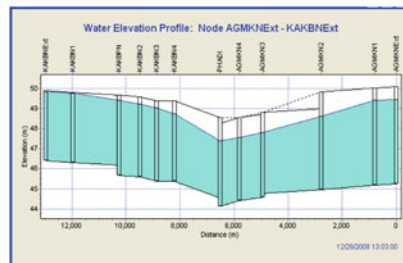
(b)



(c)



(d)



(e)

**Fig. 33.16** a Water elevation profile of the modified Kurjee drain. b Water elevation profile of the modified SK Puri and Boring canal drain. c Water elevation profile of the modified Mandri drain. d Water elevation profile of the modified Antaghat drain. e Water elevation profile of the modified Kankarbagh and Agamkhan drain

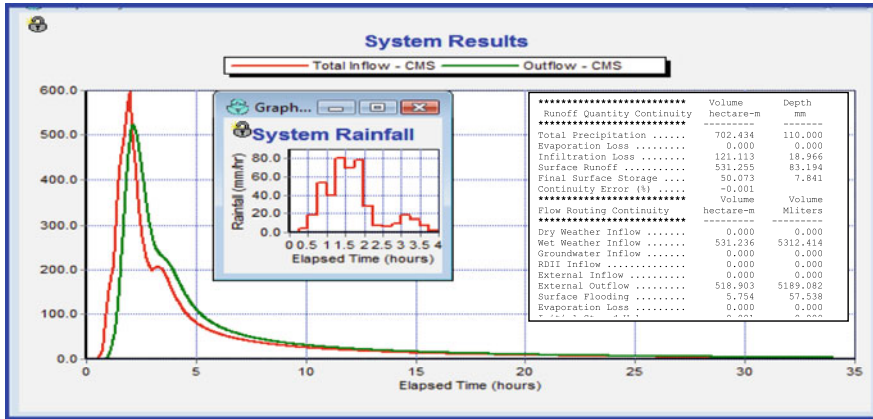


Fig. 33.17 System inflow and outflow hydrograph of the modified drainage system with observed hyetograph on 13 August 2007

at nodes of the drainage system (Figs. 33.15 and 33.16a–e). The modified designed system was verified with the observed rainfall (15 min interval) of 63 mm/h, i.e., the maximum hourly peak on 13 August 2007. This rainfall intensity was even greater than the 25 years return period hyetograph peak value. The system result shows flooding has occurred only to an extent of 5.754 ha-m (Fig. 33.17).

### 33.8 Conclusion

The SWMM model was run considering the originally designed dimensions of the drainage networks without any blockage which indicated inadequacy to dispose of the runoff. The condition of the existing drainage networks of Patna town is not even able to dispose of the rainfall depth of the 2-year return period. As a result, Patna is facing flooding and waterlogging every year. Micro-level drainage system is very poor and at many locations there is no connectivity to the macro-level drainage system. Maintenance of the conveyance system is also very poor and people are less concerned about the health of the system. The drains are choked due to dumping of garbage and polythene bags, wastages of vegetable etc. directly into the drains. Thus people need to be awakened and attention should be given to the renovation of the existing drains. The study shows that for existing drains the X-sectional area needs to be increased by 1.12–5.84 times, viz., for Kurjee—1.76, Antaghat—3.61, Mandiri—5.84, Mthapur—4.44, Boring Canal Road—2.27 and SK Puri—1.12 times to accommodate 25-year storm without spilling. Additionally, two new drains each of 1 km length were introduced in Agamkuan area (trapezoidal with a top width of 7.70 m and depth 4.8 m) and Kankarbagh area (rectangular with a top width of 8.0 m and depth 3.5 m). The analysis of the existing design drainage network and the modification made in the geometry is useful for the decision-makers to identify

critical locations and priority areas. Further, the results can also be used for the design of sumps and computing pump capacity.

## References

- Bellal M, Sillen X, Zeck Y (1996) Coupling GIS with a distributed hydrological model for studying the effect of various urban planning options on rainfall-runoff relationship in urbanized watersheds. In: Kovar K, Nachtnebel HP (eds) *Hydro GIS 96: application of GIS in hydrology and water resources management (Proceedings of the Vienna Conference)*, 99–106. International Association of Hydrological Sciences, Vienna
- Barco J, Wong KM, Stenstrom MK (2008) Automatic Calibration of the U.S. EPA SWMM model for a large urban catchment. *J Hydraulic Eng* 134(4):466–474
- Feinberg D, Uhrick SW (1997) Integrating GIS with water and wastewater hydraulic models. In: *Proceeding 1997 ESRI user conference* <http://www.esri.com/library/userconf/proc997/PROC97/TO200/PAP199/P199.htm>
- Fletcher TD, Andrieu H, Hamel P (2013) Understanding, management and modelling of urban hydrology and its consequences for receiving waters: a state of the art. *Adv Water Resour* 51:261–279
- Hellweger, Ferdi (1996) *TABHYD–TR55 tabular hydrograph method in arc view*. U.S. Department of Agriculture, Soil Conservation Service, Engineering Division
- Karla AM, Malik U (2014) Assessment of current storm water infrastructure system in lieu of flood points of interest within Union Territory, Chandigarh. In: *Published in proceedings of international symposium on integrated water management (IWRM-14) held at CWRDM, Kozhikode, Kerala, India, Volume I*, pp. 188–194
- Soil Conservation Service (SCS) (1986) *Urban hydrology for small watersheds*. U.S. department of Agriculture, Technical Release 55, Washington, DC
- Yamaguchi H, Kawamura A, Olsson J, Takasaki T (2012) Development and testing of a distributed urban storm runoff event model with a vector-based catchment delineation. *J Hydrol* 420–421:205–215
- Zellweger F, Maidment D (1999) Definition and connection of hydrologic element using geograph data. *J Hydrol Eng ASCE* 4(1):10–18

# Chapter 34

## Loss Coefficient of Expansion in Diverging Channel



M. Sahu, S. T. Biswal, and B. Naik

**Abstract** In this present work, a hydraulic study was done on the expansion section of the Kaskaskia river, Illinois (USA) (Nani G. Bhowmik). The set of flow variables was collected from the Kaskaskia river, on Reach-1. Investigation on loss coefficient was done on the two expansion sections of Kaskaskia river (1-2 and 13-15) with the diverging angle of  $0.50^\circ$  and  $0.17^\circ$ , respectively. This study was done to understand the effects of the flood on non-prismatic diverging channels. The ANSYS-FLUENT software was used for four different turbulence models, like  $k-\epsilon$ ,  $k-\omega$ , *LES* (large eddy simulation) and *RANS* (Reynolds-averaged Navier–Stokes equation) on the expansion section of Kaskaskia river. Among all the models, *LES* gave the best result. The predicted velocity was found nearly equal to the observed velocity.

**Keywords** Expansion channel · Kaskaskia river turbulence model · Non-prismatic channel · ANSYS-FLUENT ·  $k-\epsilon$  ·  $k-\omega$  · *LES* and *RANS*

### Nomenclature

$Fr$	Froude number
$Re$	Reynolds number
$Xr$	Relative distance
$B/h$	Aspect ratio
$\theta$	Expansion angle

### 34.1 Introduction

The river is the pillar of all progress inhabitants in ancient times. All the major progress and growth of cities happen at the banks of the rivers. The river is a necessary

---

M. Sahu (✉) · S. T. Biswal · B. Naik  
Department of Civil Engineering, CAPGS (BPUT), Rourkela, India

part of human beings in the past and continued in the present because it provides fertile land and sufficient water production. The river system can be divided into seasonal and year-continued flowing water. The importance was to understand the flow attributes of rivers in both the flow and overflow conditions. Flow separation in open channel expansion has been identified as one of the major problems in hydraulics structures. The open channel in which shape, size of cross-section and slope of the bed remains constant along the length of the channel is said to be a prismatic channel, and if the shape, size of the cross-section and slope remains varied along the length of the channel it is said to be non-prismatic channels. Khatua and Patra (2008) developed a new model for boundary shear stress and stage-discharge for a compound channel having a width rate of 3.67. Natural channels are examples of non-prismatic channels, and man-made open channels are examples of prismatic channels. Again non-prismatic channel was subdivided into three types: converging, diverging and skewed. Most of the research work has been worked on the prismatic channel, while most actual fact is that it does not work in the real field as it only affects the non-prismatic channels or the natural rivers. Shalmeldin et al. used ANSYS software in fluid fluent to reinvent the physical mechanism within the open channel flows and they used three different models such as  $k-\epsilon$ , *LES* and *RANS* and also compared each among them for better results. Gandhi et al. (2010) found out the velocity distribution in the tangential and lateral direction by acoustic Doppler current for finding out the flow condition and their significance. ANSYS (FLUENT) was used for the analysis of the model and its best outcomes. The important effects on the bed slope, turning point at the upstream level in the expansion and contraction of the channel, its width ratio and velocity profile have been studied at different sections. This analysis was done to know the effect of flood on the non-prismatic expansion channels. Here the aim is to find out the efficiency of *LES* (large eddy simulation), *RANS* (Reynolds-averaged Navier–Stoke equation),  $k-\epsilon$  (k-epsilon) and  $k-\omega$  (k-omega) turbulence models to determine the flow conditions in the expansion channel of Kaskaskia river, Illinois (USA) with the application of ANSYS (FLUENT).

## 34.2 Study Area

The dataset collected from the Kaskaskia river, Illinois (USA) is shown in Fig. 34.1. It consists of two reaches, namely Reach-1 and Reach-2. The total drainage area is 5801 square miles. The drainage area at Reach-1 is 1330 square miles. We have worked on the Reach-1 river using its datasets. We found four diverging sections, namely (1-2 and 13-15) and angles ( $0.50^\circ$  and  $0.17^\circ$ ), respectively. After getting these data these were analyzed using ANSYS (FLUENT) and we get the velocity contours at the inlet and outlet of the section. For the validation of the contours, actual contours were needed for which we used the software named SURFER for creating the actual contours which have been founded in the above-named river. We have also used the four turbulence models such as *LES* (large eddy simulation), *RANS*

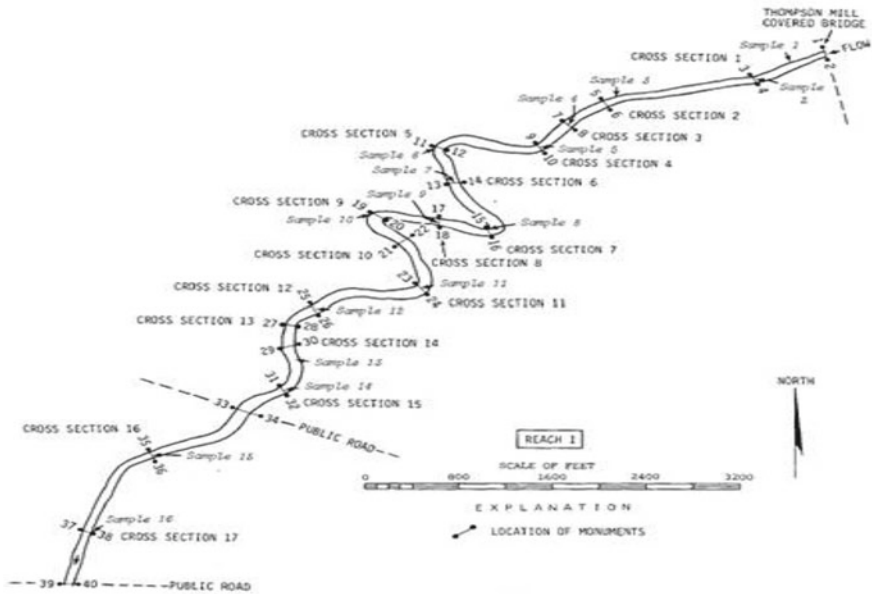


Fig. 34.1 Kaskaskia river, Illinois (USA), Reach-I (Nani G. Bhowmik)

(Reynolds-averaged Navier–Stokes equation),  $k-\omega$ ,  $k-\epsilon$  and finding which was better turbulence model among them.

### 34.3 Numerical Modelling

Various CFD packages (Fluent, CFX and Star-CD, amongst others) were used for research in water flows. In the recent past, a good number of researchers have used these software packages for the prediction of different aspects of 3D flow fields, e.g., Sahu et al. (2011). In this paper, an attempt has been made to apply to diverging channel a 3D numerical code. FLUENT has been used to test its suitability for the simulation of flood flows. The models tested here were  $k-\epsilon$ , LES,  $k-\omega$  and RANS, used for all simulation works.

#### 34.3.1 Geometry

The first step in the CFD study was the simplification and modelling of computational geometry of the fluent flow area. A constant structure of citation for the coordinate axis was adopted in the creation of geometry. In the coordinate axis, X-axis has

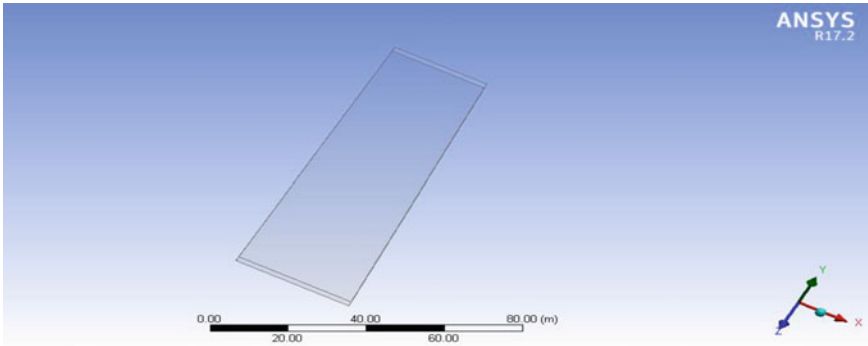


**Fig. 34.2** The geometry of the diverging channel

equivalence to the lateral direction which signifies the width of the channel bed. Y-axis combines the streamlet direction of fluid flow and the Z-axis symbolizes the vertical components or combines with the depth of water in the channel. The origin was placed at the upstream borderline and concurs with the base of the middle line of the channel. The water flows along the positive direction of the Y-axis. The simulation and modelling were done on the non-prismatic channel with the diverging channel. The geometry of diverging channel is shown in Fig. 34.2.

After geometry was done, the six faces were selected:

- Inlet
- Outlet
- Surface geometry
- Channel bottom
- Side walls

### 34.3.2 Mesh Generation

The second and most essential step in numerical analysis was setting up the individual grid corresponding to the geometry. Construction of the mesh involves discontinuous or subdividing the geometry into the section or parts at which the variables have been calculated numerically. The most fundamental form of mesh categorization is based upon the correspondence of the mesh, i.e., structured and unstructured. When each part was organized in rows and columns it is viewed as structured mesh. In this research, the flow section was separated using an unstructured grid and each coordinate. The meshing of the flow field was shown in Fig. 34.3. For temporary problems, a suitable time step needs to be accurate.



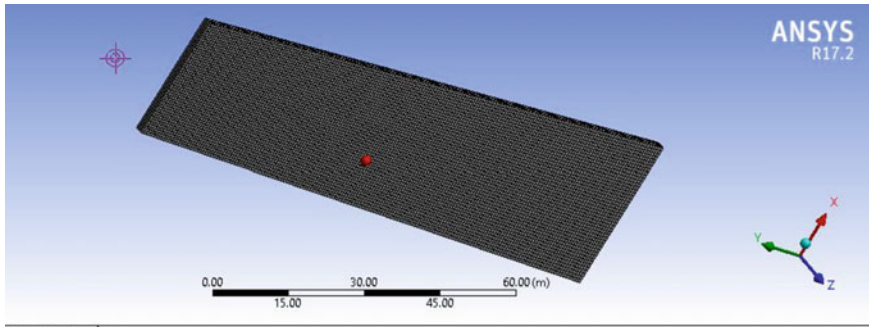


**Fig. 34.3** Mesh generation of simple diverging channel

### 34.3.3 Solver Setting

#### 34.3.3.1 Setup

After the meshing part was finished, various data were given in the Setup section. VOF (volume of fluid) model was the only design prepared for open-channel flow simulation because this numerical analysis method is concerned with the free surface flow. To attain a free surface zero friction, an instructor called “surface symmetry” was given at the named selection in the computation. Velocity for inlet and pressure for outlet are determined and the roughness coefficient was adjoining to the walls for “no slip” parameters. The temporary flow was chosen as the flow parameters were manifold in time in the experiment. Gravity was marked and the value for Z-axis was given as  $-9.81 \text{ m/s}^2$  because gravity acts downward opposing the z-direction vector. As mentioned earlier, the turbulence model was chosen such as  $k-\omega$ ,  $k-\varepsilon$ , *RANS* (Reynolds-averaged Navier–Stokes equation) and *LES* (large eddy simulation) models, which were used in our analysis. PISO was selected for solving the pressure equation as it was a pressure-based algorithm used for short-lived flow conditions. It also allows a large timestep for precise calculation. The calculation was done from the inlet after the initial values of pressure and velocity were given and the y-velocity value was given as water depth of the channel, then it is patch and close. Then it’s time for the calculation part in which the time step size was set to 0.001 s and the number of iteration given was 1000 for better accuracy and best results. After the calculation part is over then we go to the result part where the velocity contours were found at each section of the channels.

#### 34.3.3.2 Governing Equation

ANSYS-FLUENT uses the finite volume method to solve the governing equations for a fluid. Several models were studied to compare the effect of turbulent modelling

in the diverging channel, including the following: (1)  $k-\varepsilon$ , (2)  $k-\omega$ , (3) large eddy simulation ( $LES$ ) model and (4)  $RANS$ .

(i)  $k-\omega$  and  $k-\varepsilon$

$k-\omega$  model is used for turbulence modelling. The  $k-\omega$  model solves the  $k$ -transport equation and a transport equation for  $\omega$ . The  $k$ -transport equation and the transport equation for  $\omega$  can be written (Wilcox 1988) as:

$$\frac{\partial k}{\partial t} + U_i \frac{\partial k}{\partial x_i} = \frac{\partial}{\partial x_i} \left( \frac{v_t}{\sigma_k} \frac{\partial k}{\partial x_i} \right) + P - \beta' k \omega \tag{34.1}$$

$$\frac{\partial \omega}{\partial t} + U_i \frac{\partial \omega}{\partial x_i} = \frac{\partial}{\partial x_i} \left( \frac{v_t}{\sigma_\omega} \frac{\partial \omega}{\partial x_i} \right) + \alpha \frac{\omega}{k} P - \beta \omega^2 \tag{34.2}$$

And the eddy viscosity is given by:

$$v_t = k/\omega \tag{34.3}$$

where  $k$  is the turbulence energy,  $\omega$  is the turbulence dissipation rate and  $p$  is the turbulence kinetic energy production term. The turbulence equation was suggested by Menter (1994) as:

$$P = \min(P, 10\beta'k\omega) \tag{34.4}$$

(ii) Large eddy simulation ( $LES$ )

Large eddy simulation ( $LES$ ) attempts to partially resolve turbulence. The governing equation was:

$$\frac{\partial k}{\partial t} + U_i \frac{\partial k}{\partial x_i} = - \frac{\partial}{\partial x_i} \left[ \overline{u'_i \left( \frac{u_j u'_j}{2} + \frac{p}{P} \right)} \right] - \overline{u_i u_j} \frac{\partial u_i}{\partial x_j} - \overline{v \frac{\partial u'_i}{\partial x_j} \frac{\partial u'_i}{\partial x_j}} \tag{34.5}$$

(iii)  $RANS$  (Reynolds-Averaged Navier–Stokes Equation)

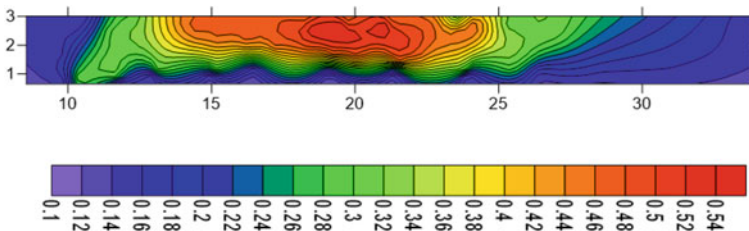
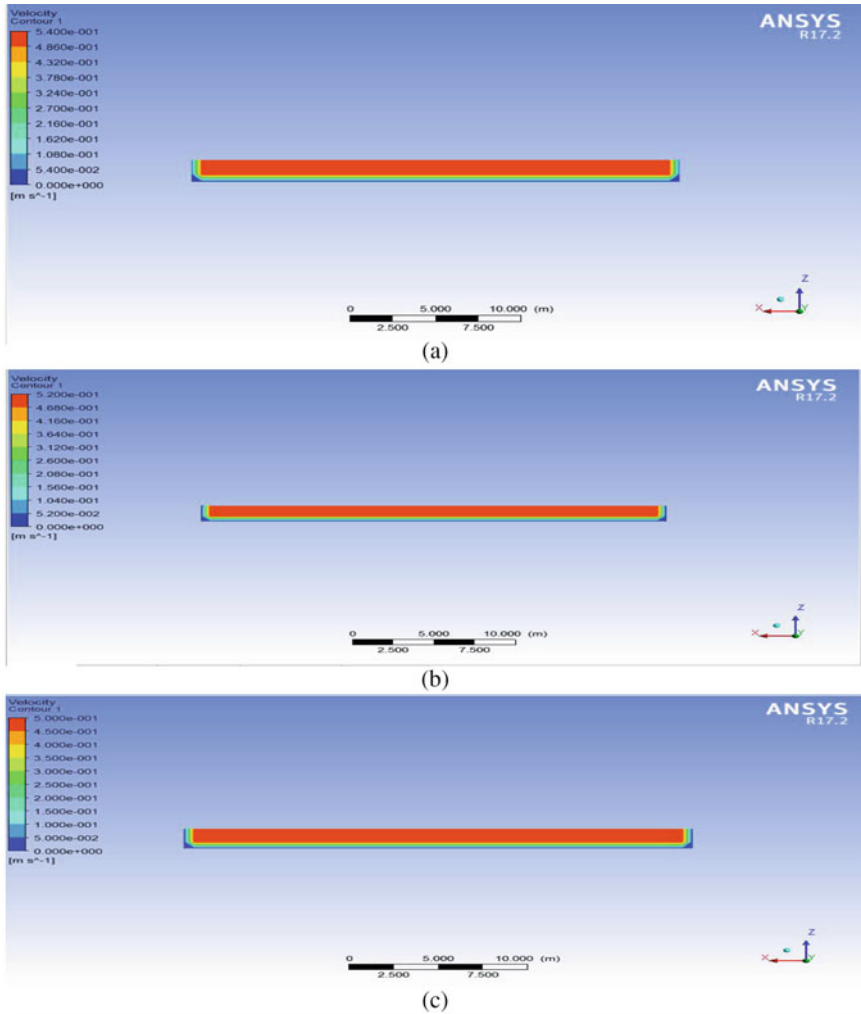


Fig. 34.4 Showing the velocity contour section

The Reynolds stress models (RSM) were more complicated than the eddy viscosity model. They provide a more accurate representation of the turbulence and are valid over a wide range of flows. The governing equation was:

$$\frac{D\overline{u'_i u'_j}}{Dt} + \frac{\partial}{\partial x_k} T_{kij} = P_{ij} + R_{ij} - \epsilon_{ij} \tag{34.6}$$



**Fig. 34.5** a The velocity contour for section-1 *LES* model for diverging angle 0.50°. b The velocity contour for section-1 *RANS* model for diverging angle 0.50°. c The velocity contour for section-1 *k-ε* model for diverging angle 0.50°. d The velocity contour for section-1 *k-ω* model for diverging angle 0.50°

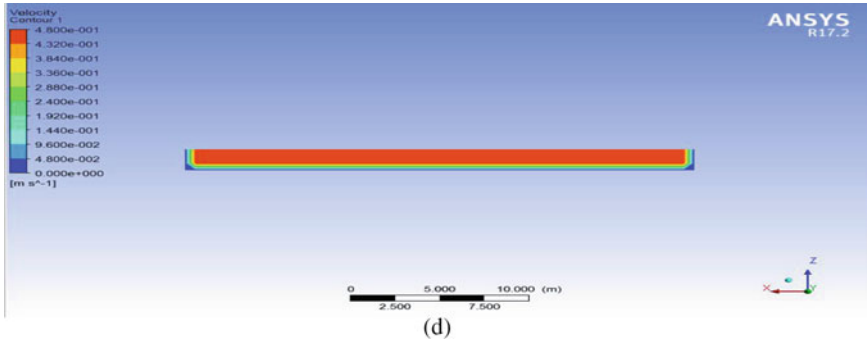


Fig. 34.5 (continued)

### 34.4 Result

#### 34.4.1 Comparison of Actual Velocity Contours and ANSYS Velocity Contours

The non-prismatic diverging sections were collected from Kaskaskia river Reach-1. After the final selection was made, the approximate location of the different sections such as sec-1, sec-2, sec-13, sec-15 was considered for diverging channel and the velocity contours of each cross-section are plotted using software called SURFER (15.0). Four turbulence models were taken such as  $k-\epsilon$ ,  $k-\omega$ , RANS, LES. Fig. 34.4 shows the actual velocity contour for section-1 and Fig. 34.5a–d) shows the ANSYS velocity contour for section-1. Fig. 34.6 shows the actual velocity contour for section-2 and Fig. 34.7a–d shows the ANSYS velocity contour for section-2 using four turbulence models. Fig. 34.8 shows the actual velocity contour for section-13 and Fig. 34.9a–d shows the ANSYS velocity contour for section-13 using four turbulence models and similar for other sections showing in Figs. 34.10 and 34.11a–d. Fig. 34.4(left) shows the velocity contour section-1.

From the above figures, it was concluded that the velocity decreased in the diverging sections and increased with the increase of flow. LES was found to be the best model among  $k-\epsilon$ ,  $k-\omega$  and RANS.

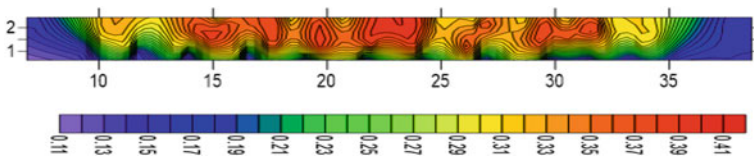
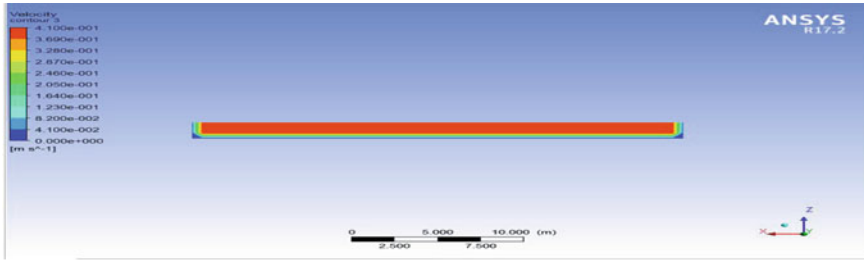
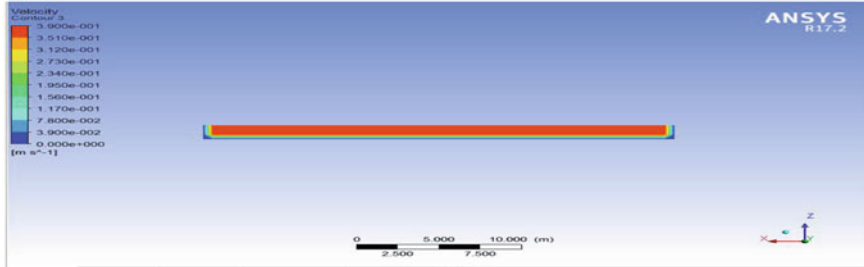


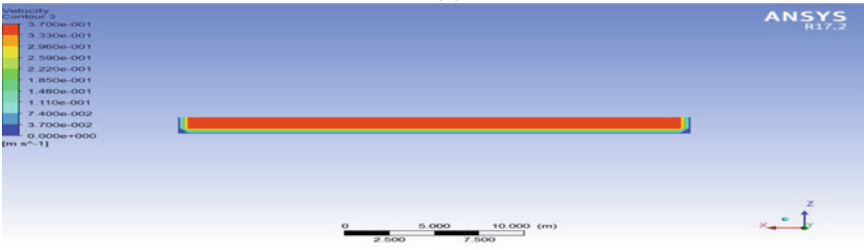
Fig. 34.6 The velocity contour of section-2



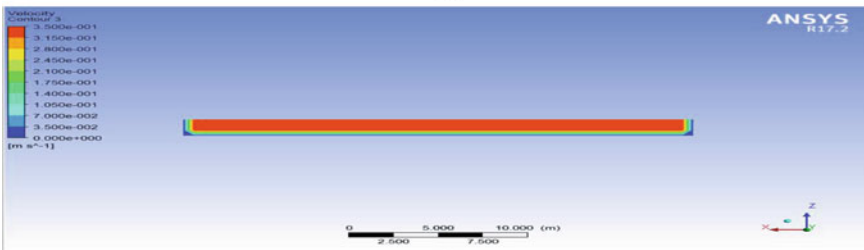
(a)



(b)



(c)



(d)

**Fig. 34.7** a The velocity contour for section-2 *LES* model for diverging angle  $0.50^\circ$ . b The velocity contour for section-2 *RANS* model for diverging angle  $0.50^\circ$ . c The velocity contour for section-2  $k-\epsilon$  model for diverging angle  $0.50^\circ$ . d The velocity contour for section-2  $k-\omega$  model for diverging angle  $0.50^\circ$

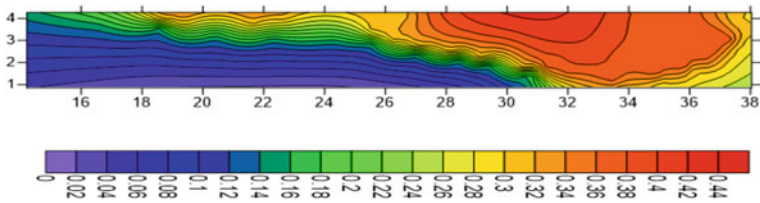
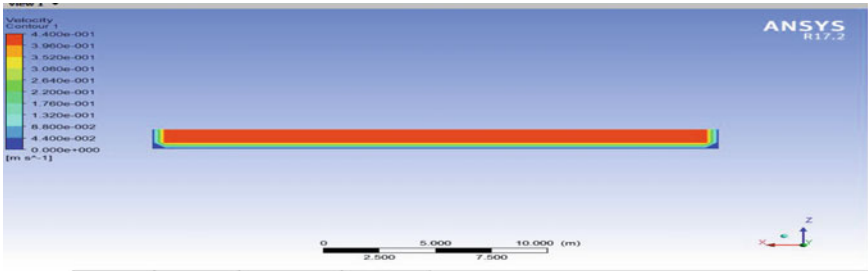
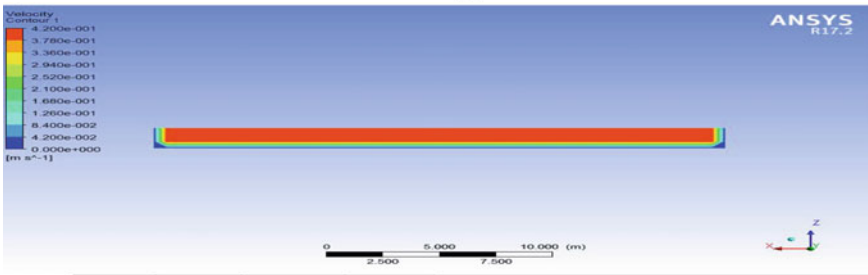


Fig. 34.8 Velocity contour of section-13



(a)

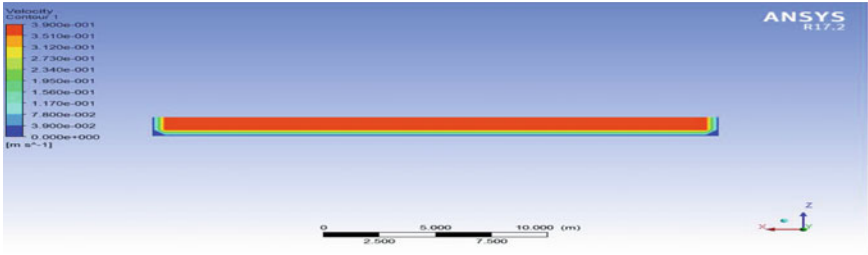


(b)

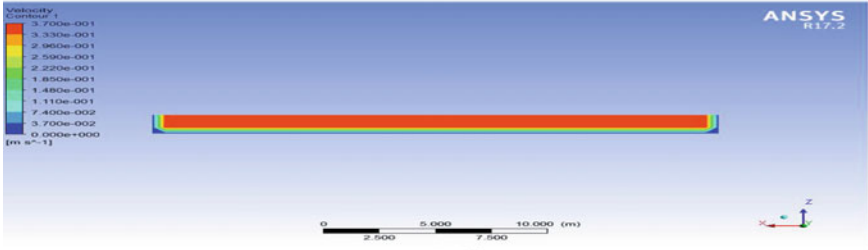
Fig. 34.9 a The velocity contour for section-13 *LES* model for diverging angle  $0.17^\circ$ . b the velocity contour for section-13 *RANS* model for diverging angle  $0.17^\circ$ . c the velocity contour for section-13 *k- $\epsilon$*  model for diverging angle  $0.17^\circ$ . d the velocity contour for section-13 *k- $\omega$*  model for diverging angle  $0.17^\circ$

### 34.5 Conclusions

The analysis was performed in Kaskaskia river, Illinois (USA) to find out the expansion section of reach-1 from it. Two expansion sections of (1-2 and 13-15) with the expansion angle of  $0.50^\circ$  and  $0.17^\circ$ , respectively, were found. The real contours were drawn from software called SURFER and validate these contours with the ANSYS contour. It was concluded that the velocity decreased in the diverging sections and increased with the increase of flow. The study of observed velocity and predicted velocity was done using ANSYS FLUENT. *LES* was found to be the best model



(c)



(d)

Fig. 34.9 (continued)

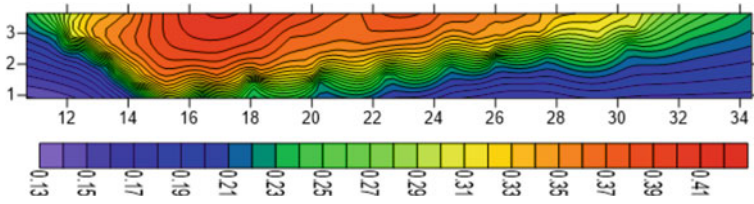
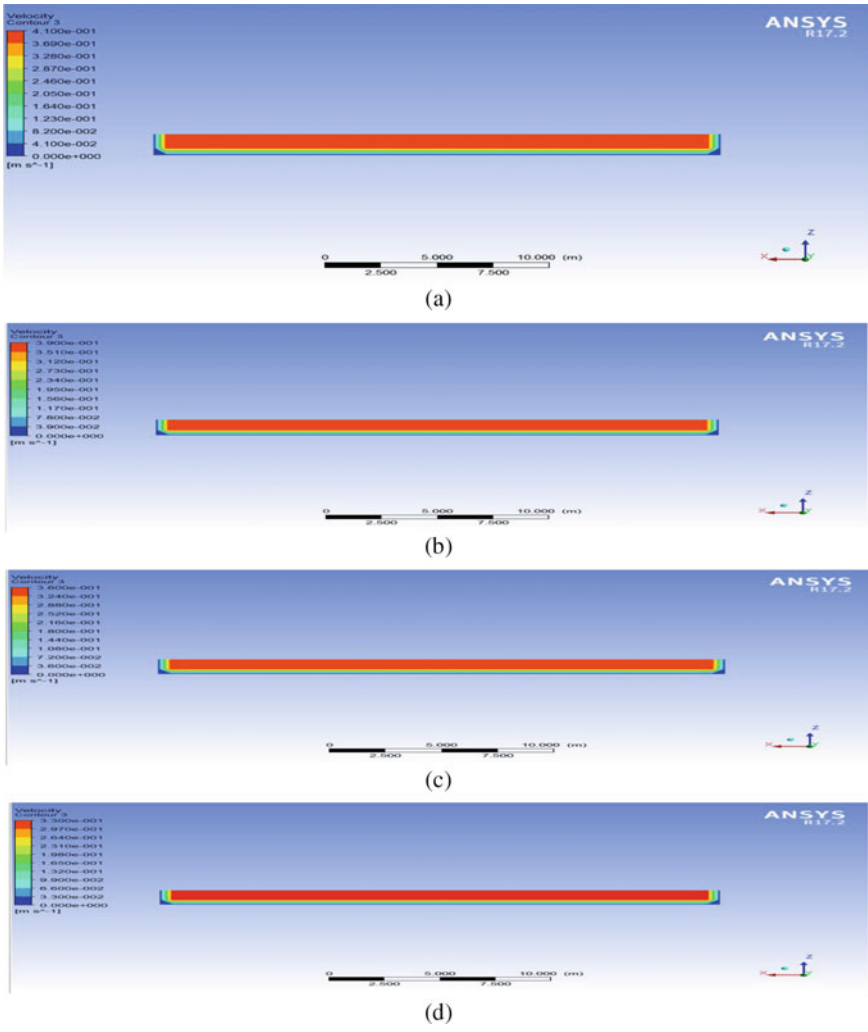


Fig. 34.10 Velocity contour of section-15

among  $k-\epsilon$ ,  $k-\omega$  and  $RANS$  for predicting velocity in the diverging channel because it is giving more accurate results than other models.



**Fig. 34.11** a The velocity contour for section-15 *LES* model for diverging angle 0.17°. b The velocity contour for section-15 *RANS* model for diverging angle 0.17°. c The velocity contour for section-15 *k-ε* model for diverging angle 0.17°. d The velocity contour for section-15 *k-ω* model for diverging angle 0.17°

### References

Gandhi BK, Verma HK, Abraham B (2010) Investigation of flow profile in open channels using CFD. Roorkee

Knight D, Shamseldin A (Eds) (2005) River basin modelling for flood risk mitigation. CRC Press

Khatua KK, Patra KC (2008) Boundary shear stress distribution in compound open channel flow. *J Hydraul Eng ISH* 12(3):39–55



- Menter FR (1994) Two-equation eddy-viscosity turbulence models for engineering applications. AIAA J 32(8):1598–1605
- Sahu M, Khatua KK, Mahapatra SS (2011) A neural network approach for prediction of discharge in straight compound open channel flow. Flow Measure Instrum 22:438–446
- Wilcox DC (1988) Reassessment of the scale-determining equation for advanced turbulence models. AIAA J 26(11):1299–2131

# Chapter 35

## Numerical Modelling of Tidal Hydrodynamics Along River Tapi, Gujarat



R. Balaji, J. SatheeshKumar, R. Cornelius, R. Naveen, G. Prasantha, and T. Prince

**Abstract** Tapi, the second-largest westward draining river in India, originates at Multai reserve forest in Betul District, Madhya Pradesh, at 752 m. It runs westward for 724 km until discharging into the Arabian Sea via the Gulf of Khambhat. The basin is located between latitudes  $20^{\circ} 5'$  and  $22^{\circ} 3'$  north, and longitudes  $72^{\circ} 38'$  and  $78^{\circ} 17'$  east. The study aims to better understand the hydrodynamics of the tidally impacted river Tapi and estimate river discharge owing to rainfall at the ONGC bridge in Surat, which is about 14 km from the Arabian Sea. In order to achieve the goals, a two-dimensional hydrodynamic model was created using the Delft3D modelling scheme. The numerical model's offshore ocean boundary is forced with tidal constituents, while the upstream river boundary is forced with discharge estimated using HEC-HMS (hydrological modelling software). The model estimated tide-induced currents are validated using observed field datasets, and it shows a good correlation. The model results indicated the tidally varying hydrodynamic behaviour during the year's pre and post-monsoon seasons.

**Keywords** Tapi river · Discharge · Delft3D-FLOW · Tidal hydrodynamics · Numerical modelling

### 35.1 Introduction

The river is an essential factor in human civilization, which provides freshwater, inland transportation, hydro energy, and helps in recreational and tourism activities. However, several risk factors are linked to this due to the current abrupt change in climate, leading to flooding or drought. Increased flooding in the coastal and riverine flood plains and the degradation of coastal ecosystems like saltmarsh are all threats from climate change. These disasters cause significant and long-term damage to coastal communities, socioeconomic activities, and the environment. Cities situated along riverine and coastal floodplain banks are particularly vulnerable to this hazard

---

R. Balaji (✉) · J. SatheeshKumar · R. Cornelius · R. Naveen · G. Prasantha · T. Prince  
Department of Civil Engineering, IIT Bombay, Mumbai 400076, India  
e-mail: [rbalaji@iitb.ac.in](mailto:rbalaji@iitb.ac.in)

(Adhikari et al. 2010). Moreover, the situation has worsened as the combination of flooding and high tide conditions in this region increases the probability of a disaster. Nowadays, numerical modelling is the most effective method for understanding this phenomenon all around the world (Cook and Merwade 2009; Gallegos et al. 2009; Mignot et al. 2006; Haider et al. 2003; Lindner and Miller 2012; Smith et al. 2005). Therefore, in the present work, the state-of-the-art Delft3D modelling system was used to understand the macro tidal river Tapi hydrodynamics, which runs along the Gujarat coast. The following sections discuss the details of the modelling and the outcomes.

## 35.2 Study Area

Tapi river is one of India's major rivers and originates from Madhya Pradesh in the Satpura range at 752 m above sea level. The river's total length is approximately 724 km, and it flows along the central part of India. The states through which the Tapi river flows include Maharashtra, Gujrat, and Madhya Pradesh. Apart from the Narmada river, Tapi is the only river that flows westward and merges into the Arabian Sea. Tapi basin is the second-largest in India with a total area of 65,145 km<sup>2</sup> and flows through major cities and discharge into the Arabian Sea about 16 km from Surat (Fig. 35.1). Therefore, Surat is frequently facing flooding problem due to river Tapi and its economy have been hit by several floods in the past few decades. During the floods, a significant portion of the city is submerged, creating a lot of damage in residential and industrial areas. Hence, it is essential to understand the hydrodynamics of the region.

## 35.3 Data and Methods

### 35.3.1 *Delft3D*

In the present study, the Delft3D modelling package (WL|Delft Hydraulics 2006) was used to simulate the hydrodynamics along the Tapi river. It is composed of multiple modules that work together to simulate processes like tidal hydrodynamics, wave transformation, water quality, sediment transport, and morphology. Delft3D-FLOW is a multi-dimensional (2D or 3D) hydrodynamic (and transport) modelling system that employs the finite-difference method to calculate non-steady flow and transport phenomena caused by tidal and meteorological forcing on a rectilinear or curvilinear boundary fitted grid with suitable initial and open boundary conditions (Lesser et al., 2004). It solves the Navier–Stokes equations for an incompressible fluid under the shallow water and Boussinesq assumptions, and it computes vertical velocities for 3D models using the continuity equation.



**Fig. 35.1** View of study area (Source Google Earth)

### 35.3.2 Hydrological Model Setup

The Tapi river monsoon discharge was estimated using a hydrological model setup using HEC-HMS. The river discharge was calculated at a specific location near Magdala Bridge in Surat, at  $21^{\circ} 8'47.25''N$  and  $72^{\circ}44'48.78''E$ . Drainage to the Arabian Sea was restricted until the Ukai Dam in Gujarat. To extract basin properties, the model was created using ArcGIS 10.5 software and HEC-GeoHMS. As illustrated in Fig. 35.2, the Tapi river's drainage lines and catchment were identified using ArcGIS 10.5 and HEC-GeoHMS, followed by terrain pre-processing to obtain watershed delineation. HEC-Geo HMS basin processing was used to integrate relatively small sub-basins. The HEC-Geo HMS characteristic tool calculates river slope, river length, basin slope, longest flow path, and basin centroid. The basin was then modelled for rainfall-runoff using monsoon rainfall data and the transfer and loss method with suitable curve numbers to estimate river discharge.

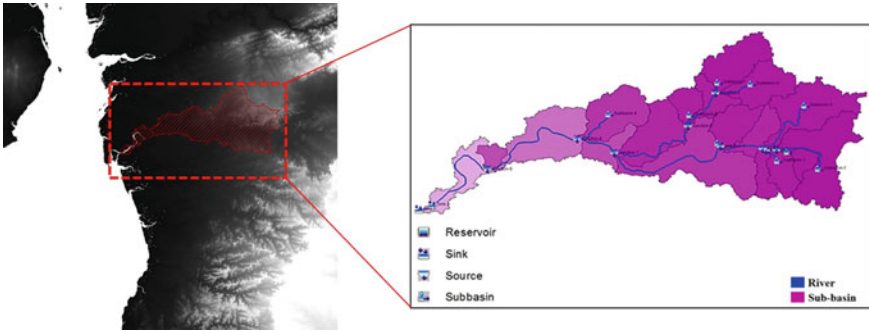


Fig. 35.2 View of river basin used for hydrologic model

### 35.3.3 Hydrodynamic Model Setup

The Delft3D computational model grid covers the entire Tapi river basin, as illustrated in Fig. 35.3. Admiralty charts (no. 1486 and 3460) were used to extract the river's bathymetry as well as nearshore coastal features such as inlets and estuaries in the region. A rectilinear grid system with a spatial resolution of 100 m was used for simulation throughout the domain. The open boundary of the model was set at 30 m of water depth, and it was forced with tidal astronomical elements from a TPXO7.1 global tidal model (Egbert et al. 1994). The HEC-HMS model was used to estimate river discharge values, which were then imposed on the upstream side of the boundary.

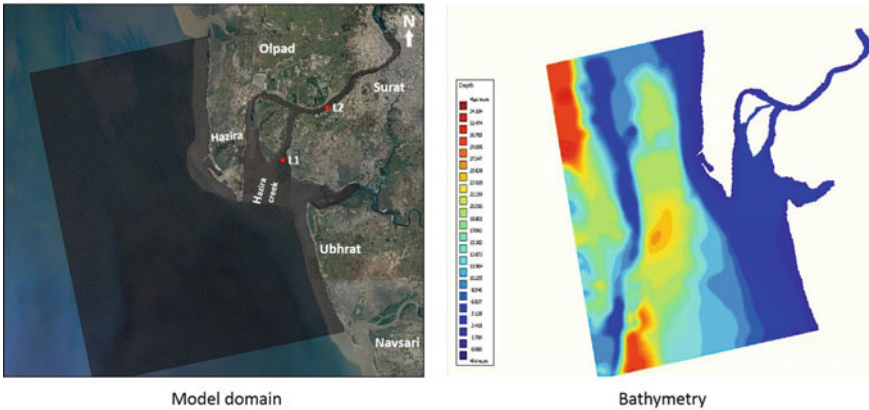
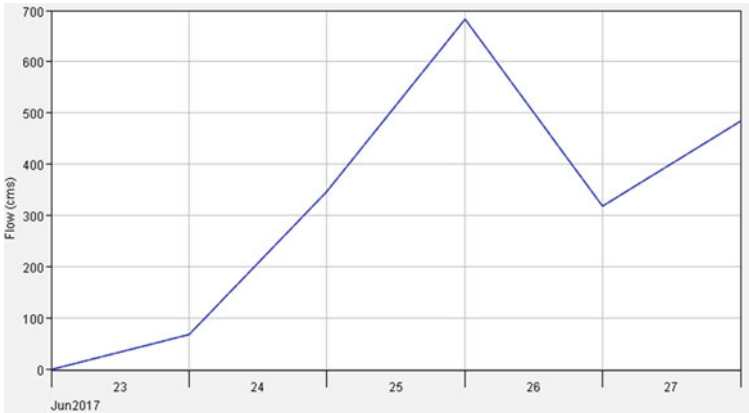


Fig. 35.3 View of study domain and bathymetry



**Fig. 35.4** Discharge hydrograph at Magdala Bridge, Tapi river

## 35.4 Results and Discussion

### 35.4.1 Hydrological Model Results

The rainfall data were obtained from GSDMA, Gujarat, for six days from 23 Jun 2017 to 28 Jun 2017, and it was observed that the peak discharge and the volume are  $5.9 \times 10^7 \text{ m}^3/\text{day}$  and  $1.4 \times 10^5 \text{ mm}$ , respectively, at the specified discharge location. The estimated discharge was shown in Fig. 35.4.

### 35.4.2 Simulated Tidal Levels and Currents

The hydrodynamic model was simulated for ten days, from 12 November to 22 November 2017. The model-simulated results are validated with the in situ field dataset carried out on 19 November 2017, to test the model's performance in the below section. The model extracted water level and velocity are shown in Fig. 35.5. It is observed that the developed model was able to simulate hydrodynamics well in the river. The observed maximum water level and velocity are 2.2 m and 1.79 m/s, respectively. Figure 35.6 depicts contour plots of water level variation.

### 35.4.3 Comparison of Measured Versus Modelled Data

On 19 November 2017, field measurements were taken to estimate the water level and flow velocity using a total station and GPS Drifters. The measured water level

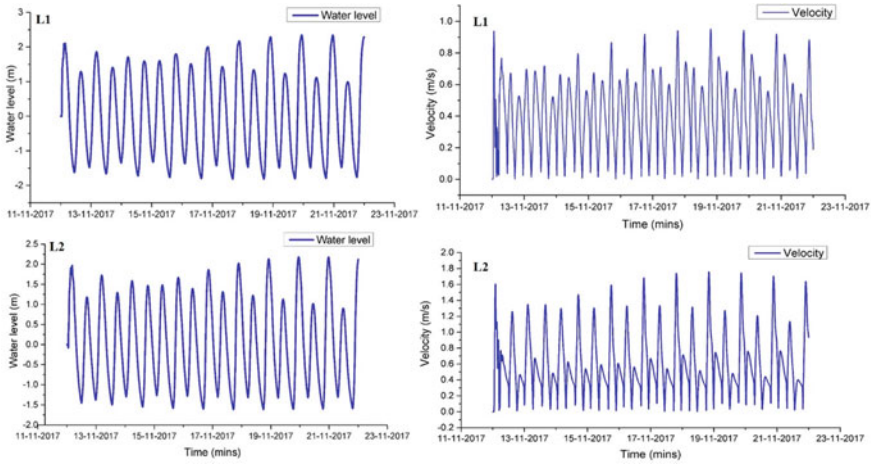


Fig. 35.5 Time series of simulated water level and velocity

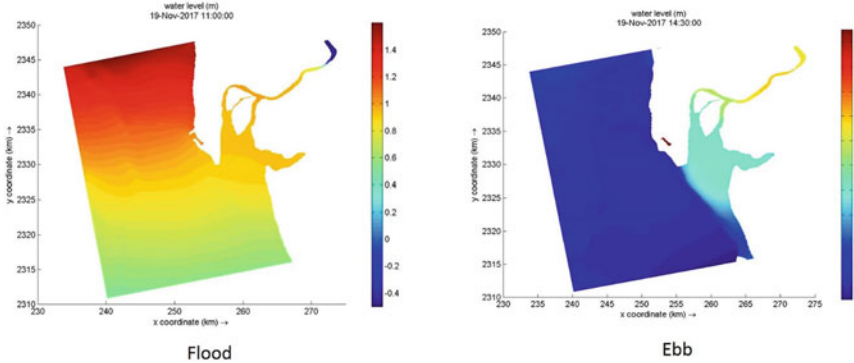


Fig. 35.6 Typical view of water level variation during flood and ebb

and velocity ranges are compared with the model outputs to validate the model successfully. The time-series comparison of measured and modelled water levels at river Tapi is presented in Fig. 35.7, and the qualitative comparison is shown in Table 35.1. Figures 35.8 and 35.9 illustrate the measured and modelled drifter velocity, and Table 35.2 provides a quantitative comparison.

### 35.5 Conclusion

The two-dimensional shallow water-based finite different model has been utilized to understand the hydrodynamics of Tapi river, Gujarat. The estimated peak discharge and water volume are  $5.9 \times 10^7 \text{ m}^3/\text{day}$  and  $1.4 \times 10^5 \text{ mm}$  at the specified discharge

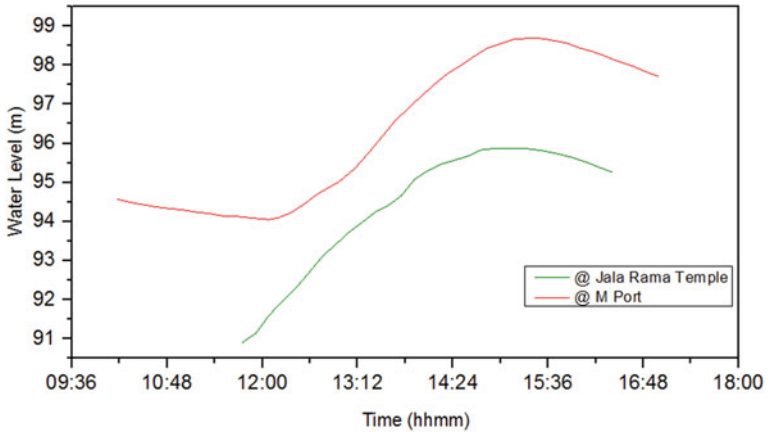


Fig. 35.7 Measured water level at two locations in Tapi river

Table 35.1 Comparison of measured versus modelled water level values

Location	Measured range (m)	Modelled range (m)
L1-joining	4.6	4.1
L2-at site	4.5	3.5



Fig. 35.8 Measured GPS drifter trajectories



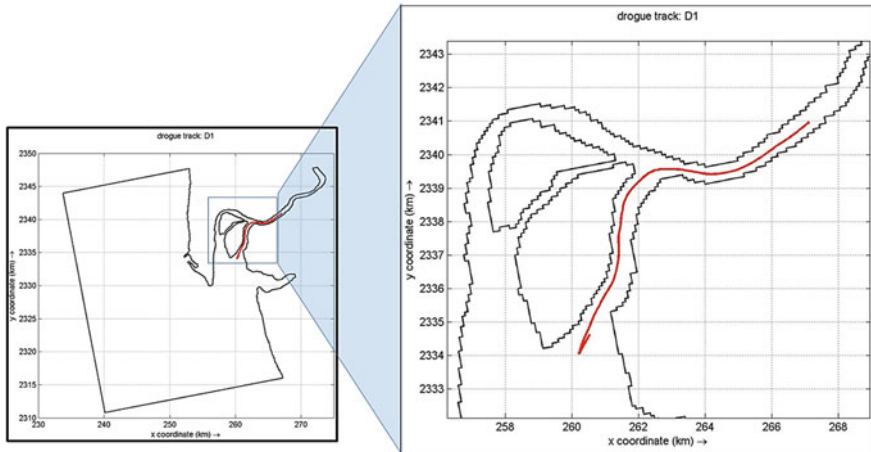


**Fig. 35.9** View of model-simulated trajectories

**Table 35.2** Comparison of measured versus modelled drifter’s surface velocity

Latitude	Longitude	Measured (m/s)	Modelled (m/s)
21.107458	72.702114	1.6	1.22
21.139184	72.711927	1.0	0.80
21.140485	72.724300	1.4	1.25

location through HEC-HMS hydrological modelling study. The tidal hydrodynamic model was forced with the estimated discharge value of different scenarios (monsoon and non-monsoon) to calculate extreme water levels and flooding. The simulated results were successfully validated against the limited available field measured data. It was further used to reproduce the spatially varying hydrodynamic characteristics such as water level and current velocity throughout the model area. It is concluded from this study, the maximum water level and velocity reach up to 2.2 m and 1.79 m/s, respectively, in the combination of spring tide and extreme discharge scenario.

## References

Adhikari Y, Osti R, Noro T (2010) Flood-related disaster vulnerability: an impending crisis of megacities in Asia. *J Flood Risk Manage* 3(3):185–191

Cook A, Merwade V (2009) Effect of topographic data, geometric configuration and modeling approach on flood inundation mapping. *J Hydrol* 377(1–2):131–142

Egbert GD, Bennett AF, Foreman MGG (1994) Topex/Poseidon tides estimated using global inverse model. *J Geophys* 99:24821–24852

Gallegos HA, Schubert JE, Sanders BF (2009) Two dimensional, high-resolution modeling of urban dam-break flooding: a case study of Baldwin Hills, California. *Adv Water Res* 32(8):1323–1335

- Haider S, Paquier A, Morel R, Champagne J-Y (2003) Urban flood modelling using computational fluid dynamics. In: Proceedings of ICE, Water Maritime Engineering 156(2):129–135
- Lesser GR, Roelvink JA, van Kester JATM, Stelling GS (2004) Development and validation of a three-dimensional morphological model. *Coast Eng* 51:883–915
- Lindner GA, Miller AJ (2012) Numerical modeling of stagedischarge relationship in urban streams. *J Hydraul Eng* 59:590–596
- Mignot E, Paquier A, Haider S (2006) Modeling floods in a dense urban area using 2D shallow water equations. *J Hydrol* 327(1–2):186–199
- Smith JA, Miller AJ, Baeck ML, Nelson PA, Fisher GT, Meierdiercks KL (2005) Extraordinary flood response of a small urban watershed to short-duration convective rainfall. *J Hydrometeorol* 6(5):599–617
- WLI/Delft Hydraulics (2006) Delft3D-FLOW User manual

# Chapter 36

## Study on the Variation of Distribution of Velocity in Accordance with Differential Roughness in a Compound Open Channel



Nirjharini Sahoo, Kishanjit Kumar Khatua, and Ramakar Jha

**Abstract** This paper presents an experimental study in which a series of measurements were carried out to investigate the hydraulic characteristics of a wide compound open channel having high width ratio and dissimilar roughness in the main channel and flood plain boundary by using pitot tube point-wise velocity measurements. Furthermore, in order to understand the effect of differential roughness (the ratio of base Manning's  $n$  value of floodplain surface roughness to that of the main channel) on the distribution of depth-averaged velocity and distribution of flow in the experimental channel, cases with different flow rates were studied. The contour plots of 2D iso-levels were drawn using SURFER software. As the channel is symmetric, half of the width is considered for point velocities. The variation of point velocities is considered along width-wise direction of the channel in order to study the depth-wise velocity profile distributions. The lateral variation of depth-averaged velocities was observed in the compound channel flow for different differential roughness ( $\gamma$ ) and the variation of flow rate in main channel is also studied with the increase in differential roughness.

**Keywords** Velocity contour · Depth-average velocity · Differential roughness · Width ratio · Distribution of flow

### 36.1 Introduction

Natural rivers seldom bear a uniform roughness throughout their main channel and floodplain. The flow process in the open channel becomes more complicated at over-bank stages due to the different hydraulic conditions prevailing in the main channel and the adjoining floodplains. Effect of differential roughness, which has a vital role

---

N. Sahoo  
Department of Civil Engineering, VSSUT, Burla, India

K. K. Khatua  
Department of Civil Engineering, NIT, Rourkela, India

R. Jha (✉)  
Department of Civil Engineering, NIT, Patna, India

in estimating flow carrying capacity of a channel; sediment transportation; erosion of river, in compound channel have been studied by many previous investigators. Ghosh and Jena (1971) studied boundary shear distribution in straight compound channels for both smooth and rough boundaries. Knight and Hamed (1984) extended the work of Knight and Knight and Demetriou (1983), to the compound channels having rough floodplains. They studied the influence of differential roughness between floodplain and main channel on the process of lateral momentum transfer. Myers and Lyness (1997) studied the behavior of two key discharge ratios, namely, total to bank full discharge and main channel to floodplain discharge in compound channels for smooth and homogeneously roughened channels of various scales with the help of acquired data of small-scale and large-scale laboratory compound channels as well as natural rivers. Myers et al. (2001) presented experimental results of a compound channel having fixed and mobile main channel along with two rough floodplains. They investigated velocity and discharge relationships illustrating the complex behavior of the compound channel river section. Hin and Bessaih (2004) investigated velocity distribution, stage–discharge relationship, and the effect of momentum transfer in a straight compound channel having a rougher floodplain than the main channel. Joo and Seng (2008) compared the different methods available for discharge prediction in a non-symmetrical compound channel with rough flood plain. Kean et al. (2009) investigated velocity and boundary shear stress distributions across the cross-section of a straight compound channel whose floodplain was roughened by cobble. Therefore, the effect of differential roughness on the velocity profile distributions, flow distribution during overbank flow conditions is retained in this study for environmental reasons.

## **36.2 Experiment's Setting in Laboratory**

### ***36.2.1 Experimental Channel***

For the aim of this study, experiments were carried out with three roughness variations in Fluid Mechanics Lab., at N.I.T. Rourkela, India. A straight compound channel of dimension 12 m long, 2 m wide, and 0.6 m depth was fabricated and used in the experiments with recirculation system of water supply.

The schematic diagram of the experimental channel with dimensions is shown in Fig. 36.1.

### ***36.2.2 Rough Channel with Mesh and Stones***

For the study of velocity distribution in a compound channel having different differential roughness, woven wire mesh and crushed stone were used as roughening

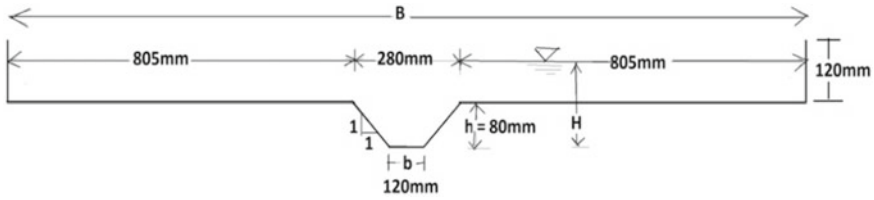


**Fig. 36.1** Systematic diagram of the compound channel (straight)

**Table 36.1** Roughness value for different set of experiments

Experiments	River channel manning's $n$ ( $n_{mc}$ )	Flood plain manning's $n$ ( $n_{fp}$ )	Roughness, ( $n_{fp}/n_{mc}$ )
Very smooth	Smooth	Smooth	1
Low roughness	Smooth	Mesh	1.12
Medium roughness	Mesh	Stone	1.32
High roughness	Smooth	Stone	1.47

materials on the flood plain and main channel to get multiple roughness patterns. In the experiments, the size of woven wire mesh was  $3 \times 3$  mm, diameter was 0.4 mm, and the diameter of the stone used in the experiment was 3.39 mm. Moreover, the values of Manning's  $n$  for different materials including wire mesh, Perspex sheet, and stones were 0.01097, 0.00983, and 0.01449, respectively. Many investigators used Manning's  $n$  for their study too (Myers and Brennan 1990; Ayyoubzadeh 1997; Atabay and Knight 2006).

During each experiment, roughness values were changed in which the flood plain was rougher than the river bed. The wetted perimeter of flood plain was set below 3% of the total wetted perimeter for the study of composite roughness. Table 36.1 shows different roughness values under a different set of experiments.

### 36.2.3 Measurement of Slope, Discharge, and Velocity

A pointer gauge having the least count of 0.1 mm was used for the experiment. The bed slope of the channel was found to be  $3.112 \times 10^{-3}$  and assumed as equal to the energy gradient slope.

The rectangular notch was calibrated and used for the discharge measurement at a given slope. The coefficient of discharge ( $C_d$ ) of the rectangular notch was 0.6792 after calibration and the mean velocity ( $U$ ) was measured at each experimental run.

In the present work, the stream-wise velocity ( $U_p$ ) at required points in the experiments was found out by using a micro-pitot tube 6.33 mm external diameter in conjunction with a suitable inclined manometer (inclined at  $24.86^\circ$  with the horizontal). As the compound channel was symmetric, only half of the channel was considered for the measurement of stream-wise velocity.

### 36.3 Results and Discussion

#### 36.3.1 Stage–Discharge Relationship

The slope was kept constant for all series of experiments in the present study. The depth of flow on the main channel ( $H$ ) was taken as the stage, which gave a particular discharge ( $Q_a$ ) only under steady and uniform conditions. From the depth of flow over the rectangular notch, the actual discharge ( $Q_a$ ) was calculated for each run of all series experiments from the equation given below:

$$Q_d = C_d * L * \sqrt{[2 * g * (H)^{(2/3)}]} \tag{36.1}$$

where  $C_d$  is the coefficient of discharge of the notch calculated from calibration,  $L$  is the length of the notch,  $H_n$  is the height of water flow above the notch, and  $g$  is the gravitational acceleration. The stage vs. discharge curves for all series of overbank flow are plotted in Fig. 36.2, where we can observe that:

- With the increase in depth of flow on main channel, discharge increases.
- For a constant depth of flow, discharge decreases with the increase in differential roughness.

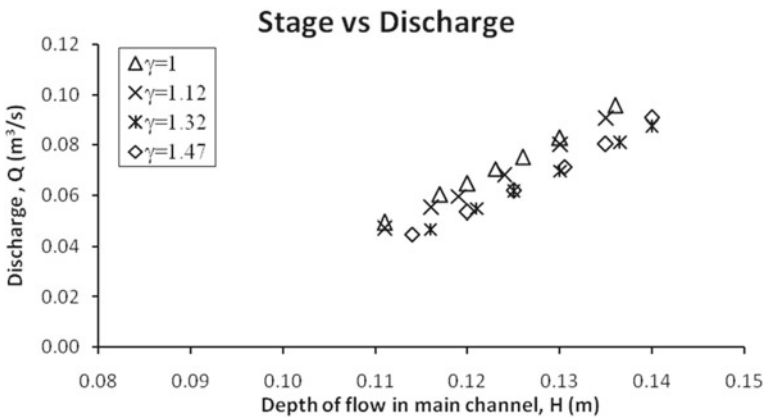


Fig. 36.2 Stage–discharge relationship for compound channels with different  $\gamma$

- Discharge of 1.12, gradually becomes closer to 1 as the depth of flow increases, i.e., the roughness effect on flow decreases slowly with an increase in depth of flow.

### 36.3.2 Distribution of Stream-Wise Velocity

For mapping of contours, the middle of the main channel is taken as origin and the base as datum. The distribution of dimensionless stream-wise velocity ( $U_p/U$ ) in contour form for a series of depth of flow in main channel ( $H = 11.6$  cm, 12.0 cm, 12.5 cm, 13.0 cm, and 13.5) for all differential roughness ( $\gamma$ ) value are shown in Figs. 36.3, 36.4, 36.5, 36.6, and 36.7. From the figures of dimensionless velocity isovels of contours, the following observation can be drawn.

- The concentration of higher velocity contour isovels increases in main channel with the increase in differential roughness, i.e., due to the effect of flood plain roughness, the velocity on flood plain decreases while the velocity becomes maximum in main channel.
- The concentration of higher velocity contours on the floodplain increases with the increase in depth of flow, which confirms that the effect of roughness gradually decreases on the flood plain flow, and the percentage of flow on the floodplain increases with increase in depth of flow.

### 36.3.3 Distribution of Depth-Averaged Velocity

A general procedure for determining the depth-averaged velocity ( $U_d$ ) is to average the velocity measured at  $0.2d'$  and  $0.8d'$  from the water surface, or the velocity measured at  $0.6d'$  from the water surface (where  $d' =$  depth of flow on a surface), Rantz (1982). Following this in the present study, the depth-averaged velocity ( $U_d$ ) was measured at  $0.6d'$  from the water surface. The distribution of ( $U_d/U$ ) across the dimensionless lateral distance ( $y/Y$ ) for all relative depth ( $\beta$ ) of all differential roughness is shown in Fig. 36.8, where  $U$  is the mean velocity of respective run,  $y$  is the lateral distance of the point (at which the  $U_d$  was measured) from the middle of the main channel toward floodplain wall, and  $Y$  is half of the compound channel width  $B$  (i.e.,  $Y = B/2$ ).

From the figures, it can be observed that:

- The variation in depth-averaged velocity, in main channel, and flood plain region is minimum in case of  $= 1$  with comparison to other three cases. The variation increases with the increase in differential roughness.
- In case of  $= 1$ , the overall depth-averaged velocity in the main channel region is lower than that of the flood plain for higher relative depth ( $\beta$ ), i.e., as the depth of flow increases.

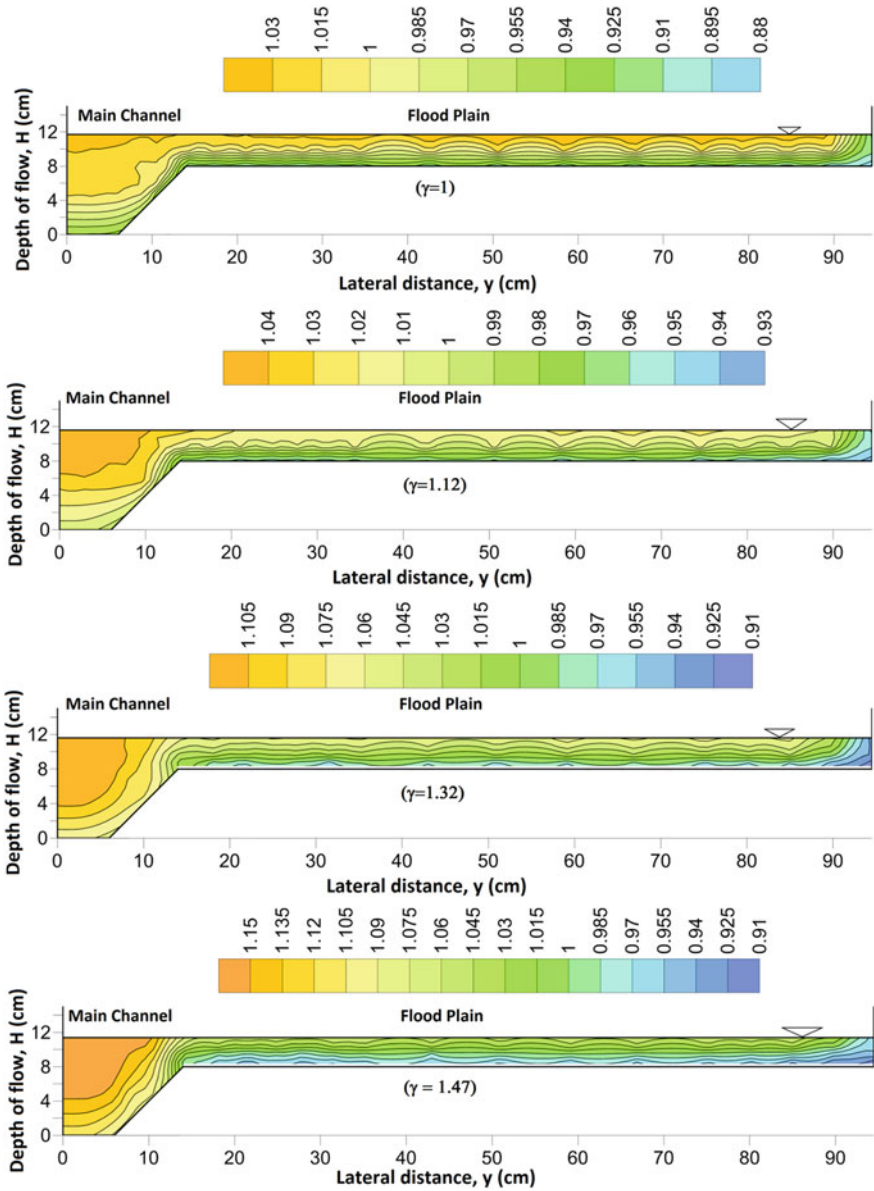


Fig. 36.3 Series I: depth flow in main channel ( $H$ ) = 11.6 cm with  $U_p/U$  isovels for different



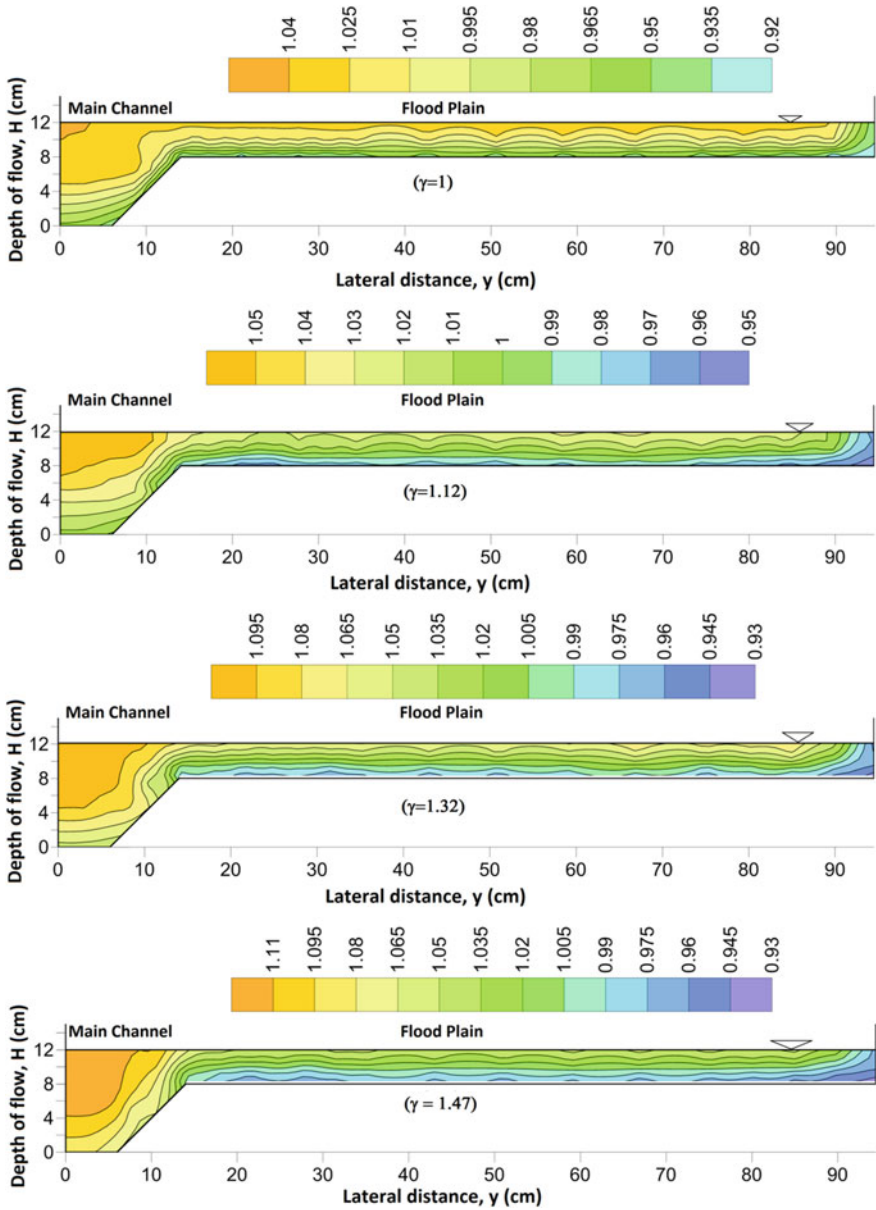


Fig. 36.4 Series II: depth flow in main channel ( $H$ ) = 12 cm with  $U_p/U$  isovels for different  $\gamma$

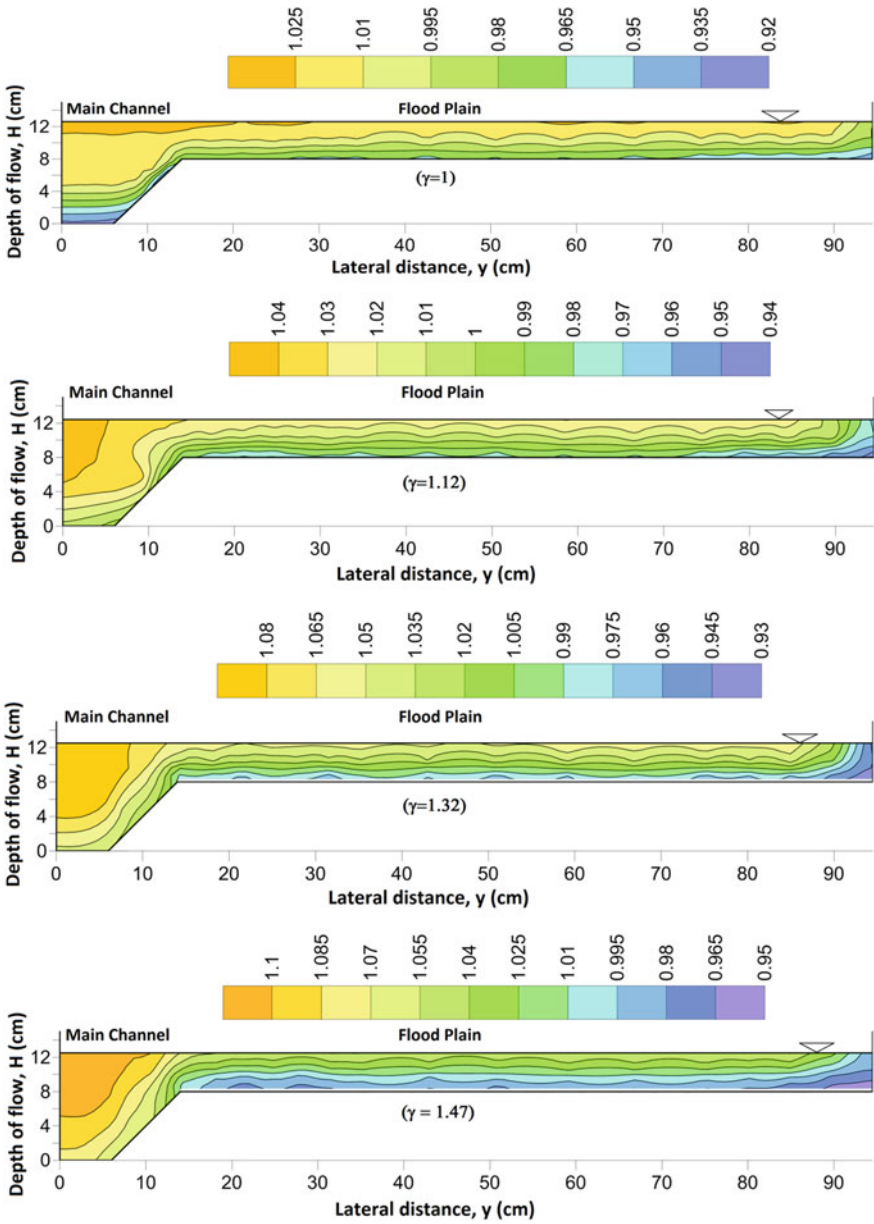


Fig. 36.5 Series III: depth flow in main channel ( $H$ ) = 12.5 cm with  $U_p/U$  isovels for different  $\gamma$

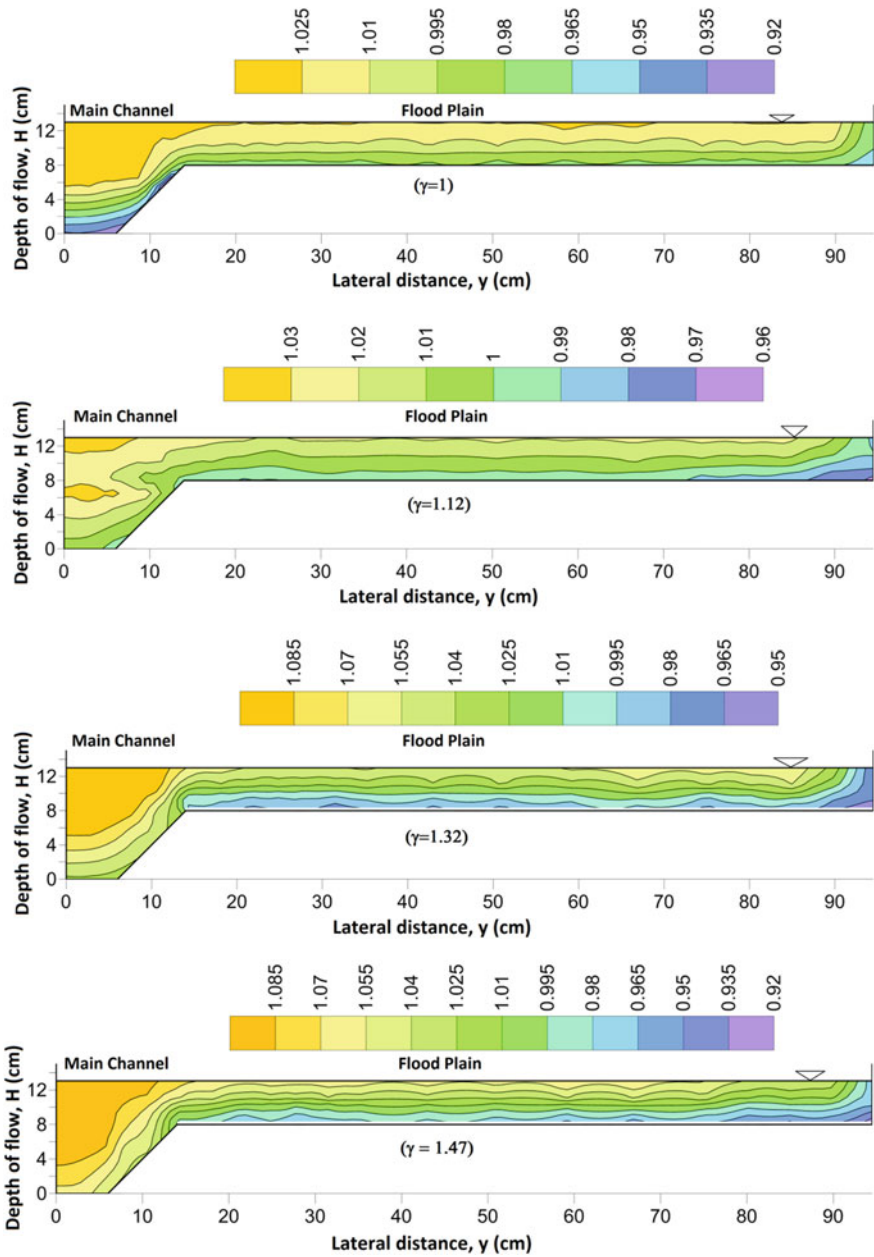


Fig. 36.6 Series IV: depth flow in main channel ( $H$ ) = 13 cm with  $U_p/U$  isovels for different  $\gamma$

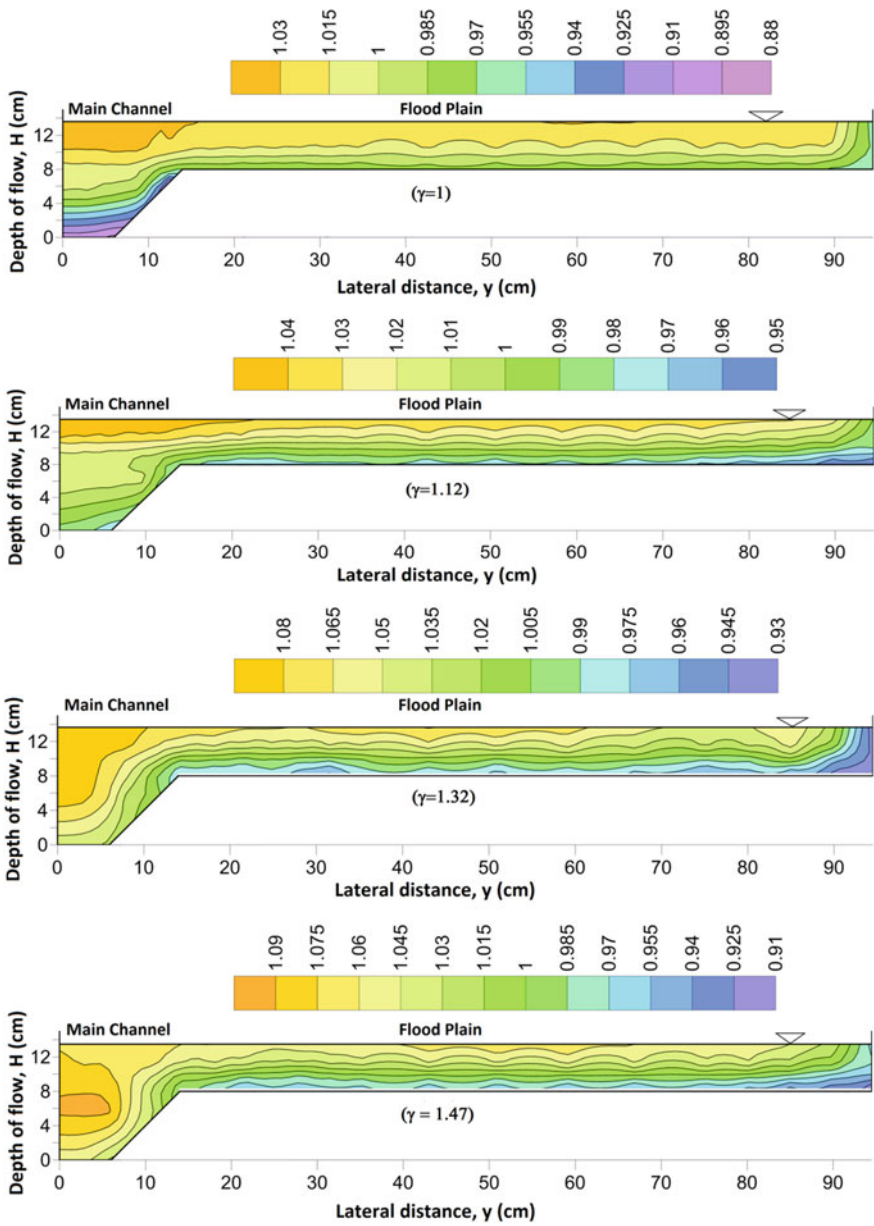


Fig. 36.7 Series V: depth flow in main channel ( $H$ ) = 13.5 cm with  $U_p/U$  isovels for different  $\gamma$

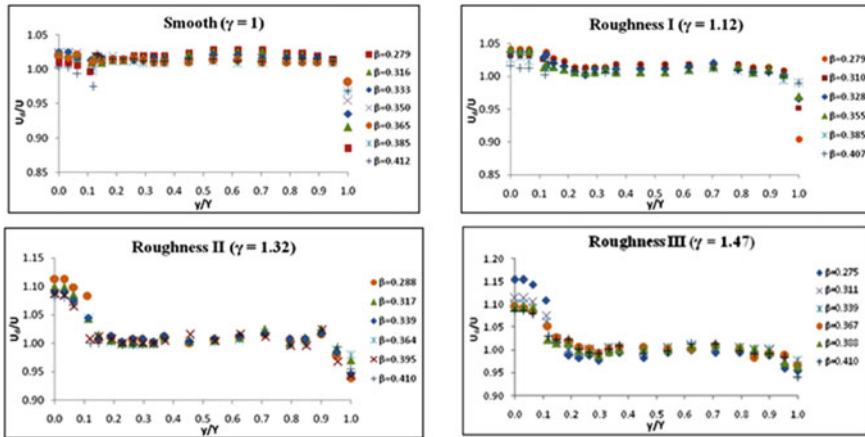


Fig. 36.8 Depth average velocity distribution for different  $\gamma$

- The depth-averaged velocity in main channel decreases with the increase in relative depth ( $\beta$ ) for all series of experiments, i.e., the resistance to the flow on floodplain by floodplain surface decreases with increase in differential roughness.
- The overall depth-averaged velocity in main channel increases with the increase in differential roughness (i.e., the percentage of flow in main channel, increases with the increase in, whereas decreases in floodplain region).

### 36.3.4 Variation in Distribution of Flow

Discharge carried by the main channel is generally calculated by separating from the compound section by vertical divided channel method. The flow in main channel was obtained by numerically integrating the depth-averaged velocity of main channel and then multiplying the integrated value with the area of main channel. Due to transfer of momentum between floodplain and main channel, the percentage of flow carried by the main channel with depth does not follow simple area ratios. At lower depths of flow over floodplain, the percentage of flow in main channel ( $\%Q_{mc}$ ) is more than that of at higher depths of flow on the same. In past, the flow and velocity distribution in compound sections have been investigated by many investigators (Knight and Demetriou 1983; Wormleaton and Hadjipanous 1985; Myers et al. 2001; Atabay and Knight 2002; Yang et al. 2004; Hin and Bessaih 2004; Khatua 2008; Absi 2011). In the present study, the variation of ( $\%Q_{mc}$ ) with the variation in differential roughness was found out and is shown in Fig. 36.9.

In the figure, we can see that with the increase in relative depth, the percentage of flow in main channel ( $\%Q_{mc}$ ) decreases due to the effect of momentum transfer between floodplain and main channel decreasing with the increase in the depth of flow. In the figure, we can also observe that the percentage of flow in main channel

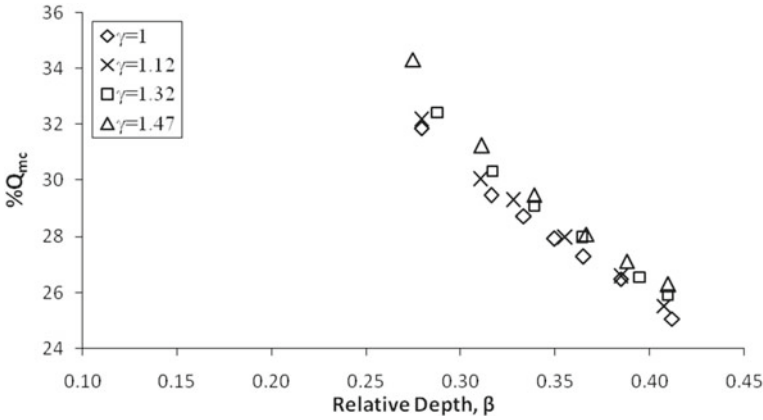


**Fig. 36.9** Variation in distribution of flow due to differential roughness ( $\gamma$ )

(% $Q_{mc}$ ) increases with the increase in differential roughness, which may be due to the resistance to flow offered by floodplain in comparison to main channel increasing with the increase in differential roughness value (as main channel is smoother than the floodplain).

### 36.4 Conclusions

- From the results of stage–discharge relationship, it can be concluded that: The overall discharge found to increase with the increase in depth of flow and decrease with the increase in differential roughness, which may be attributed to the fact that at higher depth of flow, the effect of differential roughness as well as that of the momentum transfer between main channel and flood plain, decreases.
- From stream-wise velocity ( $U_p/U$ ) in contour, it can be noted that: (i) The concentration of higher velocity contour isovels gradually increases in main channel with the increase in differential roughness, i.e., due to the effect of flood plain roughness, the velocity on flood plain decreases while the velocity becomes maximum in main channel. (ii) The concentration of higher velocity contours on the floodplain increases with the increase in depth of flow, which confirms that the effect of roughness gradually decreases on the flood plain flow, and the percentage of flow on the floodplain increases with an increase in depth of flow.
- From the observation of depth-averaged velocity, it can be noted that: Depth-averaged velocity in main channel region is found to increase and found to decrease in floodplain region with the increase in differential roughness. Depth-averaged velocity in main channel region was found to decrease with the increase in relative depth of flow.

## References

- Absi R (2011) An ordinary differential equation for velocity distribution and dip-phenomenon in open channel flows. *J Hydr Res IAHR* 49(1):82–89
- Atabay SA, Knight DW (2002) The influence of floodplain width on the stage–discharge relationship for compound channels. In: *River Flow 2002 proceedings international conference on fluvial hydraulics*. Balkema, The Netherlands, Vol. 1, pp. 197–204
- Atabay S, Knight DW (2006) 1-D modelling of conveyance, boundary shear and sediment transport in overbank flow. *J Hydr Res* 44(6):739–754
- Ayoubzadeh SA (1997) Hydraulic aspects of straight compound channel flow and bedload sediment transport. PhD thesis, The University of Birmingham, England, U.K.
- Ghosh S, Jena SB (1971) Boundary shear distribution in open channel compound. *Proceedings of the Institution of Civil Engineers, London, England* 49:417–430
- Hin LS, Bessaih N (2004) Flow in compound channels. In: *1st International conference on managing rivers in the 21st Century*. Rivers 2004
- Joo CBH, Seng DMY (2008) Study of flow in a non-symmetrical compound channel with rough floodplain. *J Inst Eng Malaysia* 69(2):18–26
- Kean JW, Kuhnle R, Smith JD, Alonso CV, Langendoen EJ (2009) Test of a method to calculate near-bank velocity and boundary shear stress. *J Hydr Eng ASCE* 135(7):588–601
- Khatua KK (2008) Interaction of flow and estimation of discharge in two stage meandering compound channels. PhD Thesis, NIT, Rourkela, India
- Knight DW, Demetriou JD (1983) Floodplain and main channel flow interaction. *J Hydr Eng ASCE* 109(8):1073–1092
- Knight DW, Hamed ME (1984) Boundary shear in symmetrical compound channels. *J Hydr Eng ASCE* 110(10):1412–1430
- Myers WRC (1987) Velocity and discharge in compound channels. *J Hydr Eng ASCE* 113(6):753–766
- Myers WRC, Brennan EK (1990) Flow resistance in compound channels. *J Hydr Res IAHR* 28(2):141–155
- Myers RC, Lyness JF (1997) Discharge ratio in smooth and rough compound channels. *J Hydr Eng ASCE* 123(3):182–187
- Myers WRC, Lyness JF, Cassells J (2001) Influence of boundary roughness on velocity and discharge in compound river channels. *J Hydr Eng ASCE* 39(3):311–319
- Rantz SE et al. (1982) Measurement and computation of streamflow: measurement of stage and discharge. U.S. Geological Survey Water-Supply, Vol. 1, p 2175
- Sahoo Nirjharini (2012) Effect of differential roughness on flow characteristics in a compound open channel. M.ech. Thesis, NIT Rourkela, India
- Wormleaton PR, Hadjipanous P (1985) Flow distribution in compound channels. *J Hydr Eng ASCE* 111(2):357–361
- Yang SQ, Tan SK, Lim SY (2004) Velocity distribution and dip-phenomenon in smooth uniform open channel flows. *J Hydr Eng ASCE* 130(12):1179–1186

# Chapter 37

## Flow Distribution in Diverging Compound Channel Using LES Models



Deepika P. Palai and K. K. Khatua

**Abstract** During flood, water from the river inundates the floodplains causing mass destruction of human lives and properties. Thus, it is more essential to evaluate flow in the floodplains. The instant study is performed to understand the flow distribution in main channel and floodplains of a compound channel having symmetrical diverging floodplains due to difference in geometry and flow properties. Numerical experimentation is performed for diverging compound channel of different geometric and hydraulic conditions using ANSYS-fluent to study the effect of geometry and flow parameters on the flow distribution of such channels. Depth averaged velocity data obtained from the numerical experimentation for different sections have been taken to compute the discharge in that section for main channel and floodplain separately. Different numerical method like , LES model, k-model is utilized for the modeling test. Among these three models, LES models provided quite good agreement with the experimental data. Hence, by taking LES model, more different diverging channel configuration has been performed and the respective flow is simulated. Using the results of LES, more data sets are extracted and a model has been developed for the computation of the proportion of rate of flow in both main channel and flood plain for various relative flow depths and for different diverging angles. The applicability of the model is proved with the observational data sets of other researchers and found to provide less error in the subsection discharge computations of a non-prismatic compound channel. The reason for higher accuracy by LES prediction has been discussed and recommended for use in non-uniform open channel flow.

**Keywords** Symmetrical diverging floodplains · LES model · ANSYS-fluent · Depth averaged velocity

---

D. P. Palai (✉)

Faculty of Civil Engineering Department, BPUT, Rourkela, Odisha 769015, India

K. K. Khatua

Associate Professor Civil Engineering Department, N.I.T, Rourkela, Odisha 769008, India



## 37.1 Introduction

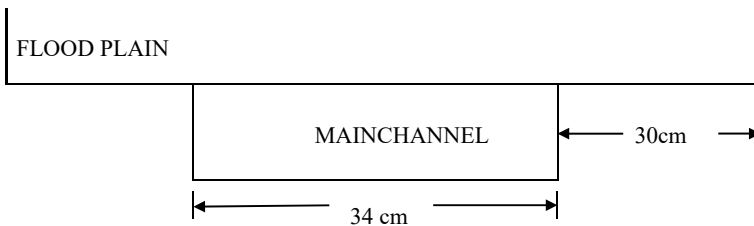
Water has ever been a fundamental piece of human progress which takes a vital role in build up and development of society. Till now, this has a disadvantage in the viewpoint that the increment in population combined with the artificial dam-related failures, landslide and so along has led to an increase in water-related catastrophe in these areas. Hence, it is basic for us to comprehend the impact of water bodies on its flood plains. The diverging channel is the sort of non-prismatic compound channel, which are separated into three types (a) diverging channel, (b) converging channel and (c) skewed channel. A diverging channel is a type of compound channel whose flood plain begins to go amiss or wandering from the primary channel is called diverging compound channel. The present undertaking work is worked on non-prismatic diverging compound channel whose diverging angle is  $9.83^\circ$  and the deviation of compound channel begins from 10m from the inlet. The length of diverging section is 3m, i.e., 10 from the inlet to 17 m.

## 37.2 Experimental Flume

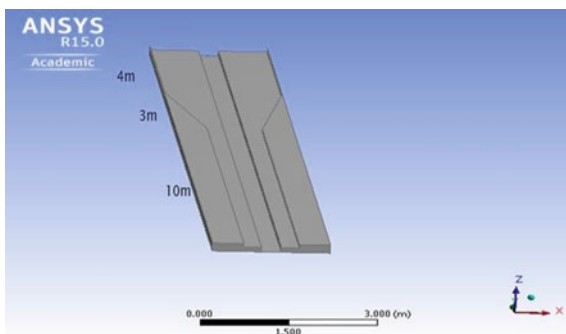
For the present-day flow research work, the analysis will be led at NIT Rourkela for compound channel hold diverging floodplain having  $9.83^\circ$ . The magnitude of NITR flume is  $20\text{ m} \times 2\text{ m} \times 0.4\text{ m}$  having bed slope 0.002. The diverging begins with 10m from the inlet. The test has directed for the above cross-sectional geometry. The dimension of this geometry helps us to calculate the various flow parameters (Figs. 37.1, 37.2, 37.3 and 37.4).

### 37.2.1 Procedure of Experiment

The entire test arrangement involves three sections such as overhead tank, compound channel and volumetric tank. The water supply needed for the test is provided from



**Fig. 37.1** Cross-sectional aspect of the channel

**Fig. 37.2** Volumetric tank**Fig. 37.3** Overhead tank and sump tank**Fig. 37.4** Image for 3 m diverging angle  $9.83^\circ$  made in ANSYS

**Table 37.1** Details of experimental parameters for diverging compound channel

Serial. No.	Items	Diverging compound channel
1	Main channel geometry	Rectangular
2	Flood plain geometry	Diverging
3	Main channel geometry	34 cm
4	Full depth of main channel	11.3 cm
5	Top width of compound channel before diverging	94 cm
6	Diverging length	3 m (completed) and 2 m (to be done)
7	Slope of the main channel	0.0014
8	Flume size	20 m × 2 m × 0.4 m

the overhead tank utilizing two electric motors and the tank is placed at a height of 3.5–4.5 m. For the flow research work, the experiment is led at NIT Rourkela for compound channel having diverging floodplain having angle  $9.83^\circ$ . The size of NITR flume is 20 m × 2 m × 0.4 m having bed slant 0.002. Diverging begins at 10m from the channel. The entire width at the inlet of channel is 0.94 m, depth of the primary channel is 11.3cm and the width of the main channel is 0.34m. The water later moving through the compound channel is gathered in a volumetric tank whose volume is known, the release of the flow can be determined. Besides this, the non-prismatic compound channel course of action with a diverging point of 9.83 degree and a length of 17m is considered in this paper. Boundary shear pressure at the predetermined area is completed utilizing the pitot tube, which was associated with manometer with static and dynamic measures. The distinction between the head of static and dynamic pressing factor is gathered. This distinction of head,  $h$  is utilized to compute the distinction of pressure (Table 37.1).

### 37.2.2 Measurement of Discharge

The volumetric tank situated toward the ending of the channel gets water flowing through with the channels. Calculating the stream rate, the time of collection of water in the volumetric tank shifted to the lower one for the higher rate of discharge. The time is recorded utilizing a stopwatch. Change in the mean water level in the tank throughout the time reaching is recorded. From the information on the volume of water gathered in the estimating tank and the comparing season of variety, the discharge flowing to the test channel for each run is acquired. At the same time, the profundity of water streaming in the channel is likewise estimated by the point check. This profundity of stream is named as a check or stage. In the following stage, the profundity of water in the channel is changed and for this new profundity of stream, stage, check, the release streaming over the channel segment is estimated as portrayed underneath. Through this manner, a bunch of information of stage and

**Table 37.2** Experimental setup at NIT Rourkela for 3 m, 2 m length diverging compound channel

Diverging length (L)	Aspect ratio	Angle	Section	Width ratio	Relative distance (Rd)	Relative depth (Dr)	Water level (H)
3	3	9.83°	1	2.764	0	0.20	0.132
3	3	9.83°	2	3.523	0.25	0.30	0.141
3	3	9.83°	3	4.288	0.50	0.35	0.150
3	3	9.83°	4	5.052	0.75	0.40	0.161
3	3	9.83°	5	5.811	1.0	0.50	0.171
2	2	14.57°	1	2.764	0	0.20	0.132
2	2	14.57°	2	3.523	0.25	0.30	0.141
2	2	14.57°	3	4.288	0.50	0.35	0.150
2	2	14.57°	4	5.052	0.75	0.40	0.161
2	2	14.57°	5	5.811	1.0	0.50	0.173

release is gathered and afterward the information is utilized to build up a phase release relationship. This phase–release relationship is useful in the calculation of release in the channel at different flow depths for the current investigation (Table 37.2).

### 37.3 Numerical Analysis

#### Results

In this chapter, the result obtained from the experiment works and LES model done in ANSYS Fluent is presented. The comparison of depth averaged velocity from section to section.

### 37.4 Graphs

The graphical represent are closed toward the data extracted from ANSYS. The diagram shown that how the depth averaged velocity (DAV) occurrence along the width of the channel at different sections like 10, 10.75, 11.5, 12.25.13 and 10m toward the inlet of the channel for different relative depths with an angle is 9.83°.

#### 37.4.1 For Aspect Ratio 9.83

See Fig. 37.5.

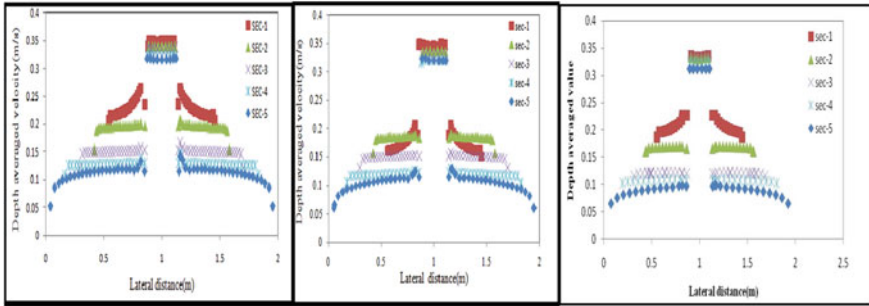


**Fig. 37.5** Comparison between DAV and position at 10 m from inlet for Angle 9.83, LES (model) from ANSYS Dr = 0.35, 0.45 and Dr = 0.55

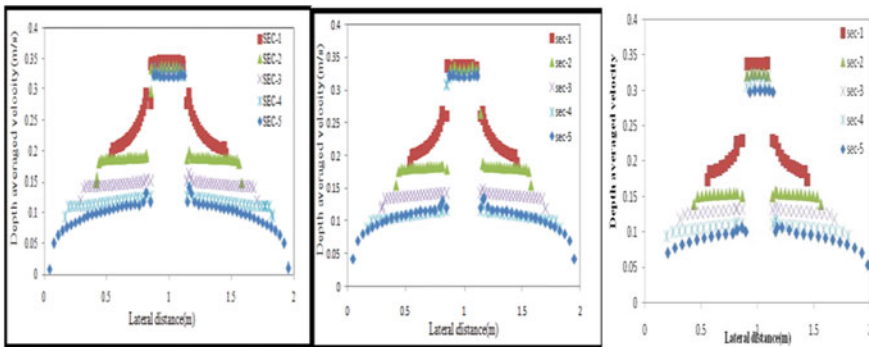


**Fig. 37.6** Comparison between DAV and position at 10 m from inlet for Angle 14.57°, LES (model) from ANSYS Dr = 0.35, 0.45 and Dr = 0.55

### 37.4.2 For Aspect Ratio 14.57

See Fig. 37.6.

## 37.5 Experimental Results

Experimental data are collected in two ways:

1. Through the methods for pitot tube, contrasts in the head of static and dynamic pressure are collected. The pitot readings are taken at a time frame narrow. This differentiation in head is utilized to figure the distinction in pressure. The tendency of the pitot tube is considered for the estimations of the speed of the stream.

2. The Acoustic Doppler Velocimeter (ADV) is utilized to record speed parts in three distinct ways. Two have been utilized for estimating the velocities; one is up probe and the other one is down probe. The ADV needs at least 5 cm of water profundity is needed for distinguishing the water flow and estimating because of this explanation, two ADVs are needed for covering full profundity of the channel. Three thousand samples of velocity are recorded at each place of the segment, and midpoints of these examples are taken to compute the DAV (Depth Averaged Velocity).
3. Comparison has been made between the ANSYS and experimental data result by covering the depth velocity graphs at each part like 10 m, 11.5 m and 13 m of channel to approve the consequences of LES model, which is utilized in ANSYS investigation.

From Figs. 37.5, 37.6, 37.7, 37.8 and 37.9, it is observed that the LES model provides the better result with experimental data has compared with other models, i.e., k-e models' model. Fig. 37.5 shows the results of different models and experimental data for starting of the diverging part, which represents the section (see Fig. 37.5) the diverging compound channel. It has been detected that each of the models over predicts the depth averaged velocity value (Fig. 37.10).

$$\%Q_{fp} = Q_{fp}/Q_t \times 100$$

$$\%Q_{mc} = Q_{mc}/Q_t \times 100$$

A floodplain or floodplain is an area of land adjacent to a stream or river that stretches from the banks of its channel to the base of the enclosing valley walls and experiences flooding during periods of high discharge the soils usually consist of levees are the heaviest fall in first, silts and sands are finer materials. In this graph, total 50% flow of water, percentage of flood plain discharge and percentage of main channel discharge are calculated. When the maximum water and minimum water flow through the main channel and flood plain, relative depth 0.35m flood plain discharge is lower than the main channel. It is the same condition that relative depth

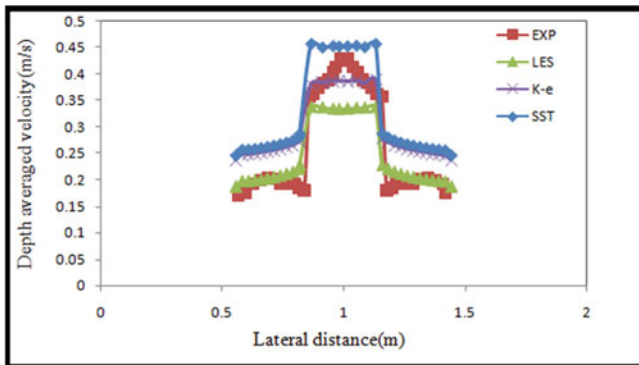
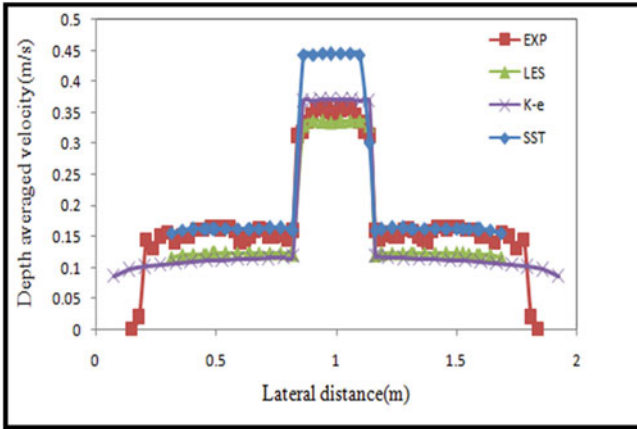
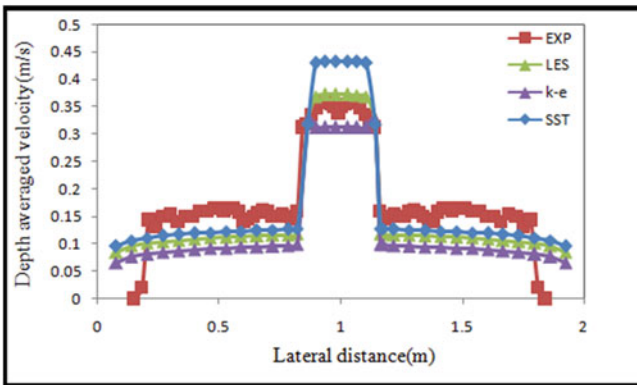


Fig. 37.7 Comparison between DAV and position at 10 m from the inlet for  $Dr = 0.5$  (ANSYS) for Section 1,  $9.83^\circ$



**Fig. 37.8** Comparison between DAV and position at 10 m from the inlet for  $Dr = 0.5$  (ANSYS) for Section 3,  $9.83^\circ$



**Fig. 37.9** Comparison between DAV and position at 10 m from the inlet for  $Dr = 0.5$  m (ANSYS) for Section 5,  $9.83^\circ$

0.4m flood plain discharge is decreased in main channel discharge, relative depth 0.5m the main channel discharge is increased and flood plain discharge is decreased (Fig. 37.11).

$$\%Q_{fp} = Q_{fp}/Q_t \times 100$$

$$\%Q_{mc} = Q_{mc}/Q_t \times 100$$

From the above discussion, LES model gives better results compared with other models. Hence, LES model is applied for the simulation of (DCC) for different geometric and hydraulic conditions. The result obtained from the LES model has been used to evaluate the percentage of flow in main channel and floodplain as shown below for different depths.

**Discussion on ANSYS result**

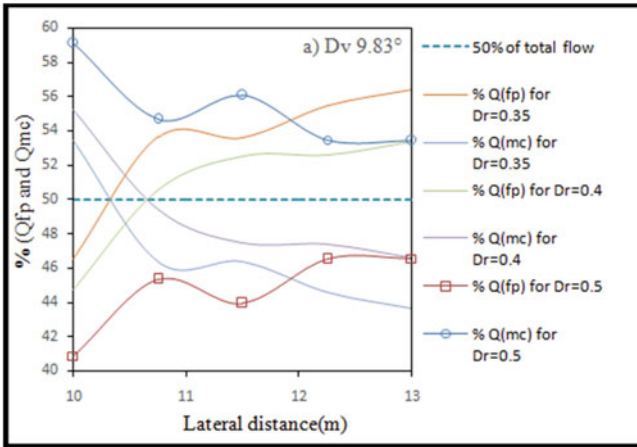


Fig. 37.10 Total % Qfp and Qmc for Dr = 0.35 m, 0.4 m and 0.5 m for 9.83°

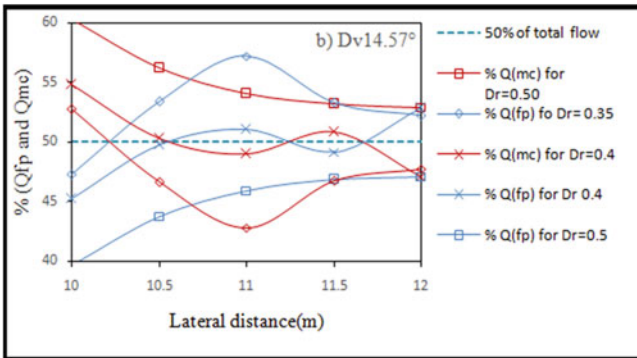


Fig. 37.11 Total, % Qfp and Qmc for Dr = 0.35 m, 0.4 m and 0.5 m for 14.57°

- A. At 10 m section: The graphs joint the flood plain of the section, the LES models give good results for K-e and SST models. The SST model data is higher than the experimental data and the floodplains are coinciding with the experimental data. Here for the peak velocity data is higher than experimental data. By the K-e model, the main channel is higher than experimental data and also avoid below the experimental data and LES model. But in case of LES model, the flood plain data is coincide with the experimental flood plain data and main channel data also.
- B. In this section (11.5 m), the LES gives good results for SST and K-e model. When the SST model gives avoid the experimental channel, flood plains are coinciding with the experimental result and SST model, experimental result, LES model under avoiding the K-e model. The LES model peak velocity is same for experimental result and ANSYS analysis.



**Table 37.3** Error analysis for diverging compound channel 9.83° for Dr 0.5 m

Section No.	LES model	K-e model	SST model
1	15	2.5	12.5
3	12	10.75	15.38
5	2.87	17.14	48.57

- C. At 13 m section: In this section good result for LES model for other models, and SST model the peak velocity is higher than the experimental result. LES model, K-e model. The floodplains are perfectly matching the other model for higher then experimental result and below the LES, K-e model.

**Error Analysis:**

Numerous attempts to categories deviation or any form that deviates from the desired target communication concentrate mainly on Chomsky’s differentiation between “competence” and “performance”. Mistakes are “errors of performance” or performance errors that have varying degrees of seriousness and are either a random guess or a “slip”, in that they are due to a “failure to utilize a known system correctly”. They are considered performance-related deviances, which can occur as a result of factors external to the competence of the speaker, such tiredness or lack of concentration (corder, 1967, 1971 mistakes are neither systematic and nor significant to the process of language learning. For LES model, the evaluation of mean absolute % error at section 1, section 3 and section 5 with Dr 0.5m and 9.83° (Table 37.3).

**37.6 Conclusions**

Later on, the existence planned through the data selected from the ANSYS just as from the experimental data and these contrasting with each other. It is observed that the outcomes are basically coordinating at main channel of areas at both 11.5 and 13m segments, and there are few similitudes among ANSYS and experimental outcomes. In every one of the three segments, top depth average velocity is almost same for both ANSYS and experimental result. As the peak velocity of the main channel is one of the principal rules in planning the water channel, LES model, K-e model. SST model is to some degree supportive in designing the progression of compound channel having the diverging segment. It is very convoluted with this outcome to remark on the precision of LES model in foreseeing the stream boundaries of separating compound segments. It is smarter to do the analyses of various separating segments having diverging points 9.83 and 14.57° and diverse relative profundities. Therefore, it gives us complete and ideal image of the exactness of LES model investigating the non-kaleidoscopic separating compound channels. From the above conversation, LES model gives better outcomes contrasted with different models. Hence, we have been applied LES model for the reproduction of DCC for various mathematical and pressure-driven conditions. The outcome acquired from the LES model has been

utilized to assess the percentage of flow in main channel and floodplain at different depths.

## References

- Deardorff J (1970) A numerical study of three dimensional turbulent channel flow at large Reynolds numbers. *J Fluid Mech* 41(2):453–480. Bibcode: 1970JFM.41.453D. <https://doi.org/10.1017/S0022112070000691>
- Ervine KDA, Jasem HK (1995) Explanations on flows in skewed compound conduits. In: *Proceedings of the ICE-water maritimes and energy*. 112(3):249–259
- Ghosh SN, Roy N (1970) Boundary shears distribution in open channel flow. *J Hydraul Div Knight Donald W, Demetrious John D* (1984) Boundary shears in the smooth Rectangular section. *J Hydraul Eng ASCE*, 18744
- Menter FR (1993) Zonal two equation  $k\omega$  turbulence models for aerodynamic flows. *AIAA Paper* 93 2906
- Myers RC, Elsayy EM (1975) Boundary shear in channel with flood plain. *J Hydraul Div*, 101 (ASCE# 11452 Proceeding)
- Proust S, Rivière N, Bousmar D, Paquier A, Zech Y, Morel R (2006) *J Hydraul Eng* 132(9):958–970
- Shiono K, Knight DW (1991) Turbulent open channel flows with variable depth across the channel. *J Fluid Mech* 222 617–646
- Tominaga A, Nezu I (1991) Turbulence flow in the compound open channel flows. *J Hydraul Eng*.117(1) 21–41
- Worm-eaten PR, Hadjipanous P (1985) Flow distribution in compound channels. *J Hydraul Eng* 111(2):357–361

# Chapter 38

## Using CARTODEM Data for Dam Break Flood Hazard Mapping in a Hilly Terrain



Pankaj Mani, Rakesh Kumar, and J. P. Patra

**Abstract** With the development of computation capability and readily available computer programs, flow inundation modelling-based flood hazard mapping is widely practiced. For such analysis, digital elevation models (DEMs) are necessary to define the river topography and terrain variability. Fine resolution DEMs are also used to extract the river cross sections that are subsequently utilized in flow model setup. But the availability of fine resolution DEM is the major constrain, especially in hilly and inaccessible terrains, etc. The satellite-based DEMs like SRTM, ASTER, CARTODEM, etc. are the alternative sources in such cases and have been used in several flow modelling studies. In this paper, dam break analysis of a small dam located in Uttarakhand in Kumaon Lesser Himalayas is reported. The various scenarios of flooding due to dam breach of the concrete face rockfill dam on Dhauliganga, a tributary of Kali river by routing flood waves in the downstream reach to compute flood inundation, time of occurrences, etc. are discussed. The hydraulic model for the river reach of about 30 km is developed in MIKE 11 using surveyed river cross sections and 10 m resolution digital elevation model of the study area generated using CartoDEM provided by NRSC, Hyderabad. Three cases of flooding are simulated: (i) flooding due to PMF in the river causing dam break condition; (ii) flooding due to PMF without dam break; and (iii) sunny day failure condition (dam failure with nominal inflow when the reservoir is full). It is observed that the time of travel of the peak flood from the dam site to the major settlement area at Dharchula, about 20 km downstream location, is 42 min for the critical case of dam failure. The maximum flood level and time of travel of the peak flood at the important locations are estimated. However, no settlement/village areas are under inundation for these conditions. The extent of flood hazards for various cases of flooding is estimated by superimposing the inundation map over Google Earth for a detailed description of inundated areas and affected infrastructures.

---

P. Mani (✉)

CFMS, National Institute of Hydrology, Patna, India

R. Kumar · J. P. Patra

SWHD, National Institute of Hydrology, Roorkee 247667, India

**Keywords** Dam break analysis · MIKE 11 · CartoDEM · Flood inundation · Flood hazard

## 38.1 Introduction

Dam break flood hazard assessment has become important as population and development are concentrated in areas downstream of the dams due to the availability of land and water. Hazard assessment helps in planning for flood mitigation plan, thus reducing the loss of life and property. Dam break flood analysis can provide useful information about the flood inundation and warning time and help in reducing the tangible and intangible losses resulting from dam failures. The flow model provides the basic inputs for flood hazard assessment, and the digital elevation model (DEM) is the most influencing input for the model. Representation of river and floodplain geometry in the flood model is established through river cross section and DEM, respectively. DEM may be characterized by spatial resolution and vertical accuracy which affect the inundation accuracy. DEM being representation of point elevation in spatial domain, its accuracy depends upon sampling and interpolation techniques in addition to its genetic source. For developing nations, the availability of accurate DEM data for the flood plain is a major hindrance to their limited resources. For many rivers and floodplains, this essential input data are either not sufficient or unavailable which is still a concern (Sanyal et al. 2014; Samantaray et al. 2015). On the other hand, the flood problem is more aggravated in this region only (WRI 2015). With the availability of inexpensive/public domain river flow models, the countries suffering from the frequent and devastating nature of flood hazards are also seeking advanced tools to plan flood mitigation. Next to a topographical survey, DEM from LiDAR data is considered to be most accurate for flood study though very costly. Satellite-based global DEMs like ASTER and SRTM are freely available, at a spatial resolution of 30 and 90 m and have been widely used in flood modelling (Tarekegn et al. 2010; Yan et al. 2013). In this series, CartoDEM provides a more finer resolution DEM derived from Cartosat-1 stereo payload launched in May 2005. The spatial resolution of CartoDEM is 2.5 m in the horizontal plane. As per the design of CartoDEM, the DEM accuracy is 8 m at LE 90 and 15 m at CE 90 for ortho data (NRSA 2015). CartoDEM is generated using Augmented Stereo Strip Triangulation (ASST), indigenously developed software by Space Application Centre, ISRO (India). The generated DEM and ortho images of each Cartosat-1 segment are cut into tiles of  $7.5' \times 7.5'$  extents and the entire Indian region is covered by approximately 500 Cartosat-1 segments with a total number of around 20,000 tile pairs, while the DEMs are available at a spatial resolution of 2.5, 10, and 30 m. In this study, 10 m DEM has been used. In the absence of surveyed river section, the cross sections are extracted from CartoDEMs. Generally, the accuracy of a DEM is evaluated with observed elevation points, although in this study, the known elevation points are selected and located mainly at the dam sections and the power house. The river cross sections are extracted from CartoDEM at 10 m resolution and used in

MIKE 11 flow model setup to compute the flooding under different scenarios. This paper discusses the dam failure analysis of Dhauliganga dam located on the Kali river in Pithoragarh district of Uttarakhand. The study envisages identification of various scenarios of flooding, estimation of breach parameters, modelling of dam break flood, and its routing in the downstream reach to compute the maximum flood inundation and its time of occurrences. The maximum flood levels and their time of occurrences have been estimated at the important locations in the downstream reach. The extent of maximum inundation for various cases of flooding has also been computed. The inundation maps are superimposed over Google Earth for a detailed description of inundated areas.

## **38.2 Study Area**

The Dhauliganga dam is part of hydropower project, is located on river Dhauliganga, and is a tributary of river Kali in Pithoragarh district of Uttarakhand. The Dhauliganga river originates in the high Himalayan mountain from the glaciers at an elevation of about 5160 m. The catchment area is 1372 Km<sup>2</sup>. The river flows in deep gorges with a very steep slope of about 48 m for every 1 Km length. The power house is located about 9.4 km downstream of the dam site.

### ***38.2.1 Description of Dhauliganga Dam***

A concrete face rockfill embankment dam is 56 m high above the riverbed level while the length of the reservoir is about 1.4 km. The elevation of the dam crest is RL 1352.0 m and the length of the crest is 270 m. The full reservoir level (FRL) of the reservoir formed by the construction of the dam is at RL 1345.0 m and the minimum drawdown level (MDDL) is at RL 1330.0 m. On the right flank of the dam are two gated spillways with open chutes and flip bucket (10 m × 6 m) with a discharge capacity of 3210 m<sup>3</sup>/s. The dam also consists of a tunnel spillway with a radial size of 9 m × 16 m.

### ***38.2.2 Downstream River Stretch***

Dam break analysis for Dhauliganga dam is carried out and its impact in the downstream river stretch up to 30 km from dam site is reported. From the dam site, Dhauliganga flows in the southeast direction up to 4.5 km and the confluence with the Kali river from where it takes a turn towards the southwest direction. The river is called now the Sharda river in its downstream stretch (from Tanakpur onwards). It outfalls in the Ghaghara river and finally joins river Ganga. The power house is



**Fig. 38.2** Design flood hydrographs at Dhauliganga dam site

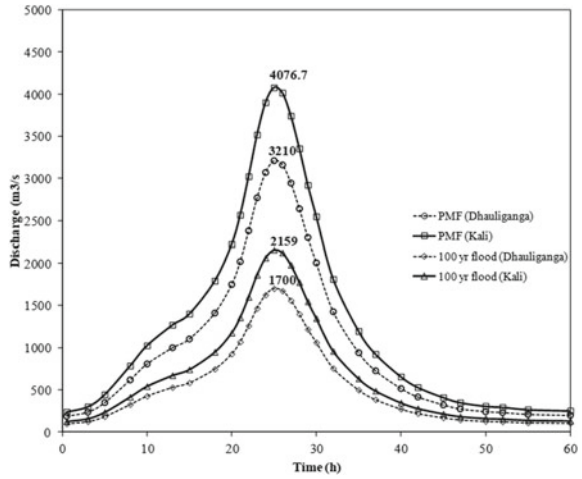


**Fig. 38.3** CartoDEM for downstream reach

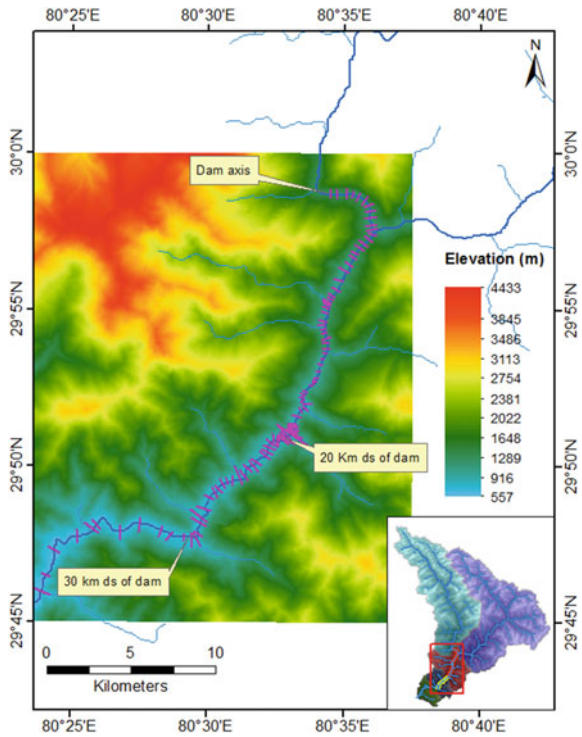


**Table 38.1** Description of breach parameters

S. No.	Approach	Average breach width (m)	Time of failure (hour)	Side slope of breach section
1	Froehlich (1995)	66	0.26	1.4:1
2	Froehlich (2008)	52	0.25	1.:1
3	MacDonald and Langridge-monopolis (1984)	310	2.82	0.5:1
4	Von Thun and Gillette	128	1.13	1.:1
5	Xu and Zhang (2009)	27	1.9	0.5:1
6	Upper bound	28	4	1:1
7	Lower bound	225	0.1	1:1
8	<b>Estimated breach parameters</b>	<b>50</b>	<b>1</b>	<b>1:1</b>

used in the 30 km study stretch. The bed resistance for the river is assigned as 0.05 in accordance with Table 38.1 of AHEC guidelines (AHEC-IITR 2013) depending upon the riverbed material as observed during field visit.

## 38.4 Methodology for Dam Break Analysis

The methodology of dam break analysis consists of two major components: estimation of breach outflow and movement of breached flow in downstream reach. The breach outflow depends upon the development of breach section in the dam. The development of the breach can either be specified as a known function of time, or it can be simulated from the sediment transport capacity of the breach flow.

### 38.4.1 Estimation of Breach Parameters

The estimation of the breach location, size, and development time are crucial in order to make an accurate estimate of the outflow hydrographs and downstream inundation. The breach parameters will directly affect the estimate of the peak flow coming out of the dam, as well as any possible warning time available to downstream locations. Unfortunately, the breach location, size, and formation time are often the most uncertain pieces of information in a dam failure analysis. A dam's potential breach characteristics can be estimated in several ways, including comparative analysis (comparing dam to historical failures of dams of similar size, materials, and water volume); regression equations (equations developed from historical dam failures in order to estimate peak outflow or breach size and development time); utilization of



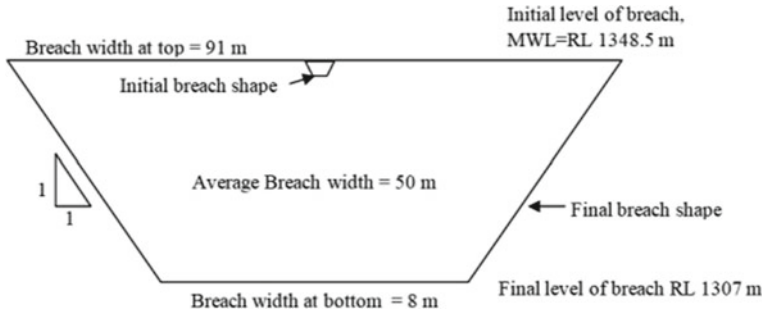


**Fig. 38.4** Estimated final breach shape for dam break analysis

velocity (or shear stress) versus erosion rates; and physically based computer models (software that attempts to model the physical breaching process by using sediment transport/erosion equations, soil mechanics, and principles of hydraulics). All of these methods are viable techniques for estimating breach characteristics. However, each of these methods has strengths and weaknesses and should be considered as a way of "estimating" the parameters and not utilized as absolute values. The breach dimensions, as well as the breach formation time, are the pre-requisite of dam break modelling and should be estimated prior to model setup. Many case studies have been performed on data from historic dam failures in the US, leading to guidelines, regression equations, and computer modelling methodologies for the prediction of the dam breach size and time. Wahl (1988) summarized a comprehensive literature on historic dam failures data and recommends a range of breach parameters for dam break analysis. The regression equations are also suggested to make estimates of the breach dimensions and failure time, namely by Froehlich (1995, 2008), and Xu and Zhang (2009). These estimates should then be used to perform a sensitivity analysis. The Federal Agencies (FA) guidelines and regression equation-based approach are widely used. In fact, the guideline provides the upper and lower bounds of parameter values while the range estimated from regression equations is used for parameter sensitivity analysis (TD-39, 2014). In this study, the breach parameters have been estimated based on various regression analyses and an average estimate for each parameter has been used for dam break analysis, as shown in Table 38.1. The progressive development of breach in the dam section is shown in Fig. 38.4.

### 38.4.2 Flood Routing

The movement of flood in the downstream reach is described through the solution of the basic Saint Venant's partial differential equations of conservation of mass and momentum as shown below.

Conservation of mass (continuity) equation

$$(\partial Q/\partial X) + \partial(A + A0)/\partial t - q = 0 \quad (38.1)$$

Conservation of momentum equation

$$(\partial Q/\partial t) + \{\partial(Q2/A)/\partial X\} + g A ((\partial h/\partial X) + S_f + S_c) = 0 \quad (38.2)$$

where Q = discharge; A = active flow area; A0 = inactive storage area; h = water surface elevation; q = lateral outflow; x = distance along waterway; t = time; S<sub>f</sub> = friction slope; S<sub>c</sub> = expansion contraction slope; g = gravitational acceleration.

The mathematical modelling of dam break flow is a cost- and time-effective approach to (approximately) solve the above governing equations. The present dam break study has been carried out using the MIKE 11 HD model developed by Danish Hydraulic Institute (DHI). The core of the MIKE 11 system consists of the HD (hydrodynamic) module, which is capable of simulating unsteady flows in a network of open channels. The results of a HD simulation consist of time series of water levels and discharges. The MIKE 11 hydrodynamic module is an implicit, finite difference model for unsteady flow computation. The model can describe sub-critical as well as supercritical flow conditions through a numerical description which is altered according to the local flow conditions (in time and space). Advanced computational modules are included for the description of flow over hydraulic structures, including possibilities to describe structure operation. The formulations can be applied for looped networks and quasi-two-dimensional flow simulation on flood plains. The computational scheme is applicable for vertically homogeneous flow conditions extending from steep river flows to tidal influenced tributaries.

## 38.5 Results and Discussions

### 38.5.1 Dam Break Analysis

The design flood of PMF and 100-year return period flood is defined in the Dhauliganga reservoir in different cases of flood simulation. The dam fails when the reservoir is at MWL of RL 1348.5 m. The failure through overtopping of the dam is considered. Further, during time of failure all the spillway gates are considered to remain fully open. The downstream boundary condition is defined at Chainage 30 km of the Kali river. The breach starts at RL 1348.5 m (MWL) and develops in a trapezoidal shape and the bottom of the section comes down to the lowest bed level of RL 1307 m (crest level of chute spillway) in a duration of 1 h. Three cases of flooding are considered in this study as follows:

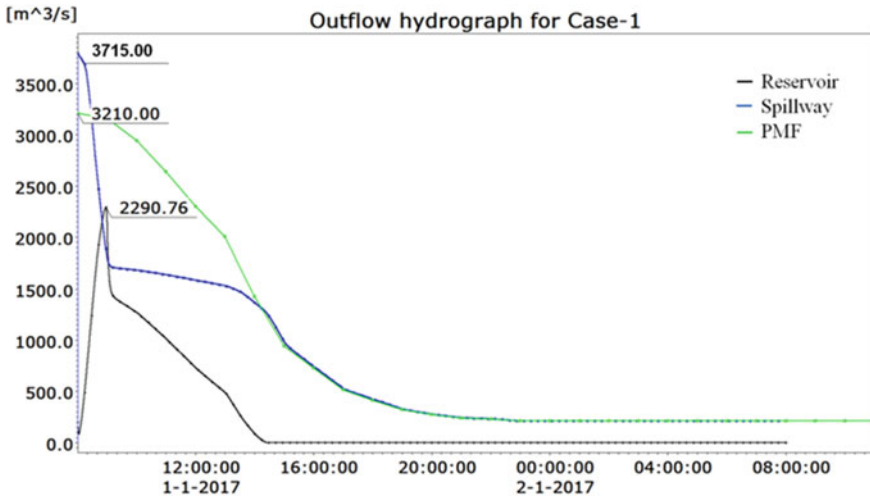


Fig. 38.5 Outflow hydrograph and design flood at dam section for Case-1

1. Case-1: breach occurs under PMF when the reservoir is at MWL.
2. Case-2: routing of PMF is simulated without dam failure.
3. Case-3: breach occurs when the reservoir is at MWL without any significant inflow (sunny day failure).

Thus, Case-1 is the critical flooding condition for dam break analysis, and Case-3 is the sunny day failure. For Case-1 when inflow (PMF) is higher compared to breach outflow from a small reservoir storage (about 2.98 MCM), the peak of breach outflow is dominated by peak inflow and storage contribution remains comparatively less significant. Further, as the spillway gates are fully opened, a significant amount of flow passes through the spillway. The flood hydrograph at the dam section for Case-1 is shown in Fig. 38.5. The figure shows the outflow hydrographs at the breach section and through spillway gates. The food in the downstream reach of the river is contributed from breach outflow and spillway outflow in addition to the contribution from the main Kali river. In the downstream river valley, the attenuation of flood hydrograph occurs as shown in Fig. 38.6. At Chainage 250, 5750, 11,750, 20,250, and 25,250 m, the peak flood is 4421.47 m<sup>3</sup>/s, 8466.55 m<sup>3</sup>/s, 8466.17 m<sup>3</sup>/s, 8466 m<sup>3</sup>/s, and 8466.02 m<sup>3</sup>/s, respectively. The increase in discharge beyond 2000 m is due to inflow from the Kali river wherein the Dhauliganga river outfalls. Further small attenuation of flood hydrograph is due to gorge-shaped river valley with steep longitudinal slope. The time of occurrence of peak flood at 20 km d/s reach from the dam site is about 42 min. The water surface profile for flooding condition in Case-1 is shown in Fig. 38.7. The maximum flood elevation maps are superimposed over the high-resolution Google Earth image to prepare the inundation maps as shown in Fig. 38.8. As the river valley is very narrow, the spread area for dam breach flood is very limited. The detailed inundation may be visualized by zooming over a

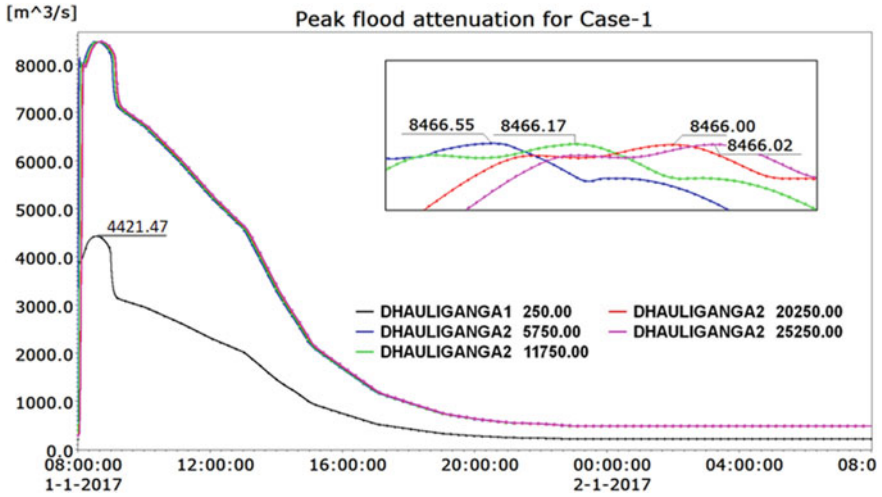


Fig. 38.6 Attenuation of flood hydrograph in downstream reach for Case-1

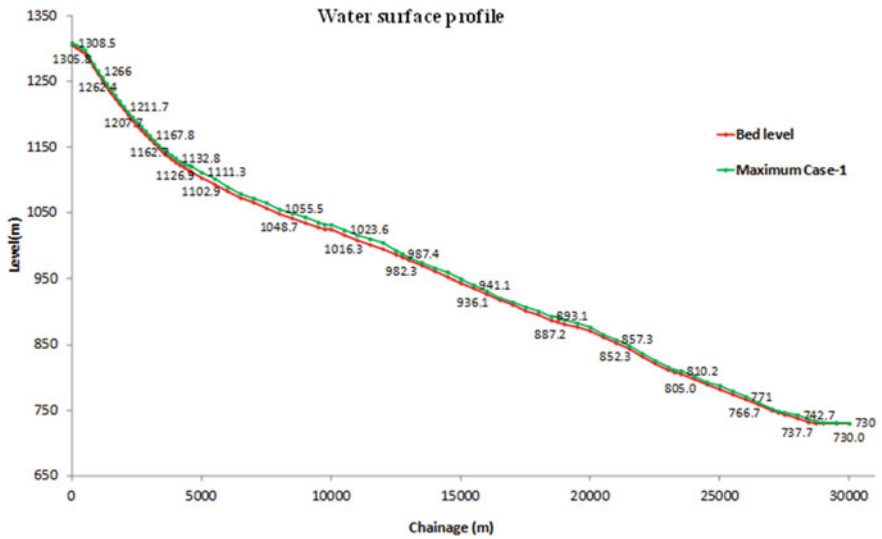


Fig. 38.7 Water surface profile for Case-1

small river stretch. The study reach is divided into seven stretches and the inundation map for each reach is prepared. Figure 38.9 shows the inundation maps for reach-5 and reach-6 where major settlements are located. Similar analysis is carried out for Case-2 and Case-3, attenuation of flood hydrographs are computed, and the extent of inundation is estimated.

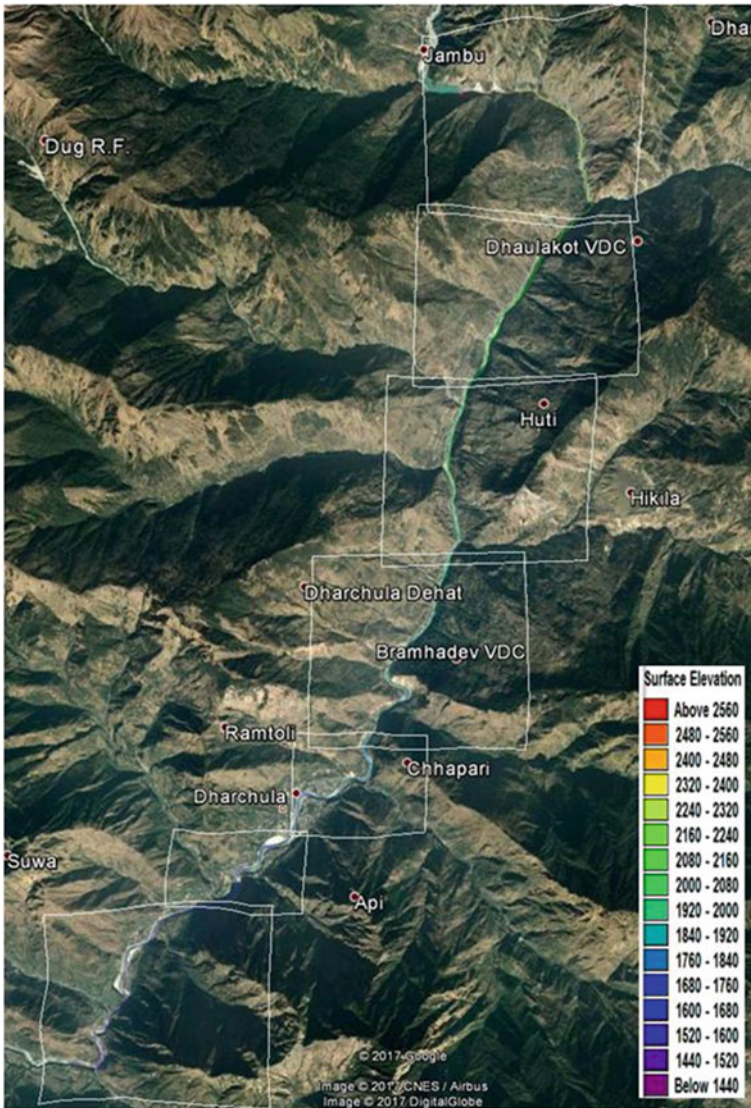


Fig. 38.8 Synoptic view of flood inundation over Google Earth for Case-1

The flood inundation attributes are computed using the results of the hydrodynamic model and CartoDEM. The maximum inundation (flood depth) depends upon the peak flood level and flood plain topography. For a flooding scenario, the flooding depths at a location depend upon the ground elevation at that location and, thus are a localized phenomenon. The flood level (mean sea level) is influenced by the topography of the entire inundated area and thus is more global and representative in

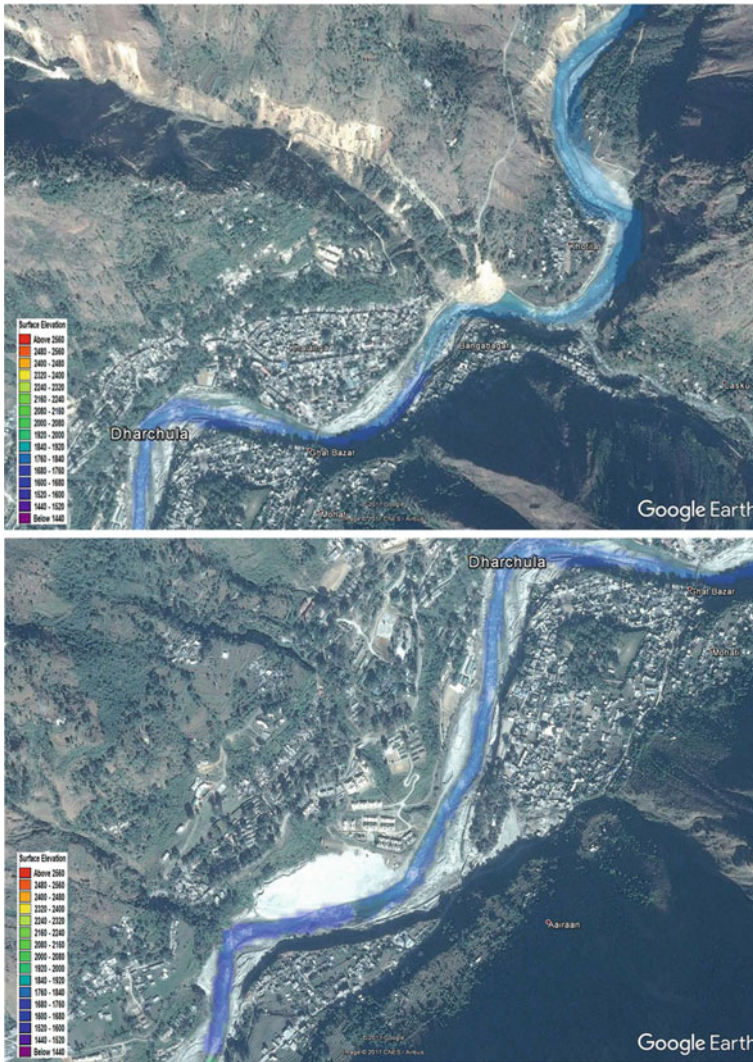


Fig. 38.9 Flood inundation map over Google Earth for Case-1 in stretch 1

quantifying flood events along with the area of inundation. The important locations in the downstream reach of the Dhauliganga dam are the Dhauliganga power house (Chainage-9.75 km) and Dharchula (Chainage 20 km) at which the maximum flood elevation (msl) has been computed for various cases of flooding. The peak flood level and its occurrence time estimated at these locations are shown in Table 38.2. The time of occurrence of maximum flood level is shown within brackets. For Case-1 in which the dam break failure under PMF is simulated, the maximum flooding time is computed since the start of a breach. For Case-2 in which PMF is simulated without

**Table 38.2** Maximum flood level at important locations for various cases of flooding

Particulars	Maximum inundation area (ha)	Important locations	
		Dhauliganga power house	Dharchula
MIKE 11 Chainage (km)		9.75	20
Case-1 (PMF flood and dam break)	163.27	1031.63 m (8:38:00 h)	857.06 m (8:42:00 h)
Case-2 (PMF flood only)	156.39	1031.36 m (21:04:00 h)	856.87 m (21:08:10 h)
Case-3 (only dam break)	94.53	1026.95 m (8:40:00 h)	853.84 m (8:43:00 min)

(Time in brackets shows the time of travel of peak flood from dam site to important locations)

dam failure, the time of the peak is considered from the instance of peak inflow at the dam site. Further, the sunny day failure of the Dhauliganga dam is also tabulated. This table also shows the maximum inundation area for various cases of flooding.

### 38.5.2 Disaster Management Plan

The maximum flood level, extent of inundation, and time of flooding (flood above a threshold level at a particular location defined locally based on the site condition) are important inputs for preparing an emergency action plan during a disaster. Table 38.2 shows that the maximum flooding is due to Case-1. The two major components for a disaster management plan are flooding extent and its time of arrival, which are shown in this table. Such information along with the geographical extent of flooding are important inputs for a disaster management plan. In this study, no important areas/locations are inundated due to critical flooding scenarios as the river is flowing through very narrow and steep terrain while settlements are located at higher elevations.

### 38.5.3 Sensitivity of Breach Parameters

As discussed earlier, the estimation of breach parameters is based on regression equations developed from observed data from historical dam failure events and

the technical guidelines based on scientific studies provided by various agencies of international repute. Still, there is uncertainty in breach parameter estimates due to several reasons including different construction techniques and workmanship, and other unforeseen conditions. The flood peak due to dam failure is highly affected by breach parameters and is influenced by the combination of various breach parameters. Hence, the sensitivity of the individual breach parameter is carried out. Sensitivity analysis for three breach parameters namely breach width, time of breach, and side slope of breach section have been done for the failure of the Dhauliganga dam. The range of estimates for various breach parameters is shown in Table 38.3.

The dam break model has been simulated with varying breach widths of 30, 50, 70, and 100 m, and the breach outflow is computed. The breach outflow hydrograph for various breach widths is shown in Fig. 38.10. With an increase in breach width, the peak flood increases. For a breach width of 30 m peak discharge is 2228.01 m<sup>3</sup>/s while for a breach width of 100 m peak, discharge is 2309.46 m<sup>3</sup>/s. With an increase in breach width by 333%, increase in peak discharge is computed to increase by 3.65% only. Similarly, the sensitivity analysis of the time of breach is carried out with varying times of failure to 0.25, 0.5, 1.0, 1.25, and 2.0 h, and its effect on breach outflow is analysed. The breach outflow hydrograph for various failure times

**Table 38.3** Breach parameters estimates for sensitivity analysis

Breach parameters	Average estimates	Estimates for parameter sensitivity			
Breach width (m)	50	30	70	100	–
Time of failure (h)	1	0.25	0.5	1.25	2
Side slope (H:V)	1:1	0.5	0.75	1.25	1.5

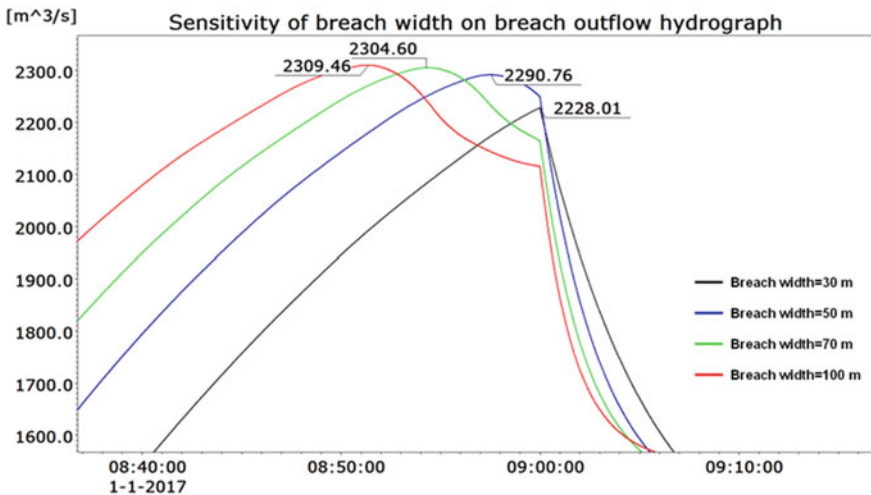


**Fig. 38.10** Sensitivity of breach width on peak discharge at breach section



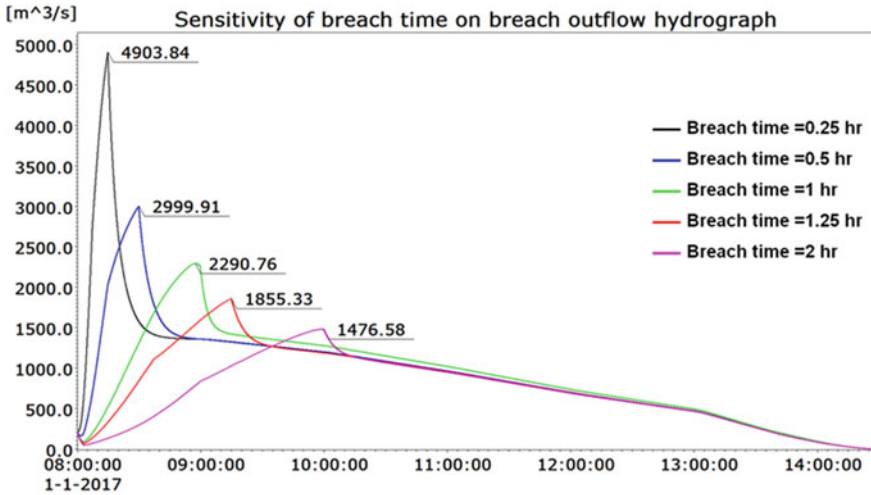


Fig. 38.11 Sensitivity of breach time on peak discharge at breach section

is shown in Fig. 38.11. With smaller breach time, the complete shape of breach develops earlier; hence higher peak discharge occurs quickly. The reverse happens with an increase in failure time, and the peak reduces as by the time breach develops to its full size, most of the upstream water outflows. The peak flow for 0.25 h is  $4903.84 m^3/s$  which reduces to  $1476.58 m^3/s$  for 2.0 h. Another effect of increased breach time is on the occurrence of peak discharge. For smaller failure time, the peak occurs earlier. The figure shows that this parameter is most sensitive in the computation of breach outflow. Another breach parameter is the shape of the breach section. The sensitivity of the breach section is shown in Fig. 38.12 which shows that this parameter is also not much sensitive.

### 38.6 Conclusions

Dam break study for the Dhauliganga dam has been carried out using the MIKE 11 model. Three cases of flooding are simulated in the study: Case-1: flooding due to PMF in the river causing dam break condition. The reservoir is considered at FRL during flooding; Case-2: flooding due to PMF without dam break. The entire flow passes through spillway; Case-3: dam break failure with nominal inflow ( $100 m^3/s$ ) in reservoir considering it at FRL (sunny day failure condition). The breach parameters have been estimated using Federal Agency Guidelines and regression equation-based approach. The average estimate of parameters has been used. The breach parameters are breach width = 50 m, breach time = 1 h, and a trapezoidal breach section of 1:1 shape is considered for this earthen concrete faced dam. Further, sensitivity analysis has been carried out for the recommended range for different breach parameters.

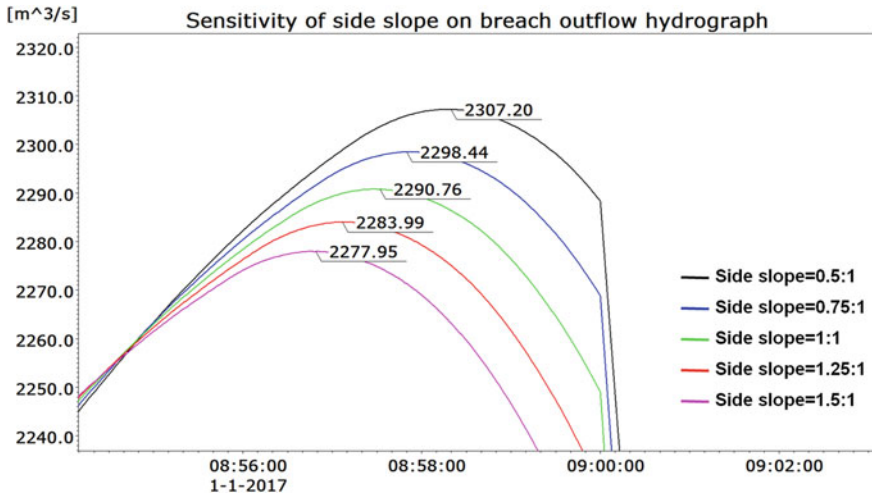


Fig. 38.12 Sensitivity of shape of breach section on peak discharge

Flood attenuation hydrograph, water surface profile, stage hydrograph at important locations, inundation maps superimposed over high-resolution satellite data, and Google Earth have been prepared for each case. The flood inundation extent overlaid in Google Earth with detailed transport networks and other features are developed to visualize the inundation over-populated/important locations. No important locations/populations are found affected by flood inundation for the severe most flooding condition. The time of travel of peak flood from the dam site to 20 km downstream end is 42 min for Case-1, 8 min for Case-2, and 43 min for Case-3. The maximum flood elevations for a critical case of flooding computed at the Dhauliganga power house and Dharchula are RL 1031.63 m and 857.06 m, respectively. No populations/settlements are under inundation due to critical cases of dam failure. Though no settlements are found under inundation areas for critical flooding scenarios, the downstream river reach is very steep and passes through densely populated Dharchula area, an effective public warning system is proposed to prevent any casualty as per the computed warning time at various locations downstream of the dam. The sensitivity of breach parameter in estimation of breach outflow has been assessed for different values of breach width and breach time. It is observed that breach time is the most sensitive parameter.

**Acknowledgments** This paper is the outcome of the study sponsored by National Hydroelectric Power Corporation (NHPC), Faridabad. The authors hereby duly acknowledge the support provided by the project authority in carrying out the study. We also acknowledge the data support obtained from NRSC, Hyderabad.

## References

- AHEC-IITR standard No. 2.2 and 2.3-hydraulic and structural design, standard/manual/guideline with support from ministry of new and renewable energy, Roorkee, July 2013
- Froehlich DC (1995) Embankment dam breach parameters revisited. In: First international conference, water resources engineering, environmental and water resources institute (EWRI), 14–18 August 1995. ASCE, Water Resources Engineering Proceeding, pp 887–891
- Froehlich DC (2008) Embankment dam breach parameters and their uncertainties. *ASCE J Hydraul Eng* 134(12):1708–1721. ISSN 0733-9429
- MacDonald TC, Langridge-Monopolis J (1984) Breaching characteristics of dam failures. *ASCE J Hydraul Eng* 110(5):567–586
- NRSA (2015) Cartosat-1, 10 years and beyond. [https://nrsc.gov.in/sites/all/pdf/Chapter\\_5.pdf](https://nrsc.gov.in/sites/all/pdf/Chapter_5.pdf)
- Samantaray D, Chatterjee C, Singh R et al (2015) Flood risk modelling for optimal rice planning for delta region of Mahanadi river basin in India. *Nat Hazards* 76:347–372. <https://doi.org/10.1007/s11069-014-1493-9>
- Sanyal J, Carbonneau P, Densmore AL (2014) Low-cost inundation modelling at the reach scale with sparse data in the Lower Damodar River basin, India. *Hydrol Sci J* 59:2086–2102. <https://doi.org/10.1080/02626667.2014.884718>
- Tarekegn TH, Haile AT, Rientjes T, Reggiani P, Alkema D (2010) Assessment of an ASTER-generated DEM for 2D hydrodynamic flood modeling. *Int J Appl Earth Obs Geoinform* 12:457–465
- TD-39 using HEC-RAS for dam break studies, U.S. army corps of engineers. Institute for Water Resources, Hydrologic Engineering Centre, 609 Second Street, Davis, CA 95616 (2014)
- Verma P, Banerji R, Sathe M, Ramteke DS, Wate SR, Singh RN (2008) Simulating lower Pedhi dam break: application of GIS and MIKE 11 model. In: Proceedings of the IASTED International symposium 638, 2008
- Wahl Tony L (1998) Prediction of embankment dam breach parameters—a literature review and needs assessment. dam safety research report, DSO-98–004. water resources research laboratory, U.S. Dept. of the interior, bureau of reclamation, dam safety office (DSO), July 1998
- WRI (2015) Annual expected populations affected by river floods compiled by world resources institute ([wri.org/floods](http://wri.org/floods)). online article available. [www.wri.org/sites/default/files/uploads/top\\_15\\_flooding\\_0.png](http://www.wri.org/sites/default/files/uploads/top_15_flooding_0.png)
- Xu Y, Zhang LM (2009) Breaching parameters for earth and rockfill dams. *ASCE J Geotech Geoenviron Eng* 135(12):1957–1970
- Yan K, Di Baldassarre G, Solomatine DP (2013) Exploring the potential of SRTM topographic data for flood inundation modelling under uncertainty. *J Hydroinform* 15(3):849. <https://doi.org/10.2166/hydro.2013.137>